frontiers | Research Topics

New challenges in space plasma physics: Open questions and future mission concepts

Edited by
Luca Sorriso-Valvo, Alessandro Retino, Christopher H. K. Chen and Daniel Verscharen

Published in
Frontiers in Astronomy and Space Sciences

ISSN 1664-8714
ISBN 978-2-83251-455-9
DOI 10.3389/978-2-83251-455-9

About Frontiers

Frontiers is more than just an open access publisher of scholarly articles: it is a pioneering approach to the world of academia, radically improving the way scholarly research is managed. The grand vision of Frontiers is a world where all people have an equal opportunity to seek, share and generate knowledge. Frontiers provides immediate and permanent online open access to all its publications, but this alone is not enough to realize our grand goals.

Frontiers journal series

The Frontiers journal series is a multi-tier and interdisciplinary set of open-access, online journals, promising a paradigm shift from the current review, selection and dissemination processes in academic publishing. All Frontiers journals are driven by researchers for researchers; therefore, they constitute a service to the scholarly community. At the same time, the *Frontiers journal series* operates on a revolutionary invention, the tiered publishing system, initially addressing specific communities of scholars, and gradually climbing up to broader public understanding, thus serving the interests of the lay society, too.

Dedication to quality

Each Frontiers article is a landmark of the highest quality, thanks to genuinely collaborative interactions between authors and review editors, who include some of the world's best academicians. Research must be certified by peers before entering a stream of knowledge that may eventually reach the public - and shape society; therefore, Frontiers only applies the most rigorous and unbiased reviews. Frontiers revolutionizes research publishing by freely delivering the most outstanding research, evaluated with no bias from both the academic and social point of view. By applying the most advanced information technologies, Frontiers is catapulting scholarly publishing into a new generation.

What are Frontiers Research Topics?

Frontiers Research Topics are very popular trademarks of the *Frontiers journals series*: they are collections of at least ten articles, all centered on a particular subject. With their unique mix of varied contributions from Original Research to Review Articles, Frontiers Research Topics unify the most influential researchers, the latest key findings and historical advances in a hot research area.

Find out more on how to host your own Frontiers Research Topic or contribute to one as an author by contacting the Frontiers editorial office: frontiersin.org/about/contact

New challenges in space plasma physics: Open questions and future mission concepts

Topic editors

Luca Sorriso-Valvo — Institute for Space Physics (Uppsala), Sweden

Alessandro Retino — UMR7648 Laboratoire de physique des plasmas (LPP), France

Christopher H. K. Chen — Queen Mary University of London, United Kingdom

Daniel Verscharen — University College London, United Kingdom

Citation

Sorriso-Valvo, L., Retino, A., Chen, C. H. K., Verscharen, D., eds. (2023). *New challenges in space plasma physics: Open questions and future mission concepts*. Lausanne: Frontiers Media SA. doi: 10.3389/978-2-83251-455-9

Table of contents

frontiers | Frontiers in Astronomy and Space Sciences

TYPE Editorial
PUBLISHED 12 January 2023
DOI 10.3389/fspas.2022.1130728

OPEN ACCESS

EDITED AND REVIEWED BY:
Joseph E. Borovsky,
Space Science Institute, United States

*CORRESPONDENCE
Luca Sorriso-Valvo,
lucasorriso@gmail.com

SPECIALTY SECTION
This article was submitted to Space Physics, a section of the journal Frontiers in Astronomy and Space Sciences

RECEIVED 23 December 2022
ACCEPTED 28 December 2022
PUBLISHED 12 January 2023

CITATION
Sorriso-Valvo L, Chen CHK, Retinò A and Verscharen D (2023), Editorial: New challenges in space plasma physics: Open questions and future mission concepts. *Front. Astron. Space Sci.* 9:1130728. doi: 10.3389/fspas.2022.1130728

Editorial: New challenges in space plasma physics: Open questions and future mission concepts

Luca Sorriso-Valvo[1,2]*, Christopher H. K. Chen[3], Alessandro Retinò[4] and Daniel Verscharen[5]

[1]CNR—Istituto per la Scienza e Tecnologia dei Plasmi (ISTP), Bari, Italy, [2]IRF—Swedish Institute of Space Physics, Uppsala, Sweden, [3]Department of Physics and Astronomy, Queen Mary University of London, London, United Kingdom, [4]LPP-CNRS/Ecole Polytechnique/UPMC/Université Paris Sud, Palaiseau, France, [5]Mullard Space Science Laboratory, University College London, Dorking, United Kingdom

KEYWORDS

plasma turbulence, *in situ* observations, numerical simulations, magnetic reconnection, dissipation processes, space physics

Editorial on the Research Topic
New challenges in space plasma physics: Open questions and future mission concepts

For over half a century, scientific space missions have provided the experimental underpinning for advances in space plasma physics. *In-situ* and remote observations have revealed an incredible variety of processes throughout the heliosphere, including the solar corona, solar wind, and planetary magnetospheres. Fundamental plasma phenomena such as turbulence, instabilities, particle acceleration, magnetic reconnection, waves, shocks, and dissipation have been widely studied but remain to be understood in depth. Each new space mission so far has driven forward our understanding of space plasmas, but has also given rise to many new questions about our solar system. This Research Topic collects novel ideas and recent results suggesting the need for innovative space measurements, new analysis methods, and pioneering instrumentation. These are presented in 12 articles demonstrating the current and future open challenges in space plasma physics, and the proposed approaches to address them.

Verscharen et al. present "The Plasma Universe" as a common and coherent science theme that transcends traditional boundaries between research communities. In their article, a group of lead authors from white papers that were submitted to the ESA Voyage 2050 process[1] give a synopsis of fundamental physics questions and processes that are linked by this common plasma science theme. The theme combines science areas that rely on remote-sensing plasma observations and *in-situ* plasma measurements stretching from UV and X-ray astronomy over solar physics, heliospheric physics, and magnetospheric physics to cometary physics.

A number of contributions to our Research Topic highlight the growing need for multi-spacecraft missions to unveil critical multi-scale phenomena in space plasma. The research

1 https://www.cosmos.esa.int/web/voyage-2050.

article by Broeren et al. proposes improved methods to reconstruct the magnetic field based on measurements by multi-point, multi-scale spacecraft observatories. By applying their reconstruction methods to test cases and simulation outputs, the authors lay important groundwork for upcoming missions like HelioSwarm or planned missions like Plasma Observatory. These missions will go beyond the tetrahedral formations of more traditional constellations to explore plasma turbulence and structures in unprecedented detail. Maruca et al. discuss the need to go beyond the number of spacecraft in currently operating and upcoming missions to fully "image" the three-dimensional structure of the interplanetary magnetic field. Their investigation suggests that a baseline design of 24 spacecraft, combined with field reconstruction techniques, could study the mesoscale magnetic structure ($\sim 10^2$ to 10^6 km) to distinguish different models of the interplanetary fluctuations and their effect on the heliosphere. They also propose the use of CubeSat designs to comply with the budget constraints of typical mission classes. Malaspina et al. envision a 34-spacecraft magnetospheric mission that uses microsatellites and small satellites. As shown in **Figure 1**, these spacecraft would carry instrumentation for radio tomography of the equatorial plasma density, combined with *in-situ* measurements of the total plasma density and extreme ultraviolet imaging of the meridional ion density and flows. With the additional *in-situ* measurements of fields and the cold and energetic particle distribution functions, the proposed mission will help us understand the processes that govern mass and energy flow through the terrestrial magnetosphere.

In the last decades, spacecraft capable of joint *in-situ* and remote observation have gained popularity due to their cross-cutting capabilities. Inspired by the recent joint observations of Solar Orbiter, Parker Solar Probe, and BepiColombo in the inner heliospehre, the perspective article by Telloni discusses a two-satellite mission crafted to maximize orbital configurations such as conjunctions, quadratures, and alignments. Combined *in-situ* and remote-sensing payload on board such a mission will enable an in-depth investigation of the heliospheric structure and of its solar and coronal drivers. Similarly, building on STEREO and Lagrange/Vigil concepts, Bemporad proposes two identical spacecraft at the Sun-Earth Lagrange points L4 and L5. Equipped with *in-situ* and remote-sensing instrumentation, this mission will enable observations of solar magnetic field evolution, from the solar interior (stereoscopic helioseismology) to the photosphere and corona (spectro-polarimetry), and into the solar wind (*in situ*). The pair of spacecraft will also serve as monitors for the Sun-Earth connection.

In order to investigate the dynamics of heliospheric magnetic and plasma structures, Borovsky and Raines present a concept for a single spacecraft mission at 1 au, equipped with high-resolution/low-noise particle and composition measurements. The fine details of the particle distributions will help to effectively distinguish the *in-situ* or coronal origin of structures such as current sheets, containing crucial information about the radial evolution of the solar wind. A key part of understanding our heliosphere is determining the conversion of energy between its different forms, including how particles are energized by electromagnetic fields, e.g., through waves, turbulence, shocks, and magnetic reconnection. Howes et al. propose new onboard field-particle correlator instrumentation, designed to study these processes with greater capability than currently possible, that could be employed on a future kinetic plasma physics mission. This method will correlate particle detections with the observations of electromagnetic fields to measure, onboard the spacecraft, energization at multiple energies simultaneously and with much higher time resolution than ever before. It will allow downlink of high-resolution data on particle energization over long periods of a mission and enable event-based triggering. These approaches will further our understanding of energization in a variety of space plasma processes. Our Research Topic also describes novel analysis methods for space plasma data. The Methods Article by Bakrania et al. explores the use of machine-learning (clustering) techniques to classify space plasma regimes. Applied to electron distribution functions observed by the Cluster mission, the method clearly identifies eight distinct plasma regions in the Earth's magnetotail. Automated classification methods are a useful and promising tool to analyse large amounts of plasma data. In the future, methods like this may even be used onboard spacecraft to reduce the dimensionality of datasets and thus the required telemetry.

The difficulty of obtaining accurate three-dimensional electric field measurements is an important limitation of experimental space physics. For instance, in their Research Article, Wilson et al. discuss specific features of high-frequency electric field fluctuations at collisionless shocks. In particular, they show observations and numerical simulations that routinely provide contradicting results. Data show consistently large-amplitude electrostatic fluctuations, while simulations produce quasi-static fields. The authors suggest that both measurements and simulations have known limitations that may explain this discrepancy, and that improvements of both are needed in order to understand the physics of collisionless shocks. In their Methods Article, Lejosne et al. address the lack of accurate electric field measurements by proposing a novel design for an instrument specifically aimed at overcoming the known limitations. Based on detectors mounted on two orthogonal rotating plates, the new concept promises continuous high-accuracy three-dimensional electric and magnetic fields measurements, at affordable price and mass.

Finally, Borovski et al. address the need for observations of the magnetic connectivity of the equatorial magnetospheric regions with the auroral arcs. This knowledge is necessary to improve our understanding of the processes leading to the aurora. This Methods Article proposes an innovative mission concept aimed at visually pinpointing the connectivity. To achieve this goal, a spacecraft located in the equatorial magnetosphere will emit a beam of energetic electrons that, if magnetic connectivity exists, will travel along the field lines and appear as a bright spot in the polar ionosphere and upper atmosphere. A ground-based optical sensor will then image and localize the bright point, allowing a reconstruction of the connecting magnetic field line.

Our Research Topic highlights that, while awaiting new insights from recently launched spacecraft, the space plasma physics community actively proposes innovative concepts for future space missions. These creative ideas, which grow in response to theoretical and numerical advances and in light of the most recent observations, have the potential to transform our understanding of our cosmic neighbourhood and of fundamental plasma physics across our Universe.

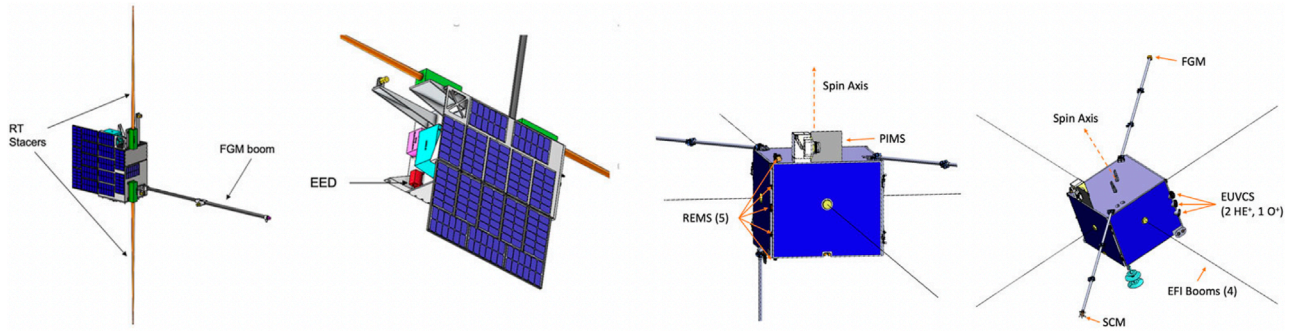

FIGURE 1
Rendering of the microsatellites equipped for radio tomography (left) and of the small satellites carrying plasma instrumentation (right). From Malaspina et al.

Author contributions

All authors listed have made a substantial, direct, and intellectual contribution to the work and approved it for publication.

Conflict of interest

The authors declare that the research was conducted in the absence of any commercial or financial relationships that could be construed as a potential conflict of interest.

Publisher's note

All claims expressed in this article are solely those of the authors and do not necessarily represent those of their affiliated organizations, or those of the publisher, the editors and the reviewers. Any product that may be evaluated in this article, or claim that may be made by its manufacturer, is not guaranteed or endorsed by the publisher.

frontiers in Astronomy and Space Sciences

METHODS
published: 21 October 2020
doi: 10.3389/fspas.2020.593516

Using Dimensionality Reduction and Clustering Techniques to Classify Space Plasma Regimes

Mayur R. Bakrania[1], I. Jonathan Rae[1,2], Andrew P. Walsh[3], Daniel Verscharen[1,4] and Andy W. Smith[1]*

[1]Department of Space and Climate Physics, Mullard Space Science Laboratory, University College London, Dorking, United Kingdom, [2]Department of Mathematics, Physics and Electrical Engineering, University of Northumbria, Newcastle, United Kingdom, [3]European Space Astronomy Centre, ESA, Madrid, Spain, [4]Space Science Center, University of New Hampshire, Durham, NH, United States

Collisionless space plasma environments are typically characterized by distinct particle populations. Although moments of their velocity distribution functions help in distinguishing different plasma regimes, the distribution functions themselves provide more comprehensive information about the plasma state, especially at times when the distribution function includes non-thermal effects. Unlike moments, however, distribution functions are not easily characterized by a small number of parameters, making their classification more difficult to achieve. In order to perform this classification, we propose to distinguish between the different plasma regions by applying dimensionality reduction and clustering methods to electron distributions in pitch angle and energy space. We utilize four separate algorithms to achieve our plasma classifications: autoencoders, principal component analysis, mean shift, and agglomerative clustering. We test our classification algorithms by applying our scheme to data from the Cluster-Plasma Electron and Current Experiment instrument measured in the Earth's magnetotail. Traditionally, it is thought that the Earth's magnetotail is split into three different regions (the plasma sheet, the plasma sheet boundary layer, and the lobes), that are primarily defined by their plasma characteristics. Starting with the ECLAT database with associated classifications based on the plasma parameters, we identify eight distinct groups of distributions, that are dependent upon significantly more complex plasma and field dynamics. By comparing the average distributions as well as the plasma and magnetic field parameters for each region, we relate several of the groups to different plasma sheet populations, and the rest we attribute to the plasma sheet boundary layer and the lobes. We find clear distinctions between each of our classified regions and the ECLAT results. The automated classification of different regions in space plasma environments provides a useful tool to identify the physical processes governing particle populations in near-Earth space. These tools are model independent, providing reproducible results without requiring the placement of arbitrary thresholds, limits or expert judgment. Similar methods could be used onboard spacecraft to reduce the dimensionality of distributions in order to optimize data collection and downlink resources in future missions.

Keywords: space plasma environments, particle populations, distribution functions, dimensionality reduction, clustering techniques

OPEN ACCESS

Edited by:
Vladislav Izmodenov, Space Research Institute (RAS), Russia

Reviewed by:
Anton Artemyev, Space Research Institute (RAS), Russia
Olga Khabarova, Institute of Terrestrial Magnetism Ionosphere and Radio Wave Propagation (RAS), Russia

****Correspondence:***
Mayur R. Bakrania
mayur.bakrania@ucl.ac.uk

Specialty section:
This article was submitted to Space Physics, a section of the journal Frontiers in Astronomy and Space Sciences

Received: *10 August 2020*
Accepted: *22 September 2020*
Published: *21 October 2020*

Citation:
Bakrania MR, Rae IJ, Walsh AP, Verscharen D and Smith AW (2020) Using Dimensionality Reduction and Clustering Techniques to Classify Space Plasma Regimes. Front. Astron. Space Sci. 7:593516. doi: 10.3389/fspas.2020.593516

1 INTRODUCTION

Particle populations in collisionless space plasma environments, such as the Earth's magnetotail, are traditionally characterized by the moments of their distribution functions. 2D distribution functions in pitch angle and energy, however, provide the full picture of the state of each plasma environment, especially when non-thermal particle populations are present that are less easily characterized by a Maxwellian fit. These non-thermal plasma populations are ubiquitous across the solar system. They make crucial contributions to the bulk properties of a plasma, such as the temperature and collisionality (Hapgood et al., 2011). Magnetic reconnection, for example, heats non-thermal seed populations in both the diffusion and outflow regions, making them an important component of the overall energization process (Øieroset et al., 2002). High-quality measurements and analysis of collisionless plasmas are consequently of key importance when attempting to understand these non-thermal populations.

Distribution functions, unlike moments, are not easily classified by a small number of parameters. We therefore propose to apply dimensionality reduction and clustering methods to particle distributions in pitch angle and energy space as a new method to distinguish between the different plasma regions. 2D distributions functions in pitch angle and energy are derived from full 3D distributions in velocity space based on the magnetic field direction and the assumption of gyrotropy of electrons. With these novel methods, we robustly classify variations in particle populations to a high temporal and spatial resolution, allowing us to better identify the physical processes governing particle populations in near-Earth space. Our method also has the advantage of being independent of the model applied, as these methods do not require prior assumptions of the distributions of each population.

1.1 Machine Learning Models

In this section, we give a detailed account of the internal operations of each of the unsupervised machine learning algorithms used in our method. In unsupervised learning, algorithms discover the internal representations of the input data without requiring training on example output data. Dimensionality reduction is a specific type of unsupervised learning in which data in high-dimensional space is transformed to a meaningful representation in lower dimensional space. This transformation allows complex datasets, such as 2D pitch angle and energy distributions, to be characterized by analysis techniques (e.g., clustering algorithms) with much more computational efficiency. Our machine learning method utilizes four separate algorithms: autoencoders (Hinton and Salakhutdinov, 2006), principal component analysis (PCA, Abdi and Williams, 2010), mean shift (Fukunaga and Hostetler, 1975), and agglomerative clustering (AC) (Lukasovā, 1979). We obtain the autoencoder algorithm from the Keras library (Chollet et al., 2015), and the PCA, mean shift, and AC algorithms from the scikit-learn library (Pedregosa et al., 2011).

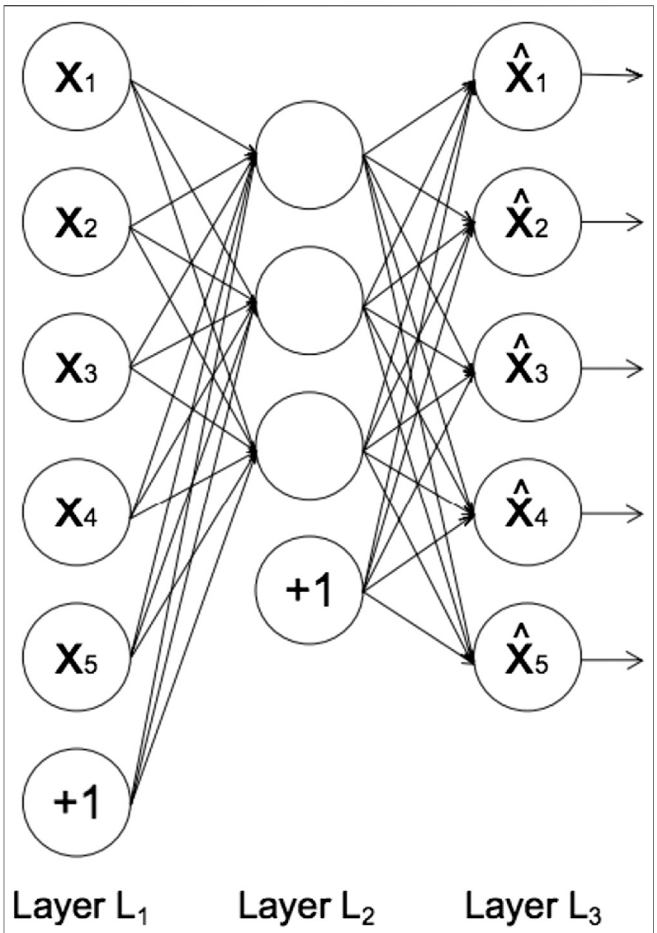

FIGURE 1 | The architecture of an autoencoder, adapted from Sakurada and Yairi (2014). Each circle represents a neuron corresponding to a data-point. Layer L1 represents the input data, layer L2 the encoded data in latent space, and layer L3 the reconstructed data. The circles labeled "+1" are known as "bias units," which are parameters that are adjusted during training to improve the performance of the neural network.

We use the autoencoder to compress the data by a factor of 10 from a high-dimensional representation. We subsequently apply the PCA algorithm to further compress the data to a three-dimensional representation. The PCA algorithm has the advantage of being a lot cheaper computationally than an autoencoder, however the algorithm only captures variations that emerge from linear relationships in the data, while autoencoders also account for non-linear relationships in the dimensionality reduction process (Bishop, 1998). For this reason, we only utilize the PCA algorithm after the data have been compressed *via* an autoencoder. After compressing the data, we use the mean shift algorithm to inform us of how many populations are present in the data using this three-dimensional representation. While the mean shift algorithm provides us with this estimate of the requisite number of clusters, the algorithm is ineffective in constraining the shapes of the clusters to determine which population each data-point belongs to. Therefore, we use an AC algorithm to assign each data-point to one of the populations.

1.1.1 Autoencoders

Autoencoders are a particular class of unsupervised neural networks. They are trained to learn compressed representations of data by using a bottleneck layer which maps the input data to a lower dimensional space, and then subsequently reconstructing the original input. By minimizing the "reconstruction error," or "loss," the autoencoder is able to retain the most important information in a representative compression and reconstruction of the data. As a result, autoencoders have applications in dimensionality reduction (e.g., Hinton and Salakhutdinov, 2006), anomaly detection (e.g., Kube et al., 2019) and noise filtering (e.g., Chandra and Sharma, 2014).

During training, an autoencoder runs two functions simultaneously. The first, called an "encoder," maps the input data, x, to the coded representation in latent space, z. The second function, called a "decoder," maps the compressed data, z, to a reconstruction of the input data, $\hat{x}$. The encoder, $E(x)$, and decoder, $D(z)$, are defined by the following deterministic posteriors:

$$\begin{aligned} E(x) &= p(z|x;\theta_E), \\ D(z) &= p(\hat{x}|z;\theta_D), \end{aligned} \tag{1}$$

where θ_E and θ_D are the trainable parameters of the encoder and decoder respectively. **Figure 1** illustrates the standard architecture of an autoencoder.

In feed-forward neural networks, such as autoencoders, each neuron computes the following sum:

$$y = \sum_i w_i x_i + b, \tag{2}$$

where x_i represents the input from the previous layer, w_i enotes the weights associated with the connections between neurons in different layers, and b denotes the bias term associated with each layer (represented by the circles labeled "+1" in **Figure 1**). The number of neurons in each layer defines the dimension of the data representation in that layer. The output of each neuron, $f(y)$, is called the activation function. Rectified Linear Unit, (Hahnioser et al., 2000) is the most commonly used activation function due to its low computational cost (Agarap, 2018). The function is described as:

$$f(y) = \max(0, y). \tag{3}$$

The sigmoid activation function (Chandra and Singh, 2004) is also commonly used. It is defined by:

$$f(y) = \frac{1}{1 + e^{-y}}, \tag{4}$$

where y is defined in **Eq. 2**. Analysis of the use of various activation functions in the remit of plasma physics are given by Kube et al. (2019).

In order to improve the representation of the compressed data in layer L2 and minimize the discrepancy between the input and reconstruction layer, the autoencoder adjusts the weights and biases by minimising a loss function through an optimiser (described below). The binary cross-entropy loss function (de Boer et al., 2005) is typically used when the input data, x, are normalized to values between 0 and 1. The loss value, c, increases as the reconstruction data, $\hat{x}$, diverge from the input data. The loss function is defined as:

$$c = -[x \ln(\hat{x}) + (1 - x)\ln(1 - \hat{x})]. \tag{5}$$

An overview of various loss functions is provided by Janocha and Czarnecki (2017). Optimisers are used to ensure the autoencoder converges quickly to a minimum loss value by finding the optimum value of the weight, w_i, of each neuron. This is achieved by running multiple iterations with different weight values, known as gradient descent (Ruder, 2016). The weights are adjusted in each iteration, t, according to:

$$w_t = w_{t-1} - \alpha \frac{\partial c}{\partial \omega}, \tag{6}$$

where $\partial c/\partial \omega$ is the gradient, which is a partial derivative of the loss value with respect to the weight. The learning rate, α, updates all the weights simultaneously with respect to the gradient descent. This learning rate is randomly initialized between 0 and 1 by the Algorithm. A low learning rate results in a slower convergence to the global minimum loss value. However a too high value for the learning rate impedes the gradient descent (**Eq. 6**) from converging on the optimum weights. The Adadelta optimiser (Zeiler, 2012) is commonly used due to its rapid convergence to the minimum loss value and its ability to adapt the learning rate depending on each parameter. The optimiser updates each parameter, θ, according to:

$$\Delta\theta_t = -\frac{\mathrm{RMS}[\Delta\theta]_{t-1}}{\mathrm{RMS}[g]_t} g_t, \tag{7}$$

where $\Delta\theta_t$ is the parameter update at the t-th iteration, g_t is the gradient of the parameters at the t-th iteration, and RMS is the root mean square. An overview of the various optimisers is provided by Khandelwal (2019).

1.1.2 Principal Component Analysis

PCA is a statistical procedure that, as well as autoencoders, also reduces the dimensionality of input data. The algorithm achieves this by transforming the input data from a large number of correlated variables to a smaller number of uncorrelated variables, known as principal components. These principal components account for most of the variation in the original input data, making them a useful tool in feature extraction.

Before the procedure, the original data, X_0, are represented by a $(n \times Q)$ matrix, where n is the number of observations and Q is the number of variables (also called dimensions). In the first step, the algorithm scales and centers the data:

$$X = (X_0 - \overline{X}_0)D^{-1}, \tag{8}$$

where $\overline{X}_0$ contains the means of each of the variables, and D is a diagonal matrix that contains the scaling coefficient of each variable. Typically, $D_{ii} = \sigma_i$ where σ_i is the standard deviation of variable with index i (Peerenboom et al., 2015). The algorithm then uses X to calculate the covariance matrix:

$$C_X = \frac{1}{n-1} X^T X, \tag{9}$$

which measures the correlation between the different variables. The principal components are calculated as the eigenvectors, A, of the covariance matrix:

$$C_X = ALA^T, \tag{10}$$

where L is a diagonal matrix containing the eigenvalues associated with A. These principal components are ordered in decreasing order, whereby the first principal components account for most of the variation in the input data. These input data are finally projected into the principal component space according to:

$$Z = XA, \tag{11}$$

where Z represents the output data containing the principal component scores. The dimensionality of these output data are determined by the number of principal components used.

1.1.3 Mean Shift

The mean shift algorithm is a non-parametric clustering technique that is used for locating the maxima of a density function in a sample space. The algorithm aims to discover the number of clusters within a dataset, meaning no prior knowledge of the number of clusters is necessary.

For a dataset containing n data-points x_i, the algorithm starts finding each maximum of the dataset's density function by randomly choosing a data-point to be the mean of the distribution, x. The algorithm then uses a kernel function, K, to determine the weights of the nearby data-points for re-estimating the mean. The variable h is the width of the kernel window. Typically, a Gaussian kernel, k, is used:

$$K\left(\frac{x-x_i}{h}\right) = c_k k\left(\left\|\frac{x-x_i}{h}\right\|^2\right) = \exp\left(-c_k\left\|\frac{x-x_i}{h}\right\|^2\right), \tag{12}$$

where c_k is the normalising constant. With the kernel function, the multivariate kernel density estimator is obtained:

$$f(x) = \frac{1}{nh^d}\sum_{i=1}^{n} K\left(\frac{x-x_i}{h}\right), \tag{13}$$

where d is the dimensionality of the dataset. The gradient of the density estimator is then:

$$\begin{aligned}\nabla f(x) &= \frac{2c_k}{nh^{d+2}}\sum_{i=1}^{n}(x_i - x)g\left(\left\|\frac{x-x_i}{h}\right\|^2\right) \\ &= \frac{2c_k}{nh^{d+2}}\left[\sum_{i=1}^{n} g\left(\left\|\frac{x-x_i}{h}\right\|^2\right)\right] m_h(x),\end{aligned} \tag{14}$$

where $g(x) = -k'(x)$. The first term is proportional to the density estimate at x, and the second term, $m_h(x)$, is:

$$m_h(x) = \frac{\sum_{i=1}^{n} x_i g\left(\left\|\frac{x-x_i}{h}\right\|^2\right)}{\sum_{i=1}^{n} g\left(\left\|\frac{x-x_i}{h}\right\|^2\right)} - x, \tag{15}$$

which is the mean shift vector and points toward the direction of the maximum increase in density. The mean shift algorithm therefore iterates between calculating the mean shift vector, $m_h(x^t)$, and translating the kernel window:

$$x^{t+1} = x^t + m_h(x^t), \tag{16}$$

where t is the iteration step. Once the window has converged to a point in feature space where the density function gradient is zero, the algorithm carries out the same procedure with a new window until all data-points have been assigned to a maximum in the density function.

1.1.4 Agglomerative Clustering

AC is a type of hierarchical clustering that uses a "bottom-up" approach, whereby each data-point is first assigned a different cluster. Then pairs of similar clusters are merged until the specified number of clusters has been reached. During each recursive step, the AC algorithm combines clusters typically using Ward's criterion (Ward, 1963), which finds pairs of clusters that lead to the smallest increase in the total intra-cluster variance after merging. The increase is measured by a squared Euclidean distance metric:

$$d_{ij} = d\left(C_i, C_j\right) = ||C_i - C_j||^2, \tag{17}$$

where C_i represents a cluster with index i. The algorithm implements Ward's criterion using the Lance–Williams formula (Lance and Williams, 1967):

$$\begin{aligned}d\left(C_i \cup C_j, C_k\right) =& \frac{n_i + n_k}{n_i + n_j + n_k} d(C_i, C_k) \\ &+ \frac{n_j + n_k}{n_i + n_j + n_k} d\left(C_j, C_k\right) - \frac{n_k}{n_i + n_j + n_k} d\left(C_i, C_j\right),\end{aligned} \tag{18}$$

where C_i, C_j, and C_k are disjoint clusters with sizes n_i, n_j, and n_k, and $d(C_i \cup C_j, C_k)$ is the squared Euclidean distance between the new cluster $C_i \cup C_j$ and C_k. The clustering algorithm uses **Eq. 18** to find the optimal pair of clusters to merge.

1.2 The Magnetotail

We use electron data from the magnetotail in order to test the effectiveness of our method. The magnetotail is traditionally divided into three different regions: the plasma sheet, the plasma sheet boundary layer, and the lobes (Hughes, 1995). These regions are defined by their plasma and magnetic field characteristics. The low temperature (~85 eV) outermost northern and southern lobes are on open magnetic field lines which results in a much lower plasma density of ~0.01 cm (Lui, 1987). The plasma sheet boundary layer exists on the reconnected magnetic field lines. This region forms the transition region in between the plasma sheet and the lobes, and is characterized by a population of field-aligned particles and a plasma β, which is the ratio of the plasma pressure to the magnetic pressure, of ~0.1 (Lui, 1987).

The innermost plasma sheet typically contains a comparatively hot (~4,250 eV) and isotropic plasma with a relatively high particle density of ~0.01 cm^{-3}. At the center of the plasma sheet is the thin neutral current sheet, which is

characterized by a relatively high plasma β of ~0, and a magnetic field strength of near zero (Lui, 1987). Although isotropic electron pitch angle distributions (PADs) are the most dominant in the plasma sheet, many cases of pitch angle anisotropy have also been found (e.g., Walsh et al., 2013; Artemyev et al., 2014; Liu et al., 2020). These intervals correspond to a colder and denser electron population and are linked to: cold anisotropic ionospheric outflows (Walsh et al., 2013), and a penetration of cold electrons from the magnetosheath near the flanks (Artemyev et al., 2014).

2 METHOD AND APPLICATION

In this section, we detail the steps required to classify different regions within a space plasma environment using machine learning techniques. As an example, we classify Cluster-Plasma Electron and Current Experiment (PEACE, Johnstone et al., 1997; Fazakerley et al., 2010) data (Laakso et al., 2010) from the Earth's magnetotail to showcase our method, as this allows us to compare to the Cluster-ECLAT (European Cluster Assimilation Technology) (Boakes et al., 2014) database for evaluation. The same method, however, can be applied to any plasma regime where energy and pitch angle measurements are available. Our steps are as follows:

(1) Data preparation: We obtain the Cluster-PEACE data from different magnetotail regions based on the Cluster-ECLAT database, and prepare the data for testing.
(2) Reducing dimensionality: We build our autoencoder and use the encoder part to reduce the dimensionality of each pitch angle and energy distribution by a factor of 10. We use a PCA algorithm to further compress each distribution to a set of coordinates in 3D space.
(3) Clustering: We apply the mean-shift algorithm to determine how many clusters exist within the compressed magnetotail electron data, and use an AC algorithm to separate the compressed dataset into this number of clusters. This allows us to determine how many plasma regimes exist within the overall dataset.
(4) Evaluation: We estimate the probabilities of the AC labels and compare our clustering results to the original ECLAT labels in order to evaluate our method.

2.1 Data Preparation

We prepare PEACE instrument data from the Cluster mission's C4 spacecraft (Escoubet et al., 2001) to test and present our method. The Cluster mission comprises of four spacecraft, each spinning at a rate of 4 s^{-1}. The PEACE data have a 4 s time resolution and are constructed from two instantaneous PAD measurements per spin. Each of our distributions is a two-dimensional differential energy flux product containing twelve 15° wide pitch angle bins and 26 energy bins, spaced logarithmically between 93 eV and 24 keV. The dimensionality of each distribution is 312 (12 × 26). We normalize the differential energy flux linearly between 0 and 1 based on the maximum flux value in the dataset. An example of an individual differential energy flux distribution used in our analysis is shown in **Figure 2**. We correct for spacecraft potential with measurements from the Cluster-EFW (Electric Field and Wave Experiment) instrument (Gustafsson et al., 2001) and corrections (19% increase) according to the results of Cully et al. (2007).

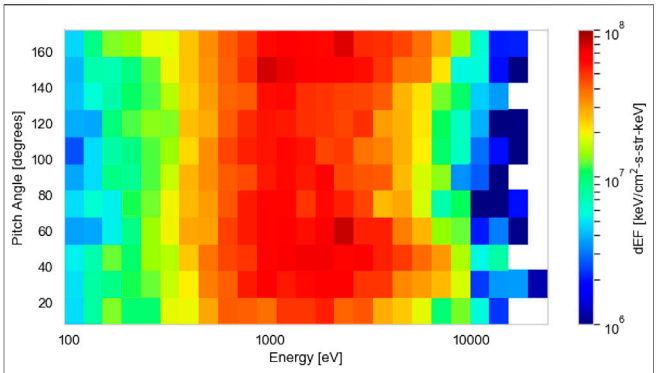

FIGURE 2 | An example two-dimensional electron differential energy flux distribution, as a function of pitch angle (°) and energy (eV), measured by the Cluster-Plasma Electron and Current Experiment instrument in the magnetotail across a 4 s window (09:51:23–09:51:27 on October 13, 2003).

The ECLAT dataset consists of a detailed list of plasma regions encountered by each of the four Cluster spacecraft in the nightside magnetosphere. The dataset is available from July to October during the years 2001–2009. Using plasma and magnetic field moments from the PEACE, Cluster Ion Spectrometry (CIS) (Rème et al., 2001), and Fluxgate Magnetometer (FGM) (Balogh et al., 1997) instruments, the dataset provides a list of (inner and outer) plasma sheet, boundary layer, and lobe times. These regions are identified based on the plasma β, the magnetic field measurements, and the current density vectors. A comprehensive account of the ECLAT identification routine for each plasma region is provided by Boakes et al. (2014). To ensure that we test our method on a large number of data from each of the magnetotail regions (>50,000 samples), we obtain PEACE data from times when the C4 spacecraft has spent at least 1 h in each region, according to ECLAT.

2.2 Reducing Dimensionality

After preparing the dataset to include a series of >50,000 time intervals, each with its associated 2D pitch angle and energy distributions (e.g., **Figure 2**), the first step toward reducing the dataset's dimensionality is to build a suitable autoencoder (described in **Section 1.1.1**). We construct our autoencoder using the Keras library. This step requires defining the number of neurons in each layer. The input and reconstruction layer should have the same number, which is equal to the dimensionality of the original dataset (312 for each time interval in this example). The middle encoded layer typically contains a compressed representation of the data that is by a factor of 10 smaller than the input data (Hinton and Salakhutdinov, 2006). We therefore specify our encoded layer to contain 32 neurons. The next step involves specifying the activation function for the neurons in the first and middle layers.

We use the standard Rectified Linear Unit activation function (Hahnioser et al., 2000) in the encoder part of our autoencoder and the sigmoid activation function (Chandra and Singh, 2004) in the decoder part, as this function is used to normalize the output between 0 and 1.

The next step defines which loss function and optimiser the autoencoder uses in order to representatively compress and reconstruct the input data. As we use normalized output data, we choose the standard binary cross-entropy loss function (de Boer et al., 2005). In terms of the optimiser, we utilize the Adadelta optimiser (Zeiler, 2012) due to its speed and versatility. All of the activation functions, loss functions, and optimisers are available in the Keras library.

In the next step, we set the hyperparameters used for training the autoencoder. These hyperparameters include: the number of epochs, the batch size, and the validation split ratio. The number of epochs represents the number of training iterations undergone by the autoencoder, with the weights and biases updated at each iteration. The batch size defines the number of samples that are propagated through the network at each iteration. It is equal to 2^n, where n is a positive integer. The batch size (256 in our case) is ideally set as close to the dimensionality of the input data as possible. The validation split ratio determines the percentage of the input data that should remain "unseen" by the autoencoder in order to verify that the algorithm is not overfitting the remaining training data. We set the validation split ratio to 1/12, which is commonly used for large datasets (Guyon, 1997). At each iteration, a training loss value and a validation loss value are produced, which are determined by the binary cross-entropy loss function. Both of these values converge to their minima after a certain number of iterations, at which point the autoencoder cannot be optimized to the input data any further. Loss values <0.01 are typically considered ideal (Le et al., 2018).

After retrieving the compressed representation of the input data from the encoding layer (with a dimensionality of 32 in our case), we apply a PCA algorithm (see **Section 1.1.2**) to the compressed data to reduce the dimensionality to 3. We obtain the PCA algorithm from the scikit-learn library. We set the output dimensionality of the PCA algorithm to 3 as the following clustering algorithms used in this method are computationally expensive and their performance scales poorly with increasing dimensionality (Lukasovã, 1979; Comaniciu and Meer, 2002). Setting the dimensionality to 3 has the added benefit that the clusters can be visualised.

2.3 Clustering

Once the dimensionality reduction stage has taken place and each pitch angle and energy distribution is represented by three PCA values, we use clustering algorithms to separate the dataset into the different particle populations. To first determine how many populations exist within the dataset (8 in our case), we apply a mean shift clustering algorithm (see **Section 1.1.3**) to the data to find the number of maxima, n_c, in the distribution of data-points. We obtain the mean shift algorithm from the scikit-learn library. We set the bandwidth, represented by h in **Eq. 15** to 1, which we find optimizes the time taken for the algorithm to converge on the maxima in the density distribution.

After determining the number of clusters in the dataset, we use an AC algorithm (see **Section 1.1.4**) to assign each data-point to one of the clusters. We obtain the AC algorithm from the scikit-learn library and instantiate the algorithm by specifying the number of clusters, n_c, before applying it to the compressed dataset. Assigning several clusters to a large dataset with three dimensions is a computationally expensive task, however we find the AC algorithm converges relatively quickly in comparison to other clustering algorithms. A further advantage of the hierarchical clustering procedure, used in the AC algorithm, is that data-points belonging to a single non-spherical structure in the 3-dimensional parameter space are not incorrectly separated into different clusters, unlike the more widely used K-means algorithm (Arthur, 2007).

Figure 3 contains a flow diagram detailing our method.

2.4 Evaluation

Figure 4 shows the training and validation loss values associated with each iteration during the training of our autoencoder. We use this graph to check if the autoencoder is overfitting to the training data, which is evident if the training loss starts to decrease more rapidly than the validation loss. In this case, our autoencoder is not overfitting at any iteration during training. **Figure 4** shows that both the loss values start to rapidly level off in less than 100 epochs. Both loss values, however, continue to decrease, with the training loss value converging to 0.0743 after 444 iterations, and the validation loss value converging to 0.0140 after 485 iterations. We therefore set the number of epochs to 500. As both loss values are lower than 0.01, we conclude the autoencoder is accurately reconstructing both sets of input data, assuring us that the encoded data with a lower dimensionality is representative of the original 2D distribution functions. The lower validation loss than training loss in **Figure 4** indicates the presence of anomalous data in the training set that is not represented in the validation set. We discuss this anomalous data later in this section.

Figure 5 shows the result of applying the AC algorithm to the compressed magnetotail electron data after the implementation of the autoencoder and PCA algorithms. The 3-dimensional representation shows that the clustering algorithm is able to assign data-points of varying PCA values to the same cluster if they belong to the same complex non-spherical structure, e.g., clusters 0, 4, and 6. The clustering algorithm is able to form clear boundaries between clusters with adjacent PCA values, e.g., between clusters 0, 1, and 7, with no mixing of cluster labels on either side of the boundaries. The clustering algorithm locates the boundaries by finding areas with a low density of data-points in comparison to the centers of the clusters.

Figure 6 shows the results of averaging the 2D differential energy flux distributions in pitch angle and energy space for each of the eight clusters. Using moments data collected by the PEACE, FGM, and CIS instruments, we compare the proton plasma βs, electron densities and temperatures, and magnetic field strengths to the average 2D distribution of each cluster. This process allows us to verify the consistency of the clustering

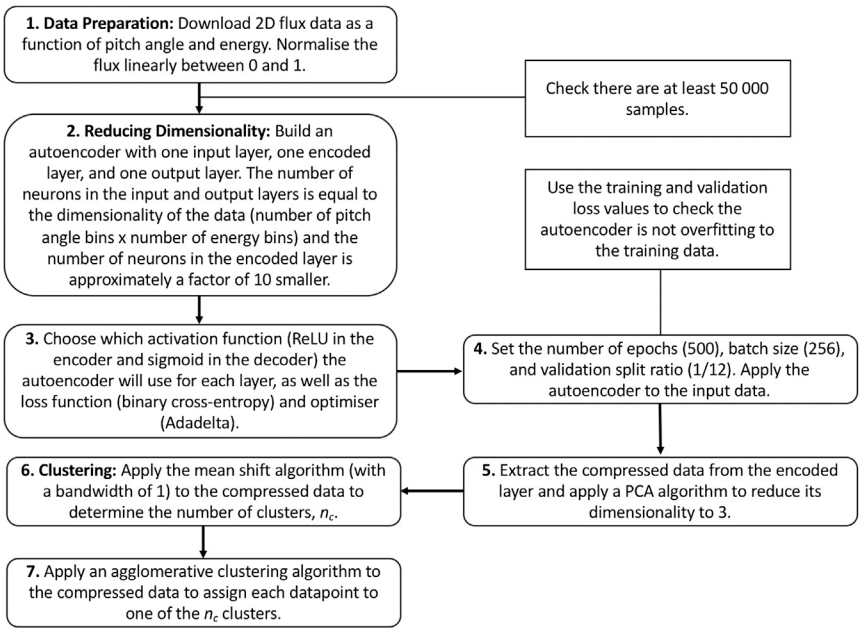

FIGURE 3 | Flow diagram illustrating the steps we take to reduce the dimensionality of the dataset and subsequently apply clustering algorithms to characterize the different populations. Our choices for the functions and input parameters necessary to train the autoencoder are shown in brackets in steps 3 and 4.

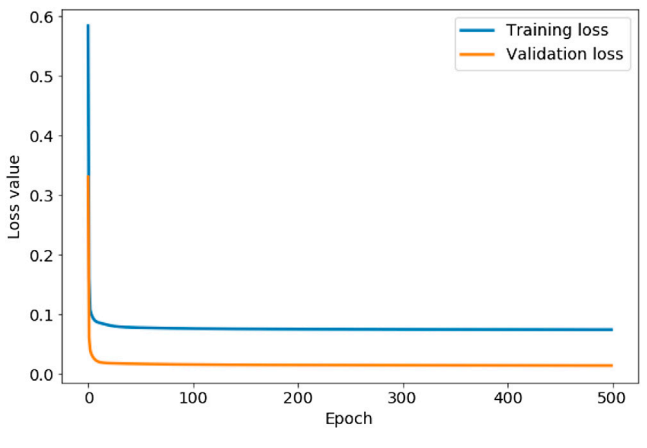

FIGURE 4 | The evolution of the training loss value and validation loss value as the autoencoder iterates through 500 steps (epochs).

method and provide general region classifications in order to make comparisons with the ECLAT labels. Our classifications (shown in the captions below each sub-figure) are produced with the aid of previous analyses of electron PADs (e.g., Walsh et al., 2011; Artemyev et al., 2014) and the plasma and magnetic field parameters (e.g., Lui, 1987; Artemyev et al., 2014) in the magnetotail.

The individual sub-figures in **Figure 6** display large differences in the average electron 2D pitch angle and energy distributions. Each average distribution differs by either: the energy of the peak flux, the peak value of the flux, or the amount of pitch angle anisotropy, i.e., the difference in flux between the parallel and perpendicular magnetic field direction. The lack of identical average distributions amongst the clusters shows the mean shift algorithm has not overestimated the number of clusters. By observing the individual 2D distributions within each cluster, we see a distinct lack of intra-cluster variance, showing the mean shift algorithm does not underestimate the number of clusters.

A limitation of using the AC algorithm is that outliers or anomalous data are not differentiated from the main clusters. Clustering a sizable number of outliers with the main populations can lead to ambiguity in the defining characteristics of each population, reducing the robustness of our method. In our case, **Figure 5** shows only nine data points, within cluster 6, that are disconnected from the main structure of cluster 6 due to their distinct PCA values. We observe similar phenomenon to a lesser extent with cluster 2. To counteract this issue, we perform an outlier detection procedure using the reconstructed output of the autoencoder. By calculating the mean square error (MSE) between each input data-point and its reconstructed output, we isolate outliers in the dataset from the AC analysis based on their large MSE values, in comparison to 99.95% of the data-points. During training, the autoencoder learns the latent space representation that defines the key characteristics of the bulk populations present in the dataset. The most relevant features of an anomalous particle distribution are not present in this subspace, resulting in a large MSE between the reconstructed data, which lacks these important features, and the original data. This technique effectively identifies the nine obvious outliers observable by eye in **Figure 5**, along with six from cluster 2 and 5 from cluster 1.

We use Gaussian mixture models (GMMs, McLachlan and Peel, 2000) to establish the probabilities of each of the data-points

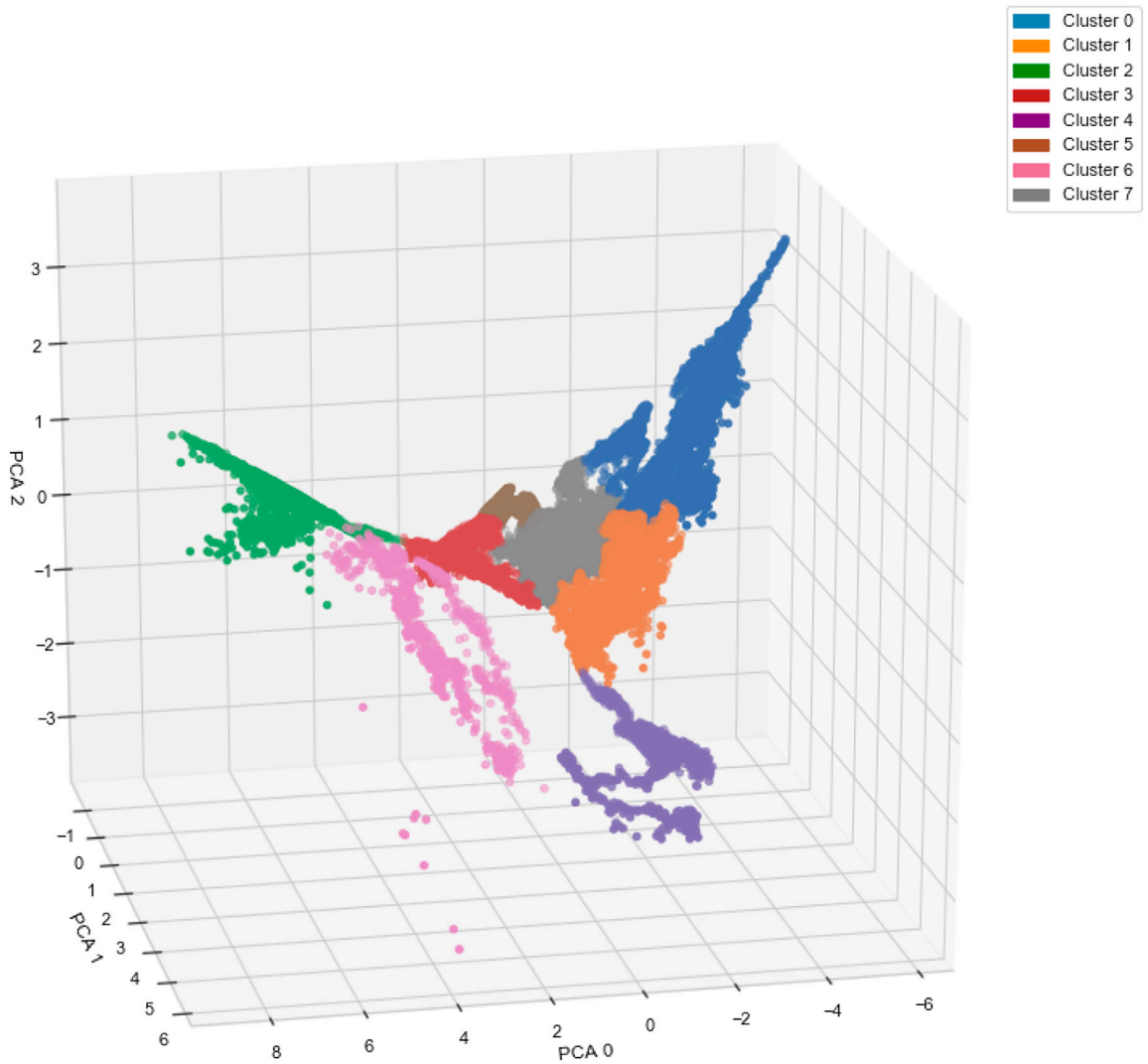

FIGURE 5 | Three-dimensional representation of the magnetotail data after undergoing dimensionality reduction *via* an autoencoder and principal component analysis (PCA) algorithm. The colors represent the clustering results from the agglomerative clustering algorithm.

belonging to the clusters they have been assigned to by the AC algorithm, providing useful information on the uncertainty associated with our region classification method. We obtain the GMM from the scikit-learn library. For each data-point, x_i, a GMM fits a normal distribution, $\mathcal{N}$, to each cluster and computes the sum of probabilities as:

$$p(x_i) = \sum_{j=1}^{k} \phi_j \mathcal{N}\left(x_i; \mu_j, \tau_j\right) = 1, \tag{19}$$

where μ_j and τ_j are the mean and covariance of the normal distribution belonging to cluster j, and ϕ_j is the mixing coefficient which represents the weight of Gaussian j and is calculated by the Expectation–Maximisation algorithm (Dempster et al., 1977). A complete description of GMMs and the Expectation–Maximisation algorithm is provided by Dupuis et al. (2020).

Figure 7 shows a histogram of the probabilities, calculated by the GMM, associated with each data-point belonging to the cluster it is assigned to by the AC algorithm. More than 92% of the data-points have a probability of over 0.9, and <1% of the data-points have a probability of <0.5. This indicates a high certainty in our clustering method and validates the high precision in our region classifications. Further investigations of the data-points with associated probabilities of <0.5 show that these data-points exist on the boundary between clusters 0 and 1, i.e., two plasma sheet populations that differ by temperature. This illustrates a small limitation in the AC method when distinguishing between relatively similar plasma regimes.

Table 1 shows the median and upper and lower quartiles of the electron density, electron temperature, magnetic field, and ion plasma β for each of the eight clusters designated by our AC algorithm. None of the eight clusters have comparable median and quartile values across all four of the chosen parameters.

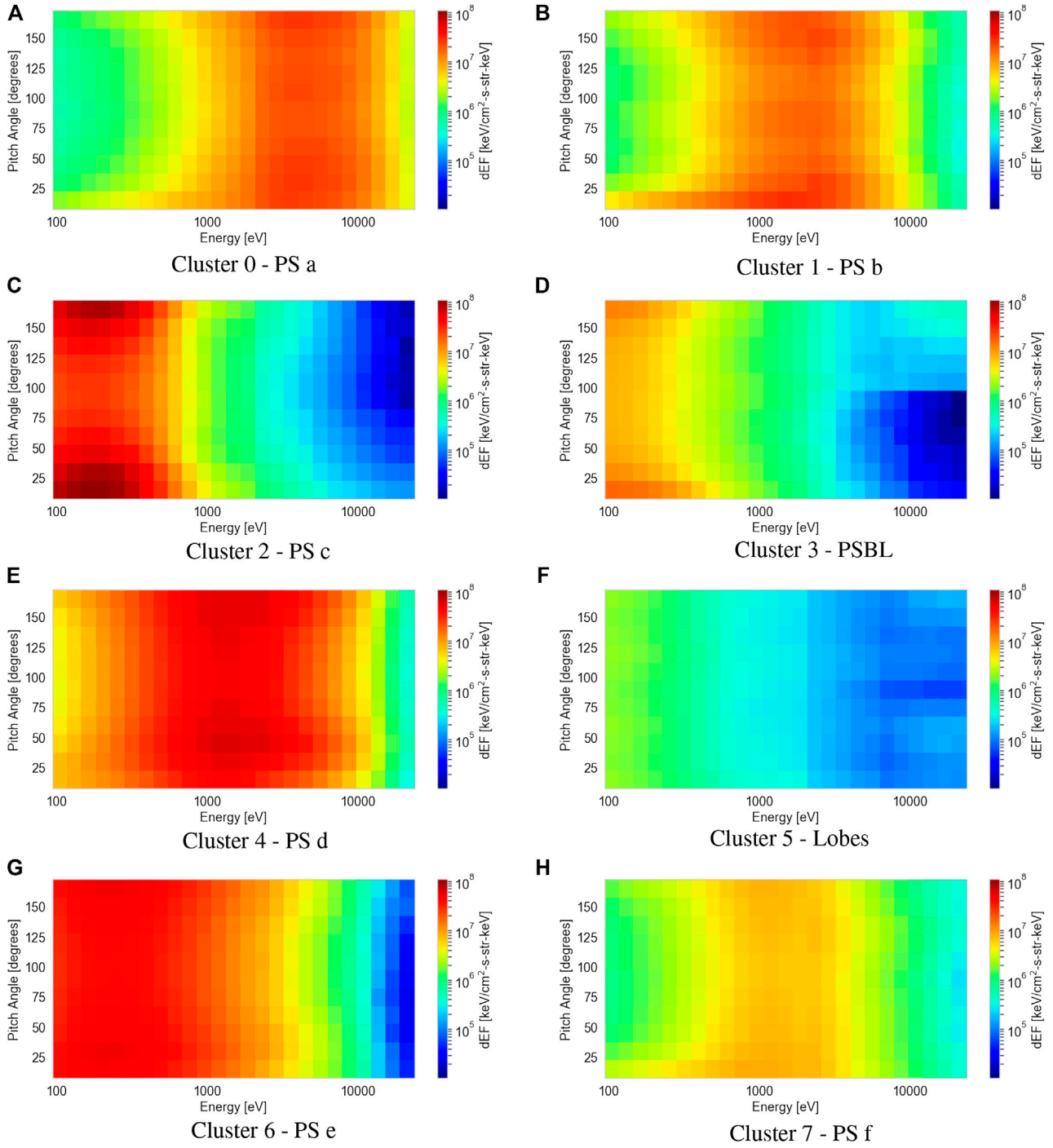

FIGURE 6 | Average electron differential energy flux distributions as a function of pitch angle and energy for each of the eight clusters **(A–H)** classified by the agglomerative clustering algorithm. Each cluster is assigned a magnetotail region (included in the subcaptions) based on our interpretation of their plasma and magnetic field parameters.

Certain pairs of clusters exhibit similarities in the median and quartile values for one or two of the four parameters, e.g., clusters 0 and 4 exhibit similar electron densities and magnetic field strengths, and clusters 3 and 6 exhibit similar magnetic field strengths. However there are large differences in the values of the remaining parameters for these pairs of clusters. These results show that clear differences in the 2D pitch angle and energy distributions (see **Figure 6**) can translate into distinctions between certain but not all plasma parameter measurements, providing a strong indicator that full 2D distributions can effectively be used to distinguish between similar particle populations. Regarding the ECLAT classifications, which are

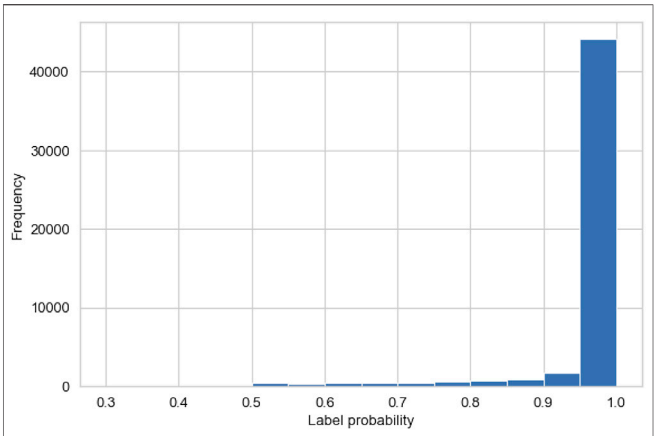

FIGURE 7 | Histogram showing the probabilities, generated by Gaussian mixture model (GMMs), that the data-points belong to the cluster assigned to them by the agglomerative clustering algorithm.

based on magnetic field and plasma β measurements, certain pairs of clusters exhibit a similar range of values in both of these measurements, e.g., clusters 0 and 4 and clusters 1 and 7. As the majority of data-points for all of these clusters are considered the same plasma sheet population by ECLAT (see **Table 2**), we conclude that using a limited number of parameters to provide classifications overlooks distinctions between different populations and incorrectly groups them into the same category.

Table 2 shows our comparison between the eight AC labels and the region names given in the ECLAT database, for the magnetotail data used in our example.

In **Table 2**, there is some disagreement with three of our clusters, namely AC labels 3, 5, and 7, which correspond to the plasma sheet boundary layer, the lobes, and a plasma sheet population respectively. However for each of these clusters, the majority of labels are in agreement with the ECLAT regions (72.4, 86.8, and 86.9% for AC clusters 3, 5, and 7 respectively). For AC labels 0, 1, 2, 4, and 6, which represent various other populations within the plasma sheet, there is 100% agreement with the ECLAT label 0, which denotes the plasma sheet. By using this method to characterize full electron pitch angle and energy distributions, instead of using the derived moments, we are successfully able to distinguish between multiple populations within what has historically been considered as one region, due to the lack of variation in the plasma moments (see **Table 1**) as well as the similarity in spatial location. Using 2D pitch angle and energy distributions also improves the time resolution of the plasma region classifications, due to a higher cadence in the spacecraft flux and counts data (e.g., 4 s resolution for the PEACE instrument) in comparison to the moments data (e.g., 8 s resolution for CIS moments and 16 s resolution for PEACE moments).

3 CONCLUSION

We present a novel machine learning method that characterizes full particle distributions in order to classify different space plasma regimes. Our method uses autoencoders and subsequently PCA to reduce the dimensionality of the 2D particle distributions to three dimensions. We then apply the mean shift algorithm to discover the number of populations in the dataset, followed by the AC algorithm to assign each data-point to a population.

To illustrate the effectiveness of our method, we apply it to magnetotail electron data and compare our results to previous classifications, i.e. the ECLAT database, that utilizes moments. With our method, we find multiple distinct electron populations within the plasma sheet, which previous studies have identified as one region (**Table 2**). These findings show that key features in particle distributions are not fully characterized by the plasma moments (e.g., **Table 1**), resulting in important distinctions between populations being overlooked. For example, we find two separate cold dense anisotropic populations in the plasma sheet (clusters 2 and 6), which are less abundant than the hotter and more isotropic plasma sheet populations. By using our clustering method to specify an exact list of times when populations like these are observed, we create a more comprehensive picture of their spatial distribution. Inherent time-dependencies may also contribute to our finding of

TABLE 1 | Comparisons of the median, Q2, and upper, Q3, and lower, Q1, quartile values of the electron density n_e, electron temperature T_e, magnetic field $|B|$, and plasma β associated with each of the eight clusters.

AC labels	n_e (cm^{-3})			T_e (eV)			$\|B\|$ (nT)			Plasma β		
	Q1	Q2	Q3	Q1	Q2	Q3	Q1	Q2	Q3	Q1	Q2	Q3
0	0.21	0.22	0.23	2,057.26	2,515.28	2,913.33	32.45	35.09	37.86	3.54	4.33	5.92
1	0.12	0.14	0.19	1,487.67	1,838.97	2,258.43	10.56	13.65	19.42	15.31	24.54	39.75
2	1.08	1.18	1.30	106.44	114.19	123.33	20.87	22.67	24.25	0.80	0.99	1.17
3	0.21	0.25	0.28	79.21	83.63	93.00	16.64	35.07	39.76	0.28	0.39	0.60
4	0.22	0.28	0.82	783.33	879.77	997.85	24.58	39.10	41.93	1.23	1.52	6.29
5	0.01	0.02	0.03	116.63	170.57	252.85	32.97	41.34	49.00	0.00	0.06	0.27
6	1.29	1.49	1.65	164.41	214.64	269.16	41.65	44.74	46.56	0.30	0.43	0.60
7	0.08	0.10	0.13	669.64	882.30	1,217.77	5.42	17.16	25.95	3.69	9.05	128.11

AC, agglomerative clustering. The AC labels 0, 1, 2, 4, 6, and 7 belong to the plasma sheet, according to ECLAT, three belongs to the plasma sheet boundary layer, and five belongs to the lobes.

TABLE 2 | Contingency table comparing the agglomerative clustering (AC) labels of the magnetotail electron data to the original ECLAT labels (0 = PS, 1 = PSBL, and 2 = lobes).

AC labels	ECLAT labels		
	0	1	2
0	6,549	0	0
1	3,074	0	0
2	5,092	0	0
3	1,590	4,188	0
4	2,097	0	0
5	156	2,228	15,641
6	1,029	0	0
7	7,020	1,057	0

The AC labels are the same as in ***Table 1****.*

multiple plasma sheet populations. Even in this case, our method is effective in characterising the evolution of particle populations, made possible by the high time resolution of our region classifications. In a follow up study, we will use this information to link the occurrence of these populations to other high-resolution spacecraft measurements in different plasma regions, in order to understand the physical processes driving changes in the less abundant particle populations. As an example analysis, our high resolution classifications of the observed anisotropic plasma sheet populations could be combined with previous theories on the sources of these populations (e.g., Walsh et al., 2013; Artemyev et al., 2014), to understand the relative contributions of particle outflows from distinct magnetospheric regions, such as the magnetosheath or ionosphere.

Comparisons between this original method and the previous classifications from ECLAT also show specific periods of disagreement (e.g., we classify a small number of ECLAT periods of plasma sheet as the plasma sheet boundary layer). This discrepancy shows that using the full 2D pitch angle and energy distributions, without requiring prior assumptions about magnetospheric plasma regions, may redefine the classifications of electron populations, along with our understanding of their plasma properties. Our method, which uses open-source and easily accessible machine learning techniques, can be used to better characterize any space plasma regime with sufficient *in-situ* observations. By not being constrained to a small number of parameters, this method allows for a more complete understanding of the interactions between various thermal and non-thermal populations. With increasingly large datasets being collected by multi-spacecraft missions, such as Cluster (Escoubet et al., 2001) (>10^9 full distributions in 20 years) and Magnetospheric Multiscale Mission (Sharma and Curtis, 2005), similar methods would provide a useful tool to reduce the dimensionality of distributions, thereby optimising data retrieval on Earth. Furthermore, combining this method with large-scale survey data, such as NASA/GSFC's OMNI database, would allow users to isolate a specific population or plasma region for analysis of its properties.

DATA AVAILABILITY STATEMENT

Publicly available datasets were analyzed in this study. This data can be found here: The datasets analysed in this study can be found in the Cluster Science Archive (https://csa.esac.esa.int/csa-web/).

AUTHOR CONTRIBUTIONS

MRB developed the method described in the manuscript, tested it on the magnetotail data and wrote the manuscript. IJR was the lead supervisor who guided the direction of the project and provided insight at every stage. AW provided expertize on the magnetotail and the various populations that we observed, aiding the evaluation of our method. DV was also important in classifying the plasma regimes and provided insights into the physical processes governing electrons in space plasmas. AWS was key to the development of the method due to his expertize in machine learning. All co-authors made important contributions to the manuscript.

FUNDING

MB is supported by a UCL Impact Studentship, joint funded by the ESA NPI program. IR the STFC Consolidated Grant ST/S000240/1 and the NERC grants NE/P017150/1, NE/P017185/1, NE/V002554/1, and NE/V002724/1. DV is supported by the STFC Consolidated Grant ST/S000240/1 and the STFC Ernest Rutherford Fellowship ST/P003826/1. AS is supported by the STFC Consolidated Grant ST/S000240/1 and by NERC Grants NE/P017150/1 and NE/V002724/1.

ACKNOWLEDGMENTS

We thank the Cluster instrument teams (PEACE, FGM, CIS, EFW) for the data used in this study, in particular the PEACE operations team at the Mullard Space Science Laboratory. We also acknowledge the European Union Framework 7 Program, the ECLAT Project FP7 Grant No. 263325, and the ESA Cluster Science Archive.

REFERENCES

Abdi, H., and Williams, L. J. (2010). Principal component analysis. *WIREs Comput. Stat.* 2, 433–459. doi:10.1002/wics.101

Agarap, A. F. (2018). Deep learning using rectified linear units (ReLU). arXiv: 1803.08375.

Artemyev, A. V., Walsh, A. P., Petrukovich, A. A., Baumjohann, W., Nakamura, R., and Fazakerley, A. N. (2014). Electron pitch angle/energy distribution in the magnetotail. *J. Geophys. Res. Space Phys.* 119, 7214–7227. doi:10.1002/2014JA020350

Arthur, D. (2007). "k-means++: the advantages of careful seeding," in Proceedings of the eighteenth annual ACM-SIAM symposium on discrete algorithms, New Orleans, United States, January 7, 2007. 1027–1035

Balogh, A., Dunlop, M. W., Cowley, S. W. H., Southwood, D. J., Thomlinson, J. G., Glassmeier, K. H., et al. (1997). The cluster magnetic field investigation. *Space Sci. Rev.* 79, 65–91. doi:10.1023/A:1004970907748

Bishop, C. M. (1998). "Bayesian PCA," in Proceedings of the 11th international conference on neural information processing systems, Denver, United States, December 1, 1997. (Cambridge, MA: MIT Press), 382–388.

Boakes, P. D., Nakamura, R., Volwerk, M., and Milan, S. E. (2014). ECLAT cluster spacecraft magnetotail plasma region identifications (2001–2009). *Dataset Papers Sci.* 2014, 684305. doi:10.1155/2014/684305

Chandra, B., and Sharma, R. K. (2014). "Adaptive noise schedule for denoising autoencoder," in *Neural information processing*. Editors C. K. Loo, K. S. Yap, K. W. Wong, A. Teoh, and K. Huang (Berlin, Germany: Springer International Publishing), 535–542.

Chandra, P., and Singh, Y. (2004). An activation function adapting training algorithm for sigmoidal feedforward networks. *Neurocomputing* 61, 429–437. doi:10.1016/j.neucom.2004.04.001

Chollet, F., Allison, K., Wicke, M., Bileschi, S., Bailey, B., Gibson, A., et al. (2015). Keras. Available at: https://keras.io (Accessed February 15, 2020).

Comaniciu, D., and Meer, P. (2002). Mean shift: a robust approach toward feature space analysis. *IEEE Trans. Pattern Anal. Machine Intell.* 24, 603–619. doi:10.1109/34.1000236

Cully, C. M., Ergun, R. E., and Eriksson, A. I. (2007). Electrostatic structure around spacecraft in tenuous plasmas. *J. Geophys. Res. Atmos.* 112, A09211. doi:10.1029/2007JA012269

de Boer, P.-T., Kroese, D. P., Mannor, S., and Rubinstein, R. Y. (2005). A tutorial on the cross-entropy method. *Ann. Oper. Res.* 134, 19–67. doi:10.1007/s10479-005-5724-z

Dempster, A. P., Laird, N. M., and Rubin, D. B. (1977). Maximum likelihood from incomplete data via the EM algorithm. *J. R. Stat. Soc. Ser. B Methodol.* 39, 1–22. doi:10.1111/j.2517-6161.1977.tb01600.x

Dupuis, R., Goldman, M. V., Newman, D. L., Amaya, J., and Lapenta, G. (2020). Characterizing magnetic reconnection regions using Gaussian mixture models on particle velocity distributions. *Astrophys J.* 889, 15. doi:10.3847/1538-4357/ab5524

Escoubet, C. P., Fehringer, M., and Goldstein, M. (2001). Introduction: the cluster mission. *Ann. Geophys.* 19, 1197–1200. doi:10.5194/angeo-19-1197-2001

Fazakerley, A. N., Lahiff, A. D., Wilson, R. J., Rozum, I., Anekallu, C., West, M., et al. (2010). "Peace data in the cluster active archive," in *The cluster active archive*. Editors H. Laakso, M. Taylor, and C. P. Escoubet (Dordrecht, Netherlands: Springer Netherlands), 129–144.

Fukunaga, K., and Hostetler, L. (1975). The estimation of the gradient of a density function, with applications in pattern recognition. *IEEE Trans. Inf. Theory.* 21, 32–40. doi:10.1109/tit.1975.1055330

Gustafsson, G., André, M., Carozzi, T., Eriksson, A. I., Fälthammar, C.-G., Grard, R., et al. (2001). First results of electric field and density observations by Cluster EFW based on initial months of operation. *Ann. Geophys.* 19, 1219–1240. doi:10.5194/angeo-19-1219-2001

Guyon, I. (1997). *A scaling law for the validation-set training-set size ratio.* Murray Hill, NJ: AT & T Bell Laboratories.

Hahnioser, R., Sarpeshkar, R., Mahowald, M., Douglas, R., and Seung, H. (2000). Digital selection and analogue amplification coexist in a cortex- inspired silicon circuit. *Nature* 405, 947–951. doi:10.1038/35016072

Hapgood, M., Perry, C., Davies, J., and Denton, M. (2011). The role of suprathermal particle measurements in crossscale studies of collisionless plasma processes. *Planet. Space Sci.* 59, 618–629. doi:10.1016/j.pss.2010.06.002

Hinton, G. E., and Salakhutdinov, R. R. (2006). Reducing the dimensionality of data with neural networks. *Science* 313, 504–507. doi:10.1126/science.1127647

Hughes, W. J. (1995). "The magnetopause, magnetotail, and magnetic reconnection," in *Introduction to space physics*. Editors M. G. Kivelson and C. T. Russell (Cambridge, UK: Cambridge University Press), Chap. 9, 227–288.

Janocha, K., and Czarnecki, W. M. (2017). On loss functions for deep neural networks in classification. arXiv.

Johnstone, A. D., Alsop, C., Burge, S., Carter, P. J., Coates, A. J., Coker, A. J., et al. (1997). *Peace: a plasma electron and current experiment*. Dordrecht, Netherlands: Springer Netherlands, 351–398

Khandelwal, R. (2019). Overview of different optimizers for neural networks. Available at: https://medium.com/datadriveninvestor/overview-of-different-optimizers-for-neural-networks-e0ed119440c3. (Accessed July 7, 2020).

Kube, R., Bianchi, F. M., Brunner, D., and LaBombard, B. (2019). Outlier classification using autoencoders: application for fluctuation driven flows in fusion plasmas. *Rev. Sci. Instrum.* 90, 013505. doi:10.1063/1.5049519

Laakso, H., Perry, C., McCaffrey, S., Herment, D., Allen, A. J., Harvey, C. C., et al. (2010). "Cluster active archive: Overview," in *The cluster active archive*. Editors H. Laakso, M. Taylor, and C. P. Escoubet (Dordrecht, Netherlands: Springer Netherlands), 3–37

Lance, G. N., and Williams, W. T. (1967). A general theory of classificatory sorting strategies: 1. Hierarchical systems. *Comput. J.* 9, 373–380. doi:10.1093/comjnl/9.4.373

Le, L., Patterson, A., and White, M. (2018). "Supervised autoencoders: improving generalization performance with unsupervised regularizers," in *Advances in neural information processing systems* (Red Hook, NY: Curran Associates, Inc.), Vol. 31, 107–117.

Liu, C. M., Fu, H. S., Liu, Y. Y., Wang, Z., Chen, G., Xu, Y., et al. (2020). Electron pitch-angle distribution in earth's magnetotail: pancake, cigar, isotropy, butterfly, and rolling-pin. *J. Geophys. Res. Space Phys.* 125, e2020JA027777. doi:10.1029/2020JA027777

Lui, A. T. Y. (1987). *Road map to magnetotail domains*. Baltimore, MD: John Hopkins University Press, 3–5.

Lukasovã, A. (1979). Hierarchical agglomerative clustering procedure. *Pattern Recogn.* 11, 365–381. doi:10.1016/0031-3203(79)90049-9

McLachlan, G., and Peel, D. (2000). *ML fitting of mixture models*. Hoboken, NJ: John Wiley & Sons, Ltd., Chap. 2, 40–80. doi:10.1002/0471721182.ch2

Øieroset, M., Lin, R. P., Phan, T. D., Larson, D. E., and Bale, S. D. (2002). Evidence for electron acceleration up to ~300 keV in the magnetic reconnection diffusion region of earth's magnetotail. *Phys. Rev. Lett.* 89, 195001. doi:10.1103/PhysRevLett.89.195001

Pedregosa, F., Varoquaux, G., Gramfort, A., Michel, V., Thirion, B., Grisel, O., et al. (2011). Scikit-learn: machine learning in Python. *J. Mach. Learn. Res.* 12, 2825–2830. doi:10.5555/1953048.2078195

Peerenboom, K., Parente, A., Kozák, T., Bogaerts, A., and Degrez, G. (2015). Dimension reduction of non-equilibrium plasma kinetic models using principal component analysis. *Plasma Sources Sci. Technol.* 24, 025004. doi:10.1088/0963-0252/24/2/025004

Rème, H., Aoustin, C., Bosqued, J. M., Dandouras, I., Lavraud, B., Sauvaud, J. A., et al. (2001). First multispacecraft ion measurements in and near the Earth's magnetosphere with the identical Cluster ion spectrometry (CIS) experiment. *Ann. Geophys.* 19, 1303–1354. doi:10.5194/angeo-19-1303-2001

Ruder, S. (2016). An overview of gradient descent optimization algorithms. arXiv e-prints.

Sakurada, M., and Yairi, T. (2014). "Anomaly detection using autoencoders with nonlinear dimensionality reduction," in Proceedings of the MLSDA 2014 2nd workshop on machine learning for sensory data analysis, Gold Coast, Australia, December 2, 2014. (New York, NY: Association for Computing Machinery), 4–11. doi:10.1145/2689746.2689747

Sharma, A. S., and Curtis, S. A. (2005). *Magnetospheric multiscale mission*. Dordrecht, Netherlands: Springer Netherlands, 179–195. doi:10.1007/1-4020-3109-28

Walsh, A. P., Fazakerley, A. N., Forsyth, C., Owen, C. J., Taylor, M. G. G. T., and Rae, I. J. (2013). Sources of electron pitch angle anisotropy in the magnetotail plasma sheet. *J. Geophys. Res. Space Phys.* 118, 6042–6054. doi:10.1002/jgra.50553

Walsh, A. P., Owen, C. J., Fazakerley, A. N., Forsyth, C., and Dandouras, I. (2011). Average magnetotail electron and proton pitch angle distributions from cluster PEACE and CIS observations. *Geophys. Res. Lett.* 38, 1029. doi:10.1029/2011GL046770

Ward, J. H. (1963). Hierarchical grouping to optimize an objective function. *J. Am. Stat. Assoc.* 58, 236–244. doi:10.1080/01621459.1963.10500845

Zeiler, M. D. (2012). Adadelta: an adaptive learning rate method. arXiv e-prints.

Conflict of Interest: The authors declare that the research was conducted in the absence of any commercial or financial relationships that could be construed as a potential conflict of interest.

frontiers in Astronomy and Space Sciences

METHODS
published: 19 November 2020
doi: 10.3389/fspas.2020.595929

A Mission Concept to Determine the Magnetospheric Causes of Aurora

Joseph E. Borovsky[1]*, *Gian Luca Delzanno*[2] and *Michael G. Henderson*[3]

[1]Center for Space Plasma Physics, Space Science Institute, Boulder, CO, United States, [2]Theoretical Division, Los Alamos National Laboratory, Los Alamos, NM, United States, [3]Intelligence and Space Research Division, Los Alamos National Laboratory, Los Alamos, NM, United States

Insufficiently accurate magnetic-field-line mapping between the aurora and the equatorial magnetosphere prevents us from determining the cause of many types of aurora. An important example is the longstanding question of how the magnetosphere drives low-latitude (growth-phase) auroral arcs: a large number of diverse generator mechanisms have been hypothesized but equatorial magnetospheric measurements cannot be unambiguously connected to arcs in the ionosphere, preventing the community from identifying the correct generator mechanisms. Here a mission concept is described to solve the magnetic-connection problem. From an equatorial instrumented spacecraft, a powerful energetic-electron beam is fired into the atmospheric loss cone resulting in an optical beam spot in the upper atmosphere that can be optically imaged from the ground, putting the magnetic connection of the equatorial spacecraft's measurements into the context of the aurora. Multiple technical challenges that must be overcome for this mission concept are discussed: these include spacecraft charging, beam dynamics, beam stability, detection of the beam spot in the presence of aurora, and the safety of nearby spacecraft.

Keywords: aurora, space experiments, magnetosphere, ionosphere, electron beams

OPEN ACCESS

Edited by:
Luca Sorriso-Valvo, National Research Council, Italy

Reviewed by:
Octav Marghitu, Space Science Institute, Romania
Hui Li, National Space Science Center (CAS), China

***Correspondence:**
Joseph E. Borovsky
jborovsky@spacescience.org

Specialty section:
This article was submitted to Space Physics, a section of the journal Frontiers in Astronomy and Space Sciences

Received: *18 August 2020*
Accepted: *28 September 2020*
Published: *19 November 2020*

Citation:
Borovsky JE, Delzanno GL and Henderson MG (2020) A Mission Concept to Determine the Magnetospheric Causes of Aurora. Front. Astron. Space Sci. 7:595929. doi: 10.3389/fspas.2020.595929

INTRODUCTION

One of the unsolved problems of magnetospheric physics is the cause of the various types of auroral forms (Lanchester, 2017; Denton, 2019). This is particularly the case for auroral arcs (Denton et al., 2016; Borovsky et al., 2020a), where an unknown generator mechanism in the equatorial and near-equatorial magnetosphere extracts power and current from the magnetosphere to drive an auroral arc that dissipates energy in the ionosphere and atmosphere. This is sketched in **Figure 1**. A large number of diverse generator mechanisms have been hypothesized (e.g., Borovsky, 1993; Haerendel, 2011; Haerendel, 2012; Borovsky et al., 2020b) but equatorial magnetospheric measurements have not been unambiguously connected to arecs in the ionosphere, preventing scientists from identifying the correct generator mechanisms. For quiescent auroral arcs, even the form of energy that is extracted from the magnetosphere (magnetic energy, ion thermal energy, electron thermal energy, flow kinetic energy, ...) is not known. The auroral community understands the near-Earth acceleration processes quite well (e.g., field-aligned potentials and Alfven-wave electron acceleration) but does not understand the equatorial energy-conversion processes driving these near-Earth processes; nor does the community understand the origin of the Alfvenic energy. The aurora is a manifestation of complex processes operating in the distant magnetosphere; the desire to use optical images of the aurora as television-screen view of magnetospheric processes (e.g., Akasofu, 1965; Mende, 2016a;

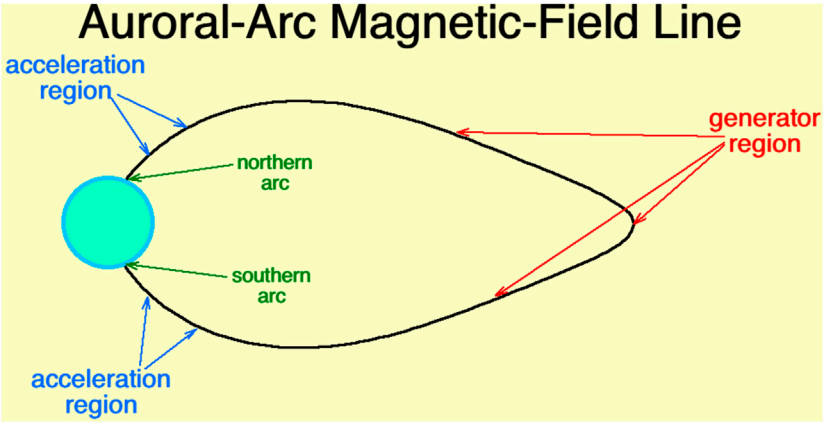

FIGURE 1 | A sketch of the equatorial magnetospheric spacecraft firing an electron beam into the northern loss cone where the beam spot can be located by a ground-based camera. Conjugate northern and southern auroral arcs are noted in the upper atmosphere, the near-Earth acceleration regions for auroral-arc electrons are indicated, and the equatorial and near-equatorial regions where the auroral-arc generator mechanisms operate are noted.

Mende, 2016b) is impeded by not knowing what processes act to create the various auroral forms.

The foundation of the auroral-cause problem is an inability to unambiguously connect equatorial magnetospheric measurements to the various auroral forms. Static magnetic models of the magnetosphere (e.g., Tsyganenko, 1989; Tsyganenko and Sitnov, 2007; Sitnov et al., 2008) are not sufficiently accurate to magnetically map ionospheric features into the equatorial electron plasma sheet, particularly into the high-Reynolds-number magnetotail (Borovsky et al., 1997; Voros et al., 2004; El-Alaoui et al., 2010; Stepanova et al., 2011; El-Alaoui et al., 2012). Tests of the accuracy of magnetic-field-line mapping with the standard magnetic-field models have found very large errors for the nightside magnetosphere (Thomsen et al., 1996; Weiss et al., 1997; Ober et al., 2000; Shevchenko et al., 2010; Nishimura et al., 2011), even in the quasi-dipolar regions. For quiescent, low-latitude (growth-phase) auroral arcs there are two schools of thought about the equatorial location of the source of the arc: one school assume that the arc is in the dipolar portion of the nightside magnetosphere (e.g., McIlwain, 1975; Meng et al., 1979; Kremser et al., 1988; Mauk and Meng, 1991; Pulkkinen et al., 1991; Lu et al., 2000; Motoba et al., 2015) and a second school has the source of the arc in the stretched magnetotail (e.g., Yahnin et al., 1997; Yahnin et al., 1999; Birn et al., 2004a; Birn et al., 2004b; Birn et al., 2012; Sergeev et al., 2012; Hsieh and Otto, 2014): our ability to map magnetic-field lines in the nightside magnetosphere is insufficient to determine which is the correct location.

Developing the technology to attain accurate "Magnetosphere-to-Ionosphere Field-Line-Tracing Technology" has been cited as an "instrument development need and emerging technology" necessary for the future of space science (National Research Council, 2012). For several decades a team of researchers centered around Los Alamos National Laboratory has worked to develop a viable spacecraft mission to unambiguously determine the magnetic connection between equatorial-magnetospheric measurements and optical auroral observations (Borovsky et al., 1998; Borovsky, 2002; NASA, 2003; NASA, 2006; Delzanno et al., 2016; Borovsky and Delzanno, 2019; Borovsky et al., 2020c). That research team has consisted of auroral observers, magnetospheric instrument designers, optical physicists, ionospheric physicists, plasma physicists, spacecraft systems scientists, and two compact-accelerator design groups. That mission concept (and the technical challenges that it must overcome) is the focus of this brief report.

THE MISSION CONCEPT: AN ELECTRON BEAM ILLUMINATING THE MAGNETIC CONNECTION BETWEEN AN EQUATORIAL MAGNETOSPHERIC SPACECRAFT AND THE ATMOSPHERE/IONOSPHERE

As sketched in **Figure 1**, the mission concept is for a magnetospheric spacecraft to carry an electron accelerator, to fire an electron beam along the magnetospheric magnetic field into the atmospheric loss cone, and with a ground-based camera to optically image the beam spot in the upper atmosphere. If that is accomplished then it is unambiguously known that a measurement taken by the magnetospheric spacecraft magnetically connects to the location in the ionosphere where the beam spot is imaged (Note that one can also approximately account for the eastward curvature-drift shift of the electron beam to more-accurately identify the magnetic location of the spacecraft.)

There are a number of challenges with this simple concept, and a good deal of research has been performed to overcome those difficulties: the technical challenges include spacecraft charging, beam aiming, beam dynamics and stability, and the detection of the beam spot in the presence of aurora. The major challenges and the associated mission-design tradeoffs are discussed in **Sections 3 and 4**.

Mission concepts have been examined that involve either (A) a single magnetospheric spacecraft making measurements and carrying an electron accelerator or (B) a swarm of measuring spacecraft with one member of the swarm carrying the electron accelerator. The spacecraft carrying the accelerator will also carry a power-storage system and a plasma contactor (for spacecraft-charging mitigation). The purpose of a swarm is to measure perpendicular-to-**B** gradients in the magnetosphere, which are important for diverting perpendicular magnetospheric currents into field-aligned currents, a critical part of the processes of driving of auroral arcs; the perpendicular gradients of interest are ion-pressure gradients, electron-pressure gradients, mass-density gradients, temperature gradients, flow shear, and gradients in the field strength, and the cross products of the various gradients are of interest (cf. **eq. 12** of Strangeway 2012 or **eq. 1** of Borovsky et al. 2020b). As analyzed in Borovsky et al. 2020c, the measurement requirements for quiescent auroral arcs in the equatorial magnetosphere appear in **Table 1**. For some theories of auroral arcs (e.g., Schindler and Birn, 2002; Birn et al., 2004a; Birn et al., 2012; Yang et al., 2013; Hsieh and Otto, 2014; Coroniti and Pritchett, 2014), Hall effects are important and so measuring both the perpendicular ion flow and the perpendicular electron flow is desirable; this can be accomplished by measuring both the ion flow and the electric field.

Two mission concepts have been considered. The first, Magnetosphere-Ionosphere Observatory (MIO) (Borovsky et al., 1998; Borovsky, 2002) consists of a tight (100's of km) swarm of spacecraft in the equator at geosynchronous orbit (6.6 R_E where R_E is the radius of the Earth), with a single ground-based observatory in the vicinity of the swarm's magnetic footpoints. In **Figure 2** the location at 100 km altitude of the magnetic footpoint of a spacecraft in the geographic equator at geosynchronous orbit is estimated using the T89 (Tsyganenko, 1989) and the IGRF (Maus et al., 2005) magnetic-field models. The spacecraft is located in the "Alaska sector" of geosynchronous orbit where the geographic and geomagnetic equators are close to each other. The "observatory" in the figure is located at Eagle, Alaska (64°47′ N,121°12′W). The red circles in **Figure 2** are the angle from zenith where the 100 km altitude is seen by the observatory. In **Figure 3** a similar plot is made for a spacecraft in the geographic equator at geosynchronous orbit in the "Scandinavian sector". The ground-based observatory would have at least one camera dedicated to beam spot imaging, although, owing to uncertainty in the estimation of the magnetic-footpoint location using magnetic-field models, a network of beamspotting cameras around the observatory location will probably be needed. The observatory would have cameras for auroral imaging and other instrumentation for ionospheric physics. In the MIO mission concept a ground-based radar could be used to help locate the beam spot (e.g., Izhovkina et al., 1980; Uspensky et al., 1980; Zhulin et al., 1980; Marshall et al., 2014); additionally the radar could be used for physics studies with the electron beam as an element of upper-atmosphere experiments. Other instrumentation at the observatory could be ionosondes, an ionospheric heater, a wave transmitter, and a magnetometer network. An important aspect of the MIO mission concept is the ability to concentrate ground-based infrastructure at a single location.

TABLE 1 | Magnetospheric measurement requirements for quiescent arcs.

Measurement quantity	Typical value	Desired accuracy
Proton number density	1 cm^{-3}	0.1 cm^{-3}
Proton temperature	10 keV	1 keV
Proton pressure	1.6 nPa	0.16 nPa
Proton pressure anisotropy	0.16 nPa	–
Electron number density	1 cm^{-3}	0.1 cm^{-3}
Electron temperature	2 keV	200 eV
Electron pressure	0.32 nPa	0.03 nPa
Electron pressure anisotropy	0.03 nPa	–
Proton flow along arc	150 km/s	15 km/s
Electron flow along arc	150 km/s	15 km/s
Proton or electron flow across arc	6.6 km/s	1.5 km/s
Magnetic-field direction vector	–	0.5°
Magnetic-field strength	80 nT	1 nT

The second mission concept, called connections (Borovsky et al., 2020c), has a swarm of spacecraft in an eccentric orbit and takes advantage of the Canadian TREx (Transition Region Explorer) (Spanswick et al., 2018) network of auroral cameras. Orbits are chosen with periods of 24 h so that the magnetic footpoint of the swarm wanders over Western Canada with a 24-h period. A 5 R_E by 8 R_E orbit was studied for its desirable footpoint locations (Borovsky et al., 2020c); note with an 8-R_E apogee, the spacecraft swarm can magnetically map further downtail than 8 R_E owing to orbital inclination and dipole tilt. The approximate magnetic-footpoint locations for the 5 R_E by 8 R_E 24-h orbit are shown as the blue curve in **Figure 4** and the approximate footpoint locations of a 4 R_E by 8 R_E 24-h orbit are also shown as the yellow curve in **Figure 4**. In **Figure 4** the field-of-views of the individual (Transition Region Explorer) TREx cameras are indicated as the red circles. An eccentric 24 h orbit can better sample the stretched-magnetotail portion of the nightside magnetosphere than can a circular geosynchronous orbit.

CHALLENGES TO OVERCOME

Four challenges that must be overcome for this magnetospheric-electron-beam mission concept are discussed in this section.

Spacecraft Charging

The most critical issue for operating a high-power electron beam from an ungrounded spacecraft in the tenuous magnetospheric plasma is spacecraft charging. The beam must deposit sufficient power (~5 kW) in the upper atmosphere to be seen in the presence of ongoing aurora: if the beam energy is 50 keV then a beam current of 100 mA is required and if the beam energy is 1 MeV then a beam current of 5 mA is required. Firing the beam will result in a fraction of a Coulomb of negative being removed from the spacecraft in a time on the order of 1 s. A substantial computer-simulation-based research effort (Delzanno et al.,

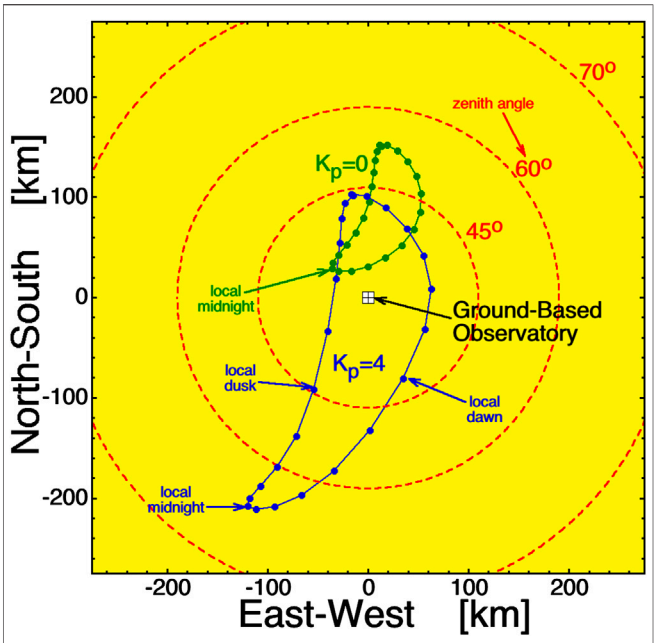

FIGURE 2 | Looking down onto Alaska, the approximate location each hour of the day in Winter of the magnetic footpoint at 100 km altitude of a spacecraft in the geosynchronous orbit geographic equator is plotted. The green points are for Kp = 0 and the blue points are for Kp = 4. The observatory is located at Eagle, Alaska. The red circles are the zenith angle of the 100 km altitude as seen from the ground-based observatory.

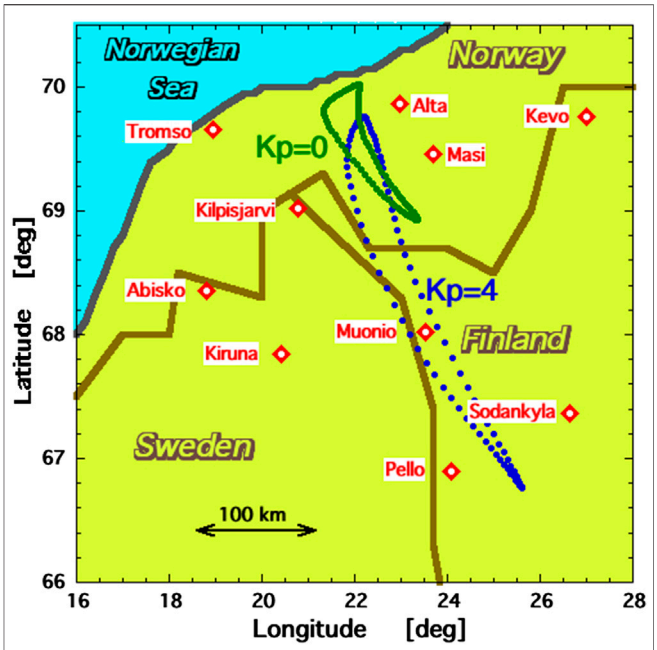

FIGURE 3 | Looking down onto Scandinavia, the approximate location each hour of the day in Winter of the magnetic footpoint at 100 km altitude of a spacecraft in the geosynchronous orbit geographic equator is plotted. The green points are for Kp = 0 and the blue points are for Kp = 4.

2015a; Delzanno et al., 2015b; Delzanno et al., 2016; Lucco Castello et al., 2018), supported by laboratory experiments (Miars et al., 2020), has demonstrated that the operation of a plasma contactor releasing a high-density charge-neutral plasma plume before and during a beam firing can greatly mitigate the charging of the spacecraft during the beam operation. Contrary to prior discussion of an emitted plasma plume acting to collect charge from the ambient plasma (e.g., Hastings and Blandino, 1989; Gerver et al., 1990; Williams and Wilbur, 1990; Davis et al., 1991), the research effort demonstrated that the surface of the plasma plume acts as an ion emitter, producing an ion current equal to the current of the electron beam.

Getting the Beam to the Atmosphere

Getting the electron beam from the spacecraft in the magnetospheric equator to the atmosphere involves aiming the beam into the atmospheric loss cone, fitting the beam within the loss cone, ensuring that the propagating beam is stable, and ensuring that the propagating beam electrons are not scattered by magnetospheric plasma waves.

Assuming that the magnetic-field strength in the auroral upper atmosphere is ~0.5 Gauss, the radius of the atmospheric loss cone is 2.5° if the spacecraft is in a 100 nT field (e.g., in geosynchronous orbit) and the radius is 1.1° if the spacecraft is in a 20 nT field (e.g., in the stretched magnetotail). Knowledge of the direction of the ambient magnetic field to an accuracy of about 0.5° is needed, and an ability to aim the beam with an accuracy of about 0.5° is also needed. A complication to the aiming into the loss cone occurs if the electron beam is very energetic: finite-gyroradii effects shift the direction of the loss cone eastward (for electrons) from the local magnetic-field direction (Il'ina et al., 1993; Mozer, 1966; Porazik et al., 2014; Powis et al., 2019; Willard et al., 2019; Borovsky et al., 2020c). For a dipole magnetic field the magnitude of this eastward angular shift is easily predictable (Mozer, 1966; Borovsky et al., 2020c), but for non-dipolar magnetic fields this shift is not predictable and a space experiment would need to determine the loss-cone shift by repeatedly test firing the electron beam with differing amounts of eastward shift while ground cameras work to detect the beam spot. If onboard energy-storage resources are limited, this would not be desirable, and if the optical beam-spot-location image analysis is not instantaneous, this trial-and-error methodology cannot be implemented.

After the electron beam is emitted from the accelerator and as it travels along the Earth's magnetic field, the nonzero net negative space charge of the beam acts to repulsively accelerate beam electrons transverse to the magnetic field; this transverse acceleration results in a spread of pitch angles of the beam electrons, turning a narrowly focused beam into a "shotgun" (cf. **Appendix B** of Borovsky, 2002). The space charge per unit length of the beam Q/L is given by $Q/L = I_{beam}/v_{beam}$, where I_{beam} is the current of the beam and v_{beam} is the speed of the beam. The beam power P_{beam} is $P_{beam} = I_{beam}V_{beam}$, where V_{beam} is the beam voltage (accelerator energy). The speed of the beam increases with the beam voltage. For the same amount of beam power, a high-voltage beam has less current and higher speed, hence it has much less charge per unit length Q/L, and the space-

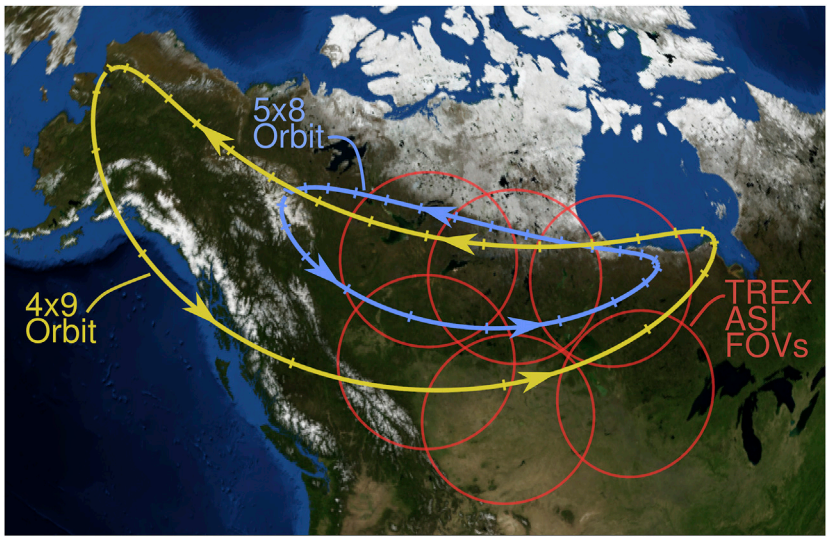

FIGURE 4 | The estimated magnetic footpoints over Canada and the (Transition Region Explorer) TREx fields of view of two elliptical orbits: a 5 R_E × 8 R_E 24 hr-period orbit (blue) and a 4 R_E × 9 R_E 24 h orbit (yellow). The arrows on the footpoint curves are the temporal direction of the movement of the footpoint relative to the ground. The red circles are the fields-of-view at 100 km altitude of the present (Transition Region Explorer) TREx cameras. The low-latitude portions of the footpoint curves correspond to spacecraft perigee's and the hash marks on the footpoint curves are at 1 h intervals in the 24 h orbits.

charge transverse spreading of the beam is much less. Figure 2 of Borovsky et al., (2020c) looks at the maximum power of a beam that will stay within the loss cone as a function of the beam voltage. Greater beam voltage is very advantageous from the beam-spreading point of view.

Calculating the stability of the electron beam propagating through the ambient magnetospheric plasma is an ongoing area of research. Fortunately, the powerful electrostatic two-stream instabilities are greatly weakened by the fact that the beam has a small cylindrical cross section (Galvez and Borovsky, 1988). Relativistic electron beams have been calculated to be stable to electromagnetic hose and filamentation instabilities (Gilchrist et al., 2001; Neubert and Gilchrist, 2002; Neubert and Gilchrist, 2004). Experimentally, similar beams have been detected after long-distance propagation through the magnetosphere. Beams with energies of up to 40 keV were propagated long distances through the magnetosphere in the Echo series of experiments (Hallinan et al., 1990; Winckler, 1992) and electron beams of 27 keV, 0.5 Amp and 15 keV, 0.5 Amp on the two ARAKS experiments were propagated 8.2 R_E through the magnetosphere without disruption (Pellat and Sagdeev, 1980; Lavergnat, 1982).

Finally, an issue of ongoing research is estimating the amount of pitch-angle scattering that beam electrons will undergo from the action of ambient magnetospheric plasma waves when the spacecraft is in various locations of the magnetosphere during different levels of geomagnetic activity. The degree of pitch-angle scattering will vary significantly with the beam voltage. At higher (relativistic) beam voltages electromagnetic ion-cyclotron (EMIC) waves and whistler-mode chorus are of concern, as is field-line curvature acting to scatter the beam. At lower beam voltages whistler-mode chorus and electromagnetic electron-cyclotron waves are of concern. Section 6.3 of Borovsky et al. (2020c) provides some preliminary estimates of the amount of pitch-angle scattering of beam electrons in the nightside magnetosphere: those estimates are favorable for the beam surviving from the equator to the atmosphere. Note also that (electromagnetic ion-cyclotron) EMIC waves are prevalent in the noon and afternoon sectors and not prevalent in the nightside auroral zone (Clausen et al., 2011; Usanova et al., 2012).

Detecting the Beam Spot

To produce a beam spot that is optically detectable from the ground in the presence of active aurora, a beam power of 5 kW or more needs to be deposited in the atmosphere. Each 1 kW of beam power results in about 1.1 W of 4278 Å emission [Bryant et al., 1970) and about 3 W of 3914 Å emission. The spectral lines emitted by the beam spot will be the same spectral lines as emitted by the electron aurora. The beam spot will be cylindrical, 10's of m in diameter across the magnetic field and ~10 km long along the magnetic field; this will produce a multi-pixel streak in the camera images. The technology of optically detecting the illuminated footpoint from the ground has been verified: electron beams with less than 5 kW of power have been optically detected from the ground after they have propagated through the magnetosphere into the upper atmosphere. Two examples are the detection of a 3.4 kW beam by Davis et al. (1980) during the NASA 12.18 NE beam experiment and the detection of a 2.4 kW beam in the Echo-4 experiment by Hallinan et al. (1990) using a ground-based image-orthicon television. In the Echo-4 experiment, the beamspot was imaged after the beam had propagated twice through the magnetosphere at L = 6.5. To identify the beam spot in the presence of aurora, an on-off temporal blink pattern of beam firings must be used along

with temporal processing of the camera images to locate the blinking streak. If the mission has a "scientist in the loop" commanding the firing of the beam as the beam spot crosses critical auroral features, the image processing must be automatic and prompt.

For beams of 10's of keV the beam spot altitude is around 90–100 km; for beams of 1 MeV the beam spot altitude is around 60 km. If the beam has a narrow spread of pitch angles, the beam spot altitude can be raised by aiming the beam away from the center of the loss cone. At 60 km there is some collisional quenching of the 3914 and 4278 Å prompt emission bands (Marshall et al., 2014; Borovsky et al., 2020c), so more beam power is required to image the beam spot. Unless it is overhead of the camera, a beam spot at 60 km altitude will also suffer more extinction from Rayleigh scattering (Penndorf, 1957; International Telephone and Telegraph Corporation, 1977), again requiring more beam power.

Safety of Other Magnetospheric Spacecraft

Since there are other spacecraft in orbit around the Earth, an important aspect to consider is whether the electron beam emitted could intercept another spacecraft and induce catastrophic charging on it. After the beam is emitted, it expands and contracts periodically with time due to space-charge and Lorentz forces as well as due to spreading in pitch angle and energy due to the electron accelerator design (Borovsky, 2002; Powis et al., 2019). As a result the beam current density will change significantly along the beam path. Any mission design will need a beam-safety plan. To estimate the beam flux to another spacecraft, the beam dynamics must be modeled and beam-connection dwell times with other spacecraft must be calculated using orbital considerations.

From preliminary calculations of the dynamics of a 1 MeV 10 mA beam in the dipolar magnetosphere with a criterion that the current flux to a second spacecraft must be less than 10^{-6} A/m^2 yields a "current safety distance" of 0.5 R_E along the Earth's magnetic field from the accelerator to another spacecraft. In the tenuous plasma of the magnetosphere an electron beam flux of 10^{-6} A/m^2 would only induce ~1 kV of spacecraft charging to the second spacecraft.

MAJOR TRADEOFFS FOR A MISSION

There are many tradeoffs that must be made in designing a mission. A major tradeoff is whether to have a single-observatory geosynchronous mission or an elliptic orbit distributed-camera-network mission (cf. Sect. 2). Two other major tradeoffs are discussed below.

Relativistic vs. Nonrelativistic Electron Beams

The accelerator technology for relativistic (~MeV) vs. nonrelativistic (10's-of-keV) beams differs:10's-of-keV beams can be produced with direct-current electron guns that accelerate the electrons through a static potential drop whereas MeV beams must be produced with a radio-frequency electron accelerator that accelerates the electrons with a propagating wavefront. Direct-current electron guns with 10's of keV energies and 10's of kW powers have been flown in space numerous times (Winckler et al., 1975; O'Neil et al., 1978; Rappaport et al., 1993; Prech et al., 1995; McNutt et al., 1995; Prech et al., 2018), while a radio-frequency accelerator has only been flown once (a 1-MeV H^- beam) (Pongratz, 2018). Designs for compact space-based relativistic-electron accelerators are underway (Lewellen et al., 2019) and spaceflight tests of the accelerator concepts are planned (Reeves et al., 2020).

The advantages of a relativistic electron accelerator over a 10's-of-keV electron gun are 1) lower beam space charge for the same beam power, resulting in a beam with less angular spread to more-easily fit into the loss cone, and 2) lower total charge removed from the spacecraft in a beam pulse, requiring less-stringent spacecraft-charging mitigation. For beam energies below a few 10's of keV, the space charge of the beam drastically limits the amount of beam power that can be delivered into the loss cone.

The disadvantages of a relativistic accelerator compared with a 10's-of-keV electron gun are 1) a lower-altitude beam spot subject to quenching, 2) for a non-dipole magnetic field the location of the loss cone is not known, 3) more difficulty in steering the beam mechanically or electrostatically, 4) there can be accelerator-thermal issues that de-tune the radio-frequency cavities after several beam firings, and 5) there are more-critical safety considerations for other spacecraft. For beams with energies above about 1 MeV, the loss-cone shift becomes severe.

The relativistic vs. nonrelativistic beams will also have tradeoffs concerning beam stability and scattering and the accelerator and gun will have tradeoffs concerning the power-conversion efficiency and mass of the required energy-storage system. For any mission with a powerful electron beam, energy storage will require substantial spacecraft mass.

Spinning vs. 3-Axis Stabilized Spacecraft

A spinning spacecraft is better, in general, for measuring plasma properties and fields. Spinning has the distinct advantage that offsets in the magnetometer can be corrected, resulting in a more-accurate determination of the magnetic field direction for beam aiming. If a relativistic accelerator is used, which will have a length of 1 m or so, mechanically steering the accelerator into the moving loss cone seen by a spinning spacecraft will be challenging. At relativistic energies, electrostatic steering of the electron beam after it exits the accelerator is very limited in angle.

A 3-axis stabilized spacecraft makes it easier to direct the beam into the loss cone, particularly if a long (0.5-s or 1-s) beam pulse is used. A de-spun platform on a spinning spacecraft is another option.

Note that if an electron drift instrument (Torbert et al., 2016) is used to measure the electric field, that instrument works in concert with a magnetometer and magnetometer offsets can be detected and corrected, even on a non-spinning spacecraft.

OTHER SCIENCE

Most of the work on the development of this magnetospheric-electron-beam mission concept has been motivated by the desire to understand the generator mechanisms of low-latitude quiescent auroral arcs (Borovsky, 2002; Delzanno et al., 2016; Borovsky et al., 2020c). However, such a beam experiment could be used to explore a wide variety of scientific problems.

The magnetospheric causes of various other types of aurora could be investigated if there is appropriate instrumentation on the magnetospheric accelerator spacecraft or the swarm spacecraft. Discerning the causes of other aurora may require wave measurements, cold-ion and cold-electron measurements, and particle-anisotropy measurements: examples of this would be the diffuse and pulsating aurora. Other auroral forms include undulations of the equatorward auroral boundary, omega bands, torches, black aurora, and patches. Investigating high-latitude auroral forms such as streamers or high-latitude Alfvenic arcs will require a spacecraft orbit that is eccentric.

The mapping of boundaries and regions between the magnetosphere and the ionosphere could be unambiguously performed with a magnetospheric-electron-beam spacecraft, provided it is instrumented to identify those boundaries and regions. Of interest are the mapping to the ionosphere of a) the inner edge of the electron plasma sheet, b) the remnant layer, c) the plasmapause, d) detached plasmasphere regions, e) ion-isotropy boundaries, f) substorm-injection boundaries, and g) the Earthward edge of the cross-tail current sheet. The magnetospheric boundaries (a)–(f) are clearly seen at the geosynchronous-orbit equator: the magnetic field at geosynchronous orbit often exhibits a stretched-tail morphology at local midningt (cf. Figure 11 of Borovsky and Denton (2010)) but boundary (g) is ambiguous to detect in the magnetosphere. Conversely, the mapping of ionospheric troughs out into the magnetosphere is of interest.

The magnetic connections between magnetospheric and ionospheric processes such as SAPS, SAID, STEVE, convection reversals, and bursty bulk flows could be determined with certainty. An eccentric orbit provides more-regular access to these various phenomena, in particular to bursty bulk flows.

Magnetosphere-ionosphere coupling can be studied by comparing temporal onsets of convection in the magnetosphere (via spacecraft flow measurements) with temporal onsets of ionospheric convection (measured, for example, by the SuperDARN radar network (Greenwald et al., 1995; Baker et al., 2011; Bristow et al., 2016)) and could answer questions about when and where the magnetosphere drives ionospheric convection and when and where the ionosphere drives magnetospheric convection.

Finally, there is an extensive literature describing how energetic electron beams could be used to study mesospheric chemistry (Neubert et al., 1990; Marshall et al., 2019), atmospheric electricity (Banks et al., 1990; Neubert et al., 1990; Neubert and Gilchrist, 2004; Marshall et al., 2019; Sanchez et al., 2019; Borovsky et al., 2020c), atmospheric electron-attachment physics and electrical conductivity (Banks et al., 1990; Neubert et al., 1996; Neubert and Gilchrist, 2004; Borovsky, 2017), and plasma-wave generation (Carlsten et al., 2018; Delzanno and Roytershteyn, 2019; Reeves et al., 2020).

DATA AVAILABILITY STATEMENT

The raw data supporting the conclusions of this article will be made available by the authors, without undue reservation, to any qualified researcher.

AUTHOR CONTRIBUTIONS

All authors performed research on this mission concept and contributed information for the manuscript.

FUNDING

Work at the Space Science Institute was supported by the NASA Heliophysics LWS program via award NNX16AB75G, and by the NSF GEM Program via grant AGS-2027569, by the NASA Heliophysics Guest Investigator Program via award NNX17AB71G, by the NSF SHINE program via grant AGS-1723416.

ACKNOWLEDGMENTS

The authors thank Phil Barker. Joachim Birn, Bruce Carlsten, Mike Collier, Eric Donovan, Eric Dors, Phil Fernandes, Reiner Friedel, Brian Gilchrist, Ray Greenwald, Herb Funsten, Gerhard Haerendel, Mike Holloway, Larry Kepko, Dave Klumpar, Dave Knudsen, Brian Larsen, Omar Leon, John Lewellen, Grant Mairs, Bob Marshall, Barry Mauk, Dave McComas, Liz McDonald, Steve Mende, Tom Moore, Dinh Nguryen, Jeff Nielsen, Craig Pollock, Tuija Pulkkinen, John Raitt, Geoff Reeves, Vadim Roytershteyn, Mike Ruohoniemi, Ennio Sanchez, Howard Singer, Jan Sojka, Emma Spanswick, Steve Storms, Bob Strangeway, Don Thompson, Michelle Thomsen. Roy Torbert, Maria Usanova, Hans Vaith, and Brent White for their assistance in developing this mission concept and in overcoming its challenges. JEB was supported by the NASA Heliophysics LWS program via award NNX16AB75G, by the NSF GEM Program via grant AGS-2027569, by the NASA Heliophysics Guest Investigator Program via award NNX17AB71G, and by the NSF SHINE program via grant AGS-1723416. GLD was supported by the Los Alamos National Laboratory (LANL) Directed Research and Development (LDRD) Program under Project 20170423ER. LANL is operated by Triad National Security, LLC, for the National Nuclear Security Administration of the U.S. Department of Energy (DOE) under Contract 89233218CNA000001.

REFERENCES

Akasofu, S. I. (1965). The Aurora. *Sci. Amer.* 213(6), 55.

Baker, J. B. H., Ruohoniemi, J. M., Ribiro, A. J., Clausen, L. B. N., Greenwald, R. A., Frissell, N. A., et al. (2011). SuperDARN ionospheric space weather. *IEEE A&E Systems Mag.* 26:30–34.

Banks, P. M., Fraser-Smith, A. C., and Gilchrist, B. E. (1990). Ionospheric modification using relativistic electron beams. *AGARD Conference Proceedings* 485, (Loughton, United Kingdom: Specialised Printing Services Limited), 22-1–22-18.

Birn, J., Dorelli, J. C., Hesse, M., and Schindler, K. (2004a). Thin current sheets and loss of equilibrium: Three-dimensional theory and simulations. *J. Geophys. Res.* 109, A02217. doi:10.1029/2003ja010303

Birn, J., Schindler, K., and Hesse, M. (2012). Magnetotail Aurora Connection: The Role of Thin Current Sheets. *Geophys. Monogr. Ser.* 197, 337. doi:10.1029/2011gm001182

Birn, J., Schindler, K., and Hesse, M. (2004b). Magnetotail aurora connections: The role of thin current sheets. *Geophys. Monogr. Ser.* 197, 337. doi:10.1029%2F2011GM001182

Borovsky, J. E. (1993). Auroral arc thicknesses as predicted by various theories. *J. Geophys. Res.* 98, 6101. doi:10.1029/92ja02242

Borovsky, J. E., Birn, J., Echim, M. M., Fujita, S., Lysak, R. L., Knudsen, D. J., et al. (2020b). Quiescent discrete auroral arcs: A review of magnetospheric generator mechanisms, *Space Sci. Rev.* 216, 1. doi:10.1007/s11214-019-0619-5

Borovsky, J. E., Delzanno, G. L., Dors, E. E., Thomsen, M. F., Sanchez, E. R., Henderson, M. G., et al. (2020c). Solving the auroral-arc-generator question by using an electron beam to unambiguously connect critical magnetospheric measurements to auroral images. *J. Atmos. Sol. Terr. Phys.* 206, 105310. doi:10.1016/j.jastp.2020.105310

Borovsky, J. E., Delzanno, G. L., Valdivia, J. A., Moya, P. S., Stepanova, M., Birn, J., et al. (2020a). Outstanding questions in magnetospheric plasma physics: The Pollenzo view. *J. Atmos. Sol. Terr. Phys.* 208, 105377. doi:10.1016/j.jastp.2020.105377

Borovsky, J. E., and Delzanno, J. L. (2019). Space active experiments: The future. *Front. Astron. Space Sci.* 6, 31. doi:10.3389/fspas.2019.00031

Borovsky, J. E., and Denton, M. H. (2010). On the heating of the outer radiation belt to produce high fluxes of relativistic electrons: Measured heating rates at geosynchronous orbit for high-speed stream-driven storms. *J. Geophys. Res.* 115, A12206. doi:10.1029/2010ja015342

Borovsky, J. E. (2017). Electrical conductivity channels in the atmosphere produced by relativistic-electron microbursts from the magnetosphere. *J. Atmos. Sol. Terr. Phys.* 155, 22. doi:10.1016/j.jastp.2017.01.004

Borovsky, J. E., Elphic, R. C., Funsten, H. O., and Thomsen, M. F. (1997). The Earth's plasma sheet as a laboratory for flow turbulence in high-β MHD. *J. Plasma Phys.* 57, 1. doi:10.1017/s0022377896005259

Borovsky, J. E., Greenwald, R. A., Hallinan, T. J., Horwitz, J. L., Kelley, M. C., Klumpar, D. M., et al. (1998). The magnetosphere-ionosphere facility: a satellite cluster in geosynchronous orbit connected to ground-based observatories. *Eos Trans. Amer. Geophys Union.* 79 (45), F744.

Borovsky, J. E., (2002). The Magnetosphere-Ionosphere Observatory (MIO). Los Alamos National Laboratory https://www.lanl.gov/csse/MIOwriteup.pdf.

Bristow, W. A., Hampton, D. L., and Otto, A. (2016). High-spatial-resolution velocity measurements derived using Local Divergence-Free Fitting of SuperDARN observations *J. Geophys. Res. Space Phys.* 121, 1349. doi:10.1002/2015ja021862

Bryant, D. A., Courtier, G. M., Skovli, G., Lindalen, H. R., Aarsnes, K., and Måseide, K. (1970). Electron density and electron flux in a glow aurora. *J. Atmos. Terr. Phys.* 32, 1695. doi:10.1016/0021-9169(70)90175-3

Carlsten, B. E., Colestock, P. L., Cunningham, G. S., Delzanno, G. L., Dors, E. E., Holloway, M. A., et al. (2018). Radiation-belt remediation using space-based antennas and electron beams. *IEEE Trans. Plasma Sci.* 47, 2045. doi:10.1109%2FTPS.2019.2910829

Clausen, L. B. N., Baker, J. B. H., Ruohoniemi, J. M., and Singer, H. J. (2011). ULF wave characteristics at geosynchronous orbit during the recovery phase of geomagnetic storms associated with strong electron acceleration. *J. Geophys. Res. Space Phys.* 116, A09203. doi:10.1029/2011ja016823

Coroniti, F. V., and Pritchett, P. L. (2014). The quiet evening auroral arc and the structure of the growth phase near-Earth plasma sheet. *J. Geophys. Res. Space Phys.* 119, 1827. doi:10.1002/2013ja019435

Davis, T. N., Hess, W. N., Trichel, M. C., Wescott, E. M., Hallinan, T. J., Stenbaek-Nielsen, H. C., et al. (1980). Artificial aurora conjugate to a rocket-borne electron accelerator. *J. Geophys. Res.* 85, 1722. doi:10.1029/ja085ia04p01722

Davis, V. A., Katz, I., Mandell, M. J., and Parks, D. E. (1991). Model of electron collecting plasma contactors. *J. Spacecr. Rockets.* 28, 292–298. doi:10.2514/3.26243

Delzanno, G. L., Borovsky, J. E., Thomsen, M. F., Gilchrist, B. E., and Sanchez, E. (2016). Can an electron gun solve the outstanding problem of magnetosphere-ionosphere connectivity?. *J. Geophys. Res. Space Phys.* 121, 6769. doi:10.1002/2016ja022728

Delzanno, G. L., Borovsky, J. E., Thomsen, M. F., and Moulton, J. D. (2015a). Future beam experiments in the magnetosphere with plasma contactors: The electron collection and ion emission routes. *J. Geophys. Res. Space Phys.* 120, 3588. doi:10.1002/2014ja020683

Delzanno, G. L., Borovsky, J. E., Thomsen, M. F., Moulton, J. D., and MacDonald, E. A. (2015b). Future beam experiments in the magnetosphere with plasma contactors: How do we get the charge off the spacecraft?. *J. Geophys. Res. Space Phys.* 120, 3647. doi:10.1002/2014ja020608

Delzanno, G. L., and Roytershteyn, V. (2019). High-Frequency Plasma Waves and Pitch Angle Scattering Induced by Pulsed electron Beams. *J. Geophys. Res. Space Phys.* 124, 7543. doi:10.1029/2019ja027046

Denton, M. H., Borovsky, J. E., Stepanova, M., and Valdivia, J. A. (2016). Unsolved Problems of Magnetospheric Physics. *J. Geophys. Res.* 121, 10783. doi:10.1002/2016ja023362

Denton, M. H. (2019). Some unsolved problems of magnetospheric physics, in *Magnetospheres in the Solar System*. Washington, DC: AGU Books, in press.

El-Alaoui, M., Ashour-Abdalla, M., Richard, R. L., Goldstein, M. L., Weygand, J. M., and Walker, R. J. (2010). Global magnetohydrodynamic simulation of reconnection and turbulence in the plasma sheet. *J. Geophys. Res.* 115, A12236. doi:10.1029/2010ja015653

El-Alaoui, M., Richard, R. L., Walker, R. J., Goldstein, M. L., R. J., et al. (2012). Turbulence in a global magnetohydrodynamic simulation of the Earth's magnetosphere during northward and southward interplanetary magnetic field. *Nonlinear Process Geophys.* 19, 165. doi:10.5194/npg-19-165-2012

Galvez, M., and Borovsky, J. E. (1988). The electrostatic two-stream instability driven by slab-shaped and cylindrical beams injected into plasmas. *Phys. Fluids.* 31, 857. doi:10.1063/1.866767

Gerver, M. J., Hastings, D. E., and Oberhardt, M. R. (1990). Theory of plasma contactors in ground-based experiments and low earth orbit. *J. Spacecr. Rockets.*, 27 (4), 391. doi:10.2514/3.26156

Gilchrist, B. E., Khazanov, G., Krause, L., and Neubert, T. (2001). Study of Relativistic electron Beam Propagation in the Atmosphere-Ionosphere-Magnetosphere. *Tech. Rep. AFRL-VS-TR-2001-1505, Air Force Research Lab*, Hanscom AFB, MA.

Greenwald, R. A., Baker, K. B., Dudeney, J. R., Pinnock, M., Jones, T. B., Thomas, E. C., et al. (1995). DARN/SuperDARN. *Space Sci. Rev.* 71, 761. doi:10.1007/bf00751350

Haerendel, G. (2012). Auroral Generators: A Survey. *Geophys. Monogr. Ser.* 197, 347. doi:10.1029/2011gm001162

Haerendel, G. (2011). Six auroral generators: A review. *J. Geophys. Res. Atmos.* 116, 347–354. doi:10.1029/2010ja016425

Hallinan, T. J., Winckler, J., Malcolm, P., Stenbaek-Nielsen, H. C., and Baldridge, J. (1990). Conjugate echoes of artificially injected electron beams detected optically by means of new image processing. *J. Geophys. Res. Space Phys.* 95, 6519. doi:10.1029/ja095ia05p06519

Hastings, D. E., and Blandino, J. (1989). Bounds on Current Collection From the Far Field by Plasma Clouds in the Ionosphere. *J. Geophys. Res.* 94, 2737. doi:10.1029/ja094ia03p02737

Hsieh, M.-S., and Otto, A. (2014). The influence of magnetic flux depletion on the magnetotail and auroral morphology during the substorm growth phase. *J. Geophys. Res. Space Physics.* 119, 3430. doi:10.1002/2013ja019459

Il'ina, A. N., Il'in, V. D., Kuznetsov, S. N., Yushkov, B. Y., Amirkhanov, I. V., and Il'in, I. V. (1993). Model of nonadiabatic charged-particle motion in the field of a magnetic dipole. *J. Exp. Theor. Phys. Lett.* 77, 246.

International Telephone and Telegraph Corporation (1977). Reference Data for Radio Engineers. *Sect. 28*, Fig. 32, Howard Sams and Co., Indianapolis, *For. Ind*.

Izhovkina, N. I., JKosik, J. C., Pyatsi, A. K., Reme, H., Saint-Marc, A., Sverdlov, J. L., et al. (1980). Comparison between experimental and theoretical conjugate points locations in the Araks experiments. *Ann. Geophys.* 36, 319.

Kremser, G., Korth, A., Ullaland, S. L., Perraut, S., Roux, A., Pedersen, A., et al. (1988). Field-aligned beams of energetic electrons (16 keV ≤E≤ 80 keV) observed at geosynchronous orbit at substorm onsets. *J. Geophys. Res.* 93, 14453. doi:10.1029/ja093ia12p14453

Lanchester, B. (2017). Some remaining mysteries in the aurora. *Astron. Geophys.* 58, 3–17. doi:10.1093/astrogeo/atx098

Lavergnat, J. (1982). The French-Soviet experiment ARAKS: Main results. in *Artificial* Particle Beams in Space Plasma Studies, B. Grandal (ed.), *pg. 87*, Plenum , New York.

Lewellen, J. W., Buechler, C. B., Carlsten, B. F., Dale, G. E., Holloway, M. A., Patrick, D., et al. (2019). Space borne electron accelerator design. *Front. Astron. Space Sci.* 6, 35. doi:10.3389/fspas.2019.00035

Lu, G., Brittnacher, M., Parks, G., and Lummerzheim, D. (2000). On the magnetospheric source regions of substorm-related field-aligned currents and auroral precipitation. *J. Geophys. Res. Atmos.* 105, 18483. doi:10.1029/1999ja000365

Lucco Castello, F., Delzanno, G. L., Borovsky, J. E., Miars, G., Leon, O., and Gilchrist, B. E. (2018). Spacecraft-charging mitigation of a high-power electron beam emitted by a magnetospheric spacecraft: simple theoretical model for the transient of the spacecraft potential. *J. Geophys. Res. Space Phys.* 123. 6424. doi:10.1029%2F1999JA000365

Marshall, R. A., Xu, W., Kero, A., Kabirzadeh, R., and Sanchez, E. (2019). Atmospheric effects of a relativistic electron beam injected from above: chemistry, electrodynamics, and radio scattering. *Front. Astron. Space Sci.* 6, 6. doi:10.3389/fspas.2019.00006

Marshall, R. A., Nicolls, M., Sanchez, E., Lehtinen, N. G., and Neilson, J. (2014). Diagnostics of an artificial relativistic electron beam interacting with the atmosphere. *J. Geophys. Res. Space Phys.* 119, 8560. doi:10.1002/2014ja020427

Mauk, B. H., and Meng, C.-I. (1991). The aurora and middle magnetospheric processes, in *Auroral Physics*, edited by C.-I. Meng, M. J. Rycroft, and L. A. Frank (Cambridge: Cambridge Press), 223.

Maus, S., Macmillan, S., Chrnova, T., Choi, S., Dater, D., Golovkov, V., et al. (2005). The 10th-generation International Geomagnetic Reference Field. *Geophys. J. Int.* 161, 561.

McIlwain, C. E. (1975). "Auroral electron beams near the magnetic equator," in *Physics of the Hot Plasma in the Magnetosphere*, Editor B. Hultqvist and L. Stenflo (New York, NY: Plenum), 91.

McNutt, R. L., Rieder, R. J., Keneshea, T. J., LePage, A. J., Rappaport, S. A., and Paulsen, D. E. (1995). Energy deposition in the upper atmosphere in the EXCEDE III experiment. *Adv. Space Res.* 15 (12), 13. doi:10.1016/0273-1177(95)00002-v

Mende, S. B. (2016a). Observing the magnetosphere through global auroral imaging: 1. Observables. *J. Geophys. Res. Space Phys.* 121, 10623. doi:10.1002/2016ja022558

Mende, S. B. (2016b). Observing the magnetosphere through global auroral imaging: 2. Observing techniques. *J. Geophys. Res. Space Phys.* 121, 10638. doi:10.1002/2016ja022607

Meng, C.-I., Mauk, B., and McIlwain, C. E. (1979). Electron precipitation of evening diffuse aurora and its conjugate electron fluxes near the magnetospheric equator. *J. Geophys. Res.* 84, 2545. doi:10.1029/ja084ia06p02545

Miars, G. C., Delzanno, G. L., Gilchrist, B. E., Leon, O., and Lucco Castello, F. (2020). Ion Emission from a Positively Biased Hollow Cathode Plasma, *IEEE Trans. Plasma Sci.* 48, 2693. doi:10.1109/tps.2020.3004553

Motoba, T., Ohtani, S., Anderson, B. J., Korth, H., Mitchell, D., Lanzerotti, L. J., et al. (2015). On the formation and origin of substorm growth phase/onset auroral arcs inferred from conjugate space-ground observations. *J. Geophys. Res. Space Phys.* 120, 8707. doi:10.1002/2015ja021676

Mozer, F. S. (1966). Proton trajectories in the radiation belts. *J. Geophys. Res.* 71, 2701. doi:10.1029/jz071i011p02701

NASA (2006). *Heliophysics: The New Science of the Sun-Solar System Connection: Recommended Roadmap for Science and Technology 2005-2035*. Washington, DC: National Aereonautics and Space Administration.

NASA, (2003). *Sun-Earth Connection Roadmap 2003-2028*, http://www.dept.aoe.vt.edu/~cdhall/courses/aoe4065/NASADesignSPs/SEC_2003_roadmap_full.pdf.

National Research Council (2012). Magnetosphere-to-ionosphere field-line tracing technology, in *Solar and Space Physics: A Science for a Technological Society*, (Washington, D. C: National Academies Press), 333–334.

Neubert, T., Banks, P. M., Gilchrist, B. E., Fraser-Smith, A. C., Williamson, P. R., Raitt, W. J., et al. (1990). The interaction of an artificial electron beam with the Earth's upper atmosphere: Effects on spacecraft charging and the near-plasma environment. *J. Geophys. Res.* 95, 12209. doi:10.1029/ja095ia08p12209

Neubert, T., and Gilchrist, B. E. (2002). Particle simulations of relativistic electron beam injection from spacecraft. *J. Geophys. Res.* 107, 1167. doi:10.1029/2001ja900102

Neubert, T., and Gilchrist, B. E. (2004). Relativistic electron beam injection from spacecraft: performance and applications. *Adv. Space Res.* 34, 2409. doi:10.1016/j.asr.2003.08.081

Neubert, T., Gilchrist, B., Wilderman, S., Habash, L., and Wang, H. J. (1996). Relativistic electron beam propagation in the Earth's atmosphere: Modeling results. *Geophys. Res. Lett.* 23, 1009. doi:10.1029/96gl00247

Nishimura, Y., Bortnik, J., Li, W., Thorne, R. M., Lyons, L. R., Angelopoulos, V., et al. (2011). Estimation of magnetic field mapping accuracy using the pulsating aurora-chorus connection. *Geophys. Res. Lett.* 38, L14110. doi:10.1029/2011gl048281

O'Neil, R. R., Shepherd, O., Reidy, W. P., Carpenter, J. W., Davis, T. N., Newell, D., et al. (1978). Excede 2 test, an artificial auroral experiment: ground-based optical measurements. *J. Geophys. Res.* 83, 3281. doi:10.1029/JA083iA07p03281

Ober, D. M., Maynard, N. C., Burke, W. J., Moen, J., Egeland, A., Sandholt, P. E., et al. (2000). Mapping prenoon auroral structures to the magnetosphere. *J. Geophys. Res.* 105, 27519. doi:10.1029/2000ja000009

Pellat, R., and Sagdeev, R. Z. (1980). Concluding remarks on the ARAKS experiments. *Ann. Geophys.* 36, 443.

Penndorf, R. (1957). Tables of the Refractive Index for Standard Air and the Rayleigh Scattering Coefficient for the Spectral Region between 02 and 200 μ and Their Application to Atmospheric Optics. *J. Opt. Soc. Am.* 47, 176. doi:10.1364/josa.47.000176

Pongratz, M. B. (2018). History of Los Alamos participation in active experiments in space. *Front. Phys.* 6, 144. doi:10.3389/fphy.2018.00144

Porazik, P., Johnson, J. R., Kaganovich, I., and Sanchez, E. (2014). Modification of the loss cone for energetic particles. *Geophys. Res. Lett.* 41, 8107. doi:10.1002/2014gl061869

Powis, A. T., Porazik, P., Greklek-Mckeon, M., Amin, K., Shaw, D., Kaganovich, I. D., et al. (2019). Evolution of a relativistic electron beam for tracing magnetospheric field lines. *Front. Astron. Space Phys.* 6, 69. doi:10.3389/fspas.2019.00069

Prech, L., Nemecek, Z., Šafránková, J., Šimunek, J., Truhlík, V., and Shutte, N. M. (1995). Response of the electron energy distribution to an artificially emitted electron beam: APEX experiment. *Adv. Space Res.* 15 (12), 33. doi:10.1016/0273-1177(95)00007-2

Prech, L., Ruzhin, Y. Y., Dokukin, V. S., Nemecek, Z., and Safrankova, J. (2018). Overview of APEX Project results. *Front. Astron. Space Sci.* 5, 46. doi:10.3389/fspas.2018.00046

Pulkkinen, T. I., Koskinen, H. E. J., and Pellinen, R. J. (1991). Mapping of auroral arcs during substorm growth phase. *J. Geophys. Res.* 96, 21087. doi:10.1029/91ja01960

Rappaport, S. A., Rieder, R. J., Reidy, W. P., McNutt, R. L., Atkinson, J. J., and Paulsen, D. E. (1993). Remote X ray measurements of the electron beam from the EXCEDE III Experiment. *J. Geophys. Res.* 98, 19093. doi:10.1029/93ja01154

Reeves, G., Delzanno, G. L., Fernandez, P., Yakymenko, K., Carlsten, B., Lewellen, J., et al. (2020). The Beam Plasma Interactions Experiment: An active experiment using pulsed electron beams. *Front. Astron. Space Sci.* 7, 23. doi:10.3389/fspas.2020.00023

Sanchez, E. R., Powis, A. T., Kagonovich, I. D., Marshall, R., Porazik, P., Johnson, J., et al. (2019). Relativistic particle beams as a resournce to solve outstanding problems in space physics. *Front. Astron. Space Sci.* 6, 71. doi:10.3389/fspas.2019.00071

Schindler, K., and Birn, J. (2002). Models of two-dimensional embedded thin current sheets from Vlasov theory. *J. Geophys. Res.* 107, SMP20. doi:10.1029/2001ja000304

Sergeev, V. A., Chernyaev, I. A., Dubyagin, S. V., Miyashita, Y., Angelopoulos, V., Boakes, P. D., et al. (2012). Energetic particle injections to geostationary orbit: Relationship to flow bursts and magnetospheric state. *J. Geophys. Res.* 117, A10207. doi:10.1029/2011ja017154

Shevchenko, I. G., Sergeev, V., Kubyshkina, M., Angelopoulos, V., Glassmeier, K. H., and Singer, H. J. (2010). Estimation of magnetosphere-ionosphere mapping accuracy using isotropy boundary and THEMIS observations. *J. Geophys. Res.* 115, A11206. doi:10.1029/2010ja015354

Sitnov, M. I., Tsyganenko, N. A., Ukhorskiy, A. Y., and Brandt, P. C. (2008). Dynamical data-based modeling of the storm-time geomagnetic field with enhanced spatial resolution. *J. Geophys. Res.* 113, A07218. doi:10.1029/2007ja013003

Spanswick, E., Donovan, E., Liang, J., Weatherwax, A. T., Skone, S., Hampton, D. L., et al. (2018). First-Light Observations from the Transition Region explorer (TREx) Ground-Based Network. American Geophysical Union, Fall Meeting, abstract SM23B-04,2018AGUFMSM23B.04S

Stepanova, M., Pinto, V., Valdivia, J. A., and Antonova, E. E. (2011). Spatial distribution of the eddy diffusion coefficients in the plasma sheet during quiet time and substorms from THEMIS satellite data. *J. Geophys. Res. Atmos.* 116, A00I24. doi:10.1029/2010ja015887

Strangeway, R. J. (2012). The relationship between magnetospheric processes and auroral field-aligned current morphology. *Geophys. Monogr. Ser.* 197, 355. doi:10.1029/2012gm001211

Thomsen, M. F., McComas, D. J., Reeves, G. D., and Weiss, L. A. (1996). An observational test of the Tsyganenko (T89a) model of the magnetospheric field. *J. Geophys. Res.* 101, 24827. doi:10.1029/96ja02318

Torbert, R. B., Vaith, H., Granoff, M., Widholm, M., Gaidos, J. A., Briggs, B. H., et al. (2016). The electron drift instrument for MMS. *Space Sci. Rev.* 199, 283. doi:10.1007/s11214-015-0182-7

Tsyganenko, N. A. (1989). A magnetospheric magnetic field model with a warped tail current sheet. *Planet. Space Sci.* 37, 5. doi:10.1016/0032-0633(89)90066-4

Tsyganenko, N. A., and Sitnov, M. I. (2007). Magnetospheric configurations from a high-resolution data-based magnetic field model. *J. Geophys. Res. Atmos.* 112, A06225. doi:10.1029/2007ja012260

Usanova, M. E., Mann, I. R., Bortnik, J., Shao, L., and Angelopoulos, V. (2012). THEMIS observations of electromagnetic ion cyclotron wave occurrence: dependence on AE, SYMH, and solar wind dynamic pressure. *J. Geophys. Res.*, 117, 172. doi:10.1029/2012ja018049

Uspensky, M. V., Timopheev, E. E., and Sverdlov, Y. L. (1980). "Araks" Doppler radar measurements of the ionospheric effects of artificial electron beam in the North hemisphere. *Ann. Geophys.* 36, 303.

Voros, Z., Baumjohann, W., Nakamura, R., Volwerk, M., Runov, A., Zhang, T. L., et al. (2004). Magnetic turbulence in the plasma sheet. *J. Geophys. Res. Atmos.* 109, A11215. doi:10.1029%2F2004JA010404

Weiss, L. A., Thomsen, M. F., Reeves, G. D., and McComas, D. J. (1997). An Examination of the Tsyganenko (T89A) Field Model Using a Database of Two-Satellite Magnetic Conjunctions. *J. Geophys. Res.* 102, 4911. doi:10.1029/96ja02876

Willard, J. M., Johnson, J. R., Snelling, J. M., Powis, A. T., Kaganovich, I. D., and Sanchez, E. R. (2019). Effect of field-line curvature on the ionospheric accessibility of relativistic electron beam experiments. *Front. Astron. Space Sci.* 6, 56. doi:10.3389/fspas.2019.00056

Williams, J. D., and Wilbur, P. J. (1990). Experimental study of plasma contactor phenomena, *J. Spacecr. Rockets.*, 27 (6), 634–641. doi:10.2514/3.26192

Winckler, J. R., Arnoldy, R. L., and Hendrickson, R. A. (1975). Echo 2: A study of electron beams injected into the high-latitude ionosphere from a large sounding rocket. *J. Geophys. Res.* 80, 2083. doi:10.1029/ja080i016p02083

Winckler, J. R. (1992). Controlled experiments in the earth's magnetosphere with artifical electron beams. *Rev. Mod. Phys.* 64, 859. doi:10.1103/revmodphys.64.859

Yahnin, A. G., Sergeev, V. A., Gvozdevsky, B. B., and Vennerstrøm, S. (1997). Magnetospheric source region of discrete auroras inferred from their relationship with isotropy boundaries of energetic particles. *Ann. Geophys.* 15, 943. doi:10.1007/s00585-997-0943-z

Yahnin, A. G., Sergeev, V. A., Gvozdevsky, B. B., and Vennerstrom, S. (1999). Reply. *Ann. Geophys.* 17, 42. doi:10.1007/s005850050734

Yang, J., Wolf, R. A., Toffoletto, F. R., and Sazykin, S. (2013). RCM-E simulation of substorm growth phase arc associated with large-scale adiabatic convection. *Geophys. Res. Lett.* 40, 6017. doi:10.1002/2013gl058253

Zhulin, I. A., Kustov, A. V., Uspensky, M. V., and Miroshnikova (1980). TV, Radar observations of the overdense ionospheric ionization created by the artificial electron beam in the "Zarnitza-2" experiment. *Ann. Geophys.* 36, 313.

Conflict of Interest: The authors declare that the research was conducted in the absence of any commercial or financial relationships that could be construed as a potential conflict of interest.

frontiers in Astronomy and Space Sciences

ORIGINAL RESEARCH
published: 25 January 2021
doi: 10.3389/fspas.2020.592634

The Discrepancy Between Simulation and Observation of Electric Fields in Collisionless Shocks

Lynn B. Wilson III[1]*, *Li-Jen Chen*[1] and *Vadim Roytershteyn*[2]

[1]NASA Goddard Space Flight Center, Heliophysics Science Division, Greenbelt, MD, United States, [2]Space Science Institute, Boulder, CO, United States

Recent time series observations of electric fields within collisionless shocks have shown that the fluctuating, electrostatic fields can be in excess of one hundred times that of the quasi-static electric fields. That is, the largest amplitude electric fields occur at high frequencies, not low. In contrast, many if not most kinetic simulations show the opposite, where the quasi-static electric fields dominate, unless they are specifically tailored to examine small-scale instabilities. Further, the shock ramp thickness is often observed to fall between the electron and ion scales while many simulations tend to produce ramp thicknesses at least at or above ion scales. This raises numerous questions about the role of small-scale instabilities and about the ability to directly compare simulations with observations.

Keywords: PIC simulation, electric field measurement, kinetic instabilities, collisionless shock, energy dissipation

OPEN ACCESS

Edited by:
Luca Sorriso-Valvo,
National Research Council, Italy

Reviewed by:
Silvia Perri,
University of Calabria, Italy
Quanming Lu,
University of Science and Technology of China, China

***Correspondence:**
Lynn B. Wilson III
lynn.b.wilson@nasa.gov

Specialty section:
This article was submitted to Space Physics, a section of the journal Frontiers in Astronomy and Space Sciences

Received: *07 August 2020*
Accepted: *02 November 2020*
Published: *25 January 2021*

Citation:
Wilson III LB, Chen L-J and Roytershteyn V (2021) The Discrepancy Between Simulation and Observation of Electric Fields in Collisionless Shocks. Front. Astron. Space Sci. 7:592634. doi: 10.3389/fspas.2020.592634

1 INTRODUCTION

Collisionless shock waves are an ubiquitous phenomenon in heliospheric and astrophysical plasmas. They most often manifest as a nonlinearly steepened fast magnetosonic-whistler wave that has reached a stable balance between steepening and some form of irreversible energy dissipation. If a balance is reached, a stationary shock ramp is formed. The shock ramp is the part of shock transition region between upstream and downstream with an abrupt, discontinuity-like change in number density (n_S where s is the particle species), pressure[1], quasi-static[2] magnetic field magnitude vector ($\mathbf{B}_o$), and bulk flow velocity ($\mathbf{V}_{bulk}$). The thickness of this ramp is thought to depend upon macroscopic shock parameters like the fast mode Mach number (M_f), shock normal angle, θ_{Bn} (e.g., quasi-perpendicular shocks satisfy $\theta_{Bn} \geq 45°$), and upstream averaged plasma beta (Sagdeev, 1966; Coroniti, 1970; Tidman & Krall, 1971; Galeev, 1976; Kennel et al., 1985).

The term collisionless derives from the fact that the shock ramp thickness ranges from several electron inertial lengths[3] to an ion inertial length with the majority below ~35 λ_e (Hobara et al., 2010; Mazelle et al., 2010). In contrast, the collisional mean free path of a thermal proton can be on the order of 1 AU or $\gtrsim 10^7$ λ_e (Wilson et al., 2018; Wilson et al., 2019a). Thus, fast mode shocks in astrophysical plasmas cannot be regulated by Coulomb collisions (with the exception of, perhaps,

[1]$P_s = n_s k_B T_s$, where T_s is the temperature of species s.

[2]Note we use the term quasi-static instead of background here since electromagnetic fluctuations near shocks in the solar wind can have amplitudes larger than the surrounding mean. That is, quasi-static refers to the lowest frequency response of an instrument, for practical purposes, but one can think of it as the effective background field.

[3]$\lambda_s = \frac{c}{\omega_{ps}}$ where s is the particle species.

TABLE 1 | Common Electrostatic Waves at/near Collisionless Shocks.

Wave Name	Polarization or waveform	Frequency[α] and/or Appearance	Scale Length[β]	Free energy source or wave source
LHW	linear $\perp$ to $\mathbf{B}_o$ or oblique to $\mathbf{B}_o$	f_{sc} ~ 5–40 Hz $f_{sc} \lesssim f_{lh}$ symmetric modulated sine waves[ρ]	$k\lambda_e \lesssim 1$	currents[κ], density gradients[λ], Electron heat flux[σ], or MTSI[θ]
IAW	linear $\parallel$ to $\mathbf{B}_o$	f_{sc} ~ 10^2–10^4 Hz $f_{rest} \lesssim f_{pi}$ symmetric[η] modulated sine waves	$\lambda \gtrsim 2\pi\lambda_{De}$	currents[δ], gyrating/reflected ions[ζ], or electron heat flux[ξ]
ECDI	elliptical or "Tear-drop"- shaped oblique to $\mathbf{B}_o$	f_{sc} ~ 10^2–10^4 Hz f_{rest} ~ mix[ϵ] asymmetric[η] modulated sine waves	$k\lambda_e \lesssim 1$ and $k\lambda_{De} \lesssim 1$	relative drift between incident electrons and reflected ions[δ]
ESW	bipolar pulse $\parallel$ to $\mathbf{B}_o$ else unipolar	f_{sc}^{-1} ~ few 10 s of ms isolated or trains of pulses	$\lambda \gtrsim \lambda_{De}$	electron beams[δ] or nonlinear wave decay[δ]
LW[ψ]	linear $\parallel$ to $\mathbf{B}_o$ or elliptical $\perp$ to $\mathbf{B}_o$	f_{sc} ~ 10–60 kHz symmetric modulated sine waves	$k\lambda_e \lesssim 1$[μ]	electron beams[χ] and/or nonlinear wave decay[γ]

[α] f_{sc} ≡ *spacecraft frame frequency;* [β] *wavelength or normalized wave number;* [δ] *[e.g., Wilson et al., 2014a, and references therein];* [ζ] *[e.g., Akimoto et al., 1985b];* [ξ] *[e.g., Dum et al., 1980];* [ψ] ***Langmuir wave****;* [χ] *[e.g., Pulupa et al., 2010];* [γ] *[e.g., Kellogg et al., 2013];* [η] *relative to oscillations about mean/average;* [κ] *[e.g., Lemons and Gary, 1978];* [λ] *[e.g., Cairns and McMillan, 2005];* [σ] *[e.g., Marsch and Chang, 1983];* [ρ] *[e.g., Walker et al., 2008];* [θ] ***modified two-stream instability*** *[e.g., Umeda et al., 2012a];* [ϵ] *mixture of IAWs and* nf_{ce} *and/or* $(n + 1/2)f_{ce}$ *harmonics;* [μ] *[e.g., Krasnoselskikh et al., 2011].*

stellar photospheres and/or chromospheres or interstellar medium) like shock waves in dense neutral fluids similar to Earth's atmosphere. The proposed phenomenon thought to act as dissipation mechanisms are dispersive radiation (Galeev and Karpman, 1963; Stringer, 1963; Morton, 1964; Sagdeev, 1966; Tidman and Northrop, 1968; Tidman and Northrop, 1968; Decker and Robson, 1972; Krasnoselskikh et al., 2002), macroscopic quasi-static field effects (Scudder et al., 1986a; Scudder et al., 1986b; Scudder et al., 1986c; Schwartz et al., 1988; Hull and Scudder, 2000; Mitchell and Schwartz, 2013; Mitchell and Schwartz, 2014), particle reflection (Edmiston and Kennel, 1984; Kennel et al., 1985; Kennel, 1987), and wave-particle interactions (Sagdeev, 1966; Coroniti, 1970; Gary, 1981; Papadopoulos, 1985).

The topic of interest for this study is electric fields in observations and simulations, so we will limit the discussion to wave-particle interactions and macroscopic quasi-static field effects. Further, given that the primary discrepancy between simulations and observations lies in the lack of large amplitude, high frequency electrostatic waves in the former, we will limit the discussion to high frequency electrostatic waves. Note that some PIC simulations do generate the electrostatic waves of interest but the simulations are often tailored to generate the modes (e.g., isolated simulation mimicking shock foot region) by artificially injecting known free energy sources (e.g., initialize with two counter-streaming beams). Therefore, all of the modes listed in the following discussion have been generated in PIC simulations (Dyrud and Oppenheim, 2006; Matsukiyo and Scholer, 2006; Matsukiyo and Scholer, 2012; Muschietti and Lembège, 2017; Saito et al., 2017). However, as will be shown, parameters like the wavelengths and amplitudes tend to differ from those in observations, sometimes significantly.

Recent work using time series electric field data has shown that the common electrostatic wave modes near collisionless shocks include lower hybrid waves (LHWs), ion acoustic waves (IAWs), electrostatic solitary waves (ESWs), waves radiated by the electron cyclotron drift instability (ECDI), and Langmuir waves (Filbert and Kellogg, 1979; Mellott and Greenstadt, 1988; Kellogg, 2003; Wilson et al., 2007; Pulupa and Bale, 2008; Walker et al., 2008; Wilson et al., 2010; Breneman et al., 2013; Wilson et al., 2014a; Wilson et al., 2014b; Chen et al., 2018; Goodrich et al., 2018; Goodrich et al., 2019). The properties of these modes are summarized in **Table 1** and discussed in detail below.

Electrostatic LHWs have been theorized to play a critical role in collisionless shock dynamics for decades (Papadopoulos, 1985; Tidman and Krall, 1971; Wu et al., 1984) but observations of their electrostatic form have been limited (Mellott and Greenstadt, 1988; Walker et al., 2008; Wygant et al., 1987). They are present in spacecraft observations at frequencies, in the spacecraft frame, near the local lower hybrid resonance frequency[4]. They are linearly polarized nearly perpendicular to $\mathbf{B}_o$ with $k\lambda_e \lesssim 1$. They are thought to be driven unstable by the free energy in currents (Lemons and Gary, 1978), ion velocity rings (Akimoto et al., 1985a), modified two stream instability (MTSI)[5], (Gladd,

[4] $f_{lh} = \sqrt{f_{ce} f_{cp}}$, where f_{cs} is the cyclotron frequency of species s ($=\frac{q_s B_o}{m_s}$ where q_s is the total charge, and m_s is the mass of species s).

[5] There are two modes radiated by the MTSI at collisionless shocks, both of which are very obliquely propagating and have real frequencies near or below f_{lh}. The two free energy sources for the MTSIs are between incident electrons and reflected ions and incident electrons and incident ions.

1976; Lemons and Gary, 1977; Wu et al., 1983; Wu et al., 1984), electron beams (Papadopoulos and Palmadesso, 1976), and/or heat flux carrying electrons (Marsch and Chang, 1983). These modes are important for collisionless shock dynamics because they can stochastically accelerate both thermal electrons (parallel to $\mathbf{B}_o$) and ions (perpendicular to $\mathbf{B}_o$) to suprathermal energies (Wu et al., 1984; Cairns and McMillan, 2005).

Electrostatic IAWs have been observed in the solar wind and near collisionless shocks for over 40 years (Fredricks et al., 1968; Fredricks et al., 1970a; Gurnett and Anderson, 1977; Gurnett et al., 1979; Kurth et al., 1979). They present in spacecraft observations at frequencies, in the spacecraft frame, above the proton plasma frequency[6] (due to the Doppler effect), typically in the ~1–10 kHz range in the solar wind near 1 AU. They are observed as linearly polarized (mostly parallel to $\mathbf{B}_o$ but sometimes at small oblique angles), modulated sine waves with bursty wave envelopes lasting 10 s of ms (Wilson et al., 2007; Wilson et al., 2010; Wilson et al., 2014a; Wilson et al., 2014b). They have been shown to have wavelengths on the order of a few to several Debye lengths[7], or 10–100 s of meters near 1 AU (Fuselier and Gurnett, 1984; Breneman et al., 2013; Goodrich et al., 2018; Goodrich et al., 2019). They are thought to be driven unstable by the free energy in currents (Biskamp et al., 1972; Lemons and Gary, 1978), temperature gradients (Allan and Sanderson, 1974), electron heat flux (Dum et al., 1980; Henchen et al., 2019), or ion/ion streaming instabilities (Auer et al., 1971; Akimoto and Winske, 1985; Akimoto et al., 1985b; Goodrich et al., 2019) or they can result from a nonlinear wave-wave process (Cairns and Robinson, 1992; Dyrud and Oppenheim, 2006; Kellogg et al., 2013; Saito et al., 2017). These modes are important for collisionless shock dynamics because they can stochastically accelerate thermal electrons (parallel to $\mathbf{B}_o$) generating self-similar velocity distribution functions (VDFs) or the so called "flattop" distributions (Vedenov, 1963; Sagdeev, 1966; Dum et al., 1974; Dum, 1975; Dyrud and Oppenheim, 2006). They are also capable of stochastically accelerating the high energy tail of the ion VDF (parallel to $\mathbf{B}_o$) (Dum et al., 1974). Note that the generation of the flattop has recently been interpreted as evidence of inelastic collisions (Wilson et al., 2019a; Wilson et al., 2019b; Wilson et al., 2020).

ESWs present in spacecraft observations as short duration (few ms), bipolar electric field pulses parallel to $\mathbf{B}_o$ and monopolar perpendicular (Behlke et al., 2004; Wilson et al., 2007; Wilson et al., 2010; Wilson et al., 2014b). They tend to be on Debye scales and are thought to be BGK phase space holes (Ergun et al., 1998; Cattell et al., 2005; Franz et al., 2005; Vasko et al., 2018). ESWs can be driven unstable by electron beams (Ergun et al., 1998; Cattell et al., 2005; Franz et al., 2005), ion beams (Vasko et al., 2018), modified two-stream instability (MTSI) (Matsukiyo and Scholer, 2006), or the produce of high frequency wave decay (Singh et al., 2000). Until recently, it was thought all ESWs outside the auroral acceleration region were electron holes. However, work by (Vasko et al., 2018) and (Wang et al., 2020) suggest that many of the ESWs in the terrestrial bow shock are not only ion holes, they do not propagate exactly along $\mathbf{B}_o$ as was previously thought. ESWs are important in collisionless shock dynamics because they can trap incident electrons (Dyrud and Oppenheim, 2006; Lu et al., 2008) or ions (Vasko et al., 2018; Wang et al., 2020), depending on the type of hole. They have also been shown to dramatically heat ions (Ergun et al., 1998), and/or couple to (or directly cause) the growth of IAWs (Dyrud and Oppenheim, 2006), whistler mode waves (Singh et al., 2001; Lu et al., 2008; Goldman et al., 2014), LHWs (Singh et al., 2000).

The ECDI is driven by the free energy in the relative drift between the incident electrons and shock-reflected ions (Forslund et al., 1970; Forslund et al., 1971; Lampe et al., 1972; Matsukiyo and Scholer, 2006; Muschietti and Lembège, 2013). They also range from Debye to electron thermal gyroradius scales (Breneman et al., 2013) and present in spacecraft observations as mixtures of Doppler-shifted IAWs and electron Bernstein modes. The polarization of these modes can be confusing, presenting as shaped like a tadpole or tear drop, with one part of the "tadpole" nearly parallel to $\mathbf{B}_o$ (i.e., IAW part) and the other nearly orthogonal (i.e., the Bernstein mode part) (Wilson et al., 2010; Breneman et al., 2013; Wilson et al., 2014b; Goodrich et al., 2018). This results from the coupling between two modes that are normally orthogonal to each other in their electric field oscillations. ECDI-driven modes are important for collisionless shocks because they can resonantly interact with the bulk of the ion VDF, generate a suprathermal tail on the ion VDF, and strongly heat the electrons perpendicular to $\mathbf{B}_o$ (Forslund et al., 1970; Forslund et al., 1972; Lampe et al., 1972; Muschietti and Lembège, 2013).

Langmuir waves have been observed upstream of collisionless shocks for decades (Gurnett and Anderson, 1977; Filbert and Kellogg, 1979; Kellogg et al., 1992; Cairns, 1994; Bale et al., 1998; Bale et al., 1999; Malaspina et al., 2009; Soucek et al., 2009; Krasnoselskikh et al., 2011). These waves have $k\lambda_e \lesssim 1$ (Soucek et al., 2009; Krasnoselskikh et al., 2011) and rest frame frequencies satisfying $f_{rest} \lesssim f_{pe}$. Langmuir waves are driven unstable by electron beams and/or nonlinear wave decay (Pulupa et al., 2010; Kellogg et al., 2013). They tend to be linearly polarized nearly parallel to $\mathbf{B}_o$ when electrostatic but some do exhibit circular polarization when electromagnetic (Bale et al., 1998; Malaspina and Ergun, 2008). Langmuir waves are relevant to collisionless shock dynamics in that they dissipate the free energy in reflected electron beams and can mode convert to generate free mode emissions that can serve as remote detection signatures (Cairns, 1994; Bale et al., 1999; Pulupa et al., 2010).

In summary, the most commonly observed electrostatic wave modes near collisionless shocks are IAWs, ESWs, ECDI-driven modes, and Langmuir waves. Electrostatic LHWs are less commonly observed, which may be due to instrumental effects

[6] $2\pi f_{ps} = \sqrt{\frac{n_s q_s^2}{\varepsilon_o m_s}}$ where s is the particle species.

[7] $\lambda_{De} = \sqrt{\frac{\varepsilon_o k_B T_e}{n_e e^2}}$ where n_e is the electron number density.

as many electric field instruments (Bonnell et al., 2008; Bougeret et al., 2008; Cully et al., 2008) have been designed with gain roll-offs at ~1–10 Hz (low- or high-pass filters), which happens to be the typical value of f_{lh} in the solar wind near 1 AU. It may also be that electrostatic LHWs are just less commonly generated or damp very quickly in collisionless shocks. Langmuir waves tend to occur upstream of the shock in regions filled with shock reflected electron beams (Cairns, 1994; Bale et al., 1999; Wilson et al., 2007; Pulupa et al., 2010). Although they can be common in the upstream, they tend to be much less so in the ramp and immediate downstream region. Therefore, the remaining discussion will focus on the most commonly observed Debye-scale, electrostatic modes: IAWs, ESWs, and ECDI-driven modes. These three modes are observed in and around both quasi-parallel and quasi-perpendicular shocks. The only macroscopic shock parameters on which they appear to depend are the shock density compression ratio and M_f [e.g., Wilson et al., 2007; Wilson et al., 2014a; Wilson et al., 2014b]. The ECDI-driven modes tend not to be observed for $M_f \lesssim 3$, since they require sufficient reflected ions to initiate the instability. Part of the reason for the lack of dependence on shock geometry is that the fluctuations in the foreshock upstream of a quasi-parallel shock, for instance, locally rotate the magnetic field to quasi-perpendicular geometries and some can even locally reflect/energize particles [e.g., Wilson et al., 2013; Wilson et al., 2016].

2 HISTORICAL CONTEXT

2.1 Spacecraft Observations

Early spacecraft electric field observers had very limited resources, compared to modern day, in memory, computational power, and spacecraft telemetry. As such, the common practice was to perform onboard computations to generate Fourier spectra for predefined frequency ranges (Fredricks et al., 1968; Fredricks et al., 1970a; Fredricks et al., 1970b; Rodriguez and Gurnett, 1975). These Fourier spectra are spectral intensity data averaged over fixed time and frequency intervals, which has been more recently shown to significantly underestimate the instantaneous wave amplitude (Tsurutani et al., 2009). The underestimation led to some confusion in multiple areas of research because the estimated wave amplitudes from the spectra were too small to noticeably impact the dynamics of the system in question.

For instance, for decades the radiation belt community had relied upon such dynamic spectra and came to conclusion that the whistler mode waves (e.g., chorus and hiss) were typically in the $\lesssim$1 mV/m amplitude range. The advent of time series electric field data led to the discovery that some of these modes could have amplitudes in excess of ~30 mV/m (Santolík et al., 2003). Later the STEREO spacecraft were launched and the electric field instruments were one of the first to be turned on. This led to the discovery of extremely large amplitude whistler mode waves with $\gtrsim$200 mV/m (Cattell et al., 2008). The discovery provoked an investigation of *Wind* observations as it passed through the radiation belt some 60+ times early in its lifetime. The result was a series of papers using *Wind* and STEREO that all showed consistent observations of large amplitude whistler mode waves with $\gtrsim$100 mV/m (Kellogg et al., 2010; Breneman et al., 2011; Kellogg et al., 2011; Kersten et al., 2011; Wilson et al., 2011; Breneman et al., 2012). These results altered the design and scientific direction of NASA's *Van Allen Probes* mission.

Similar issues arose in observations of collisionless shock waves. The early work using dynamic spectra data found electrostatic waves with spacecraft frame frequencies, f_{sc}, greater than a few hundred hertz to have amplitudes of, at most, a few 10s of mV/m but typically smaller in the few mV/m range (Fredricks et al., 1970b; Rodriguez and Gurnett, 1975). Numerous theoretical studies had suggested that small-scale, high frequency waves were an important dissipation mechanism to regulate the nonlinear steepening of collisionless shock waves (Sagdeev, 1966; Tidman and Krall, 1971; Papadopoulos, 1985). However, such small amplitude electric field observations raised doubts about the ability of the high frequency modes to supply sufficient dissipation to maintain a stable shock.

The first published example (of which the authors are aware) of a time series electric field component observed by a spacecraft within a collisionless shock was presented in Wygant et al. (1987) observed by the ISEE-1 probe. The observation was one of the first pieces of evidence that the dynamic spectra plots were not fully capturing the electric field dynamics because the data showed electric fields up to nearly ~100 mV/m. Later work using the *Wind* spacecraft found ESWs in the terrestrial bow shock with amplitudes in excess of ~100 mV/m (Bale et al., 1998; Bale et al., 2002). A few bow shock crossings were observed with the *Polar* spacecraft, which found nonlinear, electrostatic IAWs within the shock with amplitudes up to ~80 mV/m (Hull et al., 2006). The picture starting to emerge was that high frequency, electrostatic waves were common and large amplitude in collisionless shocks. Note that the occurrence rate of electrostatic waves was already implied by studies using dynamic spectra data, but not such large amplitude.

Wilson et al. (2007) examined waveform capture data of electrostatic waves above the proton cyclotron frequency, f_{pp}, from the *Wind* spacecraft finding a positive correlation between peak wave amplitude and shock strength, i.e., stronger shocks had larger amplitude waves. They also observed that ion acoustic waves were the dominant electrostatic mode within the shock ramp. Shortly after, a study (Wilson et al., 2010) of a supercritical shock showed evidence of waves radiated by the ECDI. Since then, a series of papers using MMS (Chen et al., 2018; Goodrich et al., 2018; Goodrich et al., 2019), STEREO (Breneman et al., 2013), THEMIS (Wilson et al., 2014a; Wilson et al., 2014b), and *Wind* (Breneman et al., 2013) have examined these electrostatic waves in collisionless shocks.

While the discussion has almost exclusively focused on fluctuating electric fields, δE, it is critical to discuss quasi-static electric fields, E_o, as well. The primary obstacle to accurate E_o measurements results from the lack of a stable ground in spacecraft observations (Scime et al., 1994a; Scime et al., 1994b; Scudder et al., 2000; Pulupa et al., 2014; Lavraud and Larson, 2016) and the sheath that forms around the conducting surfaces (Ergun et al., 2010), which alters how the instrument

couples to the plasma. It is beyond the scope of this study to discuss, in detail, the difficulties associated with such measurements, but some context can be gained by reviewing some recent electric field instrument papers (Wygant et al., 2013; Bale et al., 2016; Ergun et al., 2016; Lindqvist et al., 2016). In lieu of a proper E_o measurement in the plasma rest frame, we can estimate the convective electric field, $\mathbf{E}_c = -\mathbf{V}_{sw} \times \mathbf{B}_o$ (where $\mathbf{V}_{sw}$ is the bulk flow solar wind velocity in the spacecraft frame)[8]. Since the parameters in most simulations are scaled or normalized, we will use the dimensionless ratio $\delta E/E_o$ when comparing spacecraft and simulation results. Unless otherwise specified, $E_o = E_c$ in these contexts.

Prior to the launch of MMS, there were several studies that attempted to measure the cross shock electric field but each suffered from inaccuracies or under resolved electric field measurements which kept the issue of its magnitude in doubt (Dimmock et al., 2011; Dimmock et al., 2012; Wilson et al., 2014a; Wilson et al., 2014b). The launch of MMS allowed researchers, for the first time, to probe E_o with sufficient cadence and accuracy to properly measure the cross shock electric field in an interplanetary shock (Cohen et al., 2019). Note that the E_o measured in this study peaked at $\lesssim$1.5 mV/m, i.e., comparable to or smaller than the magnitude of $\mathbf{E}_c$ (which was $\lesssim$4 mV/m in this study). Therefore, we will assume E_o as being comparable to E_c in magnitude throughout and will just refer to E_o instead of both. Even so, there is some discrepancy because such a measurement is extremely difficult at the terrestrial bow shock and detailed MMS observations showed that the electron dynamics seemed to be dominated by a combination of magnetosonic-whistler modes and electrostatic IAWs and ECDI waves (Chen et al., 2018).

The current picture from observations is summarized in the following. In the studies where the quasi-static electric field could be reliably measured (Cohen et al., 2019) or approximated from measurements (Wilson et al., 2014a; Wilson et al., 2014b; Goodrich et al., 2018; Goodrich et al., 2019), the findings were that δE is consistently much larger than E_o, i.e., $\delta E \gg E_o$. Some of these works attempted to quantify the impact on the dynamics of the system due to δE vs. E_o, finding δE dominated (Wilson et al., 2014a; Wilson et al., 2014b; Chen et al., 2018; Goodrich et al., 2018). Chen et al. (Chen et al., 2018) examined in great detail the evolution of the electron distribution through the shock finding that a magnetosonic-whistler wave accelerated the bulk of the incident distribution which rapidly became unstable to high frequency, electrostatic IAWs that scattered the electrons into the often observed flattop distribution [Wilson et al., 2019b; Wilson et al., 2019a; Wilson et al., 2020, and references therein]. This seems to somewhat contradict the results of Cohen et al. (2019) and others who argued that a quasi-static cross shock potential is dominating the shock and particle dynamics. What all of these studies do agree upon is that $\delta E \gg E_o$. Note that the purpose of comparing the fluctuating to the quasi-static field here is to help compare with simulations, which normalize the electric fields by the upstream E_c value or something similar.

Figure 1 shows seven waveform captures observed by the *Wind* spacecraft's WAVES instrument (Bougeret et al., 1995) while passing through the quasi-perpendicular terrestrial bow shock. The first column shows the x-antenna electric field (δE_x), the second the y-antenna electric field (δE_y), and the third hodograms of δE_y vs. δE_x. The local $\mathbf{B}_o$ is projected onto each hodogram shown as a magenta line[9]. Each row shows a different waveform capture/snapshot that is ~17 ms in duration. The first column contains a double-ended arrow in each panel illustrating the scale associated with 200 mV/m. The first two rows show examples of ESWs mixed with ECDI-driven waves, the third and fourth rows show ECDI-driven waves, and the fifth through seventh rows show IAWs. The distinguishing features are as follows: the ESWs have an isolated, bipolar pulse with either a linear or figure eight-like polarization and a nearly flat frequency (spacecraft frame) spectrum response in the ~0.2–10 kHz range (not shown); the IAWs exhibit symmetric δE_x and δE_y about zero, are linearly polarized along $\mathbf{B}_o$, and have a broad frequency peak (spacecraft frame) in the ~2–10 kHz range (not shown); and the ECDI exhibit asymmetric δE_x and δE_y fluctuations about zero, their polarization is not always linear along $\mathbf{B}_o$, and the frequency peak (spacecraft frame) is in the ~0.5–10 kHz range with superposed cyclotron harmonics (not shown). For reference, the upstream average convective for this bow shock crossing is $E_c \sim 3.5$ mV/m.

2.2 Kinetic Simulations

Kinetic simulations of shocks are challenging due to the need to resolve global structure of the shock (generally associated with λ_i[10]) and the relatively long time scales associated with it simultaneously with short spatial (λ_{De}) and fast temporal scales (f_{pe}) associated with instabilities.

Early kinetic particle-in-cell (PIC) simulations were much more limited by computational constraints than those performed today. A common approach to scaling the problem in order reduce the computational load is to consider one- or two-dimensional problems and to reduce ratios of the ion-to-electron mass, $\frac{M_i}{m_e}$, and electron plasma-to-cyclotron frequency, $\frac{\omega_{pe}}{\Omega_{ce}}$, while keeping the plasma β and the size of the problem in units of λ_i comparable to the physical system of interest. Further computational trade-offs include altering the simulation resolution (i.e., number of grid cells), the number of particles per cell for particle codes or velocity-space resolution for continuum Vlasov codes (Yang et al., 2013). Since the frequencies and the growth rates of the instabilities of interest are associated with certain characteristic time scales, such a re-scaling may significantly alter the development and the role of instabilities in the simulations. For example, reducing $\frac{M_i}{m_e}$ lowers the threshold for Buneman instability (Hoshino and Shimada,

[8] E_c has typical values satisfying ~0.1–3 mV/m in the solar wind near Earth. In contrast, the waves shown in **Figure 1** have $\delta E \gtrsim$ 100–300 mV/m, thus $\delta E/E_o > 50$.

[9] Note that the data is taken in the ecliptic plane to within ~1° and the fraction of the local $\mathbf{B}_o$ in this plane exceeds 89% for all events except the first two rows.

[10] The size of the problem may significantly exceed λ_i, for example when upstream turbulence in quasi-parallel shocks must be included.

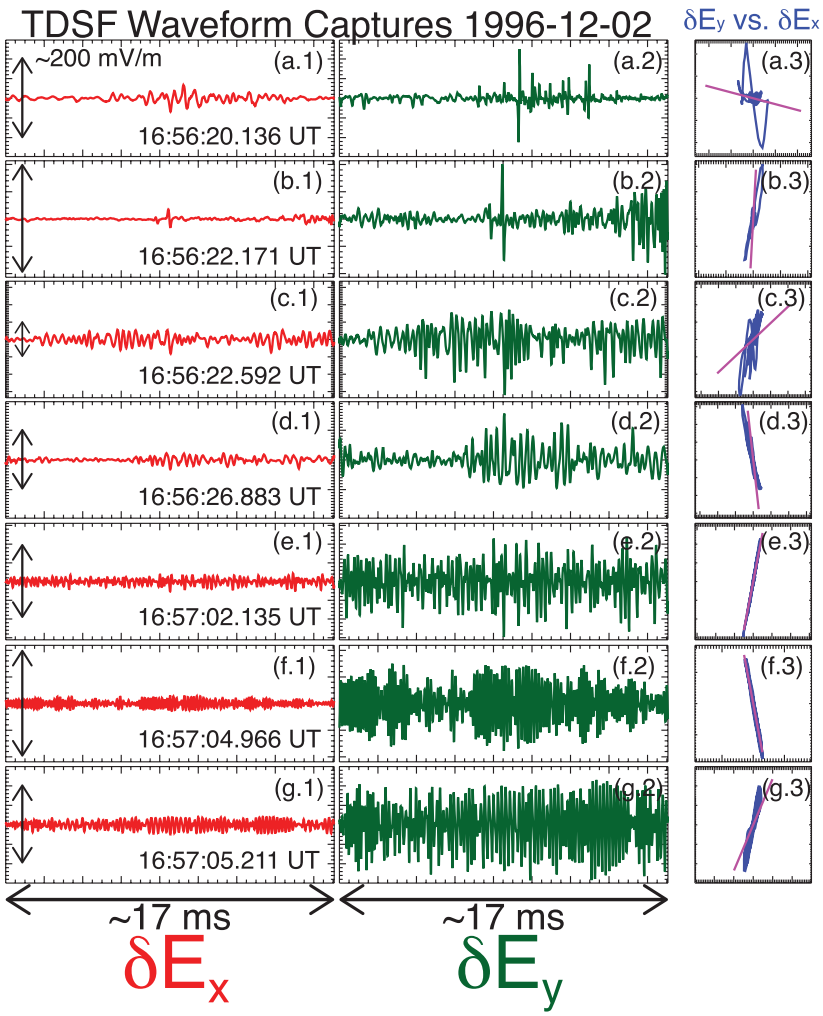

FIGURE 1 | Example of six waveform captures observed by *Wind* while crossing the Earth's quasi-perpendicular bow shock on 1996-12-02. Each row corresponds to, by column, the X vs time, Y vs time, and Y vs X hodogram (in instrument coordinates) from the *Wind*/WAVES time domain sampler (TDS) instrument (Bougeret et al., 1995). Each waveform capture/snapshot is ~17 ms in duration. The quasi-static magnetic field projection is shown as the magenta line in hodograms (Adapted from Figure 3.6 in Wilson (2010).

2002) by reducing the difference between electron and ion thermal speeds. Values of $\frac{\omega_{pe}}{\Omega_{ce}}$ were also expected and found to inhibit the growth of certain wave modes like Bernstein modes (Matsukiyo and Scholer, 2006; Muschietti and Lembège, 2013; Muschietti and Lembège, 2017). What's more, the $\frac{M_i}{m_e}$ ratio was shown to dramatically affect the macroscopic profile of the shock magnetic field (Scholer and Matsukiyo, 2004) and affect the growth of what are now viewed as critical instabilities like the MTSI (Umeda et al., 2012a; Umeda et al., 2012b; Umeda et al., 2014). Thus the re-scaling approach must be carefully chosen based upon its expected impact on the phenomena of interest.

Some of the first two-dimensional PIC simulations using realistic $\frac{M_i}{m_e}$ was presented by (Matsukiyo and Scholer, 2006). Since then, the community has made efforts to compromise somewhat on $\frac{M_i}{m_e}$ in order to increase $\frac{\omega_{pe}}{\Omega_{ce}}$, to more realistic values (i.e., 50–100 in solar wind near 1 AU) (Muschietti and Lembège, 2013) used ratios of $\frac{M_i}{m_e} = 400$ and $\frac{\omega_{pe}}{\Omega_{ce}} = 10$ to examine the higher harmonics of Bernstein modes associated with the ECDI. More typical values for the latter fall in the ~2–4 range for recent simulations (Umeda et al., 2014; Matsukiyo and Matsumoto, 2015; Zeković, 2019). However, much larger values have been used in cases where one can reduce the simulation to one spatial dimension (Umeda et al., 2019).

Despite all of the progress made since the early full PIC simulations, there still remains two striking discrepancies between observations and many simulations: the amplitude and wavelength at which the strongest electric fields are observed and inconsistencies in the thickness of the shock ramp. The second issue is more obvious from cursory examinations of simulation results, so we will discuss it first. As previously discussed, observations consistently show that the shock ramp thickness, L_{sh}, tends to satisfy $5 < L_{sh}/\lambda_e < 40$ (Hobara et al., 2010; Mazelle et al., 2010). However, PIC simulations, even with realistic mass ratio, often generate

shock ramps with thicknesses satisfying $L_{sh}/\lambda_e > 43$, i.e., exceeding proton inertial length (Scholer and Burgess, 2006), while some generate more realistically thin ramps (Matsukiyo and Scholer, 2012; Yang et al., 2013). Yang et al. (Yang et al., 2013) concluded that the shock ramp thickness decreased with increasing $\frac{M_i}{m_e}$ but increased with increasing ion plasma beta. Note however that (Matsukiyo & Scholer, 2012) used ~20% finer grid resolution, twice as many particles per cell, and smaller plasma betas than (Scholer & Burgess, 2006). However, (Yang et al., 2013) used fewer particles per cell and smaller $\frac{\omega_{pe}}{\Omega_{ce}}$ than both (Matsukiyo and Scholer, 2012) and (Scholer and Burgess, 2006). It is important to note that it's still not clear what physical or numerical parameters controls the ramp thickness in simulations or observations or even what the relevant physical scale is (e.g. λ_e or λ_{De}).

Note that the thickness of the magnetic ramp of a collisionless shock is not significantly affected by the presence of corrugation/ripples (Johlander et al., 2016) other than the temporal dependence that can occur during reformation (Mazelle et al., 2010). The spatial extent of the entire transition region can indeed be increased by such oscillations but the magnetic gradient scale length does not appear to be significantly affected. The biggest limiation to determining the shock ramp thickness in data is time resolution. More recent spacecraft like THEMIS (Angelopoulos, 2008) and MMS (Burch et al., 2016) have, for instance, fluxgate magnetometers that return 3-vector components 128 times every second, which is more than sufficient to resolve the bow shock ramp. The bow shock moves slower in the spacecraft frame than interplanetary shocks, so time resolution is more of a constraint for examining the shock ramp thickness of interplanetary shocks. Even so, the 128 sps of the THEMIS and MMS fluxgate magnetometers is still sufficient for most interplanetary shocks.

As previously discussed, observations consistently show $\delta E/E_o > 50$ for fluctuations with wavelengths at or below a few 10s of Debye lengths (Wilson et al., 2014a; Wilson et al., 2014b; Chen et al., 2018; Goodrich et al., 2018), i.e., $\lambda \lesssim$ few 10s of λ_{De}. Most shock simulations find values satisfying $\delta E/E_o < 10$ and the scales at which the largest electric field fluctuations occur tend to satisfy $k\lambda_e < 1$ (Scholer and Matsukiyo, 2004; Matsukiyo and Scholer, 2006; Scholer and Burgess, 2007; Lembège et al., 2009; Umeda et al., 2012a; Umeda et al., 2014; Matsukiyo and Matsumoto, 2015). We note that explicit fully kinetic PIC simulations tend to have spatial grid resolution of a few λ_{De}, since such scales must be resolved for numerical stability. It has long been known that unrealistically small values of $\frac{M_i}{m_e}$ and $\frac{\omega_{pe}}{\Omega_{ce}}$ can lead to unrealistically large electric field amplitudes for modes with $k\lambda_e < 1$ (Hoshino and Shimada, 2002; Comişel et al., 2011; Zeković, 2019). Although the three main modes discussed herein have been successfully identified in PIC simulations, they were either unrealistically small in amplitude or at different spatial scales or not excited unless the simulation was specifically tailored for that instability.

It is worth noting the severe computational costs of using fully realistic plasma parameters. The separation of spatial scales satisfies $\lambda_i/\lambda_{De} = \sqrt{\frac{M_i}{m_e}}\beta_e^{-1/2}\left(\frac{\omega_{pe}}{\Omega_{ce}}\right)$ or $\lambda_e/\lambda_{De} = \left(\frac{\omega_{pe}}{\Omega_{ce}}\right)\left(\frac{\sqrt{2}\,V_{Ae}}{V_{Te}}\right) = \sqrt{\frac{2}{\beta_e}}\left(\frac{\omega_{pe}}{\Omega_{ce}}\right)$ or $\lambda_e/\lambda_{De} = \frac{V_{Te}}{\sqrt{2}\,c}$, where $V_{Ae} = \frac{B_o}{\sqrt{\mu_o\, n_e\, m_e}} = \lambda_e\,\Omega_{ce}$ and $\beta_e = \frac{2\mu_o\, n_e\, k_B\, T_e}{B_o^2} = \left(\frac{V_{Te}}{\Omega\, ce\, \lambda_e}\right)^2$. If we use typical examples from 1 AU solar wind observations (see **Section 3** for values) and let $\beta_e \sim 1$, then $\lambda_i/\lambda_{De} \sim 4{,}000$–$20{,}000$. The separation of temporal scales goes as $\left(\frac{\omega_{pi}}{\Omega_{ci}}\right) = \sqrt{\frac{M_i}{m_e}}\left(\frac{\omega_{pe}}{\Omega_{ce}}\right)$, which is again $\sim 4{,}000$–$20{,}000$[11]. The computational cost of any given simulation scales as $\left(\frac{\omega_{pe}}{\Omega_{ce}}\right)^{d+1}\left(\frac{M_i}{m_e}\right)^{(d+1)/2}$, where d is the number of spatial dimensions used in the simulation. Thus, one can see that increasing $\left(\frac{\omega_{pe}}{\Omega_{ce}}\right)$ from ~10 to 100, even in a one-dimensional simulation, is at least 100 times more computationally expensive. It is also the case that simulations often use shock speeds satisfying $V_{Tp} < V_{Te} < U_{shn}$ while shocks in the solar wind tend to satisfy $V_{Tp} < U_{shn} \ll V_{Te} \ll c$ (see **Section 3** for values and definitions). For explicit PIC codes, there are additional computational expenses since the time steps are tied to the grid cell size, which raises the order of both $\frac{\omega_{pe}}{\Omega_{ce}}$ and $\frac{M_i}{m_e}$ by one. Therefore, it can be seen that we are approaching a computational wall and it may require new classes of simulation codes to overcome these limitations if we hope to use fully realistic plasma parameters.

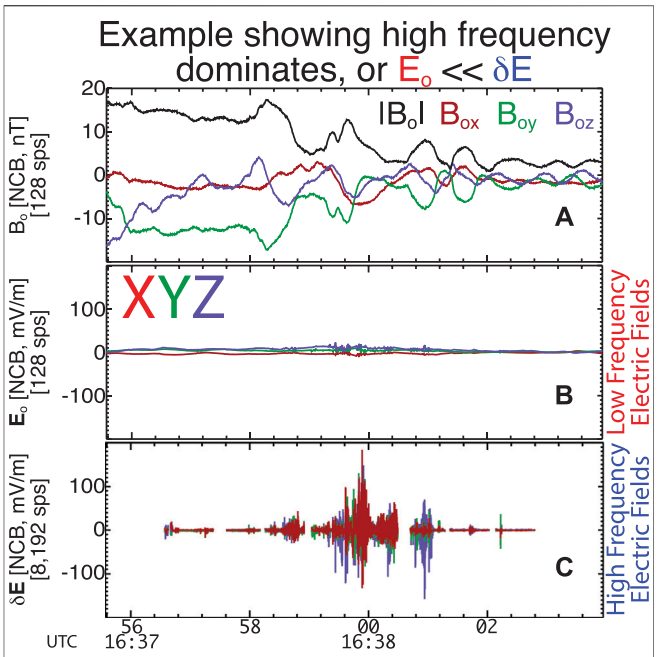

FIGURE 2 | An example terrestrial bow shock crossing observed by THEMIS-C on 2009-09-05. Panel **(A)** shows the magnetic field magnitude (black) and three normal incidence frame coordinate basis (NCB) (Scudder et al., 1986a) components vs time at 128 samples/second (sps) observed by the fluxgate magnetometer (Auster et al., 2008). Panel **(B)** shows the DC-coupled electric field at 128 sps observed by EFI (Bonnell et al., 2008; Cully et al., 2008). Panel **(C)** shows the AC-coupled electric field at 8,192 sps observed by EFI. Note that Panels **(B,C)** share the same vertical axis range for direct comparison (Adapted from Figure I:2 in Wilson et al. (2014a)).

[11]Note that ω_{pe}/Ω_{ci} is larger by an additional factor of $\sqrt{M_i/m_e}$.

3 EXAMPLE OBSERVATIONS VERSUS SIMULATIONS

In this section we will present two example observations made by the THEMIS (Angelopoulos, 2008) and MMS (Burch et al., 2016) missions to further illustrate the difference in magnitude between δE and E_o. We will also present PIC simulation results with parameters representative of a wide class of simulations discussed in the literature. The purpose is to illustrate some limitations of simulations to provoke advancement in closing the gap between observations and simulations of collisionless shocks.

Figure 2 shows a direct comparison between δE and E_o observed by THEMIS-C during a terrestrial bow shock crossing adapted from Wilson III et al. (2014a) and Wilson III et al. (2014b). The study examined the energy dissipation rates estimated from $(\mathbf{J} \cdot \mathbf{E})$ (i.e., from Poynting's theorem) due to the observed electric fields, **E**, and estimated current densities[12], **J**. They expanded $(\mathbf{j}_o + \delta\mathbf{j}) \cdot (\mathbf{E}_o + \delta\mathbf{E})$ and found that $(\mathbf{J}_o \cdot \delta\mathbf{E})$ was the dominant term[13], i.e., the fluctuating fields acted to limit the low frequency currents in/around the shock. Two important things were found: the magnitude of $(\mathbf{j}_o \cdot \delta\mathbf{E})$ and changes in this term were much larger than $(\mathbf{j}_o \cdot \mathbf{E}_o)$; the signs of the changes in $(\mathbf{j}_o \cdot \delta\mathbf{E})$ and $(\mathbf{j}_o \cdot \mathbf{E}_o)$ are opposite. The second point was interpreted to imply that the fluctuating fields were giving energy to the particles and the quasi-static fields were gaining energy from the particles. In short, the main conclusion from (Wilson III et al., 2014a; Wilson III et al., 2014b) was to illustrate that not only are the fluctuating electric fields large, they could potentially contribute enough energy transfer to compete with quasi-static fields. Prior to this study, the view by many in the community was that these fluctuating fields were completely negligible or just a minor, secondary effect. More recent, independent studies have performed similar analyses using different spacecraft and came to similar conclusions (Chen et al., 2018; Goodrich et al., 2018; Hull et al., 2020).

Figure 3 provides another example directly comparing δE and E_o observed by two MMS spacecraft during a terrestrial bow shock crossing. The electric fields are shown in the De-spun, Sun-pointing, L-vector system or DSL (Angelopoulos, 2008). For each spacecraft, $E_{o,j} \lesssim 10$ mV/m was satisfied for the entire interval with most time steps satisfying $E_{o,j} \lesssim 5$ mV/m. In contrast, the peak-to-peak δE_j values commonly exceed 100 mV/m in bursty, short duration, wave packet intervals. Note that even the electric field instrument on MMS has limitations in its accuracy for frequencies below ~1 Hz (Ergun et al., 2016; Lindqvist et al., 2016). Thus, even with the significantly improved instrument technology and design of MMS, the observations consistently show $\delta E \gg E_o$.

As a practical list of reference values, we present one-variable statistics of solar wind parameters from the same data set as in Wilson et al. (2018) and all interplanetary (IP) shocks in the Harvard

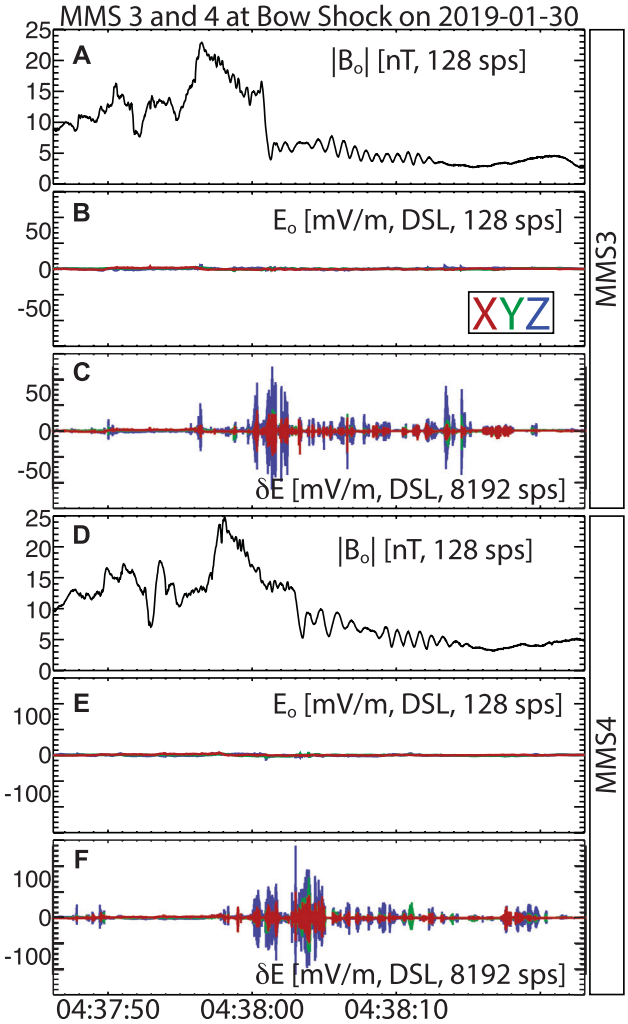

FIGURE 3 | An example terrestrial bow shock crossing observed by MMS3 and MMS4 on 2019-01-30. Panels **(A,D)** show the magnetic field magnitude (black) vs time at 128 sps observed by the fluxgate magnetometer (Russell et al., 2016). Panels **(B,E)** show the DC-coupled electric field components at 128 sps observed by the electric field instrument (Ergun et al., 2016; Lindqvist et al., 2016). Panels **(C,F)** show the AC-coupled electric field at 8,192 sps. Note that Panels **(B,C,E)** share the same vertical axis range for direct comparison.

Smithsonian's Center for Astrophysics *Wind* shock database[14]. The following will show parameters as $X_{5\%} \lesssim X \lesssim X_{95\%}, \tilde{X}$ [units], for the entire data set, where $X_{y\%}$ is the yth percentile and $\tilde{X}$ is the median. First, the typical parameters for over 400 IP shocks are as follows:

$1.10 \lesssim M_f \lesssim 4.60$, ~1.91 [N/A];
$1.15 \lesssim M_A \lesssim 6.24$, ~2.41 [N/A];
$36.6 \lesssim U_{shn} \lesssim 329.9$, ~98.2 [km/s];
$79.6 \lesssim V_{shn} \lesssim 762.3$, ~418.5 [km/s];
$22.2 \lesssim \theta_{Bn} \lesssim 87.7$, ~63.8 [deg];

[12]Note that similar current densities have been found using multi-spacecraft techniques (Hull et al., 2020) supporting the results in Wilson III et al. (2014a) and Wilson III et al. (2014b).

[13]Note that Q^o in this context is not the quasi-static terms in quasi-linear or linear theory but that from the DC-coupled measurements. Further, δQ is the fluctuating terms from these theories but the AC-coupled measurements, thus there is no a priori requirement that $\langle \delta Q \rangle = 0$.

[14]https://www.cfa.harvard.edu/shocks/wi_data/.

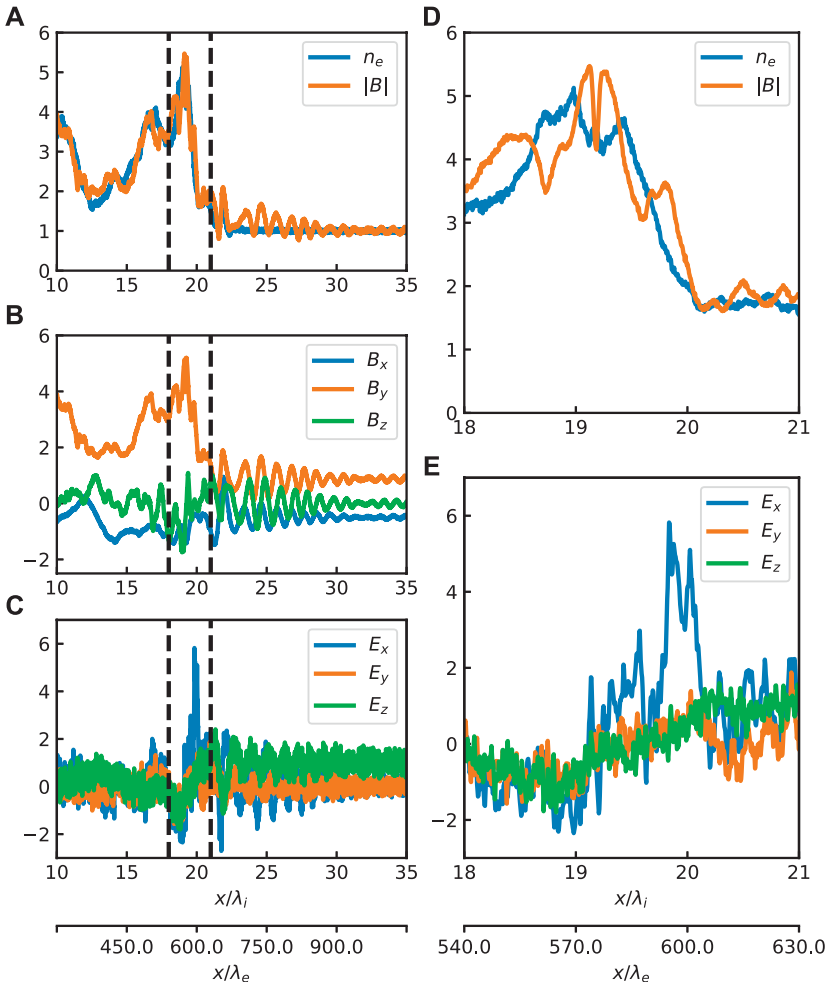

FIGURE 4 | An example taken from a PIC simulation with the shock normal along the *x*-direction. Each plot shows a 1D cut through the middle of 2D simulation domain. Panel **(A)** shows the magnetic field magnitude, *B* (orange), and the electron number density, n_e (blue), vs. spatial position *x*. Panels **(B,C)** show the components of magnetic field **(B)** and the electric field **(E)**. Panels **(D,E)** show a zoomed region of panels **(A,C)** respectively. The boundaries of the zoomed region are indicated by vertical dashed lines in panels **(A–C)**. All fields are measured in the simulation frame, where the shock moves in the positive *x* direction with the speed of ~2 V_A.

where U_{shn} is the upstream average flow speed in the shock rest frame and V_{shn} is the upstream average shock speed in the spacecraft frame. Note that the values of M_f, M_A, and U_{shn} will all be, on average, larger for most bow shocks in the interplanetary medium. These values are only meant to serve as a statistical baseline for reference. For example, the 11 bow shock crossings in Wilson et al. (2014a); Wilson et al. (2014b) satisfied $3.1 \lesssim M_A \lesssim 21.9$. Next, we present some typical plasma parameters[15] near 1 AU in the solar wind:

$80.2 \lesssim f_{ce} \lesssim 409$, ~162 [Hz];
$0.04 \lesssim f_{cp} \lesssim 0.22$, ~0.09 [Hz];
$17.2 \lesssim f_{pe} \lesssim 42.5$, ~26.3 [kHz];
$371 \lesssim f_{pp} \lesssim 944$, ~578 [Hz];
$1{,}579 \lesssim V_{Te} \lesssim 2{,}411$, ~1975 [km/s];
$21.9 \lesssim V_{Tp} \lesssim 76.9$, ~40.2 [km/s];
$1.03 \lesssim \rho_{ce} \lesssim 4.62$, ~2.28 [km];
$32.5 \lesssim \rho_{cp} \lesssim 186$, ~88.8 [km];
$1.12 \lesssim \lambda_e \lesssim 2.77$, ~1.82 [km];
$50.5 \lesssim \lambda_p \lesssim 129$, ~82.5 [km];
$4.74 \lesssim \lambda_{De} \lesssim 13.8$, ~8.58 [m];

where f_{cs} is the cyclotron frequency of species *s*, f_{ps} is the plasma frequency of species *s*, V_{Ts} is the most probable thermal speed of species *s*[16], ρ_{cs} is the thermal gyroradius of species *s*[17], λ_e is the inertial length of species *s*, and λ_{De} is the electron Debye length.

[15]Note that none of these are Doppler-shifted.

[16]$V_{Ts} = \sqrt{\frac{2k_B T_s}{m_s}}$.
[17]$\rho_{cs} = \frac{V_{Ts}}{\Omega_{cs}}$.

Next, we present ratios of some typical plasma parameters near 1 AU in the solar wind:

$176 \lesssim \lambda_e/\lambda_{De} \lesssim 269$, ~215 [N/A];
$131 \lesssim \rho_{ce}/\lambda_{De} \lesssim 670$, ~255 [N/A];
$8{,}000 \lesssim \lambda_p/\lambda_{De} \lesssim 12{,}160$, ~9,757 [N/A];
$0.34 \lesssim \lambda_e/\rho_{ce} \lesssim 1.63$, ~0.83 [N/A];
$92.4 \lesssim f_{pe}/f_{ce} \lesssim 474$, ~180 [N/A];
$4.79 \lesssim V_{Te}/\langle U_{shn}\rangle_{95\%} \lesssim 7.31$, ~5.99 [N/A];
$43.1 \lesssim V_{Te}/\langle U_{shn}\rangle_{5\%} \lesssim 65.9$, ~54.0 [N/A];
$0.53 \lesssim V_{Te}/c \lesssim 0.80$, ~0.66 [%];

where $\langle U_{shn}\rangle_{y\%}$ is the y^{th} percentile of U_{shn} presented earlier in this section and c is the speed of light in vacuum.

Figure 4 shows example one-dimensional cuts at three different time steps taken from a PIC simulation. The simulation parameters are as follows: $\theta_{Bn} \sim 60$ deg, $M_A \sim 6.5$, $\frac{\omega_{pe}}{\Omega_{ce}} \sim 4$, $\frac{M_i}{m_e} \sim 900$, $\Delta \sim 1\ \lambda_{De}$ (where Δ is the grid cell size), initially 1,000 particles per cell, and $\lambda_e/\lambda_{De} \sim 8$ (i.e., ~27 times smaller than median solar wind values near 1 AU). All of the panels show data in normalized units. The electric field is normalized to the initial upstream averaged convective electric field, $-\mathbf{V}\times\mathbf{B}$, i.e., the same E_o referenced for spacecraft observations. Thus, in the upstream the E_z component has an offset of unity. The normalization for n_e and $\mathbf{B}$ are just the initial upstream average values of the magnitude of each. All fields are measured in the simulation frame, where the shock moves in the positive x direction with the speed of approximately 2 V_A.

One can see that the largest values of $|\mathbf{E}|$ rarely exceed 2 (i.e., only short intervals >2 but peak only at ~6), similar to the simulations discussed previously. Further, the spatial scales at which these fields are maximized is on λ_e scales whereas observations show maximum electric fields at λ_{De} scales. One can also see that the ramp, e.g., B in panel (D), is about $L_{sh} \sim 28\ \lambda_e$ (or ~0.9 λ_i) thick, similar to observations that typically show ramps satisfying $L_{sh} < 35\ \lambda_e$ (or <0.8 λ_i) (Hobara et al., 2010; Mazelle et al., 2010). The simulation does, however, generate the ubiquitous whistler precursor train upstream of the shock ramp (Wilson et al., 2012; Wilson et al., 2017). Yet it is still not clear what parameter or parameters are controlling the shock ramp thickness and electric field amplitudes at very small spatial scales in simulations.

4 DISCUSSION

We have presented examples illustrating that spacecraft observations of collisionless shocks consistently show $\delta E \gg E_o$ where δE is due to electrostatic fluctuations satisfying $k\lambda_{De} \lesssim 1$ with frequencies well above f_{lh}. In contrast, most PIC simulations of collisionless shocks show considerably smaller amplitude of electrostatic fluctuations. This is true even when the simulation uses realistic $\frac{M_i}{m_e}$ and plasma betas.

Further, many simulations still generate shock ramps satisfying $L_{sh}/\lambda_e > 43$, i.e., thicker than most observations. However, much more progress has been made on this front where Yang et al. (2013) concluded that the shock ramp thickness decreased with increasing $\frac{M_i}{m_e}$ but increased with increasing ion plasma beta. There is still the question of whether $\frac{\omega_{pe}}{\Omega_{ce}}$ plays a role in the simulated values of L_{sh}, though Yang et al. (2013) was able to produce realistic thicknesses despite only having $\frac{\omega_{pe}}{\Omega_{ce}} = 2$.

Another potential issue that was not explicitly discussed in detail is that of the separation between λ_e and λ_{De}, but these are controlled by $\frac{M_i}{m_e}$ and $\frac{\omega_{pe}}{\Omega_{ce}}$. As previously shown, statistical solar wind parameters satisfy $\lambda_e/\lambda_{De} \sim 215$ (or $\lambda_p/\lambda_{De} \sim 9{,}757$) while simulations often have much smaller vales of $\lambda_p/\lambda_{De} \sim 70$–$500$ (or $\lambda_e/\lambda_{De} \sim 7$–$40$) (Umeda et al., 2011; Umeda et al., 2012a; Umeda et al., 2014; Savoini and Lembège, 2015). It is also the case that simulations often use shock speeds satisfying $V_{Tp} < V_{Te} < U_{shn} < c$ while shocks in the solar wind tend to satisfy $V_{Tp} < U_{shn} \ll V_{Te} \ll c$.

The origins of the discrepancy between the observation that $\delta E \gg E_o$ for electrostatic fluctuations satisfying $k\lambda_{De} \lesssim 1$ remain unclear. The ratios $\frac{M_i}{m_e}$ and $\frac{\omega_{pe}}{\Omega_{ce}}$ are the most likely parameters since they control the separation of spatial and temporal scales between the instabilities of interest and the global shock scales in an obvious manner. A lack of spatial resolution in most simulations may also be a factor. The purpose of this work is to motivate both observational and simulation communities to bridge the gap find closure with this issue. Without an accurate reproduction of the high frequency, large amplitude waves it is not possible to determine at what scales the electric fields dominate the energy dissipation through collisionless shocks.

DATA AVAILABILITY STATEMENT

The datasets presented in this study can be found in online repositories. The names of the repository/repositories and accession number(s) can be found below: https://cdaweb.gsfc.nasa.gov.

AUTHOR CONTRIBUTIONS

LW wrote most of the content and generated all the observational data figures presented herein. L-JC provided critical contributions to the bridge between observations and simulations. VR provided critical contributions to simulation techniques and limitations induced by the variation of different normalized parameters.

FUNDING

The work was supported by the International Space Science Institute's (ISSI) International Teams program. LW was partially supported by *Wind* MO&DA grants and a Heliophysics Innovation Fund (HIF) grant. Contributions of VR were supported by NASA grant 80NSSC18K1649. Computational resources supporting this work were provided by the NASA High-End Computing (HEC) Program through the NASA Advanced Supercomputing (NAS) Division at Ames Research Center.

ACKNOWLEDGMENTS

The authors thank B. Lembège, R. A. Treumann, M. Hesse, J. TenBarge, and J. Juno for useful discussions of kinetic simulations.

REFERENCES

Akimoto, K., and Winske, D. (1985). Ion-acoustic-like waves excited by the reflected ions at the earth's bow shock. *J. Geophys. Res.* 90, 12095. doi:10.1029/JA090iA12p12095

Akimoto, K., Papadopoulos, K., and Winske, D. (1985b). Ion-acoustic instabilities driven by an ion velocity ring. *J. Plasma Phys.* 34, 467–479. doi:10.1017/S0022377800003019

Akimoto, K., Papadopoulos, K., and Winske, D. (1985a). Lower-hybrid instabilities driven by an ion velocity ring. *J. Plasma Phys.* 34, 445–465. doi:10.1017/S0022377800003007

Allan, W., and Sanderson, J. J. (1974). Temperature gradient drive ion acoustic instability. *Plasma Phys.* 16, 753–767. doi:10.1088/0032-1028/16/8/005

Angelopoulos, V. (2008). The THEMIS mission. *Space Sci. Rev.* 141, 5–34. doi:10.1007/s11214-008-9336-1

Auer, P. L., Kilb, R. W., and Crevier, W. F. (1971). Thermalization in the earth's bow shock. *J. Geophys. Res.* 76, 2927–2939. doi:10.1029/JA076i013p02927

Auster, H. U., Glassmeier, K. H., Magnes, W., Aydogar, O., Baumjohann, W., Constantinescu, D., et al. (2008). The THEMIS fluxgate magnetometer. *Space Sci. Rev.* 141, 235–264. doi:10.1007/s11214-008-9365-9

Bale, S. D., Goetz, K., Harvey, P. R., Turin, P., Bonnell, J. W., Dudok de Wit, T., et al. (2016). The FIELDS instrument suite for solar probe plus. Measuring the coronal plasma and magnetic field, plasma waves and turbulence, and radio signatures of solar transients. *Space Sci. Rev.* 204, 49–82. doi:10.1007/s11214-016-0244-5

Bale, S. D., Hull, A., Larson, D. E., Lin, R. P., Muschietti, L., Kellogg, P. J., et al. (2002). Electrostatic turbulence and debye-scale structures associated with electron thermalization at collisionless shocks. *Astrophys. J.* 575, L25–L28. doi:10.1086/342609

Bale, S. D., Kellogg, P. J., Goetz, K., and Monson, S. J. (1998). Transverse z-mode waves in the terrestrial electron foreshock. *Geophys. Res. Lett.* 25, 9–12. doi:10.1029/97GL03493

Bale, S. D., Reiner, M. J., Bougeret, J. L., Kaiser, M. L., Krucker, S., Larson, D. E., et al. (1999). The source region of an interplanetary type II radio burst. *Geophys. Res. Lett.* 26, 1573–1576. doi:10.1029/1999GL900293

Behlke, R., André, M., Bale, S. D., Pickett, J. S., Cattell, C. A., Lucek, E. A., et al. (2004). Solitary structures associated with short large-amplitude magnetic structures (SLAMS) upstream of the Earth's quasi-parallel bow shock. *Geophys. Res. Lett.* 31, 16805. doi:10.1029/2004GL019524

Biskamp, D., von Hagenow, K. U., and Welter, H. (1972). Computer studies of current-driven ion-sound turbulence in three dimensions. *Phys. Lett.* 39, 351–352. doi:10.1016/0375-9601(72)90090-4

Bonnell, J. W., Mozer, F. S., Delory, G. T., Hull, A. J., Ergun, R. E., Cully, C. M., et al. (2008). The electric field instrument (EFI) for THEMIS. *Space Sci. Rev.* 141, 303–341. doi:10.1007/s11214-008-9469-2

Bougeret, J. L., Goetz, K., Kaiser, M. L., Bale, S. D., Kellogg, P. J., Maksimovic, M., et al. (2008). S/WAVES: the radio and plasma wave investigation on the STEREO mission. *Space Sci. Rev.* 136, 487–528. doi:10.1007/s11214-007-9298-8

Bougeret, J. L., Kaiser, M. L., Kellogg, P. J., Manning, R., Goetz, K., Monson, S. J., et al. (1995). Waves: the radio and plasma wave investigation on the wind spacecraft. *Space Sci. Rev.* 71, 231–263. doi:10.1007/BF00751331

Breneman, A., Cattell, C., Kersten, K., Paradise, A., Schreiner, S., Kellogg, P. J., et al. (2013). STEREO and Wind observations of intense cyclotron harmonic waves at the Earth's bow shock and inside the magnetosheath. *J. Geophys. Res.* 118, 7654–7664. doi:10.1002/2013JA019372

Breneman, A., Cattell, C., Wygant, J., Kersten, K., Wilson, L. B., III, Dai, L., et al. (2012). Explaining polarization reversals in STEREO wave data. *J. Geophys. Res.* 117, A04317. doi:10.1029/2011JA017425

Breneman, A., Cattell, C., Wygant, J., Kersten, K., Wilson, L. B., III, Schreiner, S., et al. (2011). Large-amplitude transmitter-associated and lightning-associated whistler waves in the Earth's inner plasmasphere at $L < 2$. *J. Geophys. Res.* 116, A06310. doi:10.1029/2010JA016288

Burch, J. L., Moor, T. E., Torbert, R. B., and Giles, B. L. (2016). Magnetospheric multiscale overview and science objectives. *Space Sci. Rev.* 199, 5–21. doi:10.1007/s11214-015-0164-9

Cairns, I. H. (1994). Fine structure in plasma waves and radiation near the plasma frequency in Earth's foreshock. *J. Geophys. Res.* 99, 23505. doi:10.1029/94JA01997

Cairns, I. H., and McMillan, B. F. (2005). Electron acceleration by lower hybrid waves in magnetic reconnection regions. *Phys. Plasmas.* 12, 102110. doi:10.1063/1.2080567

Cairns, I. H., and Robinson, P. A. (1992). Theory for low-frequency modulated Langmuir wave packets. *Geophys. Res. Lett.* 19, 2187–2190. doi:10.1029/92GL02632

Cattell, C., Dombeck, J., Wygant, J., Drake, J. F., Swisdak, M., Goldstein, M. L., et al. (2005). Cluster observations of electron holes in association with magnetotail reconnection and comparison to simulations. *J. Geophys. Res.* 110, A01211. doi:10.1029/2004JA010519

Cattell, C., Wygant, J. R., Goetz, K., Kersten, K., Kellogg, P. J., von Rosenvinge, T., et al. (2008). Discovery of very large amplitude whistler-mode waves in Earth's radiation belts. *Geophys. Res. Lett.* 35, L01105. doi:10.1029/2007GL032009

Chen, L. J., Wang, S., Wilson, L. B., III, Schwartz, S. J., Gershman, D. J., Bessho, N., et al. (2018). Electron bulk acceleration and thermalization at Earth's quasi-perpendicular bow shock. *Phys. Rev. Lett.* 120, 225101. doi:10.1103/PhysRevLett.120.225101

Cohen, I. J., Schwartz, S. J., Goodrich, K. A., Ahmadi, N., Ergun, R. E., Fuselier, S. A., et al. (2019). High-resolution measurements of the cross-shock potential, ion reflection, and electron heating at an interplanetary shock by MMS. *J. Geophys. Res.* 124, 3961–3978. doi:10.1029/2018JA026197

Comişel, H., Scholer, M., Soucek, J., and Matsukiyo, S. (2011). Non-stationarity of the quasi-perpendicular bow shock: comparison between cluster observations and simulations. *Ann. Geophys.* 29, 263–274. doi:10.5194/angeo-29-263-2011

Coroniti, F. V. (1970). Dissipation discontinuities in hydromagnetic shock waves. *J. Plasma Phys.* 4, 265–282. doi:10.1017/S0022377800004992

Cully, C. M., Ergun, R. E., Stevens, K., Nammari, A., and Westfall, J. (2008). The THEMIS digital fields board. *Space Sci. Rev.* 141, 343–355. doi:10.1007/s11214-008-9417-1

Decker, G., and Robson, A. E. (1972). Instability of the whistler structure of oblique hydromagnetic shocks. *Phys. Rev. Lett.* 29, 1071–1073. doi:10.1103/PhysRevLett.29.1071

Dimmock, A. P., Balikhin, M. A., and Hobara, Y. (2011). Comparison of three methods for the estimation of cross-shock electric potential using Cluster data. *Ann. Geophys.* 29, 815–822. doi:10.5194/angeo-29-815-2011

Dimmock, A. P., Balikhin, M. A., Krasnoselskikh, V. V., Walker, S. N., Bale, S. D., and Hobara, Y. (2012). A statistical study of the cross-shock electric potential at low Mach number, quasi-perpendicular bow shock crossings using cluster data. *J. Geophys. Res.* 117, A02210. doi:10.1029/2011JA017089

Dum, C. T. (1975). Strong-turbulence theory and the transition from Landau to collisional damping. *Phys. Rev. Lett.* 35, 947–950. doi:10.1103/PhysRevLett.35.947

Dum, C. T., Chodura, R., and Biskamp, D. (1974). Turbulent heating and quenching of the ion sound instability. *Phys. Rev. Lett.* 32, 1231–1234. doi:10.1103/PhysRevLett.32.1231

Dum, C. T., Marsch, E., and Pilipp, W. (1980). Determination of wave growth from measured distribution functions and transport theory. *J. Plasma Phys.* 23, 91–113. doi:10.1017/S0022377800022170

Dyrud, L. P., and Oppenheim, M. M. (2006). Electron holes, ion waves, and anomalous resistivity in space plasmas. *J. Geophys. Res.* 111, A01302. doi:10.1029/2004JA010482

Edmiston, J. P., and Kennel, C. F. (1984). A parametric survey of the first critical Mach number for a fast MHD shock. *J. Plasma Phys.* 32, 429–441. doi:10.1017/S002237780000218X

Ergun, R. E., Carlson, C. W., McFadden, J. P., Mozer, F. S., Muschietti, L., Roth, I., et al. (1998). Debye-scale plasma structures associated with magnetic-field-aligned electric fields. *Phys. Rev. Lett.* 81, 826–829. doi:10.1103/PhysRevLett.81.826

Ergun, R. E., Malaspina, D. M., Bale, S. D., McFadden, J. P., Larson, D. E., Mozer, F. S., et al. (2010). Spacecraft charging and ion wake formation in the near-Sun environment. *Phys. Plasmas.* 17, 072903. doi:10.1063/1.3457484

Ergun, R. E., Tucker, S., Westfall, J., Goodrich, K. A., Malaspina, D. M., Summers, D., et al. The axial double probe and fields signal processing for the MMS mission. *Space Sci. Rev.* 199, (2016). 167–188. doi:10.1007/s11214-014-0115-x

Filbert, P. C., and Kellogg, P. J. (1979). Electrostatic noise at the plasma frequency beyond the earth's bow shock. *J. Geophys. Res.* 84, 1369–1381. doi:10.1029/JA084iA04p01369

Forslund, D., Morse, R., Nielson, C., and Fu, J. (1972). Electron cyclotron drift instability and turbulence. *Phys. Fluids.* 15, 1303–1318. doi:10.1063/1.1694082

Forslund, D. W., Morse, R. L., and Nielson, C. W. Electron cyclotron drift instability. *Phys. Rev. Lett.* 25, (1970). 1266–1270. doi:10.1103/PhysRevLett.25.1266

Forslund, D. W., Morse, R. L., and Nielson, C. W. (1971). Nonlinear electron-cyclotron drift instability and turbulence. *Phys. Rev. Lett.* 27, 1424–1428. doi:10.1103/PhysRevLett.27.1424

Franz, J. R., Kintner, P. M., Pickett, J. S., and Chen, L. J. (2005). Properties of small-amplitude electron phase-space holes observed by Polar. *J. Geophys. Res.* 110, A09212. doi:10.1029/2005JA011095

Fredricks, R. W., Coroniti, F. V., Kennel, C. F., and Scarf, F. L. (1970a). Fast time-resolved spectra of electrostatic turbulence in the earth's bow shock. *Phys. Rev. Lett.* 24, 994–998. doi:10.1103/PhysRevLett.24.994

Fredricks, R. W., Crook, G. M., Kennel, C. F., Green, I. M., Scarf, F. L., Coleman, P. J., et al. (1970b). OGO 5 observations of electrostatic turbulence in bow shock magnetic structures. *J. Geophys. Res.* 75, 3751–3768. doi:10.1029/JA075i019p03751

Fredricks, R. W., Kennel, C. F., Scarf, F. L., Crook, G. M., and Green, I. M. (1968). Detection of electric-field turbulence in the earth's bow shock. *Phys. Rev. Lett.* 21, 1761–1764. doi:10.1103/PhysRevLett.21.1761

Fuselier, S. A., and Gurnett, D. A. (1984). Short wavelength ion waves upstream of the earth's bow shock. *J. Geophys. Res.* 89, 91–103. doi:10.1029/JA089iA01p00091

Galeev, A. A. (1976). "Collisionless shocks," in Physics of solar planetary environments; Proceedings of the International Symposium on Solar-Terrestrial Physics, Boulder, CO, June 7–18, 1976. Vol. 1. (A77-44201 20-88). Editor D. J. Williams (Washington, D.C.: American Geophysical Union). 464–490.

Galeev, A. A., and Karpman, V. I. (1963). Turbulence theory of a weakly nonequilibrium low-density plasma and structure of shock waves. *Sov. Phys.–JETP.* 17, 403–409.

Gary, S. P. (1981). Microinstabilities upstream of the earth's bow shock – a brief review. *J. Geophys. Res.* 86, 4331–4336. doi:10.1029/JA086iA06p04331

Gladd, N. T. (1976). The lower hybrid drift instability and the modified two stream instability in high density theta pinch environments. *Plasma Phys.* 18, 27–40. doi:10.1088/0032-1028/18/1/002

Goldman, M. V., Newman, D. L., Lapenta, G., Andersson, L., Gosling, J. T., Eriksson, S., et al. (2014). Čerenkov emission of quasiparallel whistlers by fast electron phase-space holes during magnetic reconnection. *Phys. Rev. Lett.* 112, 145002. doi:10.1103/PhysRevLett.112.145002

Goodrich, K. A., Ergun, R. E., Schwartz, S. J., Wilson, L. B., III, Johlander, A., Newman, D., et al. (2019). Impulsively reflected ions: a plausibile mechanism for ion acoustic wave growth in collisionless shocks. *J. Geophys. Res.* 124, 1855–1865. doi:10.1029/2018JA026436

Goodrich, K. A., Ergun, R. E., Schwartz, S. J., Wilson, L. B., III, Newman, D., Wilder, F. D., et al. (2018). MMS observations of electrostatic waves in an oblique shock crossing. *J. Geophys. Res.* 123, 9430–9442. doi:10.1029/2018JA025830

Gurnett, D. A., and Anderson, R. R. (1977). Plasma wave electric fields in the solar wind - initial results from HELIOS 1. *J. Geophys. Res.* 82, 632–650. doi:10.1029/JA082i004p00632

Gurnett, D. A., Neubauer, F. M., and Schwenn, R. (1979). Plasma wave turbulence associated with an interplanetary shock. *J. Geophys. Res.* 84, 541–552. doi:10.1029/JA084iA02p00541

Henchen, R. J., Sherlock, M., Rozmus, W., Katz, J., Masson-Laborde, P. E., Cao, D., et al. (2019). Measuring heat flux from collective Thomson scattering with non-Maxwellian distribution functions. *Phys. Plasmas.* 26, 032104. doi:10.1063/1.5086753

Hobara, Y., Balikhin, M., Krasnoselskikh, V., Gedalin, M., and Yamagishi, H. (2010). Statistical study of the quasi-perpendicular shock ramp widths. *J. Geophys. Res.* 115, 11106. doi:10.1029/2010JA015659

Hoshino, M., and Shimada, N. (2002). Nonthermal electrons at high Mach number shocks: electron shock surfing acceleration. *Astrophys. J.* 572, 880–887. doi:10.1086/340454

Hull, A. J., and Scudder, J. D. (2000). Model for the partition of temperature between electrons and ions across collisionless, fast mode shocks. *J. Geophys. Res.* 105, 27323–27342. doi:10.1029/2000JA900105

Hull, A. J., Larson, D. E., Wilber, M., Scudder, J. D., Mozer, F. S., Russell, C. T., et al. (2006). Large-amplitude electrostatic waves associated with magnetic ramp substructure at Earth's bow shock. *Geophys. Res. Lett.* 33, 15104. doi:10.1029/2005GL025564

Hull, A. J., Muschietti, L., Le Contel, O., Dorelli, J. C., and Lind, P. A. (2020). MMS observations of intense whistler waves within earth's supercritical bow shock: source mechanism and impact on shock structure and plasma transport. *J. Geophys. Res.* 125, e27290. doi:10.1029/2019JA027290

Johlander, A., Schwartz, S. J., Vaivads, A., Khotyaintsev, Y. V., Gingell, I., Peng, I. B., et al. (2016). Rippled quasiperpendicular shock observed by the magnetospheric multiscale spacecraft. *Phys. Rev. Lett.* 117, 165101. doi:10.1103/PhysRevLett.117.165101

Kellogg, P. J. (2003). Langmuir waves associated with collisionless shocks; a review. *Planet. Space Sci.* 51, 681–691. doi:10.1016/j.pss.2003.05.001

Kellogg, P. J., Cattell, C. A., Goetz, K., Monson, S. J., and Wilson, L. B., III (2010). Electron trapping and charge transport by large amplitude whistlers. *Geophys. Res. Lett.* 37, L20106. doi:10.1029/2010GL044845

Kellogg, P. J., Cattell, C. A., Goetz, K., Monson, S. J., and Wilson, L. B., III (2011). Large amplitude whistlers in the magnetosphere observed with wind-waves. *J. Geophys. Res.* 116, A09224. doi:10.1029/2010JA015919

Kellogg, P. J., Goetz, K., Howard, R. L., and Monson, S. J. (1992). Evidence for Langmuir wave collapse in the interplanetary plasma. *Geophys. Res. Lett.* 19, 1303–1306. doi:10.1029/92GL01016

Kellogg, P. J., Goetz, K., Monson, S. J., and Opitz, A. (2013). Observations of transverse Z mode and parametric decay in the solar wind. *J. Geophys. Res.* 118, 4766–4775. doi:10.1002/jgra.50443

Kennel, C. F. (1987). Critical Mach numbers in classical magnetohydrodynamics. *J. Geophys. Res.* 92, 13427–13437. doi:10.1029/JA092iA12p13427

Kennel, C. F., Edmiston, J. P., and Hada, T. (1985). "A quarter century of collisionless shock research," in *Collisionless shocks in the heliosphere: a tutorial review. Geophysics monograph series*. Editors R. G. Stone and B. T. Tsurutani (Washington, D.C.: AGU), Vol. 34, 1–36. doi:10.1029/GM034p0001

Kersten, K., Cattell, C. A., Breneman, A., Goetz, K., Kellogg, P. J., Wygant, J. R., et al. (2011). Observation of relativistic electron microbursts in conjunction with intense radiation belt whistler-mode waves. *Geophys. Res. Lett.* 38, L08107. doi:10.1029/2011GL046810

Krasnoselskikh, V. V., Dudok de Wit, T., and Bale, S. D. (2011). Determining the wavelength of Langmuir wave packets at the Earth's bow shock. *Ann. Geophys.* 29, (2011). 613–617. doi:10.5194/angeo-29-613-2011

Krasnoselskikh, V. V., Lembège, B., Savoini, P., and Lobzin, V. V. (2002). Nonstationarity of strong collisionless quasiperpendicular shocks: theory and full particle numerical simulations. *Phys. Plasmas.* 9, 1192–1209. doi:10.1063/1.1457465

Kurth, W. S., Gurnett, D. A., and Scarf, F. L. (1979). High-resolution spectrograms of ion acoustic waves in the solar wind. *J. Geophys. Res.* 84, 3413–3419. doi:10.1029/JA084iA07p03413

Lampe, M., Manheimer, W. M., McBride, J. B., Orens, J. H., Papadopoulos, K., Shanny, R., et al. (1972). Theory and simulation of the beam cyclotron instability. *Phys. Fluids.* 15, 662–675. doi:10.1063/1.1693961

Lavraud, B., and Larson, D. E. (2016). Correcting moments of *in situ* particle distribution functions for spacecraft electrostatic charging. *J. Geophys. Res.* 121, 8462–8474. doi:10.1002/2016JA022591

Lembège, B., Savoini, P., Hellinger, P., and Trávníček, P. M. (2009). Nonstationarity of a two-dimensional perpendicular shock: competing mechanisms. *J. Geophys. Res.* 114, A03217. doi:10.1029/2008JA013618

Lemons, D. S., and Gary, S. P. Current-driven instabilities in a laminar perpendicular shock. *J. Geophys. Res.* 83, (1978). 1625–1632. doi:10.1029/JA083iA04p01625

Lemons, D. S., and Gary, S. P. (1977). Electromagnetic effects on the modified two-stream instability. *J. Geophys. Res.* 82, 2337–2342. doi:10.1029/JA082i016p02337

Lindqvist, P. A., Olsson, G., Torbert, R. B., King, B., Granoff, M., Rau, D., et al. (2016). The spin-plane double probe electric field instrument for MMS. *Space Sci. Rev.* 199, 137–165. doi:10.1007/s11214-014-0116-9

Lu, Q. M., Lembège, B., Tao, J. B., and Wang, S. (2008). Perpendicular electric field in two-dimensional electron phase-holes: a parameter study. *J. Geophys. Res.* 113, A11219. doi:10.1029/2008JA013693

Malaspina, D. M., and Ergun, R. E. (2008). Observations of three-dimensional Langmuir wave structure. *J. Geophys. Res.* 113, A12108. doi:10.1029/2008JA013656

Malaspina, D. M., Li, B., Cairns, I. H., Robinson, P. A., Kuncic, Z., and Ergun, R. E. Terrestrial foreshock Langmuir waves: STEREO observations, theoretical modeling, and quasi-linear simulations. *J. Geophys. Res.* 114, (2009). A12101. doi:10.1029/2009JA014493

Marsch, E., and Chang, T. Electromagnetic lower hybrid waves in the solar wind. *J. Geophys. Res.* 88, (1983). 6869–6880. doi:10.1029/JA088iA09p06869

Matsukiyo, S., and Matsumoto, Y. (2015). Electron acceleration at a high beta and low Mach number rippled shock. *J. Phys. Conf.* 642, 012017. doi:10.1088/1742-6596/642/1/012017

Matsukiyo, S., and Scholer, M. (2012). Dynamics of energetic electrons in nonstationary quasi-perpendicular shocks. *J. Geophys. Res.* 117, A11105. doi:10.1029/2012JA017986

Matsukiyo, S., and Scholer, M. (2006). On microinstabilities in the foot of high Mach number perpendicular shocks. *J. Geophys. Res.* 111, A06104. doi:10.1029/2005JA011409

Mazelle, C., Lembège, B., Morgenthaler, A., Meziane, K., Horbury, T. S., Génot, V., et al. (2010). Self-reformation of the quasi-perpendicular shock: CLUSTER observations. *Proc. 12th Intl. Solar Wind Conf.* 1216, 471–474. doi:10.1063/1.3395905

Mellott, M. M., and Greenstadt, E. W. (1988). Plasma waves in the range of the lower hybrid frequency – ISEE 1 and 2 observations at the earth's bow shock. *J. Geophys. Res.* 93, 9695–9708. doi:10.1029/JA093iA09p09695

Mitchell, J. J., and Schwartz, S. J. (2014). Isothermal magnetosheath electrons due to nonlocal electron cross talk. *J. Geophys. Res.* 119, 1080–1093. doi:10.1002/2013JA019211

Mitchell, J. J., and Schwartz, S. J. Nonlocal electron heating at the Earth's bow shock and the role of the magnetically tangent point. *J. Geophys. Res.* 118, (2013). 7566–7575. doi:10.1002/2013JA019226

Morton, K. W. (1964). Finite amplitude compression waves in a collision-free plasma. *Phys. Fluids.* 7, 1800–1815. doi:10.1063/1.2746780

Muschietti, L., and Lembège, B. (2013). Microturbulence in the electron cyclotron frequency range at perpendicular supercritical shocks. *J. Geophys. Res.* 118, 2267–2285. doi:10.1002/jgra.50224

Muschietti, L., and Lembège, B. (2017). Two-stream instabilities from the lower-hybrid frequency to the electron cyclotron frequency: application to the front of quasi-perpendicular shocks. *Ann. Geophys.* 35, 1093–1112. doi:10.5194/angeo-35-1093-2017

Papadopoulos, K. (1985). "Microinstabilities and anomalous transport," in *Collisionless shocks in the heliosphere: a tutorial review. Geophysics Monograph Series*. Editors R. G. Stone and B. T. Tsurutani (Washington, DC: AGU), Vol. 34, 59–90. doi:10.1029/GM034p0059

Papadopoulos, K., and Palmadesso, P. (1976). Excitation of lower hybrid waves in a plasma by electron beams. *Phys. Fluids.* 19, 605. doi:10.1063/1.861501

Pulupa, M., and Bale, S. D. (2008). Structure on interplanetary shock fronts: type II radio burst source regions. *Astrophys. J.* 676, 1330–1337. doi:10.1086/526405

Pulupa, M. P., Bale, S. D., and Kasper, J. C. (2010). Langmuir waves upstream of interplanetary shocks: dependence on shock and plasma parameters. *J. Geophys. Res.* 115, A04106. doi:10.1029/2009JA014680

Pulupa, M. P., Bale, S. D., Salem, C., and Horaites, K. (2014). Spin-modulated spacecraft floating potential: observations and effects on electron moments. *J. Geophys. Res.* 119, 647–657. doi:10.1002/2013JA019359

Rodriguez, P., and Gurnett, D. A. (1975). Electrostatic and electromagnetic turbulence associated with the earth's bow shock. *J. Geophys. Res.* 80, 19–31. doi:10.1029/JA080i001p00019

Russell, C. T., Anderson, B. J., Baumjohann, W., Bromund, K. R., Dearborn, D., Fischer, D., et al. (2016). The magnetospheric multiscale magnetometers. *Space Sci. Rev.* 199, 189–256. doi:10.1007/s11214-014-0057-3

Sagdeev, R. Z. (1966). Cooperative phenomena and shock waves in collisionless plasmas. *Rev. Plasma Phys.* 4, 23.

Saito, S., Nariyuki, Y., and Umeda, T. (2017). Generation of intermittent ion acoustic waves in whistler-mode turbulence. *Phys. Plasmas.* 24, 072304. doi:10.1063/1.4990443

Santolík, O., Gurnett, D. A., Pickett, J. S., Parrot, M., and Cornilleau-Wehrlin, N. (2003). Spatio-temporal structure of storm-time chorus. *J. Geophys. Res.* 108, 1278. doi:10.1029/2002JA009791

Savoini, P., and Lembège, B. (2015). Production of nongyrotropic and gyrotropic backstreaming ion distributions in the quasi-perpendicular ion foreshock region. *J. Geophys. Res.* 120, 7154–7171. doi:10.1002/2015JA021018

Scholer, M., and Burgess, D. (2006). Transition scale at quasiperpendicular collisionless shocks: full particle electromagnetic simulations. *Phys. Plasmas.* 13, 062101. doi:10.1063/1.2207126

Scholer, M., and Burgess, D. (2007). Whistler waves, core ion heating, and nonstationarity in oblique collisionless shocks. *Phys. Plasmas.* 14, 072103. doi:10.1063/1.2748391

Scholer, M., and Matsukiyo, S. (2004). Nonstationarity of quasi-perpendicular shocks: a comparison of full particle simulations with different ion to electron mass ratio. *Ann. Geophys.* 22, 2345–2353. doi:10.5194/angeo-22-2345-2004

Schwartz, S. J., Thomsen, M. F., Bame, S. J., and Stansberry, J. (1988). Electron heating and the potential jump across fast mode shocks. *J. Geophys. Res.* 93, 12923–12931. doi:10.1029/JA093iA11p12923

Scime, E. E., Bame, S. J., Feldman, W. C., Gary, S. P., Phillips, J. L., and Balogh, A. (1994b). Regulation of the solar wind electron heat flux from 1 to 5 AU: ULYSSES observations. *J. Geophys. Res.* 99, 23401–23410. doi:10.1029/94JA02068

Scime, E. E., Phillips, J. L., and Bame, S. J. (1994a). Effects of spacecraft potential on three-dimensional electron measurements in the solar wind. *J. Geophys. Res.* 99, 14769–14776. doi:10.1029/94JA00489

Scudder, J. D., Aggson, T. L., Mangeney, A., Lacombe, C., and Harvey, C. C. (1986a). The resolved layer of a collisionless, high beta, supercritical, quasi-perpendicular shock wave. I–rankine-Hugoniot geometry, currents, and stationarity. *J. Geophys. Res.* 91, 11019–11052. doi:10.1029/JA091iA10p11019

Scudder, J. D., Aggson, T. L., Mangeney, A., Lacombe, C., and Harvey, C. C. (1986b). The resolved layer of a collisionless, high beta, supercritical, quasi-perpendicular shock wave. II - dissipative fluid electrodynamics. *J. Geophys. Res.* 91, 11053–11073. doi:10.1029/JA091iA10p11053

Scudder, J. D., Cao, X., and Mozer, F. S. (2000). Photoemission current-spacecraft voltage relation: key to routine, quantitative low-energy plasma measurements. *J. Geophys. Res.* 105, 21281–21294. doi:10.1029/1999JA900423

Scudder, J. D., Mangeney, A., Lacombe, C., Harvey, C. C., and Wu, C. S. (1986c). The resolved layer of a collisionless, high beta, supercritical, quasi-perpendicular shock wave. III – Vlasov electrodynamics. *J. Geophys. Res.* 91, 11075–11097. doi:10.1029/JA091iA10p11075

Singh, N., Loo, S. M., Wells, B. E., and Deverapalli, C. (2000). Three-dimensional structure of electron holes driven by an electron beam. *Geophys. Res. Lett.* 27, 2469–2472. doi:10.1029/2000GL003766

Singh, N., Loo, S. M., and Wells, B. E. (2001). Electron hole as an antenna radiating plasma waves. *Geophys. Res. Lett.* 28, 1371–1374. doi:10.1029/2000GL012652

Soucek, J., Santolík, O., Dudok de Wit, T., and Pickett, J. S. (2009). Cluster multispacecraft measurement of spatial scales of foreshock Langmuir waves. *J. Geophys. Res.* 114, A02213. doi:10.1029/2008JA013770

Stringer, T. E. (1963). Low-frequency waves in an unbounded plasma. *J. Nuclear Energy.* 5, 89–107. doi:10.1088/0368-3281/5/2/304

Tidman, D. A., and Krall, N. A. (1971). *Shock waves in collisionless plasmas*. New York, NY: John Wiley & Sons.

Tidman, D. A., and Northrop, T. G. (1968). Emission of plasma waves by the Earth's bow shock. *J. Geophys. Res.* 73, 1543–1553. doi:10.1029/JA073i005p01543

Tsurutani, B. T., Verkhoglyadova, O. P., Lakhina, G. S., and Yagitani, S. (2009). Properties of dayside outer zone chorus during HILDCAA events: loss of energetic electrons. *J. Geophys. Res.* 114, A03207. doi:10.1029/2008JA013353

Umeda, T., Kidani, Y., Matsukiyo, S., and Yamazaki, R. (2014). Dynamics and microinstabilities at perpendicular collisionless shock: a comparison of large-scale two-dimensional full particle simulations with different ion to electron mass ratio. *Phys. Plasmas.* 21, 022102. doi:10.1063/1.4863836

Umeda, T., Kidani, Y., Matsukiyo, S., and Yamazaki, R. (2012b). Microinstabilities at perpendicular collisionless shocks: a comparison of full particle simulations with different ion to electron mass ratio. *Phys. Plasmas.* 19, 042109. doi:10.1063/1.3703319

Umeda, T., Kidani, Y., Matsukiyo, S., and Yamazaki, R. (2012a). Modified two-stream instability at perpendicular collisionless shocks: full particle simulations. *J. Geophys. Res.* 117, A03206. doi:10.1029/2011JA017182

Umeda, T., Yamao, M., and Yamazaki, R. (2011). Cross-scale coupling at a perpendicular collisionless shock. *Planet. Space Sci.* 59, 449–455. doi:10.1016/j.pss.2010.01.007

Umeda, T., Yamazaki, R., Ohira, Y., Ishizaka, N., Kakuchi, S., Kuramitsu, Y., et al. (2019). Full particle-in-cell simulation of the interaction between two plasmas for laboratory experiments on the generation of magnetized collisionless shocks with high-power lasers. *Phys. Plasmas.* 26, 032303. doi:10.1063/1.5079906

Vasko, I. Y., Mozer, F. S., Krasnoselskikh, V. V., Artemyev, A. V., Agapitov, O. V., Bale, S. D., et al. (2018). Solitary waves across supercritical quasi-perpendicular shocks. *Geophys. Res. Lett.* 45, 5809–5817. doi:10.1029/2018GL077835

Vedenov, A. A. (1963). Quasi-linear plasma theory (theory of a weakly turbulent plasma). *J. Nucl. Energy.* 5, 169–186. doi:10.1088/0368-3281/5/3/305

Walker, S. N., Balikhin, M. A., Alleyne, H. S. C. K., Hobara, Y., André, M., and Dunlop, M. W. (2008). Lower hybrid waves at the shock front: a reassessment. *Ann. Geophys.* 26, 699–707. doi:10.5194/angeo-26-699-2008

Wang, R., Vasko, I. Y., Mozer, F. S., Bale, S. D., Artemyev, A. V., Bonnell, J. W., et al. (2020). Electrostatic turbulence and debye-scale structures in collisionless shocks. *Astrophys. J. Lett.* 889, L9. doi:10.3847/2041-8213/ab6582

Wilson, L. B., III (2010). The microphysics of collisionless shocks. PhD thesis, University of Minnesota. Publication Number: AAT 3426498; ISBN: 9781124274577; Minneapolis, MN: Advisor: Cynthia Cattell.

Wilson, L. B., III, Cattell, C., Kellogg, P. J., Goetz, K., Kersten, K., Hanson, L., et al. (2007). Waves in interplanetary shocks: a wind/WAVES study. *Phys. Rev. Lett.* 99, 041101. doi:10.1103/PhysRevLett.99.041101

Wilson, L. B., III, Cattell, C. A., Kellogg, P. J., Goetz, K., Kersten, K., Kasper, J. C., et al. (2010). Large-amplitude electrostatic waves observed at a supercritical interplanetary shock. *J. Geophys. Res.* 115, A12104. doi:10.1029/2010JA015332

Wilson, L. B., III, Cattell, C. A., Kellogg, P. J., Wygant, J. R., Goetz, K., Breneman, A., et al. (2011). The properties of large amplitude whistler mode waves in the magnetosphere: propagation and relationship with geomagnetic activity. *Geophys. Res. Lett.* 38, L17107. doi:10.1029/2011GL048671

Wilson, L. B., III, Chen, L. J., Wang, S., Schwartz, S. J., Turner, D. L., Stevens, M. L., et al. (2019a). Electron energy partition across interplanetary shocks: II. Statistics. *Astrophys. J.* 245. doi:10.3847/1538-4365/ab5445

Wilson, L. B., III, Chen, L. J., Wang, S., Schwartz, S. J., Turner, D. L., Stevens, M. L., et al. (2020). Electron energy partition across interplanetary shocks: III. Analysis. *Astrophys. J.* 893. doi:10.3847/1538-4357/ab7d39

Wilson, L. B., III, Chen, L. J., Wang, S., Schwartz, S. J., Turner, D. L., Stevens, M. L., et al. (2019b). Electron energy partition across interplanetary shocks: I. Methodology and data product. *Astrophys. J.* 243. doi:10.3847/1538-4365/ab22bd

Wilson, L. B., III, Koval, A., Sibeck, D. G., Szabo, A., Cattell, C. A., Kasper, J. C., et al. (2013). Shocklets, SLAMS, and field-aligned ion beams in the terrestrial foreshock. *J. Geophys. Res.* 118, 957–966. doi:10.1029/2012JA018186

Wilson, L. B., III, Koval, A., Szabo, A., Breneman, A., Cattell, C. A., Goetz, K., et al. (2012). Observations of electromagnetic whistler precursors at supercritical interplanetary shocks. *Geophys. Res. Lett.* 39, L08109. doi:10.1029/2012GL051581

Wilson, L. B., III, Koval, A., Szabo, A., Stevens, M. L., Kasper, J. C., Cattell, C. A., et al. (2017). Revisiting the structure of low Mach number, low beta, quasi-perpendicular shocks. *J. Geophys. Res.* 122, 9115–9133. doi:10.1002/2017JA024352

Wilson, L. B., III, Sibeck, D. G., Breneman, A. W., Le Contel, O., Cully, C., Turner, D. L., et al. (2014a). Quantified energy dissipation rates in the terrestrial bow shock: 1. Analysis techniques and methodology. *J. Geophys. Res.* 119, 6455–6474. doi:10.1002/2014JA019929

Wilson, L. B., III, Sibeck, D. G., Breneman, A. W., Le Contel, O., Cully, C., Turner, D. L., et al. (2014b). Quantified energy dissipation rates in the terrestrial bow shock: 2. Waves and dissipation. *J. Geophys. Res.* 119, 6475–6495. doi:10.1002/2014JA019930

Wilson, L. B., III, Sibeck, D. G., Turner, D. L., Osmane, A., Caprioli, D., and Angelopoulos, V. (2016). Relativistic electrons produced by foreshock disturbances observed upstream of the Earth's bow shock. *Phys. Rev. Lett.* 117, 215101. doi:10.1103/PhysRevLett.117.215101

Wilson, L. B., III, Stevens, M. L., Kasper, J. C., Klein, K. G., Maruca, B., Bale, S. D., et al. (2018). The Statistical Properties of Solar Wind Temperature Parameters Near 1 au. *Astrophys. J. Suppl.* 236, 41. doi:10.3847/1538-4365/aab71c

Wu, C. S., Winske, D., Papadopoulos, K., Zhou, Y. M., Tsai, S. T., and Guo, S. C. (1983). A kinetic cross-field streaming instability. *Phys. Fluids.* 26, 1259–1267. doi:10.1063/1.864285

Wu, C. S., Winske, D., Tanaka, M., Papadopoulos, K., Akimoto, K., Goodrich, C. C., et al. (1984). Microinstabilities associated with a high Mach number, perpendicular bow shock. *Space Sci. Rev.* 37, 63–109. doi:10.1007/BF00213958

Wygant, J. R., Bensadoun, M., and Mozer, F. S. (1987). Electric field measurements at subcritical, oblique bow shock crossings. *J. Geophys. Res.* 92, 11109–11121. doi:10.1029/JA092iA10p11109

Wygant, J. R., Bonnell, J. W., Goetz, K., Ergun, R. E., Mozer, F. S., Bale, S. D., et al. (2013). The electric field and waves instruments on the radiation belt storm probes mission. *Space Sci. Rev.* 179, 183–220. doi:10.1007/s11214-013-0013-7

Yang, Z., Lu, Q., Gao, X., H, C., Yang, H., Liu, Y., et al. (2013). Magnetic ramp scale at supercritical perpendicular collisionless shocks: full particle electromagnetic simulations. *Phys. Plasmas.* 20, 092116. doi:10.1063/1.4821825

Zeković, V. (2019). Resonant micro-instabilities at quasi-parallel collisionless shocks: cause or consequence of shock (re)formation. *Phys. Plasmas.* 26, 032106. doi:10.1063/1.5050909

Conflict of Interest: The authors declare that the research was conducted in the absence of any commercial or financial relationships that could be construed as a potential conflict of interest.

frontiers in Astronomy and Space Sciences

PERSPECTIVE
published: 31 March 2021
doi: 10.3389/fspas.2021.627576

Possible Advantages of a Twin Spacecraft Heliospheric Mission at the Sun-Earth Lagrangian Points L4 and L5

A. Bemporad *

INAF, Turin Astrophysical Observatory, Pino Torinese, Italy

After the launch of STEREO twin spacecraft, and most recently of Solar Orbiter and Parker Solar Probe spacecraft, the next mission that will explore Sun-Earth interactions and how the Sun modulates the Heliosphere will be the "Lagrange" mission, which will consist of two satellites placed in orbit around L1 and L5 Sun-Earth Lagrangian points. Despite the significant novelties that will be provided by such a double vantage point, there will be also missing information, that are briefly discussed here. For future heliospheric missions, an alternative advantageous approach that has not been considered so far would be to place two twin spacecraft not in L1 and L5, but in L4 and L5 Lagrangian points. If these two spacecraft will be equipped with *in situ* instruments, and also remote sensing instruments measuring not only photospheric but also coronal magnetic fields, significant advancing will be possible. In particular, data provided by such a twin mission will allow to follow the evolution of magnetic fields from inside the Sun (with stereoscopic helioseismology), to its surface (with classical photospheric magnetometers), and its atmosphere (with spectro-polarimeters); this will provide a tremendous improvement in our physical understanding of solar activity. Moreover, the L4-L5 twin satellites will take different interesting configurations, such as relative quadrature, and quasi-quadrature with the Earth, providing a baseline for monitoring the Sun-to-Earth propagation of solar disturbances.

Keywords: space weather, future missions, open problems, solar physics, solar eruptions

OPEN ACCESS

Edited by:
Luca Sorriso-Valvo, Institute for Space Physics (Uppsala), Sweden

Reviewed by:
Scott William McIntosh, National Center for Atmospheric Research (UCAR), United States
Emilia Kilpua, University of Helsinki, Finland

***Correspondence:**
A. Bemporad
alessandro.bemporad@inaf.it

Specialty section:
This article was submitted to Space Physics, a section of the journal Frontiers in Astronomy and Space Sciences

Received: *09 November 2020*
Accepted: *20 January 2021*
Published: *31 March 2021*

Citation:
Bemporad A (2021) Possible Advantages of a Twin Spacecraft Heliospheric Mission at the Sun-Earth Lagrangian Points L4 and L5. Front. Astron. Space Sci. 8:627576. doi: 10.3389/fspas.2021.627576

INTRODUCTION: STATE OF THE ART

One of the main target of Space Weather is to provide alerts to the human society before the occurrence of a geomagnetic storm, within the reasonable amount of time required to prevent possible consequences for human technologies and activities (see e.g., Schrijver et al., 2015; Eastwood et al., 2018). For these reasons, in 2009 ESA started the Space Situation Awareness (SSA) program (see e.g., Opgenoorth et al., 2019 and references therein), working on three main areas: Space Weather (SWE), Near-Earth Objects (NEO), and Space Surveillance and Tracking (SST), with SSA Program Office located at ESOC Darmstad (Germany). Focusing on main progresses for SW activities, over the last 12 years lot of developments have been implemented, such as (but not limited to) the SW data center (SWDC) located at ESA Redu Space Services Station in Belgium, and the ESA SSA SW coordination center (SSCC) in Bruxelles (established in 2013), with integrate information provided also by the Met Office Space Weather Operations Center in United Kingdom (established in 2014).

In particular, SSCC is coordinating a common effort at European level, the SW Service Network including 5 "Expert Service Centers" (ESCs) and consisting of ~40 European teams collaborating to provide products and services for customers. These centers heavily rely on space-based data provided by remote sensing instruments. Hence, under the SSA program ESA is also expanding the use of data provided by existing missions (e.g., PROBA-2, SOHO, Gaia, SWARM), but also studying the deployment of new SW sensors to be hosted on future missions, and supporting the development of a new mission called "Lagrange" (Hapgood, 2017). This mission will be entirely dedicated to SW monitoring, and will consist of two satellites placed in orbit around the Sun-Earth Lagrangian points L1 and L5; the mission development is now in Phase B, and its launch is planned for 2025, when the development of SW services mentioned above will also be ready to integrate the data coming from "Lagrange" mission (Kraft, 2017).

Among the different Sun-Earth Lagrangian points, in the development of the "Lagrange" mission a preference was given to L1 and L5 points mostly because L1 offers a very good vantage point to measure local conditions of interplanetary plasma just before its interaction with the Earth's magnetosphere, and a good point to monitor the solar hemisphere facing the Earth, while L5 offers a good vantage point to constrain the arrival time of CMEs (Vourlidas, 2015; Rodriguez et al., 2020) and detect with remote sensing instruments the arrival of Active Regions or equatorial coronal holes before their appearance behind the solar limb visible from the Sun-Earth line (Hapgood, 2017).

Given the inherent complexity of physical phenomena related with solar activity (including for instance the emergence of magnetic flux, the accumulation of magnetic energy in the solar atmosphere, the destabilization of magnetic configurations, the acceleration of plasma and particles, etc . . .), the research dealing with single specific case studies failed so far to identify clear and common universal phenomena occurring in every event (see e.g., Chen, 2011; Liu, 2020), although unified models have been recently proposed (Wyper et al., 2017). On the other hand, the huge number of studies performed over the last decades on eruptive events from the Sun demonstrates that a statistical knowledge of these phenomena (e.g., Wheatland, 2005; McKenna-Lawlor et al., 2006; Song et al., 2009; Ma et al., 2010; Morgan et al., 2012) based on large catalogs (e.g., Gopalswamy et al., 2009; Rotti et al., 2020) is not sufficient to provide reliable forecast of Space Weather conditions, also because of limited duration of solar-terrestrial datasets (see e.g., discussion by Hapgood, 2011). Over the last ~10 years, a rising number of researchers moved their interest to the promising research fields of Artificial Intelligence and Machine Learning (see review by Camporeale, 2019) applied to solar and i.p. physics data for SW forecasting purposes, for instance to predict the occurrence of solar eruptions and flares (e.g., Ahmed et al., 2013; Benvenuto et al., 2018; Florios et al., 2018), predict geomagnetic storms (e.g., Sexton et al., 2019), and to detect and classify solar events (Martens et al., 2012; Armstrong and Fletcher 2019; Hughes et al., 2019). These methods are really promising, but it is maybe too early to know what will be the new results that these methods will provide in the end.

MOTIVATIONS: THE NEED FOR MAGNETIC FIELD MEASUREMENTS

In general, *learning* a phenomenon does not necessarily imply a real physical understanding of it, but the latter is needed to generalize new discoveries about Sun-Earth interactions (Hapgood, 2011), and also to apply the same concepts for instance to the interaction of other planets in the Solar System with the Sun, or to other planetary systems orbiting solar-type stars in our Galaxy. Without a real understanding of solar-terrestrial physics (e.g., Tsurutani et al., 2020), any significant change in the background, stationary, or "average" conditions that were used to "learn" anything about the complex behavior of the Sun-Earth system even over one full solar cycle, will make the system likely unpredictable when extreme Carrington-like events will happen (Riley et al., 2018). In this perspective, SW prediction capabilities we are developing could fail just when we will need them most. Hence, it is hard to believe that real SW prediction capabilities will ever be developed in the end without going through a real understanding of physical phenomena driving the solar variability and the corresponding planetary response. Moreover, significant advancing in our forecasting capabilities will necessary require a much deeper understanding of the origin on the Sun and propagation/evolution in the interplanetary medium of these disturbances.

Now, because the majority of phenomena occurring on the Sun are driven by magnetic fields and related plasma physical phenomena, this means in particular that we need a better understanding of how the magnetic fields are generated in the solar interior, how their emergence through the photosphere, their storage and release in the lower corona, and the final connection with our planet. Hence, a mission specifically dedicated to these objectives is needed. In fact, previous solar missions demonstrate the potential of remote sensing observations combined with *in situ* instrument data acquired from multiple points of view, but much more attention is required to the origin and evolution of solar magnetic fields.

Unfortunately, continuous monitoring of the magnetic fields on the Sun is currently possible only for one single layer of this star: the photosphere (see Kleint and Gandorfer 2017). Over this surface, magnetic field measurements are possible thanks to the Zeeman splitting of some spectroscopic lines, related with the strength of the magnetic field. These measurements are currently available 24 h per day only for the solar hemisphere visible along the Sun-Earth line. On the other hand, field measurements in the above layers of the Sun have been proven to be possible with spectro-polarimetry both in the chromosphere (e.g., Kano et al., 2012) and the corona (Tomczyk and McIntosh 2009) by using Zeeman and Hanle effects (see also Raouafi et al., 2016; Yang et al., 2020). Unfortunately, coronal field measurements are acquired so far only along the Sun-Earth line, hence on the plane of sky of the solar corona as seen from Earth. This means that at present (under favorable conditions) we can measure coronal magnetic fields related with sunspots and active regions located on the limb whose photospheric fields cannot be measured, while we can measure photospheric fields of these regions when they are located in the visible hemisphere when the

corresponding coronal fields cannot be measured. So, at present magnetic fields cannot be measured at the same time from the photosphere to the corona. As a result, it is at present impossible to fully understand how the magnetic energy is transferred from the photosphere to the corona, how it is stored in the corona, and why the excess energy is finally released when the system is destabilized, leading to solar flares, CMEs, and SEP acceleration. Having information of photospheric-to-coronal magnetic fields is of paramount importance to forecast geomagnetic storms in advance, because the magnetic structure of the flux rope embedded in the eruption is the most crucial parameter to determine the strength of the space weather effects (see e.g., Kilpua et al., 2019), and our current capability to provide that information is very modest.

To solve this significant lack of information, many different extrapolation methods have been developed to reconstruct the coronal fields starting from the measured photospheric fields (see Wiegelmann, 2008; Régnier, 2013 and references therein), but the agreement between the location and orientation of the reconstructed fieldlines and the observed EUV coronal loops (usually assumed to match the fieldlines) is only marginal (Sandman et al., 2009), in particular above active regions where significant deviations from the lower energy potential field configuration are present (Aschwanden, 2013). A better correspondence with EUV features is provided for instance by non-linear Force-free field extrapolations (e.g., Guo et al., 2012; James et al., 2018) or time-dependent magneto-frictional methods (e.g., Pomoell et al., 2019), but these models provide a good reconstruction only for regions located near the solar disk center, and because measurements of the above coronal fields are missing, more quantitative comparisons are not possible. Moreover, these extrapolation methods start from photospheric field measurements acquired when the active regions are observed in the visible hemisphere, and these fields can be compared only with EUV features visible on-disk in the inner corona ($h < 1.3\ R_{sun}$), while a comparison with coronal features extending at higher altitudes requires off-limb observations (as those recently provided by PAROBA2/SWAP; O'Hara et al., 2019), and again these observations are daily available only along the Sun-Earth line. Hence, a comparison between the extrapolated coronal fieldlines and the observed coronal features requires to assume that these fields are not changed significantly over the time required (3–7 days) for the active region observed on disk to move at the limb dragged by solar rotation.

The situation was marginally improved thanks to the STEREO mission (Kaiser et al., 2008), that provided for the first time observations of coronal structures on a plane of the sky aligned with the Sun-Earth line, but (because STEREO spacecraft are orbiting the Sun along the Earth orbit, but drifting away from Earth at an average rate of about 22.5° per year) this happened only for short periods during the mission. Moreover, unfortunately the STEREO spacecraft didn't have on-board any photospheric field magnetometer, and not even any coronal field magnetometer. In the near future the situation will be slightly improved thanks to Solar Orbiter mission (Müller et al., 2013), which is carrying on-board a photospheric magnetometer (Solanki et al., 2020), a coronagraph (Antonucci et al., 2020) and a Heliospheric Imager (Howard et al., 2020), but remote sensing observations will be acquired only during specific time windows, and only a few of them will occur with the spacecraft in quadrature with respect to the Earth.

As anticipated, to overcome these limits ESA is now developing the "Lagrange" mission (Hapgood, 2017), with the aim to put in stable orbits two satellites around the L1 and L5 Sun-Earth Lagrangian points. In particular, the real novelty of the mission will be represented by the satellite put in orbit around the L5 point, something that has never been attempted before. From this vantage point, the remote sensing instruments on-board the spacecraft (including a photospheric field magnetometer) will continuously monitor coronal off-limb features located near the plane of the sky close to the Sun-Earth line, and the interplanetary propagation of solar disturbances expanding toward Earth. It will be possible for the first time to measure with remote sensing data photospheric fields of active regions crossing the solar limb as seen from Earth and before their arrival with solar rotation on the hemisphere pointing toward our planet. Moreover, *in situ* data acquired in L5 will detect possible high-speed streams and Stream Interaction Regions before their arrival on Earth ~4.5 days later dragged by rotation of the Parker spiral. These are likely the main reasons why the L5 point was chosen instead of L4 for the "Lagrange" mission.

Nevertheless, there are few important considerations to be made. First of all, neither of the two "Lagrange" satellites will carry on-board an instrument to measure with spectro-polarimetry coronal magnetic fields. Hence, without a coronal magnetometer, it will be again necessary to extrapolate these fields in the corona, starting from photospheric field measurements: a mission carrying on board such an instrument will be still missing in the near future. For this reason, similar instruments have been proposed as a payload not only for past missions (e.g., Peter et al., 2012), but also more recently[1] in response to the call for "white papers" for the long-term planning of ESA science program (MiMOSA mission).

Second, we have to consider that the L5 point is not located in quadrature with the Earth, but at an angle from the Sun-Earth line of 60°, which is not the ideal location to monitor solar eruptions propagating toward the Earth. This angular separation may not appear significant, considering also the angular expansion of solar eruptions, but the visible light emission observed by coronagraphs maximizes on the so-called "Thomson sphere," and this limit their visibility in the inner corona to the instrument plane-of-sky (see review by Rouillard, 2011). The spacecraft in L5 will be likely placed in a stable "Trojan" orbit (Llanos et al., 2012), which is almost elliptical, with amplitude of the orbit depending mostly on the chosen transfer trajectory and transfer time from the low Earth parking orbit, and two extreme cases can be considered here. For instance, if the spacecraft will be inserted in a small amplitude Trojan orbit (even down to ~100 km)

[1]https://www.cosmos.esa.int/web/voyage-2050/white-papers

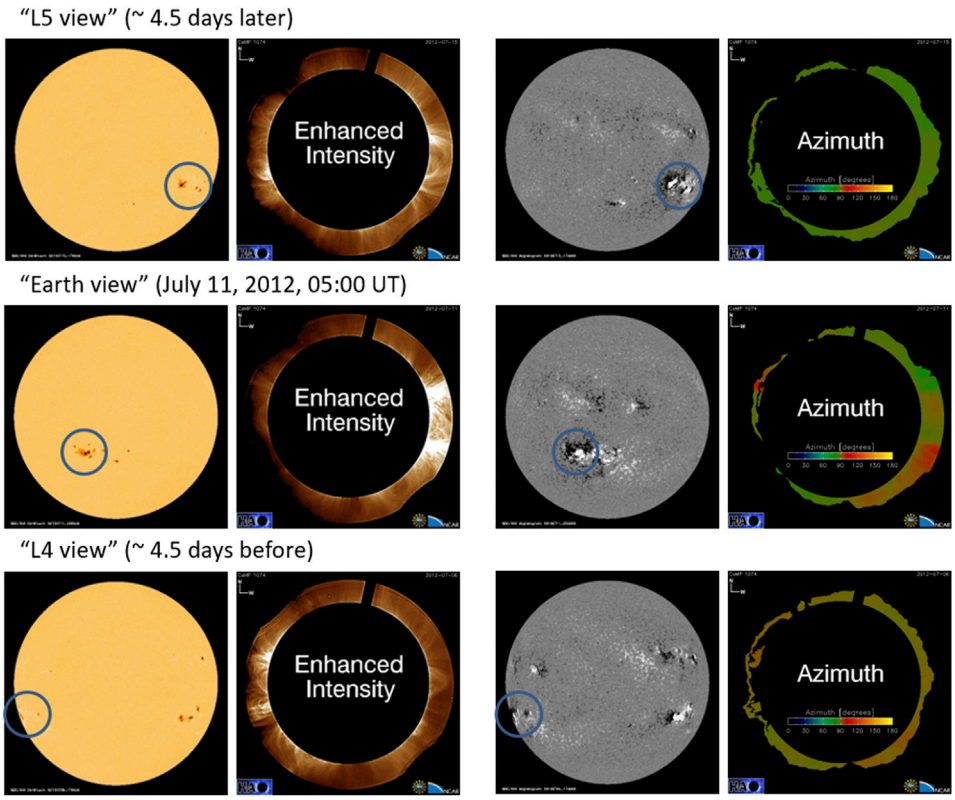

FIGURE 1 | Example of a possible combination of data acquired from L5 **(top row)**, L1 **(middle row)**, and L4 **(bottom row)** vantage point. The different columns show the visible photosphere **(left column)**, the inner corona **(middle left column)**, and the corresponding photospheric fields **(middle right column)** and coronal field azimuth **(right column)**. The location of the same sunspot group is outlines with a circle.

around L5, the remote sensing instruments will never observe the corona in quadrature with the Earth. On the other hand, if the spacecraft will be inserted in a large amplitude Trojan orbit (up to ~0.25–0.50 AU), the spacecraft will spend a half of its time very close to the quadrature configuration, and the second half very far from this configuration. The period of any of these orbits around L5 is about one year (Llanos et al., 2012). In summary: both in the first and in the second case a single spacecraft placed in L5 will never be able to monitor continuously the Sun in quasi-quadrature with respect to the Earth.

Third, we also have to remember that, considering the path followed by Solar Energetic Particles (SEPs) during their propagation in the interplanetary space, the most dangerous Active Regions (in terms of possible SW effects) are those located not at the center of the solar hemisphere as seen from the Sun-Earth line, but those located Westward, typically around 45–60° West (see review by Reames, 2013). This phenomenon is related with the Sun-Earth magnetic connectivity through the Parker spiral of interplanetary magnetic field, making an angle of about 45° with respect to the radial direction at the Earth's orbit. As a consequence, photospheric magnetic fields for these dangerous Active Regions cannot be observed at all from a spacecraft located in L5 (because the region will appear behind the limb as seen from that vantage point), and can be only marginally observed from a spacecraft located in L1 or along the Sun-Earth line (because the best measurement of photospheric fields provides the line-of-sight component of these fields, unless vector magnetograms are employed, whose data have a well-known ±180° azimuthal ambiguity, Gary and Hagyard, 1990). Hence, the best location to measure magnetic fields of Active Regions magnetically connected with the Earth will be nor L5, neither L1, but the L4 Lagrangian point.

LOOKING FORWARD: THE ADVANTAGES OF A TWIN L4-L5 MISSION

A solution to all the above missing capabilities of the previous (e.g., STEREO), current (e.g., Solar Orbiter), and near future (e.g., "Lagrange") missions will be covered instead by a new mission concept, consisting of twin spacecraft to L4 and L5, briefly described here. An example of a combined views of photosphere and corona that will be provided by L4 and L5 is shown in **Figure 1**: the unique combination of these data would allow to monitor the same Active Region and its impact on the overlying atmosphere from the limb to the disk center at the same time, allowing to follow the emergence of photospheric fields, the accumulation of coronal fields, and their release from a side and face perspectives. Considering the limited amount of space and the aims of this paper, I will not review here the need for a mission

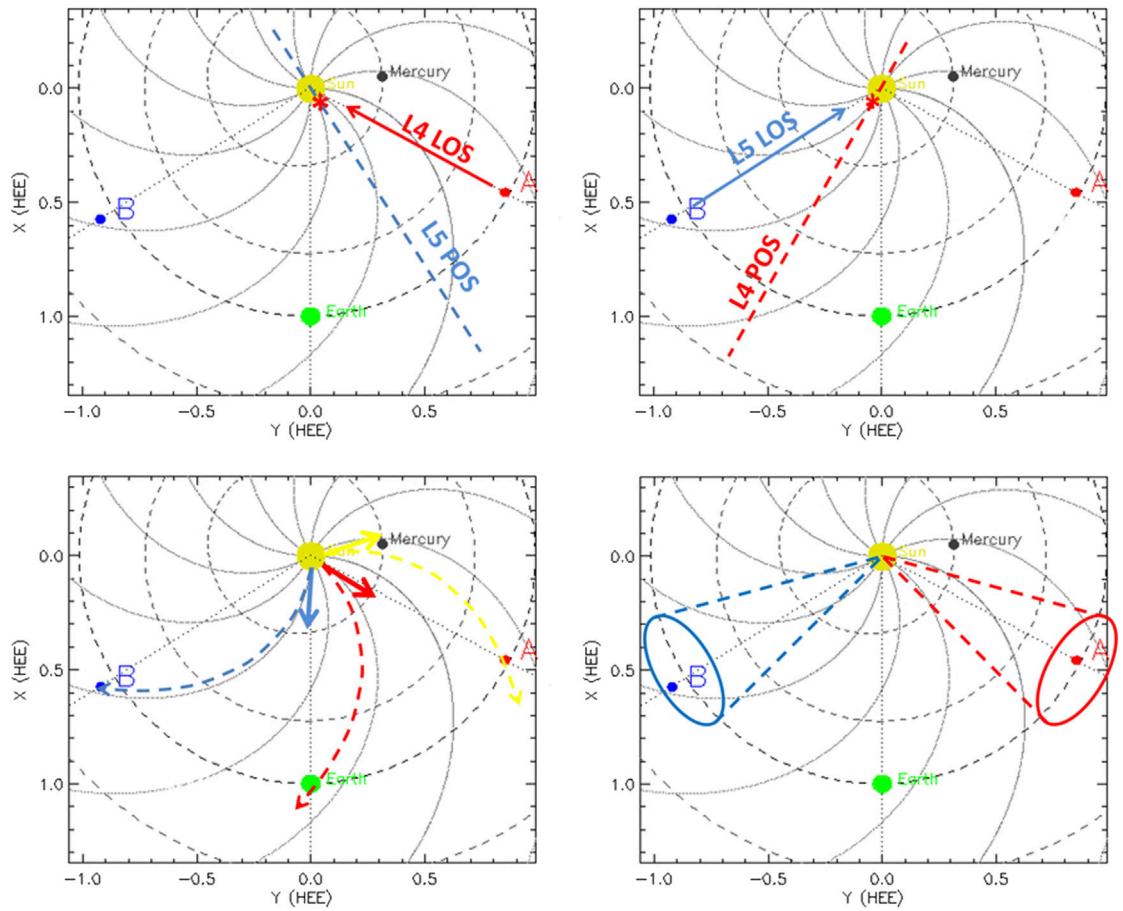

FIGURE 2 | Example of possible advantages offered by the twin L4-L5 mission proposed here. Top panels: the plane-of-sky (POS) of remote sensing instruments will allow to observe limb events from one spacecraft that will be observed as events at the center of solar disk from the other spacecraft. **Bottom left**: combinations of remote sensing and *in situ* data will allow to study CMEs propagating at different direction (blue, red, and yellow arrows) and also to sample the associated SEP fluxes propagating along the Parker spiral arms (blue, red, and yellow dashed lines). **Bottom right**: during their Trojan stable orbits around L4 and L5 the twin spacecraft will go from relative quadrature to quasi-quadrature with the Earth (dashed lines). These drawings are based on the plot provided by the STEREO orbit tool[2] and showing the location of STEREO spacecraft when the mission passed nearby L4 and L5 points (October 2009).

carrying remote sensing instruments capable to measure at the same time not only the photospheric, but also the coronal magnetic fields with spectro-polarimetry. The interested reader may refer for instance to the recent paper by Raouafi et al. (2016), or to the review by Kleint and Gandorfer (2017), and references therein.

What will be discussed here instead is the importance to consider a similar suite of instruments on-board a twin mission to the L4 and L5 vantage points; this idea was first proposed by Bemporad et al. (2014) in a mission concept named "HeMISE (Helio-Magnetism Investigation from the Sun to Earth)." Let us consider here two twin spacecraft, carrying *in situ* and remote sensing instruments measuring photospheric and coronal fields, and being located in stable orbits around L4 and L5 Lagrangian points. This configuration will have many advantages, briefly summarized here. The two spacecraft could be placed both in close orbit around L4 and L5, thus keeping almost all the time a relative separation angle of about ~120° each other, and ~60° with respect to the Sun-Earth line. During a solar eruption, the same event would be observed expanding above the limb from one view point (thus allowing an early determination of kinematical properties of CMEs and shocks), and face-on above the disk (the perfect location to study the flare and SEP acceleration), as it is shown in **Figure 2** bottom left panel. Nevertheless, this configuration seems not the best option for scientific and monitoring purposes.

More interestingly, the two spacecraft could be placed in a much broader Trojan orbit around L4 and L5, having for instance an orbital amplitude (corresponding to two times the maximum radius measured from center of the libration orbit) of about 0.52 AU (Llanos et al., 2012). In this case, during the orbital period of about one year, each spacecraft will change its longitudinal angle with respect to the Sun-Earth line from a maximum amplitude of about 75°, down to a minimum amplitude around 45° (**Figure 2**, bottom right panel). Then, with two spacecraft in L4 and L5 two possible cases can be considered: 1) synchronous orbits, and 2) asynchronous orbits shifted by half a orbital period. If the two orbits around L4 and L5 (separated by an angular distance by 120°) are synchronized, then the separation angle between the two spacecraft will change from a maximum of 150° (quasi-opposition) to

a minimum of 90° (quadrature), with both spacecraft closer/farther to the quasi-quadrature configuration with the Earth in the same period of time. On the other hand, in the case of asynchronous orbits shifted by half a orbital period, the separation angle between the two spacecraft will be almost constant during the mission, and the two spacecraft will move alternatively closer and farther from the quasi-quadrature with the Earth.

The first configuration 1) will provide very interesting cases from the scientific point of view. In particular, during quadratures between the two spacecraft photospheric fields sampled by one view point will be observed at the same time in the lower corona, off-limb with coronagraphic spectro-polarimetric data acquired from the second view-point. Photospheric fields measured by one spacecraft will be combined with coronal fields measured by the second spacecraft in quasi-quadrature, thus providing for the first time a continuous coverage of solar magnetic fields through the solar atmosphere. Hence, it will be possible for the first time to really understand how the emergence of magnetic fields in the photosphere directly affect the coronal structures, providing completely new information for the origin of solar eruptions, occurrence of impulsive events, acceleration of solar wind (stereoscopic coronal magnetometry). More than that, during the rest of the whole mission it will be possible in general to perform 3D reconstruction of solar stationary features in the inner corona, 3D reconstructions of CMEs and their kinematic, and stereoscopic helioseismology. In particular, it will be possible to study the 3D propagation of waves in the solar interior down to the tachocline from two points of view, opening the possibility for stereoscopic global helioseismology. The feasibility of research in this latter topic will be tested for the first time with the forthcoming Solar Orbiter data, but this mission will acquire only limited datasets during specific remote sensing periods, while satellites in stable orbits around L4 and L5 will cover potentially years of evolution of the Sun, and a long-term data coverage is of fundamental importance to understand the whole solar cycle evolution.

On the other hand, the second configuration 2) with the two orbits around L4 and L5 shifted by half a period will be the more suitable one for SW monitoring applications. The reason is that in this case one of the two spacecraft will be alternatively closer and farther from the quasi-quadrature configuration with the Earth. This means that among two spacecraft, one of them will be ever closer to the best configuration to monitor solar transients propagating toward the Earth. These resulting will be sampled by the heliospheric imagers on-board the spacecraft, covering almost the whole range of distances from the Sun to the Earth (like H1 and H2 imagers on-board STEREO). This will allow continuous 3D reconstructions of solar transients propagating to the Earth, hence providing a ideal mission for space weather studies. The same scientific cases mentioned above (3D reconstructions and stereoscopic helioseismology) will be also possible, with the advantage that the separation angle between the twin spacecraft will be almost constant with time, and this will reduce the long-term variability of data analysis for helioseismology. This configuration of L4-L5 satellites, complemented with measurements from L1 or from the Earth, would provide nearly continuous boundary conditions for coronal field models.

Moreover, considering again the geometry of interplanetary magnetic field spiral, very interesting science cases will be provided by the possible combinations of remote sensing and *in situ* data. The unique vantage point offered by the spacecraft in L5 will allow to detect *in situ* SEPs propagating along the Parker spiral and related with geo-effective ICMEs with the source region located near the center of the visible hemisphere as seen from the Sun-Earth line. On the other hand, the spacecraft in L4 will detect *in situ* the transit of ICMEs associated with SEP streams affecting the Earth. When the spacecraft will be in quasi-quadrature configuration, in the case of a CME directed toward one of them, the same eruption will be observed with remote sensing data as limb event from one spacecraft, and sampled later on with *in situ* data from the other spacecraft (**Figure 2**, bottom left panel). Last but not least, the L4 vantage point will allow to monitor Active Regions magnetically connected with the Earth with standard photopsheric magnetograms, thus helping the forecasting of flares accelerating SEP fluxes toward the Earth.

SUMMARY AND CONCLUSION

This paper briefly summarized the current state and future directions of solar and heliospheric physics human investigation. Among the current and proposed future missions exploring the Heliosphere, a possible combination of twin satellites orbiting around the L4 and L5 Sun-Earth Lagrangian point has never been proposed. The advantages and new knowledge of such a configuration were briefly described here: in particular, if the spacecraft will be equipped not only with "classical" remote sensing and *in situ* instruments, but also with coronal magnetometers, the combination of data acquired by the L4-L5 perspectives will provide a new knowledge of magnetic fields evolution across different layers of the Sun, and will also allow to monitor almost continuously in quasi-quadrature configuration the Sun-Earth interactions.

DATA AVAILABILITY STATEMENT

The original contributions presented in the study are included in the article/Supplementary Material, further inquiries can be directed to the corresponding author.

AUTHOR CONTRIBUTIONS

The author confirms being the sole contributor of this work and has approved it for publication.

ACKNOWLEDGMENTS

The author acknowledges S. Fineschi and M. Romoli for useful discussions in the preparation of some of the ideas proposed here.

REFERENCES

Ahmed, O. W., Qahwaji, R., Colak, T., Higgins, P. A., Gallagher, P. T., Bloomfield, D. S., et al. (2013). Solar flare prediction using advanced feature extraction, machine learning, and feature selection. *Sol. Phys.* 283 (1), 157–175. doi:10.1007/s11207-011-9896-1

Antonucci, E., Romoli, M., Andretta, V., Fineschi, S., Heinzel, P., Moses, J. D., et al. (2020). Metis: the solar orbiter visible light and ultraviolet coronal imager. *Astron. Astrophys.* 642, A10. doi:10.1051/0004-6361/201935338

Armstrong, J. A., and Fletcher, L. (2019). Fast solar image classification using deep learning and its importance for automation in solar physics. *Sol. Phys.* 294 (6), 80. doi:10.1007/s11207-019-1473-z

Aschwanden, M. J. (2013). A nonlinear force-free magnetic field approximation suitable for fast forward-fitting to coronal loops. III. the free energy. *Sol. Phys.* 287 (1-2), 369–389. doi:10.1007/s11207-012-0203-6

Bemporad, A., Fineschi, S., Focardi, M., Landini, F., Romoli, M., and Pancrazzi, M. (2014). "HeMISE (Helio-Magnetism Investigation from the Sun to Earth): a twin spacecraft mission at the Sun-Earth Lagrangian points L4 and L5" in 40th COSPAR scientific assembly, Moscow, Russia, 2-10 August 2014, 15–14.

Benvenuto, F., Piana, M., Campi, C., and Massone, A. M. (2018). A hybrid supervised/unsupervised machine learning approach to solar flare prediction. *Astrophys. J.* 853 (1), 90. doi:10.3847/1538-4357/aaa23c

Camporeale, E. (2019). The challenge of machine learning in space weather: nowcasting and forecasting. *Space Weather* 17 (8), 1166. doi:10.1029/2018sw002061

Chen, P. F. (2011). Coronal mass ejections: models and their observational basis. *Living Rev. Solar Phys.* 8, 1. doi:10.12942/lrsp-2011-1

Eastwood, J. P., Hapgood, M., Biffis, E., Benedetti, D., Bisi, M. M., Green, L., et al. (2018). Quantifying the economic value of space weather forecasting for power grids: an exploratory study. *Space Weather* 16, 2052–2067. doi:10.1029/2018sw002003

Florios, K., Kontogiannis, I., Park, S.-H., Guerra, J. A., Benvenuto, F., Bloomfield, D. S., et al. (2018). Forecasting solar flares using magnetogram-based predictors and machine learning. *Sol. Phys.* 293 (2), 28. doi:10.1007/s11207-018-1250-4

Gary, G. A., and Hagyard, M. J. (1990). Transformation of vector magnetograms and the problems associated with the effects of perspective and the azimuthal ambiguity. *Sol. Phys.* 126, 21.

Gopalswamy, N., Yashiro, S., Michalek, G., Stenborg, G., Vourlidas, A., Freeland, S., et al. (2009). The SOHO/LASCO CME catalog. *Earth, Moon Planets* 104 (1), 295. doi:10.1007/s11038-008-9282-7

Guo, Y., Ding, M. D., Liu, Y., Sun, X. D., DeRosa, M. L., Wiegelmann, T., et al. (2012). Modeling magnetic field structure of a solar active region corona using nonlinear force-free Fields in spherical geometry. *Astrophys. J.* 760, 47. doi:10.1088/0004-637x/760/1/47

Hapgood, M. (2017). L1L5Together: report of workshop on future missions to monitor space weather on the Sun and in the solar wind using both the L1 and L5 Lagrange points as valuable viewpoints. *Space Weather* 15, 654. doi:10.1002/2017sw001638

Hapgood, M. A. (2011). Towards a scientific understanding of the risk from extreme space weather. *Adv. Space Res.* 47, 2059. doi:10.1016/j.asr.2010.02.007

Howard, R. A., Vourlidas, A., Colaninno, R. C., Korendyke, C. M., Plunkett, S. P., Carter, M. T., et al. (2020). The solar orbiter heliospheric imager (SoloHI). *Astron. Astrophys.*. 642, A13. doi:10.1051/0004-6361/201935202

Hughes, J. M., Hsu, V. W., Seaton, D. B., Bain, H. M., Darnel, J. M., Krista, L., et al. (2019). Real-time solar image classification: assessing spectral, pixel-based approaches. *J. Space Weather Space Clim.* 9, A38. doi:10.1051/swsc/2019036

James, A. W., Valori, G., Green, L. M., Liu, Y., Cheung, M. C. M., Guo, Y., and Driel-Gesztelyi, L. v. (2018). An observationally constrained model of a flux rope that formed in the solar corona. *Astrophys. J. Lett.* 855, L16. doi:10.3847/2041-8213/aab15d

Kaiser, M. L., Kucera, T. A., Davila, J. M., Cyr, O. C. St., Guhathakurta, M., Christian, E., et al. (2008). The STEREO mission: an introduction. *Space Sci. Rev.* 136 (1), 5. doi:10.1007/s11214-007-9277-0

Kano, R., Bando, T., Narukage, N., Ishikawa, R., Tsuneta, S., Katsukawa, Y., et al. (2012). Chromospheric Lyman-alpha spectro-polarimeter (CLASP). *Proc. SPIE* 8443, 84434F. doi:10.1117/12.925991

Kilpua, E. K. J., Lugaz, N., Mays, M. L., and Temmer, M. (2019). Forecasting the structure and orientation of earthbound coronal mass ejections. *Space Weather* 17, 498–526. doi:10.1029/2018sw001944

Kraft, S. (2017). Remote sensing optical instrumentation for enhanced space weather monitoring from the L1 and L5 Lagrange points. *Proc. SPIE* 10562, 105620F–105622F. doi:10.1117/12.2296100

Kleint, L., and Gandorfer, A. (2017). Prospects of solar magnetometry-from ground and in space. *Space Sci. Rev.* 210, 397. doi:10.1007/s11214-015-0208-1

Liu, R. (2020). Magnetic flux ropes in the solar corona: structure and evolution toward eruption. *Res. Astron. Astrophys.* 20 (10), 165. doi:10.1088/1674-4527/20/10/165

Llanos, P. J., Miller, J. K., and Hintz, G. (2012). Navigation analysis for an L5 mission in the Sun-Earth system. *Adv. Astronautical. Sci.* 142, 11–503. doi:10.13140/2.1.2069.4402

Ma, S., Attrill, G. D. R., Golub, L., and Lin, J. (2010). Statistical study of coronal mass ejections with and without distinct low coronal signatures. *Astrophys. J.* 722 (1), 289. doi:10.1088/0004-637x/722/1/289

Martens, P. C. H., Attrill, G. D. R., Davey, A. R., Engell, A., Farid, S., Grigis, P. C., et al. (2012). Computer vision for the solar dynamics observatory (SDO). *Sol. Phys.* 275 (1-2), 79. doi:10.1007/s11207-010-9697-y

McKenna-Lawlor, S. M. P., Dryer, M., Kartalev, M. D., Smith, Z., Fry, C. D., Sun, W., et al. (2006). Near real-time predictions of the arrival at Earth of flare-related shocks during Solar Cycle 23. *J. Geophys. Res.* 111 (A11), A11103. doi:10.1029/2005ja011162

Morgan, H., Byrne, J. P., and Habbal, S. R. (2012). Automatically detecting and tracking coronal mass ejections. I. separation of dynamic and quiescent components in coronagraph images. *Astrophys. J.*, 752 (2), 144. doi:10.1088/0004-637x/752/2/144

Müller, D., Marsden, R. G., Cyr, O. C. St., and Gilbert, H. (2013). Solar orbiter. exploring the Sun-Heliosphere connection. *Sol. Phys.* 285 (1-2), 25. doi:10.1007/s11207-012-0085-7

Opgenoorth, H. J., Wimmer-Schweingruber, R. F., Belehaki, A., Berghmans, D., Hapgood, M., Hesse, M., et al. (2019). Assessment and recommendations for a consolidated European approach to space weather - as part of a global space weather effort. *J. Space Weather Space Clim.* 9, A37. doi:10.1051/swsc/2019033

O'Hara, J. P., Mierla, M., Podladchikova, O., D'Huys, E., and West, M. J. (2019). Exceptional extended field-of-view observations by PROBA2/SWAP on 2017 April 1 and 3. *Astrophys. J.* 883, 59. doi:10.3847/1538-4357/ab3b08

Peter, H., Abbo, L., Andretta, V., Auchère, F., Bemporad, A., Berrilli, F., et al. (2012). Solar magnetism eXplorer (SolmeX). Exploring the magnetic field in the upper atmosphere of our closest star. *Exp. Astron.* 33 (2-3), 271. doi:10.1007/s10686-011-9271-0

Pomoell, J., Lumme, E., and Kilpua, E. (2019). Time-dependent data-driven modeling of active region evolution using energy-optimized photospheric electric fields. *Sol. Phys.* 294 (4), 41. doi:10.1007/s11207-019-1430-x

Raouafi, N. E., Riley, P., Gibson, S., Fineschi, S., and Solanki, S. K. (2016). Diagnostics of coronal magnetic fields through the Hanle Effect in UV and IR lines. *Front. Astron. Space Sci.* 3. doi:10.3389/fspas.2016.00020

Reames, D. V. (2013). The two sources of solar energetic particles. *Space Sci. Rev.* 175 (1-4), 53–92. doi:10.1007/s11214-013-9958-9

Régnier, S. (2013). Magnetic field extrapolations into the corona: success and future improvements. *Sol. Phys.* 288 (2), 481. doi:10.1007/s11207-013-0367-8

Riley, P., Baker, D., Liu, Y. D., Verronen, P., Singer, H. J., and Güdel, M. (2018). Extreme space weather events: from cradle to grave. *Space Sci. Rev.*, 214 (1), 21. doi:10.1007/s11214-017-0456-3

Rodriguez, L., Scolini, C., Mierla, M., Zhukov, A. N., and West, M. J. (2020). Space weather monitor at the L5 point: a case study of a CME observed with STEREO B. *Space Weather* 18 (10), e02533. doi:10.1029/2020sw002533

Rotti, S. A., Martens, P. C. H., and Aydin, B. (2020). A catalog of solar flare events observed by the SOHO/EIT. *ApJS* 249 (2), 20. doi:10.3847/1538-4365/ab9a42

Rouillard, A. P. (2011). Relating white light and *in situ* observations of coronal mass ejections: a review. *J. Atmos. Solar-Terrestrial Phys.* 73 (10), 1201. doi:10.1016/j.jastp.2010.08.015

Sandman, A. W., Aschwanden, M. J., DeRosa, M. L., Wülser, J. P., and Alexander, D. (2009). Comparison of STEREO/EUVI loops with potential magnetic field models. *Sol. Phys.* 259 (1), 1–11. doi:10.1007/s11207-009-9383-0

Schrijver, C. J., Kauristie, K., Aylward, A. D., Denardini, D. M., Gibson, S. E., Glover, A., et al. (2015). Understanding space weather to shield society: A global

road map for 2015–2025 commissioned by COSPAR and ILWS. *Adv. Space Res.* 55 (12), 2745–2807. doi:10.1016/j.asr.2015.03.023

Sexton, S., Nykyri, K., and Ma, X. (2019). Kp forecasting with a recurrent neural network. *J. Space Weather Space Clim.* 9, A19. doi:10.1051/swsc/2019020

Solanki, S. K., del Toro Iniesta, J. C., Woch, J., Gandorfer, A., Hirzberger, J., Alvarez-Herrero, A., et al. (2020). The polarimetric and helioseismic imager on solar orbiter. *Astron. Astrophys.* 642, A11. doi:10.1051/0004-6361/201935325

Song, H., Tan, C., Jing, J., Wang, H., Yurchyshyn, V., and Abramenko, V. (2009). Statistical assessment of photospheric magnetic features in imminent solar flare predictions. *Sol. Phys.* 254 (1), 101. doi:10.1007/s11207-008-9288-3

Tomczyk, S., and McIntosh, S. W. (2009). Time-distance seismology of the solar corona with CoMP. *Astrophys. J.* 697 (2), 1384. doi:10.1088/0004-637x/697/2/1384

Tsurutani, B. T., Lakhina, G. S., and Hajra, R. (2020). The physics of space weather/solar-terrestrial physics (STP): what we know now and what the current and future challenges are. *Nonlin. Process. Geophys.* 27, 7. doi:10.5194/npg-27-75-2020

Vourlidas, A. (2015). Mission to the sun-earth L5Lagrangian point: an optimal platform for space weather research. *Space Weather* 13, 197–201. doi:10.1002/2015sw001173

Wheatland, M. S. (2005). A statistical solar flare forecast method. *Space Weather* 3 (7), S07003. doi:10.1029/2004sw000131

Wiegelmann, T. (2008). Nonlinear force-free modeling of the solar coronal magnetic field. *J. Geophys. Res.* 113 (A3), A03S02. doi:10.1029/2007ja012432

Wyper, P. F., Antiochos, S. K., and DeVore, C. R. (2017). A universal model for solar eruptions. *Nature* 544 (7651), 452. doi:10.1038/nature22050

Yang, Z., Bethge, C., Tian, H., Tomczyk, S., Morton, R., Del Zanna, G., et al. (2020). Global maps of the magnetic field in the solar corona. *Science* 369, 694. doi:10.1126/science.abb4462

Conflict of Interest: The author declares that the research was conducted in the absence of any commercial or financial relationships that could be construed as a potential conflict of interest.

frontiers in Astronomy and Space Sciences

PERSPECTIVE
published: 14 April 2021
doi: 10.3389/fspas.2021.651070

The Plasma Universe: A Coherent Science Theme for Voyage 2050

Daniel Verscharen[1,2], Robert T. Wicks[3], Graziella Branduardi-Raymont[1], Robertus Erdélyi[4,5,6], Filippo Frontera[7], Charlotte Götz[8], Cristiano Guidorzi[7], Vianney Lebouteiller[9,10], Sarah A. Matthews[1], Fabrizio Nicastro[11], Iain Jonathan Rae[3], Alessandro Retinò[12], Aurora Simionescu[13,14,15], Paolo Soffitta[16], Phil Uttley[17] and Robert F. Wimmer-Schweingruber[18,19]*

[1]Mullard Space Science Laboratory, University College London, Dorking, United Kingdom, [2]Space Science Center, University of New Hampshire, Durham, NH, United States, [3]Department of Mathematics, Physics and Electrical Engineering, Northumbria University, Newcastle upon Tyne, United Kingdom, [4]Solar Physics and Space Plasma Research Centre, University of Sheffield, Sheffield, United Kingdom, [5]Department of Astronomy, Eötvös Loránd University, Budapest, Hungary, [6]Gyula Bay Zoltán Solar Observatory (GSO), Hungarian Solar Physics Foundation (HSPF), Gyula, Hungary, [7]Department of Physics and Earth Sciences, University of Ferrara, Ferrara, Italy, [8]ESTEC, European Space Agency, Noordwijk, Netherlands, [9]AIM, CEA, CNRS, Université Paris-Saclay, Université Paris Diderot, Sorbonne Paris Cité, Gif-sur-Yvette, France, [10]Department of Physics and Astronomy, University of North Carolina, Chapel Hill, NC, United States, [11]Italian National Institute for Astrophysics (INAF), Rome Astronomical Observatory, Rome, Italy, [12]Laboratoire de Physique des Plasmas, École Polytechnique, Palaiseau, France, [13]SRON Netherlands Institute for Space Research, Utrecht, Netherlands, [14]Leiden Observatory, Leiden University, Leiden, Netherlands, [15]Kavli Institute for the Physics and Mathematics of the Universe (WPI), The University of Tokyo, Kashiwa, Japan, [16]Italian National Institute for Astrophysics (INAF), Istituto di Astrofisica e Planetologia Spaziali, Rome, Italy, [17]Anton Pannekoek Institute, University of Amsterdam, Amsterdam, Netherlands, [18]Institute of Experimental and Applied Physics, Kiel University, Kiel, Germany, [19]National Space Science Center, Chinese Academy of Sciences, Beijing, China

OPEN ACCESS

Edited by:
Vladislav Izmodenov, Space Research Institute (RAS), Russia

Reviewed by:
Jonathan Squire, University of Otago, New Zealand
John Charles Raymond, Center for Astrophysics, Harvard University, United States

***Correspondence:**
Daniel Verscharen
d.verscharen@ucl.ac.uk

Specialty section:
This article was submitted to Space Physics, a section of the journal Frontiers in Astronomy and Space Sciences

Received: *08 January 2021*
Accepted: *17 February 2021*
Published: *14 April 2021*

Citation:
Verscharen D, Wicks RT, Branduardi-Raymont G, Erdélyi R, Frontera F, Götz C, Guidorzi C, Lebouteiller V, Matthews SA, Nicastro F, Rae IJ, Retinò A, Simionescu A, Soffitta P, Uttley P and Wimmer-Schweingruber RF (2021) The Plasma Universe: A Coherent Science Theme for Voyage 2050. Front. Astron. Space Sci. 8:651070. doi: 10.3389/fspas.2021.651070

In review of the White Papers from the Voyage 2050 process[1] and after the public presentation of a number of these papers in October 2019 in Madrid, we as White Paper lead authors have identified a coherent science theme that transcends the divisions around which the Topical Teams are structured. This note aims to highlight this synergistic science theme and to make the Topical Teams and the Voyage 2050 Senior Committee aware of the wide importance of these topics and the broad support that they have across the worldwide science community.

Keywords: plasma, space physics, astrophysics, european space agency—ESA, voyage 2050

Baryonic matter in the Universe is almost exclusively in the plasma state. It forms structures on a huge range of scales, reaching from the kinetic electron and ion microscales to the size of the entire observable Universe. These plasmas include very diverse objects such as magnetic cavities around comets, planetary magnetospheres, the solar atmosphere, the outer heliosphere, accretion discs around compact objects, galaxy-scale "Fermi bubbles," the intracluster medium, and the intergalactic medium permeating the cosmic web. The key difficulty in understanding of all these objects lies in the two-way nature of the intrinsic multi-scale physics of plasmas: processes on the largest scales affect the small-scale physics, and processes on the smallest scales affect the large-scale evolution of plasmas.

[1]All Voyage 2050 White Papers are available online at https://www.cosmos.esa.int/web/voyage-2050/white-papers.

These multi-scale processes are united by *fundamental physics questions* that underpin the physics addressed in all of the 18 White Papers referenced below, e.g.

- How are electrons and ions heated and accelerated, and how is energy partitioned?
- What is the role of the magnetic field?
- What are the properties and roles of different energisation regions in plasma structures?
- What is the role of plasma physics in the formation and evolution of different processes and objects including flux tubes, turbulence, waves, flows, jets, discs, magnetospheres, coronae, and halos?
- What are the effects of rapid and discontinuous processes such as shocks and reconnection?

The answers to these *fundamental questions* are very important for a wide range of processes in the Universe including:

- accretion of matter onto compact objects,
- cosmic-ray acceleration,
- galaxy formation,
- heat and energy transfer, conduction, diffusion, and turbulence in plasma flows on all scales, in intergalactic, interstellar, and interplanetary media,
- magnetic-field generation through dynamo processes,
- magnetospheric dynamics,
- stellar activity and coronal dynamics, and
- space weather.

We have specifically identified four fields of study in the proposed Voyage 2050 White Papers that are linked by this common theme:

Astronomy from the UV to soft and hard X-ray wavelengths is a powerful tool to explore different parameter regimes and examples of plasma environments on large scales based on a whole-system overview. They allow us to identify plasma shocks, thermal processes in accretion flows onto compact objects such as neutron stars and black holes, the large-scale geometry of matter, and even elemental and charge-state composition through the effective use of spectroscopy and polarimetry [Lebouteiller et al., 2019; Frontera et al., 2021; Guidorzi et al., 2021; Nicastro et al., 2021; Simionescu et al., 2021; Soffitta et al., 2021; Uttley et al., 2021].

Solar physics investigates processes on intermediate scales and links the physics explored by X-ray and UV astronomy to the local environment of the solar system. It allows us to obtain detailed spectroscopic imagery of plasma phenomena that we can interpret directly (Branduardi-Raymont et al., 2021; Erdélyi et al., 2021; Matthews et al., 2021; Peter et al., 2021).

Heliospheric, magnetospheric, and cometary physics studies of *in-situ* plasma phenomena such as the acceleration and heating of particles can be directly linked to larger structures with a good level of system-wide imagery and context (McCrea et al., 2019; Branduardi-Raymont et al., 2021; Erdélyi et al., 2021; Götz et al., 2021; Matthews et al., 2021; Peter et al., 2021; Rae et al., 2021; Roussos et al., 2021; Wimmer-Schweingruber et al., 2021).

In-situ plasma physics explores the near-Earth plasma environment (e.g., pristine and shocked solar wind, bow shock, and magnetosphere) and the plasma environment around other solar-system objects. It allows us to analyse the detailed fundamental interactions and the micro-scale processes that determine the large-scale evolution and thermodynamics of matter (Branduardi-Raymont et al., 2021; Götz et al., 2021; Rae et al., 2021; Retinò et al., 2021; Verscharen et al., 2021; Wimmer-Schweingruber et al., 2021).

Although these science topics appear quite diverse and each White Paper is being evaluated on its own merit by their respective Topical Team, we emphasise that all of them will mutually benefit from each other. For instance, the interpretation of X-ray and UV observations, reaching from compact objects to the largest structures in the Universe, depends on a solid understanding of fundamental *in-situ* plasma physics. On the other hand, the *in-situ* plasma community will benefit from cross-disciplinary collaboration with plasma astrophysicists by studying a much wider range of plasma conditions, some of which cannot be studied *in situ*. The same benefit applies likewise to the solar, heliospheric, magnetospheric, and cometary fields. Moreover, numerical modelling of plasmas in different regimes with shared physical understanding will underpin much of the developments in these fields.

The synopsis above and the related Voyage 2050 White Papers show that a common and coherent science theme has emerged from the Voyage 2050 process. This theme is linked by the common interest across large parts of the ESA-science community in exploring structures in the Universe that are shaped by plasma processes across a large variety of scales. This science theme spans across all of the installed Topical Teams. We are convinced that the adoption of this coherent science theme by ESA through a programme of missions addressing plasma physics in its many forms will make transformative advances in our knowledge of fundamental plasma physics questions and of a wide range of processes that are of greatest importance for our understanding of the Universe.

DATA AVAILABILITY STATEMENT

The original contributions presented in the study are included in the article, further inquiries can be directed to the corresponding author.

AUTHOR CONTRIBUTIONS

All authors contributed to the writing of this article.

FUNDING

DV is supported by Science and Technology Facilities Council (STFC) Ernest Rutherford Fellowship ST/P003826/1. DV, GBR, and SAM are supported by STFC Consolidated Grant ST/S000240/1. RTW and IJR are supported by STFC

Consolidated Grant ST/V006320/1. RE is grateful to STFC (grant number ST/M000826/1) and the Royal Society for enabling this research. RE also acknowledges the support received by the CAS President's International Fellowship Initiative Grant No.2019VMA052 and the warm hospitality received at USTC of CAS, Hefei, where part of his contribution was made. SAM is also supported by UKSA Hinode Operations Continuation grant ST/S006532/1.

REFERENCES

Branduardi-Raymont, G., Berthomier, M., Bogdanova, Y., Carter, J. C., Collier, M., Dimmock, A., et al. (2021). Exploring solar-terrestrial interactions via multiple observers. *Voyage 2050 White Paper and submitted to Experimental Astronomy*. Available at: https://www.cosmos.esa.int/documents/1866264/3219248/Branduardi-RaymontG_Voyage2050_WP_Solar-Terrestrial_exploration.pdf.

Erdélyi, R., Damé, L., Fludra, A., Mathioudakis, M., Amari, T., Belucz, B., et al. (2021). HiRISE – high-Resolution Imaging and Spectroscopy Explorer – ultrahigh resolution, interferometric and external occulting coronagraphic science. *Voyage 2050 White Paper and submitted to Experimental Astronomy*. Available at: https://www.cosmos.esa.int/documents/1866264/3219248/ErdelyiR_HiRISE_ESA-VOYAGE2050_WP.pdf

Frontera, F., Virgilli, E., Guidorzi, C., Rosati, P., Diehl, R., Siegert, T., et al. (2021). Understanding the origin of the positron annihilation line and the physics of the supernova explosions. *Voyage 2050 White Paper and submitted to Experimental Astronomy*. Available at: https://www.cosmos.esa.int/documents/1866264/3219248/FronteraF_White_Paper_FFrontera-ESA-voyage2050.pdf.

Götz, C., Gunell, H., Volwerk, M., Beth, A., Eriksson, A., Galand, M., et al. (2021). Cometary plasma science. *Voyage 2050 White Paper and submitted to Experimental Astronomy*. Available at: https://www.cosmos.esa.int/documents/1866264/3219248/GoetzC_wp_comet_plasma_goetz.pdf.

Guidorzi, C., Frontera, F., Ghirlanda, G., Stratta, G., Mundell, C. G., Virgilli, E., et al. (2021). A deep study of the high-energy transient sky. *Voyage 2050 White Paper and submitted to Experimental Astronomy*. Available at: https://www.cosmos.esa.int/documents/1866264/3219248/GuidorziC_WP_ESA_Voyage_2050.pdf.

Lebouteiller, V., Yan, C. G. H., Richter, P., Godard, B., Jenkins, E. B., Welty, D., et al. (2019). A complete census of the gas phases in and around galaxies, far-UV spectropolarimetry as a prime tool for understanding galaxy evolution and star formation. *ESA Voyage 2050 White Paper (2019) arXiv:1909.03056*. Available at: https://www.cosmos.esa.int/documents/1866264/3219248/LebouteillerV_ESA_white_paper_Lebouteiller.pdf.

Matthews, S. A., Reid, H. S., Baker, D., Bloomfield, D. S., Browning, P. K., Calcines, A., et al. (2021). Solar particle acceleration, radiation & kinetics (SPARK). *Voyage 2050 White Paper and submitted to Experimental Astronomy*. Available at: https://www.cosmos.esa.int/documents/1866264/3219248/MatthewsS_Solar_Particle_Acceleration_Radiation_Kinetics.pdf.

McCrea, I., Davies, J., Dunlop, M., Erdélyi, R., Forsyth, C., Harra, L., et al. (2019). The grand European heliospheric observatory–an integrated ESA approach to challenges in solar and solar-terrestrial physics. *ESA Voyage 2050 White Paper*. Available at: https://www.cosmos.esa.int/documents/1866264/3219248/McCrea_Heliophysics_Observatory_WP_20190805_fontfix.pdf.

Nicastro, F., Kaastra, J., Argiroffi, C., Behar, E., Bianchi, S., Bocchino, F., et al. (2021). The voyage of metals in the universe from cosmological to planetary scales: the need for a very high-resolution, high throughput soft X-ray spectrometer. *Experimental Astronomy*. Available at: https://ui.adsabs.harvard.edu/abs/2021ExA...tmp...17N.

Peter, H., Alsina Ballester, E., Andretta, V., Auchere, F., Belluzzi, L., Bemporad, A., et al. (2021). Magnetic imaging of the outer solar atmosphere (MImOSA): unlocking the driver of the dynamics in the upper solar atmosphere. *Voyage 2050 White Paper and submitted to Experimental Astronomy*. Available at: https://www.cosmos.esa.int/documents/1866264/3219248/PeterH_voy2050_submitted.pdf.

ACKNOWLEDGMENTS

Apart from minor edits, this article was submitted as a supporting statement in response to the European Space Agency's (ESA's) long-term planning cycle Voyage 2050. We are grateful to ESA's Directorate of Science, the Science Programme Committee (SPC), the Voyage 2050 Senior Committee, and the Voyage 2050 Topical Teams for the consideration of the community's input.

Rae, I. J., Forsyth, C., Dunlop, M., Palmroth, M., Lester, M., Friedel, R., et al. (2021). What are the fundamental modes of energy transfer and partitioning in the coupled Magnetosphere-Ionosphere system?. *Voyage 2050 White Paper and submitted to Experimental Astronomy*. Available at: https://www.cosmos.esa.int/documents/1866264/3219248/RaeJ_ESA_whitepaper_draft_v16.pdf.

Retinò, A., Khotyaintsev, Y., Le Contel, O., Marcucci, M. F., Plaschke, F., Vaivads, A., et al. (2021). Particle energization in space plasmas: towards a multi-point, multi-scale plasma observatory. *Voyage 2050 White Paper and submitted to Experimental Astronomy*. Available at: https://www.cosmos.esa.int/documents/1866264/3219248/RetinoA_esa-voyage-2050-white-paper-retino.pdf.

Roussos, E., Allanson, O., André, N., Bertucci, B., Branduardi-Raymont, G., Clark, G., et al. (2021). The *in-situ* exploration of Jupiter's radiation belts. *Voyage 2050 White Paper and submitted to Experimental Astronomy*. Available at: https://www.cosmos.esa.int/documents/1866264/3219248/RoussosE_Roussos_Voyage2050_Jupiter_Radiation_Belts.pdf.

Simionescu, A., Ettori, S., Werner, N., Nagai, D., Vazza, F., Akamatsu, H., et al. (2021). Voyage through the hidden physics of the cosmic web. *Voyage 2050 White Paper and submitted to Experimental Astronomy*. Available at: https://www.cosmos.esa.int/documents/1866264/3219248/SimionescuA_Voyage2050_cosmicweb.pdf.

Soffitta, P., Bucciantini, N., Churazov, E., Costa, E., Dovciak, M., Feng, H., et al. (2021). A polarized view of the hot and violent Universe. *Voyage 2050 White Paper and submitted to Experimental Astronomy*. Available at: https://www.cosmos.esa.int/documents/1866264/3219248/SoffittaP_PolarizedUniverse_PaoloSoffitta.pdf.

Uttley, P., den Hartog, R., Bambi, C., Barret, D., Bianchi, S., Bursa, M., et al. (2021). The high energy universe at ultra-high resolution: the power and promise of X-ray interferometry. *Voyage 2050 White Paper and submitted to Experimental Astronomy*. Available at: https://www.cosmos.esa.int/documents/1866264/3219248/UttleyP_Voyage_2050_XRI_WP.pdf.

Verscharen, D., Wicks, R. T., Alexandrova, O., Bruno, R., Burgess, D., Chen, C. H. K., et al. (2021). A case for electron-astrophysics. *Voyage 2050 White Paper and submitted to Experimental Astronomy*. Available at: https://www.cosmos.esa.int/documents/1866264/3219248/VerscharenD_electrons_white_paper_final.pdf.

Wimmer-Schweingruber, R. F., Cairns, I., Veronig, A., Poedts, S., Zong, Q., Nickeler, D., et al. (2021). *In-situ* investigations of the local interstellar medium. *Voyage 2050 White Paper and submitted to Experimental Astronomy*. Available at: https://www.cosmos.esa.int/documents/1866264/3219248/Wimmer-SchweingruberR_2019-08-04-interstellar-whitepaper.pdf.

Conflict of Interest: The authors declare that the research was conducted in the absence of any commercial or financial relationships that could be construed as a potential conflict of interest.

frontiers in Astronomy and Space Sciences

METHODS
published: 29 July 2021
doi: 10.3389/fspas.2021.665885

MagneToRE: Mapping the 3-D Magnetic Structure of the Solar Wind Using a Large Constellation of Nanosatellites

Bennett A. Maruca[1,2], Jeffersson A. Agudelo Rueda[3], Riddhi Bandyopadhyay[4], Federica B. Bianco[1,5,6,7], Alexandros Chasapis[8], Rohit Chhiber[1,9], Haley DeWeese[1], William H. Matthaeus[1,2], David M. Miles[10], Ramiz A. Qudsi[1,11], Michael J. Richardson[1], Sergio Servidio[12], Michael A. Shay[1,2], David Sundkvist[13], Daniel Verscharen[3,14], Sarah K. Vines[15], Joseph H. Westlake[15] and Robert T. Wicks[16]*

[1]Department of Physics and Astronomy, University of Delaware, Newark, DE, United States, [2]Bartol Research Institute, University of Delaware, Newark, DE, United States, [3]Mullard Space Science Laboratory, University College London, Dorking, United Kingdom, [4]Department of Astrophysical Sciences, Princeton University, Princeton, NJ, United States, [5]Joseph R. Biden, Jr, School of Public Policy and Administration, University of Delaware, Newark, DE, United States, [6]Data Science Institute, University of Delaware, Newark, DE, United States, [7]Center for Urban Science and Progress, New York University, Brooklyn, NY, United States, [8]Laboratory for Atmospheric and Space Physics, University of Colorado, Boulder, CO, United States, [9]Heliophysics Science Division, NASA Goddard Space Flight Center, Greenbelt, MD, United States, [10]Department of Physics and Astronomy, University of Iowa, Iowa City, IA, United States, [11]Center for Space Physics, Boston University, Boston, MA, United States, [12]Department of Physics, University of Calabria, Rende, Italy, [13]Space Sciences Laboratory, University of California, Berkeley, CA, United States, [14]Space Science Center, University of New Hampshire, Durham, NH, United States, [15]Applied Physics Laboratory, Johns Hopkins University, Laurel, MD, United States, [16]Department of Mathematics, Physics and Electrical Engineering, Northumbria University, Newcastle upon Tyne, United Kingdom

OPEN ACCESS

Edited by:
Rudolf A. Treumann, Ludwig Maximilian University of Munich, Germany

Reviewed by:
Yasuhito Narita, Austrian Academy of Sciences (OeAW), Austria
Ferdinand Plaschke, Austrian Academy of Sciences, Austria

***Correspondence:**
Bennett A. Maruca
bmaruca@udel.edu

Specialty section:
This article was submitted to Space Physics, a section of the journal Frontiers in Astronomy and Space Sciences

Received: *09 February 2021*
Accepted: *08 June 2021*
Published: *29 July 2021*

Citation:
Maruca BA, Agudelo Rueda JA, Bandyopadhyay R, Bianco FB, Chasapis A, Chhiber R, DeWeese H, Matthaeus WH, Miles DM, Qudsi RA, Richardson MJ, Servidio S, Shay MA, Sundkvist D, Verscharen D, Vines SK, Westlake JH and Wicks RT (2021) MagneToRE: Mapping the 3-D Magnetic Structure of the Solar Wind Using a Large Constellation of Nanosatellites. Front. Astron. Space Sci. 8:665885. doi: 10.3389/fspas.2021.665885

Unlike the vast majority of astrophysical plasmas, the solar wind is accessible to spacecraft, which for decades have carried *in-situ* instruments for directly measuring its particles and fields. Though such measurements provide precise and detailed information, a single spacecraft on its own cannot disentangle spatial and temporal fluctuations. Even a modest constellation of *in-situ* spacecraft, though capable of characterizing fluctuations at one or more scales, cannot fully determine the plasma's 3-D structure. We describe here a concept for a new mission, the Magnetic Topology Reconstruction Explorer (MagneToRE), that would comprise a large constellation of *in-situ* spacecraft and would, for the first time, enable 3-D maps to be reconstructed of the solar wind's dynamic magnetic structure. Each of these nanosatellites would be based on the CubeSat form-factor and carry a compact fluxgate magnetometer. A larger spacecraft would deploy these smaller ones and also serve as their telemetry link to the ground and as a host for ancillary scientific instruments. Such an ambitious mission would be feasible under typical funding constraints thanks to advances in the miniaturization of spacecraft and instruments and breakthroughs in data science and machine learning.

Keywords: turbulence, space plasma, solar wind, interplanetary magnetic field, magnetometer, nanosatellite, CubeSat

1 INTRODUCTION

1.1 Mission Motivation

The interplanetary magnetic field (IMF) emerges from the Sun and extends throughout the heliosphere (Parker, 1958). It plays a fundamental role in initially heating and accelerating the solar wind and continues to shape the dynamics of the expanding plasma. It propagates energy through linear and nonlinear dynamical couplings, participates in energy transfer and conversion across scales, and regulates the transport of solar energetic particles (SEPs).

The IMF's structure is defined by the magnetic field's strength and direction. These properties vary across many spatial and temporal scales (Owens and Forsyth, 2013; Verscharen et al., 2019) that are roughly grouped into three categories of descending size (**Figure 1**):

- Macroscales (~ 10^6 to 10^9 km at 1 au from the Sun) are dominated by the large-scale flux tubes that emerge from the Sun. Images of the solar corona and nascent solar wind reveal that the macroscale IMF is defined by the Parker spiral, interactions among solar wind streams, coronal mass ejections (CMEs), and other global structures and events (Balogh and Erdõs, 2013).
- Mesoscales (~ 10^2 to 10^6 km) include the complex structures that arise from the interaction and "tearing" of flux tubes that occur as the plasma expands through the heliosphere.
- Microscales (~ 10^{-2} to 10^2 km) consist of the smallest-scale structures, whose dynamics are governed by the field-particle interactions of kinetic physics: heating, kinetic waves, microinstabilities, and magnetic reconnection (Marsch, 2006; Alexandrova et al., 2013; Osman et al., 2014).

The mesoscale IMF plays a crucial but poorly understood role in solar-wind energy dynamics (Tu and Marsch, 1995). Energy is injected at macroscales by large-scale drivers (effectively "stirring" plasma streams) and passes through mesoscales via a combination of turbulent fluctuations and MHD waves that interact through shears and compressions. Ultimately, the energy in these complex mesoscale structures arrives at the microscales, where it dissipates as heating and particle acceleration (Alexandrova et al., 2009). The mesoscales, though, are not a mere conduit for the energy: rather, they process and transform the energy in ways that both impact the ultimate microscale dissipation and feed back on macroscale phenomena (Bruno and Carbone, 2005; 2013, 2016). To date, there have been no studies to comprehensively catalog individual mesoscale structures in 3-D: their morphology (shape), topology (relative placement), and interactions.

Mesoscale IMF structures constitute an important "missing link" in our understanding of solar-wind dynamics (**Figure 1**). Through remote imaging, we have traced the macroscale IMF, and, with *in-situ* measurements from single spacecraft and small constellations of spacecraft, we have observed microscale structures. To close this observational gap that limits our understanding of the mesoscale IMF, we describe herein a new mission concept, the Magnetic Topology Reconstruction Explorer (MagneToRE), which calls for a large constellation of nanosatellites to produce the first dynamic, 3-D maps of mesoscale structures in any space plasma. MagneToRE targets the smaller IMF structures of the mesoscale range: those a few orders-of-magnitude larger than the microscale range. Magnetic structures of this size have been nearly fully processed by mesocale dynamics and provide the 3-D context for microscale phenomena.

1.2 Overview and Outline

In this Article, we describe the MagneToRE mission concept and show how it would characterize the full, 3-D structure of the solar wind's mesoscale magnetic field. Just as the mesoscales connect

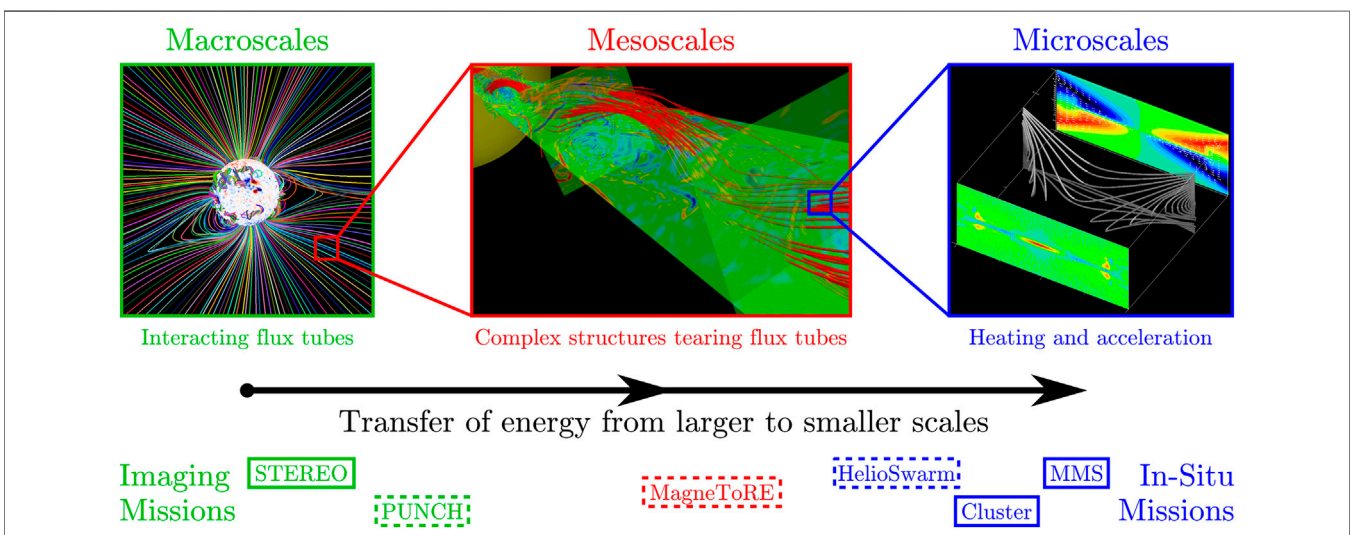

FIGURE 1 | Representation of the three primary size scales in the interplanetary magnetic field (IMF). The approximate scales explored by select past/present (solid) and future (dashed) missions are also indicated. Left image: prediction of the solar corona's magnetic field during the 21 August 2017 total solar eclipse performed by the team at Predictive Science, Inc., San Diego, CA, United States (Mikić et al., 2018). Center image: rendering of magnetic-field lines from simulations of reflection-driven Alfvén-wave turbulence inside a narrow magnetic flux tube (Jean C. Perez, Florida Institute of Technology). Right image: simulation of a magnetic reconnection region by Zenitani et al. (2011).

the energy dynamics of the IMF's macro- and microscales, MagneToRE's unique design would serve as a hybrid between *in-situ* and remote-imaging instrumentation (**Figure 1**). By utilizing a sufficiently large constellation of small, *in-situ* spacecraft, this mission would enable 3-D "images" of the magnetic structure to be reconstructed via advanced machine-learning techniques. These 3-D reconstructions of passing magnetic structures would be MagneToRE's ultimate data product and would allow competing theories of solar-wind energy dynamics to be directly assessed. Our goal in this Article is to demonstrate the scientific importance and technological feasibility of MagneToRE. Though specific details of MagneToRE's implementation require further study, the mission science and architecture presented here are targeted to fit within the scope of NASA's Explorers Program (SMEX or MIDEX).

The outline of the remainder of this Article is as follows. **Section 2** provides a brief overview of the theory and observations of IMF structure and its dynamics at mesoscales. We describe MagneToRE in **Sections 3** and **4**, which respectively contain the mission objectives and requirements and a high-level overview of possible mission implementation. We summarize the scientific impact of MagneToRE and possible augmentations to the mission in **Section 5** and offer concluding remarks in **Section 6**.

2 SCIENTIFIC BACKGROUND

At mesoscales, turbulent fluctuations dominate solar-wind dynamics (Matthaeus, 2021). Energy injected by the Sun at macroscales cascades down through the mesoscales and dissipates at microscales (Coleman, 1968; Goldstein et al., 1994; Petrosyan et al., 2010; Kiyani et al., 2015; Bruno and Carbone, 2005, 2013, 2016). At 1 au from the Sun, mesoscales extend from the correlation length ($\approx 10^6$ km) down to about d_i, the proton inertial length (≈ 100 km for nominal solar wind conditions; see **Figure 2**):

$$d_i = \frac{c}{\omega_{plas,p}}, \tag{1}$$

where $\omega_{plas,p}$ is the proton plasma frequency.

The solar wind's high speed ($v \approx 300$ to 800 km/s) means that temporal variations in IMF structures are minimal compared to their convection time. Taylor's hypothesis (Taylor, 1938) links the frequency, f, of *in-situ* plasma measurements with the wavevector, $\mathbf{k}$, of a passing structure:

$$2\pi f \approx \mathbf{k} \cdot \mathbf{v}, \tag{2}$$

where $\mathbf{v}$ is the solar-wind velocity.

Via Taylor's hypothesis, time series of *in-situ* measurements from a single spacecraft provide essentially 1-D, straight-line cuts through the structure of the IMF (Wicks et al., 2010; Horbury et al., 2012). Such data are typically analyzed with statistical methods: e.g., Fourier power spectra, structure functions, and wavelet transforms (Matthaeus and Goldstein, 1982; Burlaga, 1991; Greco et al., 2012). Though useful, such

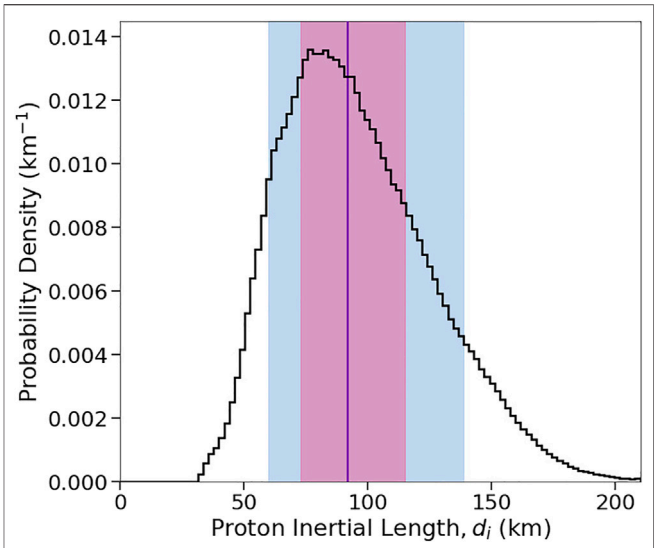

FIGURE 2 | Probability distribution of proton inertial length, d_i, from the Wind spacecraft (Acuña et al., 1995; Ogilvie et al., 1995; Wilson et al., 2018). Shaded regions show the (magenta) 25th to 75th percentiles and (blue) 10th to 90th percentiles.

methods fail to reveal the IMF's 3-D structure, and thus single-point measurements cannot distinguish between spatial and temporal variations. Constellations of four or five spacecraft – the Cluster, Magnetospheric Mulsticale (MMS), and Time History of Events and Macroscale Interactions during Substorms (THEMIS) missions – addressed some of these shortcomings (Escoubet et al., 2001; Angelopoulos, 2008; Burch et al., 2016). These missions yielded important new information about IMF processes through the use of groundbreaking data-analysis techniques: e.g., wave telescope (Neubauer and Glassmeier, 1990; Motschmann et al., 2000; Pinçon and Motschmann, 2000) and discontinuity analysis (Russell et al., 1983; Mottez and Chanteur, 1994; Dunlop and Woodward, 2000). Nevertheless, because of the limited number of spacecraft in each of these missions, none could fully map out 3-D IMF structures. Even proposed missions with moderately larger numbers of spacecraft – e.g., Cross-Scale (Horbury et al., 2006), EIDOSCOPE (Vaivads et al., 2012), and HelioSwarm (Klein et al., 2019; Matthaeus et al., 2019; Spence, 2019; TenBarge et al., 2019) missions – would suffer this limitation.

In the following sections, we demonstrate that MagneToRE's large nanosatellite constellation would transcend the capabilities of these other missions by simultaneously measuring the solar wind's magnetic field at enough points in space to enable the first 3-D "images" of the IMF. These images would include the full, dynamic, 3-D information about the morphology and topology of the magnetic field. In the past, 3-D dynamic reconstructions of space plasmas have been pursued for understanding the Birkeland currents in Earth's polar ionosphere (via the AMPERE missions; Anderson et al., 2000, Anderson et al., 2014), the magnetic reconnection X-line in the Earth's

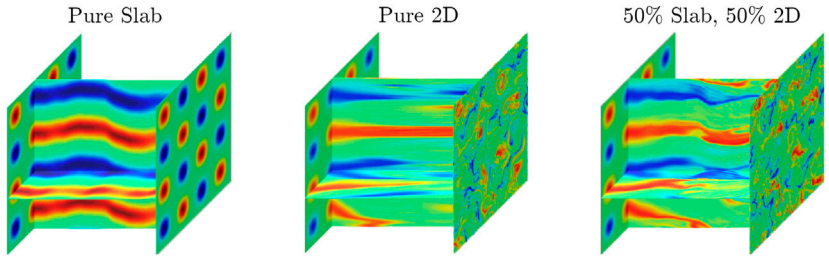

FIGURE 3 | After Bieber et al. (1996), simulations of magnetic flux tubes perturbed by three types of fluctuations (injected at the left of each box), which evolve into vastly different structures.

TABLE 1 | Comparison of prominent theories of solar-wind turbulence.

Turbulence theory	3-D structures
Isotropic turbulence: Kolmogorov (1941)	Multi-scale eddies without preferred direction
Slab + 2-D: Matthaeus et al. (1990); Zank et al. (2017)	Multi-scale eddies elongated along B_0; waves propagating along B_0
Critical balance: Goldreich and Sridhar (1995); Schekochihin et al. (2009)	Anisotropic fluctuations with wave-like polarization and propagation properties
Reduced MHD: Montgomery (1982); Shalchi and Hussein (2014); Oughton et al. (2017)	Elongated flux tubes including non-propagating structures and propagating waves

magnetotail (Denton et al., 2020; Torbert et al., 2020), and the global magnetic field and large-scale current morphology throughout Earth's magnetosphere (via a collection of decades of magnetic field measurements; Sitnov et al., 2019; Stephens et al., 2019). In contrast, we have optimized MagneToRE to enable the 3-D reconstruction of the solar wind's magnetic field, which, unlike Earth's magnetic field, is far weaker and subject to rapid convection.

In the absence of 3-D measurements from a mission such as MagneToRE, simulations have given rise to competing theories for the structure and evolution of the mesoscale IMF (Mininni et al., 2008; Eyink et al., 2013) and how it affects the solar wind's overall dynamics at all scales. **Table 1** summarizes the most prominent models. Though single-spacecraft observations have afforded plausibility to all these theories (Verscharen et al., 2019, and refs. therein), only a truly 3-D reconstruction of the IMF, such as the one MagneToRE would provide, can distinguish among them.

The difference among the turbulence theories in **Table 1** is not merely an academic abstraction but rather one with profound, multifaceted consequences for our understanding of the heliosphere. As the simulations in **Figure 3** show, different types of turbulent fluctuations produce vastly different magnetic structures, which, e.g., substantially affect the transport of energetic particles and plasma heating near intermittent structures (Bieber et al., 1996; Marsch and Tu, 1997). By creating 3-D images of the mesoscale IMF, MagneToRE would determine how wave-like IMF structures are (Belcher and Davis, 1971), what impact propagation effects have (Howes, 2015), the accuracy of force-free field approximations (Burlaga et al., 1998), and the presence of scale-dependent anisotropies and magnetic geometries potentially unstable to reconnection (Retinò et al., 2007; Priest and Pontin, 2009; Howes, 2016).

3 MISSION OVERVIEW

3.1 Mission Objectives

The MagneToRE mission's large constellation of nanosatellites, would simultaneously fulfill three science objectives:

Objective 1: Determine the 3-D morphology and topology of mesoscale IMF structures. The turbulence theories listed in **Table 1** predict different morphologies (shapes and "aspect ratios") and topologies (orientations and placements) for magnetic structures. This information could be captured in 3-D "images" of the magnetic field, which would require measurements across at least one order-of-magnitude in scale. Since the mesoscale IMF provides the context for the kinetic processes at microscales, MagneToRE would target the lower end of the mesocale range: 10's of d_i (1,000's of km) and above.

Objective 2: Determine how time variations affect the mesoscale IMF. This objective relates to distinguishing between spatial and temporal variations in the IMF. Different turbulence theories (**Table 1**) predict different types of temporal fluctuations, which define the IMF's wave, dispersion, and propagation properties. MagneToRE would determine scale-dependent time decorrelation rates, which are crucial for interpreting the nature of IMF fluctuations. (Edwards, 1964; Zhou et al., 2004; Lugones et al., 2016).

Objective 3: Determine how the mesoscale IMF varies with solar-wind conditions. MagneToRE would need to sample many different streams of solar wind – fast and slow wind, co-rotating interaction region (CIR) interfaces, and coronal mass ejections (CMEs) – to fully characterize the breadth of turbulence behavior in the mesoscale IMF. These wind types and large-scale structures originate in different source regions of the solar corona and experience different expansion histories, so they may exhibit differences in magnetic structure and fluctuations (Bruno and Carbone, 2005, 2013, 2016; Chapman et al., 2009; Wicks et al., 2009).

Scientific measurements in support of these three objectives need not necessarily be collected simultaneously. Indeed, some distributions of spacecraft within the constellation will be more conducive to one objective than another. For example,

TABLE 2 | Science traceability matrix (STM) for MagneToRE.

Science objectives	Science questions	Investigation objective requirements			Mission requirements
		Measurement	**Requirement**	**Projected performance**	
Objective 1: Determine the 3-D morphology and topology of mesoscale IMF structures	What is the static and dynamic structure of the mesocale IMF?	Magnetic field			*In-situ* solar-wind measurements
		Locations	≥ 22 points	24 points	
		Range	± 200 nT	± 1000 nT	
Objective 2: Determine how time variations affect the mesoscale IMF		Resolution	≤ 30 pT	10 pT	
		Noise (at 1 Hz)	≥ 10 sps	≥ 16 sps	Many magnetometers over 1,000's of km
		Sample rate	≤ 30 pT/$\sqrt{\text{Hz}}$	10 pT/$\sqrt{\text{Hz}}$	
		Proton distributions			
		Maximum energy	4000 eV	6000 eV	Single, ion Faraday cup or electrostatic analyzer
Objective 3: Determine how the mesoscale IMF varies with solar wind conditions	How does the nature of mesocale IMF structure vary?	Energy resolution	≤ 10%	≤ 6%	
		Cadence	0.5 Hz	1 Hz	
		Magnetic field			Many intervals ≥ 1 h over ≥ 1 year
		No requirements beyond those above			

Objective 1 would be well served by a relatively planar constellation oriented perpendicular to the solar wind's flow (**Section 4.1.2**). Conversely, **Objective 2** favors a constellation that is more elongated along the flow – especially one in which multiple spacecraft are nearly aligned with the flow. Most of the trajectory options (**Section 4. 2**) for MagneToRE would allow the constellation to naturally evolve over the course of the mission.

3.2 Science Traceability

Table 2 shows the science traceability matrix (STM) for MagneToRE. In order to achieve science closure on the mission objectives (**Section 3.1**), two types of *in-situ* measurements are required: vector magnetic field observations at multiple points for 3-D image reconstruction (**Section 4.1.2**) and bulk proton moments (density, velocity, and temperature) at a single point to gauge overall plasma conditions and aid in the 3-D magnetic reconstructions.

3.2.1 Vector Magnetic Field

Distributed measurements of the vector magnetic field are needed to fully characterize the IMF's spatiotemporal variations. To explore mesoscale structures in particular, spatial separations $\gtrsim$10's of d_i (**Eq. 1**) are required to avoid the transition into microscales. Furthermore, to "image" the 3-D magnetic structures, the range of spatial separations between measurements should span at least about one order of magnitude (**Section 4.1.2**).

Assuming the validity of Taylor's hypothesis (**Eq. 2**), regular measurements at the same point in space correspond to spatial measurements along the plasma's flow direction. We use Taylor's hypothesis here only to make a rough estimate of the minimum sampling frequency. To keep that estimate conservative, we set the lower limit on the size of structures that we seek to resolve at one d_i (≈100 km at 1 au; **Figure 2**). Applying the Nyquist criterion, this corresponds to a sampling frequency of the magnetic field of least $2v/d_i \approx 10$ Hz, where $v \approx 500$ km/s is a typical solar wind speed.

The sensitivity of each magnetic-field measurement must be $\lesssim 30\ \text{pT}/\sqrt{\text{Hz}}$ at 1 Hz, which is one order-of-magnitude below the typical turbulence power at the d_i-scale according to previous single-spacecraft measurements (Alexandrova et al., 2009; Woodham et al., 2018).

3.2.2 Proton Moments

Assuming an inter-spacecraft spacing of $\gtrsim 20\, d_i$, the Nyquist criterion gives a minimum sampling frequency for the proton moments of about 0.5 Hz. For image reconstruction, the uncertainty in proton speed would need to be $\lesssim$5% ($\lesssim$25 km/s) and the uncertainty in flow direction $\lesssim 5^\circ$. To distinguish high- and low-β_p plasma, where

$$\beta_p \equiv \left(\frac{2\,\mu_0\, n_p\, k_B\, T_p}{B_0^2} \right), \tag{3}$$

proton density (n_p) and temperature (T_p) uncertainties need only be $\lesssim$10% and $\lesssim$20%, respectively.

3.2.3 Sampling Duration and Mission Lifetime

Though MagneToRE need not continuously collect scientific measurements, the operations plan should ensure that it remains in its science mode for intervals of $\gtrsim$1 hour. This roughly corresponds to the correlation time, which defines

the boundary between the macro- and mesoscales. MagneToRE, over the course of its lifetime, should collect data over many such intervals. A mission lifetime of $\gtrsim 1$ year would ensure that multiple Carrington rotations are sampled, which would provide a wide variety of plasma conditions for statistical studies.

3.2.4 Data Analysis and Science Closure

Science closure would require physics-based reconstructions that employ modern data science approaches (see **Section 4.1.2**) alongside the computation of field-line topologies (e.g., Priest and Pontin, 2009; Tooprakai et al., 2016) and the morphology and complexity of flux surfaces (e.g., Mininni et al., 2008; Servidio et al., 2014). Algorithms for identifying likely critical points (e.g., X- and O-points) would need to be developed based on those employed for MMS and other missions (Denton et al., 2010; Fu et al., 2015) and would be essential for assessing magnetic structure. Higher-order statistics of the magnetic field (e.g., scale-dependent kurtosis and multifractal analysis), which quantify the intermittency of structures (Kiyani et al., 2007; Chhiber et al., 2018), would also be employed.

4 MISSION IMPLEMENTATION

Dynamic, 3-D maps of the mesoscale IMF could be effectively reconstructed (**Section 4.1**) from *in-situ* magnetic-field measurements from MagneToRE's large constellation (**Section 4.2**) of spacecraft. Each of MagneToRE's nanosatellite "probe" spacecraft (**Section 4.3**) would carry a compact fluxgate magnetometer. A larger "prime" spacecraft (**Section 4.4**) would be required to deploy the probe spacecraft, serve as their telemetry link to the ground, and host a Faraday cup or electrostatic analyzer (ESA) for measuring proton moments.

4.1 Magnetic Reconstruction

4.1.1 Select Existing Methods

Determining the structure of magnetic fields is a fundamental aspect of multi-spacecraft missions in heliophysics. The analysis of spatial gradients and volumetric tensors (Harvey, 1998) requires simultaneous, *in-situ* measurements from 4 or more spacecraft (Shen et al., 2003, Shen et al., 2007). Trilinear methods (Haynes and Parnell, 2007) and first-order Taylor expansion (Fu et al., 2016; Chen et al., 2019) are also useful in identifying and characterizing magnetic structures. These methods do not rely on Taylor's hypothesis (**Eq. 2**), but they typically require that measurements be made at a minimum of 4 points (or 8 points in the case of trilinear methods) and perform best under specific spatial arrangements of the spacecraft. With more simultaneous measurement points, better estimates are possible of the volumetric tensor and gradients – even when the measurement points are randomly distributed (Watanabe and Nagata, 2017).

4.1.2 Case Study: A Novel Method

Though we are actively exploring extensions of the methods described in **Section 4.1.1**, we focus here on an alternative approach that utilizes modern machine-learning algorithms to reconstruct 3-D maps of the magnetic field from multi-point *in-situ* measurements. Development of this new method remains ongoing and will be the subject of a publication that is currently in preparation. Here, we present a case study to demonstrate the feasibility of the algorithm and to establish a baseline number of probe spacecraft for MagneToRE.

We began by using the output from a fully kinetic, 3-D plasma simulation (Roytershteyn et al., 2015) to generate synthetic, ~ 13 Hz time series of magnetic-field measurements for various constellations (number and arrangement) of probe spacecraft. For simplicity, we have initially focused on constellations in which the spacecraft are in a plane perpendicular to the plasma flow; under Taylor's hypothesis (**Eq. 2**), applying a phase shift to any probe's time series effectively shifts its location along the flow direction.

We carried out magnetic reconstruction in 3-D using the complete time-series from all spacecraft as a single dataset versus carrying out a series of 2-D, planar reconstructions. We interpolated the magnetic-field via the Gaussian Processes (GP) method (Rasmussen and Williams, 2006) as implemented in the scikit-learn package (Pedregosa et al., 2011; Buitinck et al., 2013) and with a Matern kernel, which is based on modified Bessel functions (Abramowitz et al., 1965).

Figure 4 shows one "slice" through our 3-D spatial reconstruction of the magnetic field. The constellation of spacecraft was distributed in the xy-plane, and the plasma flowed along the z-axis (perpendicular to the page). For brevity, **Figure 4** only shows the x-component (B_x); the **Appendix** shows renderings of the y and z-components (B_y and B_z) and the magnitude ($B \equiv |\mathbf{B}|$). Panel **A** shows a slice of the 3-D simulation (Roytershteyn et al., 2015), and Panels **B–H** show GP reconstructions based on synthetic time-series from various constellations (black dots). For constellations of 4 or 8 spacecraft (**Panels B** and **C**), the reconstruction poorly matches the original (**Panel A**). With 16 spacecraft (**Panel D**), some structure is captured, but the shape of the boundary between the red and blue regions (positive and negative B_x) is distorted. A constellation of 24 spacecraft (**Panel E**) provides a far better reconstruction, but 34 spacecraft (**Panel F**) provide little further improvement. Even when the 24 spacecraft have randomized positions (**Panel G**) and 2 spacecraft are removed (**Panel H**) to simulate unfavorable alignments or equipment failure, a reasonable reconstruction is still produced.

These results of our case study indicate that the baseline design for MagneToRE should be measuring the magnetic field at 24 points in space to enable a sufficiently detailed reconstruction of the 3-D magnetic field. These results also suggest that strict control over the trajectory of the individual spacecraft is not necessary since the algorithm performs well even when the spacecraft locations are randomly perturbed.

Nevertheless, our algorithm remains in active development, and we are focusing on several key areas of improvement. First, the current algorithm interpolates each component of the vector magnetic field independently of the other two. We are currently testing alternative implementations of the GP method that would simultaneously

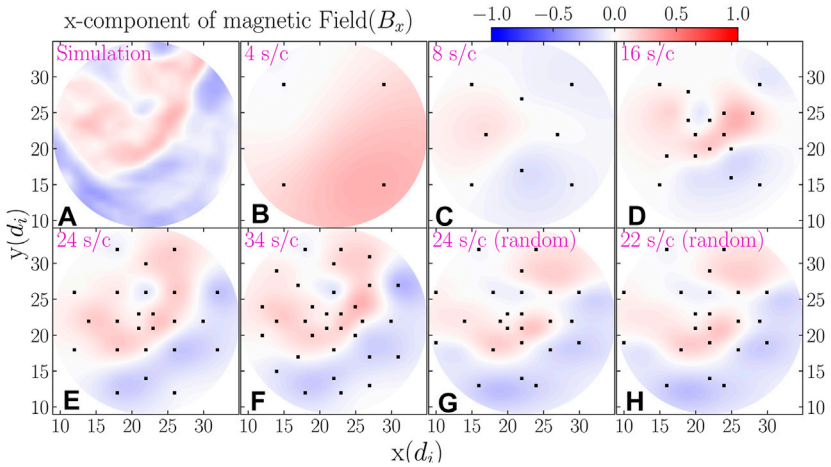

FIGURE 4 | Plots of the normalized *x*-component of magnetic field (B_x) over the *xy*-plane (coordinates normalized by d_i): **(A)** slice from the 3-D simulation (Roytershteyn et al., 2015) and **(B–H)** GP reconstructions from synthetic time series from various constellations of spacecraft (black dots).

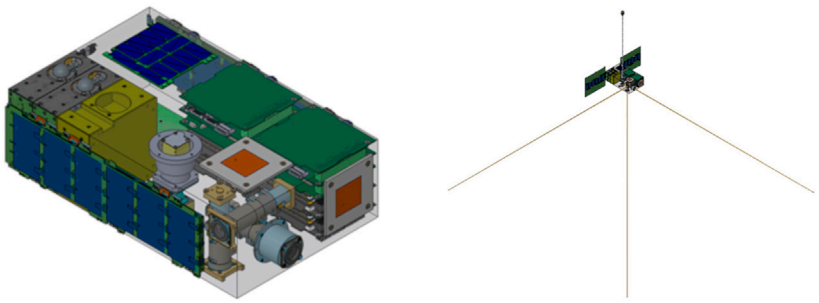

FIGURE 5 | A "strawman" probe 6U Cubesat with stacer antennas, solar panels, and a placeholder magnetometer (left) stowed and (right) deployed. Note that the two images are shown at different scales.

interpolate all three components and automatically enforce the requirement that the magnetic field be divergence-less, which could significantly improve the quality of the magnetic reconstructions. Second, we are developing methods for quantitatively comparing our algorithm's magnetic reconstructions to each other and to the original simulation. These comparisons would be based on the automated identification and characterization of magnetic structures (see **Section 3.2.4**).

4.2 Constellation Orbits and Operations

The science requirements dictate that the MagneToRE constellation would need to spend $\gtrsim 1$ hour at a time in the solar wind for multiple periods over $\gtrsim 1$ year, which could be achieved under various launch scenarios. The Earth-Sun L1 point affords continuous solar-wind observations, but insertion into lunar orbit may be more feasible for a rideshare (e.g., via the Artemis program). A rideshare with a deep-space (e.g., planetary) mission could also be suitable and offer the added benefits of easier constellation management and the opportunity to explore changes in IMF structure with distance from the Sun.

The launch, commission, and operation of 25 spacecraft poses significant logistical challenges that would require very careful consideration and planning. Nevertheless, in both the public and private sector, multi-spacecraft missions (including those utilizing CubeSats) are becoming increasingly common and often use some degree of semi-autonomous control. Operations for MagneToRE would be aided by having only a single science mode: e.g., no burst modes are anticipated. Likewise, while the relative positions of the spacecraft must be carefully measured, the controlling of those positions through precision formation flying is not required (**Section 4.1.2**).

4.3 Probe Spacecraft

Until recently, a large constellation mission such as MagneToRE would have been cost-prohibitive under most funding programs due to the number of large and sophisticated spacecraft required. However, recent advancements in nanosatellites and instrument miniaturization now make such a constellation feasible (Liemohn et al., 2021). Each probe spacecraft could be built from a custom bus based on the well-established 6U CubeSat form factor (**Figure 5**) and designed to have a modest magnetic signature (**Section 4.3.6**).

TABLE 3 | Summary of design for probe spacecraft.

Subsystem	Description	Heritage/ Vendor
Chassis	Modified 6U CubeSat	CURIE
Solar panels	Two, custom, trifold panels Nominal power output: 18 W each	Spectrolab, CURIE
Attitude control	Commercial star tracker Commercial reaction wheels	Blue Canyon Technologies
Propulsion	Multiple (≥ 4), CO_2-propelled thrusters Nominal thrust: 3 mN each	CURIE
Inter-spacecraft communications	Three, custom, deployable, stacer antennas Chip-scale atomic clock for radio ranging Nominal frequency: 20 MHz Estimated data rate: $\approx$ 20 kpbs	CURIE, Microsemi
Magnetometer	Miniaturized, low-noize fluxgate sensor Foldable boom	Ex-Alta 1, ICI-5, TRACERS ACES-II, BLAZE

FIGURE 6 | A deployed CURIE stacer antenna undergoing ground testing.

Because all of the probe spacecraft would be identical, substantial resources could be used to formulate, implement, and validate their design. These development costs would be roughly independent of the number of spacecraft, so, for a large number, the incremental cost of each spacecraft would be modest. This would also make it practical for the probe spacecraft's design to comply with all the requirements of NASA's Explorers Program, which are far more rigorous than is typical for CubeSat missions.

In this Section, we describe one possible implementation of MagneToRE's probe spacecraft that would satisfy the mission objectives described above (**Section 3.1**). In this scenario, which is summarized in **Table 3**, many of the spacecraft support systems would be based on components developed at the Space Sciences Laboratory at the University of California, Berkeley (UCB/SSL) for the Cubesat Radio Interferometry Experiment (CURIE) mission (Sundkvist et al., 2016), which is slated to launch and operate in late 2021. Likewise, the probe magnetometers would be based on instruments and technology (e.g., Miles et al., 2019) developed at the University of Iowa (UIowa).

4.3.1 Power

Off-the-shelf electrical power systems (EPSs) and batteries from Clyde Space could be used to power each probe. Input power could be derived from trifold, deployable solar panels developed at UCB/SSL for CURIE (**Figure 5**). Each trifold panel provides up to 18 W of power (for a total of 36 W) via Spectrolab space-rated photovoltaic cells.

4.3.2 Guidance and Navigation

Attitude control for each probe could be provided by a Blue Canyon XACT Attitude Control System (ACS), which has both a star tracker and reaction wheels. Deployment and control of the constellation could utilize a UCB/SSL propulsion unit based on that developed for the CURIE mission. Multiple thruster nozzles, each with a 3 mN nominal thrust and a 0.6 mN impulse burst bit, would allow on-axis thrusting and momentum dumping from the reaction wheels.

4.3.3 Radio Communications

The large separations (1,000's of km) required for the probe spacecraft poses a challenge for probe-to-probe and probe-to-prime communications. Using high-frequency transceivers would require narrow antenna beam patterns and accurate pointing ability to function over such large distances. This would impose severe restrictions and complicate the design of the probe's bus and ACS. Instead, given the moderate data-rates required, omnidirectional UCB/SSL stacer antennas (**Figure 6**) and a high-frequency (HF) transceiver system (about 20 MHz and 20 kbps) based on CURIE heritage could comfortably close the link budget at these distances.

4.3.4 Radio Ranging and Position Reconstruction

The communication stacers would double as antennas for a radio ranging system that would deduce relative spacecraft positions and establish constellation geometry. Two-way transfer is a two-way radio-ranging method for accurately measuring the time-of-flight between two nodes. Each node is responsible for accurately measuring the local time delay between a receive and transmit pulse, which can be accomplished with nanosecond resolution

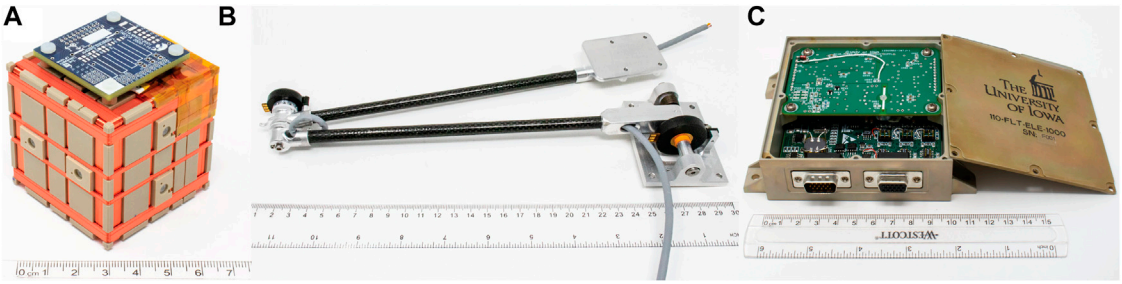

FIGURE 7 | (A) Prototype magnetometer sensor for TRACERS. **(B)** BLAZE magnetometer boom. **(C)** Fluxgate electronics as-flown on the ICI-5 sounding rocket (November 2019).

using commercial, chip-scale atomic clocks (e.g., the Microsemi devices used on CURIE). The scalar distance between two nodes can be deduced by measuring the total time-of-flight from one node, to another, and back again. This method results in a distance measurement with an accuracy $\lesssim 10$ m – more than sufficient for orbit station-keeping as well as baseline science. Together with a simultaneous goniopolarimetric measurement of the direction of radio propagation, position vectors can be established and the overall geometery of the spacecraft constellation determined.

4.3.5 Magnetometer

Each probe's magnetometer system would consist of a vector fluxgate sensor, segmented boom, and radiation tolerant electronics package (Miles et al., 2013) such as has been developed at UIowa (**Figures 7A–C**, respectively). This system, based on the MGF instrument (Wallis et al., 2015) on Cassiope/e-POP, also draws heritage from the fluxgate magnetometer (Miles et al., 2016) for the Ex-Alta 1 CubeSat (Mann et al., 2020) in the QB50 constellation (Wicks and Miles, 2019). The next-generation, nanosatellite-scale "Tesseract" magnetometer sensor (**Figure 7A**) leverages low-noise custom fluxgate cores (Miles et al., 2019) to create a compact, rigid, symmetric, and magnetically stable probe. This sensor design also incorporates temperature compensation (Miles et al., 2017), which may be advantageous for some potential trajectories (e.g., lunar orbit; **Section 4.2**). Each magnetometer would deploy 60 cm from its probe via the BLAZE magnetometer boom (**Figure 7B**), which is composed of non-magnetic materials (titanium and carbon-fiber with phosphor bronze springs).

4.3.6 Magnetic Cleanliness

Given the central role that magnetic-field measurements play in effecting science closure (**Table 2**), maintaining appropriate magnetic cleanliness in the probe spacecraft would be essential and would require careful management. A magnetometer boom (**Figure 7B**) would separate the fluxgate sensor from the spacecraft by 60 cm. This approach proved highly effective for the 3U Ex-Alta 1 CubeSat (Miles et al., 2016). Active noise removal (e.g., Ness et al., 1971; Constantinescu et al., 2020) is also possible using an alternative gradiometer setup (e.g., two separated miniature sensors on the outer boom segment).

Since some prior CubeSat missions have encountered magnetic contamination from commercial components (e.g., Miles et al., 2016), the design and fabrication of the probe spacecraft would be largely kept "in house" and carefully managed to ensure compliance. At the prototype stage, potential parts and subsystems would be screened magnetically and, where appropriate, replaced with preferred materials such as titanium, aluminum, or engineering plastic. Custom solar panels (**Section 4.3.1**) would be wired to minimize their stray magnetic-field. Similarly, battery arrays would be selected and arranged to minimize stray field during charge/discharge. Though commercial reaction wheels would be required, these would have a custom control-system and be augmented by thrusters, which together would be used to keep the wheels from generating interference either at the base-band (DC) or at the second harmonic of the fluxgate drive frequency (~16 kHz).

Particular attention would be paid to time-varying stray magnetic fields, which are the most challenging to remove in post-processing. Static offsets and long-duration trends can likely be mitigated using vector-vector calibration across the constellation of spacecraft. Over a sufficiently long interval, we can assume that all spacecraft will experience a common environment in the solar wind. Therefore, long-term deviations by an individual spacecraft from the ensemble average, particularly if the offset is constant in the frame of the spacecraft/instrument, likely result from local fields or instrumental offsets and can be trended and removed. Time varying fields, particularly those occurring on time-scales comparable to the measurement requirements, cannot be easily removed this way and must be mitigated by design pre-launch.

4.4 Prime Spacecraft

MagneToRE's single prime spacecraft would have four main functions: transporting the probe spacecraft to their orbit insertion point, releasing the probes into a constellation, relaying data between the probes and the Earth, and obtaining solar-wind proton moments. The design and implementation of the prime spacecraft would follow the example of single-spacecraft missions from NASA's Explorers Program and emphasize the use of components with extensive flight heritage.

4.4.1 Bus, Avionics, and Guidance

Various satellite designs could be used for the prime spacecraft. The EELV Secondary Payload Adapter (ESPA) is an existing

design with low development-costs, high heritage, and compatibility with rideshares. An ESPA would accommodate commercial propulsion, avionics, and power systems. For a dedicated launch, a custom spacecraft could be designed with substantially lower mass.

4.4.2 Communications

The prime spacecraft would carry two radio systems. An HF transceiver, identical to that on each probe, would be used for communicating with the probes. An X-band system with a high-gain dish would communicate with the ground.

4.4.3 Ion Faraday Cup or Electrostatic Analyzer

The prime spacecraft's only required scientific instrument would be an ion Faraday cup or electrostatic analyzer (ESA), which would measure bulk proton moments (density, velocity, and temperature), with nominal energies of ~ 500–1,000 eV. The scientific requirements on the ion measurements (**Section 3.2**) are relatively modest, so various designs could be employed for this instrument. The important consideration for this measurement is that the instrument resolve the solar-wind proton population, which is supersonic and nearly unidirectional.

4.4.4 Magnetic Cleanliness

Since the prime spacecraft would not operate its own magnetometer, its requirements for magnetic cleanliness would be far less stringent than those on the probe spacecraft (**Section 4.3.6**). Only relatively modest efforts to control magnetic contamination would be needed to protect the unactivated probe spacecraft that it would carry and deploy.

Though, in principle, the prime spacecraft could include one or more magnetometers, doing so is not a requirement for mission success and would substantially increase the mission's cost and complexity. Even if the prime spacecraft used the same magnetometer sensor and electronics (**Section 4.3.5**) as the probe spacecraft, it would require a different and larger boom to account for the prime spacecraft's much larger size. Additionally, operating a magnetometer on the prime spacecraft would require much greater attention to magnetic cleanliness, which would almost certainly eliminate the possibility of using an existing commercial design for the spacecraft system (e.g., an ESPA; **Section 4.4.1**).

5 DISCUSSION

5.1 Programmatic Context

The implementation of MagneToRE would enable substantial progress toward Key Science Goal 4 of the Heliophysics Decadal Survey (Committee on a Decadal Strategy for Solar and Space Physics, 2013), which seeks to "discover and characterize fundamental processes that occur within the heliosphere." Analyses of MagneToRE's observations would definitively characterize the mesoscale magnetic structure of the solar wind – including that upstream of Earth, which drives space weather. Moreover, different theories of IMF turbulent structure lead to drastically different predictions for the propagation of energetic particles (**Section 2**). Thus, MagneToRE would further our "understanding of the Sun and its effects on the Earth," as sought by **Objective 1** of NASA's, 2018 Strategic Plan (NASA, 2018).

MagneToRE's unique design and innovative data-processing algorithms would lay important groundwork for future multi-spacecraft missions such as the Magnetospheric Constellation (MagCon). The final report of the National Academies' Committee on Achieving Science Goals with CubeSats (Committee on Achieving Science Goals with CubeSats, 2016) emphasizes that "constellations of 10–100 science spacecraft have the potential to enable critical measurements for space science."

MagneToRE could also provide unique rideshare opportunities to other, smaller missions. In particular, if an ESPA bus was used as the mission's prime spacecraft, it would have substantial capacity for additional payloads. This could enable missions-of-opportunity, which could include instruments fixed to the prime spacecraft and CubeSats deployed from it. Such small projects often have few options for accessing deep space, so they would greatly benefit from MagneToRE's trajectory –whether that be to L1, lunar orbit, or beyond. Additionally, since the prime spacecraft would already be designed as a communications relay, it could potentially provide the smaller projects with data and power at very little additional cost.

5.2 Mission Augmentations

Though the MagneToRE mission concept as presented offers a compelling science case, it could be augmented in several ways to enhance its science return. A full trade study would be required to determine whether the additional science enabled by these augmentations would justify higher mission costs.

Given the importance of mesoscale IMF structure to the propagation of energetic particle populations – including solar energetic particles (SEPs), shock-accelerated particles associated with CMEs and CIRs, and galactic cosmic rays (GCRs) – adding instruments to detect and characterize such particles could be valuable for MagneToRE. While one or more large, sophisticated energetic-particle instruments could be added to the prime spacecraft, the probe spacecraft may be able to accommodate simpler, miniaturized detectors.

MagneToRE would be able to achieve all of its objectives (**Section 3.1**) with only a single thermal-particle instrument located on the prime spacecraft. Nevertheless, adding a thermal-particle instrument to some or all of the probe spacecraft would enable some additional science objectives – especially those related to field-particle correlation. An electrostatic analyzer or Faraday cup on each probe would provide the most detailed information but may require a larger chassis for the probes, which in turn could substantially increase the mission's cost. Langmuir probes, Mach probes, or quasi-thermal noise instruments would return less information on the particles but would likely be less costly.

6 CONCLUSION

As **Figure 1** shows, the MagneToRE mission concept described above would fill a critical gap in our understanding of the IMF's

dynamic structure. Energy in the solar wind is widely understood to be injected at large scales and then to shift to progressively smaller scales, but the process of this kind of turbulent cascade remains poorly understood and an active area of research. Indeed, two, multi-spacecraft missions – one upcoming and another under review – seek to begin exploring mesocale IMF turbulence with complementary techniques. First, PUNCH (DeForest et al., 2017) will use imaging instruments to explore the larger end of the mesoscale range. Second, HelioSwarm (Klein et al., 2019; Matthaeus et al., 2019; Spence, 2019; TenBarge et al., 2019) would be an *in-situ* mission that spans the transition from mesoscales to microscales. However, the number of spacecraft that would comprise the HelioSwarm mission would not fully allow for the "imaging" of the 3-D IMF structure and magnetic field reconstruction described here. MagneToRE would provide the "missing link" between these two missions by producing the first-ever, truly 3-D maps of the IMF at any scale.

DATA AVAILABILITY STATEMENT

Publicly available datasets from the Wind spacecraft used for **Figure 2** are available from NASA's Coordinated Data Analysis Web (CDAWeb; https://cdaweb.gsfc.nasa.gov/index.html/).

AUTHOR CONTRIBUTIONS

All authors listed have made a substantial, direct, and intellectual contribution to the work and approved it for publication.

FUNDING

BAM and RAQ are partially supported by NSF Award Number 1931435. JAAR is supported by the European Space Agency's Networking/Partnership Initiative (NPI) programme and the Colombian programme Pasaporte a la Ciencia, Foco Sociedad - Reto 3 (Educación de calidad desde la ciencie, la tecnología y la innovación (CTel)), ICETEX. RB is partially supported by NASA award 80NSSC21K0739. RC and WHM are supported by NASA HSR grant 80NSSC18K1648. DMM is supported by NASA under grants and contracts 80NSSC19K0491, 80GSFC18C0008, 80NSSC18K1293, and 80NSSC20K1842. SS is supported by the European Union's Horizon 2020 research and innovation program under Grant Agreement No. 776262 (AIDA, www.aida-space.eu). DS is supported by NASA award 80NSSC17K0032. SKV is supported by NASA contract NNG04EB99C and by NSF grants ATM-0739864 and ATM-1420184. DV is supported by STFC Ernest Rutherford Fellowship ST/P003826/1 and STFC Consolidated Grant ST/S000240/1. RTW is supported by STFC Consolidated Grant ST/V006320/1.

ACKNOWLEDGMENTS

The authors thank Zoran Mikić, Jean C. Perez, and Seiji Zenitani for permission to reproduce their images in **Figure 1**. BAM and DV gratefully acknowledge the NSF's SHINE program (https://shinecon.org/), whose 2019 annual meeting served as a venue for preliminary discussions about this mission concept. BAM and SKV extend further thanks to Erika Hamden and the 2019 NASA PI Launchpad workshop, which offered invaluable instruction and enabled refinement of the mission. The authors also thank George C. Ho, Clint T. Apland, and Michael V. Paul for fruitful discussions. This research made use of PlasmaPy, a community-developed open-source Python package for plasma science (PlasmaPy Community, 2020). The preparation of this manuscript made use of the SAO/NASA Astrophysics Data System (ADS): https://ui.adsabs.harvard.edu/.

REFERENCES

Abramowitz, M., Stegun, I. A., and Miller, D. (1965). Handbook of Mathematical Functions with Formulas, Graphs and Mathematical Tables (National Bureau of Standards Applied Mathematics Series No. 55). *J. Appl. Mech.* 32, 239. doi:10.1115/1.3625776

Acuña, M. H., Ogilvie, K. W., Baker, D., Curtis, S. A., Fairfield, D., and Mish, W. (1995). The Global Geospace Science Program and its investigations. *Space Sci. Rev.* 71, 5–21. doi:10.1007/BF00751323

Alexandrova, O., Chen, C. H. K., Sorriso-Valvo, L., Horbury, T. S., and Bale, S. D. (2013). Solar Wind Turbulence and the Role of Ion Instabilities. *Space Sci. Rev.* 178, 101–139. doi:10.1007/s11214-013-0004-8

Alexandrova, O., Saur, J., Lacombe, C., Mangeney, A., Mitchell, J., Schwartz, S. J., et al. (2009). Universality of Solar-Wind Turbulent Spectrum from Mhd to Electron Scales. *Phys. Rev. Lett.* 103, 165003. doi:10.1103/PhysRevLett.103.165003

Anderson, B. J., Korth, H., Waters, C. L., Green, D. L., Merkin, V. G., Barnes, R. J., et al. (2014). Development of Large-Scale Birkeland Currents Determined from the Active Magnetosphere and Planetary Electrodynamics Response experiment. *Geophys. Res. Lett.* 41, 3017–3025. doi:10.1002/2014GL059941

Anderson, B. J., Takahashi, K., and Toth, B. A. (2000). Sensing Global Birkeland Currents with Iridium Engineering Magnetometer Data. *Geophys. Res. Lett.* 27, 4045–4048. doi:10.1029/2000GL000094

Angelopoulos, V. (2008). The THEMIS mission. *Space Sci. Rev.* 141, 5–34. doi:10.1007/s11214-008-9336-1

Balogh, A., and Erdõs, G. (2013). The Heliospheric Magnetic Field. *Space Sci. Rev.* 176, 177–215. doi:10.1007/s11214-011-9835-3

Belcher, J. W., and Davis, L. (1971). Large-amplitude Alfvén Waves in the Interplanetary Medium, 2. *J. Geophys. Res.* 76, 3534–3563. doi:10.1029/JA076i016p03534

Bieber, J. W., Wanner, W., and Matthaeus, W. H. (1996). Dominant Two-Dimensional Solar Wind Turbulence with Implications for Cosmic ray Transport. *J. Geophys. Res.* 101, 2511–2522. doi:10.1029/95JA02588

Bruno, R., and Carbone, V. (2005). The Solar Wind as a Turbulence Laboratory. *Living Rev. Solar Phys.* 2, 4. doi:10.12942/lrsp-2005-4

Bruno, R., and Carbone, V. (2013). The Solar Wind as a Turbulence Laboratory. *Living Rev. Solar Phys.* 10, 2. doi:10.12942/lrsp-2013-2

Bruno, R., and Carbone, V. (2016). *Turbulence in the Solar Wind*. Switzerland: Springer. doi:10.1007/978-3-319-43440-7

Buitinck, L., Louppe, G., Blondel, M., Pedregosa, F., Mueller, A., Grisel, O., et al. (2013). *API Design for Machine Learning Software: Experiences from the Scikit-Learn Project*. ECML PKDD Workshop: Languages for Data Mining and Machine Learning, 108–122.

Burch, J. L., Moore, T. E., Torbert, R. B., and Giles, B. L. (2016). Magnetospheric Multiscale Overview and Science Objectives. *Space Sci. Rev.* 199, 5–21. doi:10.1007/s11214-015-0164-910.1007/978-94-024-0861-4_2

Burlaga, L. F. (1991). Intermittent Turbulence in the Solar Wind. *J. Geophys. Res.* 96, 5847–5851. doi:10.1029/91JA00087

Burlaga, L., Fitzenreiter, R., Lepping, R., Ogilvie, K., Szabo, A., Lazarus, A., et al. (1998). A Magnetic Cloud Containing Prominence Material: January 1997. *J. Geophys. Res.* 103, 277–285. doi:10.1029/97JA02768

Chapman, S. C., Nicol, R. M., Leonardis, E., Kiyani, K., and Carbone, V. (2009). Observation of Universality in the Generalized Similarity of Evolving Solar Wind Turbulence as Seen by ulysses. *ApJ* 695, L185–L188. doi:10.1088/0004-637X/695/2/L185

Chen, Z., Fu, H., Wang, T., Cao, D., Peng, F., Yang, J., et al. (2019). Reconstructing the Flux-Rope Topology Using the Fote Method. *Sci. China Technol. Sci.* 62, 144–150. doi:10.1007/s11431-017-9201-1

Chhiber, R., Chasapis, A., Bandyopadhyay, R., Parashar, T. N., Matthaeus, W. H., Maruca, B., et al. (2018). Higher-order Turbulence Statistics in the Earth's Magnetosheath and the Solar Wind Using Magnetospheric Multiscale Observations. *J. Geophys. Res. Space Phys.* 123, 9941–9954. doi:10.1029/2018JA025768

Coleman, P. J. J., Jr. (1968). Turbulence, Viscosity, and Dissipation in the Solar-Wind Plasma. *ApJ* 153, 371. doi:10.1086/149674

Committee on a Decadal Strategy for Solar and Space Physics (2013). *Solar and Space Physics: A Science for a Technological Society*. Washington, DC: Tech. rep. National Research Council. doi:10.17226/13060

Committee on Achieving Science Goals with CubeSats (2016). *Achieving Science with Cubesats: Thinking inside the Box*. Washington, DC: Tech. rep.National Academies of Sciences, Engineering, and Medicine. doi:10.17226/23503

Constantinescu, O. D., Auster, H.-U., Delva, M., Hillenmaier, O., Magnes, W., and Plaschke, F. (2020). Maximum-variance Gradiometer Technique for Removal of Spacecraft-Generated Disturbances from Magnetic Field Data. *Geosci. Instrum. Method. Data Syst.* 9, 451–469. doi:10.5194/gi-9-451-2020

DeForest, C. E., de Koning, C. A., and Elliott, H. A. (2017). 3d Polarized Imaging of Coronal Mass Ejections: Chirality of a Cme. *ApJ* 850, 130. doi:10.3847/1538-4357/aa94ca

Denton, R. E., Sonnerup, B. U. Ö., Birn, J., Teh, W.-L., Drake, J. F., Swisdak, M., et al. (2010). Test of Methods to Infer the Magnetic Reconnection Geometry from Spacecraft Data. *J. Geophys. Res.* 115, a–n. doi:10.1029/2010JA015420

Denton, R. E., Torbert, R. B., Hasegawa, H., Dors, I., Genestreti, K. J., Argall, M. R., et al. (2020). Polynomial Reconstruction of the Reconnection Magnetic Field Observed by Multiple Spacecraft. *J. Geophys. Res. Space Phys.* 125, 027481. doi:10.1029/2019JA027481

Dunlop, M. W., and Woodward, T. I. (2000). "Multi-spacecraft Discontinuity Analysis: Orientation and Motion," in *Analysis Methods For Multi-Spacecraft Data*. Editors G. Paschmann and P. W. Daly 1 edn (Bern, Switzerland: International Space Science Institute (ISSI)), 271–306. no. SR-001 in ISSI Scientific Reportchap. 11. 1.

Edwards, S. F. (1964). The Statistical Dynamics of Homogeneous Turbulence. *J. Fluid Mech.* 18, 239–273. doi:10.1017/S0022112064000180

Escoubet, C. P., Fehringer, M., and Goldstein, M. (2001). IntroductionThe Cluster mission. *Ann. Geophys.* 19, 1197–1200. doi:10.5194/angeo-19-1197-2001

Eyink, G., Vishniac, E., Lalescu, C., Aluie, H., Kanov, K., Bürger, K., et al. (2013). Flux-freezing Breakdown in High-Conductivity Magnetohydrodynamic Turbulence. *Nature* 497, 466–469. doi:10.1038/nature12128

Fu, H. S., Cao, J. B., Vaivads, A., Khotyaintsev, Y. V., Andre, M., Dunlop, M., et al. (2016). Identifying Magnetic Reconnection Events Using the Fote Method. *J. Geophys. Res. Space Phys.* 121, 1263–1272. doi:10.1002/2015ja021701

Fu, H. S., Vaivads, A., Khotyaintsev, Y. V., Olshevsky, V., André, M., Cao, J. B., et al. (2015). How to Find Magnetic Nulls and Reconstruct Field Topology with Mms Data? *J. Geophys. Res. Space Phys.* 120, 3758–3782. doi:10.1002/2015JA021082

Goldreich, P., and Sridhar, S. (1995). Toward a Theory of Interstellar Turbulence. 2: Strong Alfvenic Turbulence. *ApJ* 438, 763. doi:10.1086/175121

Goldstein, M. L., Roberts, D. A., and Fitch, C. A. (1994). Properties of the Fluctuating Magnetic Helicity in the Inertial and Dissipation Ranges of Solar Wind Turbulence. *J. Geophys. Res.* 99, 11519–11538. doi:10.1029/94JA00789

Greco, A., Matthaeus, W. H., D'Amicis, R., Servidio, S., and Dmitruk, P. (2012). Evidence for Nonlinear Development of Magnetohydrodynamic Scale Intermittency in the Inner Heliosphere. *ApJ* 749, 105. doi:10.1088/0004-637X/749/2/105

Harvey, C. (1998). Use of sandy beach Habitat by *Fundulus majalis*, a Surf-Zone Fish. *Mar. Ecol. Prog. Ser.* 164, 307–310. doi:10.3354/meps164307

Haynes, A. L., and Parnell, C. E. (2007). A Trilinear Method for Finding Null Points in a Three-Dimensional Vector Space. *Phys. Plasmas* 14, 082107. doi:10.1063/1.2756751

Horbury, T., Louarn, P., Fujimoto, M., Baumjohann, W., Blomberg, L. G., Barabash, S., et al. (2006). "Cross-scale: a Multi-Spacecraft mission to Study Cross-Scale Coupling in Space Plasmas," in *Cluster and Double Star Symposium*. Editor K Fletcher (ESA Special Publication), 598, 77.

Horbury, T. S., Wicks, R. T., and Chen, C. H. K. (2012). Anisotropy in Space Plasma Turbulence: Solar Wind Observations. *Space Sci. Rev.* 172, 325–342. doi:10.1007/s11214-011-9821-9

Howes, G. G. (2015). A Dynamical Model of Plasma Turbulence in the Solar Wind. *Phil. Trans. R. Soc. A.* 373, 20140145. doi:10.1098/rsta.2014.0145

Howes, G. G. (2016). The Dynamical Generation of Current Sheets in Astrophysical Plasma Turbulence. *ApJ* 827, L28. doi:10.3847/2041-8205/827/2/L28

Kiyani, K., Chapman, S. C., Hnat, B., and Nicol, R. M. (2007). Self-similar Signature of the Active Solar corona within the Inertial Range of Solar-Wind Turbulence. *Phys. Rev. Lett.* 98, 211101. doi:10.1103/PhysRevLett.98.211101

Kiyani, K. H., Osman, K. T., and Chapman, S. C. (2015). Dissipation and Heating in Solar Wind Turbulence: from the Macro to the Micro and Back Again. *Phil. Trans. R. Soc. A.* 373, 20140155. doi:10.1098/rsta.2014.0155

Klein, K. G., Alexandrova, O., Bookbinder, J., Caprioli, D., Case, A. W., Chandran, B. D. G., et al. (2019). *Multipoint Measurements of the Solar Wind: A Proposed advance for Studying Magnetized Turbulence*. arXiv:1903. 05740.

Kolmogorov, A. N. (1941). The Local Structure of Turbulence in Incompressible Viscous Fluid for Very Large Reynolds' Numbers. *Doklady Akademii Nauk SSSR* 30, 301–305.

Liemohn, M. W., Keesee, A. M., Kepko, L., and Moldwin, M. B. (2021). *Instigators of Future Change in Magnetospheric Research*. American Geophysical Union, 753–763. chap. 47. doi:10.1002/9781119815624.ch47

Lugones, R., Dmitruk, P., Mininni, P. D., Wan, M., and Matthaeus, W. H. (2016). On the Spatio-Temporal Behavior of Magnetohydrodynamic Turbulence in a Magnetized Plasma. *Phys. Plasmas* 23, 112304. doi:10.1063/1.4968236

Mann, I. R., Nokes, C. D. A., Cupido, C., Miles, D. M., Bruner, B., Elliott, D. G., et al. (2020). The Experimental Albertan Satellite #1 (Ex-Alta 1) Cube-Satellite mission. *Space Sci. Rev.* 216, 96. doi:10.1007/s11214-020-00720-8

Marsch, E. (2006). Kinetic Physics of the Solar corona and Solar Wind. *Living Rev. Solar Phys.* 3, 1. doi:10.12942/lrsp-2006-1

Marsch, E., and Tu, C.-Y. (1997). Intermittency, Non-gaussian Statistics and Fractal Scaling of Mhd Fluctuations in the Solar Wind. *Nonlin. Process. Geophys.* 4, 101–124. doi:10.5194/npg-4-101-1997

Matthaeus, W. H., Bandyopadhyay, R., Brown, M. R., Borovsky, J., Carbone, V., Caprioli, D., et al. (2019). *The Essential Role of Multi-point Measurements in Turbulence Investigations: The Solar Wind beyond Single Scale and beyond the taylor Hypothesis*. arXiv:1903.06890.

Matthaeus, W. H. (2021). Turbulence in Space Plasmas: Who Needs it? *Phys. Plasmas* 28, 032306, 2021. (in press). doi:10.1063/5.0041540

Matthaeus, W. H., and Goldstein, M. L. (1982). Measurement of the Rugged Invariants of Magnetohydrodynamic Turbulence in the Solar Wind. *J. Geophys. Res.* 87, 6011–6028. doi:10.1029/JA087iA08p06011

Matthaeus, W. H., Goldstein, M. L., and Roberts, D. A. (1990). Evidence for the Presence of Quasi-Two-Dimensional Nearly Incompressible Fluctuations in the Solar Wind. *J. Geophys. Res.* 95, 20673–20683. doi:10.1029/JA095iA12p20673

Mikić, Z., Downs, C., Linker, J. A., Caplan, R. M., Mackay, D. H., Upton, L. A., et al. (2018). Predicting the corona for the 21 August 2017 Total Solar Eclipse. *Nat. Astron.* 2, 913–921. doi:10.1038/s41550-018-0562-5

Miles, D. M., Bennest, J. R., Mann, I. R., and Millling, D. K. (2013). A Radiation Hardened Digital Fluxgate Magnetometer for Space Applications. *Geosci. Instrum. Method. Data Syst.* 2, 213–224. doi:10.5194/gi-2-213-2013

Miles, D. M., Ciurzynski, M., Barona, D., Narod, B. B., Bennest, J. R., Kale, A., et al. (2019). Low-noise Permalloy Ring Cores for Fluxgate Magnetometers. *Geosci. Instrum. Method. Data Syst.* 8, 227–240. doi:10.5194/gi-8-227-2019

Miles, D. M., Mann, I. R., Ciurzynski, M., Barona, D., Narod, B. B., Bennest, J. R., et al. (2016). A Miniature, Low-Power Scientific Fluxgate Magnetometer: A Stepping-Stone to Cube-Satellite Constellation Missions. *J. Geophys. Res. Space Phys.* 121, 11839–11860. doi:10.1002/2016JA023147

Miles, D. M., Mann, I. R., Kale, A., Milling, D. K., Narod, B. B., Bennest, J. R., et al. (2017). The Effect of Winding and Core Support Material on the thermal Gain Dependence of a Fluxgate Magnetometer Sensor. *Geosci. Instrum. Method. Data Syst.* 6, 377–396. doi:10.5194/gi-6-377-2017

Mininni, P., Lee, E., Norton, A., and Clyne, J. (2008). Flow Visualization and Field Line Advection in Computational Fluid Dynamics: Application to Magnetic fields and Turbulent Flows. *New J. Phys.* 10, 125007. doi:10.1088/1367-2630/10/12/125007

Montgomery, D. (1982). Major Disruptions, Inverse Cascades, and the Strauss Equations. *Phys. Scr.* T2A, 83–88. doi:10.1088/0031-8949/1982/T2A/009

Motschmann, U., Glassmeier, K. H., and Pinçon, J. L. (2000). "Multi-spacecraft Filtering: Plasma Mode Recognition," in *Analysis Methods For Multi-Spacecraft Data*. Editors G Paschmann and PW Daly. 1 edn (Bern, Switzerland: International Space Science Institute (ISSI)), 79–90. no. SR-001 in ISSI Scientific Reportchap. 4. 1.

Mottez, F., and Chanteur, G. (1994). Surface Crossing by a Group of Satellites: A Theoretical Study. *J. Geophys. Res.* 99, 13499–13507. doi:10.1029/93JA03326

NASA (2018). *Strategic Plan*. Tech. rep.NASA.

Ness, N. F., Behannon, K. W., Lepping, R. P., and Schatten, K. H. (1971). Use of Two Magnetometers for Magnetic Field Measurements on a Spacecraft. *J. Geophys. Res.* 76, 3564–3573. doi:10.1029/JA076i016p03564

Neubauer, F. M., and Glassmeier, K.-H. (1990). Use of an Array of Satellites as a Wave Telescope. *J. Geophys. Res.* 95, 19115–19122. doi:10.1029/JA095iA11p19115

Ogilvie, K. W., Chornay, D., Fritzenreiter, R., Hunsaker, F., Keller, J., Lobell, J., et al. (1995). SWE, a comprehensive plasma instrument for the WIND spacecraft. *Space Sci. Rev.* 71, 55–77. doi:10.1007/BF00751326

Osman, K. T., Matthaeus, W. H., Gosling, J. T., Greco, A., Servidio, S., Hnat, B., et al. (2014). Magnetic Reconnection and Intermittent Turbulence in the Solar Wind. *Phys. Rev. Lett.* 112, 215002. doi:10.1103/PhysRevLett.112.215002

Oughton, S., Matthaeus, W. H., and Dmitruk, P. (2017). Reduced MHD in Astrophysical Applications: Two-Dimensional or Three-Dimensional? *ApJ* 839, 2. doi:10.3847/1538-4357/aa67e2

Owens, M. J., and Forsyth, R. J. (2013). The Heliospheric Magnetic Field. *Living Rev. Solar Phys.* 10, 5. doi:10.12942/lrsp-2013-5

Parker, E. N. (1958). Dynamics of the Interplanetary Gas and Magnetic fields. *ApJ* 128, 664–676. doi:10.1086/146579

Pedregosa, F., Varoquaux, G., Gramfort, A., Michel, V., Thirion, B., Grisel, O., et al. (2011). Scikit-learn: Machine Learning in Python. *J. Machine Learn. Res.* 12, 2825–2830.

Petrosyan, A., Balogh, A., Goldstein, M. L., Léorat, J., Marsch, E., Petrovay, K., et al. (2010). Turbulence in the Solar Atmosphere and Solar Wind. *Space Sci. Rev.* 156, 135–238. doi:10.1007/s11214-010-9694-3

Pinçon, J. L., and Motschmann, U. (2000). "Multi-spacecraft Filtering: General Framework," in *Analysis Methods For Multi-Spacecraft Data*. Editors G Paschmann and PW Daly. 1 edn (Bern, Switzerland: International Space Science Institute (ISSI)), 65–78. SR-001 in ISSI Scientific Reportchap. 3. 1.

PlasmaPy Community (2020). Plasmapy Version 0.5.0. doi:10.5281/zenodo.4313063

Priest, E. R., and Pontin, D. I. (2009). Three-dimensional Null point Reconnection Regimes. *Phys. Plasmas* 16, 122101. doi:10.1063/1.3257901

Rasmussen, C. E., and Williams, C. K. I. (2006). *Gaussian Processes for Machine Learning*. MIT Press. Available at: http://www.gaussianprocess.org/gpml/chapters/. (Accessed date February 9, 2021).

Retinò, A., Sundkvist, D., Vaivads, A., Mozer, F., André, M., and Owen, C. J. (2007). *In Situ* evidence of Magnetic Reconnection in Turbulent Plasma. *Nat. Phys.* 3, 235–238. doi:10.1038/nphys574

Roytershteyn, V., Karimabadi, H., and Roberts, A. (2015). Generation of Magnetic Holes in Fully Kinetic Simulations of Collisionless Turbulence. *Phil. Trans. R. Soc. A.* 373, 20140151. doi:10.1098/rsta.2014.0151

Russell, C. T., Mellott, M. M., Smith, E. J., and King, J. H. (1983). Multiple Spacecraft Observations of Interplanetary Shocks: Four Spacecraft Determination of Shock Normals. *J. Geophys. Res.* 88, 4739–4748. doi:10.1029/JA088iA06p04739

Schekochihin, A. A., Cowley, S. C., Dorland, W., Hammett, G. W., Howes, G. G., Quataert, E., et al. (2009). Astrophysical Gyrokinetics: Kinetic and Fluid Turbulent Cascades in Magnetized Weakly Collisional Plasmas. *ApJS* 182, 310–377. doi:10.1088/0067-0049/182/1/310

Servidio, S., Matthaeus, W. H., Wan, M., Ruffolo, D., Rappazzo, A. F., and Oughton, S. (2014). Complexity and Diffusion of Magnetic Flux Surfaces in Anisotropic Turbulence. *ApJ* 785, 56. doi:10.1088/0004-637X/785/1/56

Shalchi, A., and Hussein, M. (2014). Perpendicular Diffusion of Energetic Particles in Noisy Reduced Magnetohydrodynamic Turbulence. *ApJ* 794, 56. doi:10.1088/0004-637X/794/1/56

Shen, C., Li, X., Dunlop, M., Liu, Z., Balogh, A., Baker, D., et al. (2003). Analyses on the Geometrical Structure of Magnetic Field in the Current Sheet Based on Cluster Measurements. *J. Geophys. Res. Space Phys.* 108, 1168. doi:10.1029/2002ja009612

Shen, C., Li, X., Dunlop, M., Shi, Q., Liu, Z., Lucek, E., et al. (2007). Magnetic Field Rotation Analysis and the Applications. *J. Geophys. Res. Space Phys.* 112, A06211. doi:10.1029/2005ja011584

Sitnov, M. I., Stephens, G. K., Tsyganenko, N. A., Miyashita, Y., Merkin, V. G., Motoba, T., et al. (2019). Signatures of Nonideal Plasma Evolution during Substorms Obtained by Mining Multimission Magnetometer Data. *J. Geophys. Res. Space Phys.* 124, 8427–8456. doi:10.1029/2019JA027037

Spence, H. E. (2019). Helioswarm: Unlocking the Multiscale Mysteries of Weakly-Collisional Magnetized Plasma Turbulence and Ion Heating. AGU Fall Meeting 9-13 December 2019 in San Francisco, CA, United States. Th. SH11B–04. Abstracts.

Stephens, G. K., Sitnov, M. I., Korth, H., Tsyganenko, N. A., Ohtani, S., Gkioulidou, M., et al. (2019). Global Empirical Picture of Magnetospheric Substorms Inferred from Multimission Magnetometer Data. *J. Geophys. Res. Space Phys.* 124, 1085–1110. doi:10.1029/2018JA025843

Sundkvist, D. J., Saint-Hilaire, P., Bain, H. M., Bale, S. D., Bonnell, J. W., Hurford, G. J., et al. (2016). "Curie: Cubesat Radio Interferometry experiment," in AGU Fall Meeting 12-16 December 2016 in San Francisco, CA, United States., SH11C–2271. Abstracts.

Taylor, G. I. (1938). The Spectrum of Turbulence. *Proc. R. Soc. A.* 164, 476–490. doi:10.1098/rspa.1938.0032

TenBarge, J. M., Alexandrova, O., Boldyrev, S., Califano, F., Cerri, S. S., Chen, C. H. K., et al. (2019). *Disentangling the Spatiotemporal Structure of Turbulence Using Multi-Spacecraft Data*. arXiv:1903.05710.

Tooprakai, P., Seripienlert, A., Ruffolo, D., Chuychai, P., and Matthaeus, W. H. (2016). Simulations of Lateral Transport and Dropout Structure of Energetic Particles from Impulsive Solar Flares. *ApJ* 831, 195. doi:10.3847/0004-637X/831/2/195

Torbert, R. B., Dors, I., Argall, M. R., Genestreti, K. J., Burch, J. L., Farrugia, C. J., et al. (2020). A New Method of 3-D Magnetic Field Reconstruction. *Geophys. Res. Lett.* 47, 085542. doi:10.1029/2019GL085542

Tu, C.-Y., and Marsch, E. (1995). MHD Structures, Waves and Turbulence in the Solar Wind: Observations and Theories. *Space Sci. Rev.* 73, 1–210. doi:10.1007/BF00748891

Vaivads, A., Andersson, G., Bale, S. D., Cully, C. M., De Keyser, J., Fujimoto, M., et al. (2012). Eidoscope: Particle Acceleration at Plasma Boundaries. *Exp. Astron.* 33, 491–527. doi:10.1007/s10686-011-9233-6

Verscharen, D., Klein, K. G., and Maruca, B. A. (2019). The Multi-Scale Nature of the Solar Wind. *Living Rev. Sol. Phys.* 16, 5. doi:10.1007/s41116-019-0021-0

Wallis, D. D., Miles, D. M., Narod, B. B., Bennest, J. R., Murphy, K. R., Mann, I. R., et al. (2015). The Cassiope/e-Pop Magnetic Field Instrument (Mgf). *Space Sci. Rev.* 189, 27–39. doi:10.1007/s11214-014-0105-z

Watanabe, T., and Nagata, K. (2017). Gradients Estimation from Random Points with Volumetric Tensor in Turbulence. *J. Comput. Phys.* 350, 518–529. doi:10.1016/j.jcp.2017.08.057

Wicks, R. T., Chapman, S. C., and Dendy, R. O. (2009). Spatial Correlation of Solar Wind Fluctuations and Their Solar Cycle Dependence. *ApJ* 690, 734–742. doi:10.1088/0004-637X/690/1/734

Wicks, R. T., Horbury, T. S., Chen, C. H. K., and Schekochihin, A. A. (2010). Power and Spectral index Anisotropy of the Entire Inertial Range of Turbulence in the Fast Solar Wind. *Monthly Notices R. Astronomical Soc.* 407, L31–L35. doi:10.1111/j.1745-3933.2010.00898.x

Wicks, R. T., and Miles, D. M. (2019). Editorial: Topical Collection on Multi-point Measurements of the Thermosphere with the Qb50 mission. *Space Sci. Rev.* 215, 15. doi:10.1007/s11214-019-0588-8

Wilson, L. B., Stevens, M. L., Kasper, J. C., Klein, K., Maruca, B., Bale, S., et al. (2018). The Statistical Properties of Solar Wind Temperature Parameters Near 1 au. *Astrophys. J. Suppl.* 236, 41. doi:10.3847/1538-4365/aab71c

Woodham, L. D., Wicks, R. T., Verscharen, D., and Owen, C. J. (2018). The Role of Proton Cyclotron Resonance as a Dissipation Mechanism in Solar Wind Turbulence: A Statistical Study at Ion-Kinetic Scales. *ApJ* 856, 49. doi:10.3847/1538-4357/aab03d

Zank, G. P., Adhikari, L., Hunana, P., Shiota, D., Bruno, R., and Telloni, D. (2017). Theory and Transport of Nearly Incompressible Magnetohydrodynamic Turbulence. *ApJ* 835, 147. doi:10.3847/1538-4357/835/2/147

Zenitani, S., Hesse, M., Klimas, A., Black, C., and Kuznetsova, M. (2011). The Inner Structure of Collisionless Magnetic Reconnection: The Electron-Frame Dissipation Measure and Hall fields. *Phys. Plasmas* 18, 122108. doi:10.1063/1.3662430

Zhou, Y., Matthaeus, W., and Dmitruk, P. (2004). Colloquium: Magnetohydrodynamic Turbulence and Time Scales in Astrophysical and Space Plasmas. *Rev. Mod. Phys.* 76, 1015–1035. doi:10.1103/RevModPhys.76.1015

Conflict of Interest: The authors declare that the research was conducted in the absence of any commercial or financial relationships that could be construed as a potential conflict of interest.

The reviewer FP declared a past co-authorship with the authors BAM, SS, DV, JHW and RTW to the handling editor.

APPENDIX

As described in **Section 4.1.2**, we used the 3-D kinetic plasma simulations of Roytershteyn et al. (2015) to generate synthetic *in-situ* magnetometer measurements, which we then used to reconstruct 3-D maps of the magnetic field. Though **Section 4.1.2** focuses on the magnetic field's x-component (B_x; **Figure 4**) as an example, we also considered the y- and z-components (B_y and B_z; **Figures A1**, **A2**) and the magnitude of the magnetic field (**Figure A3**). Note that these figures show only a single slice (parallel to the xy-plane) from our 3-D reconstructions.

The key results of **Section 4.1.2** are supported by any one of these figures. A constellation of 4 or 8 spacecraft provides insufficient spacial coverage for this type of magnetic reconstruction. Though a 16-spacecraft constellation offers significant improvement, the reconstruction still contains major defects. Only with a constellation of $\gtrsim 24$ spacecraft is the reconstruction sufficiently robust for magnetic structure (i.e., morphology and topology) to be accurately discerned.

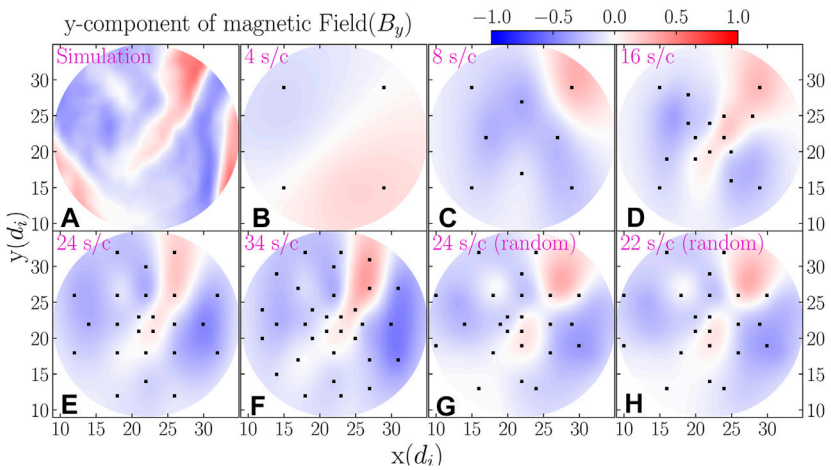

FIGURE A1 | Same as **Figure 4**, but for B_y, the y-component of the magnetic field.

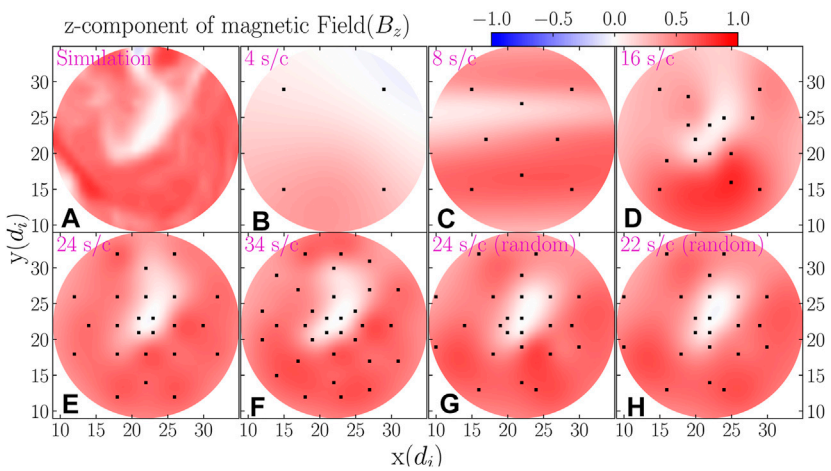

FIGURE A2 | Same as **Figure 4**, but for B_z, the z-component of the magnetic field.

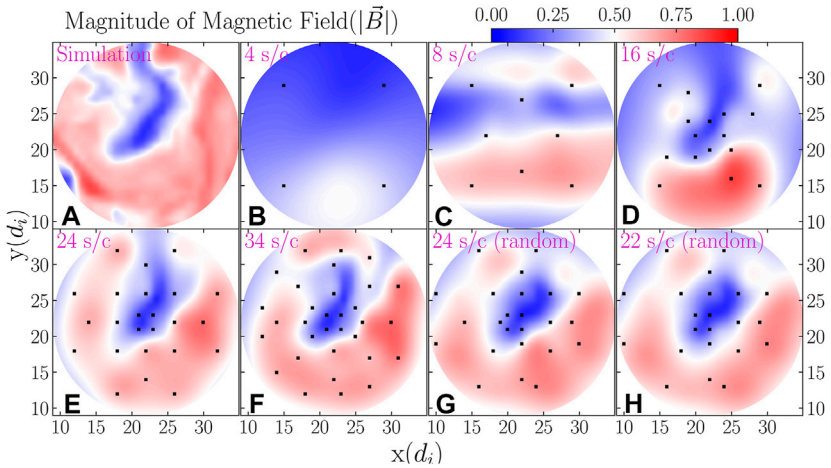

FIGURE A3 | Same as **Figure 4**, but for $B \equiv |\mathbf{B}|$, the magnitude of the magnetic field.

frontiers in Astronomy and Space Sciences

ORIGINAL RESEARCH
published: 13 September 2021
doi: 10.3389/fspas.2021.727076

Magnetic Field Reconstruction for a Realistic Multi-Point, Multi-Scale Spacecraft Observatory

T. Broeren[1], K. G. Klein[2], J. M. TenBarge[3], Ivan Dors[4], O. W. Roberts[4] and D. Verscharen[5,6]*

[1]Department of Applied Mathematics, University of Arizona, Tucson, AZ, United States, [2]Lunar and Planetary Laboratory, University of Arizona, Tucson, AZ, United States, [3]Department of Astrophysical Sciences, Peyton Hall, Princeton University, Princeton, NJ, United States, [4]Space Research Institute, Austrian Academy of Sciences, Graz, Austria, [5]Mullard Space Science Laboratory, University College London, Surrey, United Kingdom, [6]Space Science Center, University of New Hampshire, Durham, NH, United States

Future *in situ* space plasma investigations will likely involve spatially distributed observatories comprised of multiple spacecraft, beyond the four and five spacecraft configurations currently in operation. Inferring the magnetic field structure across the observatory, and not simply at the observation points, is a necessary step towards characterizing fundamental plasma processes using these unique multi-point, multi-scale data sets. We propose improvements upon the classic first-order reconstruction method, as well as a second-order method, utilizing magnetometer measurements from a realistic nine-spacecraft observatory. The improved first-order method, which averages over select ensembles of four spacecraft, reconstructs the magnetic field associated with simple current sheets and numerical simulations of turbulence accurately over larger volumes compared to second-order methods or first-order methods using a single regular tetrahedron. Using this averaging method on data sets with fewer than nine measurement points, the volume of accurate reconstruction compared to a known magnetic vector field improves approximately linearly with the number of measurement points.

Keywords: plasma physics, magnetic fields, spacecraft, vector field reconstruction, space physics, curlometer, space mission analysis, multi-spacecraft analysis

OPEN ACCESS

Edited by:
Georgios Balasis, National Observatory of Athens, Greece

Reviewed by:
Bogdan Hnat, University of Warwick, United Kingdom
Arnaud Masson, European Space Astronomy Centre (ESAC), Spain
Uwe Motschmann, Technische Universitat Braunschweig, Germany

****Correspondence:***
T. Broeren
broeren@email.arizona.edu

Specialty section:
This article was submitted to Space Physics, a section of the journal Frontiers in Astronomy and Space Sciences

Received: *18 June 2021*
Accepted: *13 August 2021*
Published: *13 September 2021*

Citation:
Broeren T, Klein KG, TenBarge J M, Dors I, Roberts OW and Verscharen D (2021) Magnetic Field Reconstruction for a Realistic Multi-Point, Multi-Scale Spacecraft Observatory. Front. Astron. Space Sci. 8:727076. doi: 10.3389/fspas.2021.727076

1 INTRODUCTION

Plasmas, which are ubiquitous throughout the Universe, are readily available for study in the natural laboratory of space. Electromagnetic fields play a fundamental role in the transport, heating, and acceleration of charged particles that compose plasmas. In order to characterize fundamental processes governing heliospheric plasmas, the space plasma community has utilized *in-situ* spacecraft measurements of electromagnetic fields and charged particles. These *in-situ* measurements include the characterization of the vector magnetic field **B** at a spacecraft via magnetometers; see §2.4 of Verscharen et al. (2019).

Knowledge of **B** from a single magnetometer is limited; single-point measurements can not construct the full three-dimensional structure characteristic of processes such as magnetic reconnection and plasma turbulence. To avoid this shortcoming, ESA's CLUSTER (Escoubet et al., 2001), NASA's THEMIS (Angelopoulos, 2008) and MMS (Burch et al., 2016) missions have employed four- and five-spacecraft configurations, where each spacecraft is equipped with an

instrument suite that includes a magnetometer. These missions study the boundaries of the Earth's magnetosphere, including how magnetic reconnection transfers magnetic energy into kinetic energy of plasma particles.

Analysis techniques have been created for multi-spacecraft missions, such as CLUSTER, which search for specific types of plasma waves (Constantinescu et al., 2006) and which analyze current sheet structure (Narita et al., 2013) for a four spacecraft configuration. Knowledge of the direction of wave propagation allows us to use multi-spacecraft filtering (Pinçon and Motschmann. 1998) to determine the general polarisation properties of any multi-point measurement of a wave field in space plasmas. Measurements from exactly four spacecraft (e.g., a tetrahedron of spacecraft) can be used to estimate current density via the Curlometer technique (Robert et al., 1998).

The Cluster and MMS missions have also utilized the Curlometer technique to interpolate the value of the magnetic field over a region near the tetrahedron's barycenter, regardless of the field's geometry. However, these interpolations are limited to measuring fluctuations on a scale on the same order as that of their inter-spacecraft distances (e.g., Robert et al., 1998; Forsyth et al., 2011). To study multi-scale processes, such as plasma turbulence, with structures on characteristic length scales that cover many orders of magnitude, we must employ measurements from more than four spacecraft. Therefore, we develop a method which extends the magnetic field reconstruction technique Curlometer to configurations of more than four spacecraft.

Many such multi-spacecraft missions have been proposed, e.g., Cross-scale (Schwartz et al., 2009), AME (Dai et al., 2020) and HelioSwarm (Klein et al., 2019), but in order to optimize such missions, it is urgent to robustly quantify the impact of particular spacecraft configurations on multi-point analysis methods, capturing the effects of the physical scales spanned by the spacecraft in the observatory and the geometry of the polyhedra that can be drawn from the constituent spacecraft. Such quantification will help demonstrate that a proposed mission will be able to usefully analyze a large number of magnetometer measurements made in the pristine solar wind,magnetosphere, and magnetosheath. It will also assist in the optimization of spacecraft configurations and quantification of errors derived from multi-point, multi-scale measurements. In this paper, we focus on the fidelity of the reproduction of the magnetic field using a sparsely sampled set of measurements whose spatial configuration is based upon realistic configurations of the proposed nine-spacecraft HelioSwarm observatory, described for instance by Plice et al. (2020).

The reconstruction method is described in §2, the results are applied to two magnetic field models, including a numerical simulation of turbulence, in §3, with a concluding discussion in §4.

2 METHODOLOGY

2.1 Geometrical Definitions

Given N spacecraft, we identify $C(N, k)$ polyhedra with k vertices. As spatial divergence analysis methods (e.g., Dunlop et al., 1988; Paschmann and Daly, 1998, 2008) require at least four vertices to resolve three-dimensional structure, we only consider polyhedra with at least four vertices, known as tetrahedra. For $N = 9$, there are 126 (i.e., 9 choose 4) tetrahedra, 126 polyhedra with five vertices, 84 with six vertices, 36 with seven vertices, 9 with 8 vertices, and 1 with 9 vertices, for a total of 382 polyhedra with at least four vertices.

Each polyhedron is characterized in terms of its size and shape. Because measurements from all d spacecraft are weighted equally, we define the *barycenter* of the qth polyhedron with set $\mathbf{D}$ of d vertices drawn from the $N \geq d$ spacecraft positions $\mathbf{x}_i$ as

$$\mathbf{x}_0^{q,d} = \frac{1}{d}\sum_{i\in\mathbf{D}} \mathbf{x}_i. \tag{1}$$

Given the barycenter, we then define the volumetric tensor of the qth polyhedra with set $\mathbf{D}$ of d vertices as

$$R_{jk}^{q,d} = \frac{1}{d}\sum_{i\in\mathbf{D}} \left(x_{ij} - x_{0j}^{q,d}\right)\left(x_{ik} - x_{0k}^{q,d}\right). \tag{2}$$

Here x_{ij} represents the $jth \in \{x, y, z\}$ component of the position vector for the ith spacecraft. The eigenvectors of the tensor $\mathbf{R}^{q,d}$ represent the three semi-axes of the polyhedra and are associated with the eigenvalues $a^{q,d} = \sqrt{R_1^{q,d}}$ (major axis), $b^{q,d} = \sqrt{R_2^{q,d}}$ (middle axis), and $c^{q,d} = \sqrt{R_3^{q,d}}$ (minor axis), where $a \geq b \geq c$ (a more detailed analysis of the eigenvalues can be found in Chapt 12 of Paschmann and Daly, 1998).

To provide a useful geometric interpretation of these shapes, we define a *characteristic size* L, as well as an *elongation* E and a *planarity* P (see chapter 16.3 of Paschmann and Daly, 1998)[1]:

$$\begin{aligned} L &= 2a \\ E &= 1 - b/a \\ P &= 1 - c/b. \end{aligned} \tag{3}$$

2.2 Reconstruction Techniques

2.2.1 First-Order Method

In a first-order Taylor series expansion, we use the values of the magnetic field, $\mathbf{B}$, measured at four spacecraft positions $\mathbf{x}_i$ to estimate the value of $\mathbf{B}$ (and its corresponding directional derivatives) at any other point in space, ξ (Fu et al., 2015, 2020). The Taylor expansion is:

$$\hat{B}_m^i = B_m + \sum_{k\in\{x,y,z\}} \partial_k B_m r_k^i \forall i \in \{1,2,3,4\}, m \in \{x,y,z\}. \tag{4}$$

In this equation $\hat{B}_m^i$ is the measured mth component of $\mathbf{B}$ at the ith spacecraft, B_m is the computed mth component of $\mathbf{B}$ at ξ, $\partial_k B_m$ is the computed derivative of the mth component of $\mathbf{B}$ with respect to the kth direction at ξ, and r_k^i is the relative position of

[1]Note that there is some discrepancy in the community about pif the elongation should be defined as $E = 1$ — b=a or $E = 1$ —1; (b=a)2, with a similarly subjective choice for planarity. Both definitions span the same range, and we have opted for the former definition.

spacecraft i with respect to ξ. In other words, if x_{ik} is the kth component of spacecraft i's location, then $r_k^i := x_{ik} - \xi_k$.

This is a system of 12 equations with 12 unknowns, where the 12 equations represent the x, y, and z components of **B** for each of the four spacecraft. The 12 unknowns are the x, y, and z components of **B** at ξ and the nine terms in the Jacobian of **B** at ξ.

This system can be reformatted into linear ($A\mathbf{x} = \mathbf{b}$) form and solved with a common linear system solver. This 12-dimensional linear system (shown in full detail in **Supplementary Appendix SA**, Eq. A8) comprises the first-order reconstruction method.

This magnetic field reconstruction method is related to the Curlometer method (Dunlop et al., 1988; Robert et al., 1998), which utilizes Ampère's law to calculate the current density **J** as the curl of **B**. The Curlometer solves the same set of equations, but uses the partial derivatives to estimate the current density at the center of each tetrahedron. The Curlometer method has been widely applied to four-spacecraft magnetic field measurements made for instance by Cluster and MMS (c.f. Chapter 16.2 of Paschmann and Daly, 1998). Future missions, such as the proposed HelioSwarm Observatory (Klein et al., 2019), will have more than four spacecraft. Therefore, for every reconstructed point, ξ, we can apply this reconstruction method for each of the $C(N, 4)$ tetrahedra and average the reconstructed values, yielding a statistically larger base of estimates and improving the accuracy of the reconstruction.

2.2.2 Second-Order Method

Because the proposed HelioSwarm Observatory has nine spacecraft, we can use measurements of **B** from all nine spatial points simultaneously to apply a second-order reconstruction method. This method, also based on a Taylor series expansion, is more accurate for values located near the center of the expansion (i.e., near the barycenter of the nine-spacecraft constellation) than a single implementation of the first-order method. Following the work of Torbert et al. (2020), we write:

$$\hat{B}_m^i = B_m + \sum_{k\in\{x,y,z\}} \partial_k B_m r_k^i + \frac{1}{2} \sum_{j,k\in\{x,y,z\}} \partial_j \partial_k B_m r_k^i r_j^i \; \forall i \in \{1,\ldots,9\}, m \in \{x,y,z\}. \tag{5}$$

These terms are the same as in the first-order method, with the addition of $\partial_j\partial_k B_m$, the second derivative of the mth component of **B** with respect to the kth and jth directions, at ξ.

This is a system of 31 equations with 30 unknowns. 27 of these equations are associated with the x, y, and z components of **B** from the nine spacecraft. There are four additional constraints, imposed by the magnetic field having zero divergence, as well as the divergence of the magnetic field having zero gradient. The 30 unknowns are the x, y, and z components **B** at ξ, the nine terms in the Jacobian of **B** at ξ, and the 18 terms in the Hessian of **B** at ξ (excluding the 9 redundant terms).

This system can be reformatted into linear ($A\mathbf{x} = \mathbf{b}$) form where A is a 31 × 30 matrix (shown in full detail in **Supplementary Appendix SB**, Eq. B16). This system is over-determined, therefore in general, an exact solution does not exist. However, we can find an approximate solution via the method of ordinary least squares. This method finds the solution to the problem $A\mathbf{x} = \mathbf{b}$ which minimizes the two-norm of the error, i.e.

$$\mathbf{x} = \underset{\mathbf{x}}{\operatorname{argmin}} \|A\mathbf{x} - \mathbf{b}\|_2. \tag{6}$$

This second-order reconstruction method is referred to as M_2 throughout this paper.

2.2.3 Quantifying Error

We define the error at any point in space, ξ, as:

$$\theta = 100 \frac{\|\mathbf{B}_{calc}(\xi) - \mathbf{B}_{true}(\xi)\|_2}{\|\mathbf{B}_{true}(\xi)\|_2} \tag{7}$$

where $\mathbf{B}_{true}(\xi)$ is the magnetic field vector at point ξ and $\mathbf{B}_{calc}(\xi)$ is the reconstructed magnetic field vector at point ξ.

Given that we can determine the value of this error at all points in a simulation or for a given analytic field, we also define $\epsilon(\theta)$ as the proportion of the volume that is reconstructed with less than θ% error. For a sufficiently dense grid of $N_x \times N_y \times N_z$ uniformly-spaced points, $\epsilon(\theta)$ can be estimated as

$$\epsilon(\theta) = \frac{\#\text{points with} \le \theta\% \text{ error}}{N_x N_y N_z}. \tag{8}$$

To define the physical volume in which a given magnetic field reconstruction is accurate, $\epsilon(\theta)$ is translated into a dimensional quantity by multiplying it by the total volume covered by the $N_x \times N_y \times N_z$ grid.

2.2.4 Error Minimization Techniques

As the first-order method (§2.2.1) only requires a single tetrahedron of spacecraft to estimate **B**, in this paper we will test four selection methods for using a subset of the 126 tetrahedra to improve the reconstruction. These methods combine the statistically large set of tetrahedra with our knowledge of the spacecraft positions relative to ξ and the geometry of all 126 tetrahedra.

For the first method, $M_{1.1}$, at each point in space we reconstruct the magnetic field using all 126 tetrahedra to produce 126 estimates for $\mathbf{B}(\xi)$. We then average over these $\mathbf{B}(\xi)$ values component-wise to estimate $\mathbf{B}(\xi)$.

For the second method, $M_{1.2}$, we perform the same averaging as method one, but only include tetrahedra whose barycenter are within a characteristic distance of ξ. i.e., for each reconstructed point ξ, only include tetrahedra j in the average which satisfy

$$\|(r_0)_j - \xi\|_2 < L_j, \tag{9}$$

where L_j is the characteristic size and $(r_0)_j$ is the barycenter of the jth tetrahedron.

For the third method, $M_{1.3}$, we perform the same selection as method two, but with the added restriction that the shape of tetrahedron j must be quasi-regular. In terms of the geometric quantities of the spacecraft configuration (defined in **Eq. 3**), this translates to elongation E and planarity P being sufficiently small. Because E and P are symmetric with respect to orientation, we will define a composite geometric parameter χ_j

$$\chi_j = \sqrt{E_j^2 + P_j^2}. \tag{10}$$

Small χ_j implies that both the elongation and planarity of tetrahedron j are small. For method $M_{1,3}$, we restrict our averaging to only include tetrahedra where

$$\begin{aligned} \chi_j &\leq 1 \\ \|(r_0)_j - \xi\|_2 &< L_j. \end{aligned} \tag{11}$$

For the fourth method, $M_{1,4}$, we perform the same selection of tetrahedra as method three, but require the tetrahedra included in the averaging to be more regular. For method $M_{1,4}$, our shape and position requirement is

$$\begin{aligned} \chi_j &\leq 0.6 \\ \|(r_0)_j - \xi\|_2 &< L_j. \end{aligned} \tag{12}$$

The value of 0.6 was selected because page 408 of Paschmann and Daly (1998) shows it be a threshold value for elongation and planarity which separates the well performing 'pseudo-sphere type' and 'potato type' spacecraft configurations from the poorer performing 'knife blade type', 'cigar type', and 'pancake type' configurations.

The first-order methods $M_{1,1}$, $M_{1,2}$, $M_{1,3}$, $M_{1,4}$ will be compared to the second-order method M_2 as well as the first-order method applied to a single regular (i.e., $\chi = 0$) tetrahedron of spacecraft. This single regular tetrahedron will have the same characteristic scale as the nine-spacecraft configuration it is compared to.

2.3 Models

To validate and quantify the errors of our reconstruction, we implement our reconstruction methods on two magnetic field models, a simple current sheet and a numerical simulation of turbulence.

2.3.1 Simple Current Sheet

For our first model, we define a magnetic field where **B** is analytically defined at all spatial points. This field, which represents a simple current sheet, can be described in cylindrical coordinates as

$$\mathbf{B}(r) = \mu_0 J_0 \sigma [\sigma/r - e^{-r\sigma}(1 + \sigma/r)]\hat{\theta}. \tag{13}$$

The variable σ represents the current sheet characteristic width and J_0 represents the magnitude of the current at its center.

2.3.2 Turbulence Simulation

Physically realistic fields, such as those generated by turbulence in the solar wind, are significantly more complex than the simple current sheet model of **Eq. 13**. We therefore test our reconstruction techniques on magnetic fields drawn from numerical simulations of turbulence. In particular, we utilize the magnetic fields from a fully developed turbulence simulation performed with the five moment, multi-fluid solver within the Gkeyll simulation framework (Hakim et al., 2006; Wang et al., 2015, 2020). This turbulence simulation is designed to represent plasma behavior in the pristine solar wind at 1AU.

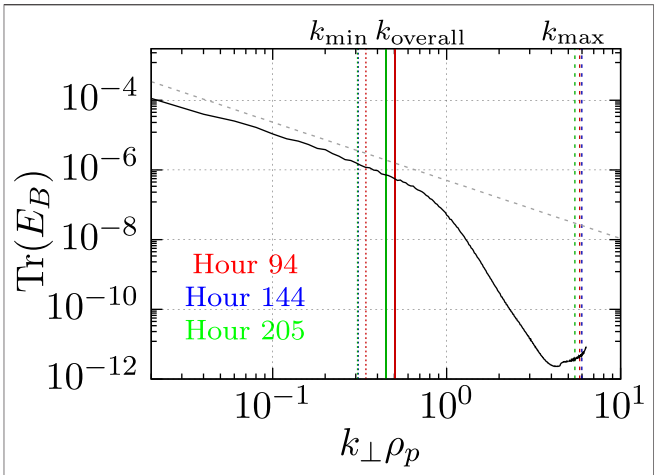

FIGURE 1 | Trace magnetic field spectrum (solid black) from the Gkeyll simulation computed at $t = 1500/\Omega_p$, with a $k_\perp^{-5/3}$ dashed line plotted for reference. The characteristic scales associated with the three spacecraft configurations, Hours 94, 144, and 205, drawn from the HelioSwarm DRM are shown as vertical colored lines.

We use the five moment (n_s, $\mathbf{u}_s$, p_s), two fluid ($s = p, e$) plasma model to evolve a proton-electron plasma. We note that the five moment, two fluid model formally reduces to Hall MHD in the limit $m_e \to 0$ and $\epsilon_0 \to 0$ (Srinivasan and Shumlak, 2011), where ϵ_0 is the vacuum permittivity. We use a reduced (proton to electron) mass ratio of $m_p/m_e = 100$, a temperature ratio of $T_p/T_e = 1$, Alfvén velocity of $v_A/c = B/\sqrt{\mu_0 n_p m_p c^2} = 0.02$, plasma beta (ratio of plasma thermal pressure to magnetic pressure) of $\beta_p = 2\mu_0 n_p T_p/B^2 = 1$, and adiabatic index $\gamma = 5/3$. We employ an elongated domain $L_x = L_y = 0.2L_z = 100\pi\rho_p$ with resolution $n_x = n_y = n_z = 448$. Lengths are normalized to the proton gyroradius $\rho_p = v_{tp}/\Omega_p$, the ratio of the proton thermal speed $v_{tp} = \sqrt{2T_p/m_p}$ and the proton cyclotron frequency $\Omega_p = q_p B/m_p$. We choose a uniform background density and magnetic field, $\mathbf{B}_0 = B_0\hat{\mathbf{z}}$, and initialize the simulation with the three dimensional extension of the Orszag-Tang vortex (Orszag and Tang, 1979) described in Li et al. (2016).

$$\begin{aligned} \frac{\mathbf{z}_1^+}{v_A} &= -\frac{2z_0}{v_A}\sin(k_\perp y - k_z z)\hat{\mathbf{x}}, \frac{z_1^-}{v_A} = 0 \\ \frac{\mathbf{z}_2^\pm}{v_A} &= \frac{z_0}{v_A}\sin(k_\perp x \mp k_z z)\hat{\mathbf{y}} \\ \frac{\mathbf{z}_3^\pm}{v_A} &= \pm\frac{z_0}{v_A}\sin(2k_\perp x \mp k_z z)\hat{\mathbf{y}}, \end{aligned} \tag{14}$$

where $\mathbf{z}^\pm = \delta\mathbf{u} \pm \delta\mathbf{B}/\sqrt{\mu_0\rho_0}$ are the Elsasser variables (Elsasser, 1950), $k_{x,y} = 2\pi/L_{x,y}$, and $k_z = 2\pi/L_z$. The initial amplitude, $z_0 = 0.2$, is chosen to satisfy the critical balance condition, $k_x z_0/k_z v_A = 1$ (Goldreich and Sridhar, 1995).

The simulation is run for one Alfvén crossing time, $t_A = 1500/\Omega_p$, at which point the turbulence has fully developed and reached

TABLE 1 | Characteristic geometric parameters for the three nine-spacecraft configurations under consideration and the minimum/maximum characteristic geometric parameters created from choosing any four of the nine spacecraft of each configuration.

Hour		L (km)	E	P
94	Overall	1,245	0.48	0.60
	Min	108	0.14	0.10
	Max	1834	0.93	0.99
144	Overall	1,395	0.42	0.70
	Min	108	0.06	0.23
	Max	2030	0.95	0.99
205	Overall	1,401	0.45	0.75
	Min	115	0.32	0.26
	Max	2045	0.97	0.99

a steady state. In **Figure 1**, we plot the trace magnetic energy spectrum as a function of $k_\perp = \sqrt{k_x^2 + k_y^2}$, with a $k_\perp^{-5/3}$ dashed line plotted for reference. The steep roll-over in the spectrum at $k_\perp \rho_p \simeq 1$ is due to numerical diffusion from the finite volume scheme employed by Gkeyll.

To compare the simulation to the selected spacecraft configurations with separations in physical units, we note that the proton gyroradius can be written as

$$\rho_p = \sqrt{\frac{m_p}{m_e}}\sqrt{\beta_p}\ \frac{c}{\omega_{pe}}. \tag{15}$$

With the constants in the turbulence simulation of $m_p/m_e = 100$, $\beta_p = 1$, $\omega_{pe} = \frac{c}{d_e} = 5.64 \times 10^4 \sqrt{n}$, we set $n_e = 0.2829$ cm^{-3}, so that $\rho_p = 100$ km.

We extract from this simulation a 3-dimensional grid of values representing the plasma's physical parameters at different points in space. From this grid, we use trilinear interpolation to estimate the value of **B** at any point in the simulation volume.

2.3.3 Spacecraft Configurations

To illustrate our reconstruction methods for realistic spacecraft configurations, we study these methods using three different nine-spacecraft configurations. The spacecraft configurations are selected from the phase A design reference mission (DRM) of the proposed HelioSwarm Observatory concept, corresponding to hours 94, 144, and 205 of the science phase. These hours are selected because they represent a selection of spacecraft tetrahedra that have significantly different distributions of their elongation, planarity, and length. In **Table 1** we note the geometric characteristics of the overall nine-vertex polyhedra for each of the three configurations. We also calculate the size, elongation, and planarity of all 126 tetrahedron in each configuration and display them in **Figure 2**, noting the minimum and maximum values of these three parameters for each configuration in **Table 1**. The wavelengths associated with the overall, minimum, and maximum scales, $k\rho_p = 2\pi\rho_p/L$, are overlaid on **Figure 1**, using a fiducial value of $\rho_p = 100$ km.

3 APPLICATION OF RECONSTRUCTION

To find the expected error at all points in space near a particular spacecraft configuration, we take a Monte Carlo approach and place the barycenter of each nine-spacecraft configuration into a known magnetic field at random locations. We then reconstruct the magnetic field on a grid of points centered at the barycenter of the nine-spacecraft configuration using the first- and second-order reconstruction methods. The location of each point in the reconstructed grid is constant with respect to the spacecraft configuration. Therefore, we find the average of the errors, θ, at all reconstructed grid points for all elements of the Monte Carlo ensemble, allowing the calculation of the expected value of error at each point on the grid.

Additionally, we compare the divergence found on a grid of points sampled from the baseline current sheet and turbulence simulation magnetic fields with that of the same points sampled from the fields reconstructed using our first-order reconstruction methods. This comparison yields divergence values of similar magnitude in the baseline and reconstructed fields, which indicates that our reconstruction methods do not introduce nonphysical values of divergence.

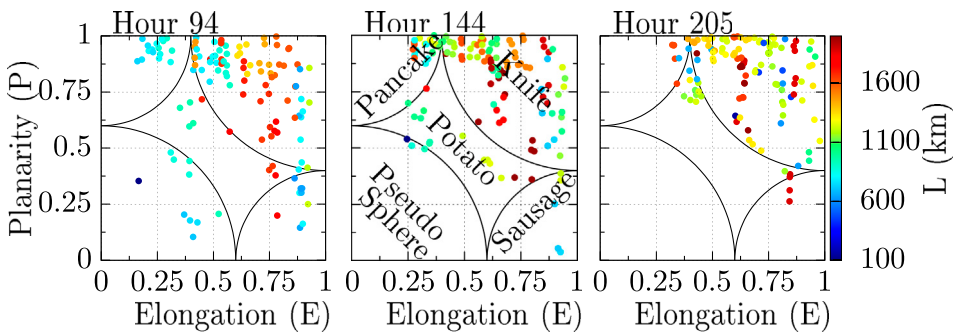

FIGURE 2 | Elongation and planarity of the 126 tetrahedron associated with the three nine-spacecraft configurations under consideration, with characteristic lengths shown in color.

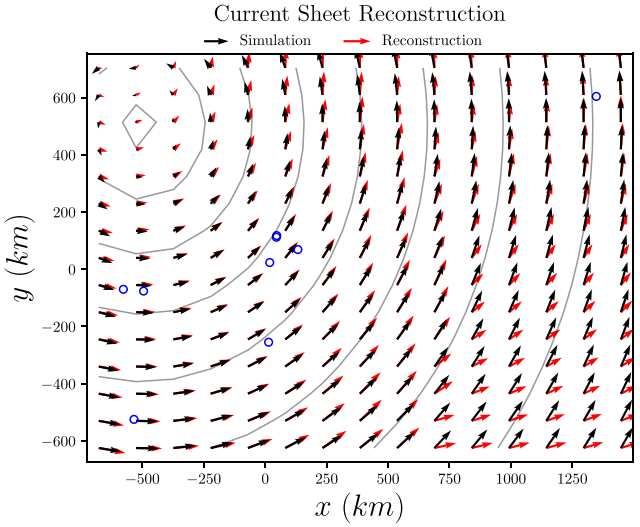

FIGURE 3 | An example of the spacecraft configuration at hour 94, pictured as the blue circles, reconstructing the magnetic field associated with a simple current sheet using first-order method $M_{1,3}$. The true magnetic field is shown as black arrows, and the reconstructed magnetic field is shown as red arrows. This current sheet, centered at (–500, 500) km, has characteristic width $\sigma = 2000$ km. Contour lines of the $\hat{z}$ component of current density **J** are shown in gray.

3.1 Current Sheet

We present an example magnetic field reconstruction of the simple current sheet model (§2.3.1) in **Figure 3**. Here, we use the first-order method $M_{1,3}$ to reconstruct the magnetic field in the $z = 0$ plane for the simple current sheet, **Eq. 13** with $\sigma = 2000$ km using the hour 94 spacecraft configuration. There is little difference between the reconstructed and original fields near the center of the spacecraft configuration, and the difference in vectors increases with distance from the spacecraft configuration's center.

We perform 200 Monte Carlo iterations of reconstruction using each method, observing that 200 was sufficient to point-wise converge in error. The characteristic width of the current sheet is chosen as a uniform random variable $\sigma \sim U$ [500, 5000] km, while the barycenter of the nine-spacecraft configuration is selected as a 3D uniform random variable $r_0 \sim U$ [−1000,1000] ^{3} km. We reconstruct a $30 \times 30 \times 30$ grid of points ξ that extends 100 km past the furthest spacecraft in all directions.

The errors computed for the reconstruction of the simple current sheet are displayed in **Figures 4–6** for the hour 94, 144, and 205 configurations respectively. These figures illustrate the ensemble-averaged errors along a 2D plane orthogonal to the current intersecting a given nine-spacecraft configuration's barycenter. The first four panels correspond to the four first-order reconstruction methods, $M_{1,1}$, $M_{1,2}$, $M_{1,3}$ and $M_{1,4}$, the fifth panel corresponds to the second-order method M_2, and the final

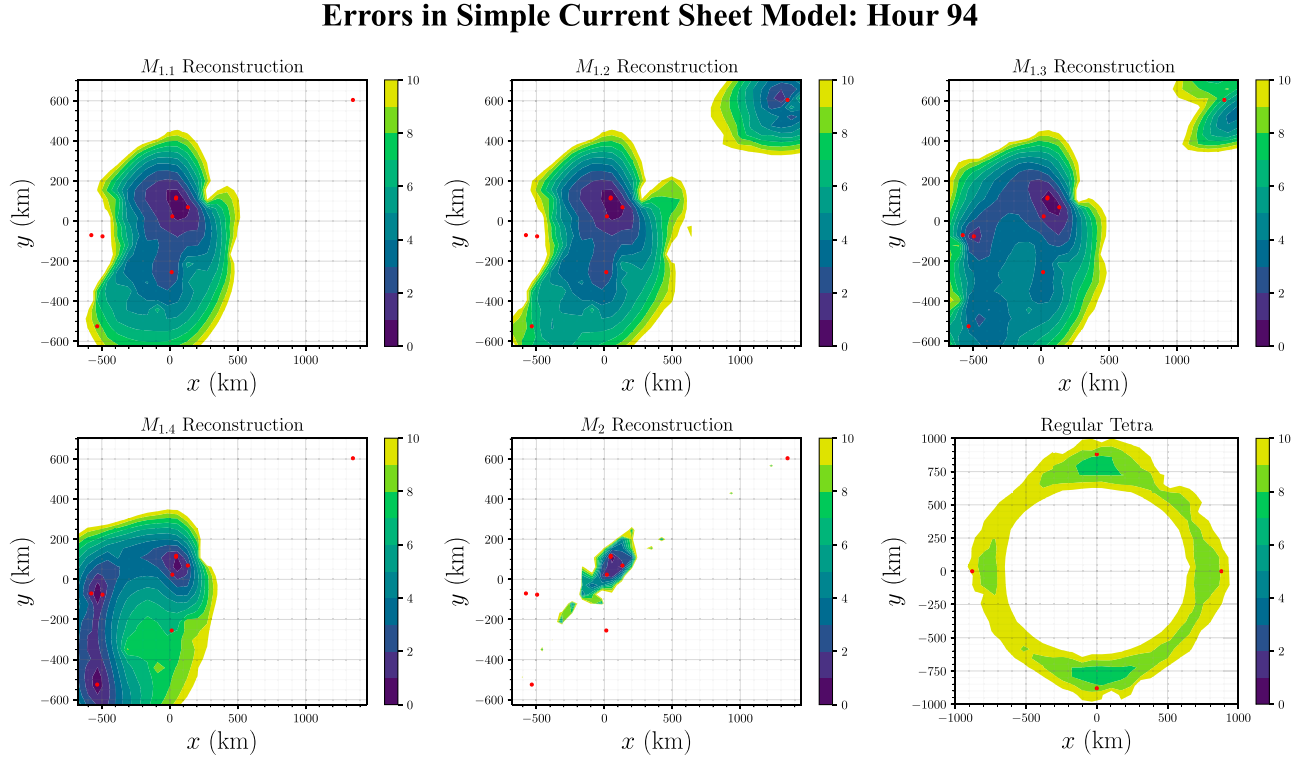

FIGURE 4 | Computation error (defined in **Eq. 7**) at all points on the $z = 0$ plane of the simple current sheet model, using the swarm configuration at hour 94 of the HelioSwarm DRM using first-order methods $M_{1,1}$, $M_{1,2}$, $M_{1,3}$ and $M_{1,4}$, the second-order method, M_2 and a single regular tetrahedron. The red points represent the spacecraft locations. Areas in white either have a reconstruction error above 10%, or have no tetrahedron satisfying reconstruction method condition, resulting in no reconstructed field values.

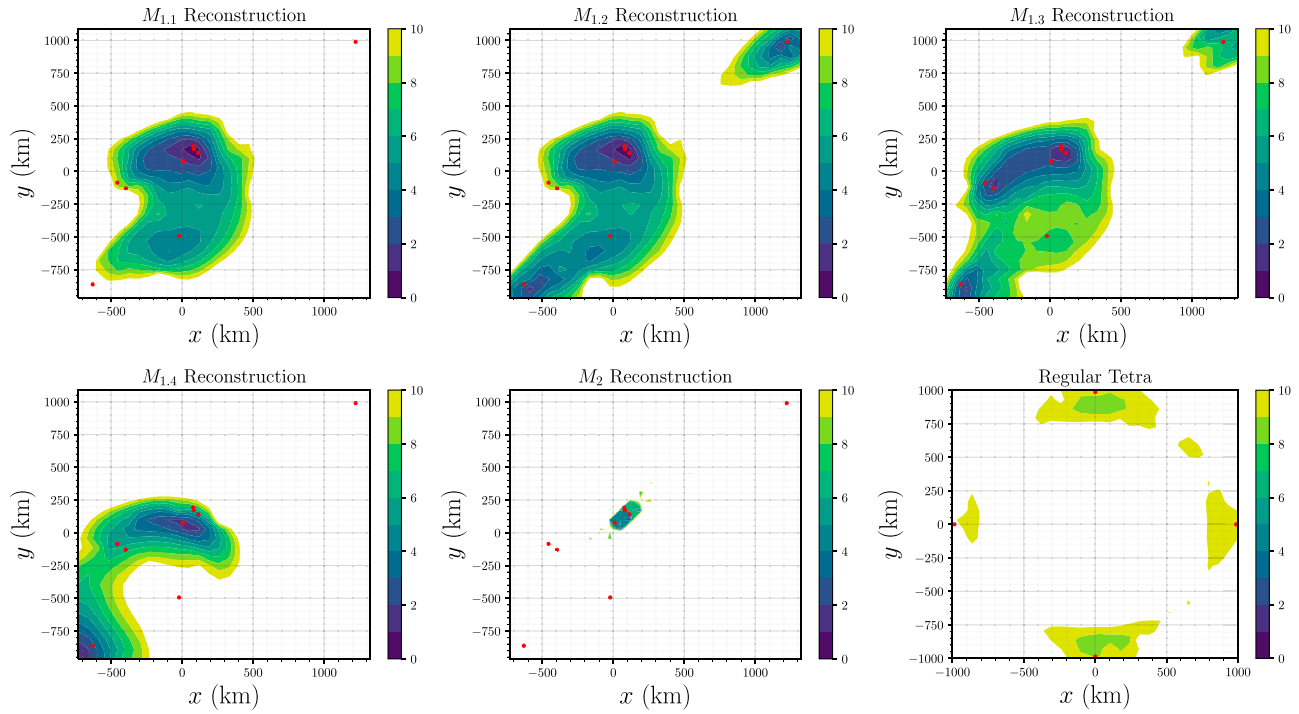

FIGURE 5 | Computation error (defined in **Eq. 7**) at all points on the $z = 0$ plane of the simple current sheet model, using the swarm configuration at hour 144 of the HelioSwarm DRM. The layout is identical to **Figure 4**.

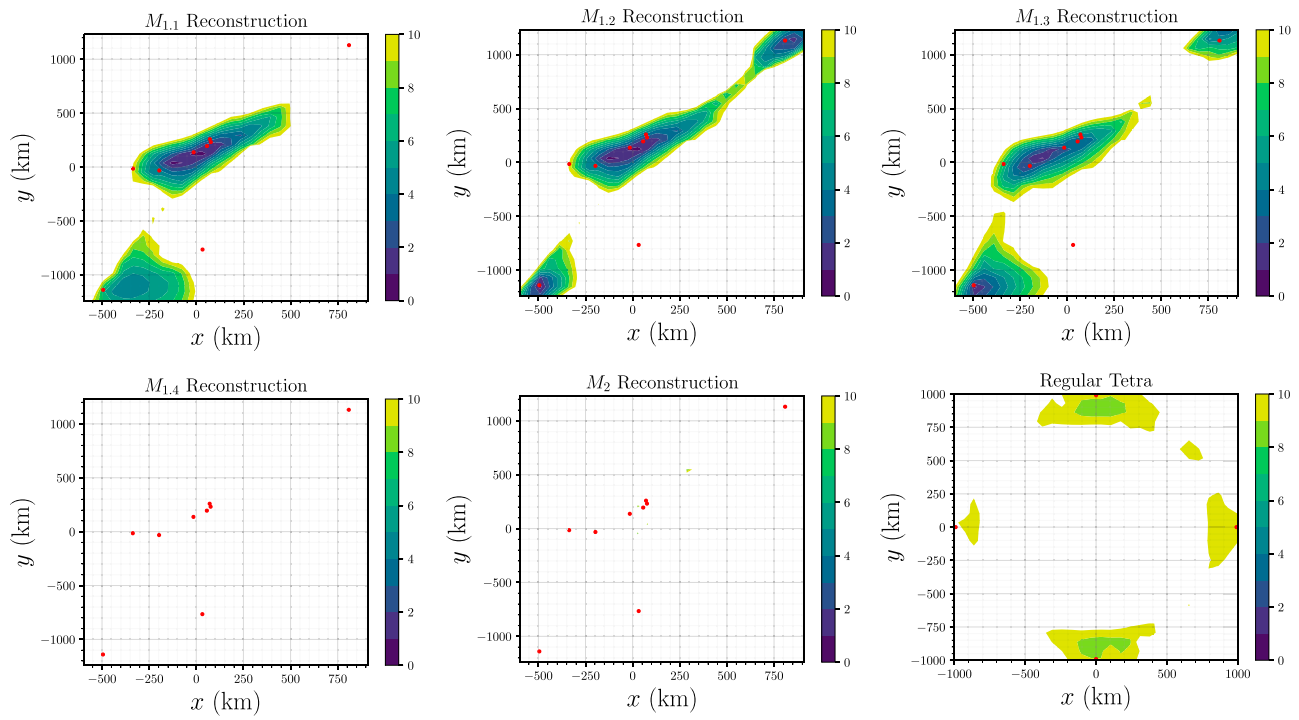

FIGURE 6 | Computation error (defined in **Eq. 7**) at all points on the $z = 0$ plane of the simple current sheet model, using the swarm configuration at hour 205 of the HelioSwarm DRM. The layout is identical to **Figure 4**.

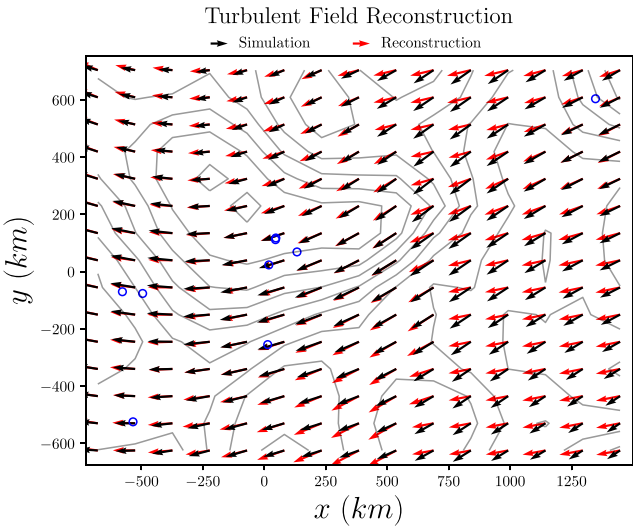

FIGURE 7 | An example of the spacecraft configuration at hour 94, pictured as blue circles, reconstructing the magnetic field associated with a turbulence simulation using first-order method $M_{1.3}$. The simulation's magnetic field is shown as black arrows, and the reconstructed magnetic field is shown as red arrows. Contour lines of the $\hat{z}$ component of current density **J** are shown in gray.

panel corresponds to the reconstruction obtained from the standard first-order method applied to a single regular tetrahedron, with $E = P = 0$. This single tetrahedron has the same characteristic size L as the overall nine-spacecraft configuration, calculated as twice the major axis of the volumetric tensor, **Eq. 2**, evaluated using all nine points. With four spacecraft, we cannot reconstruct the magnetic field with the second-order method, nor can we select subsets of tetrahedra with advantageous geometric characteristics, so only the first-order reconstruction method from a single tetrahedron is used.

We see that near the barycenter of each of the nine-spacecraft configurations (located at the origin of **Figures 4–6**) the magnetic field can be reconstructed to within 1% accuracy. By comparing method $M_{1.1}$ with methods $M_{1.2}$ and $M_{1.3}$ in these figures, we also conclude that leveraging knowledge of the tetrahedral shapes and positions expands the region of high-accuracy reconstruction. Unfortunately, overly restrictive conditions limit the number of tetrahedra available to average over, limiting the size of the reconstructed region. In fact, the bottom left panel of **Figure 6** is empty because none of the 126 tetrahedra in the hour 205 configuration satisfy the geometric requirement that $\chi_j \leq 0.6$ demanded by $M_{1.4}$. Additionally, the second-order reconstruction method M_2 is accurate for only a small volume

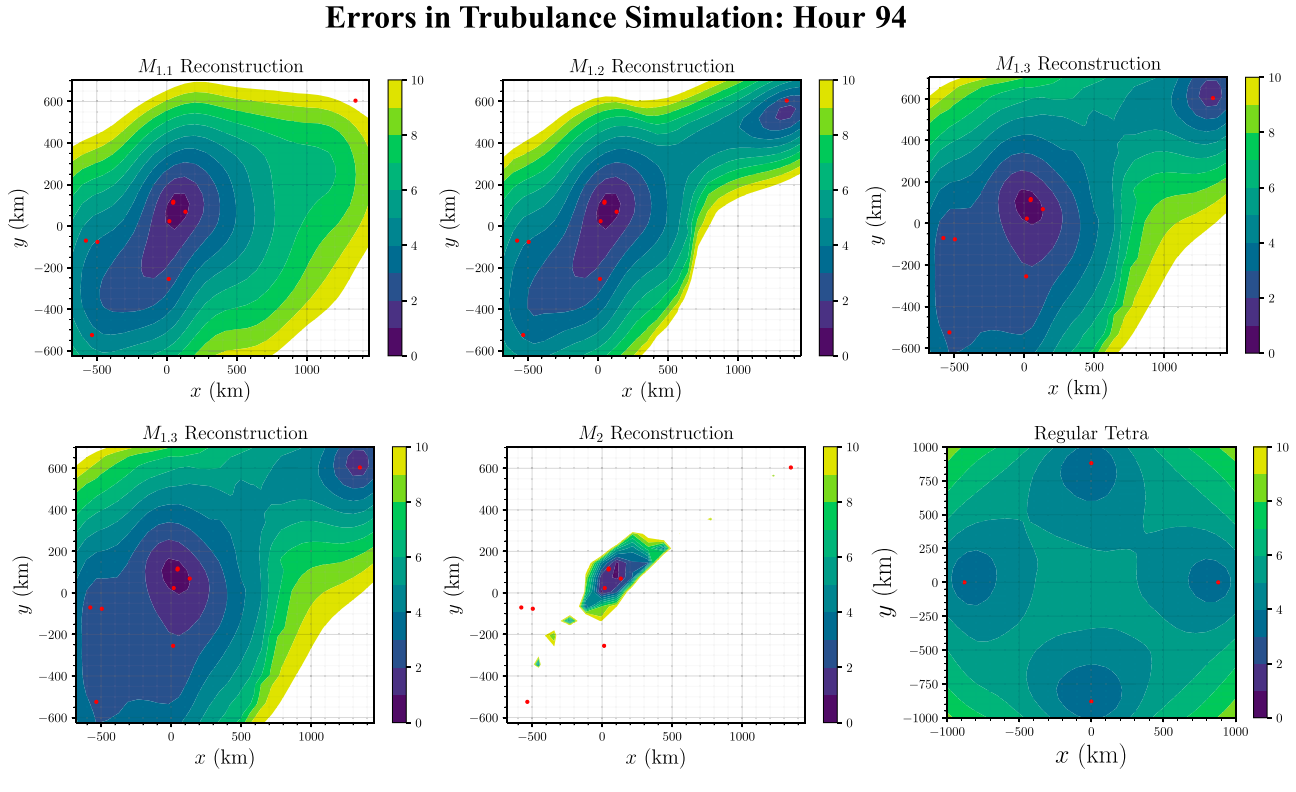

FIGURE 8 | Computation error (defined in **Eq. 7**) at all points on the $z = 0$ plane of the turbulent magnetic field (from the Gkeyll Simulation), using the swarm configuration at hour 94 of the HelioSwarm DRM. The layout is identical to **Figure 4**.

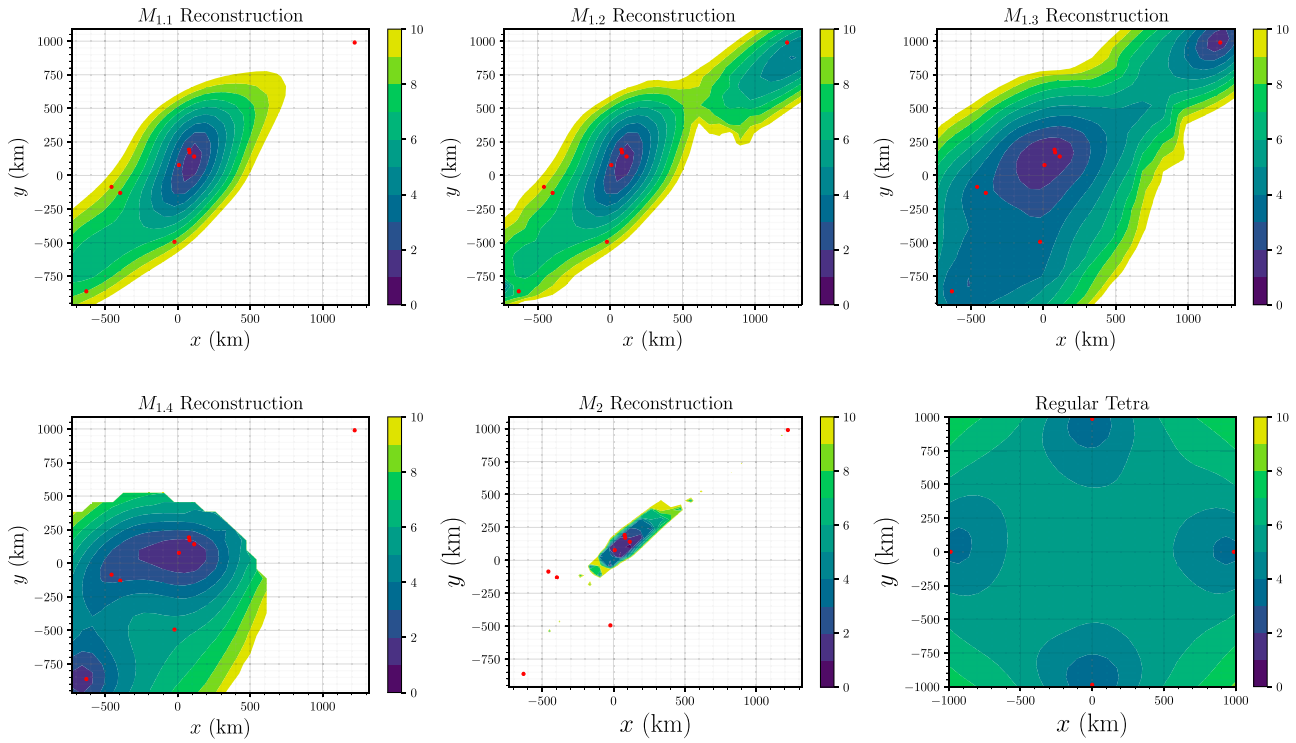

FIGURE 9 | Computation error (defined in **Eq. 7**) at all points on the $z = 0$ plane of the turbulent magnetic field (from the Gkeyll Simulation), using the swarm configuration at hour 144 of the HelioSwarm DRM. The layout is identical to **Figure 4**.

when compared with the first-order methods $M_{1.1}$, $M_{1.2}$, $M_{1.3}$, and $M_{1.4}$.

By comparing the bottom right panel to the other five in **Figures 7–10**, we see that the behavior of methods $M_{1.1}$, $M_{1.2}$, $M_{1.3}$, $M_{1.4}$, and M_2 is distinct to that of the reconstruction using a single regular tetrahedron. The single regular tetrahedron only accurately reconstructs the magnetic field of the current sheet near each of the four spacecraft. Due to the angular symmetry in the current sheet and the fact that none of the four spacecraft are positioned on the $z = 0$ plane, the area of most accurate reconstruction appears to be a ring on the bottom right panel of **Figures 4–6**.

3.2 Turbulence Simulation

We present an example magnetic field reconstruction of the turbulence simulation (§2.3.2) in **Figure 7**. Here, we use the first-order method $M_{1.3}$ to reconstruct the magnetic field in the $z = 0$ plane in the turbulence simulation. Mirroring the behavior described in **Figure 3**, there is little difference between the reconstructed and original fields near the center of the spacecraft configuration.

We perform 50 Monte Carlo iterations of reconstruction using each method, observing that 50 was more than enough to point-wise converge in error. The barycenter is chosen as a uniform random variable so that all spacecraft remained in the 31415 × 31415 × 157079 km simulation cube. We then construct a 30 × 30 × 30 grid of points ξ. Each dimension of this grid is selected so that the overall size of the grid extends 100 km past the furthest spacecraft in all directions.

The errors computed from the turbulence simulation reconstruction are displayed in **Figures 8–10** for the configurations at hours 94, 144, and 205 respectively. The panels shown are organized in the same order as the simple current sheet reconstruction. In **Table 2** we show the volume (in units of 10^6 km^3) of the magnetic field that can be reconstructed with errors less than 1, 5, and 10%. This is done for all three of the investigated spacecraft configurations, and using all five of the nine-spacecraft reconstruction methods, $M_{1.1}$, $M_{1.2}$, $M_{1.3}$, $M_{1.4}$, and M_2. In the bottom half of this table, we compare the volume reconstructed using a single regular tetrahedron to that of our five reconstruction methods.

Near the barycenter of each of the nine-spacecraft configurations, located at the origin of **Figures 8–10**, the magnetic field can be reconstructed to within 1% accuracy. The second-order method, M_2, can only reconstruct the magnetic field to within 10% accuracy in a small region near the barycenter of the configuration, while the first-order methods can reconstruct the magnetic field within 10% over a much greater area. This is the case because the second-order Taylor series expansion diverges quadratically with distance away from

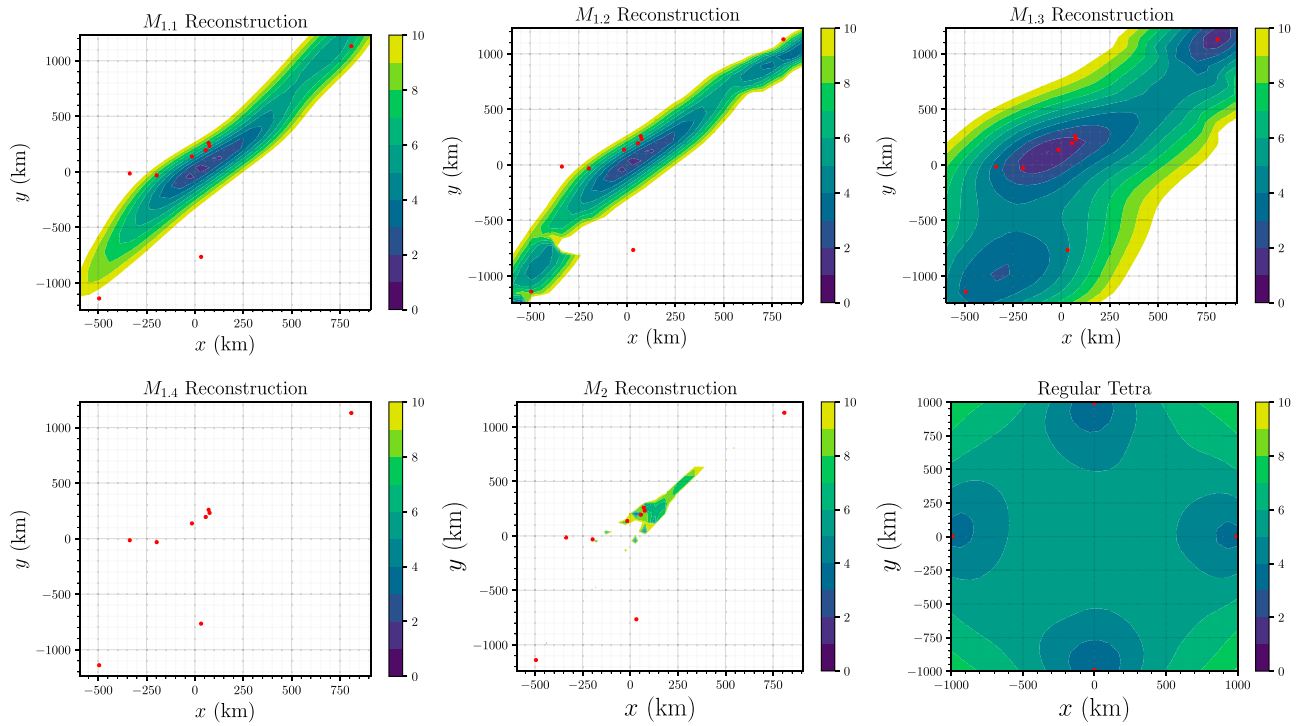

FIGURE 10 | Computation error (defined in **Eq. 7**) at all points on the $z = 0$ plane of the turbulent magnetic field (from the Gkeyll Simulation), using the swarm configuration at hour 205 of the HelioSwarm DRM. The layout is identical to **Figure 4**.

TABLE 2 | Volumes (in units of 10^6 km^3) with reconstructed magnetic field error less than 1, 5, or 10% for the three configurations using the four first-order methods and the second-order method discussed in §2.2. These volumes are compared to the equivalent regions reconstructed from a single regular tetrahedron with the same characteristic size as the overall nine-spacecraft configuration.

	Hour 94			**Hour 144**			**Hour 205**		
Volume	$\epsilon(1)$	$\epsilon(5)$	$\epsilon(10)$	$\epsilon(1)$	$\epsilon(5)$	$\epsilon(10)$	$\epsilon(1)$	$\epsilon(5)$	$\epsilon(10)$
$M_{1.1}$	17.56	1,057	3,095	2.95	324.4	2021	1.325	145.7	1,231
$M_{1.2}$	17.93	1,197	2,425	3.686	387.8	2,330	1.325	218.6	1,047
$M_{1.3}$	21.30	1816	3,208	9.584	2,151	4,722	12.59	1,556	4,334
$M_{1.4}$	30.26	1,189	1,679	17.69	1,169	2,281	0.0	0.0	0.0
M_2	3.363	47.45	118.1	5.898	48.66	137.9	3.975	33.79	103.3
Vs Regular Tetrahedron (%)	$\epsilon(1)$	$\epsilon(5)$	$\epsilon(10)$	$\epsilon(1)$	$\epsilon(5)$	$\epsilon(10)$	$\epsilon(1)$	$\epsilon(5)$	$\epsilon(10)$
$M_{1.1}$	137.20	54.31	38.70	24.58	23.75	25.26	13.80	10.77	15.39
$M_{1.2}$	140.12	61.51	30.32	30.72	28.40	29.13	13.80	16.16	13.08
$M_{1.3}$	166.39	93.33	40.12	79.87	157.54	59.04	131.12	115.03	54.18
$M_{1.4}$	236.44	61.06	21.00	147.45	85.62	28.51	0.0	0.0	0.0
M_2	26.27	2.44	1.48	49.15	3.56	1.72	41.41	2.50	1.29

the barycenter of the spacecraft configuration, while the first-order Taylor series only diverges linearly with distance. Since our goal is to maximize the volume of accurate reconstruction, the first-order methods are superior. However, the second-order method may be more accurate at reconstructing the values of the magnetic field very close to the barycenter of a spacecraft configuration.

The largest disparity compared to the current sheet simulations occurs for the single regular tetrahedron case, on the bottom right panels of each figure. The magnetic field is again only reconstructed accurately near each of the spacecraft, but because the turbulence simulation lacks angular symmetry, these regions manifest as spheres centered around each spacecraft. These four spheres appear to be the same size on the bottom

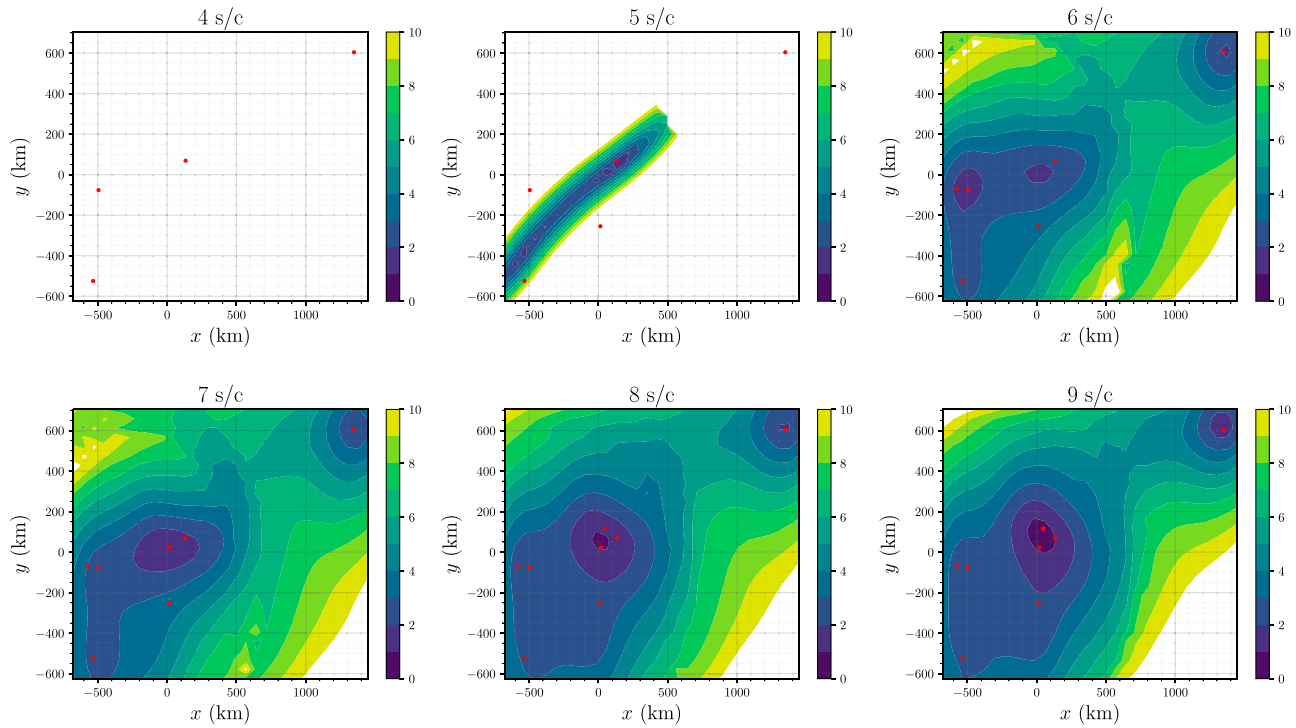

FIGURE 11 | Computation error (defined in **Eq. 7**) at all points on the $z = 0$ plane of the turbulent magnetic field (from the Gkeyll Simulation), using the first-order method $M_{1,3}$ with a subset of the spacecraft from the hour 94 configuration of the HelioSwarm DRM.

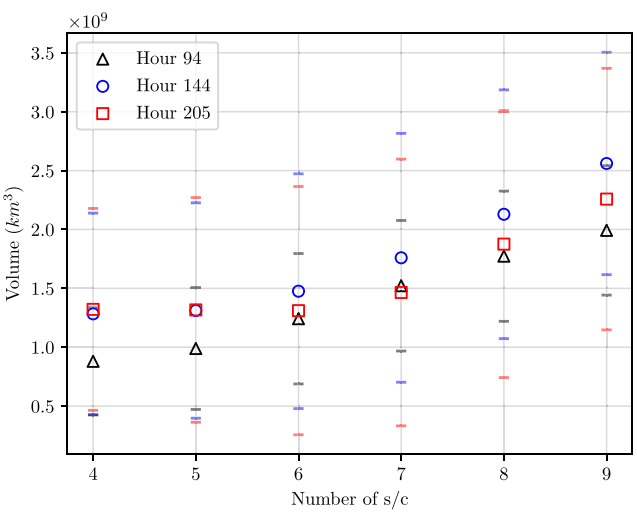

FIGURE 12 | Mean values of volume which were reconstructed with less than 5% error for the three nine-spacecraft configurations analyzed. The dashes above/below the markers represent one standard deviation away from the mean volume for each configuration.

right panel of each figure because the spacecraft are equidistant from the $z = 0$ plane.

Shown in **Table 2**, the single regular tetrahedron reconstructs the largest volume with less than 10% error,

TABLE 3 | From the nine-spacecraft configurations of hours 94, 144, and 205, we select a subset of $N \in \{4, 5, 6, 7, 8, 9\}$ spacecraft. We determine the probability that this N spacecraft configuration does not contain a tetrahedron which passes the threshold shape requirements of first-order reconstruction method $M_{1,3}$.

N	4	5	6	7	8	9
Hour 94	57.1	13.5	1.2	0	0	0
Hour 144	71.4	36.5	9.5	0	0	0
Hour 205	77.8	51.6	20.2	0	0	0

however the first-order methods reconstruct larger volumes with smaller errors. To maximize the volume reconstructed with less than 1% error, it appears it is best to use the first-order method $M_{1,4}$, detailed in §2.2.4 (if a sufficient number of quasi-regular tetrahedra can be formed from the nine spacecraft configuration).

3.3 Sensitivity to Number of Spacecraft

We analyze how the volume reconstructed with less than 5% error varies as a function of the number of spacecraft. This analysis was completed using the Monte Carlo sampling of the turbulent simulation as described in §3.

For $N \in \{4, 5, 6, 7, 8, 9\}$ spacecraft, we reconstructed the value of the magnetic field at all $30 \times 30 \times 30$ points ξ using all $C(N, 4)$ tetrahedra. We then use the $M_{1,3}$ first-order reconstruction method of §2.2.4 to reconstruct **B** at all points ξ. The errors everywhere are computed using **Eq. 7**, and the volume where the

error is less than 5% is computed using **Eq. 8** multiplied by the total reconstructed volume. We visualize the errors of this method for the hour 94 configuration in **Figure 11**. In this example, we find that as the number of spacecraft is increased, the area which is reconstructed with a high accuracy also increases. As this result depends on which particular subset of spacecraft are chosen for a given N, we next investigate whether this increase is holds for an arbitrary selection of spacecraft.

We start by choosing four out of the 9 spacecraft of the hour 94 configuration. These spacecraft measurements are used to estimate the value of **B** everywhere via the first-order reconstruction method $M_{1.3}$. We find the volume over which we can reconstruct **B** with an error less than 5%. This process is repeated for all 126 possible choices of four spacecraft. We repeat all of these volume calculations, initializing the spacecraft configuration at 50 different locations within the simulated turbulent **B** field. Finally, we take the mean of all 126 × 50 volume values and plot them in **Figure 12**. In these averages, we omit the instances where no tetrahedra pass the selection criteria of method $M_{1.3}$. We repeat this process for $N = 5$, 6, 7, 8, and 9 spacecraft from the hour 94 configuration, as well as for the hour 144 and 205 configurations.

As shown in **Figure 12**, we see that increasing the number of spacecraft measurements available increases the volume of the magnetic field reconstructed with less than 5% error. The variance of this reconstructed volume is smallest for the hour 94 configuration, which contains the most tetrahedra which are quasi-regular ($\chi_j \leq 1$). However, it is not the case that the hour 94 configuration has the highest average volume which is reconstructed with less than 5% error.

We also track the instances where zero of the available tetrahedra in the set of N spacecraft meet the shape threshold of $\chi_j \leq 1$ for the $M_{1.3}$ method. The percentage of arrangements where this occurs is shown in **Table 3** as a function of spacecraft configuration (hour) and number of spacecraft, N. We see from this table that for the analyzed configurations, there must be at least seven spacecraft measurements to guarantee that at least one tetrahedron passes the previously stated shape criteria.

4 DISCUSSION

We have demonstrated that our reconstruction methods are an effective way to leverage magnetometer measurements from a configuration consisting of more than four spacecraft. We have defined a shape metric, χ, for a tetrahedron of spacecraft which can be used as a threshold criterion. Estimates of magnetic field derived from tetrahedron which do meet the threshold value of χ will be discarded, as they are misshapen and therefore more likely to produce erroneous estimates. Finally, we have shown that increasing the number of spacecraft in a configuration will increase the volume over which the magnetic field can be accurately reconstructed, as well as increase the likelihood that some tetrahedra of spacecraft in the configuration are well shaped.

In **Table 2** we demonstrated that our second-order reconstruction method M_2 does not reconstruct the magnetic field with high accuracy over a large volume. However, we have shown that methods $M_{1.3}$ and $M_{1.4}$, which average over a subset of the many available tetrahedra formed by nine spacecraft, improves the field reconstruction. This work indicates that the subset of tetrahedra which should be averaged over needs to consider each tetrahedron's spacial proximity to the reconstructed point as well as its geometric properties. By comparing results from spacecraft configurations with different tetrahedral geometric configurations, we find that designing spacecraft trajectories which maximize the number of tetrahedra that are quasi-regular (i.e., $\chi \leq 1$) is essential to improving the accuracy of the reconstructed magnetic field.

This work can help optimize future multi-spacecraft missions, such as HelioSwarm. The selection of tetrahedra which are included in the calculation of **B** can be tuned to maximize the volume over which the field is reconstructed accurately, or it can be tuned to recreate **B** as accurately as possible over a small volume. The first-order methods discussed here can be applied to reconstruct any vector field which is sparsely sampled by *in-situ* measurements, as no assumptions are made about the physical properties of the field.

The first-order reconstruction method applied to a single tetrahedron reconstructs the magnetic field perfectly at each spacecraft location. However, using any of our proposed composite first-order reconstruction methods, which average over many of these reconstructions, negates this behavior. In future work, we plan to construct a weight function which, when introduced into the tetrahedral averaging, returns this desired limiting behavior. Additional future work could include characterizing methods of predicting the surface inside-of-which we have less than a prescribed error value for an arbitrary configuration of spacecraft.

The authors would like to thank the HelioSwarm Science and Flight Dynamics teams for discussions and comments during the execution of this project, in particular Laura Plice and Jonathan Niehof. This material is based upon High Performance Computing (HPC) resources supported by the University of Arizona TRIF, UITS, and Research, Innovation, and Impact (RII) and maintained by the UArizona Research Technologies department. The authors acknowledge the Texas Advanced Computing Center (TACC) at The University of Texas at Austin for providing HPC resources that have contributed to the research results reported within this paper. D.V. is supported by the Science and Technology Facilities Council (STFC) Ernest Rutherford Fellowship ST/P003826/1 and STFC Consolidated Grant ST/S000240/1. J.M.T is supported by NSF STR award AGS-1842638.

DATA AVAILABILITY STATEMENT

The raw data supporting the conclusions of this article will be made available by the authors, without undue reservation.

AUTHOR CONTRIBUTIONS

TB conducted the numerical experiments, analyzed the results, and wrote the majority of the paper, with guidance and oversight

from KK on all steps. JT supplied the turbulence simulation results and wrote up its description. ID provided background work on second order methods which served as a starting point for the one we developed. OR and DV provided knowledge of previous missions and context to the results.

REFERENCES

Angelopoulos, V. (2008). The THEMIS Mission. *Space Sci. Rev.* 141, 5–34. doi:10.1007/s11214-008-9336-1

Burch, J. L., Moore, T. E., Torbert, R. B., and Giles, B. L. (2016). Magnetospheric Multiscale Overview and Science Objectives. *Space Sci. Rev.* 199, 5–21. doi:10.1007/s11214-015-0164-9

Constantinescu, O. D., Glassmeier, K.-H., Motschmann, U., Treumann, R. A., Fornaçon, K.-H., and Fränz, M. (2006). Plasma Wave Source Location Using CLUSTER as a Spherical Wave Telescope. *J. Geophys. Res.* 111, A09221. doi:10.1029/2005JA011550

Dai, L., Wang, C., Cai, Z., Gonzalez, W., Hesse, M., Escoubet, P., et al. (2020). AME: A Cross-Scale Constellation of CubeSats to Explore Magnetic Reconnection in the Solar–Terrestrial Relation. *Front. Phys.* 8, 89. doi:10.3389/fphy.2020.00089

Dunlop, M. W., Southwood, D. J., Glassmeier, K. H., and Neubauer, F. M. (1988). Analysis of Multipoint Magnetometer Data. *Adv. Space Res.* 8, 273. doi:10.1016/0273-1177(88)90141-X

Elsasser, W. M. (1950). The Hydromagnetic Equations. *Phys. Rev.* 79, 183. doi:10.1103/PhysRev.79.183

Escoubet, C. P., Fehringer, M., and Goldstein, M. (2001). IntroductionThe Cluster mission. *Ann. Geophys.* 19, 1197–1200. doi:10.5194/angeo-19-1197-2001

Forsyth, C., Lester, M., Fazakerley, A. N., Owen, C. J., and Walsh, A. P. (2011). On the Effect of Line Current Width and Relative Position on the Multi-Spacecraft Curlometer Technique. *Planet. Space ScienceSpace Sci.* 59, 598–605. doi:10.1016/j.pss.2009.12.007

Fu, H. S., Vaivads, A., Khotyaintsev, Y. V., Olshevsky, V., André, M., Cao, J. B., et al. (2015). How to Find Magnetic Nulls and Reconstruct Field Topology with MMS Data? *J. Geophys. Res. Space Phys.* 120, 3758–3782. doi:10.1002/2015JA021082

Fu, H. S., Wang, Z., Zong, Q., Chen, X. H., He, J. S., Vaivads, A., et al. (2020). Methods for Finding Magnetic Nulls and Reconstructing Field Topology. *Am. Geophys. Union.*, 153–172. doi:10.1002/9781119509592.ch9

Goldreich, P., and Sridhar, S. (1995). Toward a Theory of Interstellar Turbulence. 2: Strong Alfvenic Turbulence. *Astrophysical J.* 438, 763. doi:10.1086/175121

ISSI book (2008). "Multi-Spacecraft Analysis Methods Revisited," in *ISSI Scientific Report SR-008*. Editors G. Paschmann and P. W. Daly (Bern, Switzerland: International Space Science Institute).

Hakim, A., Loverich, J., and Shumlak, U. (2006). A High Resolution Wave Propagation Scheme for Ideal Two-Fluid Plasma Equations. *J. Comput. Phys.* 219, 418–442. doi:10.1016/j.jcp.2006.03.036

Klein, K. G., Alexandrova, O., Bookbinder, J., Caprioli, D., Case, A. W., Chandran, B. D. G., et al. (2019). Plasma 2020 Decadal] Multipoint Measurements of the Solar Wind: A Proposed Advance for Studying Magnetized Turbulence. arXiv:1903.05740. Available at: https://arxiv.org/abs/1903.05740.

Li, T. C., Howes, G. G., Klein, K. G., and TenBarge, J. M. (2016). Energy Dissipation and Landau Damping in Two- and Three-Dimensional Plasma Turbulence. *Astrophysical J.* 832, L24. doi:10.3847/2041-8205/832/2/L24

Narita, Y., Nakamura, R., and Baumjohann, W. (2013). Cluster as Current Sheet Surveyor in the Magnetotail. *Ann. Geophys.* 31, 1605–1610. doi:10.5194/angeo-31-1605-2013

Orszag, S. A., and Tang, C.-M. (1979). Small-Scale Structure of Two-Dimensional Magnetohydrodynamic Turbulence. *J. Fluid Mech.* 90, 129–143. doi:10.1017/S002211207900210X

Paschmann, G., and Daly, P. W. (1998). *Analysis Methods for Multi-Spacecraft Data*. Netherlands: The International Space Science Institute, Hallerstr. 6, CH-3012 Bern, Switzerland. ESA Publications Division, Noordwjik. Copyright: 1998 ISSI/ESA. ISSI Scientific Report SR-001.

Pinçon, J.-L., and Motschmann, U. (1998). "Multi-spacecraft Filtering: General Framework," in *Analysis Methods for Multi-Spacecraft Data, ISSI Scientific Reports Series*. Editors G. Paschmann and P. W. Daly, 1, 65.

Plice, L., Perez, A. D., and West, S. (2020). Advances in the Astronautical Sciences, 171.

Robert, P., Dunlop, M. W., Roux, A., and Chanteur, G. (1998). Tetrahedron Geometric Factors. *ISSI Scientific Rep. Ser.* 1, 323–348.

Schwartz, S., Bale, S. D., Fujimoto, M., Hellinger, P., Kessel, M., Le, G., et al. (2009). Cross-Scale: Multi-Scale Coupling in Space Plasma, Assessment Study Report. arXiv:0912.0856. Available at: https://arxiv.org/abs/0912.0856.

Srinivasan, B., and Shumlak, U. (2011). Analytical and Computational Study of the Ideal Full Two-Fluid Plasma Model and Asymptotic Approximations for Hall-Magnetohydrodynamics. *Phys. Plasmas.* 18, 092113. doi:10.1063/1.3640811

Torbert, R. B., Dors, I., Argall, M. R., Genestreti, K. J., Burch, J. L., Farrugia, C. J., et al. (2020). A New Method of 3-D Magnetic Field Reconstruction. *Geophys. Res. Lett.* 47, e85542. doi:10.1029/2019GL085542

Verscharen, D., Klein, K. G., and Maruca, B. A. (2019). The Multi-Scale Nature of the Solar Wind. *Living Rev. Sol. Phys.* 16, 5. doi:10.1007/s41116-019-0021-0

Wang, L., Hakim, A. H., Bhattacharjee, A., and Germaschewski, K. (2015). Comparison of Multi-Fluid Moment Models with Particle-In-Cell Simulations of Collisionless Magnetic Reconnection. *Phys. Plasmas.* 22, 012108. doi:10.1063/1.4906063

Wang, L., Hakim, A. H., Ng, J., Dong, C., and Germaschewski, K. (2020). Exact and Locally Implicit Source Term Solvers for Multifluid-Maxwell Systems. *J. Comput. Phys.* 415, 109510. doi:10.1016/j.jcp.2020.109510

SUPPLEMENTARY MATERIAL

The Supplementary Material for this article can be found online at: https://www.frontiersin.org/articles/10.3389/fspas.2021.727076/full#supplementary-material

Conflict of Interest: The authors declare that the research was conducted in the absence of any commercial or financial relationships that could be construed as a potential conflict of interest.

frontiers | Frontiers in Astronomy and Space Sciences

PERSPECTIVE
published: 30 May 2022
doi: 10.3389/fspas.2022.923463

SQUARE^2: Spacecraft in QUAdrature for Solar Exploration—A Mission Concept for Synergetic Observations of the Sun and Heliosphere

D. Telloni *

National Institute for Astrophysics, Astrophysical Observatory of Torino, Pino Torinese, Italy

SQUARE^2 is the acronym for Spacecraft in QUAdrature for solaR Exploration, and is a mission concept for multi-instrumental two-point observations of the Sun and its environment. It stems from the need to have two probes that are systematically in orbital configurations of interest, such as quadratures or radial alignments, in order to successfully address some science topics that joint measurements by different spacecraft, not specifically designed though to operate in synergy, can only partially solve. This perspective paper describes the mission profile that SQUARE^2 should have in order to achieve a better understanding of how the Sun creates and controls the heliosphere. Specifically, the combined use of remote-sensing and *in-situ* instrumentation aboard the twin SQUARE^2 probes would allow the connection of the locally sampled solar-wind plasma flow with its coronal drivers and a proper investigation of solar wind evolution, dynamics, and transient events in the inner heliosphere. The potential impact of SQUARE^2 and the science topics covered by such a solar mission are here discussed.

Keywords: space probes, space vehicle instruments, orbits, the Sun, heliosphere, space plasmas, solar wind, solar coronal mass ejections

OPEN ACCESS

Edited by:
Alessandro Retino, UMR7648 Laboratoire de physique des plasmas, France

Reviewed by:
Feng Wang, Guangzhou University, China

***Correspondence:**
D. Telloni
daniele.telloni@inaf.it

Specialty section:
This article was submitted to Space Physics, a section of the journal Frontiers in Astronomy and Space Sciences

Received: *19 April 2022*
Accepted: *02 May 2022*
Published: *30 May 2022*

Citation:
Telloni D (2022) SQUARE^2: Spacecraft in QUAdrature for Solar Exploration—A Mission Concept for Synergetic Observations of the Sun and Heliosphere. Front. Astron. Space Sci. 9:923463. doi: 10.3389/fspas.2022.923463

1 INTRODUCTION

Some of the most important scientific advances in the investigation of the Sun and its region of influence, the heliosphere, came from coordinated multi-spacecraft, multi-instrument observations. The study of the evolution of the dynamical/energetic properties of Coronal Mass Eruptions (CMEs, e.g., Nakwacki et al., 2011; Telloni et al., 2020) or solar wind turbulence (e.g., D'Amicis et al., 2010; Alberti et al., 2022), the investigation of the origin and propagation of the solar wind plasma (e.g., Poletto et al., 2002; Telloni et al., 2021a), the stereoscopic reconstructions of eruptive phenomena (such as prominences or CMEs, Gissot et al., 2008; Wood et al., 2009) or large-scale coronal structures (e.g., Aschwanden et al., 2008; Decraemer et al., 2019), the analysis of widespread solar energetic particle events in interplanetary space (e.g., Kollhoff et al., 2021; Mason et al., 2021), are just some of the many possible examples. Such investigations are performed by exploiting particular orbital configurations between two or more spacecraft. Radial alignments between the Sun and two different probes, when crossed by a same solar event (whether it is a transient structure, such as a CME, or the same solar-wind plasma parcel), represent the only way to study its evolution during expansion throughout heliosphere (e.g., Witasse et al., 2017; Telloni et al., 2021b). It is true that other approaches, based for example on the statistical study of many events observed by different spacecraft, at different distances from the Sun and at different times, provide information, e.g.,

on how the morphology of CMEs varies with distance from the Sun (e.g., Janvier et al., 2019) or the fast solar wind becomes more and more turbulent as it expands into interplanetary space (e.g., Telloni et al., 2015), but these are far from being satisfactory, as they provide just average information, which does not take into account, for example, the different solar cycle (and, therefore, the different background conditions) in which the observations are performed. On the other hand, during quadrature configurations, obtained when the angular separation between the two spacecraft is 90° with the Sun at the apex of the angle, one of the two probes remotely observes the coronal/heliospheric plasma that lately impinges on the second one: therefore, this orbital geometry allows the study of the magnetic connection of the plasma observed *in situ* to its solar source (Telloni et al., 2021a). The conjunction between two or more spacecraft finally allows local two-point studies, thus providing three-dimensional information of solar events, otherwise not feasible with single-spacecraft measurements (e.g., Davies et al., 2021).

Synergetic studies, based on joint remote-sensing and *in-situ* instrument observations from different solar observatories, represent the cutting edge of the potential of space missions currently probing the Sun and the heliosphere. This is evidenced by the growing number of international Working Groups and International Space Science Institute (ISSI) proposed teams established to coordinate activities between traditionally disjoint space plasma communities and to maximize the scientific return of spacecraft configurations in the inner heliosphere. Nevertheless, such a multi-spacecraft approach remains one of the largest unexplored territories in the field of heliophysics. Its limited blossoming undoubtedly depends on the fact that the solar missions launched so far comprise only a single probe (excluding some magnetospheric missions, such as Cluster (Escoubet et al., 2001) or Magnetospheric MultiScale (MMS, Burch et al., 2016), consisting of four-spacecraft constellation in a tetrahedral flight formation and only sporadically entering the solar wind). Exception is the Solar TErrestrial RElations Observatory (STEREO, Kaiser et al., 2008), a solar mission consisting of two nearly identical probes, carrying both *in-situ* and remote-sensing instrumentation, placed in orbit around the Sun at different positions along Earth's orbit, with the ahead spacecraft (STEREO-A) preceding Earth and the behind spacecraft (STEREO-B) following it. This enabled the first ever stereoscopic view of the Sun and its large-scale manifestations (such as CMEs, see the review by Thernisien et al., 2011, and references therein).

Most of the current understanding of how the Sun creates and controls the heliosphere comes from near-Earth space observatories, resulting in a limited view of the Sun's environment. The most recent heliospheric missions, namely BepiColombo (BC, Benkhoff et al., 2010), Parker Solar Probe (PSP, Fox et al., 2016), and Solar Orbiter (SO, Müller et al., 2020), which are probing *in situ* and remotely the inner heliosphere along complementary trajectories, has partially overcome this gap, while providing exciting and unprecedented opportunities for coordinated studies, in conjunction with the current near-Earth orbiting fleet, of the complex heliospheric dynamics and structures. Preliminary investigations were carried out by Velli et al. (2020) and Hadid et al. (2021) to identify the useful spacecraft configurations for such synergistic studies and highlight their potential for discovery. Since the first studies relying on these special orbital configurations (Jannet et al., 2021; Telloni et al., 2021a,b; Davies et al., 2021; Weiss et al., 2021; Musset et al., 2021; Möstl et al., 2022; Alberti et al., 2022; Réville et al., 2022), it became immediately clear that multi-point, multi-instrument observations by BC, PSP, and SO represent an exceptional added value in order to successfully address all the scientific goals the three heliospheric missions aim at. Nevertheless, the BC, PSP, and SO space missions, specifically their instrumentation payload and orbits, are not designed to operate in synergy. It follows that the potential science return of the interconnected science is not fully exploited. For this purpose it would be useful an "ad hoc" solar mission consisting of two (or more) twin probes placed in different orbits around the Sun, but optimized to maximize the number of orbital geometries, i.e., quadratures, radial alignments, conjunctions and so on.

SQUARE^2 is a twin-probe solar mission concept specifically tailored for multi-spacecraft studies of solar interconnected processes in the heliosphere. It stands for Spacecraft in QUAdrature for solaR Exploration, and the superscript "2" both indicates that the mission consists of twin probes and recalls the concept of "squared", namely that one of the goals of the mission is to maximize the quadrature configurations between the two probes. This perspective paper is devoted to describing SQUARE^2, i.e., what its orbital features should be (§2), what scientific questions would be addressed (§3), and a concluding outlook (§4).

2 SQUARE^2 ORBITAL GEOMETRIES

This section deals with the orbital characteristics that SQUARE^2 should have in order to maximize the number of time windows in which the two probes are in particular geometries useful for multi-spacecraft studies. It should be immediately stressed that the orbits shown in the following are unrealistic examples helpful only for the purpose of presenting what should be the spacecraft configurations to be maximized during the SQUARE^2 solar mission. The actual mission design, the different and complementary trajectories of the two probes eventually combined with multiple gravitational assists (at Earth, Venus, or Mercury), are the subject of the mission profile development that is obviously beyond the scope of this paper, which instead aims only to present the potential richness of such a solar mission. It is only worth noting here that the two probes are expected to have very different and complementary orbits, with different eccentricities, periods of revolution, and distances from the Sun (provided that the number of useful geometries is maximized), eventually including periods of quasi-co-rotation between the two spacecraft. Both probes would be then equipped with both remote-sensing (disk imager, magnetograph, coronagraph, spectrometer, heliospheric imager) and *in-situ* (plasma sensors, magnetometers, particle detector, radio antenna) instruments in order to address all the science objectives of SQUARE^2. To satisfy telemetry requirements,

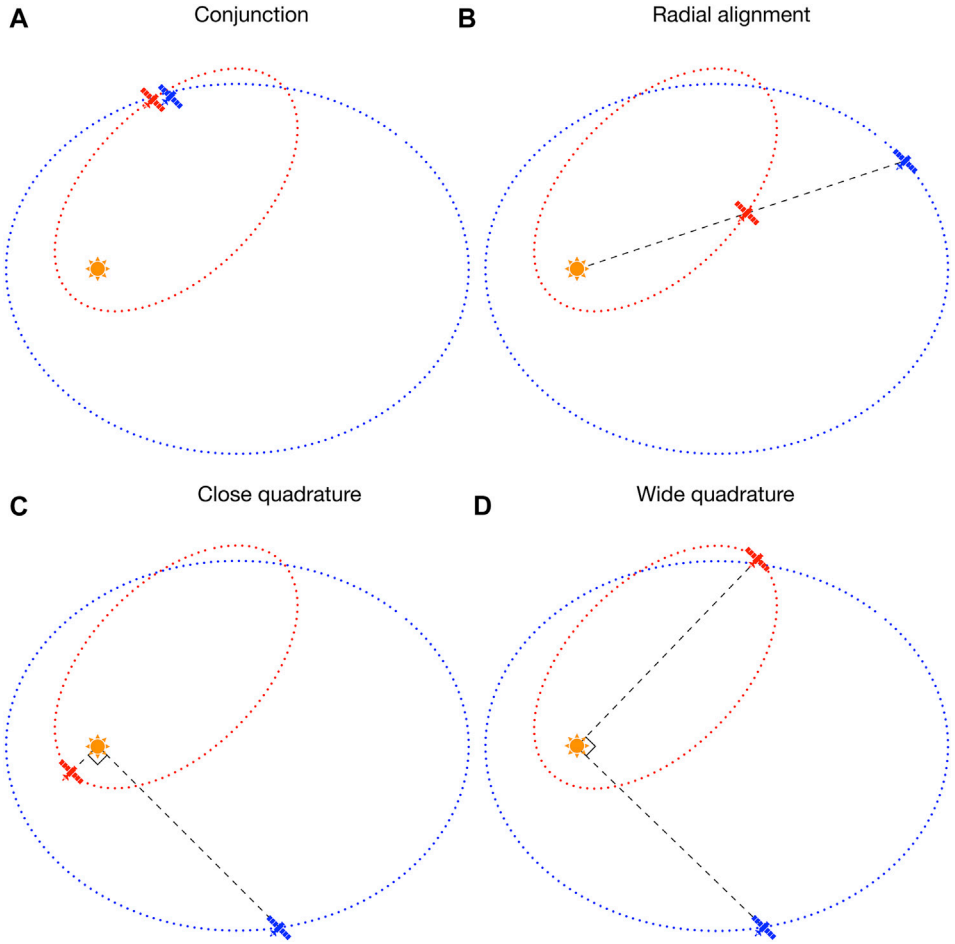

FIGURE 1 | Sketches of particular geometrical configurations between SQUARE^2 s/c #1 (red) and s/c #2 (blue) while orbiting around the Sun (yellow star) along their relative trajectories (color-coded dotted lines): spacecraft conjunction **(A)**, radial alignment **(B)**, close **(C)** and wide **(D)** quadratures. The s/c—Sun lines, during alignments and quadratures, are marked as dashed lines.

remote-sensing instruments would observe only during relevant orbital configurations, while *in-situ* sensors would operate continuously.

Figure 1 displays four interesting orbital geometries between the two SQUARE^2 twin probes s/c #1 and #2 (in red and blue, respectively) orbiting along different trajectories (color-coded dotted lines) around the Sun (yellow star).

Spacecraft conjunctions (**Figure 1A**) occur when the s/c #1—s/c #2 longitudinal and radial separation is very small, and enable two-point *in-situ* investigations of the evolving 3D properties of the solar wind turbulence or transient (if any). Indeed, probing the same region of space at two distinct points and at different times would allow scientists to overcome the spatiotemporal ambiguity intrinsic to any single-spacecraft measurement, thus disentangling temporal from spatial fluctuations.

When s/c #1 and s/c #2 are radially aligned (i.e., their longitudinal separation is very small, even though orbiting at different distances from the Sun, **Figure 1B**), the evolution of solar wind properties and turbulence, as well as of the heliospheric counterpart of CMEs, while propagating into interplanetary space, can be studied. Different radial alignments, with the probes having different radial separations, over the whole course of the SQUARE^2 mission would allow extensive analysis of the evolution of the expanding solar plasma fairly uniformly throughout the inner heliosphere.

Unlike the previous orbital configurations, during close or wide spacecraft quadratures (**Figures 1C,D**, respectively), occurring when the s/c #1—Sun—s/c #2 angle is 90°, remote-sensing observations of the Sun and its atmosphere play a crucial role. Indeed, quadratures enable studies on the magnetic connection of solar wind plasma measured locally by *in-situ* instrumentation to its solar sources observed remotely in coronagraphic images. In this context, remote-sensing observations from the first spacecraft gather information on the large-scale configuration of the coronal drivers of the plasma flows later crossing the second spacecraft, which measures *in situ* its physical properties. However, all quadratures are not equal, and the scientific targets that can be achieved depend greatly on the relative distance of the two

probes from the Sun. Solar-wind connectivity can indeed be successfully addressed only in the case of a close quadrature (**Figure 1C**), with one of the two probes observing the Sun from afar and the second locally sampling the wind plasma very close to the Sun (which ensures that the plasma has not been significantly reprocessed during its propagation from the Sun to the spacecraft, i.e., it is still pristine). When the observation points of both probes in quadrature are very far from the Sun (**Figure 1D**), this kind of investigation is in fact (at least partially) prevented, and other (and complementary with respect to close quadratures) science objectives are enabled. For instance, observations of the solar corona from two (widely separated) vantage points would provide information about the 3D structure and dynamics of the large-scale solar atmosphere. Furthermore, local measurements of interplanetary CMEs by in-quadrature spacecraft at small radial separations but larger longitudinal separations (as in **Figure 1D**) shed light on their 3D structure.

In addition, if the two probes experienced, when in particular orbital configurations, periods of quasi-co-rotation with the Sun and/or each other, this would provide interesting opportunities to lengthen the periods of connection with solar sources, thus allowing the possibility to answer long-standing question such as the origin of the slow solar wind, to distinguish between temporal and spatial scales of locally sampled small-scale variations (and, in turn, between turbulence-related fluctuations and flux-tube-like structures), and to monitor the evolution of CMEs and the associated post-CME current sheets. Finally, noteworthy is that, being different from each other, the various orbits should be dedicated to specific science topics, as discussed in the following section.

3 MAJOR SCIENCE TOPICS ADVANCED BY SQUARE^2

SQUARE^2 could potentially advance the current understanding of the Sun—heliosphere coupling, by providing an unprecedented large set of useful orbital configurations for enhancing the study of the 3D structure of the heliosphere, the origin of the solar wind, transient events, and, most importantly, their connection to the coronal drivers. Specifically, the SQUARE^2 systematic two-point, multi-instrument observations would be used to address, mainly yet not exclusively, the following science topics and their interplay.

Solar wind origin and propagation By simultaneously measuring the solar atmosphere, from the photosphere to the corona, remotely and the solar wind plasma and magnetic field *in situ* during systematic s/c #1—s/c #2 quadratures, SQUARE^2 would efficiently link the small-scale properties of the plasma flow with the large-scale structures of solar drivers at the Sun (Telloni et al., 2021a). This would provide a plethora of observations to potentially represent a breakthrough in the investigation of the origin of the slow solar wind, which is still matter of strong debate (Abbo et al., 2016). In addition, joint remote-sensing and *in-situ* observations of coronal flows would provide insight into the link and interplay between macrophysics and microphysics in the processes underlying the evolution of the solar wind, and a better understanding of how stream-stream interactions reprocess the plasma during its expansion. Radial alignments would be of critical importance in this context, representing in fact the only way to satisfactorily study the propagation of solar wind from the very inner heliosphere to Earth's orbit and beyond, and its interaction with the surrounding environment. Finally, combined observations at both coronal and heliospheric heights during quadratures and/or alignments would contribute significantly to solving the question of how the plasma is heated and accelerated as it escapes from the outer layers of the solar atmosphere. Comparison of SQUARE^2 results of outflow velocity and plasma density of accelerating coronal flows with currently existing solar wind models (see the exhaustive review by Zank et al., 2021, and reference therein) would represent a significant step forward in ascertaining what processes regulate the heating and acceleration of coronal plasma.

Turbulence, waves, kinetic physics in the solar wind The investigation of the radial evolution of turbulence, waves and kinetic phenomena in the solar wind is primarily based on large sets of measurements belonging to different plasma streams, acquired at different times and distances from the Sun (e.g., Bruno et al., 2014; Alberti et al., 2020; Chen et al., 2020), and therefore inevitably suffers from the natural inhomogeneity and non-stationarity of the solar wind and its solar drivers, thus yielding results at least partially biased by the different solar conditions pertinent to the different observations. It turns out that the only really accurate way to learn about the evolution of turbulence, waves and heating is to rely on the same solar-wind plasma parcel observed at different heliocentric distances during radial lineups between two or more space vehicles (e.g., D'Amicis et al., 2010; Bruno and Telloni, 2015; Telloni et al., 2021b). In this context, SQUARE^2 would provide a major improvement in the availability of instances for exploring how turbulence/waves of the same solar flow evolve while expanding in the inner heliosphere, as it would maximize the number of radial alignments between the twin probes comprising the space mission. By comparing remote observations of the solar drivers and *in-situ* measurements of the plasma and magnetic field fluctuations, SQUARE^2 would help address the origin of plasma turbulence, diagnose wave-particle interactions, and advance understanding of the role of turbulence/instabilities/kinetic processes in heating the solar wind plasma. Finally, SQUARE^2's observations would be of critical importance in distinguishing between competing theories of the generation, transport and dissipation of the magnetohydrodynamic (MHD) turbulence (Zank et al., 2021).

Solar wind transient events The investigation of the solar-wind transient perturbations, such as interplanetary counterpart of CMEs, would also benefit greatly from the multi-point observations provided by SQUARE^2. The availability of systematic measurements in the corona and the very inner heliosphere, i.e., the region where the transient structures evolve more rapidly, would indeed ensure to gain insights on a wide variety of their properties at both large and small scales. Specifically, wide s/c #1—s/c #2 quadratures would allow studies of the global morphology, i.e., the 3D structure, of erupting phenomena, and their propagation in the extended corona, during the initial acceleration phases. Should and when the interplanetary CME hit the two SQUARE^2 probes, widely separate in longitude but at approximately the same

heliocentric distance, this would provide information on the extent and/or distortion of the CME structure. Relying on close quadratures, on the other hand, it would be possible to assess the local properties of the still fast-evolving CMEs. However, the maximum scientific return would be obtained during the s/c #1—s/c #2 radial alignments. Indeed, when the two probes are lined up, the radial evolution of the CME MHD properties, such as the degree of twisting of the embedded flux rope and its energetic budget (Telloni et al., 2020) or the turbulence and plasma heating development (Sorriso-Valvo et al., 2021), as well as the local dynamical interaction with the ambient solar wind, could be estimated. The joint operation of the SQUARE^2 twin spacecraft over a wide range of distances from the Sun would thus provide a powerful analysis platform for studying the interplay between the various physical processes underlying the onset, acceleration and propagation/evolution of the most important manifestation of solar activity.

4 CONCLUDING REMARKS

The launch in just 3 years, from 2018 to 2020, of the three fantastic inner heliospheric missions BepiColombo, Parker Solar Probe, and Solar Orbiter has opened a new era in the exploration of the inner heliosphere and its complex dynamics, while showing the potential of the multi-spacecraft approach in solar physics studies. Yet, it also showed the need for a space mission comprising multiple twin probes and specifically dedicated to multi-point, multi-instrument observations of the Sun and its environment. SQUARE^2, Spacecraft in QUAdrature for solaR Exploration, is a solar mission concept specifically conceived to address this need and perform synergetic observations of the Sun and heliosphere, in order to fully capture the temporal and spatial dynamical evolution of the solar wind and transient events, and connect them to their coronal sources. Its mission profile is precisely designed to maximize the number of useful orbital configurations (such as conjunctions, radial alignments, and quadrature). This paper has briefly summarized the SQUARE^2 characteristics and orbital geometries, as well as the advantages and new insights of such a space mission. In particular, it has appeared evident that systematic coordinated observations of several *in-situ* and remote-sensing instruments would enable breakthrough science in a way no other solar mission could, allowing the scientific community to successfully address still unsolved and profoundly interconnected problems, such as the origin, acceleration and propagation of the coronal plasma flows, the spatiotemporal evolution of turbulence, waves, and kinetic processes, and dynamical interaction of transient events with the surrounding solar wind throughout interplanetary space.

DATA AVAILABILITY STATEMENT

All relevant data to the present work are included in the paper, further inquiries can be addressed to the corresponding author.

AUTHOR CONTRIBUTIONS

The author confirms being the sole contributor to this paper, having conceived and written it, and approved it for publication.

FUNDING

The author was partially supported by the Italian Space Agency (ASI) under contract 2018-30-HH.0.

REFERENCES

Abbo, L., Ofman, L., Antiochos, S. K., Hansteen, V. H., Harra, L., Ko, Y.-K., et al. (2016). Slow Solar Wind: Observations and Modeling. *Space Sci. Rev.* 201, 55–108. doi:10.1007/s11214-016-0264-1

Alberti, T., Laurenza, M., Consolini, G., Milillo, A., Marcucci, M. F., Carbone, V., et al. (2020). On the Scaling Properties of Magnetic-Field Fluctuations through the Inner Heliosphere. *Astrophys. J.* 902, 84. doi:10.3847/1538-4357/abb3d2

Alberti, T., Milillo, A., Heyner, D., Hadid, L. Z., Auster, H.-U., Richter, I., et al. (2022). The "Singular" Behavior of the Solar Wind Scaling Features during Parker Solar Probe-BepiColombo Radial Alignment. *Astrophys. J.* 926, 174. doi:10.3847/1538-4357/ac478d

Aschwanden, M. J., Wülser, J.-P., Nitta, N. V., and Lemen, J. R. (2008). First Three-Dimensional Reconstructions of Coronal Loops with the STEREO A and B Spacecraft. I. Geometry. *Astrophys. J.* 679, 827–842. doi:10.1086/529542

Benkhoff, J., van Casteren, J., Hayakawa, H., Fujimoto, M., Laakso, H., Novara, M., et al. (2010). BepiColombo—Comprehensive Exploration of Mercury: Mission Overview and Science Goals. *Planet. Space Sci.* 58, 2–20. doi:10.1016/j.pss.2009.09.020

Bruno, R., Telloni, D., Primavera, L., Pietropaolo, E., D'Amicis, R., Sorriso-Valvo, L., et al. (2014). Radial Evolution of the Intermittency of Density Fluctuations in the Fast Solar Wind. *Astrophys. J.* 786, 53. doi:10.1088/0004-637X/786/1/53

Bruno, R., and Telloni, D. (2015). Spectral Analysis of Magnetic Fluctuations at Proton Scales from Fast to Slow Solar Wind. *Astrophys. J. Lett.* 811, L17. doi:10.1088/2041-8205/811/2/L17

Burch, J. L., Moore, T. E., Torbert, R. B., and Giles, B. L. (2016). Magnetospheric Multiscale Overview and Science Objectives. *Space Sci. Rev.* 199, 5–21. doi:10.1007/s11214-015-0164-9

Chen, C. H. K., Bale, S. D., Bonnell, J. W., Borovikov, D., Bowen, T. A., Burgess, D., et al. (2020). The Evolution and Role of Solar Wind Turbulence in the Inner Heliosphere. *Astrophys. J. Suppl. Ser.* 246, 53. doi:10.3847/1538-4365/ab60a3

D'Amicis, R., Bruno, R., Pallocchia, G., Bavassano, B., Telloni, D., Carbone, V., et al. (2010). Radial Evolution of Solar Wind Turbulence during Earth and Ulysses Alignment of 2007 August. *Astrophys. J.* 717, 474–480. doi:10.1088/0004-637X/717/1/474

Davies, E. E., Möstl, C., Owens, M. J., Weiss, A. J., Amerstorfer, T., Hinterreiter, J., et al. (2021). *In Situ* multi-spacecraft and Remote Imaging Observations of the First CME Detected by Solar Orbiter and BepiColombo. *Astron. Astrophys.* 656, A2. doi:10.1051/0004-6361/202040113

Decraemer, B., Zhukov, A. N., and Van Doorsselaere, T. (2019). Three-dimensional Density Structure of a Solar Coronal Streamer Observed by SOHO/LASCO and STEREO/COR2 in Quadrature. *Astrophys. J.* 883, 152. doi:10.3847/1538-4357/ab3b58

Escoubet, C. P., Fehringer, M., and Goldstein, M. (2001). Introduction the Cluster Mission. *Ann. Geophys* 19, 1197–1200. doi:10.5194/angeo-19-1197-2001

Fox, N. J., Velli, M. C., Bale, S. D., Decker, R., Driesman, A., Howard, R. A., et al. (2016). The Solar Probe Plus Mission: Humanity's First Visit to Our Star. *Space Sci. Rev.* 204, 7–48. doi:10.1007/s11214-015-0211-6

Gissot, S. F., Hochedez, J. F., Chainais, P., and Antoine, J. P. (2008). 3D Reconstruction from SECCHI-EUVI Images Using an Optical-Flow Algorithm: Method Description and Observation of an Erupting Filament. *Sol. Phys.* 252, 397–408. doi:10.1007/s11207-008-9270-0

Hadid, L. Z., Génot, V., Aizawa, S., Milillo, A., Zender, J., Murakami, G., et al. (2021). BepiColombo's Cruise Phase: Unique Opportunity for Synergistic Observations. *Front. Astron. Space Sci.* 8, 154. doi:10.3389/fspas.2021.718024

Jannet, G., Dudok de Wit, T., Krasnoselskikh, V., Kretzschmar, M., Fergeau, P., Bergerard-Timofeeva, M., et al. (2021). Measurement of Magnetic Field Fluctuations in the Parker Solar Probe and Solar Orbiter Missions. *J. Geophys. Res. Space Phys.* 126, e28543. doi:10.1029/2020JA028543

Janvier, M., Winslow, R. M., Good, S., Bonhomme, E., Démoulin, P., Dasso, S., et al. (2019). Generic Magnetic Field Intensity Profiles of Interplanetary Coronal Mass Ejections at Mercury, Venus, and Earth from Superposed Epoch Analyses. *J. Geophys. Res. Space Phys.* 124, 812–836. doi:10.1029/2018JA025949

Kaiser, M. L., Kucera, T. A., Davila, J. M., Cyr, St. O. C., Guhathakurta, M., and Christian, E. (2008). The STEREO Mission: An Introduction. *Space Sci. Rev.* 136, 5–16. doi:10.1007/s11214-007-9277-0

Kollhoff, A., Kouloumvakos, A., Lario, D., Dresing, N., Gómez-Herrero, R., Rodríguez-García, L., et al. (2021). The First Widespread Solar Energetic Particle Event Observed by Solar Orbiter on 2020 November 29. *Astron. Astrophys.* 656, A20. doi:10.1051/0004-6361/202140937

Mason, G. M., Cohen, C. M. S., Ho, G. C., Mitchell, D. G., Allen, R. C., Hill, M. E., et al. (2021). Solar Energetic Particle Heavy Ion Properties in the Widespread Event of 2020 November 29. *Astron. Astrophys.* 656, L12. doi:10.1051/0004-6361/202141310

Möstl, C., Weiss, A. J., Reiss, M. A., Amerstorfer, T., Bailey, R. L., Hinterreiter, J., et al. (2022). Multipoint Interplanetary Coronal Mass Ejections Observed with Solar Orbiter, BepiColombo, Parker Solar Probe, Wind, and STEREO-A. *Astrophys. J. Lett.* 924, L6. doi:10.3847/2041-8213/ac42d0

Müller, D., Cyr, St. O. C., Zouganelis, I., Gilbert, H. R., Marsden, R., Nieves-Chinchilla, T., et al. (2020). The Solar Orbiter Mission. *Sci. overviewAstron. Astrophys.* 642, A1. doi:10.1051/0004-6361/202038467

Musset, S., Maksimovic, M., Kontar, E., Krupar, V., Chrysaphi, N., Bonnin, X., et al. (2021). Simulations of Radio-Wave Anisotropic Scattering to Interpret Type III Radio Burst Data from Solar Orbiter, Parker Solar Probe, STEREO, and Wind. *Astron. Astrophys.* 656, A34. doi:10.1051/0004-6361/202140998

Nakwacki, M. S., Dasso, S., Démoulin, P., Mandrini, C. H., and Gulisano, A. M. (2011). Dynamical Evolution of a Magnetic Cloud from the Sun to 5.4 AU. *Astron. Astrophys.* 535, A52. doi:10.1051/0004-6361/201015853

Poletto, G., Suess, S. T., Biesecker, D. A., Esser, R., Gloeckler, G., Ko, Y. K., et al. (2002). Low-latitude Solar Wind during the Fall 1998 SOHO-Ulysses Quadrature. *J. Geophys. Res. Space Phys.* 107, 1300. doi:10.1029/2001JA000275

Réville, V., Fargette, N., Rouillard, A. P., Lavraud, B., Velli, M., Strugarek, A., et al. (2022). Flux Rope and Dynamics of the Heliospheric Current Sheet. Study of the Parker Solar Probe and Solar Orbiter Conjunction of June 2020. *Astron. Astrophys.* 659, A110. doi:10.1051/0004-6361/202142381

Sorriso-Valvo, L., Yordanova, E., Dimmock, A. P., and Telloni, D. (2021). Turbulent Cascade and Energy Transfer Rate in a Solar Coronal Mass Ejection. *Astrophys. J. Lett.* 919, L30. doi:10.3847/2041-8213/ac26c5

Telloni, D., Andretta, V., Antonucci, E., Bemporad, A., Capuano, G. E., Fineschi, S., et al. (2021a). Exploring the Solar Wind from its Source on the Corona into the Inner Heliosphere during the First Solar Orbiter-Parker Solar Probe Quadrature. *Astrophys. J. Lett.* 920, L14. doi:10.3847/2041-8213/ac282f

Telloni, D., Bruno, R., and Trenchi, L. (2015). Radial Evolution of Spectral Characteristics of Magnetic Field Fluctuations at Proton Scales. *Astrophys. J.* 805, 46. doi:10.1088/0004-637X/805/1/46

Telloni, D., Sorriso-Valvo, L., Woodham, L. D., Panasenco, O., Velli, M., Carbone, F., et al. (2021b). Evolution of Solar Wind Turbulence from 0.1 to 1 au during the First Parker Solar Probe-Solar Orbiter Radial Alignment. *Astrophys. J. Lett.* 912, L21. doi:10.3847/2041-8213/abf7d1

Telloni, D., Zhao, L., Zank, G. P., Liang, H., Nakanotani, M., Adhikari, L., et al. (2020). Magnetohydrodynamic Turbulent Evolution of a Magnetic Cloud in the Outer Heliosphere. *Astrophys. J. Lett.* 905, L12. doi:10.3847/2041-8213/abcb03

Thernisien, A., Vourlidas, A., and Howard, R. A. (2011). CME Reconstruction: Pre-STEREO and STEREO Era. *J. Atmos. Sol.-Terr. Phys.* 73, 1156–1165. doi:10.1016/j.jastp.2010.10.019

Velli, M., Harra, L. K., Vourlidas, A., Schwadron, N., Panasenco, O., Liewer, P. C., et al. (2020). Understanding the Origins of the Heliosphere: Integrating Observations and Measurements from Parker Solar Probe, Solar Orbiter, and Other Space- and Ground-Based Observatories. *Astron. Astrophys.* 642, A4. doi:10.1051/0004-6361/202038245

Weiss, A. J., Möstl, C., Davies, E. E., Amerstorfer, T., Bauer, M., Hinterreiter, J., et al. (2021). Multi-point Analysis of Coronal Mass Ejection Flux Ropes Using Combined Data from Solar Orbiter, BepiColombo, and Wind. *Astron. Astrophys.* 656, A13. doi:10.1051/0004-6361/202140919

Witasse, O., Sánchez-Cano, B., Mays, M. L., Kajdič, P., Opgenoorth, H., Elliott, H. A., et al. (2017). Interplanetary coronal mass ejection observed at STEREO-A, Mars, comet 67P/Churyumov-Gerasimenko, Saturn, and New Horizons en route to Pluto: Comparison of its Forbush decreases at 1.4, 3.1, and 9.9 AU. *J. Geophys. Res. Space Phys.* 122, 7865–7890. doi:10.1002/2017JA023884

Wood, B. E., Howard, R. A., Thernisien, A., Plunkett, S. P., and Socker, D. G. (2009). Reconstructing the 3D Morphology of the 17 May 2008 CME. *Sol. Phys.* 259, 163–178. doi:10.1007/s11207-009-9391-0

Zank, G. P., Zhao, L. L., Adhikari, L., Telloni, D., Kasper, J. C., and Bale, S. D. (2021). Turbulence Transport in the Solar Corona: Theory, Modeling, and Parker Solar Probe. *Phys. Plasmas* 28, 080501. doi:10.1063/5.0055692

Conflict of Interest: The author declares that the research was conducted in the absence of any commercial or financial relationships that could be construed as a potential conflict of interest.

frontiers | Frontiers in Astronomy and Space Sciences

ORIGINAL RESEARCH
published: 17 June 2022
doi: 10.3389/fspas.2022.910730

Plasma Imaging, LOcal Measurement, and Tomographic Experiment (PILOT): A Mission Concept for Transformational Multi-Scale Observations of Mass and Energy Flow Dynamics in Earth's Magnetosphere

David Malaspina[1,2], Robert Ergun[1,2], Jerry Goldstein[3], Constance Spittler[2], Laila Andersson[2], Joseph Borovsky[4], Xiangning Chu[2], Lauren De Moudt[5], Dennis Gallagher[6], Vania Jordanova[7], Solène Lejosne[8], Jason Link[2], Naomi Maruyama[2], Jeffery Parker[5], Scott Thaller[2], Bryce Unruh[2] and Brian Walsh[9]*

[1]Astrophysical and Planetary Sciences Department, University of Colorado, Boulder, CO, United States, [2]Laboratory for Atmospheric and Space Physics, University of Colorado, Boulder, CO, United States, [3]Southwest Research Institute, San Antonio, TX, United States, [4]Space Science Research Institute, Boulder, CO, United States, [5]Advanced Space LLC, Westminster, CO, United States, [6]NASA Marshall Spaceflight Research Center, Huntsville, AL, United States, [7]Los Alamos National Laboratory, Los Alamos, NM, United States, [8]Space Sciences Laboratory, University of California, Berkeley, Berkeley, CA, United States, [9]College of Engineering, Boston University, Boston, MA, United States

OPEN ACCESS

Edited by:
Luca Sorriso-Valvo, Institute for Space Physics (Uppsala), Sweden

Reviewed by:
Filomena Catapano, European Space Research Institute (ESRIN), Italy
Rungployphan Om Kieokaew, UMR5277 Institut de Recherche en Astrophysique et Planétologie (IRAP), France

***Correspondence:**
David Malaspina
David.Malaspina@colorado.edu

Specialty section:
This article was submitted to Space Physics, a section of the journal Frontiers in Astronomy and Space Sciences

Received: *01 April 2022*
Accepted: *17 May 2022*
Published: *17 June 2022*

Citation:
Malaspina D, Ergun R, Goldstein J, Spittler C, Andersson L, Borovsky J, Chu X, De Moudt L, Gallagher D, Jordanova V, Lejosne S, Link J, Maruyama N, Parker J, Thaller S, Unruh B and Walsh B (2022) Plasma Imaging, LOcal Measurement, and Tomographic Experiment (PILOT): A Mission Concept for Transformational Multi-Scale Observations of Mass and Energy Flow Dynamics in Earth's Magnetosphere. Front. Astron. Space Sci. 9:910730. doi: 10.3389/fspas.2022.910730

We currently do not understand the fundamental physical processes that govern mass and energy flow through the Earth's magnetosphere. Knowledge of these processes is critical to understanding the mass loss rate of Earth's atmosphere, as well as for determining the role that a planetary magnetic field plays in atmospheric retention, and therefore habitability, for Earth-like planets beyond the solar system. Mass and energy flow processes are challenging to determine at Earth in part because Earth's planetary magnetic field creates a complex "system of systems" composed of interdependent plasma populations and overlapping spatial regions that perpetually exchange mass and energy across a broad range of temporal and spatial scales. Further, the primary mass carrier in the magnetosphere is cold plasma (as cold as ~0.1 eV), which is invisible to many space-borne instruments that operate in the inner magnetosphere. The Plasma Imaging LOcal and Tomographic experiment (PILOT) mission concept, described here, provides the transformational multi-scale observations required to answer fundamental open questions about mass and energy flow dynamics in the Earth's magnetosphere. PILOT uses a constellation of spacecraft to make radio tomographic, remote sensing, and *in-situ* measurements simultaneously, fully capturing cold plasma mass dynamics and its impact on magnetospheric systems over an unprecedented range of spatial and temporal scales. This article details the scientific motivation for the PILOT mission concept as well as a potential mission implementation.

Keywords: inner magnetosphere, plasmasphere, cold plasma, mission concept, mass transport

1 INTRODUCTION

Magnetospheric physics has a massive problem: we have not yet determined the fundamental processes that govern plasma mass and energy flow through the terrestrial magnetosphere, nor the degree to which these flows regulate key magnetospheric subsystems.

Hundreds of metric tons of ionized atmospheric gases pass into and through Earth's magnetic field. This mass accumulates in inner magnetospheric reservoirs, is transported through the magnetosphere, where it profoundly regulates magnetospheric subsystems, and can eventually be lost to the solar wind. Cold plasma (< 1–100 eV) carries the overwhelming majority of this mass, and tracking its flow is the weakest link in our chain of understanding for magnetospheric physics (Delzanno et al., 2021). Currently, we understand more about the physics of atmospheric mass loss at Mars and Venus than we do at Earth (Titov et al., 2006; Jakosky, 2015). Understanding magnetospheric mass flows and associated energy flows is critical to understanding the mass loss rate of Earth's atmosphere, as well as to determining the importance of a planetary magnetic field for atmospheric retention (Ramstad and Barabash, 2021), and therefore habitability, for Earth-like planets beyond the solar system.

Knowledge gaps related to the processes that govern plasma mass and energy flow through the magnetosphere have persisted through decades of magnetospheric measurements due to three primary limitations. First, the Earth's planetary magnetic field creates a complex "system of systems" composed of interdependent plasma populations and overlapping spatial regions that perpetually exchange mass and energy. Because of this complexity, inherent to any planet with an internal dynamo-driven magnetic field, measurements are required that span a broad range of temporal and spatial scales in order to disentangle the coupled processes that drive mass and energy flow. Second, cold plasma is not directly detectable by most space-borne particle instruments traversing the inner magnetosphere, because its thermal energy is well below the floating electrical potential of spacecraft surfaces immersed in the ambient plasma (Delzanno et al., 2021). To make new progress, instrumentation specifically designed to detect cold plasma is required. Third, prior observations of mass flow and its impact on magnetospheric subsystems are limited to either single-spacecraft local measurements of total plasma density with limited composition data and no contextual mass spatial distribution information (Engwall et al., 2009; Kurth et al., 2015; Andriopoulou et al., 2018), or to single-view line-of-sight integrated measurements of minor ion species without *in-situ* measurements embedded in the imaged plasma (Sandel et al., 2001). New progress requires combining measurements of the plasma mass spatial distribution in the inner magnetosphere with simultaneous embedded *in-situ* measurements.

The Plasma Imaging LOcal and Tomographic experiment (PILOT) mission concept overcomes all three of these limitations by using a constellation of 34 spacecraft to simultaneously make rapidly refreshing, spatially resolved images of total plasma density in the equatorial plane, images of ion density and flows in the meridional plane, and *in-situ* ground-truth measurements embedded within the imaged regions.

The PILOT mission concept constellation consists of 30 identical microsat spacecraft ('RadioSats') and four smallsat spacecraft ("PlasmaSats") in two near-equatorial orbits. The network of RadioSats produce equatorial plasma density images through radio tomographic inversion of a network of line-of-sight total electron content (TEC) measurements (see **Supplementary Appendix S1** and Ergun et al. (2000)), combined with *in-situ* total plasma density measurements. The resulting density images have high spatial ($\sim 0.5\ R_E$) and temporal ($\sim 15\ s$) resolution. Meridional ion density and flows are determined by imaging extreme ultraviolet (EUV) photons at 30.4 nm (He^+) and 83.4 nm (O^+/O^{++}) (Sandel et al., 2001; Burch et al., 2001a; Burch et al., 2001b; Burch, 2001; Goldstein et al., 2003; Goldstein et al., 2018; Goldstein et al., 2019), with high spatial ($\sim 0.05\ R_E$) and temporal ($< 15\ s$) resolution. Two of the four PlasmaSats carry EUV instruments. All four PlasmaSats are equipped to make embedded *in-situ* measurements of both DC-coupled and AC-coupled electric and magnetic fields, cold plasma composition, flux, and distribution functions, as well as energetic proton and electron flux and distribution functions.

The PILOT spacecraft are arranged in two highly-elliptical orbits (1.52 R_E x 4.25 R_E and 1.10 R_E x 6.25 R_E). The orbits are optimized to enable 1) near-equatorial radio tomographic images with instantaneous coverage over a large region of the inner magnetosphere: ~ 3 Earth radii (R_E) in radial distance and ~ 3 hrs in MLT, 2) coverage in the meridional plane of ±4.8 R_E for He^+ images and ±2.2 R_E for O^+ images, and 3) *in-situ* measurements along orbits with apogees near L-shells of 4 and 6, embedded within the imaged plasma.

The PILOT implementation leverages several technological innovations to support a fully feasible mission. First, spacecraft manufacturing has matured to the point where numerous commercial vendors exist that can produce spacecraft in the quantities needed for radio tomographic imaging (a few tens of spacecraft). Second, instrumentation miniaturization has progressed such that relatively small spacecraft can host the range of instruments needed for PILOT *in-situ* measurements. Third, the launch and deployment of large spacecraft constellations has become commonplace, and a number of technologies that enable constellation deployment are now available.

By taking advantage of these technological advancements, the PILOT mission concept makes the transformational measurements needed to close fundamental and persistent knowledge gaps about mass and energy flow through the magnetosphere of a magnetized terrestrial planet.

The following sections first lay out the specific science goals and objectives that motivate the PILOT mission concept, then discuss the measurements required to achieve them. A mission implementation is then described, including notional orbits, spacecraft bus configurations, and instrumentation. A detailed discussion on the generation of plasma density images by radio tomography for PILOT is included in **Supplementary Appendix S1**. Finally, inversion and forward model algorithms that can be

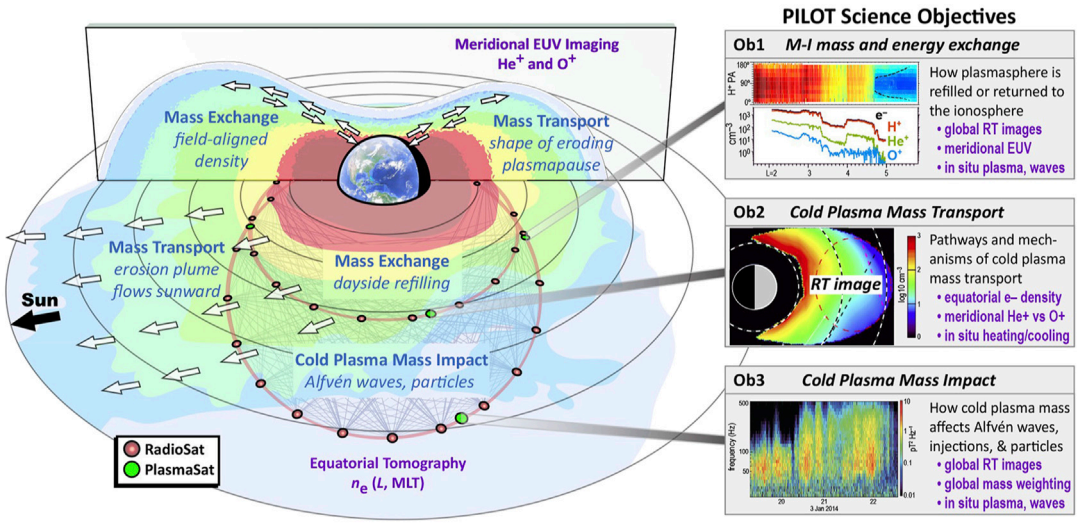

FIGURE 1 | Overview of PILOT science objectives and high-level measurement strategy. Black solid lines indicate radial distance (1 Earth radius intervals) in the equatorial plane. The light red solid lines show the two orbital paths of PILOT spacecraft. See text for details. The sub-figure illustrating objective 1 is adapted from Figure 3 in Goldstein et al. (2019). The sub-figure illustrating objective 3 is adapted from Figure 1 in Breneman et al. (2015).

used for EUV image deconvolution are discussed in **Supplementary Appendix S2**.

2 MOTIVATING SCIENCE GOALS AND OBJECTIVES

The driving science goal of PILOT is to determine the primary pathways of mass and energy flow through the coupled systems of the terrestrial magnetosphere. This goal motivates three specific science objectives. Each targets a critical aspect of mass and energy exchange among the plasma populations that make up the magnetospheric meta-system. The science objectives are arranged to "follow the mass" as ionized gases exit the ionosphere, enter and are transported through and out of the inner magnetosphere, and profoundly modify magnetospheric systems and magnetospheric energy transport along their journey.

The PILOT science objectives are: 1) Identify and quantify the key processes that govern mass and energy exchange between the ionosphere and the magnetosphere, 2) Discover the pathways and processes governing cold plasma mass transport through and out of the inner magnetosphere, and 3) Determine how, where, and when cold plasma mass acts most efficiently to regulate coupling between magnetospheric regions and between plasma populations. Achieving each science objective requires addressing specific science questions, listed and described below.

Figure 1 presents an overview of PILOT's science objectives and high-level measurement strategy: simultaneous radio tomography, EUV imaging, and embedded *in-situ* measurement. The radio tomographic mesh formed by the RadioSats is shown in the equatorial plane, the meridional plane imaged by the outer-orbit PlasmaSatEUV instruments is shown, and locations of all four *in-situ* measurements (PlasmaSats) are indicated. RadioSats and PlasmaSats are discussed in **Section 3.1**. Plasma density is represented by colored contours, where the equatorial mass distribution is adapted from an EUV image in Figure 2B of Goldstein et al. (2004a). The meridional mass distribution is schematic, based on simulated EUV images created using the forward model of Goldstein et al. (2018). PILOT's three science objectives (Ob1, Ob2, and Ob3) are indicated on the right of the figure. The science questions that underpin those objectives are discussed in detail next.

2.1 Objective 1, Science Question 1a: How Is the Plasmasphere Refilled From Ionospheric Sources?

When atmospheric gases are ionized, by solar radiation or electron bombardment, electromagnetic interaction with the solar wind causes them to flow out of the ionosphere (e.g., Banks, 1968; Banks, 1969; Singh and Horwitz, 1992). Earth's planetary magnetic field traps much of this plasma in the plasmasphere, preventing it from escaping directly to the solar wind (Chappell, 2015). During geomagnetic storms, some of the mass held in this reservoir is forced into the solar wind and lost from the magnetosphere. Ionospheric outflow then refills the plasmaspheric reservoir and the process repeats (Hultqvist et al., 1999; Welling et al., 2015).

After decades of research, fundamental questions concerning plasmaspheric refilling remain unanswered. The observations required to address these questions do not yet exist (Gallagher et al., 2021). In this observational void, gaps in our basic knowledge persist: What causes refilling rates to vary by orders of magnitude? Why is the amount of mass trapped by the magnetosphere only weakly correlated with the polar

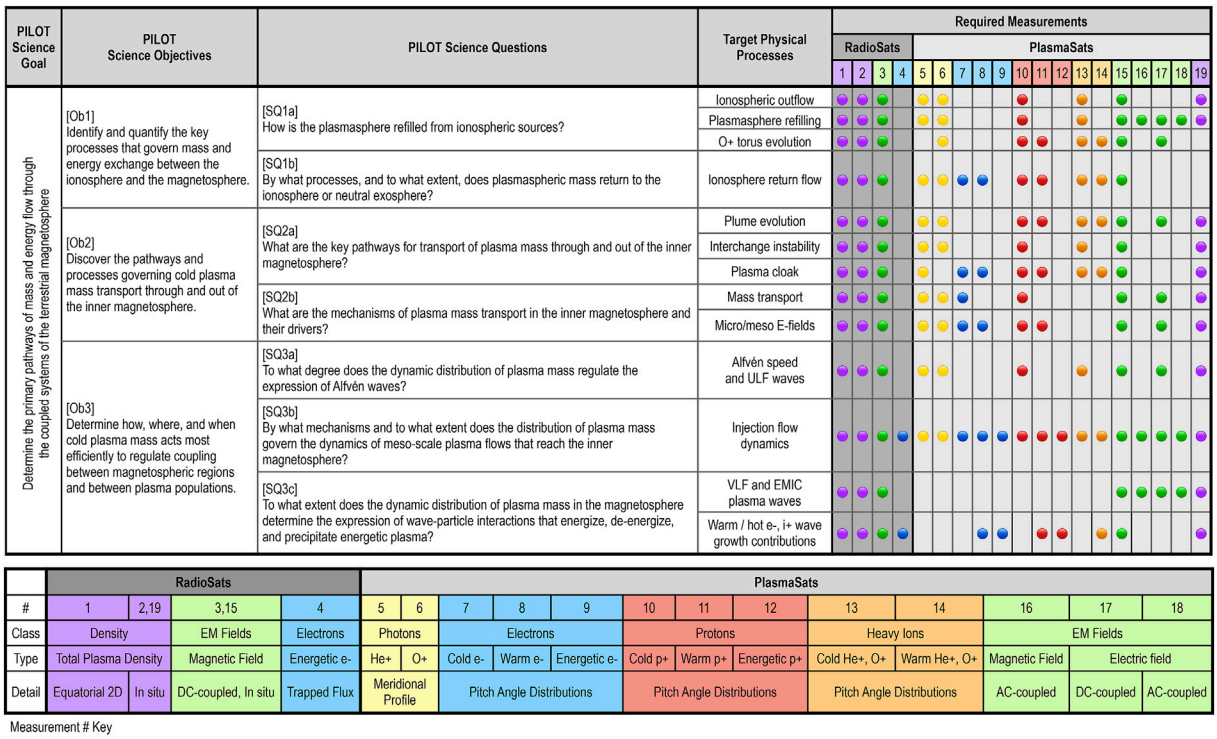

FIGURE 2 | Logical flow from PILOT science goal, to science questions, to targeted physical processes, to required measurements.

outflow rates (Denton et al., 2012)? What fundamental plasma processes are responsible for trapping new ions in the plasmasphere torus (Goldstein et al., 2020; Goldstein et al., 2021)?

Ionospheric outflow and plasmaspheric refilling shows intense variability (Gallagher et al., 2021). For $2.5 \leq L \leq 4.5$ refilling rates range from 4 to 800 cm^{-3} day^{-1} (Park, 1973; Park, 1974; Farrugia et al., 1989; Carpenter et al., 1993; Reinisch et al., 2004; Dent et al., 2006; Sandel and Denton, 2007; Gallagher et al., 2021). At geosynchronous orbit, quiet-time refilling rates range from as little as ~0.6 cm^{-3} day^{-1} (Lawrence et al., 1999) to as much as 50 cm^{-3} day^{-1} (Sojka et al., 1986). In stark contrast, Borovsky et al. (2014) discovered long-lived plasmaspheric plume active-time events at geosynchronous orbit that could only persist if fueled by refilling rates of 100–500 cm^{-3} day^{-1}.

We lack basic knowledge about the formation of the dense O^+ torus in the outer plasmasphere (Horwitz and Lockwood, 1985; Roberts et al., 1987; Andersson et al., 2005; Goldstein et al., 2018; Hull et al., 2019). Two possible origins for the O^+ torus have been identified: it may originate from the local ionosphere near the magnetic equator, or it could arrive in part or in total from high latitude as the low energy portion of the warm plasma cloak (Chappell et al., 2008).

The PILOT mission concept achieves closure on this science question by comparing multi-scale measurements of cold plasma mass flow and variability over a broad swath of the inner magnetosphere against theories for ion trapping (Hrbáčková et al., 2015), refilling variability (Gallagher et al., 2021), refilling mass dependence (Sandel, 2011), and O^+ torus formation (Goldstein et al., 2018).

These comparisons are enabled by direct and simultaneous measurement of: 1) spatially and temporally resolved plasma density across a broad region of the near-equatorial inner magnetosphere [≥ 3 h Magnetic Local Time (MLT)], covering radial distances (3 < L-shell < 6) where field aligned ions are converted into trapped isotropic distributions during plasmasphere refilling, 2) global meridional EUV-He measurements to quantify the spatial and temporal evolution of field-aligned light ion distributions, 3) *in-situ* observations, embedded within the imaged regions, of cold (0.1–100 eV) H^+, He^+, and O^+ distribution functions, densities, and temperatures, as well as plasma waves that may isotropize outflowing ions (Gurnett, 1976; Olsen et al., 1987; Boardsen et al., 1992; Singh, 1996; Hrbáčková et al., 2015), and 4) EUV global meridional imaging of O^+, to determine the extent to which O^+ torus ions are supplied from the ionosphere, by cusp outflow, or directly from the auroral zone (Horwitz and Lockwood, 1985; Roberts et al., 1987; Hull et al., 2019). Imaging the O^+ torus enables its basic morphology to be quantified, including its symmetry (or lack thereof) in MLT, its latitudinal extent, and what processes control these attributes (Nosé et al., 2011; Nosé et al., 2015; Goldstein et al., 2018; Nosé et al., 2018). *In-situ* observations for this science question must cover radial distances where refilling is most dynamic (3 < L-shell < 6), in the minutes, hours, and days that follow geomagnetically active times.

2.2 Objective 1, Science Question 1b: By What Processes, and to What Extent, Does Plasmaspheric Mass Return to the Ionosphere or Neutral Exosphere?

A full accounting of mass flow between the ionosphere and plasmasphere must include flow from the plasmasphere back into the ionosphere (Lemaire and Gringauz, 1998) or neutral exosphere (Nass and Fahr, 1984). There is a large knowledge gap related to this mass flow pathway. In the absence of sunlight, low-altitude recombination reduces ion pressure gradients, which is expected to cause downward transport (Lemaire and Gringauz, 1998; Gallagher et al., 2021), allowing nightside flux tubes to return plasmaspheric mass to the ionosphere. This mechanism may explain the anomalous mass loss reported on L-shells far from the eroded plasmapause boundary (Gallagher et al., 2021). However, the cross-scale measurements required to test this hypothesis, or to identify a new one, currently do not exist.

PILOT achieves closure on this science question by comparing existing predictions for downward ion transport of plasmaspheric mass (Gallagher et al., 2021) with direct multi-scale measurements of cold plasma mass content and its variability.

Making these comparisons requires direct and simultaneous measurements of: 1) spatially and temporally resolved total plasma density over several hours of MLT and several L-shell, 2) meridional imaging of ionospheric plasma inflows (of both light ions and O^+), and 3) *in-situ* observations of cold (0.1–100 eV) proton and heavy ion distribution functions embedded in the imaged regions. The observations most effective at addressing this science question will be within 3 < L-shell < 5, where plasmapause erosion is weakly active during quiet or moderately-disturbed times.

2.3 Objective 2, Science Question 2a: What Are the Key Pathways for Transport of Plasma Mass Through and Out of the Inner Magnetosphere?

After cold plasma mass reaches the plasmasphere, it is distributed and transported to other magnetospheric regions. Known and speculated mass transport pathways include plasmaspheric plume flows (Darrouzet et al., 2009), interchange instability (Pierrard and Lemaire, 2004), and the warm plasma cloak (Borovsky et al., 2013; Gallagher and Comfort, 2016). Each transport pathway is driven by different, sometimes competing, physical mechanisms. Limited existing measurements prevent us from knowing which mass flow pathways are most important under which geomagnetic conditions, what feedback exists among transport mechanisms, and how these mechanisms combine to produce the observed distribution of mass in the magnetosphere.

A plasmaspheric plume is a dramatic structure formed by sunward plasma transport, where the density can be 50–100 times greater than adjacent regions. A plume can span many Earth radii (5 R_E or more) or be narrow (< 1 R_E). A plume can detach from the plasmasphere and extend into the dayside magnetopause. A basic understanding of how a plasmaspheric plume forms and maintains itself is lacking. A plume can form over the course of tens of minutes. It can be short lived (hours) or last for weeks (Borovsky et al., 2014; Krall et al., 2018). The physics that drives the refilling necessary to sustain this structure and quantification of the appropriate refilling rates both remain poorly determined (Denton and Borovsky, 2014; Gallagher and Comfort, 2016).

The warm plasma cloak is a population outside the plasmasphere transported in from the magnetotail, rich with oxygen (Chappell et al., 2008; Nose et al., 2015; Jahn et al., 2017). Many key questions remain about the transport and coupling of this population. What mechanism is responsible for heating the cloak plasma (Hill et al., 2020)? Does the plasma cloak play a dominant role in mass loading the dayside magnetosphere (Borovsky et al., 2013)? Is the cloak a candidate for nightside plasmasphere refilling (Gallagher and Comfort, 2016)?

PILOT achieves closure on this science question by comparing the observed morphology of cold plasma flows in the near-equatorial magnetosphere, and signatures of cold ion heating or cooling, against theoretical expectations for each pathway.

These comparisons require measurement of rapidly refreshing images of total plasma density in the near-equatorial plane across several MLT in the inner magnetosphere. Observations must target radial distances where strong transport is observed ($3 < L < 6$). Simultaneously, meridional plasma flows of He^+ and O^+ must be imaged to determine whether equatorial plasma density changes are due to flows out of the equatorial plane or within it. Embedded *in-situ* observations of heavy (He^+, O^+) and light (H^+) ion distributions spanning 0.1–100 eV are required to observe heating or cooling of cold plasma that may be a prerequisite for some transport pathways (Borovsky et al., 2013).

2.4 Objective 2, Science Question 2b: What Are the Mechanisms of Plasma Mass Transport and Their Drivers?

Once ionospheric plasma mass reaches the plasmasphere, it may go sunward to the dayside magnetopause and participate in reconnection, or it may be diverted to the flanks and travel anti-sunward to load the plasmasheet. What fundamental mechanisms dictate the transport and distribution of this mass?

Mass transport is expected to be primarily determined by the dynamic electric and magnetic fields in the magnetosphere. While the geomagnetic field is relatively well-known, the electric (E) field is more elusive. Single-point *in-situ* E-field measurements have been leveraged to create empirical models, i.e., statistical maps. However, empirical models usually impose an electrostatic assumption ($\nabla \times E = 0$). Although it facilitates visualization of convective pathways (Matsui et al., 2013), the validity of this assumption is questionable, in particular at higher L-shells. It is also difficult to quantify the extent to which statistical models can accurately describe dynamical evolution in case studies.

Moreover, statistical data analysis blurs/obscures small scale features and/or highly structured features naturally present in the database. These features include sub-auroral polarization streams (SAPS) (Foster et al., 2007) and sub-auroral ion drifts (SAID) (Anderson et al., 1991). While statistical experimental models for

SAPS exist (Kunduri et al., 2018), how they connect to the global topology of the electric fields, thus, how they organize plasma mass transport, remains unclear (Elphic et al., 1997; Liemohn et al., 2004; Foster et al., 2020).

Small-scale features are definitely present in the global electric field topology, but their role in plasma transport remains to be determined. For instance, to what extent is plasmasphere erosion governed by global vs. local electric field dynamics? Observations from the IMAGE EUV instrument revealed the existence of many small scale structures on the plasmasphere boundary, including notches, crenulations, fingers and shoulders. The time evolution of these structures was leveraged to extract information about the average spatial variability of the large-scale DC electric field (Galvan et al., 2010). Yet statistical models for the electric field dynamics seldom accurately reproduce such features (Goldstein and Sandel, 2005).

PILOT achieves closure on this science question by comparing electric field drivers and magnetic field context with the resulting plasma mass motion, allowing key transport mechanisms to be identified.

Measuring bulk plasma motion requires rapidly refreshing images of total density in the equatorial plane. Embedded in the image plane, *in-situ* point observations of DC-coupled electric and magnetic fields, along with measurements of cold proton, electron, and heavy ion distribution functions, provide ground truth point-sampling of the cold plasma bulk motion and the electric fields that drive it. Simultaneous meridional imaging of cold plasma flow is required to quantify transport into and out of the equatorial plane. This set of measurements enables determination of the mechanisms and drivers of cold plasma mass transport.

2.5 Objective 3, Science Question 3a: To What Degree Does the Dynamic Distribution of Plasma Mass Regulate the Expression of Alfvén Waves?

Propagating at the Alfvén speed, Ultra Low Frequency (ULF) waves carry information via magnetic field fluctuations that enable magnetosphere-ionosphere coupling (Lysak, 1990), magnetosphere-solar wind coupling (Wright, 1996), as well as radiation belt energization and particle transport via radial diffusion (Elkington et al., 2003).

The inner magnetosphere supports various ULF modes, including those that carry energy Earthward from the magnetotail and from the magnetopause (Takahashi et al., 2015). These energy inputs can either drive propagating waves, or drive field line resonances and cavity modes (Dungey, 1955; Samson and Rostoker, 1972; Kivelson and Southwood, 1985; Lee and Lysak, 1989; Samson et al., 1992). Energy flux transport *via* these modes, and energy exchange between these modes is critically sensitive to the Alfvén speed.

Modeling has shown that the spatial distribution of plasma mass should significantly alter the ULF wave power distribution, both radially and in MLT. For example, the plasma mass distribution determines the radial location where the compressional (fast mode) radial wavenumber goes to zero, beyond which compressional waves transfer energy into local field line resonances (Claudepierre et al., 2016).

PILOT achieves closure on this science question by measuring the dynamic spatial distribution of Alfvén speed, across scale sizes, over a broad region of the inner magnetosphere, while simultaneously quantifying the degree to which this distribution regulates ULF plasma wave properties.

Determining the spatial distribution of Alfvén speed requires a network of magnetic field measurements and total plasma density images. This information must be sampled on timescales faster than plasma mass is redistributed in order to resolve temporal changes to this distribution (likely minutes or faster). A network of magnetic field measurements over a broad region of space is required to measure fluctuating ULF-wave magnetic fields to establish how ULF wave amplitudes and modes (e.g., field line resonance or propagating mode) are determined by the spatial distribution of total plasma density. The Alfvén speed is also a function of plasma mass density. Therefore, point measurements of ion composition (H^+, He^+, and O^+) embedded within the total plasma density image plane are required to determine the extent to which the spatial distribution of cold ions significantly impacts ULF wave properties.

2.6 Objective 3, Science Question 3b: By What Mechanisms and to What Extent Does the Distribution of Plasma Mass Govern the Dynamics of Meso-Scale Plasma Flows That Reach the Inner Magnetosphere?

The Dungey cycle (Dungey, 1961) describes the fundamental flow of magnetic energy and flux through Earth's solar-wind driven magnetosphere. A key portion of the Dungey cycle involves the return flow of magnetic field and plasma sunward from the magnetotail. Numerous studies have established that these return flows take the form of structured plasma flows, often called Bursty Bulk Flows (BBFs) (Baumjohann et al., 1989; Angelopoulos et al., 1992; Angelopoulos et al., 1994; Runov et al., 2011; Wiltberger et al., 2015). The evolution of BBFs is well understood $> \sim 8R_E$ from Earth. BBFs originate in the magnetotail beyond $\sim 15R_E$ (Ohtani et al., 2006; Sitnov et al., 2009; Runov et al., 2011). They are accompanied by dipolarization of the Earth's magnetic field (Angelopoulos, 2008). BBFs are known to be responsible for much of the energy transport from the Earth's magnetotail into the inner magnetosphere [Turner et al. (2015); Stawarz et al. (2016) and references therein] and are known to drive ionospheric energy deposition, as demonstrated by their association with specific auroral forms (Sergeev et al., 1999; Sergeev et al., 2000; Nakamura et al., 2001; Stawarz et al., 2015).

BBF velocities slow to the order of 100 km/s as they travel from $\sim 12R_E$ to $\sim 8R_E$ and the Earth's magnetic field becomes stronger. This region, called the BBF braking region (McPherron et al., 2011), displays strong turbulence, wherein ions and electrons are energized and Alfvén waves are launched toward Earth's ionosphere (Ergun et al., 2015). The fate of BBFs is not well understood Earthward of $\sim 8R_E$, where their flow speed is again dramatically reduced (Reeves et al., 1996; Malaspina et al., 2015).

One of the many unknowns is how BBFs inject energetic particles and heavy ions into the inner magnetosphere (Takada et al., 2006; Dubyagin et al., 2011; Gkioulidou et al., 2014; Turner et al., 2015).

Mounting evidence indicates that the distribution of plasmaspheric mass determines the final deceleration of Earthward plasma flows (Li et al., 2011; Khoo et al., 2018; Glocer et al., 2020; Allison et al., 2021), thereby regulating the deposition of their remaining flow energy into the inner magnetosphere, and their ability to transport plasmasheet particles into the inner magnetosphere (Sorathia et al., 2018). Further, the Poynting flux generated during BBF breaking is implicated in the energization of ions in the ionosphere and subsequent production of low-energy ion outflow that contributes to re-population of the outer plasmasphere (Chaston et al., 2016).

Fundamental aspects of Earthward flow physics cannot be determined using single-point or serendipitous multi-point *in-situ* measurements. A lack of coordinated *in-situ* and context imaging measurements prevents quantitative evaluation of how the energy and mass carried by these flows is redistributed through the inner magnetosphere as they slow and stop. Evidence from multi-spacecraft case studies (Motoba et al., 2020) supports the long-suspected [e.g., Turner et al. (2015) and Turner et al. (2017)] and references therein connection between BBFs and the particle injections that supply the ring current (Gkioulidou et al., 2014), as well as radiation belt source and seed particles (Jaynes et al., 2015).

PILOT achieves closure on this SQ by determining the extent to which cold plasma regulates plasma flow evolution in the inner magnetosphere, including particle injection physics and energy transfer from flows to plasma waves.

A network of magnetic field sensors and rapidly refreshing total density maps are required to end long-persistent questions about the flow spatial structure and deceleration in the inner magnetosphere (e.g., Reeves et al., 1996; Wiltberger et al., 2015; Khoo et al., 2018)). A network of energetic electron flux measurements are required to definitively connect flow deceleration with electron injection spatial and temporal evolution, including energy-dependent radial penetration (Li et al., 2011; Turner et al., 2015; Turner et al., 2017; Khoo et al., 2018; Glocer et al., 2020; Motoba et al., 2020; Allison et al., 2021). Embedded within the density image plane, *in-situ* ground-truth observations are needed. Electron, proton, and heavy ion distribution functions across a wide range of energies (0.1 eV–1 MeV for e- and p+, up to 50 keV for heavy ions) are required to determine the evolution of flow-entrained particles. DC-coupled electric and magnetic field observations are required to definitively identify injection flows. AC-coupled electric and magnetic field measurements are needed to observe dissipation of flow energy into plasma waves. Meridional cold plasma observations, made in concert with the previously described measurements, are needed to constrain the amount of new ion outflow that results from flow-breaking energy input into the ionosphere (Chaston et al., 2016) during the dissipation of flow events. A typical flow is expected to be 1 to $2R_E$ in radial and azimuthal spatial extent, traveling Earthward at 35 km/s with a total plasma density (n_e) fractional depletion of $\Delta n_e/n_e \approx 50\%$ (Reeves et al., 1996; Runov et al., 2011; Fletcher et al., 2019). Given these parameters, a density image spatial resolution of $\leq 0.5\ R_E$ and temporal resolution of < 20 s are needed to fully characterize these flows (Yang et al., 2014; Liu et al., 2015).

2.7 Objective 3, Science Question 3c: To What Extent Does the Dynamic Distribution of Plasma Mass in the Magnetosphere Determine the Expression of Wave-Particle Interactions That Energize, De-Energize, and Precipitate Energetic Plasma?

Plasma waves are a fundamental driver of particle energization and loss in the inner magnetosphere (Horne et al., 2005; Thorne, 2010; Jaynes et al., 2015). Ambient cold plasma density and magnetic field strongly determine the efficiency of the relevant wave-particle interactions on kinetic scales (Young et al., 1981; Kozyra et al., 1984; Summers et al., 1998; Omura et al., 2007). However, our knowledge of the spatial extent of these processes currently relies on an elaborate chain of complex modeling and statistical inference (Ni et al., 2014; Meredith et al., 2018; Zhang et al., 2018; He et al., 2020; Malaspina et al., 2020; Meredith et al., 2020; Delzanno et al., 2021). Predictions resulting from this chain often sharply disagree with any individual geomagnetic event (Jaynes et al., 2018; Watt et al., 2019), especially for extreme driving cases, blurring the picture as to which plasma wave processes are most relevant under which geomagnetic conditions.

Some of the plasma wave modes most effective at sculpting particle populations in the inner magnetosphere are Very Low Frequency (VLF) waves such as chorus and hiss (e.g., Horne et al., 2005; Thorne, 2010; Ripoll et al., 2014; Breneman et al., 2015), and electromagnetic ion cyclotron (EMIC) waves (e.g. Sandanger et al., 2007; Usanova et al., 2014; Shprits et al., 2016).

Plasma density regulates the growth and damping of these wave modes (Nicholson, 1983; Summers et al., 1998; Agapitov et al., 2019). Because of this, the plasmapause defines a sharp boundary between hiss (radiation-belt loss) and chorus (radiation-belt energization and/or loss) (Thorne, 2010; Malaspina et al., 2016; Malaspina et al., 2018), making it a critical boundary for radiation belt dynamics (Baker et al., 2013), auroral precipitation (He et al., 2020) and ionospheric heating (Liang et al., 2018).

The generation and propagation of EMIC waves depend strongly on plasma density and ion composition (Young et al., 1981; Kozyra et al., 1984). In a multi-component plasma, EMIC waves appear frequency bands separated by the cyclotron frequencies of individual ion species. Models show that EMIC source regions overlap with regions of anisotropic ring current protons and plasmaspheric drainage plumes (Jordanova et al., 2001; Chen et al., 2010). Simulated global images of proton precipitation match the temporal and spatial evolution of IMAGE observations of subauroral proton arcs, indicating that cyclotron resonant wave-particle interactions are a viable mechanism for their generation (Jordanova et al., 2007). Observationally, however, the dependence of EMIC waves on cold plasma density and/or density gradients is controversial

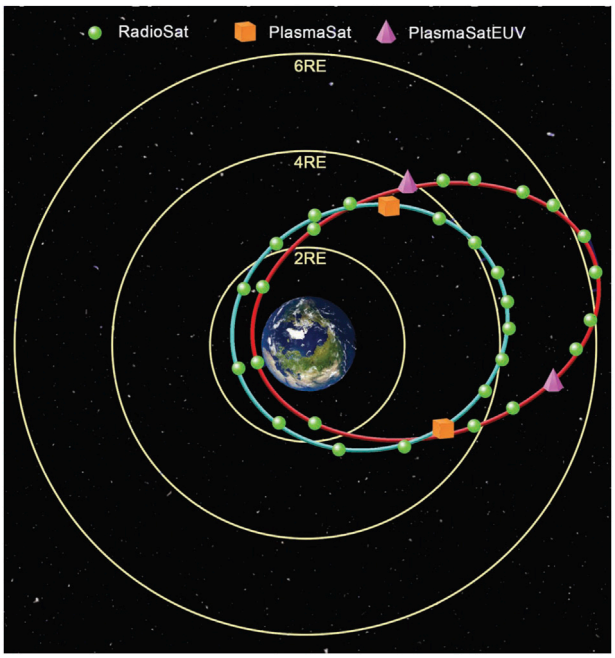

FIGURE 3 | PILOT spacecraft orbits, shown from a vantage point orthogonal to the orbit plane, which has a 0^o latitude inclination.

(Usanova et al., 2013; Engebretson et al., 2015; Halford et al., 2015).

PILOT achieves closure on this science question by determining the degree to which the dynamic spatial distribution of cold plasma mass and magnetic field controls the expression (growth, damping) of plasma waves over a broad region of the inner magnetosphere.

A network of magnetic field measurements and rapidly refreshing total plasma density images are required to define the two-dimensional spatial distribution of plasma wave growth conditions near the magnetic equatorial plane. Embedded in this two-dimensional space, *in-situ* measurements of electron, proton, and heavy ion distribution functions, along with AC-coupled electric and magnetic fields, are needed to provide ground-truth point-sampling of energy transfer from particles to plasma waves as the surrounding density and magnetic field conditions that regulate wave properties vary in time and space.

2.8 Science Objectives to Measurements

Figure 2 shows the flow from PILOT's science goal to its science objectives to specific science questions, to targeted physical processes, and finally to required measurements. The required measurements are separated into those made by RadioSats and those made by PlasmaSats. A key maps each measurement number to the physical property being measured.

Cold particles are defined here as having thermal energy between ~0.1 and ~100 eV. Warm particles are defined from ~100 eV to ~50 keV, and energetic particles are those with thermal energy from ~100 keV to 1 MeV. DC-coupled electric and magnetic fields are defined as fields with fluctuation frequencies between quasi-static and ~20 Hz. AC-coupled fields are defined by frequencies between ~10 Hz and 15 kHz for magnetic fields, and between ~10 Hz and ~500 kHz for electric fields.

The next section describes a mission implementation that is fully capable of making the required PILOT measurements and thereby addressing the PILOT science objectives and questions.

3 MISSION IMPLEMENTATION CONCEPT

3.1 Mission Overview

PILOT uses a constellation of 30 identical microsat spacecraft (RadioSats) and four smallsat spacecraft (PlasmaSats) in two near-equatorial, highly-elliptical orbits. The PILOT orbits are 1.52 R_E x 4.25 R_E and 1.10 R_E x 6.25 R_E (**Figure 3**). These orbits are chosen to optimize measurements of the most mass-dynamic regions of the inner magnetosphere, particularly near the plasmapause. Over the course of a three-year primary mission, PILOT measures near-equatorial plasma density with images constructed from radio tomography measurements, measures meridional plasma flows with EUV images, and makes embedded *in-situ* fields and particle measurements.

Radio tomography, active plasma sounding, *in-situ* magnetic field, and *in-situ* energetic electron flux measurements are made by 14 RadioSats in the inner orbit and 16 RadioSats in the outer orbit. The RadioSat instrument complement and the heritage of notional instruments is shown in **Table 1**. RadioSat measurements are complemented by PlasmaSat measurements of DC and AC electric and magnetic fields, as well as proton, ion, and electron distribution functions, as well as local total electron density. These measurements are made by four PlasmaSats, which are identical except that the two PlasmaSats in the outer orbit, PlasmaSatEUVs, also carry EUV cameras that image the spatial distribution and flow of He^+ and O^+ ions in the meridional plane. The PlasmaSat instrument complement and heritage of notional instruments is shown in **Table 2**.

The PILOT flight system design is driven primarily by the orbits required to achieve PILOT science. To maintain the radio tomographic mesh, the two orbits are required to have parallel lines of apsides and precess at the same rate for the full mission duration through all MLTs, and necessarily traverse a high-radiation environment. An orbit design that meets this co-precession requirement uses an inner orbit perigee of 1.52 R_E. The orbit selected precessed through all MLTs each 1.7 years, allowing 1.75 full precessions through MLT during the nominal 3 year mission. To dispose of the spacecraft on this orbit within 25 years, 40 m/s of delta-V is required to place the inner orbit spacecraft into a graveyard orbit. The outer spacecraft are deorbited into the Earth's atmosphere, requiring 57 m/s of delta-V. The PILOT mission design includes ample propellant to accommodate collision avoidance maneuvers. Parts selection and shielding mass are driven by the requirement to withstand up to 125 krad-Si/year of radiation. The PILOT spacecraft are launched by two Falcon Heavy launch vehicles, one for each orbit, from Cape Canaveral, FL. It should be noted that near-future launch vehicles (for example, the SpaceX Starship), allow the deployment of all PILOT spacecraft in one launch at significantly reduced cost.

TABLE 1 | RadioSat instruments and heritage.

Acronym	Instrument type	Measurement	Heritage
RT	Radio Tomography, relaxation sounder	Total e- content, *in-situ* e- density	N/A (radio tomography), MAVEN LPW (sounder)
EED	Energetic electron detector	Energetic e- flux	AeroCube10 μCPT
FGM	Fluxgate Magnetometer	Vector DC magnetic fields	ST-5, GTOsat

TABLE 2 | PlasmaSat instruments and heritage.

Acronym	Instrument type	Measurement	Heritage
EMF FGM	Fluxgate magnetometer	DC magnetic fields	ST-5
EMF SCM	Search coil magnetometer	AC magnetic fields	Van Allen Probes EMFISIS
EMF EFI	Electric field double probes	AC and DC electric fields	Van Allen Probes EFW
EMF APPS	Relaxation sounder	*In-situ* e- density	MAVEN LPW
PIMS	Ion mass spectrometer	Cold and warm, e^-, p+, He^+, O^+ PADs	Van Allen Probes HOPE
EPS	Energetic particle spectrometer	Energetic e^-/p + PADs	GTOsat REMS
EUVCS EUV-He	He^+ imager	He^+ from 30.4 nm intensity	IMAGE EUV (sensor) JUNO UVS (electronics)
EUVCS EUV-O	O^+/O^{++} imager	O^+/O^{++} from 83.4 nm intensity	IMAGE EUV (sensor) JUNO UVS (electronics)

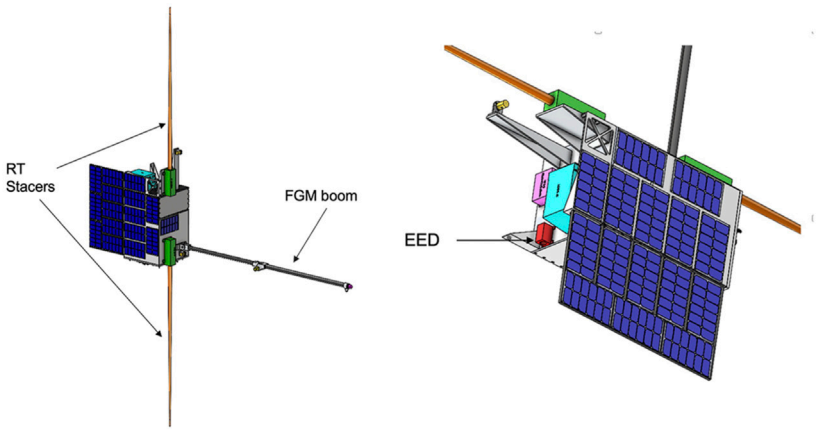

FIGURE 4 | Notional RadioSat spacecraft, with instruments indicated.

PILOT's mission architecture is resilient to risks associated with the loss of a spacecraft. For example, if up to four RadioSats fail before reaching the baseline mission duration, the remaining RadioSats can be re-positioned to meet the resolution requirement for tomographic imaging with a reduced duty cycle.

3.2 RadioSat

PILOT uses 30 RadioSats: 16 in the inner orbit and 14 in the outer orbit. An industry survey was conducted to determine the capability of current spacecraft providers to produce 30 RadioSats that meet PILOT science and environment requirements. Multiple providers were identified, and the PILOT mission concept adopts a representative RadioSat spacecraft design from this survey.

To facilitate the production of large-quantity RadioSat instruments, PILOT's approach is to have instruments designed by universities or research institutes, but to have instrument manufacture, as well as integration and test completed by commercial companies.

3.2.1 Instrument Payload Description

Each RadioSat carries three scientific instruments: Radio Tomography (RT), Fluxgate Magnetometer (FGM), and Energetic Electron Detector (EED).

The RT instrument consists of two subsystems: Radio Frequency (RF) and Active and Passive Plasma Sounder (APPS), both of which share the same dipole pair of axially-deployed 1.5 m stacer antennas (**Figure 4**) for transmitting and receiving signals. RF transmits dual frequency (50 and 150 MHz) radio signals from each RadioSat to all other RadioSats. The RF on each RadioSat receives these signals and measures their relative phase delay to determine the TEC along the line of sight between spacecraft (Ergun et al., 2000). Two-dimensional total plasma density images are derived from this network of TEC measurements via tomographic inversion. APPS is a relaxation sounder, similar to Cluster Whisper (Trotignon et al., 2003) and the relaxation sounding portion of MAVEN/LPW (Andersson et al., 2015), that measures *in-situ* electron density needed for radio

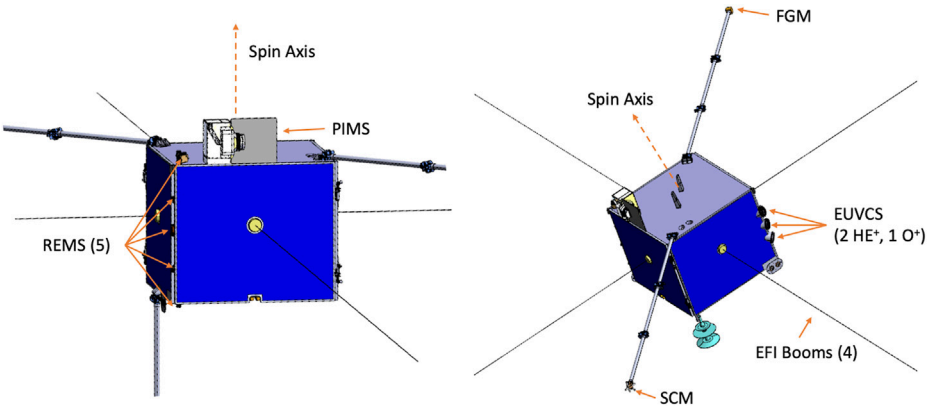

FIGURE 5 | PlasmaSatEUV spacecraft, with instruments indicated. The EFI booms are shown truncated. Their nominal base-to-tip length is 50 m each.

tomographic inversion. APPS stimulates the ambient plasma with a low-power electrostatic signal and measures the frequency of the resultant plasma-resonant waves, both actively and passively. The FGM is located at the end of a 2 m boom and measures the DC-coupled three-axis magnetic field. The network of FGMs measure the detailed terrestrial magnetic field configuration, as well as spatial variation in ULF wave properties. The EED is a compact solid state telescope that measures fluxes of trapped (~ 90^o pitch angle) electrons in the 50 keV–3 MeV range. The science goal of the EED instruments is to resolve time variability of trapped electron fluxes at many locations simultaneously (e.g., observing a front of newly injected electrons pass over each spacecraft in sequence). Therefore, EED does not need to resolve pitch angle, and larger measurement errors compared to non-miniaturized solid-state particle instruments are acceptable for PILOT.

A discussion and demonstration of how RT RF measurements are used to produce images of plasma density for PILOT is presented in **Supplementary Appendix S1**.

3.2.2 Spacecraft

RadioSat spacecraft (**Figure 4**) are three-axis stabilized and carry an X-band high-gain antenna and S-band patch antenna. They contact an Amazon Web Services ground station at each perigee for data downlink and commanding. Their pointing knowledge is determined by combining data from six sun sensors with comparisons between FGM measurements and geomagnetic field models near perigee. Position knowledge is determined via GPS near perigee combined with orbit modeling. Reaction wheels are used for attitude control. RadioSats are deployed on two SpaceX Falcon Heavy launch vehicles, one for each orbit, with four RadioSats mounted per ESPA-Grande port. Once deployed from the launch vehicle, they use on-board propulsion to achieve spacing in mean anomaly to optimize radio tomography image resolution.

3.3 PlasmaSat

PILOT has four PlasmaSat spacecraft. The two on the outer orbit carry EUV imaging instruments (PlasmaSatEUVs), and the two on the inner orbit do not (PlasmaSats). The PlasmaSat design is driven by the need to spin for particle and fields measurements.

3.3.1 Instrument Payload Description

All four PlasmaSats have identical spacecraft busses, and carry identical copies of the Electromagnetic Fields (EMF) instrument suite, Energetic Particle Sensors (EPS), and the Plasmasphere Ion Mass Spectrometer (PIMS). The two outer-orbit PlasmaSatEUVs also carry an EUV Camera System (EUVCS).

The EMF suite measures *in-situ* electric and magnetic fields across a range of frequencies using several sensors. The Electric Field Instrument (EFI) measures electric fields from DC to ~500 kHz along two axes, as well as the spacecraft floating potential, using the double probe technique (Mozer, 2016). A fluxgate magnetometer (FGM) identical to the one flown on the RadioSats, measures the DC-coupled magnetic field vector, and a search coil magnetometer (SCM) measures the AC magnetic field vector. EMF includes identical APPS electronics to the RadioSats. The PlasmaSat APPS uses EFI booms to broadcast and receive relaxation sounding signals. EMF-suite instruments have extensive heritage on magnetospheric missions including the Van Allen Probes (Kletzing et al., 2013; Mauk et al., 2013; Wygant et al., 2013), THEMIS (Angelopoulos, 2008; Bonnell et al., 2008), and MMS (Burch et al., 2015; Torbert et al., 2016).

PIMS obtains *in-situ* distribution functions (flux versus engery, pitch angle, gyrophase angle) and derived moments (density, temperature) for three major ion species (H^+, He^+, and O^+) and electrons. PIMS is a nearly identical copy of the Van Allen Probes HOPE instrument that comprises an electrostatic analyzer (ESA) with a time of flight (TOF) subsystem (Funsten et al., 2013). Measurement of full cold ion distributions (down to ~0 eV) is enabled by the Sensor-Panel Bias (SPB) system, which applies a voltage to the entire PIMS instrument and its adjacent spacecraft panel relative to the spacecraft chassis ground, allowing cold ions to reach PIMS while minimizing angular deflection.

EPS consists of five electron and proton magnetic spectrometers per PlasmaSat. Together, they measure the *in-situ* distribution functions of energetic electrons (~0.2 to ~1.5 MeV) and protons (~0.15 to ~8 MeV). Each spectrometer has a 20^o x 10^o field of

view, and five spectrometers are arranged on each PlasmaSat such that the 20^o portion of their fields of view are symmetrically distributed along the 180^o between PlasmaSat spin axes. This arrangement, combined with spacecraft rotation, enables a nearly 4π steradian coverage of the sky. The baseline for the PILOT EPS spectrometer is the REMS instrument on GTOSat (Blum et al., 2020). REMS is a miniaturized version of the MagEIS-Medium instrument on Van Allen Probes (Blake et al., 2013).

EUVCS comprises two imager instruments: EUV-He and EUV-O. EUVCS provides global images of EUV light scattered from He^+ at 30.4 nm (EUV-He, two cameras) and O^+/O^+ + at 83.4 nm (EUV-O, one camera). EUVCS images meridional ion distribution, orthogonal and complementary to the equatorial distribution obtained via radio tomography. The optical design shared by EUV-He and EUV-O is an evolution of the IMAGE EUV instrument (Sandel et al., 2000), with an expanded 40^o field of view and improved 0.45^o resolution (Davis et al., 2013; Goldstein et al., 2022) to image structures as small as 0.05 R_E.

A discussion of inversion and forward modeling algorithms for EUV image deconvolution is given in **Supplementary Appendix S2**.

3.3.2 Spacecraft

PlasmaSat and PlasmaSatEUV spacecraft (**Figure 5**) are identical except for the EUVCS instrument. The bus design is driven by instrument power, mass, and accommodation requirements, the radiation environment, and propellant needed for disposal delta-V. PlasmaSat spacecraft spin at ~5 RPM, and the spin axis is nearly orthogonal to the spacecraft orbital plane. Each PlasmaSat carries a high-gain omnidirectional X-band antenna and contacts Amazon Web Services ground station throughout the orbit to downlink data, and uplink commands once per day. Star trackers are used for attitude determination. Position knowledge is determined using single-way ranging. PlasmaSats are designed with avionics radiation tolerant to 100 krad, and use shielding to provide additional radiation mitigation.

4 CONCLUSION

There are currently large gaps in our understanding of the physical processes that transport mass into, through, and out of the magnetosphere. These processes are fundamental to our understanding of the role that planetary magnetic fields may play in atmospheric retention at terrestrial planets. A comprehensive picture of mass flow dynamics is also critical to understanding how the evolving spatial distribution of magnetospheric plasma mass regulates the behavior of key magnetospheric subsystems, and binds these subsystems together into a coherent whole.

These considerations motivate the primary science goal of PILOT: to determine the primary pathways of mass and energy flow through the coupled systems of the terrestrial magnetosphere. Three science objectives flow from this goal: 1) Identify and quantify the key processes that govern mass and energy exchange between the ionosphere and the magnetosphere, 2) Discover the pathways and processes governing cold plasma mass transport through and out of the inner magnetosphere, and 3) Determine how, where, and when cold plasma mass acts most efficiently to regulate coupling between magnetospheric regions and between plasma populations. To address these science objectives, the PILOT mission concept 'follows the mass' through the magnetosphere, combining simultaneous measurements of the spatial distribution of total plasma density in the near-equatorial plane, the ion density distribution in the meridional plane, and ground-truth *in-situ* measurements of particles and fields.

The PILOT mission implementation concept leverages technological innovations to construct a fully realizable mission from 34 spacecraft: 30 RadioSats that create a radio tomographic mesh for plasma density images, and 4 PlasmaSats carrying comprehensive *in-situ* payloads, with 2 of those 4 also carrying EUV imaging payloads. These 34 spacecraft are arrayed in two co-precessing orbits to provide high spatial and temporal coverage of a large swath of the inner magnetosphere.

The PILOT mission concept is fully capable of making the transformational measurements needed to close fundamental and persistent knowledge gaps about mass and energy flow through the magnetosphere of a magnetized terrestrial planet.

DATA AVAILABILITY STATEMENT

The original contributions presented in the study are included in the article/**Supplementary Material**, further inquiries can be directed to the corresponding author.

AUTHOR CONTRIBUTIONS

All authors supported this mission concept through the development of science objectives, questions and/or instrument or spacecraft implementation. All authors contributed to the text and/or figures included in the manuscript.

FUNDING

Work on the PILOT mission concept was funded by the NASA Heliophysics Mission Concept Studies (HMCS) program *via* award # 80NSSCK0110.

ACKNOWLEDGMENTS

The authors would like to acknowledge helpful discussions and input from the following commercial companies: Aerojet Rocketdyne, The Aerospace Corporation, Amazon Web Services, Ball Aerospace, Blue Canyon Technologies, Blue Origin, Exolaunch GmbH, Microchip Technology Inc., Muon Space, and SpaceX. The companies were not involved in the study design, collection, analysis, interpretation of data, the writing of this article or the decision to submit it for publication.

SUPPLEMENTARY MATERIAL

The Supplementary Material for this article can be found online at: https://www.frontiersin.org/articles/10.3389/fspas.2022.910730/full#supplementary-material

REFERENCES

Agapitov, O., Mourenas, D., Artemyev, A., Hospodarsky, G., and Bonnell, J. W. (2019). Time Scales for Electron Quasi-linear Diffusion by Lower-Band Chorus Waves: The Effects of ω Pe/Ω Ce Dependence on Geomagnetic Activity. *Geophys. Res. Lett.* 46, 6178–6187. doi:10.1029/2019GL083446

Allison, H. J., Shprits, Y. Y., Zhelavskaya, I. S., Wang, D., and Smirnov, A. G. (2021). Gyroresonant Wave-Particle Interactions with Chorus Waves during Extreme Depletions of Plasma Density in the Van Allen Radiation Belts. *Sci. Adv.* 7. doi:10.1126/sciadv.abc0380

Anderson, P. C., Heelis, R. A., and Hanson, W. B. (1991). The Ionospheric Signatures of Rapid Subauroral Ion Drifts. *J. Geophys. Res.* 96, 5785–5792. doi:10.1029/90ja02651

Andersson, L., Peterson, W. K., and McBryde, K. M. (2005). Estimates of the Suprathermal O+outflow Characteristic Energy and Relative Location in the Auroral Oval. *Geophys. Res. Lett.* 32, L09104. doi:10.1029/2004GL021434

Andersson, L., Weber, T. D., Malaspina, D., Crary, F., Ergun, R. E., Delory, G. T., et al. (2015). Dust Observations at Orbital Altitudes Surrounding Mars. *Science* 350, 0398. doi:10.1126/science.aad0398

Andriopoulou, M., Nakamura, R., Wellenzohn, S., Torkar, K., Baumjohann, W., Torbert, R. B., et al. (2018). Plasma Density Estimates from Spacecraft Potential Using Mms Observations in the Dayside Magnetosphere. *J. Geophys. Res. Space Phys.* 123, 2620–2629. doi:10.1002/2017JA025086

Angelopoulos, V., Baumjohann, W., Kennel, C. F., Coroniti, F. V., Kivelson, M. G., Pellat, R., et al. (1992). Bursty Bulk Flows in the Inner Central Plasma Sheet. *J. Geophys. Res.* 97, 4027–4039. doi:10.1029/91JA02701

Angelopoulos, V., Kennel, C. F., Coroniti, F. V., Pellat, R., Kivelson, M. G., Walker, R. J., et al. (1994). Statistical Characteristics of Bursty Bulk Flow Events. *J. Geophys. Res.* 99, 21257–21280. doi:10.1029/94JA01263

Angelopoulos, V. (2008). The THEMIS Mission. *Space Sci. Rev.* 141, 5–34. doi:10.1007/s11214-008-9336-1

Baker, D. N., Kanekal, S. G., Hoxie, V. C., Batiste, S., Bolton, M., Li, X., et al. (2013). The Relativistic Electron-Proton Telescope (REPT) Instrument on Board the Radiation Belt Storm Probes (RBSP) Spacecraft: Characterization of Earth's Radiation Belt High-Energy Particle Populations. *Space Sci. Rev.* 179, 337–381. doi:10.1007/s11214-012-9950-9

Banks, P. M. (1968). Hydrogen Ion Velocity Distributions in the Ionosphere. *Planet. Space Sci.* 16, 759–773. doi:10.1016/0032-0633(68)90080-9

Banks, P. M. (1969). The Thermal Structure of the Ionosphere. *Proc. IEEE* 57, 258–281. doi:10.1109/proc.1969.6959

Baumjohann, W., Paschmann, G., and Cattell, C. A. (1989). Average Plasma Properties in the Central Plasma Sheet. *J. Geophys. Res.* 94, 6597–6606. doi:10.1029/JA094iA06p06597

Bernhardt, P. A., McCoy, R. P., Dymond, K. F., Picone, J. M., Meier, R. R., Kamalabadi, F., et al. (1998). Two-dimensional Mapping of the Plasma Density in the Upper Atmosphere with Computerized Ionospheric Tomography (CIT). *Phys. Plasmas* 5, 2010–2021. doi:10.1063/1.872872

Blake, J. B., Carranza, P. A., Claudepierre, S. G., Clemmons, J. H., Crain, W. R., Dotan, Y., et al. (2013). The Magnetic Electron Ion Spectrometer (MagEIS) Instruments Aboard the Radiation Belt Storm Probes (RBSP) Spacecraft. *Space Sci. Rev.* 179, 383–421. doi:10.1007/s11214-013-9991-8

Blum, L. W., Kepko, L., Turner, D., Gabrielse, C., Jaynes, A., Kanekal, S., et al. (2020). "The GTOSat CubeSat: Scientific Objectives and Instrumentation," in *Micro- and Nanotechnology Sensors, Systems, and Applications XII*. Editors T. George. and M. S. Islam (International Society for Optics and Photonics (SPIE)), 62–71. doi:10.1117/12.2556268

Boardsen, S. A., Gallagher, D. L., Gurnett, D. A., Peterson, W. K., and Green, J. L. (1992). Funnel-shaped, Low-Frequency Equatorial Waves. *J. Geophys. Res.* 97, 14967–14976. doi:10.1029/92JA00827

Bonnell, J. W., Mozer, F. S., Delory, G. T., Hull, A. J., Ergun, R. E., Cully, C. M., et al. (2008). The Electric Field Instrument (EFI) for THEMIS. *Space Sci. Rev.* 141, 303–341. doi:10.1007/s11214-008-9469-2

Borovsky, J. E., Denton, M. H., Denton, R. E., Jordanova, V. K., and Krall, J. (2013). Estimating the Effects of Ionospheric Plasma on Solar Wind/magnetosphere Coupling via Mass Loading of Dayside Reconnection: Ion-Plasma-Sheet Oxygen, Plasmaspheric Drainage Plumes, and the Plasma Cloak. *J. Geophys. Res. Space Phys.* 118, 5695–5719. doi:10.1002/jgra.50527

Borovsky, J. E., Welling, D. T., Thomsen, M. F., and Denton, M. H. (2014). Long-lived Plasmaspheric Drainage Plumes: Where Does the Plasma Come from? *J. Geophys. Res. Space Phys.* 119, 6496–6520. doi:10.1002/2014JA020228

Breneman, A. W., Halford, A., Millan, R., McCarthy, M., Fennell, J., Sample, J., et al. (2015). Global-scale Coherence Modulation of Radiation-Belt Electron Loss from Plasmaspheric Hiss. *Nature* 523, 193–195. doi:10.1038/nature14515

Burch, J. L., Mende, S. B., Mitchell, D. G., Moore, T. E., Pollock, C. J., Reinisch, B. W., et al. (2001a). Views of Earth's Magnetosphere with the IMAGE Satellite. *Science* 291, 619–624. doi:10.1126/science.291.5504.619

Burch, J. L., Mitchell, D. G., Sandel, B. R., Brandt, P. C., and Wüest, M. (2001b). Global Dynamics of the Plasmasphere and Ring Current during Magnetic Storms. *Geophys. Res. Lett.* 28, 1159–1162. doi:10.1029/2000GL012413

Burch, J. L., Moore, T. E., Torbert, R. B., and Giles, B. L. (2015). Magnetospheric Multiscale Overview and Science Objectives. *Space Sci. Rev.* 199, 5–21. doi:10.1007/s11214-015-0164-9

Burch, J. L. (2001). The Fury of Space Storms. *Sci. Am.* 284, 86–94. doi:10.1038/scientificamerican0401-86

Carpenter, D. L., Giles, B. L., Chappell, C. R., Décréau, P. M. E., Anderson, R. R., Persoon, A. M., et al. (1993). Plasmasphere Dynamics in the Duskside Bulge Region: A New Look at an Old Topic. *J. Geophys. Res.* 98, 19243–19271. doi:10.1029/93JA00922

Celnikier, L. M., Harvey, C. C., Jegou, R., Moricet, P., and Kemp, M. (1983). A Determination of the Electron Density Fluctuation Spectrum in the Solar Wind, Using the ISEE Propagation Experiment. *Astronomy Astrophysics* 126, 293–298.

Chappell, C. R., Huddleston, M. M., Moore, T. E., Giles, B. L., and Delcourt, D. C. (2008). Observations of the Warm Plasma Cloak and an Explanation of its Formation in the Magnetosphere. *J. Geophys. Res.* 113, a–n. doi:10.1029/2007JA012945

Chappell, C. R. (2015). The Role of the Ionosphere in Providing Plasma to the Terrestrial Magnetosphere - an Historical Overview. *Space Sci. Rev.* 192, 5–25. doi:10.1007/s11214-015-0168-5

Chaston, C. C., Bonnell, J. W., Reeves, G. D., and Skoug, R. M. (2016). Driving Ionospheric Outflows and Magnetospheric O + Energy Density with Alfvén Waves. *Geophys. Res. Lett.* 43, 4825–4833. doi:10.1002/2016GL069008

Chen, L., Thorne, R. M., Jordanova, V. K., Wang, C.-P., Gkioulidou, M., Lyons, L., et al. (2010). Global Simulation of EMIC Wave Excitation during the 21 April 2001 Storm from Coupled RCM-RAM-HOTRAY Modeling. *J. Geophys. Res. (Space Phys.* 115, A07209. doi:10.1029/2009JA015075

Claudepierre, S. G., Toffoletto, F. R., and Wiltberger, M. (2016). Global MHD Modeling of Resonant ULF Waves: Simulations with and without a Plasmasphere. *J. Geophys. Res. Space Phys.* 121, 227–244. doi:10.1002/2015JA022048

Darrouzet, F., Gallagher, D. L., André, N., Carpenter, D. L., Dandouras, I., Décréau, P. M. E., et al. (2009). Plasmaspheric Density Structures and Dynamics: Properties Observed by the Cluster and Image Missions. *Space Sci. Rev.* 145, 55–106. doi:10.1007/s11214-008-9438-9

Davis, M. W., Gladstone, G. R., Goldstein, J., Sandel, B. R., Greathouse, T. K., Retherford, K. D., et al. (2013). "An Improved Wide-Field Camera for Imaging Earth's Plasmasphere at 30.4 Nm," in *UV, X-Ray, and Gamma-Ray Space Instrumentation for Astronomy XVIII*. Editor O. H. Siegmund (International Society for Optics and Photonics (SPIE)), 227–235. doi:10.1117/12.2024440

Delzanno, G. L., Borovsky, J. E., Henderson, M. G., Resendiz Lira, P. A., Roytershteyn, V., and Welling, D. T. (2021). The Impact of Cold Electrons and Cold Ions in Magnetospheric Physics. *J. Atmos. Solar-Terrestrial Phys.* 220, 105599. doi:10.1016/j.jastp.2021.105599

Dent, Z. C., Mann, I. R., Goldstein, J., Menk, F. W., and Ozeke, L. G. (2006). Plasmaspheric Depletion, Refilling, and Plasmapause Dynamics: A Coordinated Ground-Based and IMAGE Satellite Study. *J. Geophys. Res.* 111, A03205. doi:10.1029/2005JA011046

Denton, M. H., and Borovsky, J. E. (2014). Observations and Modeling of Magnetic Flux Tube Refilling of the Plasmasphere at Geosynchronous Orbit. *J. Geophys. Res. Space Phys.* 119, 9246–9255. doi:10.1002/2014ja020491

Denton, R. E., Goldstein, J., Lee, D.-H., King, R. A., Dent, Z. C., Gallagher, D. L., et al. (2006). Realistic Magnetospheric Density Model for 29 August 2000. *J. Atmos. Solar-Terrestrial Phys.* 68, 615–628. doi:10.1016/j.jastp.2005.11.009

Denton, R. E., Wang, Y., Webb, P. A., Tengdin, P. M., Goldstein, J., Redfern, J. A., et al. (2012). Magnetospheric electron density long-term (> 1 day) refilling rates inferred from passive radio emissions measured by IMAGE RPI during

geomagnetically quiet times. *J. Geophys. Res.* 117, a–n. doi:10.1029/2011JA017274

Dubyagin, S., Sergeev, V., Apatenkov, S., Angelopoulos, V., Runov, A., Nakamura, R., et al. (2011). Can Flow Bursts Penetrate into the Inner Magnetosphere? *Geophys. Res. Lett.* 38, a–n. doi:10.1029/2011GL047016

Dungey, J. W. (1955). Electrodynamics of the Outer Atmosphere. *Phys. Ionos.* 229.

Dungey, J. W. (1961). Interplanetary Magnetic Field and the Auroral Zones. *Phys. Rev. Lett.* 6, 47–48. doi:10.1103/PhysRevLett.6.47

Elkington, S. R., Hudson, M. K., and Chan, A. A. (2003). Resonant Acceleration and Diffusion of Outer Zone Electrons in an Asymmetric Geomagnetic Field. *J. Geophys. Res.* 108, 1116. doi:10.1029/2001JA009202

Elphic, R. C., Thomsen, M. F., and Borovsky, J. E. (1997). The Fate of the Outer Plasmasphere. *Geophys. Res. Lett.* 24, 365–368. doi:10.1029/97GL00141

Engebretson, M. J., Posch, J. L., Wygant, J. R., Kletzing, C. A., Lessard, M. R., Huang, C. L., et al. (2015). Van Allen Probes, NOAA, GOES, and Ground Observations of an Intense EMIC Wave Event Extending over 12 H in Magnetic Local Time. *J. Geophys. Res. Space Phys.* 120, 5465–5488. doi:10.1002/2015JA021227

Engwall, E., Eriksson, A. I., Cully, C. M., André, M., Torbert, R., and Vaith, H. (2009). Earth's Ionospheric Outflow Dominated by Hidden Cold Plasma. *Nat. Geosci.* 2, 24–27. doi:10.1038/ngeo387

Ergun, R. E., Goodrich, K. A., Stawarz, J. E., Andersson, L., and Angelopoulos, V. (2015). Large-amplitude Electric Fields Associated with Bursty Bulk Flow Braking in the Earth's Plasma Sheet. *J. Geophys. Res. Space Phys.* 120, 1832–1844. doi:10.1002/2014JA020165

Ergun, R. E., Larson, D. E., Phan, T., Taylor, D., Bale, S., Carlson, C. W., et al. (2000). Feasibility of a Multisatellite Investigation of the Earth's Magnetosphere with Radio Tomography. *J. Geophys. Res.* 105, 361–373. doi:10.1029/1999JA900170

Farrugia, C. J., Young, D. T., Geiss, J., and Balsiger, H. (1989). The Composition, Temperature, and Density Structure of Cold Ions in the Quiet Terrestrial Plasmasphere: GEOS 1 Results. *J. Geophys. Res.* 94, 11865–11891. doi:10.1029/JA094iA09p11865

Fletcher, A. C., Crabtree, C., Ganguli, G., Malaspina, D., Tejero, E., and Chu, X. (2019). Kinetic Equilibrium and Stability Analysis of Dipolarization Fronts. *J. Geophys. Res. Space Phys.* 124, 2010–2028. doi:10.1029/2018JA026433

Foster, J. C., Erickson, P. J., Walsh, B. M., Wygant, J. R., Coster, A. J., and Zhang, Q. H. (2020). *Multi-Point Observations of the Geospace Plume*. American Geophysical Union, 243–264. chap. 14. doi:10.1002/9781119509592.ch14

Foster, J. C., Rideout, W., Sandel, B., Forrester, W. T., and Rich, F. J. (2007). On the Relationship of Saps to Storm-Enhanced Density. *J. Atmos. Solar-Terrestrial Phys.* 69, 303–313. doi:10.1016/j.jastp.2006.07.021

Funsten, H. O., Skoug, R. M., Guthrie, A. A., MacDonald, E. A., Baldonado, J. R., Harper, R. W., et al. (2013). Helium, Oxygen, Proton, and Electron (HOPE) Mass Spectrometer for the Radiation Belt Storm Probes Mission. *Space Sci. Rev.* 179, 423–484. doi:10.1007/s11214-013-9968-7

Gallagher, D. L., and Adrian, M. L. (2007). Two-dimensional Drift Velocities from the IMAGE EUV Plasmaspheric Imager. *J. Atmos. Solar-Terrestrial Phys.* 69, 341–350. doi:10.1016/j.jastp.2006.05.028

Gallagher, D. L., Comfort, R. H., Katus, R. M., Sandel, B. R., Fung, S. F., and Adrian, M. L. (2021). The Breathing Plasmasphere: Erosion and Refilling. *J. Geophys. Res. Space Phys.* 126, e2020JA028727. doi:10.1029/2020JA028727

Gallagher, D. L., and Comfort, R. H. (2016). Unsolved Problems in Plasmasphere Refilling. *J. Geophys. Res. Space Phys.* 121, 1447–1451. doi:10.1002/2015ja022279

Galvan, D. A., Moldwin, M. B., Sandel, B. R., and Crowley, G. (2010). On the Causes of Plasmaspheric Rotation Variability: IMAGE EUV Observations. *J. Geophys. Res. (Space Phys.* 115, A01214. doi:10.1029/2009JA014321

Gkioulidou, M., Ukhorskiy, A. Y., Mitchell, D. G., Sotirelis, T., Mauk, B. H., and Lanzerotti, L. J. (2014). The Role of Small-Scale Ion Injections in the Buildup of Earth's Ring Current Pressure: Van Allen Probes Observations of the 17 March 2013 Storm. *J. Geophys. Res. Space Phys.* 119, 7327–7342. doi:10.1002/2014JA020096

Glocer, A., Welling, D., Chappell, C. R., Toth, G., Fok, M.-C., Komar, C., et al. (2020). A Case Study on the Origin of Near-Earth Plasma. *J. Geophys. Res. Space Phys.* 125, e2020JA028205. doi:10.1029/2020JA028205

Goldstein, J., Chappell, C. R., Davis, M. W., Denton, M. H., Denton, R. E., Gallagher, D. L., et al. (2018). Imaging the Global Distribution of Plasmaspheric Oxygen. *J. Geophys. Res. Space Phys.* 123, 2078–2103. doi:10.1002/2017JA024531

Goldstein, J., Gallagher, D., Craven, P. D., Comfort, R. H., Genestreti, K. J., Mouikis, C., et al. (2019). Temperature Dependence of Plasmaspheric Ion Composition. *J. Geophys. Res. Space Phys.* 124, 6585–6595. doi:10.1029/2019JA026822

Goldstein, J., Gallagher, D. L., Molyneux, P., and Reeves, G. D. (2021). "Core-Plasma Refilling and Erosion: Science Justification," in Heliophysics 2050 White Papers *(NASA Heliophysics Division)* (MAGNETOSPHERE SCIENCE, #4063).

Goldstein, J., Gallagher, D. L., Sandel, B. R., Davis, M., Molyneux, P., Veach, T., et al. (2020). "The Future of Plasmaspheric Extreme Ultraviolet (EUV) Imaging," in *Magnetospheric Imaging* (Elsevier), 231. Chapter 6. doi:10.1016/B978-0-12-820630-0.00010-6

Goldstein, J., Gallagher, D. L., Sandel, B. R., Davis, M., Molyneux, P., Veach, T., et al. (2022). "The Future of Plasmaspheric Extreme Ultraviolet (EUV) Imaging," in *Understanding the Space Environment through Global Measurements*. Editors Y. Colado-Vega, D. Gallagher, H. Frey, and S. Wing (Elsevier), 231–286. doi:10.1016/B978-0-12-820630-0.00010-6

Goldstein, J., and Sandel, B. R. (2005). The Global Pattern of Evolution of Plasmaspheric Drainage Plumes. *Wash. D.C. Am. Geophys. Union Geophys. Monogr. Ser.* 159, 1–22. doi:10.1029/159gm02

Goldstein, J., Sandel, B. R., Thomsen, M. F., Spasojeviá, M., and Reiff, P. H. (2004a). Electric Fields Deduced from Plasmapause Motion in IMAGE EUV Images. *Geophysical Research Letters* 31 (1), L01801–22. doi:10.1029/2003GL018797

Goldstein, J., Spasojević, M., Reiff, P. H., Sandel, B. R., Forrester, W. T., Gallagher, D. L., et al. (2003). Identifying the Plasmapause in IMAGE EUV Data Using IMAGE RPI *In Situ* Steep Density Gradients. *J. Geophys. Res.* 108, 1147. doi:10.1029/2002JA009475

Goldstein, J., Wolf, R. A., Sandel, B. R., and Reiff, P. H. (2004b). Electric Fields Deduced from Plasmapause Motion in IMAGE EUV Images. *Geophys. Res. Lett.* 31, L01801. doi:10.1029/2003GL018797

Gurnett, D. A. (1976). Plasma Wave Interactions with Energetic Ions Near the Magnetic Equator. *J. Geophys. Res.* 81, 2765–2770. doi:10.1029/JA081i016p02765

Halford, A. J., Fraser, B. J., and Morley, S. K. (2015). EMIC Waves and Plasmaspheric and Plume Density: CRRES Results. *J. Geophys. Res. Space Phys.* 120, 1974–1992. doi:10.1002/2014JA020338

He, F., Guo, R.-L., Dunn, W. R., Yao, Z.-H., Zhang, H.-S., Hao, Y.-X., et al. (2020). Plasmapause Surface Wave Oscillates the Magnetosphere and Diffuse Aurora. *Nat. Commun.* 11, 1668. doi:10.1038/s41467-020-15506-3

Hill, S., Buzulukova, N., Boardsen, S., and Fok, M.-C. (2020). Local Heating of Oxygen Ions in the Presence of Magnetosonic Waves: Possible Source for the Warm Plasma Cloak? *J. Geophys. Res. Space Phys.* 125, e2019JA027210. doi:10.1029/2019ja027210

Horne, R. B., Thorne, R. M., Shprits, Y. Y., Meredith, N. P., Glauert, S. A., Smith, A. J., et al. (2005). Wave Acceleration of Electrons in the Van Allen Radiation Belts. *Nature* 437, 227–230. doi:10.1038/nature03939

Horwitz, J. L., and Lockwood, M. (1985). The Cleft Ion Fountain: A Two-Dimensional Kinetic Model. *J. Geophys. Res.* 90, 9749. doi:10.1029/JA090iA10p09749

Hrbáčková, Z., Santolík, O., Němec, F., Macúšová, E., and Cornilleau-Wehrlin, N. (2015). Systematic Analysis of Occurrence of Equatorial Noise Emissions Using 10 Years of Data from the Cluster Mission. *J. Geophys. Res. Space Phys.* 120, 1007–1021. doi:10.1002/2014JA020268

Hull, A. J., Chaston, C. C., Bonnell, J. W., Wygant, J. R., Keltzing, C. A., Reeves, G. D., et al. (2019). Dispersive Alfven Wave Control of O^+ Ion Outflow and Energy Densities in the Inner Magnetosphere. *Geophys. Res. Lett.* 46. doi:10.1002/2019GL08380810.1029/2019gl083808

Hultqvist, B., Øieroset, M., Paschmann, G., and Treumann, R. A. (1999). *Magnetospheric Plasma Sources and Losses*. Springer. doi:10.1007/978-94-011-4477-3

Jahn, J.-M., Goldstein, J., Reeves, G. D., Fernandes, P. A., Skoug, R. M., Larsen, B. A., et al. (2017). The Warm Plasma Composition in the Inner Magnetosphere during 2012–2015. *J. Geophys. Res. Space Phys.* 122, 11–018. doi:10.1002/2017ja024183

Jakosky, B. M. (2015). MAVEN Explores the Martian Upper Atmosphere. *Science* 350, 643. doi:10.1126/science.aad3443

Jaynes, A. N., Ali, A. F., Elkington, S. R., Malaspina, D. M., Baker, D. N., Li, X., et al. (2018). Fast Diffusion of Ultrarelativistic Electrons in the Outer Radiation Belt: 17 March 2015 Storm Event. *Geophys. Res. Lett.* 45, 10,874–10,882. doi:10.1029/2018GL079786

Jaynes, A. N., Baker, D. N., Singer, H. J., Rodriguez, J. V., Loto'aniu, T. M., Ali, A. F., et al. (2015). Source and Seed Populations for Relativistic Electrons: Their Roles in Radiation Belt Changes. *J. Geophys. Res. Space Phys.* 120, 7240–7254. doi:10.1002/2015JA021234

Jordanova, V. K., Farrugia, C. J., Thorne, R. M., Khazanov, G. V., Reeves, G. D., and Thomsen, M. F. (2001). Modeling Ring Current Proton Precipitation by Electromagnetic Ion Cyclotron Waves during the May 14-16, 1997, Storm. *J. Geophys. Res.* 106, 7–22. doi:10.1029/2000JA002008

Jordanova, V. K., Spasojevic, M., and Thomsen, M. F. (2007). Modeling the Electromagnetic Ion Cyclotron Wave-Induced Formation of Detached Subauroral Proton Arcs. *J. Geophys. Res.* 112, a–n. doi:10.1029/2006JA012215

Khoo, L. Y., Li, X., Zhao, H., Sarris, T. E., Xiang, Z., Zhang, K., et al. (2018). On the Initial Enhancement of Energetic Electrons and the Innermost Plasmapause Locations: Coronal Mass Ejection-Driven Storm Periods. *J. Geophys. Res. Space Phys.* 123, 9252–9264. doi:10.1029/2018JA026074

Kivelson, M. G., and Southwood, D. J. (1985). Resonant ULF Waves: A New Interpretation. *Geophys. Res. Lett.* 12, 49–52. doi:10.1029/GL012i001p00049

Kletzing, C. A., Kurth, W. S., Acuna, M., MacDowall, R. J., Torbert, R. B., Averkamp, T., et al. (2013). The Electric and Magnetic Field Instrument Suite and Integrated Science (EMFISIS) on RBSP. *Space Sci. Rev.* 179, 127–181. doi:10.1007/s11214-013-9993-6

Kozyra, J. U., Cravens, T. E., Nagy, A. F., Fontheim, E. G., and Ong, R. S. B. (1984). Effects of Energetic Heavy Ions on Electromagnetic Ion Cyclotron Wave Generation in the Plasmapause Region. *J. Geophys. Res.* 89, 2217–2234. doi:10.1029/JA089iA04p02217

Krall, J., Huba, J. D., and Borovsky, J. E. (2018). Sami3 Simulations of a Persistent Plasmasphere Plume. *Geophys. Res. Lett.* 45, 3374–3381. doi:10.1002/2017gl076448

Kunduri, B. S. R., Baker, J. B. H., Ruohoniemi, J. M., Nishitani, N., Oksavik, K., Erickson, P. J., et al. (2018). A New Empirical Model of the Subauroral Polarization Stream. *J. Geophys. Res. Space Phys.* 123, 7342–7357. doi:10.1029/2018JA025690

Kurth, W. S., De Pascuale, S., Faden, J. B., Kletzing, C. A., Hospodarsky, G. B., Thaller, S., et al. (2015). Electron Densities Inferred from Plasma Wave Spectra Obtained by the Waves Instrument on Van Allen Probes. *J. Geophys. Res. Space Phys.* 120, 904–914. doi:10.1002/2014JA020857

Lawrence, D. J., Thomsen, M. F., Borovsky, J. E., McComas, D. J., and McComas, D. J. (1999). Measurements of Early and Late Time Plasmasphere Refilling as Observed from Geosynchronous Orbit. *J. Geophys. Res.* 104, 14691–14704. doi:10.1029/1998JA900087

Lee, D.-H., and Lysak, R. L. (1989). Magnetospheric ULF Wave Coupling in the Dipole Model: the Impulsive Excitation. *J. Geophys. Res.* 94, 17097–17103. doi:10.1029/JA094iA12p17097

Leitinger, R., Ladreiter, H.-P., and Kirchengast, G. (1997). Ionosphere Tomography with Data from Satellite Reception of Global Navigation Satellite System Signals and Ground Reception of Navy Navigation Satellite System Signals. *Radio Sci.* 32, 1657–1669. doi:10.1029/97RS01027

Lemaire, J. F., Gringauz, K. I., Carpenter, D. L., and Bassolo, V. (1998). *The Earth's Plasmasphere*. Cambridge: Cambridge University Press. doi:10.1017/CBO9780511600098

Li, S. S., Angelopoulos, V., Runov, A., Zhou, X. Z., McFadden, J., Larson, D., et al. (2011). On the Force Balance Around Dipolarization Fronts within Bursty Bulk Flows. *J. Geophys. Res. (Space Phys.* 116, A00I35. doi:10.1029/2010JA015884

Liang, J., Donovan, E., Reimer, A., Hampton, D., Zou, S., and Varney, R. (2018). Ionospheric Electron Heating Associated with Pulsating Auroras: Joint Optical and Pfisr Observations. *J. Geophys. Res. Space Phys.* 123, 4430–4456. doi:10.1029/2017JA025138

Liemohn, M. W., Ridley, A. J., Gallagher, D. L., Ober, D. M., and Kozyra, J. U. (2004). Dependence of Plasmaspheric Morphology on the Electric Field Description during the Recovery Phase of the 17 April 2002 Magnetic Storm. *J. Geophys. Res.* 109, A03209. doi:10.1029/2003JA010304

Liu, J., Angelopoulos, V., Zhou, X.-Z., Yao, Z.-H., and Runov, A. (2015). Cross-tail Expansion of Dipolarizing Flux Bundles. *J. Geophys. Res. Space Phys.* 120, 2516–2530. doi:10.1002/2015JA020997

Lysak, R. L. (1990). Electrodynamic Coupling of the Magnetosphere and Ionosphere. *Space Sci. Rev.* 52, 33–87. doi:10.1007/BF00704239

Malaspina, D. M., Jaynes, A. N., Boulé, C., Bortnik, J., Thaller, S. A., Ergun, R. E., et al. (2016). The Distribution of Plasmaspheric Hiss Wave Power with Respect to Plasmapause Location. *Geophys. Res. Lett.* 43, 7878–7886. doi:10.1002/2016GL069982

Malaspina, D. M., Ripoll, J. F., Chu, X., Hospodarsky, G., and Wygant, J. (2018). Variation in Plasmaspheric Hiss Wave Power with Plasma Density. *Geophys. Res. Lett.* 45, 9417–9426. doi:10.1029/2018GL078564

Malaspina, D. M., Zhu, H., and Drozdov, A. Y. (2020). A Wave Model and Diffusion Coefficients for Plasmaspheric Hiss Parameterized by Plasmapause Location. *J. Geophys. Res. (Space Phys.* 125, e27415. doi:10.1029/2019JA027415

Malaspina, D., Wygant, J., Ergun, R., Reeves, G., Skoug, R., and Larsen, B. (2015). Electric Field Structures and Waves at Plasma Boundaries in the Inner Magnetosphere. *J. Geophys. Res. (Space Phys.* 120. doi:10.1002/2015JA021137

Maruyama, N., Sun, Y. Y., Richards, P. G., Middlecoff, J., Fang, T. W., Fuller-Rowell, T. J., et al. (2016). A New Source of the Midlatitude Ionospheric Peak Density Structure Revealed by a New Ionosphere-Plasmasphere Model. *Geophys. Res. Lett.* 43, 2429–2435. doi:10.1002/2015GL067312

Matsui, H., Torbert, R. B., Spence, H. E., Khotyaintsev, Y. V., and Lindqvist, P.-A. (2013). Revision of Empirical Electric Field Modeling in the Inner Magnetosphere Using Cluster Data. *J. Geophys. Res. Space Phys.* 118, 4119–4134. doi:10.1002/jgra.50373

Mauk, B. H., Fox, N. J., Kanekal, S. G., Kessel, R. L., Sibeck, D. G., and Ukhorskiy, A. (2013). Science Objectives and Rationale for the Radiation Belt Storm Probes Mission. *Space Sci. Rev.* 179, 3–27. doi:10.1007/s11214-012-9908-y

McPherron, R. L., Hsu, T.-S., Kissinger, J., Chu, X., and Angelopoulos, V. (2011). Characteristics of Plasma Flows at the Inner Edge of the Plasma Sheet. *J. Geophys. Res. (Space Phys.* 116, A00I33. doi:10.1029/2010JA015923

Meier, R. R., Nicholas, A. C., Picone, J. M., Melendez-Alvira, D. J., Ganguli, G. I., Reynolds, M. A., et al. (1998). Inversion of Plasmaspheric EUV Remote Sensing Data from the STP 72-1 Satellite. *J. Geophys. Res.* 103, 17505–17518. doi:10.1029/98JA01175

Meredith, N. P., Horne, R. B., Kersten, T., Li, W., Bortnik, J., Sicard, A., et al. (2018). Global Model of Plasmaspheric Hiss from Multiple Satellite Observations. *J. Geophys. Res. Space Phys.* 123, 4526–4541. doi:10.1029/2018JA025226

Meredith, N. P., Horne, R. B., Shen, X.-C., Li, W., and Bortnik, J. (2020). Global Model of Whistler Mode Chorus in the Near-Equatorial Region (— λ_m—¡ 18°). *Geophys. Res. Lett.* 47, e87311. doi:10.1029/2020GL087311

Morton, Y. J., Yang, Z., Breitsch, B., Bourne, H., and Rino, C. (2020). *Ionospheric Effects, Monitoring, and Mitigation Techniques*. John Wiley & Sons, 879–937. chap. 31. doi:10.1002/9781119458449.ch31

Motoba, T., Ohtani, S., Claudepierre, S. G., Reeves, G. D., Ukhorskiy, A. Y., and Lanzerotti, L. J. (2020). Dynamic Properties of Particle Injections inside Geosynchronous Orbit: A Multisatellite Case Study. *J. Geophys Res. Space Phys.* 125, e2020JA028215. doi:10.1029/2020JA028215

Mozer, F. S. (2016). DC and Low-Frequency Double Probe Electric Field Measurements in Space. *J. Geophys. Res. (Space Phys.* 121, 10,942–10,953. doi:10.1002/2016JA022952

Nakamura, R., Baumjohann, W., Schödel, R., Brittnacher, M., Sergeev, V. A., Kubyshkina, M., et al. (2001). Earthward Flow Bursts, Auroral Streamers, and Small Expansions. *J. Geophys. Res.* 106, 10791–10802. doi:10.1029/2000JA000306

Nakano, S., Fok, M.-C., Brandt, P. C., and Higuchi, T. (2014a). Estimation of Temporal Evolution of the Helium Plasmasphere Based on a Sequence of IMAGE/EUV Images. *J. Geophys. Res. Space Phys.* 119, 3708–3723. doi:10.1002/2013JA019734

Nakano, S., Fok, M.-C., Brandt, P. C., and Higuchi, T. (2014b). Estimation of the Helium Ion Density Distribution in the Plasmasphere Based on a Single IMAGE/EUV Image. *J. Geophys. Res. Space Phys.* 119, 3724–3740. doi:10.1002/2013JA019733

Nass, H. U., and Fahr, H. J. (1984). Plasma-gas Interactions in Planetary Atmospheres and Their Relevance for the Terrestrial Hydrogen Budget. *J. Geophys. Zeitschrift Geophys.* 56, 34–46.

Ni, B., Li, W., Thorne, R. M., Bortnik, J., Ma, Q., Chen, L., et al. (2014). Resonant Scattering of Energetic Electrons by Unusual Low-Frequency Hiss. *Geophys. Res. Lett.* 41, 1854–1861. doi:10.1002/2014GL059389

Nicholson, D. R. (1983). *Introduction to Plasma Theory*. New York: John Wiley & Sons.

Nosé, M., Matsuoka, A., Kumamoto, A., Kasahara, Y., Goldstein, J., Teramoto, M., et al. (2018). Longitudinal Structure of Oxygen Torus in the Inner Magnetosphere: Simultaneous Observations by Arase and Van Allen Probe A. *Geophys. Res. Lett.* 45. doi:10.1002/2018GL08012210.1029/2018gl080122

Nosé, M., Oimatsu, S., Keika, K., Kletzing, C. A., Kurth, W. S., Pascuale, S. D., et al. (2015). Formation of the Oxygen Torus in the Inner Magnetosphere: Van Allen Probes Observations. *J. Geophys. Res. Space Phys.* 120, 1182–1196. doi:10.1002/2014ja020593

Nosé, M., Oimatsu, S., Keika, K., Kletzing, C. A., Kurth, W. S., Pascuale, S. D., et al. (2015). Formation of the Oxygen Torus in the Inner Magnetosphere: Van Allen Probes Observations. *J. Geophys. Res. Space Phys.* 120, 1182–1196. doi:10.1002/2014JA020593

Nosé, M., Takahashi, K., Anderson, R. R., and Singer, H. J. (2011). Oxygen Torus in the Deep Inner Magnetosphere and its Contribution to Recurrent Process of O+-rich Ring Current Formation. *J. Geophys. Res.* 116, a–n. doi:10.1029/2011JA016651

Ohtani, S., Singer, H. J., and Mukai, T. (2006). Effects of the Fast Plasma Sheet Flow on the Geosynchronous Magnetic Configuration: Geotail and GOES Coordinated Study. *J. Geophys. Res.* 111, A01204. doi:10.1029/2005JA011383

Olsen, R. C., Shawhan, S. D., Gallagher, D. L., Green, J. L., Chappell, C. R., and Anderson, R. R. (1987). Plasma Observations at the Earth's Magnetic Equator. *J. Geophys. Res.* 92, 2385–2407. doi:10.1029/JA092iA03p02385

Omura, Y., Furuya, N., and Summers, D. (2007). Relativistic Turning Acceleration of Resonant Electrons by Coherent Whistler Mode Waves in a Dipole Magnetic Field. *J. Geophys. Res. (Space Phys.* 112, A06236. doi:10.1029/2006JA012243

Park, C. G. (1974). Some Features of Plasma Distribution in the Plasmasphere Deduced from Antarctic Whistlers. *J. Geophys. Res.* 79, 169–173. doi:10.1029/JA079i001p00169

Park, C. G. (1973). Whistler Observations of the Depletion of the Plasmasphere during a Magnetospheric Substorm. *J. Geophys. Res.* 78, 672–683. doi:10.1029/JA078i004p00672

Pierrard, V., and Lemaire, J. (2004). Development of Shoulders and Plumes in the Frame of the Interchange Instability Mechanism for Plasmapause Formation. *Geophys. Res. Lett.* 31. doi:10.1029/2003gl018919

Ramstad, R., and Barabash, S. (2021). Do Intrinsic Magnetic Fields Protect Planetary Atmospheres from Stellar Winds? *Space Sci. Rev.* 217, 36. doi:10.1007/s11214-021-00791-1

Reeves, G. D., Henderson, M. G., McLachlan, P. S., Belian, R. D., Friedel, R. H. W., and Korth, A. (1996). "Radial Propagation of Substorm Injections," in International Conference on Substorms, Vol. 389. ESA Special Publication. Editors E. J. Rolfe. and B. Kaldeich (Paris: European Space Agency), 579.

Reinisch, B. W., Huang, X., Song, P., Green, J. L., Fung, S. F., Vasyliunas, V. M., et al. (2004). Plasmaspheric Mass Loss and Refilling as a Result of a Magnetic Storm. *J. Geophys. Res.* 109, A01202. doi:10.1029/2003JA009948

Ripoll, J.-F., Albert, J. M., and Cunningham, G. S. (2014). Electron Lifetimes from Narrowband Wave-Particle Interactions within the Plasmasphere. *J. Geophys. Res. Space Phys.* 119, 8858–8880. doi:10.1002/2014JA020217

Roberts, W. T., Horwitz, J. L., Comfort, R. H., Chappell, C. R., Waite, J. H., and Green, J. L. (1987). Heavy Ion Density Enhancements in the Outer Plasmasphere. *J. Geophys. Res.* 92, 13499. doi:10.1029/JA092iA12p13499

Roelof, E. C., Mauk, B. H., and Meier, R. R. (1992). "Instrument Requirements for Imaging the Magnetosphere in Extreme Ultraviolet and Energetic Neutral Atoms Derived from Computer-Simulated Images," in Instrumentation for Magnetospheric Imagery, Vol. 1744 of Society of Photo-Optical Instrumentation Engineers (SPIE) Conference Series. Editor S. Chakrabarti (SPIE), 19–30. doi:10.1117/12.60576

Runov, A., Angelopoulos, V., Zhou, X.-Z., Zhang, X.-J., Li, S., Plaschke, F., et al. (2011). A THEMIS Multicase Study of Dipolarization Fronts in the Magnetotail Plasma Sheet. *J. Geophys. Res.* 116, A05216. doi:10.1029/2010JA016316

Samson, J. C., Harrold, B. G., Ruohoniemi, J. M., Greenwald, R. A., and Walker, A. D. M. (1992). Field Line Resonances Associated with MHD Waveguides in the Magnetosphere. *Geophys. Res. Lett.* 19, 441–444. doi:10.1029/92GL00116

Samson, J. C., and Rostoker, G. (1972). Latitude-dependent Characteristics of High-Latitude Pc 4 and Pc 5 Micropulsations. *J. Geophys. Res.* 77, 6133–6144. doi:10.1029/JA077i031p06133

Sandanger, M., Søraas, F., Aarsnes, K., Oksavik, K., and Evans, D. S. (2007). Loss of Relativistic Electrons: Evidence for Pitch Angle Scattering by Electromagnetic Ion Cyclotron Waves Excited by Unstable Ring Current Protons. *J. Geophys. Res. (Space Phys.* 112, A12213. doi:10.1029/2006JA012138

Sandel, B. R., Broadfoot, A. L., Curtis, C. C., King, R. A., Stone, T. C., Hill, R. H., et al. (2000). The Extreme Ultraviolet Imager Investigation for the IMAGE Mission. *Space Sci. Rev.* 91, 197–242. doi:10.1023/A:1005263510820

Sandel, B. R. (2011). Composition of the Plasmasphere and Implications for Refilling. *Geophys. Res. Lett.* 38, a–n. doi:10.1029/2011GL048022

Sandel, B. R., and Denton, M. H. (2007). Global View of Refilling of the Plasmasphere. *Geophys. Res. Lett.* 34, L17102. doi:10.1029/2007GL030669

Sandel, B. R., King, R. A., Forrester, W. T., Gallagher, D. L., Broadfoot, A. L., and Curtis, C. C. (2001). Initial Results from the IMAGE Extreme Ultraviolet Imager. *Geophys. Res. Lett.* 28, 1439–1442. doi:10.1029/2001GL012885

Sergeev, V. A., Liou, K., Meng, C.-I., Newell, P. T., Brittnacher, M., Parks, G., et al. (1999). Development of Auroral Streamers in Association with Localized Impulsive Injections to the Inner Magnetotail. *Geophys. Res. Lett.* 26, 417–420. doi:10.1029/1998GL900311

Sergeev, V. A., Sauvaud, J.-A., Popescu, D., Kovrazhkin, R. A., Liou, K., Newell, P. T., et al. (2000). Multiple-spacecraft Observation of a Narrow Transient Plasma Jet in the Earth's Plasma Sheet. *Geophys. Res. Lett.* 27, 851–854. doi:10.1029/1999GL010729

Shprits, Y. Y., Drozdov, A. Y., Spasojevic, M., Kellerman, A. C., Usanova, M. E., Engebretson, M. J., et al. (2016). Wave-induced Loss of Ultra-relativistic Electrons in the Van Allen Radiation Belts. *Nat. Commun.* 7, 12883. doi:10.1038/ncomms12883

Singh, N. (1996). Effects of Electrostatic Ion Cyclotron Wave Instability on Plasma Flow during Early Stage Plasmaspheric Refilling. *J. Geophys. Res.* 101, 17217–17227. doi:10.1029/96JA01008

Singh, N., and Horwitz, J. L. (1992). Plasmasphere Refilling: Recent Observations and Modeling. *J. Geophys. Res.* 97, 1049. doi:10.1029/91JA02602

Sitnov, M. I., Swisdak, M., and Divin, A. V. (2009). Dipolarization Fronts as a Signature of Transient Reconnection in the Magnetotail. *J. Geophys. Res.* 114, a–n. doi:10.1029/2008JA013980

Sojka, J. J., Rasmussen, C. E., and Schunk, R. W. (1986). An Interplanetary Magnetic Field Dependent Model of the Ionospheric Convection Electric Field. *J. Geophys. Res.* 91, 11281–11290. doi:10.1029/JA091iA10p11281

Sorathia, K. A., Ukhorskiy, A. Y., Merkin, V. G., Fennell, J. F., and Claudepierre, S. G. (2018). Modeling the Depletion and Recovery of the Outer Radiation Belt during a Geomagnetic Storm: Combined MHD and Test Particle Simulations. *J. Geophys. Res. Space Phys.* 123, 5590–5609. doi:10.1029/2018JA025506

Stawarz, J. E., Ergun, R. E., and Goodrich, K. A. (2015). Generation of High-Frequency Electric Field Activity by Turbulence in the Earth's Magnetotail. *J. Geophys. Res. Space Phys.* 120, 1845–1866. doi:10.1002/2014JA020166

Stawarz, J. E., Eriksson, S., Wilder, F. D., Ergun, R. E., Schwartz, S. J., Pouquet, A., et al. (2016). Observations of Turbulence in a Kelvin-Helmholtz Event on 8 September 2015 by the Magnetospheric Multiscale Mission. *J. Geophys. Res. Space Phys.* 121, 11,021–11,034. doi:10.1002/2016JA023458

Summers, D., Thorne, R. M., and Xiao, F. (1998). Relativistic Theory of Wave-Particle Resonant Diffusion with Application to Electron Acceleration in the Magnetosphere. *J. Geophys. Res.* 103, 20487–20500. doi:10.1029/98JA01740

Takada, T., Nakamura, R., Baumjohann, W., Asano, Y., Volwerk, M., Zhang, T. L., et al. (2006). Do BBFs Contribute to Inner Magnetosphere Dipolarizations: Concurrent Cluster and Double Star Observations. *Geophys. Res. Lett.* 33, L21109. doi:10.1029/2006GL027440

Takahashi, K., Denton, R. E., Kurth, W., Kletzing, C., Wygant, J., Bonnell, J., et al. (2015). Externally Driven Plasmaspheric ULF Waves Observed by the Van Allen Probes. *J. Geophys. Res. Space Phys.* 120, 526–552. doi:10.1002/2014JA020373

Thorne, R. M. (2010). Radiation Belt Dynamics: The Importance of Wave-Particle Interactions. *Geophys. Res. Lett.* 37, a–n. doi:10.1029/2010GL044990

Titov, D. V., Svedhem, H., McCoy, D., Lebreton, J.-P., Barabash, S., Bertaux, J.-L., et al. (2006). Venus Express: Scientific Goals, Instrumentation, and Scenario of the Mission. *Cosm. Res.* 44, 334–348. doi:10.1134/S0010952506040071

Torbert, R. B., Russell, C. T., Magnes, W., Ergun, R. E., Lindqvist, P.-A., LeContel, O., et al. (2016). The FIELDS Instrument Suite on MMS: Scientific Objectives, Measurements, and Data Products. *Space Sci. Rev.* 199, 105–135. doi:10.1007/s11214-014-0109-8

Trotignon, J. G., Décréau, P. M. E., Rauch, J. L., Le Guirriec, E., Canu, P., and Darrouzet, F. (2003). The Whisper Relaxation Sounder Onboard Cluster: A Powerful Tool for Space Plasma Diagnosis Around the Earth. *Cosmic Res.* 41, 345–348. doi:10.1023/a:1025045308666

Turner, D. L., Claudepierre, S. G., Fennell, J. F., O'Brien, T. P., Blake, J. B., Lemon, C., et al. (2015). Energetic Electron Injections Deep into the Inner Magnetosphere Associated with Substorm Activity. *Geophys. Res. Lett.* 42, 2079–2087. doi:10.1002/2015GL063225

Turner, D. L., Fennell, J. F., Blake, J. B., Claudepierre, S. G., Clemmons, J. H., Jaynes, A. N., et al. (2017). Multipoint Observations of Energetic Particle Injections and Substorm Activity during a Conjunction between Magnetospheric Multiscale (MMS) and Van Allen Probes. *J. Geophys. Res. Space Phys.* 122, 11,481–11,504. doi:10.1002/2017JA024554

Usanova, M. E., Darrouzet, F., Mann, I. R., and Bortnik, J. (2013). Statistical Analysis of EMIC Waves in Plasmaspheric Plumes from Cluster Observations. *J. Geophys. Res. Space Phys.* 118, 4946–4951. doi:10.1002/jgra.50464

Usanova, M. E., Drozdov, A., Orlova, K., Mann, I. R., Shprits, Y., Robertson, M. T., et al. (2014). Effect of EMIC Waves on Relativistic and Ultrarelativistic Electron Populations: Ground-Based and Van Allen Probes Observations. *Geophys. Res. Lett.* 41, 1375–1381. doi:10.1002/2013GL059024

Watt, C. E. J., Allison, H. J., Meredith, N. P., Thompson, R. L., Bentley, S. N., Rae, I. J., et al. (2019). Variability of Quasilinear Diffusion Coefficients for Plasmaspheric Hiss. *J. Geophys. Res. Space Phys.* 124, 8488–8506. doi:10.1029/2018JA026401

Welling, D. T., André, M., Dandouras, I., Delcourt, D., Fazakerley, A., Fontaine, D., et al. (2015). The Earth: Plasma Sources, Losses, and Transport Processes. *Space Sci. Rev.* 192, 145–208. doi:10.1007/s11214-015-0187-2

Wiltberger, M., Merkin, V., Lyon, J. G., and Ohtani, S. (2015). High-resolution Global Magnetohydrodynamic Simulation of Bursty Bulk Flows. *J. Geophys. Res. Space Phys.* 120, 4555–4566. doi:10.1002/2015ja021080

Wright, A. N. (1996). Transfer of Magnetosheath Momentum and Energy to the Ionosphere along Open Field Lines. *J. Geophys. Res.* 101, 13169–13178. doi:10.1029/96JA00541

Wygant, J. R., Bonnell, J. W., Goetz, K., Ergun, R. E., Mozer, F. S., Bale, S. D., et al. (2013). The Electric Field and Waves Instruments on the Radiation Belt Storm Probes Mission. *Space Sci. Rev.* 179, 183–220. doi:10.1007/s11214-013-0013-7

Yang, J., Toffoletto, F. R., and Wolf, R. A. (2014). RCM-E Simulation of a Thin Arc Preceded by a North-South-Aligned Auroral Streamer. *Geophys. Res. Lett.* 41, 2695–2701. doi:10.1002/2014GL059840

Young, D. T., Perraut, S., Roux, A., de Villedary, C., Gendrin, R., Korth, A., et al. (1981). Wave-particle Interactions Near Ω_{He+} Observed in GEOS 1 and 2 1. Propagation of Ion Cyclotron Waves in He^+ -rich Plasma. *J. Geophys. Res.* 86, 6755–6772. doi:10.1029/JA086iA08p06755

Zhang, W., Fu, S., Gu, X., Ni, B., Xiang, Z., Summers, D., et al. (2018). Electron Scattering by Plasmaspheric Hiss in a Nightside Plume. *Geophys. Res. Lett.* 45, 4618–4627. doi:10.1029/2018GL077212

Conflict of Interest: Authors LD and JP are employed by Advanced Space LLC.

The remaining authors declare that the research was conducted in the absence of any commercial or financial relationships that could be construed as a potential conflict of interest.

Publisher's Note: All claims expressed in this article are solely those of the authors and do not necessarily represent those of their affiliated organizations, or those of the publisher, the editors, and the reviewers. Any product that may be evaluated in this article, or claim that may be made by its manufacturer, is not guaranteed or endorsed by the publisher.

frontiers | Frontiers in Astronomy and Space Sciences

METHODS
published: 29 June 2022
doi: 10.3389/fspas.2022.912868

Revolutionizing Our Understanding of Particle Energization in Space Plasmas Using On-Board Wave-Particle Correlator Instrumentation

Gregory G. Howes[1], Jaye L. Verniero[2], Davin E. Larson[3], Stuart D. Bale[3,4], Justin C. Kasper[5,6], Keith Goetz[7], Kristopher G. Klein[8,9], Phyllis L. Whittlesey[3], Roberto Livi[3], Ali Rahmati[3], Christopher H. K. Chen[10], Lynn B. Wilson[2], Benjamin L. Alterman[11] and Robert T. Wicks[12]*

[1]Department of Physics and Astronomy, University of Iowa, Iowa City, IA, United States, [2]Goddard Space Flight Center, Heliophysics Science Division, NASA, Greenbelt, MD, United States, [3]Space Science Laboratory, University of California, Berkeley, Berkeley, CA, United States, [4]Physics Department, University of California, Berkeley, Berkeley, CA, United States, [5]Climate and Space Sciences and Engineering, University of Michigan, Ann Arbor, MI, United States, [6]BWX Technologies, Inc., Washington, DC, United States, [7]School of Physics and Astronomy, University of Minnesota, Minneapolis, MN, United States, [8]Lunar and Planetary Laboratory, University of Arizona, Tucson, AZ, United States, [9]Department of Planetary Sciences, University of Arizona, Tucson, AZ, United States, [10]Department of Physics and Astronomy, Queen Mary University of London, London, United Kingdom, [11]Southwest Research Institute, San Antonio, TX, United States, [12]Department of Mathematics, Physics and Electrical Engineering, Northumbria University, Newcastle Upon Tyne, United Kingdom

OPEN ACCESS

Edited by:
Jiansen He,
Peking University, China

Reviewed by:
Tieyan Wang,
Rutherford Appleton Laboratory, United Kingdom
Jinsong Zhao,
Purple Mountain Observatory (CAS), China

***Correspondence:**
Gregory G. Howes
gregory-howes@uiowa.edu

Specialty section:
This article was submitted to Space Physics, a section of the journal Frontiers in Astronomy and Space Sciences

Received: *05 April 2022*
Accepted: *02 May 2022*
Published: *29 June 2022*

Citation:
Howes GG, Verniero JL, Larson DE, Bale SD, Kasper JC, Goetz K, Klein KG, Whittlesey PL, Livi R, Rahmati A, Chen CHK, Wilson LB, Alterman BL and Wicks RT (2022) Revolutionizing Our Understanding of Particle Energization in Space Plasmas Using On-Board Wave-Particle Correlator Instrumentation. Front. Astron. Space Sci. 9:912868. doi: 10.3389/fspas.2022.912868

A leap forward in our understanding of particle energization in plasmas throughout the heliosphere is essential to answer longstanding questions in heliophysics, including the heating of the solar corona, acceleration of the solar wind, and energization of particles that lead to observable phenomena, such as the Earth's aurora. The low densities and high temperatures of typical heliospheric environments lead to weakly collisional plasma conditions. Under these conditions, the energization of particles occurs primarily through collisionless interactions between the electromagnetic fields and the individual plasma particles with energies characteristic of a particular interaction. To understand how the plasma heating and particle acceleration impacts the macroscopic evolution of the heliosphere, impacting phenomena such as extreme space weather, it is critical to understand these collisionless wave-particle interactions on the characteristic ion and electron kinetic timescales. Such understanding requires high-cadence measurements of both the electromagnetic fields and the three-dimensional particle velocity distributions. Although existing instrument technology enables these measurements, a major challenge to maximize the scientific return from these measurements is the limited amount of data that can be transmitted to the ground due to telemetry constraints. A valuable, but underutilized, approach to overcome this limitation is to compute on-board correlations of the maximum-cadence field and particle measurements to improve the sampling time by several orders of magnitude. Here we review the fundamentals of the innovative field-particle correlation technique, present a formulation of the technique that can be implemented as an on-board wave-particle correlator, and estimate results that can be

achieved with existing instrumental capabilities for particle velocity distribution measurements.

Keywords: plasma heating, particle acceleration, plasma turbulence, collisionless shocks, magnetic reconnection, kinetic instabilities, wave-particle correlator

1 INTRODUCTION

One of the key goals in heliophysics and astrophysics is to discover and characterize the processes controlling the flow of energy and the impact of that energy on the evolution of the space plasma environment. For example, although the source of energy in the heliosphere is nuclear fusion occurring at the heart of the Sun, the mechanisms which mediate the flow of some fraction of that energy into the solar corona—where it ultimately heats the coronal plasma to temperatures in excess of one million Kelvin—remain poorly understood. In particular, the fundamental plasma physics mechanisms of turbulence, magnetic reconnection, shocks, and instabilities (e.g., see Howes, 2017; Hesse and Cassak, 2020; Verscharen et al., 2019; Wilson et al., 2021b,Wilson et al., 2021a, and references therein) play crucial roles in mediating the transport of energy in space and astrophysical plasmas, and have been identified as grand challenge problems in the 2013–2022 Decadal Survey in Solar and Space Physics by the National Research Council.

Under the typically low-density and high-temperature conditions of turbulent plasmas in the heliosphere and planetary magnetospheres, the energization of particles occurs primarily through the collisionless interaction between the electromagnetic fields and the individual plasma particles (Howes, 2017; Wilson et al., 2018). To understand how the consequent plasma heating and particle acceleration impacts the macroscopic evolution of the heliosphere, driving phenomena such as extreme space weather, it is critical to understand these collisionless wave-particle interactions on their characteristic ion and electron kinetic timescales. Such understanding requires high-cadence measurements of both the electromagnetic fields and the three-dimensional particle velocity distributions. Although existing instrument technology enables these measurements, a major challenge to maximize the scientific return from these measurements is the limited amount of data that can be transmitted to the ground due to telemetry constraints. A valuable, but not widely used, approach to overcome this limitation is to compute on-board correlations of the maximum-cadence field and particle measurements. Here we propose a novel spacecraft mission concept focused on the coordinated operation of field and particle instruments that has the potential to achieve an improvement in sampling time by orders of magnitude, opening the door for transformative progress in our understanding of particle energization in the heliosphere.

Nonlinear plasma kinetic theory dictates that the collisionless interactions between the electromagnetic fields and charged particles in weakly collisional heliospheric plasmas necessarily lead to correlations between the fields and fluctuations in the particle velocity distributions. This fundamental insight lead to the recent develoment of the *field-particle correlation technique* (Klein and Howes, 2016; Howes et al., 2017; Klein et al., 2017), which employs *single-point* measurements of the electromagnetic fields and particle velocity distributions to determine not only the net energy transfer between the fields and particles, but also how that transferred energy is distributed in particle velocity space. A variation of this technique, denoted the Particle Arrival Time Correlation for Heliophysics (PATCH) method (Verniero et al., 2021b), was devised specificially for implementation with on-board wave-particle correlator instrumentation. These developments provide a solid theoretical foundation for the pursuit of a new mission based on novel wave-particle correlator instrumentation.

1.1 History of Wave-Particle Correlator Instrumentation

Several previous rocket and spacecraft missions have indeed sought to perform on-board mathematical correlations between field measurements and particle measurements at the same point in space, thereby preserving the valuable phase information needed to establish definitively an interaction between the fields and particles. The earliest attempts to identify wave-particle interactions in space plasmas sought to measure the phase bunching of resonant electrons predicted to occur in the presence of sufficiently large-amplitude Langmuir wave fluctuations (Melrose, 1986). On-board particle auto-correlator instruments were developed to detect electron phase bunching at $f \sim 10^6$ Hz frequencies in the auroral ionosphere, even when electron count rates were $\nu \lesssim 10^5$ Hz (Spiger et al., 1974; 1976; Gough, 1980; Gough et al., 1980), providing a critical foundation for the subsequent development of wave-particle correlators.

The first conclusive wave-particle correlator, that performed a direct correlation of the arrival times of electrons with the phase of the high-frequency wave field, flew on a sounding rocket in the auroral zone (Ergun et al., 1991a; b). This experiment indeed detected electron phase bunching during periods of intense Langmuir waves, driving subsequent theoretical work to develop refined theoretical predictions for finite-size Langmuir wavepackets (Muschietti et al., 1994). A wave-particle correlator was attempted on the *Wind* spacecraft (Wilson et al., 2021a between the WAVES and 3DP instruments but it did not correctly trigger. Another wave-particle correlator was flown on the NASA *Combined Release and Radiation Effects Satellite* (*CRRES*), computing correlations onboard between the Low Energy Plasma Analyzer and the electric field/Langmuir probe instrument (Watkins et al., 1996), and later a refined wave-particle correlator was implemented as a component of the Fields instrument on the *FAST* spacecraft (Ergun et al., 1998,

2001). Subsequent development lead to an improved wave-particle correlator design with higher phase resolution than previous instruments, flown on an auroral sounding rocket, which measured the reactive component of the electron phase bunching in a Langmuir wave (Kletzing et al., 2005; Kletzing and Muschietti, 2006). Further developments in wave-particle correlator instrumentation have continued (Fukuhara et al., 2009), with the latest implementation of a Software-type Wave-Particle Interaction Analyzer (S-WPIA) on-board the Japanese *Arase* spacecraft (Miyoshi et al., 2018) to study the energy transfer process between energetic electrons and whistler-mode chorus emissions in the Earth's inner magnetosphere (Katoh et al., 2013; Katoh et al., 2018).

All of these previous wave-particle correlator instruments were specially designed to explore the energy transfer to particles from waves that have frequencies at or above the particle detector counting rate, $f \gtrsim \nu$, for example studying the interaction of electrons with whistler waves or Langmuir waves in the Earth's magnetosphere. But the Alfvénic turbulent fluctuations in the magnetosheath, solar wind, and solar corona have a much lower frequency than the whistler and Langmuir wave fluctuations of interest in the magnetosphere. Furthermore, current spacecraft missions—such as the *Magnetospheric Multiscale* (*MMS*) (Burch et al., 2016), *Parker Solar Probe* (Bale et al., 2016; Fox et al., 2016; Kasper et al., 2016; Whittlesey et al., 2020; Livi et al., 2021), and *Solar Orbiter* (Müller et al., 2013) missions—boast fast, three-dimensional particle velocity measurements at a sampling rate approaching or surpassing the frequency of the fluctuations involved in the collisionless transfer of energy between fields and particles, $f \lesssim \nu$. These unprecedented measurement capabilities, coupled with recent advances in plasma kinetic theory for determining particle energization from single-point measurements of electromagnetic field and particle velocity distribution measurements (Klein and Howes, 2016; Howes et al., 2017; Klein et al., 2017), make possible an *entirely new approach* to understanding particle energization using an on-board field-particle correlator, providing a strong motivation for the mission concept proposed here.

2 MATERIALS AND EQUIPMENT

In this section, we describe the heritage Electrostatic Analyzer (ESA) particle instrumentation, electromagnetic fields instrumentation, and electronics digital processing units (DPUs) that comprise the base elements upon which an onboard wave-particle correlator instrument would be designed. The specific details arise from two of the key instrument suites on the *Parker Solar Probe* (*PSP*) mission: 1) the Solar Wind Electron Alphas and Protons (SWEAP) investigation (Kasper et al., 2016) that measures the core (thermal) plasma populations; and 2) the FIELDS investigation (Bale et al., 2016) that measures the two-dimensional electric and three-dimensional magnetic fields.

2.1 Electrostatic Analyzer Instruments

Three of the four SWEAP sensors on *PSP* are electrostatic analyzers (2 electron and 1 ion) that detect single particles and return total accumulated counts within a short (~1 ms) time interval that represents only one point in phase space (Kasper et al., 2016; Whittlesey et al., 2020; Livi et al., 2021). Even though this intrinsic time resolution may seem short, it is long compared to the time duration of some field-particle interactions. The goal is to use on-board electronics to correlate the particle counts from the electrostatic analyzer instruments with measurements of the electromagnetic fields simultaneous with the particle detections, yielding a new instrument denoted an Integrated Field-Particle Correlator (IFPC) instrument.

Current heritage instrument operational parameters are listed in **Table 1** compared to the predicted requirements for an IFPC ion and electron instruments. Note that the requirements for ions and electrons are different. Although the process for modifying the SPAN-E heritage sensor to perform onboard field-particle correlation measurements is identical for ions and electrons (excepting the micro-channel plate supply modification), the science requirements for the electron IFPC and the ion IFPC are different, with electron IFPC requiring a substantially faster measurement cadence. Increasing the measurement cadence of the heritage electron instrument is achievable with an increase in consumed instrument power (currently ~2 W depending on the area of phase space being scanned at the time) and additional modifications to the Field-Programmable Gate Array (FPGA) design.

In the heritage wave-particle correlator instrument on *Parker Solar Probe*, SPAN-E, the correlator subsection is located on another board: in the case of *PSP*, the SPAN-E particle counts from either one or many anodes are summed together into a single channel, and are sent to the FIELDS suite, where they are correlated onboard the Time Domain Sampler (TDS) board (Bale et al., 2016). Modifications to implement an IFPC require upgrading the heritage instrument's digital board and FPGA to preserve the angular resolution from the individual separate anodes in the correlation with electric and magnetic fields signals. The optimal method of doing this is to modify the FPGA firmware to perform correlations onboard the heritage instrument, where all 16 anodes' channels are preserved separately, instead of running 16 output signals to an external instrument, which would then need 16 dedicated channels to process the correlations separately. Thus, instead of conducting correlations on a summation of 16 channels' worth of signal with fields externally, we propose to introduce new input channels to the SPAN-E Engineering Test Unit's (ETU) digital board to perform correlations internally.

2.2 Electromagnetic Fields Instruments

The detailed specifications of the electromagnetic fields instruments on *Parker Solar Probe* are presented in Bale et al. (2016), and so we only briefly describe the relevant fields instruments to be incorporated into a proposed IFPC here.

The electric fields essential to the computing field-particle correlations that probe the rate of energization of particles (see **Section 3.1**) are measured using four voltage sensors deployed in nearly orthogonal, co-linear pairs slightly behind the plane of the spacecraft heat shield. These voltage sensors are implemented as a current-biased resistively-coupled double probe instrument.

TABLE 1 | Heritage electrostatic analyzer for electrons (SPAN-E) measurement performance and predicted performance requirements of proposed ion and electron Integrated Field-Particle Correlator (IFPC) instruments.

	Energy Range	Cadence	# Of phase Space Bins	$\Delta E/E$	$\Delta\theta \times \Delta\phi$	Field of View
SPAN-E	5eV - 30 keV	0.218s 3D VDF	256	7%	$6^\circ \times 3.75^\circ$	$247^\circ \times 120^\circ$
IFPC i^+	10eV-2 keV	0.3s 3D VDF	-	< 10%	$15^\circ \times 10^\circ$	$180^\circ \times 30^\circ$
IFPC e^-	5eV-5 keV	0.06s 3D VDF	-	< 10%	$10^\circ \times 10^\circ$	$200^\circ \times 90^\circ$

Providing measurements at 2M samples/s, this instrument returns two-component electric field measurements over a bandwidth from DC up to 1 MHz. A calibration procedure to process these voltage measurements and return 2D electric field data is detailed in Mozer et al. (2020).

The magnetic fields are measured using both fluxgate and search-coil (induction) magnetometers mounted on a deployable boom. The fluxgate magnetometers measure the 3D magnetic field at 293 samples/s, covering a bandwidth from DC up to 140 Hz, with dynamic range of ±65,536 nT and a resolution of 16 bits. The search-coil magnetometer measures all three components of the AC magnetic signature of solar wind fluctuations, from 10 Hz up to 50 kHz and a single component from 1 kHz to 1 MHz.

The wide bandwidth and dynamic range of these electric and magnetic field instruments allows FIELDS to investigate transients caused by interplanetary shocks and reconnection, the turbulent cascade beyond the electron kinetic scale, and also numerous plasma wave modes. Within different plasma environments in the heliosphere, these processes are predicted to play a role in the energization of particles. These heritage instruments are sufficiently capable that, when integrated with the particle instrumentation described in **Section 2.1**, an IFPC can be developed to provide high-cadence and long-time statistical sampling of the heliospheric plasma dynamics to discover and characterize the dominant mechanisms of particle energization.

2.3 Electronic Digital Processing Units

The FIELDS instrument on *Parker Solar Probe* includes a waveform capture instrument which is intended to capture voltage time-series waveform bursts, $V(t)$, from the FIELDS detectors. The FIELDS Time Domain Sampler (TDS) samples five analog voltage channels at a sampling speed of ~ 2M samples/s. This can include sampling any of the five FIELDS voltage probes (V1, V2, V3, V4 or V5) or the dipoles formed by sampling V1-V2 or V3-V4. In addition, the TDS can sample one mid-frequency winding of the magnetic search coil sensor.

TDS bursts are triggered to allow the capture of waveforms using a peak triggering mechanism. Triggered bursts are saved to catalog of bursts in instrument memory. Evaluation of waveforms using a combination of waveform RMS amplitude and waveform frequency provide selection criteria for sending "interesting" waveforms to the ground.

The TDS also incorporates a single-channel wave-particle correlator on *Parker Solar Probe*, as depicted in the diagram in **Figure 1**. The additional of a single connection (red) directly between the SWEAP Electronics Module (SWEM) and the FIELDS Time Domain Sampler (TDS) enables a simple implementation of a wave-particle correlator. In addition to the five analog channels of the TDS described above, each sampled at 2M samples/s, or 500 ns/sample, the TDS simultaneously counts incoming particles from the SWEAP instrument in an accumulator. As the analog samples are acquired during each 500ns sampling period, the number of accumulated particle pulses are also sampled and stored in TDS instrument memory. In this way, complete TDS bursts are returned to the ground with high-time resolution waveforms of electric and magnetic field values obtained simultaneously with the corresponding particle count time series.

The wave-particle correlator implemented on *Parker Solar Probe* is rather limited in capability relative to the IFPC proposed here, and was included primarily as a proof-of-principle demonstration of a correlator instrument. Some of the shortcomings of this limited implementation are: 1) the duty cycle of selected events is extremely small; 2) correlations are not done on board, and thus there is no way to trigger on correlated events; 3) the on-board burst selection criteria is based only on wave amplitude, not on field-particle correlations; and 4) only a single point in phase space (1 of 16 anodes) can be correlated at a time.

3 METHODS

In this section, we explain how the field-particle correlation technique is derived from the Boltzmann equation for the evolution of a weakly collisional plasma, detail refinements of the implementation of the technique for application to the discrete phase-space measurements of the particle velocity distributions provided by modern electrostatic analyzer instruments, describe modifcations of the technique for application to on-board wave-particle correlator instrumentation, and finally present the proposed design of a multi-channel, dedicated On-Board Wave-Particle Correlator instrument.

3.1 The Field-Particle Correlation Technique

The nonlinear evolution of a kinetic plasma is governed by the Maxwell-Boltzmann equations. Under the weakly collisional conditions typical of heliospheric plasmas, we can drop the collision term in the Boltzmann equation, which is

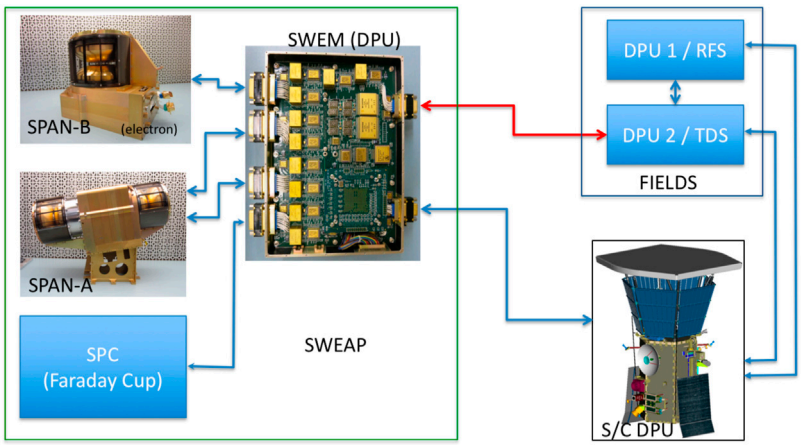

FIGURE 1 | The SWEAP/FIELDS interface on *PSP*: the Wave-Particle Correlator (WPC). The additional hardware (mass resource) consists of a single cable (red) that allows the SWEAP and FIELDS instruments to communicate to each other without the need to pass through the spacecraft interface. Wires in this cable conduct a 200 ns long particle pulse signal every time a particle is detected in a SPAN. From Verniero et al. (2021b).

unnecessary to describe the collisionless transfer of energy between fields and particles, to obtain the Vlasov equation.

To explore the energy transfer between fields and particles, we define the *phase-space energy density* for a particle species s by $w_s(\mathbf{r}, \mathbf{v}, t) = m_s v^2 f_s(\mathbf{r}, \mathbf{v}, t)/2$. Multiplying the Vlasov equation by $m_s v^2/2$, we obtain an expression for the rate of change of the phase-space energy density,

$$\frac{\partial w_s(\mathbf{r},\mathbf{v},t)}{\partial t} = -\mathbf{v}\cdot\nabla w_s - q_s\frac{v^2}{2}\mathbf{E}\cdot\frac{\partial f_s}{\partial \mathbf{v}} - \frac{q_s}{c}\frac{v^2}{2}(\mathbf{v}\times\mathbf{B})\cdot\frac{\partial f_s}{\partial \mathbf{v}}. \quad (1)$$

Integrating over all velocity space and all physical space eliminates the first and third terms (Howes et al., 2017), yielding an equation for the rate of change of the energy W_s of a particle species s

$$\frac{\partial W_s}{\partial t} = -\int d^3\mathbf{r}\int d^3\mathbf{v}\, q_s\frac{v^2}{2}\frac{\partial f_s}{\partial \mathbf{v}}\cdot\mathbf{E} = \int d^3\mathbf{r}\left(\int d^3\mathbf{v}\, q_s\mathbf{v}f_s\right)\cdot\mathbf{E} = \int d^3\mathbf{r}\,\mathbf{j}_s\cdot\mathbf{E}, \quad (2)$$

where an integration by parts in velocity has been used between the second and third forms above. This expression shows that the change in species energy W_s is due to work done on that species by the electric field, $\mathbf{j}_s\cdot\mathbf{E}$. The two middle expressions also make clear the concept that measurements of the electric field $\mathbf{E}$ and particle velocity distribution $f_s(\mathbf{v})$ contain sufficient information to determine the rate of energy transfer between the fields and particle species s.

Unfortunately spacecraft measurements provide information on the fields and particle velocity distributions at only one (or, for multi-spacecraft missions, a few) points in space as a function of time, a spatial sampling that is insufficient to perform the spatial integration in **Eq. 2**. To determine the energy transfer between fields and particles at a single point in space, we return to **Eq. 2** which provides the rate of change of phase-space energy density $\partial w_s(\mathbf{r}_0, \mathbf{v})/\partial t$ at a single point in space $\mathbf{r}_0$.

From the previous analysis, we know that only the second term on the right-hand side of **Eq. 1**, $-q_s(v^2/2)\mathbf{E}\cdot\partial f_s/\partial\mathbf{v}$, leads to a net change of particle energy when integrated over position and velocity. However, if the fields are oscillatory in time—for example, in the case of plasma turbulence—this term includes both contributions from the conservative *oscillating energy transfer* associated with undamped wave motion and from the *secular energy transfer* associated with the collisionless damping of the turbulent fluctuations (Klein and Howes, 2016; Howes et al., 2017). To eliminate the often larger amplitude oscillating energy transfer, we perform an unnormalized correlation (essentially a sliding time-average) between the particle and field measurements over a suitable correlation interval τ.

Note that the optimal choice of correlation interval τ depends on the physical mechanism under investigation. For turbulent fluctuations damped by collisionless wave-particle interactions (through resonant mechanisms such as Landau damping or ion cyclotron damping or other mechanisms such as stochastic ion heating, for example), it is generally necessary to choose an interval τ that is longer than several of the oscillation periods of the turbulent fluctuations at the scales suffering the collisionless damping (Klein and Howes, 2016; Howes et al., 2017; Klein et al., 2017).

To help diagnose the nature of the physical mechanism governing the energization of the particles, it is beneficial to separate out the contributions to the dot product in the second term on the right-hand side of **Eq. 1** from the different components of $\mathbf{E}$. For some cases, such as plasma turbulence, it can be beneficial to decompose $\mathbf{E}$ in a field-aligned coordinate (FAC) system, $(E_{\perp 1}, E_{\perp 2}, E_\parallel)$. Thus, the field-particle correlations for each of the components[1] are given by

$$C_{E_\parallel}(\mathbf{v},t,\tau) = C\left(-q_s\frac{v_\parallel^2}{2}\frac{\partial f_s(\mathbf{r}_0,\mathbf{v},t)}{\partial v_\parallel}, E_\parallel(\mathbf{r}_0,t)\right) \quad (3)$$

[1]Note that the physically essential boundary condition that $f(v) \to 0$ as $|v| \to \infty$ can be exploited to reduce the v^2 factor in the jth component of the dot product to v_j^2 (Klein et al., 2017).

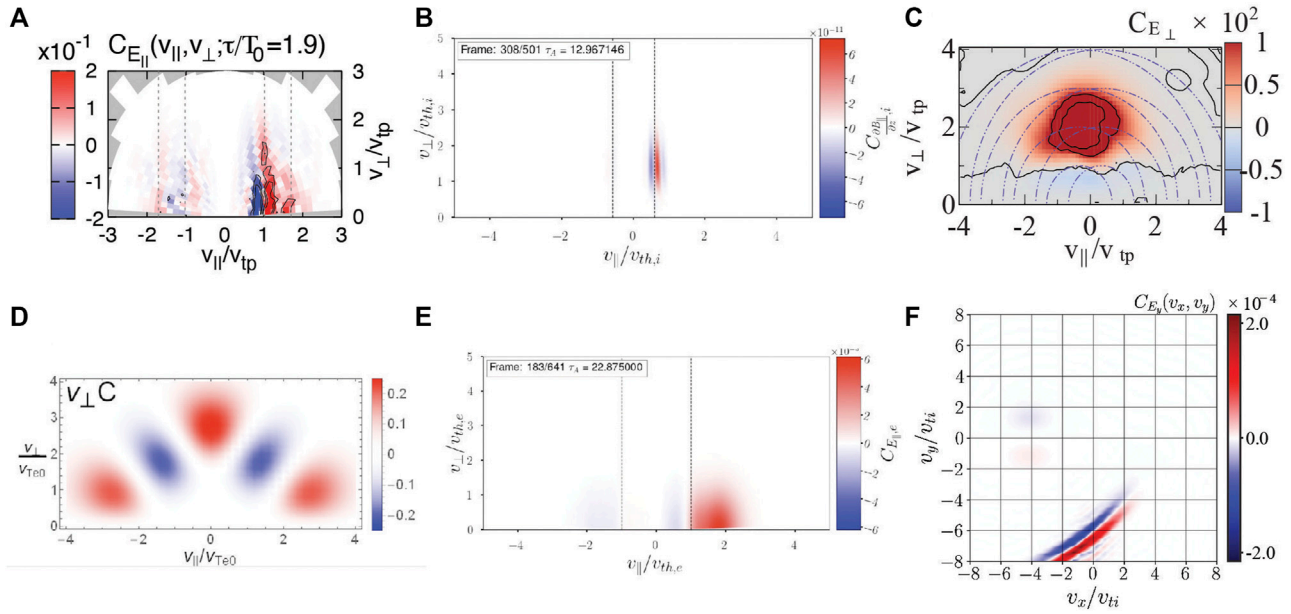

FIGURE 2 | Velocity-space signatures from the application of the field-particle correlation technique to numerous kinetic particle energization mechanisms: **(A)** gyrotropic velocity-space signature from the standard parallel field-particle correlation $C_{E_\parallel}(v_\parallel, v_\perp)$ for ion Landau damping in a gyrokinetic simulation of plasma turbulence (Klein et al., 2017); **(B)** parallel field-particle correlation for transit-time damping by the magnetic mirror force $C_{\delta B_\parallel}(v_\parallel, v_\perp)$ for a linear kinetic Alfvén wave; **(C)** perpendicular field-particle correlation $C_{E_\perp}(v_\parallel, v_\perp)$ for ion cyclotron damping from a hybrid Vlasov-Maxwell simulation of high-frequency plasma turbulence (Klein et al., 2020); **(D)** total field-particle correlation $C_{\mathbf{E}}(v_\parallel, v_\perp)$ for electron heating from a numerical model of magnetic pumping (Montag and Howes, 2022); **(E)** parallel field-particle correlation $C_{E_\parallel}(v_\parallel, v_\perp)$ for electron energization from a strong-guide field reconnection simulation (McCubbin et al., 2022); and **(F)** velocity-space signature of shock-drift acceleration $C_{E_y}(v_x, v_y)$ from a Vlasov simulation of a perpendicular collisionless shock with Alfvén Mach number $M_A \approx 5$ (Juno et al., 2021).

$$C_{E_{\perp 1}}(\mathbf{v},t,\tau) = C\left(-q_s\frac{v_{\perp 1}^2}{2}\frac{\partial f_s(\mathbf{r}_0,\mathbf{v},t)}{\partial v_{\perp 1}}, E_{\perp 1}(\mathbf{r}_0,t)\right) \quad (4)$$

$$C_{E_{\perp 2}}(\mathbf{v},t,\tau) = C\left(-q_s\frac{v_{\perp 2}^2}{2}\frac{\partial f_s(\mathbf{r}_0,\mathbf{v},t)}{\partial v_{\perp 2}}, E_{\perp 2}(\mathbf{r}_0,t)\right). \quad (5)$$

Here, the unnormalized, time-centered correlation $C(A, B)$ is essentially a sliding time average, and is defined at the discrete measurement time t_i by

$$C(A,B) \equiv \frac{1}{n}\sum_{j=i-n/2}^{i+n/2} A_j B_j, \quad (6)$$

for quantities A and B, which together as a product represent a rate of change of energy density, measured at discrete times $t_j = j\Delta t$, with their product averaged over n measurements over a correlation interval of duration $\tau \equiv n\Delta t$ (Klein et al., 2017). Applying this correlation to a time series of electric field and particle velocity distribution measurements at a single point yields the *velocity-space signature* of the secular energy transfer.

In general, each component E_j of the electric field yields a signature in three-dimensional velocity space (3V). To aid in visualization of the rate of energy transfer in velocity space, it is useful to reduce these 3V determinations to a two-dimensional form for ease of visualization. The optimal choice for such a two-dimensional reduction depends on the physical process under investigation. In the case of plasma turbulence, the typically low-frequency dynamics (relative to the cyclotron frequencies of the particle species) can be usefully represented in the 2V gyrotropic phase space ($v_\parallel$, $v_\perp$), where one integrates over the gyroangle about the magnetic field to obtain variations as a function of the perpendicular velocity coordinate $v_\perp = \sqrt{v_{\perp 1}^2 + v_{\perp 2}^2}$. For collisionless shocks, which generate decidedly agyrotropic distributions, one may integrate a general 3V velocity space (v_x, v_y, v_z) over each velocity dimension separately, obtaining three 2V representations (v_x, v_y), (v_y, v_z), and (v_z, v_x).

The application of the field-particle correlation technique yields a velocity-space signature of the rate of particle energization as a function of velocity. The qualitative and quantitative features of this velocity-space signature can typically be used to identify the physical mechanism responsible for the particle energization. In **Figure 2**, we show the velocity-space signatures of six different kinetic particle energization mechanisms, all of which are sufficiently unique to distinguish one mechanism from another. From a simulation of weakly collisional electromagnetic turbulence in a $\beta_i = 1$ and $T_i/T_e = 1$ plasma using the Astrophysical Gyrokinetics Code (AstroGK) (Numata et al., 2010), we plot in 1) the velocity-space signature of ion Landau damping using a visualization of the standard parallel field-particle correlation $C_{E_\parallel}(v_\parallel, v_\perp)$ on the gyrotropic velocity-space (Klein et al., 2017). The characteristic signature of Landau damping shows a loss of energy (blue) below the resonant velocity (vertical dashed line at $v_\parallel/v_{tp} \simeq 1$) and a gain of energy (red) above, corresponding to the familiar quasi-linear flattening of the distribution function (Howes et al., 2017). In

panel 2) is the velocity-space signature of transit-time damping (Barnes, 1966) of a linear kinetic Alfvén wave in a $\beta_i = 3$ plasma due to the magnetic mirror force $-\mu\nabla_\parallel|\mathbf{B}|$ acting on the magnetic moment of the particle's gyromotion $\mu = mv_\perp^2/(2B)$, given by $C_{\delta B_\parallel}(v_\parallel, v_\perp)$, where $\nabla_\parallel$ is the gradient along the magnetic field. In panel 3) is plotted the velocity-space signature of ion cyclotron damping $C_{E_\perp}(v_\parallel, v_\perp)$ from a Hybrid Vlasov-Maxwell (HVM) (Valentini et al., 2007) simulation of high-frequency plasma turbulence (Klein et al., 2020). In panel 4) is plotted the total field-particle correlation $C_{\mathbf{E}}(v_\parallel, v_\perp)$ for electron heating from a numerical model of magnetic pumping (Montag and Howes, 2022). In panel 5) is plotted the velocity-space signature of electron energization from a gyrokinetic simulation of magnetic reconnection in the strong-guide-field limit in a $\beta_i = 0.01$ plasma (McCubbin et al., 2022) using the parallel field-particle correlation $C_{E_\parallel}(v_\parallel, v_\perp)$. Finally, from a Gkeyll Vlasov simulation (Juno et al., 2018) of a perpendicular collisionless shock with Alfvén Mach number $M_A \simeq 5$, we show the velocity-space signature of shock-drift acceleration $C_{E_y}(v_x, v_y)$ (Juno et al., 2021). Together, these results show that the velocity-space signatures of these different kinetic energization mechanisms are qualitatively and quantitatively unique, providing a "Rosetta stone" for the identification of the physical mechanisms of particle energization. The results also strongly motivate the development on a dedicated instrument to provide velocity-space signatures from onboard computations of high-cadence field-particle correlations.

3.2 Refinements of the Implementation for Analysis of Spacecraft Measurements

The application of the field-particle correlation technique to data from kinetic simulations codes using a continuum representation of velocity space—where a complete grid of velocity space points is known at each point $\mathbf{r}$ in configuration space—is relatively straightforward. Specifically, one can simply implement a finite difference, or other discrete representation, of the derivative in velocity space needed in the field-particle correlations **Eqs. 3–5**. But for kinetic simulations codes that employ a Monte-Carlo sampling of velocity-space at a disordered set of velocity points (Juno et al., 2022), or for spacecraft instruments where the velocity phase-space measurements may not be uniformly distributed (Chen et al., 2019; Afshari et al., 2021), the computation of the velocty-space derivative $\partial f_s/\partial\mathbf{v}$ represents a non-trivial exercise. Here we describe a specific implementation of the technique for these latter two cases that yields usable results.

First, we note that substituting for $f_s = 2w_s/(m_s v^2)$ in the Vlasov equation and solving for the evolution of the phase-space energy density w_s along trajectories in 3D-3V phase space yields

$$\frac{\partial w_s}{\partial t} + \mathbf{v}\cdot\nabla w_s + \frac{q_s}{m_s}\left(\mathbf{E} + \frac{\mathbf{v}}{c}\times\mathbf{B}\right)\cdot\frac{\partial w_s}{\partial\mathbf{v}} = q_s\mathbf{v}\cdot\mathbf{E}f_s. \tag{7}$$

We define the right-hand side of **Eq. 7** as the *alternative field-particle correlation*

$$C'_{E_j}(\mathbf{v}, t, \tau) = C\Big(q_s v_j f_s(\mathbf{r}_0, \mathbf{v}, t), E_j(\mathbf{r}_0, t)\Big), \tag{8}$$

for the electric field component E_j. Note that when integrated over all velocity space, this alternative form yields the same net rate of change of spatial energy density as the forms in **Eqs. 3–5**. The difference between the two forms of the field-particle correlation is that the standard correlation $C(\mathbf{v})$ takes an Eulerian view of velocity space, showing which parts of velocity space are gaining or losing energy density, whereas the alternative correlation $C'(\mathbf{v})$ takes a Lagrangian view of velocity space, showing how small volumes of phase space gain or lose energy along their Lagrangian particle trajectories in 3D-3V phase space. A key advantage of the alternative form **Eq. 8** is that does not require velocity-space derivatives.

Here we describe specific choices for the implementation of the field-particle correlation technique to spacecraft measurements (Chen et al., 2019); the same choices can be used for an implementation with particle-based kinetic simulation codes, such as particle-in-cell (PIC) codes. First, the particle distribution measurements and electric field measurements are Lorentz transformed to the mean bulk flow velocity of species s over the interval to be analyzed. Second, it is also desirable to determine the mean velocity distribution $f_{s0}(\mathbf{v})$ averaged over the same interval and substract it to obtain the perturbed velocity distribution $\delta f_s(\mathbf{v}, t) = f_s(\mathbf{v}, t) - f_{s0}(\mathbf{v})$, computing the correlation with δf_s instead of f_s, although this is not strictly necessary. Third, the time-series of electric field measurements, which is usually sampled at a much higher cadence than the velocity distributions, is downsampled to the cadence of the velocity distribution measurements. With the $\delta f_s(\mathbf{v}, t)$ and $\mathbf{E}(t)$ measurements now at the same cadence, the alternative field-particle correlation $C'_{E_j}(\mathbf{v}_j, t_n) = q_s v_j E_j(t_n)\delta f_s(\mathbf{v}_j, t_n)$ is computed at each point in 3V velocity space $\mathbf{v}_j$ for each timeslice t_n. Next, the alternative correlation $C'_{E_j}(\mathbf{v}_j, t_n)$ is binned in velocity space, with the choice of bins tailored for investigation of a particular particle energization process—for the application to turbulence, it is binned into 2V gyrotropic phase space $(v_\parallel, v_\perp)$. The velocity derivatives needed to obtain the standard field-particle correlation $C_{E_j}(\mathbf{v}_j, t_n)$ can be computed at this point; for the parallel correlation in the 2V gyrotropic velocity space, it would take the form

$$C_{E_{\parallel,e}}(v_\parallel, v_\perp) = -\frac{v_\parallel}{2}\frac{\partial C'_{E_{\parallel,e}}(v_\parallel, v_\perp)}{\partial v_\parallel} + \frac{C'_{E_{\parallel,e}}(v_\parallel, v_\perp)}{2}, \tag{9}$$

For the analysis of particle energization by the dissipation of broadband plasma turbulence, it can be helpful to high-pass filter the electric field measurements to eliminate the large-amplitude contribution from the electric field fluctuations associated with large-scale, low-frequency waves—such waves typically have negligible net secular energy transfer associated with collisionless damping, so eliminating the often large-amplitude contribution to the rate of energy transfer due to undamped oscillations at large scales helps to expose the energy transfer due to smaller scale, higher frequency waves that dominate the collisionless damping of the turbulent fluctuations.

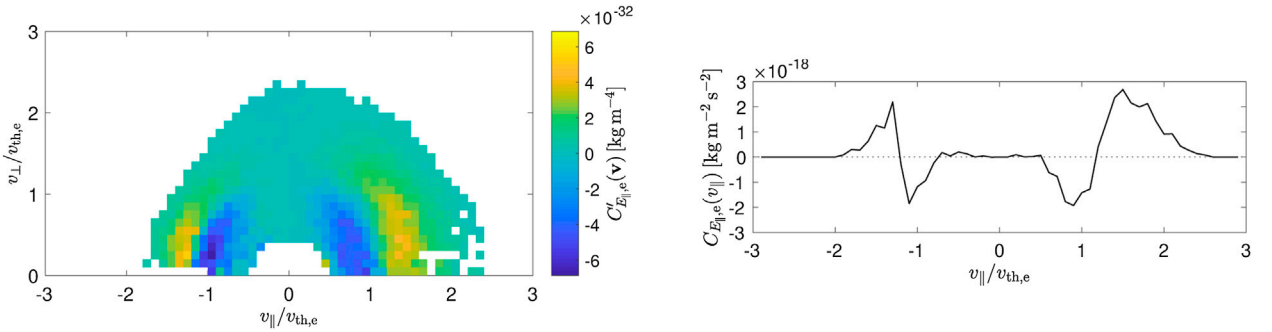

FIGURE 3 | Parallel alternative field-particle correlation for electrons, $C'_{E_\parallel,e}(v_\parallel, v_\perp)$, measured in the Earth's magnetosheath from *MMS* data (left). Same data integrated over $v_\perp$ and converted to the standard field-particle correlation $C_{E_\parallel,e}(v_\parallel)$. Both show a clear signature of electron Landau damping at $v_\parallel \sim \pm v_{th,e}$. Figures from Chen et al. (2019).

To demonstrate how these refinements of the implementation can yield a clear velocity-space signature, we present in **Figure 3** the results from Chen et al. (2019) showing the 2D alternative field-particle correlation $C'_{E_\parallel,e}(v_\parallel, v_\perp)$ and 1D standard field-particle correlation $C_{E_\parallel,e}(v_\parallel)$ for electrons measured using 70 s of data from the *MMS* spacecraft in the Earth's magnetosheath. The 2D correlation shows velocity-space structure primarily in $v_\parallel$ rather than $v_\perp$, and the 1D correlation directly represents the energy transfer at each parallel velocity. Since the energy transfer is from fields to particles ($C_{E_\parallel,e} > 0$) at $|v_\parallel| > v_{th,e}$ and from particles to fields ($C_{E_\parallel,e} < 0$) at $|v_\parallel| < v_{th,e}$, and the expected resonant velocity for which the kinetic Alfvén wave damping becomes strong is $\sim v_{th,e}$, this provides a clear signature that is consistent with the Landau damping of kinetic Alfvén turbulence in this region of space. Afshari et al. (2021) performed a follow-up study, applying this technique to 20 similar intervals, finding 95% displayed Landau-like signatures although most were more asymmetrical than in **Figure 3**, which is consistent with imbalanced turbulence, and is supported by kinetic numerical simulations (Horvath et al., 2020). Both Chen et al. (2019) and Afshari et al. (2021) noted that the total integrated transfer rate is comparable to the turbulent energy cascade rate, indicating that electron Landau damping plays a significant role in the dissipation of turbulence here. These results indicate that the field-particle correlation technique holds a lot of promise for answering important questions in space plasma physics.

3.3 The PATCH Algorithm

To take advantage of the high time resolution achievable with a Wave-Particle Correlator instrument that utilizes the particle arrival times, the field-particle correlation technique must be modified to exploit the arrival time information. Here we briefly describe the *Particle Arrival Time Correlation for Heliophysics* (*PATCH*) algorithm for determining the rate of energy transfer between electromagnetic fields and plasma particles using measurements at a single point in space; a detailed derivation of the PATCH algorithm from plasma kinetic theory is presented elsewhere (Verniero et al., 2021b).

An illustration of the concept of the PATCH algorithm for the correlation of field and particle measurements is shown in **Figure 4**, where we consider a single spatial dimension for simplicity, with a particle velocity distribution $f(x, v, t)$ and an electric field $E(x, t)$. Consider a single phase-space bin centered at velocity v_p with bin width Δv measured by the particle instrumentation at position x_p within a 1D spatial volume Δx. The distribution function at the 1D-1V phase-space position (x_p, v_p) is given by

$$f(x_p, v_p, t) = \frac{N(t)}{\Delta x \Delta v}, \tag{10}$$

where the number of particles within the 1D-1V phase-space volume $\Delta x \Delta v$ is given by $N(t)$. In **Figure 4**, we plot electric field measured by the probe $E(x_p, t)$ (red) and the time-varying number of particles in the phase-space volume $\Delta x \Delta v$, given by $N(t)$ (blue). Note that the probability that a particle in this phase-space bin is counted by the instrument is proportional to $N(t)$.

The PATCH algorithm is based on the alternative correlation C' given by **Eq. 8**, which essentially computes the rate of work done on a charged particle by the electric field. In **Figure 4**, we use Poisson statistics to determine whether a particle is counted by the detector based on the probabilities related to $N(t)$, and each particle count is denoted as a green vertical line at the time of arrival at the bottom of figure. As detailed in Verniero et al. (2021b), the net rate of energy transfer to the particle distribution by the electric field E can be determined by the summing the rate of work done by the electric field on each particle that is counted, qEv_p. The resulting sum yields a discrete sampling of the in-phase component between $N(t)$ and $E(t)$, which determines the net energy transfer between the electric field and the particles over the correlation interval τ. Note that the weighting by the particle phase-space density $f(x, v)$ is naturally included when summing the electric field at each particle arrival time, capturing the relative phases of the perturbations to $f(x, v, t)$ and $E(x, t)$.

For a particle instrument, such as the electrostatic analyzers on the *MMS* or *PSP* missions (Pollock et al., 2016; Whittlesey et al., 2020), the PATCH algorithm is relatively easy to implement in

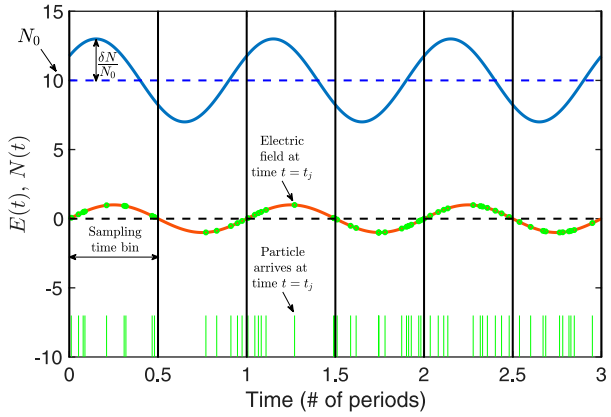

FIGURE 4 | Demonstration of the concept underlying the PATCH algorithm: the variation of the particle number in a particular phase bin $\Delta x \Delta v$ is given by $N(t)$ (blue) and the electric field $E(t)$ (red). Individual particles, with a probability of detection proportional to $N(t)$, arrive at discrete times t_j (vertical green lines). The PATCH correlation, C_τ' gives the rate of work done by the electric field on the particles, and it is essentially the summed values of the electric field at the particle arrival times. From Verniero et al. (2021b).

the 3D-3V phase space of an astrophysical plasma. The PATCH correlation $C_\tau^\star$ over a correlation interval τ is defined by

$$C_\tau^* = \frac{1}{\tau}\frac{1}{\Delta \mathbf{r}_p \Delta \mathbf{v}_p}\sum_{j=1}^{N_\tau} q\mathbf{v}_p \cdot \mathbf{E}\left(t_j\right) \tag{11}$$

where the measurement bin in 3D-3V phase space is given by $\Delta \mathbf{r}_p \Delta \mathbf{v}_p$, the 3V velocity of the phase bin is $\mathbf{v}_p$, the number of particles counted in the phase bin over the correlation interval τ is N_τ, and the electric field at each particle arrival time is $\mathbf{E}$ (t_j). Note that the contributions to the dot product $\mathbf{v}_p \cdot \mathbf{E} = v_{px}E_x + v_{py}E_y + v_{pz}E_z$ from each component of the electric field can be computed and saved separately, enabling a subsequent rotation of the coordinate system in post-processing, *e.g.,* rotating to magnetic field aligned coordinates (FAC).

A demonstration of how the PATCH algorithm can be used to produce a velocity-space signature that can be used to identify a particular particle energization mechanism is shown in **Figure 5**. From a gyrokinetic simulation of strong plasma turbulence in a $\beta_i = 1$ and $T_i/T_e = 1$ plasma over the range $0.25 \le k_\perp \rho_i \le 5.5$ (Klein et al., 2017), we can compute the alternative correlation with the parallel component of the electric field $C'_{E_\parallel}(v_\parallel, v_\perp)$. The high velocity-space resolution simulation data has been downsampled to the *PSP* velocity-space resolution, and the pattern of $C'_{E_\parallel}(v_\parallel, v_\perp)$ in **Figure 5A** shows a peak in the rate of change of the phase-space energy density at $v_\parallel/v_{ti} \simeq 1.1$, indicative of ion Landau damping. The PATCH algorithm, with only 25 ions counted in the phase-space bin at the peak of the distribution, is used to compute the correlation $C^\star_{E_\parallel}(v_\parallel, v_\perp)$, recovering most of the qualitative and quantitative details of the velocity-space signature, as shown in **Figure 5B** (Verniero et al., 2021b). This result shows that an on-board implementation of the field-particle correlation technique, specifically the PATCH algorithm, indeed is able to recover the velocity-space signature of the ion energization, opening up many new opportunities in understanding energy transfer in space plasmas.

3.4 A Multi-Channel, Integrated Field-Particle Correlator Instrument

Previous applications of the field-particle correlation technique to spacecraft measurements (Chen et al., 2019; Afshari et al., 2021) have relied on the downlink of burst-mode data for the electromagnetic field and particle velocity distribution measurements separately to implement later a ground-based computation of the field-particle correlations. Although this approach has indeed met with success—achieving the first definitive identification of electron Landau damping in a turbulent space plasma and assessing the importance of this particle energization channel to the total turbulent plasma heating—the limitations on telemetry of burst-mode data restricts such studies to a moderate sample size relative to the total sampling time in space. With the exception of the single-channel correlator connecting the FIELDS and SWEAP instrument suites on *Parker Solar Probe*, a dedicated, multi-channel *Integrated Field-Particle Correlator* (*IFPC*) instrument has never been developed. Here we describe a preliminary design concept for such an instrument.

Fortunately, the implementation of an IFPC can exploit the heritage instrumentation used on previous missions for the electromagnetic field and particle velocity distribution measurements, requiring only the development of the cables and firmware to interface these instruments with the digital processing unit (DPU) and the software to compute the correlations. In discussion below, let us consider the heritage instrumentation from the *Parker Solar Probe* mission, specifically the FIELDS (Bale et al., 2016) and SWEAP (Kasper et al., 2016) instrument suites as a specific example of modern instrumentation that could be incorporated into an IFPC.

The key principle of operation of the proposed IFPC follows. When the particle instrument detects a single particle (ion or electron) in a particular energy-angle bin (dictated by the energy sweep and deflector sweep voltages at that moment), it sends a $\delta t_p = 200$ *ns* pulse to the DPU with only a few ns delay. In addition, the FIELDS instrument provides two-component electric field measurements (strictly, differential voltage measurements from the dipole antennas) to the DPU at a 2 MHz sampling frequency and three-component magnetic field measurements at a 100 kHz sampling frequency (Bale et al., 2016). The PATCH algorithm for computing on-board correlations, described in **Section 3.3**, simply requires the electric field measurement at the time of the particle arrival and the 3V velocity representative of the energy-angle bin (dictated by the table for energy sweep and deflector sweep voltages). In addition, the local magnetic field direction at the particle arrival time can also be saved for subsequent projection of the PATCH correlation into magnetic field aligned coordinates (FAC), if desired.

The single-channel correlator implemented on Parker Solar Probe can only correlate the fields with a single phase-space bin. But the SWEAP electrostatic analyzer instruments actually count particles in the 16 azimuthal anodes simultaneously, so in

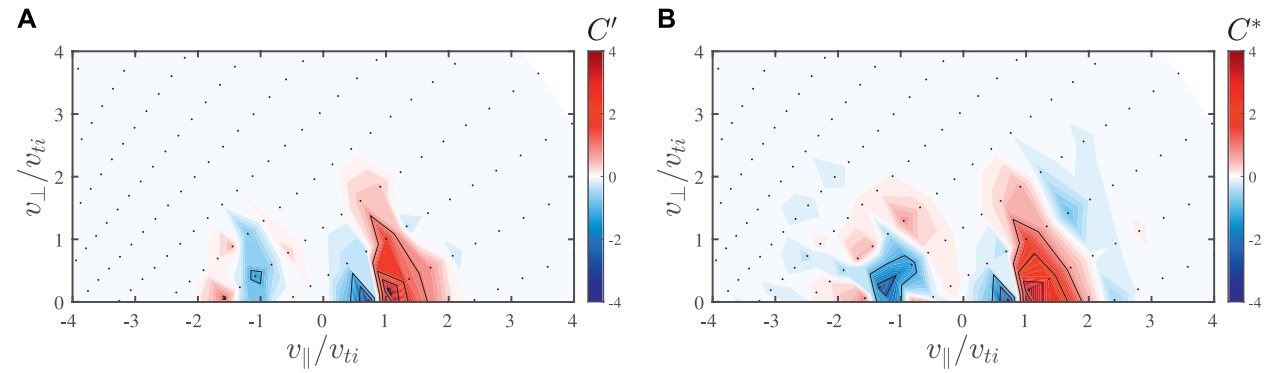

FIGURE 5 | (A) Example of the alternative parallel electric field correlation $C'_{E_\parallel}(v_\parallel, v_\perp)$ computed at a single spatial point in a gyrokinetic simulation of plasma turbulence and downsampled to the phase-space resolution of the SPAN-I instrument on *Parker Solar Probe* (Verniero et al., 2021a), compared to **(B)** the signature determined from applying the PATCH algorithm $C'_\tau(v_\parallel, v_\perp)$, computed using $N = 25$ counts in the maximum density phase-space bin at the same phase-space resolution. From Verniero et al. (2021b).

principle 16 phase-bins can be correlated simultaneously. With minor modifications to the digital electronics board and some significant reprogramming of the FPGA firmware, it would be possible to convert the existing single-channel implementation into a 16-channel correlator. Fortuitously, the design of the heritage digital electronic board on Parker Solar Probe already has two 12-bit Analog to Digital Converter (ADC) chips which can be repurposed to process FIELDS measurements from an external source.

In the development of a dedicated IFPC instrument, there is one key difference from the implmentation of the single-channel correlator implemented on Parker Solar Probe. The existing correlator sends to the particle counts from SWEAP to the digital processing unit in the FIELDS suite, so to implement separate channels from multiple anodes would require multiple dedicated cables to transmit the signal from each anode. Instead, for a dedicated IFPC instrument, the measurements of the electric and magnetic fields would be transmitted to the electronic firmware for the particle instrument, enabling the correlation to be processed locally within the processing unit for the particle instrument.

The data products returned from the high-TRL, heritage electrostatic analyzer instruments are formatted by 16 discrete anodes and 256 energy times deflector bins. These three dimensions (anode, deflector, energy) can be summed in any direction to make smaller dimension products, but the primary data product from the heritage instrument is a 4,116 byte (16 Anodes x 8 Deflections x 32 Energies x 1 byte each +20 bytes of packet header) Low Voltage Differential Signal (LVDS) formatted packet that is produced every 0.218 s. After modification of the digital board and FPGA, we anticipate producing correlation plots such as those seen from previous work (see **Figure 3**) in addition to the same 4,116 byte science packets.

4 ANTICIPATED RESULTS

4.1 Laboratory Tests of a Wave-Particle Correlator

In order to test the *PSP* correlator system in the laboratory, our team devised a method to modulate the particle flux impinging on the *PSP* ion analyzer (SPAN-I) using an experimental setup with an ion source. An oscillating voltage applied to Vgate of the ion source resulted in a modulated ion flux while the ion beam energy remained constant in time. The same signal that controls the ion flux was also fed into the FIELDS instrument Time Domain Sampler (TDS), where it was digitized and recorded.

The top panel in **Figure 6** (left) shows 2 cycles of a 200 Hz signal of the voltage that controlled the particle flux. The middle panel shows the number of particles detected within each 0.5μs time bin, where one 5 ms wave period contains 10,000 of these high-resolution time bins. Most bins have zero counts and the probability of obtaining more than 1 count is very low, indicating Poisson statistics are applicable for this implementation. The bottom panel of **Figure 6** (left) shows the counts binned at the intrinsic time resolution of a single phase-space bin the *PSP*/SPAN instrument, $\delta t = 0.85$ ms. At this field modulation frequency, much faster than the fastest full SPAN energy-angle sweep of $\Delta t = 0.218$ s, the variation in the particle count rate can be resolved.

Note that an implementation of a wave-particle correlator which bins all of the counts within each $\delta t = 0.85$ ms measurements for a particular energy-angle phase bin cannot access signals at frequencies $f \gtrsim 588$ Hz, but the implementation of the PATCH algorithm, because it uses the time of arrival of the particle, should in principle be able to probe physics at kHz frequencies and higher, such as Type III bursts. Note also that the current *PSP* flight software burst selection is based on the product of the root mean square wave amplitude and the frequency in one of the analog channels. This produces a nice sampling of, for example, Langmuir wave packets. It would be possible to include some aspects of the simultaneous particle count time series which could enhance the returned wave-particle correlator bursts. Finally, correlating with 16 channels of particle data would be possible with only minor modifications to the SPAN digital electronics board, shown in **Figure 6** (right), along with some significant reprogramming of the Field-Programmable Gate Array (FPGA) firmware.

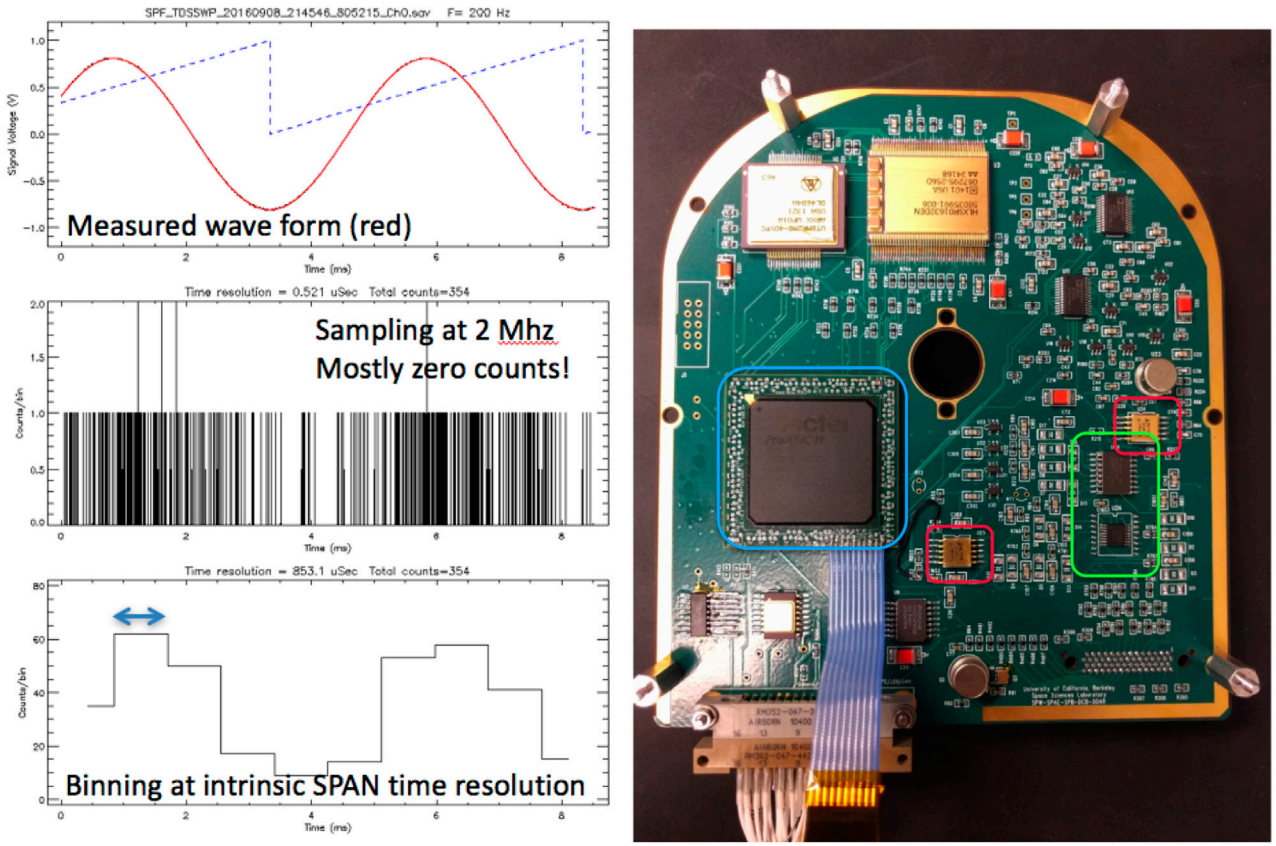

FIGURE 6 | (Left top) Waveform of the oscillating voltage applied to modulate the ion source (red) at f = 200 Hz frequency. (Left middle) Particles counted within 0.5μs time bins, showing mostly 0 or 1 counts, indicating Poisson counting statistics. (Left bottom) At the SPAN phase-space bin time resolution of δt = 0.85 ms, the modulation in the number of detected ions at the f = 200 Hz frequency. (Right) Photograph of the SPAN-E digital electronics board.

4.2 Predicted Capabilities of an Integrated Field-Particle Correlator

The energy transfer governed by the physics of particle energization in space plasmas—whether through the dissipation of plasma turbulence, through the release of magnetic energy via magnetic reconnection, or through the compression of the plasma and the acceleration of particles at plasma shocks—generally occurs on the characteristic kinetic timescales. Although a recent analysis has shown clearly that, with a sufficiently long correlation interval, the field-particle correlation technique can indeed recover the physics of particle occuring on frequencies above the Nyquist frequency of the sampling (Horvath et al., 2022), to resolve fully the details of the particle energization, one must generally sample the plasma at a faster cadence than the timescale of the process. For example, at a heliocentric distance of 1 AU in the solar wind, the frequency associated with fluctuations at ion length scales convected past a spacecraft at the solar wind velocity is typically $f_i \sim 1$ Hz. For the frequency of the convected ion gyroradius, for example, this frequency scales as $f_i \propto V_{sw} B/T_i^{1/2}$. Estimates of the changes in solar wind flow velocity, magnetic field, and ion temperature enable predictions of these characteristic frequencies at different heliocentric distances (Bale et al., 2016). For example, at the heliocentric distance of the first perihelion of *Parker Solar Probe* at $r \simeq 36R_\odot$, this frequency rises to $f_i \gtrsim 5$ Hz; near the predicted Alfvén radius of the Sun at $r \simeq 10R_\odot$, the frequency may rise to $f_i \gtrsim 30$ Hz. Additional collisionless energy transfer with electrons occurs at yet higher frequencies.

The most significant obstacles to investigating the particle energization in space plasmas are 1) the limited cadence of particle instrumentation, such as electrostatic analyzers and 2) telemetry limitations that constrain the amount of measured data that can be transmitted back to the Earth for analysis. An on-board wave-particle correlator, such as the Integrated Field-Particle Correlator (IFPC) described in **Section 3.4**, is a potential approach to overcome both of these obstacles. Here we estimate the capabilities of an IFPC incorporating electromagnetic field and plasma instruments equivalent to those on the *Parker Solar Probe* mission.

The SPAN-E electrostatic analyzer instrument for electrons on *PSP* (Whittlesey et al., 2020) is capable of performing a full energy sweep of 32 steps in energy E and 8 steps in deflector angle θ over a sampling interval of Δt = 0.218 s. All 16 anodes covered the azimuthal angles ϕ are measured simultaneously, for a total of 4,096 (E, θ, ϕ) phase-space bins sampled in that interval. Each phase-bin is therefore measured in a time $\delta t = \Delta t/(32 \times 8) =$ 0.85 ms, equivalent to a sampling frequency greater than 1 kHz. The electric field components necessary to determine the rate of particle energization are measured by the FIELDS instrument at sampling

frequency of 2 MHz (Bale et al., 2016). By combining the electric field and particle counts on-board using the PATCH algorithm, the effective sampling time is reduced from $\Delta t = 0.218$ s to $\delta t = 0.85$ ms, an improvement by a factor of 256, with a corresponding Nyquist frequency of the measurements of $f \simeq 587$ Hz.

The improvement in sampling cadence is actually even larger using the PATCH algorithm, since one of its key features is that the electric field used in the calculation is measured at the time of the arrival of the particle in the detector. For the $\delta t_p = 200$ ns pulse sent from the detector to the digital processing unit (DPU) when a particle arrives, the effective sampling frequency is 2.5 MHz, actually faster than the electric field measurement cadence. So within the $\delta t = 0.85$ ms measurement interval for a single phase-space bin, one obtains a Nyquist frequency of 1.25 MHz. Therefore, the improvement in time resolution from existing particle instrumentation could be up to a factor of $\Delta t/\delta t_p \sim 10^6$.

One significant caveat is that each individual phase-bin is only sampled once over an interval $\delta t = 0.85$ ms every $\Delta t = 0.218$ s. Therefore, one must interpret the correlated measurements carefully. For example, for the PATCH correlation of the parallel electric field $C^*_{E_\parallel}(v_\parallel, v_\perp)$ over the full velocity-space sweep interval of $\Delta t = 0.218$ s, which would appear similar to the right panel of **Figure 5**, each individual phase bin measurement over $\delta t = 0.85$ ms would be measured at a different time during the sweep. So, a plot of a single entire velocity-space sweep combines these measurements at different times, but the electric field and particle measurements in each of the phase bins would use a time accurate to approximately 200 ns. Significant modeling efforts would be needed to ensure that the results returned by the implementation of the PATCH algorithm can be interpreted accurately to reflect the underlying kinetic physics of particle energization.

Another potential capability of an IFPC is to enable alternative operating modes that are designed to sweep over a reduced region of 3V velocity-space on a much faster cadence. For example, one could select a single deflector angle θ and perform a sweep over all 32 energies with a sampling interval of $\Delta t = 0.0273$ s, improving time resolution by a factor of 8 by eliminating the deflector angle sweep; alternatively, one could select a single energy and sweep over only deflector angles with a sampling interval of $\Delta t = 0.00068$ s, improving time resolution by a factor of 32 by eliminating the energy sweep. This is not dissimilar from the existing alternating full and targeted sweeps that are already used by the SPAN-E electrostatic analyzer instrument. With scientific insight guiding the selection of a reduced sampling region in 3V velocity-space, one would potentially be able to tailor different operating modes to tackle different science questions.

5 DISCUSSION

5.1 Improvements in Understanding Plasma Heating and Particle Acceleration in Space Plasmas

A spacecraft mission including an Integrated Field-Particle Correlator (IFPC) instrument, as described in **Section 3.4**, would enable significant advances in our understanding of particle energization in space plasmas, including plasma heating and particle acceleration. Note that, unlike previous applications of a wave-particle correlator that sorted the particle counts by wave phase (see **Section 1.1**), and therefore required a dominant single wave mode, because the IFPC correlates each particle count with the instantaneous field measurements, no single wave is necessary. The successful application of the ground-based FPC method on measurements of broadband turbulence in Earth's magnetosheath to identify for the first time electron Landau damping in a space plasma is a proof of principle of the field-particle correlation technique (Chen et al., 2019; Afshari et al., 2021).

For key science questions, such as how the solar corona is heated and the solar wind accelerated—two of the primary science questions of both the *Parker Solar Probe* and *Solar Orbiter* missions—the vast improvement in the cadence of measurements using an IFPC would enable the kinetic physics of both ion and electron energization to be investigated in detail. Within the outer boundary of the solar corona, inside the Alfvén point, the frequencies of ion energization are likely tens of Hz, and the electron frequencies are up to $\sqrt{m_i/m_e} \simeq 43$ times higher, or approaching kHz frequencies. The much lower sampling frequency of existing particle velocity distribution instruments, with measurement cadences of $\Delta t = 0.218$ s, constitutes a significant obstacle in illuminating the kinetic physics involved. But with an IFPC, one can achieve sampling at or above the frequencies of these physical energy transfer mechanisms. In addition, kinetic instabilities may play an important role in the energetics of the solar wind (Bale et al., 2009), and since the energy transfer from the particle velocity distributions to unstable electromagnetic fluctuations can equally be explored with the field-particle correlation technique (Klein, 2017), an IFPC would be a valuable tool to explore this avenue of energy flow in the heliospheric plasma.

The higher effective cadence of an IFPC also enables new science investigations of collisionless field-particle interactions that simply cannot be considered using existing instrumentation. For example, Type III radio bursts with frequencies in the few MHz range can be scattered from density fluctuations in the solar wind turbulence (Krupar et al., 2020), so an IFPC could potentially explore the physics of this scattering using *in situ* measurements of the electrons and the electric field of these bursts. Furthermore, in the investigation of collisionless shocks, such as Earth's bow shock or interplanetary shocks, a spacecraft passes through the ramp of the shock in a very short time interval. Being able to correlate the detection of particles with the electric fields at the time of detection will likely open up new avenues for the observational analysis of particle acceleration mechanisms, such as shock drift acceleration (Paschmann et al., 1982; Sckopke et al., 1983; Juno et al., 2021). For some of these new science targets, alternative operating modes may be utilized to focus on the regions of interest in phase-space for a given process, as described in **Section 4.2**, further increasing the time resolution of the observations.

In addition to new science targets enabled by the development and implementation of an IFPC instrument on an upcoming spacecraft mission, the on-board correlations can improve the

statistics of sampling by orders of magnitude. For example, the *MMS* S-band downlink of 4 Gb/day allows only about 20 min of full-cadence, burst-mode data to be transmitted to the ground for analysis per day, even though the instruments are always sampling at burst-mode cadence. This leads to an effective duty cycle of 1.4%. In principle, on-board correlations could utilize the full 24 h of burst-mode measurements per day in computing correlations, leading to a factor of 72 improvement in total sampling time. For more distant spacecraft that are limited to lower downlink rates, such as *Parker Solar Probe* and *Solar Orbiter*, the improvement factor can be even larger. With the potential for the velocity-space signatures generated by the PATCH algorithm to be used to identify different physical mechanisms of particle energization and to quantify the rate of energization, this major improvement in sampling time would enable statistical studies of the fraction of turbulent energy dissipation via different mechanisms, a long term goal of the heliophysics community.

Additional opportunities are made possible by an IFPC, such as event-based triggering. Existing spacecraft can implement triggering based on the amplitude of field fluctuations or rapid changes in field direction, but these events do not necessarily correlate with significant energy transfer between particles and fields. By triggering on the amplitude of the PATCH correlation (possibly averaged over some suitably chosen time interval to eliminate large amplitude oscillatory energy transfer that yields little net particle energization), the operators can be alerted intervals of interest for deeper investigation, or the spacecraft can switch into an appropriate alternative operating mode. Overall, the development of an IFPC using heritage field and particle instrumentation opens up potentially transformative new avenues for investigating the physics of space plasmas.

5.2 Caveats and Challenges

The development of an IFPC instrument for the exploration of the kinetic physics of particle energization in space plasmas faces certain challenges that will need to be addressed before such an instrument can incorporated into a future spacecraft mission. Specific issues include performing the instrument calibration, transformation of electromagnetic fields and velocity coordinates to the frame of the plasma bulk flow, filtering in frequency, potential instrumental limitations of electric field measurements to only two of the three spatial dimensions, and developing the foundation of knowledge needed to interpret the velocity-space signatures of particle energization returned by the correlator measurements.

Data on-board spacecraft are stored in raw format, which does not include calibration factors that are typically determined on the ground. This impacts all of the measurements that PATCH, or any wave-particle correlation method, requires: magnetic field vector, electric field vector, velocity space values of particle measurements, and particle distribution functions. Magnetometers require an absolute calibration, often provided by rotating the spacecraft, to remove background fields caused by the spacecraft and remove drift of the sensor with time. Electric fields measurements by dipole antennas often require extensive calibration to convert the differential voltage measurements into electric field measurements, using cross-instrument calibration to determine DC offsets, effective antenna length, and an angular correction, all as a function of frequency (Mozer et al., 2020).

For ions, the common calibration issue is sensor efficiency (*e.g.*, as set by micro-channel plate gain and threshold voltages) which will change in time as the sensor material ages and settings change to compensate (Lavraud and Larson, 2016). For electrons, the spacecraft charging environment strongly affects the low energy electrons. Most spacecraft charge up to approximately 10 V depending on size, orientation and surface material properties. The thermal energy of electrons in the solar wind is of order 10 eV and in the magnetosheath of order 100 eV and so the spacecraft potential magnitude and structure is frequently important for thermal electron calibration (Scime et al., 1994; Szita et al., 2001). The spacecraft potential accelerates the ambient electrons, both the space plasma populations, changing both energy and direction, and also photoelectrons generated from the spacecraft body, creating a high-density low energy contaminating population. This matters for the PATCH method because photoelectrons will contaminate the triggering events and the velocity of the particles being measured must be corrected for the spacecraft potential, and so the absolute value of correlation $C_\tau^\star$ will have a systematic error based on the magnitude of the spacecraft potential (Lewis et al., 2010).

Typically, correction to the electron energy is performed on the ground, which removes photoelectrons at low energies and shifts the energy of the observed distribution to remove the spacecraft contribution. For most past and existing missions the spacecraft potential is estimated on the ground from the electron distribution and the DC electric field measurements, if they are available. One method to include the calibration factors in on-board data processing for field-particle correlators is to perform regular in flight calibrations on the ground and up-link calculated correction factors to the spacecraft to be included in calculations on board. This has the advantage that the calibration can be performed by a person on the ground, but the disadvantage that the calibration factors would be determined for a typical case and would not change with ambient conditions, as spacecraft potential does. A mission that includes electric potential measurements can provide an on-board estimate of spacecraft potential that can be included in the calibration of the energy of the electrons, but this requires accurate calibration of the spacecraft potential measurement on-board. The spacecraft potential environment can be modelled before launch (Guillemant et al., 2017), but the calibration of the electron distribution for this effect must be done in flight and so this leads to a necessary mission requirement of a time period for instrument calibration in space that is perhaps more extensive than usual in order to update on-board calibrations and not rely on the ground processing.

A significant challenge for the operation of an on-board field-particle correlator is how to implement the field-particle correlations in the appropriate frame of reference for the investigation of particle energization. The standard application to spacecraft measurements is to shift the measurements into the frame of the bulk flow of the plasma species (Chen et al., 2019; Afshari et al., 2021), taking care to perform the appropriate

Lorentz transform of the electromagnetic fields. Consider transforming from the spacecraft rest frame $\mathcal{K}'$ (primed) to the plasma species rest frame $\mathcal{K}$ (unprimed) moving at velocity $\mathbf{U}$ relative to the spacecraft frame. The particle velocity transforms as $\mathbf{v} = \mathbf{v}' - \mathbf{U}$, and for typical non-relativistic conditions in the heliosphere, the electromagnetic fields transform by $\mathbf{E} = \mathbf{E}' + \mathbf{U} \times \mathbf{B}'$ and $\mathbf{B} = \mathbf{B}'$ (Howes et al., 2014). The PATCH correlation in the plasma frame can be expressed in terms of the spacecraft frame measurements by

$$C_\tau^* \propto \sum_{j=1}^{N_\tau} q\mathbf{v}_p \cdot \mathbf{E}\left(t_j\right)$$

$$= \sum_{j=1}^{N_\tau} \left\{ q\left(\mathbf{v}_p' - \mathbf{U}\right) \cdot \mathbf{E}'\left(t_j\right) - q\mathbf{v}_p' \cdot \left[\mathbf{U} \times \mathbf{B}'\left(t_j\right)\right] \right\} \qquad (12)$$

To implement this transformation on-board requires saving at each particle arrival time t_j the instantaneous (spacecraft frame) electric and magnetic field measurements $\mathbf{E}'(t_j)$ and $\mathbf{B}'(t_j)$ over the correlation time τ. Note that $\mathbf{v}_p'$ is the spacecraft frame velocity for each phase-bin, and is known from the applied operating voltages of the instrument at t_j. Over the correlation time, the average bulk fluid velocity of plasma species p is given by $\mathbf{U} = \langle \mathbf{U}_p(t) \rangle_\tau$, where the angle brackets indicate the time-average over the correlation interval τ. At the end of each correlation interval τ, the PATCH correlation C_τ^* can be computed on-board using the known $\mathbf{U}$ and measurements $\mathbf{E}'(t_j)$ and $\mathbf{B}'(t_j)$. Another complication of an on-board implementation of the field-particle correlation technique is how to high-pass filter the electric field measurements to eliminate large-amplitude, low frequency oscillations that yield zero net energy transfer (Chen et al., 2019; Afshari et al., 2021). One could, of course, design a high-pass electronic circuit to eliminate the low-frequency components, but since transformation to the plasma rest frame requires storage of data and on-board processing, a preferred approach is to perform on-board high-pass filtering of the high-cadence electric field measurements in flight software. To do so, one again uses a chosen correlation interval τ over which to save the highest cadence electric field time series $\mathbf{E}'(t)$, performs a Fourier transform in time $\mathbf{E}'(f)$, applies the appropriate filtering in frequency $\tilde{\mathbf{E}}'(f)$, and then inverse transforms back to a time series $\tilde{\mathbf{E}}'(t)$. One then simply replaces the $\mathbf{E}'(t_j)$ values in **Eq. 12** with the filtered values $\tilde{\mathbf{E}}'(t_j)$. Such a software-based filtering approach would enable high-pass, band-pass, or low-pass filtering, potentially enabling energy transfers at different frequencies to be isolated. Determining the appropriate correlation intervals τ (likely numerous operating modes with different τ will be designed to tackle different science targets) and the optimal algorithms for on-board frequency filtering will require substantial design work.

A final complication with the implementation of an IFPC instrument is that many spinning spacecraft obtain high-quality electric field measurements in the 2D spin-plane, but poor quality or no electric field measurements along the spin axis. Without full 3D electric field measurements, it is not possible to determine the rate of particle energization due to the unmeasured component of the electric field. But, one can still determine the energization by the two in-plane components of the electric field. Whether the missing component yields an important contribution to the total particle energization depends on the physical mechanism of energy transfer and the orientation of the magnetic field relative to the unmeasured direction, so the limitation must be assessed on a case-by-case basis. In general, selecting an electric field instrument that can provide reliable 3D electric field measurements should be prioritized highly for a proposed mission based on an IFPC instrument to ensure that all aspects of the particle energization can be probed.

In addition to these significant instrumental challenges with calibration, understanding and interpreting the velocity-space signatures generated by the correlated field and particle measurements represents a significant challenge for theory and computation. Significant progress has already been made using the field-particle correlation technique, from its initial conception in 2016 (Klein and Howes, 2016) to the first successful identification of electron Landau damping in a turbulent space plasma using *MMS* measurements in 2019 (Chen et al., 2019), to a moderate statistical sample demonstrating the relative contribution of electron Landau damping to the total dissipation in 2021 (Afshari et al., 2021). Nonetheless, theoretical and numerical investigations to identify new velocity-space signatures of different proposed particle energization mechanisms are ongoing, identifying electrostatic counterstreaming beam instabilities (Klein, 2017), ion Landau damping (Klein et al., 2017), ion cyclotron damping (Klein et al., 2020), magnetic pumping (Montag and Howes, 2022), electron energization in strong-guide-field collisionless magnetic reconnection (McCubbin et al., 2022), shock-drift acceleration of ions at a perpendicular collisionless shock (Juno et al., 2021), and adiabatic electron heating through the ramp of a perpendicular collisionless shock (Juno et al., 2021). But many more particle energization mechansisms are expected to play a role in space plasmas, and much more work to identify qualitatively their unique velocity-space signatures and to characterize quantitatively the energization rates of all of these mechanisms is necessary to exploit fully the promise of an IFPC instrument.

Furthermore, to take full advantage of the 100% duty cycle of correlated burst-mode measurements, it would be ideal to be able to automatically identify the signatures of different energization mechanisms to compile large statistical studies. Machine learning, and in particular the proven capabilities of Convolutional Neural Networks (CCNs) to learn geometric patterns in images (LeCun and Bengio, 1995, 2015), provide a potentially powerful avenue for classifying and identifying different mechanisms in the investigation of the physics of plasma heating and particle acceleration in space plasmas.

Finally, particle detector design can also be refined to employ more efficient representation of velocity distribution functions (VDFs), where the quest to optimize the scientific return of a mission based on the tragedy of insufficient downlink capabilities is universal among the astrophysical community. Ongoing efforts for tackling this hurdle show promise. For example, a wavelet-based compression for particle count data was explored on *MMS*

data (Barrie et al., 2019). In addition, optimization of VDF basis functions using neural networks was performed to mitigate lossy compression artifacts (da Silva et al., 2020). Representation of the electron VDF using Legendre polynomials has shown to be useful in diagnosing anisotropies signifying net energy transfer (Carcaboso et al., 2020). In a similar vein, a spherical expansion of the ion VDF has been applied to *Cluster* data to show that only the coefficients of the expansion are needed to obtain the plasma moment information (Viñas and Gurgiolo, 2009). Based on these recent findings regarding optimal spacecraft data compression techniques, it is apparent the physical geometry of the detector is crucial for extracting the most optimal information. Further onboard methodologies considering optimal basis functions (such as polynomial expansion coefficients) for transmitting back both the particle and wave data will be developed in future work toward enhancement of scientific data return.

5.3 Future Mission Concepts

Due to the requirement for simultaneous and triggered measurements of multiple variables, the most effective way to perform the most accurate measurements of field-particle correlations is with a dedicated and specifically designed sensor payload. Future missions dedicated to plasma physics and the role of field-particle correlations are currently proposed, for example the Debye mission (Verscharen et al., 2021) with the European Space Agency, that could include such an Integrated Field-Particle Correlator (IFPC) instrument. As well as a coordinated payload, there are potentially changes to the design of the particle detectors themselves that can improve, or at least change, the performance of an IFPC.

Electrostatic analysers cycle through energy and look-direction by changing voltages in time. This means that different energies and different directions in elevation are not seen simultaneously, although different azimuths are. It is not clear that this kind of operation is optimized for a dedicated field-particle correlation mission. There are two different options that can change this set-up. First, there are novel designs of electrostatic sensors that use multiple entry apertures with distinct electrostatic deflection voltages to sample half of the sky simultaneously at one energy (Skoug et al., 2016; Morel et al., 2017). Thus field-particle correlations could be measured simultaneously in different directions but with different energies separated in time. The second option is to sample multiple energies simultaneously. This is possible using a magnetic field to deflect incoming particles and then separate energies using anodes on a micro-channel plate (MCP) at different distances from the entry aperture (Criton et al., 2020). Different look directions could then be sampled in time, but the energy distribution of the correlation could be measured very rapidly. Both of these ideas offer the opportunity to increase the speed of the particle observations by removing one dimension of the two-dimensional voltage sweeping in traditional ESAs. An alternative is that the time resolution can be kept as it is, but the count-rate will be increased due to the reduction in instrument dead time and increase in geometric factor for these designs, which will increase the accuracy and number of observations made by the instrument.

As highlighted above, the IFPC concept requires a dedicated data processing unit that links particle and field sensors. This has become more common in recent missions, for example the Solar Orbiter mission has shared DPU for the Solar Wind Analyser (SWA) (Owen et al., 2020) *in-situ* plasma detectors and a similar approach is proposed for Debye. However, these designs do not take into account the specialised needs of correlation measurements, such as the rapid pulse required for individual particle arrival time measurement.

The Debye mission has science goals to measure the energy transfer between fields and particles at electron scales. This requires high time-resolution measurements of fields and electron velocity distributions, so the application of the field-particle correlation techniques described here are of fundamental importance to this question. There is the potential to enhance the Debye mission with the integration of field-particle correlation measurements as a central feature of the mission. The payload includes all of the instruments required and a dedicated DPU—only the harnessing to provide the connections between the instruments and the firmware on the DPU is required to make the Debye proposal the first dedicated design for a field-particle correlation mission (Verscharen et al., 2021).

In conclusion, innovative wave-particle correlator instrumentation, in particular the proposal here for the design of a new Integrated Field-Particle Correlator (IFPC) instrument, show significant promise in overcoming the limits of telemetry to maximize the scientific return from upcoming spacecraft missions. Concerted efforts to develop such new instrumentation for onboard correlations are ongoing, with the potential for transformative progress in our understanding of particle energization mechanisms, leading to plasma heating and particle acceleration, operating in the heliosphere.

DATA AVAILABILITY STATEMENT

The original contributions presented in the study are included in the article/Supplementary Materials, further inquiries can be directed to the corresponding author.

AUTHOR CONTRIBUTIONS

GH organized the team and wrote much of the manuscript. Authors and contributors for sections of the manuscript follow: (**Section 1**) GH and LW; (**Section 1.1**) GH and JV; (**Section 2.1**) DL, JP, PW, RL and AR; (**Section 2.2**) SB; (**Section 2.3**) SB and KG; (**Section 3.1**) GH and KK; (**Section 3.2**) CC, KK and GH; (**Section 3.3**) JV and GH; (**Section 3.4**) GH, DL, PW, RL and JV; (**Section 4.1**) DL, KG, SB, PW and RL; (**Section 4.2**) GH, JV, SB, KG, DL, PW and RL; (**Section 5.1**) GH, SB and KG; (**Section 5.2**) RW, GH, JV and DL; (**Section 5.3**) RW and GH. All authors participated in discussions about the mission concept and contributed to comments, references, and interpretative feedback on the manuscript.

FUNDING

GGH was supported by NASA grants 80NSSC18K0643, 80NSSC18K1371, and 80NSSC20K1273, and by NSF grant AGS-1842561. CHKC was supported by STFC Consolidated Grant ST/T00018X/1. The *PSP*/FIELDS experiment was developed and is operated under NASA contract NNN06AA01C. RTW was supported by STFC Consolidated Grant ST/V006320/1. KK was supported by NASA ECIP Grant 80NSSC19K0912 and SWEAP contract NNN06AA01C. LW was supported by *Wind* MO&DA funds and two NASA grants.

ACKNOWLEDGMENTS

The mission concept proposed here was developed and refined as part of the *Parker Solar Probe* Wave-Particle Correlator Working Group, led by GGH. The work was supported by the International Space Science Institute's (ISSI) International Teams programme ("Resolving the Microphysics of Collisionless Shock Waves" led by LW III) and the Geospace Environment Modeling (GEM) Focus Group "Particle Heating and Thermalization in Collisionless Shocks in the MMS Era" led by LW III.

REFERENCES

Afshari, A. S., Howes, G. G., Kletzing, C. A., Hartley, D. P., and Boardsen, S. A. (2021). The Importance of Electron Landau Damping for the Dissipation of Turbulent Energy in Terrestrial Magnetosheath Plasma. *JGR Space Phys.* 126, e29578. doi:10.1029/2021JA029578

Bale, S. D., Goetz, K., Harvey, P. R., Turin, P., Bonnell, J. W., Dudok de Wit, T., et al. (2016). The FIELDS Instrument Suite for Solar Probe Plus. Measuring the Coronal Plasma and Magnetic Field, Plasma Waves and Turbulence, and Radio Signatures of Solar Transients. *Space Sci. Rev.* 204, 49–82. doi:10.1007/s11214-016-0244-5

Bale, S. D., Kasper, J. C., Howes, G. G., Quataert, E., Salem, C., and Sundkvist, D. (2009). Magnetic Fluctuation Power Near Proton Temperature Anisotropy Instability Thresholds in the Solar Wind. *Phys. Rev. Lett.* 103, 211101. doi:10.1103/PhysRevLett.103.211101

Barnes, A. (1966). Collisionless Damping of Hydromagnetic Waves. *Phys. Fluids* 9, 1483–1495. doi:10.1063/1.1761882

Barrie, A. C., Smith, D. L., Elkington, S. R., Sternovsky, Z., da Silva, D., Giles, B. L., et al. (2019). Wavelet Compression Performance of Mms/fpi Plasma Count Data with Plasma Environment. *Earth Space Sci.* 6, 116–135. doi:10.1029/2018EA000430

Burch, J. L., Moore, T. E., Torbert, R. B., and Giles, B. L. (2016). Magnetospheric Multiscale Overview and Science Objectives. *Space Sci. Rev.* 199, 5–21. doi:10.1007/s11214-015-0164-9

Carcaboso, F., Gómez-Herrero, R., Espinosa Lara, F., Hidalgo, M. A., Cernuda, I., and Rodríguez-Pacheco, J. (2020). Characterisation of Suprathermal Electron Pitch-Angle Distributions - Bidirectional and Isotropic Periods in Solar Wind. *A&A* 635, A79. doi:10.1051/0004-6361/201936601

Chen, C. H. K., Klein, K. G., and Howes, G. G. (2019). Evidence for Electron Landau Damping in Space Plasma Turbulence. *Nat. Comm.* 10, 740. doi:10.1038/s41467-019-08435-3

Criton, B., Nicolaou, G., and Verscharen, D. (2020). Design and Optimization of a High-Time-Resolution Magnetic Plasma Analyzer (Mpa). *Appl. Sci.* 10. doi:10.3390/app10238483

da Silva, D., Barrie, A., Gershman, D., Elkington, S., Dorelli, J., Giles, B., et al. (2020). Neural Network Repair of Lossy Compression Artifacts in the September 2015 to March 2016 Duration of the Mms/fpi Data Set. *J. Geophys. Res. Space Phys.* 125, e2019JA027181. doi:10.1029/2019JA027181

Ergun, R. E., Carlson, C. W., McFadden, J. P., Clemmons, J. H., and Boehm, M. H. (1991a). Langmuir Wave Growth and Electron Bunching - Results from a Wave-Particle Correlator. *J. Geophys. Res.* 96, 225–238. doi:10.1029/90JA01596

Ergun, R. E., Carlson, C. W., McFadden, J. P., Tonthat, D. M., and Clemmons, J. H. (1991b). Observation of Electron Bunching during Landau Growth and Damping. *J. Geophys. Res.* 96, 11. doi:10.1029/91JA00658

Ergun, R. E., Carlson, C. W., Mozer, F. S., Delory, G. T., Temerin, M., McFadden, J. P., et al. (2001). The FAST Satellite Fields Instrument. *Space Sci. Rev.* 98, 67–91. doi:10.1007/978-94-010-0332-2_3

Ergun, R. E., McFadden, J. P., and Carlson, C. W. (1998). "Wave-Particle Correlator Instrument Design," in *Measurement Techniques in Space Plasmas:Particles* (Washington DC: American Geophysical Union), 102, 325.

Fox, N. J., Velli, M. C., Bale, S. D., Decker, R., Driesman, A., Howard, R. A., et al. (2016). The Solar Probe Plus Mission: Humanity's First Visit to Our Star. *Space Sci. Rev.* 204, 7–48. doi:10.1007/s11214-015-0211-6

Fukuhara, H., Kojima, H., Ueda, Y., Omura, Y., Katoh, Y., and Yamakawa, H. (2009). A New Instrument for the Study of Wave-Particle Interactions in Space: One-Chip Wave-Particle Interaction Analyzer. *Earth, Planets, Space* 61, 765–778. doi:10.1186/bf03353183

Gough, M. P. (1980). A Technique for Rocket-Borne Detection of Electron Bunching at Megahertz Frequencies. *Nucl. Instrum. Methods* 177, 581–587. doi:10.1016/0029-554X(80)90074-9

Gough, M. P., Martelli, G., Smith, P. N., Maehlum, B. N., and Ventura, G. (1980). Bunching of 8-10 keV Auroral Electrons Near an Artificial Electron Beam. *Nature* 287, 15–17. doi:10.1038/287015a0

Guillemant, S., Maksimovic, M., Hilgers, A., Pantellini, F., Lamy, L., Louarn, P., et al. (2017). A Study of Solar Orbiter Spacecraft–Plasma Interactions Effects on Electric Field and Particle Measurements. *IEEE Trans. Plasma Sci.* 45, 2578–2587. doi:10.1109/TPS.2017.2731054

Hesse, M., and Cassak, P. A. (2020). Magnetic Reconnection in the Space Sciences: Past, Present, and Future. *J. Geophys. Res.* 125, e25935. doi:10.1029/2019JA02593510.1029/2018ja025935

Horvath, S. A., Howes, G. G., and McCubbin, A. J. (2020). Electron Landau Damping of Kinetic AlfvÃ © N Waves in Simulated Magnetosheath Turbulence. *Phys. Plasmas* 27, 102901. doi:10.1063/5.0021727

Horvath, S. A., Howes, G. G., and McCubbin, A. J. (2022). Observing Particle Energization above the Nyquist Frequency: An Application of the Field-Particle Correlation Technique. *Phys. Plasmas*. in press.

Howes, G. G. (2017). A Prospectus on Kinetic Heliophysics. *Phys. Plasmas* 24, 055907. doi:10.1063/1.4983993

Howes, G. G., Klein, K. G., and Li, T. C. (2017). Diagnosing Collisionless Energy Transfer Using Field-Particle Correlations: Vlasov-Poisson Plasmas. *J. Plasma Phys.* 83, 705830102. doi:10.1017/S0022377816001197

Howes, G. G., Klein, K. G., and TenBarge, J. M. (2014). Validity of the Taylor Hypothesis for Linear Kinetic Waves in the Weakly Collisional Solar Wind. *Astrophys. J.* 789, 106. doi:10.1088/0004-637X/789/2/106

Juno, J., Brown, C., Howes, G. G., and Haggerty, C. (2022). A Field-Particle Correlation Analysis of a Quasiperpendicular Magnetized Collisionless Shock. *J. Plasma Phys*. In preparation.

Juno, J., Hakim, A., TenBarge, J., Shi, E., and Dorland, W. (2018). Discontinuous Galerkin Algorithms for Fully Kinetic Plasmas. *J. Comp. Phys.* 353, 110–147. doi:10.1016/j.jcp.2017.10.009

Juno, J., Howes, G. G., TenBarge, J. M., Wilson, L. B., Spitkovsky, A., Caprioli, D., et al. (2021). A Field-Particle Correlation Analysis of a Perpendicular Magnetized Collisionless Shock. *J. Plasma Phys.* 87, 905870316. doi:10.1017/S0022377821000623

Kasper, J. C., Abiad, R., Austin, G., Balat-Pichelin, M., Bale, S. D., Belcher, J. W., et al. (2016). Solar Wind Electrons Alphas and Protons (SWEAP) Investigation: Design of the Solar Wind and Coronal Plasma Instrument Suite for Solar Probe Plus. *Space Sci. Rev.* 204, 131–186. doi:10.1007/s11214-015-0206-3

Katoh, Y., Kitahara, M., Kojima, H., Omura, Y., Kasahara, S., Hirahara, M., et al. (2013). Significance of Wave-Particle Interaction Analyzer for Direct Measurements of Nonlinear Wave-Particle Interactions. *Ann. Geophys.* 31, 503–512. doi:10.5194/angeo-31-503-2013

Katoh, Y., Kojima, H., Hikishima, M., Takashima, T., Asamura, K., Miyoshi, Y., et al. (2018). Software-type Wave-Particle Interaction Analyzer on Board the Arase Satellite. *Earth, Planets, Space* 70, 4. doi:10.1186/s40623-017-0771-7

Klein, K. G. (2017). Characterizing Fluid and Kinetic Instabilities Using Field-Particle Correlations on Single-point Time Series. *Phys. Plasmas* 24, 055901. doi:10.1063/1.4977465

Klein, K. G., and Howes, G. G. (2016). Measuring Collisionless Damping in Heliospheric Plasmas Using Field-Particle Correlations. *Astrophys. J. Lett.* 826, L30. doi:10.3847/2041-8205/826/2/L30

Klein, K. G., Howes, G. G., and TenBarge, J. M. (2017). Diagnosing Collisionless Enegy Transfer Using Field-Particle Correlations: Gyrokinetic Turbulence. *J. Plasma Phys.* 83, 535830401. doi:10.1017/S0022377817000563

Klein, K. G., Howes, G. G., TenBarge, J. M., and Valentini, F. (2020). Diagnosing Collisionless Energy Transfer Using Field-Particle Correlations: Alfvén-Ion Cyclotron Turbulence. *J. Plasma Phys.* 86, 905860402. doi:10.1017/S0022377820000689

Kletzing, C. A., Bounds, S. R., LaBelle, J., and Samara, M. (2005). Observation of the Reactive Component of Langmuir Wave Phase-Bunched Electrons. *Geophys. Res. Lett.* 32, L05106. doi:10.1029/2004GL021175

Kletzing, C. A., and Muschietti, L. (2006). "Phase Correlation of Electrons and Langmuir Waves," in *Geospace Electromagnetic Waves and RadiationBerlin Springer Verlag*. Editors J. W. Labelle and R. A. Treumann, 687, 313. Lect. Notes Phys.

Krupar, V., Szabo, A., Maksimovic, M., Kruparova, O., Kontar, E. P., Balmaceda, L. A., et al. (2020). Density Fluctuations in the Solar Wind Based on Type III Radio Bursts Observed by Parker Solar Probe. *Astrophys. J. Supp.* 246, 57. doi:10.3847/1538-4365/ab65bd

Lavraud, B., and Larson, D. E. (2016). Correcting Moments of *In Situ* Particle Distribution Functions for Spacecraft Electrostatic Charging. *J. Geophys. Res. Space Phys.* 121, 8462–8474. doi:10.1002/2016JA022591

LeCun, Y., and Bengio, Y. (1995). "Convolutional Networks for Images, Speech, and Time Series," in *The Handbook of Brain Theory and Neural Networks* (Cambridge, MA: MIT Press), 3361.

LeCun, Y., Bengio, Y., and Hinton, G. (2015). Deep Learning. *Nature* 521, 436. doi:10.1038/nature14539

Lewis, G., Arridge, C., Linder, D., Gilbert, L., Kataria, D., Coates, A., et al. (2010). The Calibration of the Cassini–Huygens Caps Electron Spectrometer. *Planet. Space Sci.* 58, 427–436. doi:10.1016/j.pss.2009.11.008

Livi, R., Larson, D. E., Kasper, J. C., Abiad, R., Case, A. W., Klein, K. G., et al. (2021). The Solar Probe Analyzer-Ions on Parker Solar Probe. *Astrophys. J. Supp*. in press

McCubbin, A. J., Howes, G. G., and TenBarge, J. M. (2022). Characterizing Velocity-Space Signatures of Electron Energization in Large-Guide-Field Collisionless Magnetic Reconnection. *Phys. Plasmas* 29, 052105. doi:10.1063/5.0082213

Melrose, D. B. (1986). *Instabilities in Space and Laboratory Plasmas*. Cambridge, UK: Cambridge University Press.

Miyoshi, Y., Shinohara, I., Takashima, T., Asamura, K., Higashio, N., Mitani, T., et al. (2018). Geospace Exploration Project ERG. *Earth, Planets, Space* 70, 101. doi:10.1186/s40623-018-0862-0

Montag, P., and Howes, G. G. (2022). A Field-Particle Correlation Analysis of Magnetic Pumping. *Phys. Plasmas* 29, 032901. doi:10.1063/5.0036825

Morel, X., Berthomier, M., and Berthelier, J.-J. (2017). Electrostatic Analyzer with a 3-d Instantaneous Field of View for Fast Measurements of Plasma Distribution Functions in Space. *J. Geophys. Res. Space Phys.* 122, 3397–3410. doi:10.1002/2016JA023596

Mozer, F. S., Agapitov, O. V., Bale, S. D., Bonnell, J. W., Bowen, T. A., and Vasko, I. (2020). DC and Low-Frequency Electric Field Measurements on the Parker Solar Probe. *J. Geophys. Res.* 125, e27980. doi:10.1029/2020JA027980

Müller, D., Marsden, R. G., Cyr, St. O. C., and Gilbert, H. R. (2013). Solar Orbiter . Exploring the Sun-Heliosphere Connection. *Sol. Phys.* 285, 25–70. doi:10.1007/s11207-012-0085-7

Muschietti, L., Roth, I., and Ergun, R. (1994). Interaction of Langmuir Wave Packets with Streaming Electrons: Phase-Correlation Aspects. *Phys. Plasmas* 1, 1008–1024. doi:10.1063/1.870781

Numata, R., Howes, G. G., Tatsuno, T., Barnes, M., and Dorland, W. (2010). AstroGK: Astrophysical Gyrokinetics Code. *J. Comp. Phys.* 229, 9347. doi:10.1016/j.jcp.2010.09.006

Owen, C. J., Bruno, R., Livi, S., Louarn, P., Al Janabi, K., Allegrini, F., et al. (2020). The Solar Orbiter Solar Wind Analyser (SWA) Suite. *Astron. Astrophys.* 642, A16. doi:10.1051/0004-6361/201937259

Paschmann, G., Sckopke, N., Bame, S. J., and Gosling, J. T. (1982). Observations of Gyrating Ions in the Foot of the Nearly Perpendicular Bow Shock. *Geophys. Res. Lett.* 9, 881–884. doi:10.1029/GL009i008p00881

Pollock, C., Moore, T., Jacques, A., Burch, J., Gliese, U., Saito, Y., et al. (2016). Fast Plasma Investigation for Magnetospheric Multiscale. *Space Sci. Rev.* 199, 331–406. doi:10.1007/s11214-016-0245-4

Scime, E. E., Phillips, J. L., and Bame, S. J. (1994). Effects of Spacecraft Potential on Three-Dimensional Electron Measurements in the Solar Wind. *J. Geophys. Res. Space Phys.* 99, 14769–14776. doi:10.1029/94JA00489

Sckopke, N., Paschmann, G., Bame, S. J., Gosling, J. T., and Russell, C. T. (1983). Evolution of Ion Distributions across the Nearly Perpendicular Bow Shock - Specularly and Non-specularly Reflected-Gyrating Ions. *J. Geophys. Res.* 88, 6121–6136. doi:10.1029/JA088iA08p06121

Skoug, R. M., Funsten, H. O., Mobius, E., Harper, R. W., Kihara, K. H., and Bower, J. S. (2016). A Wide Field of View Plasma Spectrometer. *J. Geophys. Res. Space Phys.* 121, 6590–6601. doi:10.1002/2016JA022581

Spiger, R. J., Murphree, J. S., Anderson, H. R., and Loewenstein, R. F. (1976). Modulation of Auroral Electron Fluxes in the Frequency Range 50 kHz to 10 MHz. *J. Geophys. Res.* 81, 1269–1278. doi:10.1029/JA081i007p01269

Spiger, R. J., Oehme, D., Loewenstein, R. F., Murphree, J., Anderson, H. R., and Anderson, R. (1974). A Detector for High Frequency Modulation in Auroral Particle Fluxes. *Rev. Sci. Instrum.* 45, 1214–1220. doi:10.1063/1.1686462

Szita, S., Fazakerley, A. N., Carter, P. J., James, A. M., Trávnícek, P., Watson, G., et al. (2001). Cluster Peace Observations of Electrons of Spacecraft Origin. *Ann. Geophys.* 19, 1721–1730. doi:10.5194/angeo-19-1721-2001

Valentini, F., Trávníček, P., Califano, F., Hellinger, P., and Mangeney, A. (2007). A Hybrid-Vlasov Model Based on the Current Advance Method for the Simulation of Collisionless Magnetized Plasma. *J. Comp. Phys.* 225, 753–770. doi:10.1016/j.jcp.2007.01.001

Verniero, J. L., Howes, G. G., Stewart, D. E., and Klein, K. G. (2021a). Determining Threshold Instrumental Resolutions for Resolving the Velocity Space Signature of Ion Landau Damping. *J. Geophys. Res. (Space Phys.* 126, e28361. doi:10.1029/2020JA028361

Verniero, J. L., Howes, G. G., Stewart, D. E., and Klein, K. G. (2021b). PATCH: Particle Arrival Time Correlation for Heliophysics. *J. Geophys. Res. (Space Phys.* 126, e28940. doi:10.1029/2020JA028940

Verscharen, D., Klein, K. G., and Maruca, B. A. (2019). The Multi-Scale Nature of the Solar Wind. *Living Rev. Sol. Phys.* 16, 1. doi:10.1007/s41116-019-0021-0

Verscharen, D., Wicks, R. T., Alexandrova, O., Bruno, R., Burgess, D., Chen, C. H., et al. (2021). A Case for Electron-Astrophysics. *Exp. Astron.* 57, 1. doi:10.1007/s10686-021-09761-5

Viñas, A. F., and Gurgiolo, C. (2009). Spherical Harmonic Analysis of Particle Velocity Distribution Function: Comparison of Moments and Anisotropies Using Cluster Data. *J. Geophys. Res. Space Phys.* 114. doi:10.1029/2008JA013633

Watkins, N. W., Bather, J. A., Chapman, S. C., Mouikis, C. G., Gough, M. P., Wygant, J. R., et al. (1996). Suspected Wave-Particle Interactions Coincident with a Pancake Distribution as Seen by the CRRES Spacecraft. *Adv. Space Res.* 17, 83–87. doi:10.1016/0273-1177(95)00698-E

Whittlesey, P. L., Larson, D. E., Kasper, J. C., Halekas, J., Abatcha, M., Abiad, R., et al. (2020). The Solar Probe ANalyzers—Electrons on the Parker Solar Probe. *Astrophys. J. Supp.* 246, 74. doi:10.3847/1538-4365/ab7370

Wilson, L. B., III, Brosius, A. L., Gopalswamy, N., Nieves-Chinchilla, T., Szabo, A., Hurley, K., et al. (2021a). A Quarter Century of *Wind* Spacecraft Discoveries. *Rev. Geophys.* 59, e2020RG000714. doi:10.1029/2020RG000714

Wilson, L. B., III, Chen, L.-J., and Roytershteyn, V. (2021b). The Discrepancy between Simulation and Observation of Electric Fields in Collisionless Shocks (Invited). *Front. Astron. Space Sci.* 7, 14. doi:10.3389/fspas.2020.592634

Wilson, L. B., III, Stevens, M. L., Kasper, J. C., Klein, K. G., Maruca, B., Bale, S. D., et al. (2018). The Statistical Properties of Solar Wind Temperature Parameters Near 1 au. *Astrophys. J. Suppl.* 236, 41. doi:10.3847/1538-4365/aab71c

Conflict of Interest: Author JK was employed by company BWX Technologies, Inc.

The remaining authors declare that the research was conducted in the absence of any commercial or financial relationships that could be construed as a potential conflict of interest.

Publisher's Note: All claims expressed in this article are solely those of the authors and do not necessarily represent those of their affiliated organizations, or those of the publisher, the editors and the reviewers. Any product that may be evaluated in this article, or claim that may be made by its manufacturer, is not guaranteed or endorsed by the publisher.

frontiers | Frontiers in Astronomy and Space Sciences

ORIGINAL RESEARCH
published: 12 July 2022
doi: 10.3389/fspas.2022.919755

Heliospheric Structure Analyzer (HSA): A Simple 1-AU Mission Concept Focusing on Large-Geometric-Factor Measurements

Joseph E. Borovsky[1]* *and Jim M. Raines*[2]

[1]Center for Space Plasma Physics, Space Science Institute, Boulder, CO, United States, [2]Climate and Space Sciences and Engineering, University of Michigan, Ann Arbor, MI, United States

To obtain measurements that will address some outstanding questions about the properties and origin of the magnetic and plasma structure of the heliosphere a simple single-spacecraft mission at one AU is outlined. By focusing on large-geometric-factor measurements of particles (protons, alphas, heavy ions, and electrons) several longstanding questions can be answered. The key objectives of the large-geometric-factor measurements are lower noise and faster time resolution. Much of the focus is on critical measurements associated with the ubiquitous current sheets (directional discontinuities) of the solar wind that provide information about the origin and evolution of the current sheets and about the origin and evolution of the magnetic and plasma structures that they define.

Keywords: heliospheric structure, solar wind, current sheets, magnetic flux tubes, directional discontinuities, turbulence

OPEN ACCESS

Edited by:
Alessandro Retino, UMR7648 Laboratoire de physique des plasmas (LPP), France

Reviewed by:
Roman Kislov, Space Research Institute (RAS), Russia
Lingling Zhao, University of Alabama in Huntsville, United States

***Correspondence:**
Joseph E. Borovsky
jborovsky@spacescience.org

Specialty section:
This article was submitted to Space Physics, a section of the journal Frontiers in Astronomy and Space Sciences

Received: *13 April 2022*
Accepted: *07 June 2022*
Published: *12 July 2022*

Citation:
Borovsky JE and Raines JM (2022) Heliospheric Structure Analyzer (HSA): A Simple 1-AU Mission Concept Focusing on Large-Geometric-Factor Measurements. Front. Astron. Space Sci. 9:919755. doi: 10.3389/fspas.2022.919755

1 INTRODUCTION

A simple single-spacecraft mission at one AU that focuses on large-geometric-factor (effective large collecting area) ion and electron measurements could greatly advance the understanding of the heliosphere, specifically on two outstanding questions in heliospheric physics: (A) What is the magnetic and plasma structure of the heliosphere? and (B) Where does that structure come from?

It is critical to unambiguously detect subtle changes in the particle properties (protons, alphas, heavy ions, electrons) across solar-wind directional discontinuities (current sheets). Focusing on obtaining accurate measurements of the changes in the ion and electron properties across solar-wind discontinuities, the mission would determine 1) which discontinuities are fossils from the Sun and which discontinuities could have been created in the solar wind away from the Sun, 2) which discontinuities in the solar wind are rotational discontinuities (propagating Alfvénic field kinks) and which are tangential discontinuities (plasma boundaries), and 3) the fingerprints of discontinuity-evolution processes acting in the solar wind away from the Sun.

Making these determinations about solar-wind discontinuities is important because these determinations 1) provide remote information about processes acting in the solar corona, 2) provide information about the nature and origin of the magnetic ductwork that transports energetic particles and solar heat flux, 3) provide an assessment as to the impact of turbulence on the evolution of the solar wind and the heliospheric structure, 4) provide information about the origin and evolution of the solar wind from an individual-flux-tube point of view, and 5) connect the

intermittent driving of the Earth's magnetosphere-ionosphere system to structure in the corona and to processes occurring in the solar wind.

In this note we will make the case for lower-noise and higher-time-resolution measurements of ions and electrons in the solar wind at one AU. Basically, the push will be to field instruments with larger geometric factors to obtain improved particle count rates resulting in lower statistical noise for ion and electron measurements. Of particular interest will be heavy-ion spectrometers that can measure ion-charge-state ratios with higher time resolution than present spectrometers can.

2 THE MEASUREMENTS OF INTEREST

The measurements of interest are high-time-resolution and low-noise measurements of particle boundaries and their association with current sheets. The particle populations of interest are protons, alphas, heavy-ion charge states, core electrons, and the electron strahl.

2.1 Crossing Current Sheets

Vital information about the structure of the heliosphere and the origin of that structure comes from comparing the plasmas on the two sides of a directional discontinuity (current sheet). Note that there are common thin current sheets and there are rarer thick current sheets in the solar wind, the thick current sheets being for example the heliospheric current sheet that separates magnetic sectors of the heliosphere (Smith, 2001) and current sheets associated with the corotating-interaction-region stream interfaces (Borovsky, 2006). The focus here is not on these thick current-sheet structures, but on the ubiquitous thin current sheets of the solar wind. At 1 AU these current sheets have thicknesses on the order of 1,000 km (Siscoe et al., 1968; Vasquez et al., 2007; Borovsky and Steinberg, 2014) as determined using the Taylor hypothesis with each current sheet passing a spacecraft in 1–4 s. The current sheet thicknesses are much larger than the plasma kinetic scales ion gyroradii and ion inertial lengths (Vasquez et al., 2007) so they tend to be stable against Petschek-type collisionless-plasma reconnection. Additionally, the solar wind plasma is everywhere expanding (except across interplanetary shocks), so the strong current sheets will not thin by compression. (But see Lazarian and Vishniac (1999), Artemyev (2008), Zelenyi et al. (2011), Zelenyi et al. (2021), Lazarian et al. (2020) for other ideas about current-sheet reconnection). Solar-wind current sheets pass a spacecraft at a rate of a few per hour, which is about 30,000 per year. (The current sheet collection of Borovsky (2008) was about 10,000 per year, but that collection only selected very strong current sheets). Each current sheet spatially separates two plasmas. A current sheet is characterized by a sudden large change in the direction of the magnetic field from the one plasma to the other. Examination of the spacings and orientations of the current sheets in the solar wind leads to a "flux-tube spaghetti" picture of the heliospheric magnetic structure with the magnetic flux tubes meandering along the Parker-spiral direction (McCracken and Ness, 1966; Michel, 1967; Bruno et al., 2001; Borovsky, 2008, Borovsky, 2010a; Greco et al., 2008; Pecora et al., 2019). The spacings and orientations of the current sheets in the solar wind are consistent with a flux-tube spaghetti picture of the heliospheric magnetic structure and this will be the picture used in this manuscript. A depiction of the background flux-tube heliosphere appears in **Figure 1**. In the spaghetti, large temporal changes in the magnetic-field direction are seen when a spacecraft crosses a current sheet and smaller angular wiggles of the magnetic-field direction are seen within the flux tubes (Bruno et al., 2001; Borovsky, 2008).

Besides the flux-tube-spaghetti depiction, there are other depictions of the magnetic structure of the solar wind, e.g., an admixture of flux tubes, plasmoids (flux ropes), magnetic islands, and localized magnetic structures (e.g., Tamano, 1991; Khabarova et al., 2015; Khabarova et al., 2016; Adhikari et al., 2019; Malandraki et al., 2019; Khabarova et al., 2020), depicted in Figure 24c of Khabarova et al. (2021). Flux ropes and plasma blobs are important constituents of the very slow sector-reversal-region plasma originating from coronal streamer stalks (Wang et al., 1999; Sheeley and Rouillard, 2010; Viall et al., 2010; Viall and Vourlidas, 2015; Kepko et al., 2016; Di Matteo et al., 2019). Relatedly, sector-reversal-region plasma at one AU tends to have magnetic fields that are not Parker-spiral oriented (Borovsky, 2020a) and tends to have a weak electron strahl (Borovsky, 2021b), both being indicative of impulsive emission of plasma from the Sun with poor magnetic connections back to the Sun.

The origin of this flux-tube magnetic structure (and the intermittent driving of the Earth) is still an outstanding issue (Neugebauer and Giacalone, 2010, Neugebauer and Giacalone, 2015; Li and Qin, 2011; Owens et al., 2011; Telloni et al., 2016; Tu et al., 2016; Viall and Borovsky, 2020). The origins might involve fossil magnetic flux tubes from the corona (McCracken and Ness, 1966; Borovsky, 2008, Borovsky, 2016), current sheets created by MHD turbulence in the solar wind (Greco et al., 2009; Zhdankin et al., 2012; Vasquez et al., 2013), evolving Alfvén waves propagating out from the Sun (Tsurutani and Ho, 1999; Vasquez and Hollweg, 1999), or advected pressure-balance structures (Riazantseva et al., 2005a; Zhang et al., 2008; Tu et al., 2016).

Current sheets (directional discontinuities) dominate the magnetic structure of the heliosphere, cellularizing the field and plasma into a spaghetti of tubes, as indicated by the common plasma-property jumps seen when crossing current sheets [cf. Figures 3, 5 of Borovsky (2008)]. These tubes form the magnetic ductwork of the heliosphere that enables the long-distance transport of energetic particles and solar heat flux along magnetic-field lines. This transport ductwork is readily seen in the changes of strahl intensity across current sheets (Gosling et al., 2004a,b; Borovsky, 2020b) and the changes in SEP flux from tube to tube (Trenchi et al., 2013). The current sheets that separate the tubes dominate the Fourier power of the solar wind (Siscoe et al., 1968; Borovsky, 2010b) and current-sheet properties (occurrence distribution, thicknesses, and profiles) determine the details of the Fourier magnetic power spectral density that has been analyzed for decades (Borovsky and Podesta, 2015; Borovsky and Burkholder, 2020). As the

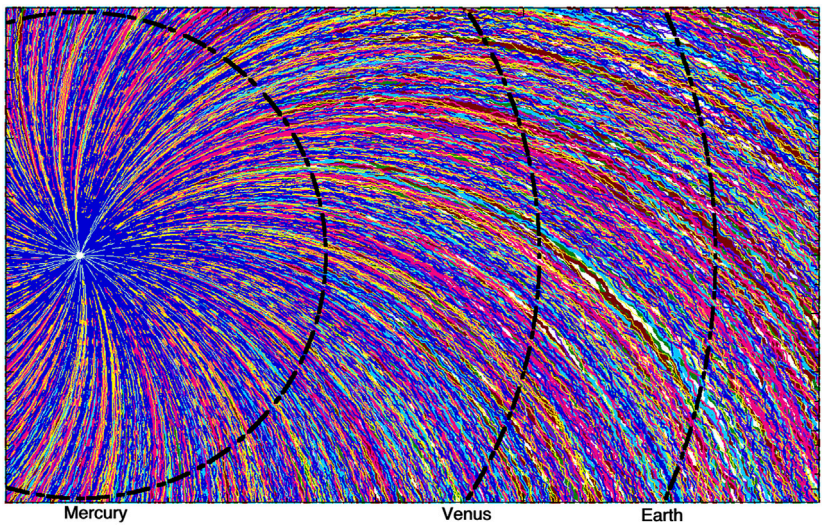

FIGURE 1 | A simple sketch (to scale) of the background heliospheric structure that forms a magnetic ductwork for the transport of energetic particles and that produces the intermittent driving of the Earth's magnetosphere. In the sketch no fast-versus-slow wind is depicted and no ejecta is depicted.

spaghetti of flux tubes passes the Earth, the Earth sees sudden changes in the orientation of the solar-wind magnetic field from flux tube to flux tube. The driving of the Earth's magnetosphere by the solar wind is very sensitive to the orientation ("clock angle") of the solar wind magnetic field (Komar and Cassak, 2016) so flux tube to flux tube the rate of driving changes, resulting in an temporally on-off driving of the Earth (Borovsky, 2020a). The ultimate cause of this intermittent driving of the Earth is unknown: it could be solar-wind turbulence or it could be coronal magnetic structure.

Early analysis of the background heliospheric magnetic structure and its origin focused on the question of whether current sheets (directional discontinuities) are tangential discontinuities (plasma boundaries) versus rotational discontinuities (propagating field kinks) (e.g., Burlaga and Ness, 1969; Turner and Siscoe, 1971; Neugebauer et al., 1984; Lepping and Behannon, 1986; Soding et al., 2001). To discern whether a directional discontinuity is a rotational discontinuity versus a tangential discontinuity, the focus historically has been 1) to determine the orientation of the current sheet, 2) to determine the local magnetic-field direction, and then 3) to discern by the orientation whether or not the magnetic-field lines are crossing the current sheet. Field lines crossing a current sheet indicates that it is a rotational discontinuity. [Another possibility that could be considered for field lines crossing the current sheet is a "contact discontinuity" (e.g., Burlaga, 1971), however indications are that contact discontinuities cannot persist in collisionless plasmas such as the solar wind (cf. Lapenta and Brackbill, 1996)]. When current sheets are highly oblique to the magnetic-field direction [which multispacecraft measurements indicate that they tend to be (Horbury et al., 2001; Knetter et al., 2003,2004; Riazantseva et al., 2005b,c)] this rotational-versus-tangential determination is difficult and tends to yield

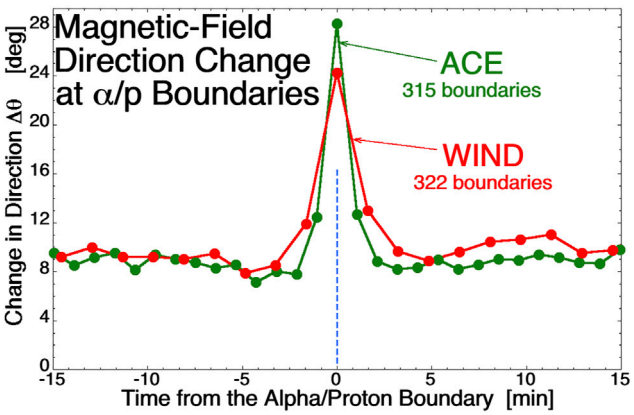

FIGURE 2 | Superposed epoch averages of change in the direction of the solar-wind magnetic field with the zero epoch being an ion-composition boundary as identified by a sudden change in the α/*p* value. The green curve plots the 64-s change in the field direction for 315 α/p boundaries identified with the ACE spacecraft and the red curve plots the 97-s change in the field direction 322 for α/p boundaries identified with the WIND spacecraft.

ambiguous classifications about rotational versus tangential discontinuities (Neugebauer, 2006; Paschmann et al., 2013; Artemyev et al., 2019; Sonnerup, 2022).

When a spacecraft crosses a current sheet from the plasma on one side of the sheet into the plasma on the other side, often changes other than the direction of the magnetic field can be seen. Current-sheet crossings can exhibit "jumps" in the value of the magnetic-field strength $|\mathbf{B}|$, in the value of the proton and electron number densities n_p and n_e, in the proton temperature T_p, in the proton specific entropy $S_p = T_p/n_p^{2/3}$, in the proton-beta $\beta_p = 8\pi n_p k_B T_p/B^2$, in the core electron temperature $T_{e\ core}$, in the intensity of the electron strahl, and

in the alpha-to-proton number-density ratio α/p (helium abundance).

An example of this appears in **Figure 2** where jumps in the α/p time series at one AU are statistically examined from measurements onboard ACE and separately from measurements onboard WIND (cf. Borovsky, 2020b). The measurements utilized for the α/p number-density ratio were 64-s resolution measurements from ACE SWEPAM (McComas et al., 1998) and 97-s resolution measurements from WIND SWE (Ogilvie et al., 1995; Kasper et al., 2006). Times when distinct changes in the α/*p* value are seen are collected: to be collected, the changes in α/p must be clearly larger than the "shot noise" of the α/p measurements in the time series. Then the temporal changes Δθ in the direction of the solar wind magnetic field at each spacecraft are calculated in the time series. **Figure 2** shows superposed-epoch averages of the temporal-field-change angle Δθ for the two collections of α/p jumps with the zero epoch (t = 0) at the time of each α/p jump. The large values of Δθ at the times of the α/p jumps indicate that these α/p jumps are occurring across current sheets in the solar wind. α/p ion-composition boundaries cannot be created in the solar wind away from the Sun. If the plasma has a uniform ion composition, there are no *in situ* processes that can change that composition. Hence the observed α/p boundary seen at one AU must have been created in the corona and survived intact advected to one AU. It follows that the current sheets observed at one AU that have α/p jumps across them are fossil current sheets from the corona. These particular current sheets are inconsistent with current-sheet formation by MHD turbulence or by other *in situ* processes in the solar wind. The current sheets being fossils from the Sun implies also that the magnetic-flux tubes adjacent to the current sheets are magnetic fossils from the corona.

Note that aside from identifying individual fossil current sheets *via* α/p boundaries, there are statistical methods that indicate that most of the current sheets of the solar wind are fossils (Borovsky, 2021a): these methods examine the statistical properties of the current-sheet orientations and compare those properties with estimates of the unidirectional compression or rarefaction of the solar-wind plasma (Borovsky and Denton, 2016; Borovsky, 2020e).

The association of jumps in ion and electron parameters at current sheets are in general demonstrated in Figure 3 of Borovsky (2008). The association of proton-specific-entropy jumps with current sheets is shown in Figure 5A of Borovsky (2008). The associations of jumps in the proton number density, the proton specific entropy, and the proton beta with current sheets is shown in Figure 6 of Borovsky (2012). The association of α/p ion-composition boundaries with current sheets is shown in Figure 5B of Borovsky (2008) and examined extensively in Borovsky (2020b). The association of strahl-intensity boundaries with current sheets is discussed in Gosling et al. (2004a,b) and Borovsky (2021b) and studied extensively in Borovsky (2020b). The association of jumps in the electron number density and core-electron temperature with current sheets was studied extensively in Borovsky et al. (2021).

2.2 What the Tube-To-Tube Jumps Indicate

Observing changes in different quantities when crossing a current sheet from one flux tube into another flux tube provides information about the heliospheric magnetic structure and its origins: specifically about the current sheet and about the two adjacent flux tubes. For structure that can be identified as fossil, information about coronal processes might be obtainable. **Table 1** summarizes some of the information that is obtained by observing jumps in specific quantities across the solar-wind current sheets.

As noted above, an observable jump in the alpha-to-proton number-density ratio α/p (helium abundance) across a current sheet indicates that current sheet is a fossil (relic) from the solar corona (first row of **Table 1**). A jump in a heavy-ion charge-state ratio would also indicate a fossil current sheet, however the time resolution of present-day heavy-ion spectrometers is too slow to perform such a measurement across a current sheet. Charge-state-ratio measurements across a current sheet would provide unique insight into the differences in magnetic mapping of the two adjacent flux tubes into the corona and provide information about the magnetic mapping of the corona out into the heliosphere. As noted in **Table 1**, a change of α/p or the charge-state ratio across a current sheet also indicates that current sheet is a tangential discontinuity, not a rotational discontinuity.

The electron strahl at one AU is a field-aligned population of energetic electrons that are the coronal hot electrons escaping along magnetic field lines out into the heliosphere (Feldman et al., 1976; Pilipp et al., 1987; Maksimovic et al., 2005). This standard picture of the origin of the strahl emanating from the corona is supported by statistical observations of the strahl evolving into the halo-electron population with distance from the Sun (e.g., Stverak et al., 2009), although there are suggestions that strahl-electron populations can be created *in situ* away from the Sun by whistler waves (Vocks et al., 2005) or by reconnection (Khabarova et al., 2020). Electron-strahl-intensity jumps across current sheets indicate either 1) that the plasma on the two sides of the current sheet magnetically connect to two different regions of the corona (e.g., Gosling et al., 2004a,b; Borovsky, 2021b) or 2) that physical processes in the plasmas on the two sides of the current sheet produce different amounts of scattering of the strahl electrons. Either indication implies that the current sheet is coherent back to the Sun. As noted in the second row of **Table 1**, a clear conclusion of a current sheet exhibiting a jump in the strahl intensity is that current sheet is not a rotational discontinuity, rather it is a tangential discontinuity (plasma boundary).

Jumps in the core electron temperature $T_{e\ core}$ from flux tube to flux tube were examined by Borovsky et al. (2021). In exobase models of the solar wind the local value of the core-electron temperature $T_{e\ core}$ is a direct measure of the local value of the interplanetary electrical potential ϕ with respect to infinity (Feldman et al., 1975; Boldyrev et al., 2020; Moncuquet et al., 2020). As noted in **Table 1**, differences in $T_{e\ core}$ across a current sheet imply differences in ϕ in the two flux tubes. Differences in ϕ from tube to tube imply that the exobase model operates independently from one flux tube to another. This leads to a

TABLE 1 | Information that is obtained by observing a jump in a specific quantity when crossing a current sheet from flux tube A into flux tube B. (TD = tangential discontinuity and RD = rotational discontinuity).

Quantity changing across current sheet	Information yielded	Implication about adjacent flux tubes
α/p number-density ratio Heavy-ion charge-state ratio	• Fossil current sheet • Current sheet is a TD not an RD	Tube A and Tube B map to different spots in corona
Electron Strahl Intensity	• Current sheet is coherent back to the Sun • Current sheet is a TD not an RD	Tube A and Tube B map to different spots in corona
$T_{e\ corr}$	• Current sheet is a TD not an RD	Different interplanetary potential ϕ in Tube A versus Tube B
S_p, n, T_p, B_{mag}, β_p	• Current sheet is a TD not an RD	
$(\Delta v \bullet \Delta B)/(\lvert\Delta v\rvert\lvert\Delta B\rvert) \approx 1$ $(\Delta v \times \Delta B)/(\lvert\Delta v\rvert\lvert\Delta B\rvert) \approx 0$	• Current sheet in a CDE	

system-science picture of flux tubes (Borovsky, 2021c), each flux tube being an independent system wherein its particle populations (protons, proton beam, alpha particles, heavy ions, core electrons, strahl electrons, and halo electrons) evolve with distance from the Sun independently from the particle populations in adjacent flux tubes. In that picture a spacecraft making measurements from flux tube to flux tube at one AU is seeing independent realizations of system evolution.

General plasma and field variations across current sheets are commonly seen [cf. Figure 3 of Borovsky (2008)]. As noted in the fourth row of **Table 1** these jumps are a clear indication that the current sheet is a tangential discontinuity (plasma boundary) and not a rotational discontinuity (propagating Alfvénic kink in the field). These plasma variations often fall into the categorization of "pressure balanced structures" that advect out from the Sun in the solar wind flow (Tu and Marsch, 1993; Riazantseva et al., 2005a; Zhang et al., 2008; Tu et al., 2016). Note that Fourier analysis of variations in the solar-wind magnetic-field strength B_{mag} and plasma number density n are often interpreted as evidence that there are dynamic fluctuations in the solar wind that have a "compressible" aspect: however, an interpretation that the solar-wind plasma is "inhomogeneous" or "lumpy" is more physically accurate (cf. Borovsky, 2020c).

For understanding the magnetic structure of the heliosphere it is important to discuss the Chandrasekhar dynamical equilibrium (CDE). In the Alfvénic fast wind and in the Alfvénic slow wind the magnetic structure of the heliosphere moves out from the Sun faster than the proton solar wind plasma. The relative speed between the magnetic structure and the proton plasma is about 0.7 v_A in the outward-Parker-spiral direction (Borovsky, 2020d; Nemecek et al., 2020). In a temporal block of solar-wind data a single reference frame can be found (the reference frame moving with the magnetic structure) wherein the proton flow has $v_\perp \approx 0$ and essentially all flow is parallel to the local magnetic-field direction. [In Borovsky, 2020d this reference frame is found using a genetic algorithm in the data analysis that finds the vector reference frame minimizing arccos $(v_{proton} \bullet B)$]. Hence, with $v_\perp \approx 0$ the magnetic structure moves outward from the Sun without discernable time evolution. This case is discussed in Sect. 7.2 of Parker (1979) with an illustration in Figure 7.1 of Parker (1979) where Parker referred to it as Chandrasekhar's "dynamical equilibrium solution" (Chandrasekhar, 1961). (See also Birn (1991), Tenerani et al. (2020) for nonlinear V parallel to B equilibrium solutions). Essentially, a nonlinear tangle of magnetic field will propagate through a plasma without evolution. For flux tubes in a CDE spaghetti, a vector jump in the proton flow velocity Δv is seen across each current sheet owing to the sudden rotation of the magnetic-field direction and the proton flow being everywhere parallel to the local field direction. As noted in the last row of **Table 1**, for those vector velocity jumps $\Delta\underline{\mathbf{v}}$ and vector magnetic-field jumps $\Delta\mathbf{B}$ in a CDE it is the case that $(\Delta\mathbf{v} \bullet \Delta\mathbf{B})/(|\Delta\mathbf{v}||\Delta\mathbf{B}|) \approx 1$ and $(\Delta\mathbf{v} \times \Delta\mathbf{B})/(|\Delta\mathbf{v}||\Delta\mathbf{B}|) \approx 0$.

3 WHAT LEVEL OF JUMPS CAN BE UNAMBIGUOUSLY IDENTIFIED TODAY AT 1 AU IN THE DATA

Owing to "shot noise" in the measurement time series, only jumps in the values of measured quantities that are larger than the measurement noise level can be confidently identified. Three examples of the sizes of changes in the solar wind particle properties that can be confidently identified have appeared in the literature.

For the study of α/p number-density-ratio changes in the solar wind at one AU (Borovsky, 2020b) only changes in the ratio that were larger than about 25% of the α/*p* value could be identified in either the ACE SWEPAM measurements or the WIND SWE measurements (cf. **Figure 1** of Borovsky (2020b)). With the faster, multi-head BMSW instrument on the Spektr-R spacecraft jumps in the α/p ratio that are smaller than 25% could probably be identified (e.g., Safrankova et al., 2013; Zastenker et al., 2013), however the Spektr-R spacecraft does not have a magnetometer to correlate the α/p ion-composition jumps with current sheets.

For the study of core-electron-temperature changes in the solar wind, changes of $T_{e\ core}$ that were larger than about 1 eV could be confidently identified (cf. Figure 5B of Borovsky et al., 2021).

In the study of electron-strahl-intensity changes in the solar wind, changes in the flux of the electron strahl that were greater

than about 25% of the flux value could be identified with confidence (cf. **Figure 2** of Borovsky, 2020b).

Faster and lower-noise measurements can be obtained with improved particle instrumentation aimed at higher particle count rates *via* 1) larger geometric factors and 2) multi-head instruments that eliminate energy sweeps. This would enable smaller changes in the ion and electron properties of the solar wind to be confidently identified, enabling the analysis of a much larger fraction of the current sheets of the solar wind to be analyzed and assessed according to **Table 1**.

The need for larger-geometric-factor heavy-ion spectrometers is particularly acute. Present-day spectrometers with time resolutions of a fraction of an hour have proven very useful for studying the large-scale structure of the solar wind and its origin from the various large-scale regions of the solar corona like coronal holes versus streamer belts versus ejecta (e.g., Geiss et al., 1995; Wimmer-Schweingruber et al., 1997; Zurbuchen et al., 1999; Burton et al., 1999; von Steiger et al., 2001; Zhao et al., 2009) and for studying the heliospheric-plasma-sheet region (Simunac et al., 2012) and large-scale "microstreams" and plumes in coronal-hole-origin plasma (von Steiger et al., 1999; Neugebauer, 2012). Here, with higher time resolution we are calling for heavy-ion spectrometers to be used to study the finer-scale magnetic structure of the heliosphere and the coronal physical processes creating that structure: i.e., flux-tube to flux-tube measurements in the solar wind at one AU that may correspond to loop-to-loop variations in the solar corona. For heavy-ion spectrometers to be useful for this, time resolutions of 1 min or better are critical.

For particle-counting instruments the combination of lower noise and higher time resolution is difficult, with poorer counting statistics being a consequence of shorter measuring intervals. For the solar wind there is an argument that higher-frequency fluctuations have smaller amplitudes than lower-frequency fluctuations, making the higher-time-resolution measurements need even more accuracy and lower noise. That argument is likely false, and it is addressed in the Appendix.

4 THE FUTURE WITH IMPROVED MEASUREMENTS

Some specific measurement needs to better evaluate **Table 1** are discussed and the resulting improvements to our knowledge are outlined. In all cases lower-noise measurements are needed to be able to locate subtle but distinct changes in the levels of the measurements and measure tube-to-tube variations in particle properties. For this lower-noise measurements with cadences of a fraction of a minute will suffice.

Note that any measurement improvement will lead to progress and lower-noise measurements will enable the exploration of solar wind features that were hidden in the shot noise of the present-day measurements.

Heavy-Ion Charge States: As stated above, time resolutions of about 1 min or better are needed for heavy-ion charge-state ratios. To confidently locate a boundary, several data points are needed on each side of a jump in the charge-state ratio, and of course the jump must be larger than the measurement shot noise. Perhaps designing spectrometers than concentrate their measurement time on specific heavy-ion charge states (e.g., O^{7+}/O^{6+} or C^{6+}/C^{5+} or C^{6+}/C^{4+}) would enable the needed faster-yet-low-noise measurements. The proper charge-state measurements would not only identify what is a magnetic fossil at one AU, but perhaps where in the corona it came from and how it was made.

Alpha-to-Proton Number-Density Ratios: α/p ratios (helium abundance) are available at present with fast time resolution at one AU, but in the present data sets the measurement shot noise is very large. Improved geometric factors to lower the shot noise would greatly enhance the ability to identify current sheets that are definitely fossils from the corona. In the count-rate data analysis, sacrificing the time resolution to integrate the count-rates longer to lower the shot noise is also a clear option for the analysis of jumps across current sheets. Reading the changes in α/p from one fossil flux tube to the next might provide information about the coronal origins of the two flux tubes, if the physics driving the solar-wind α/p helium abundance can be sorted out (e.g., Wang, 2008, 2016; Byhring, 2011; McIntosh et al., 2011; Rakowski and Laming, 2012; Fu et al., 2018).

Proton Flow-Velocity Vectors: In analyzing the evolution (or not) of CDEs, it is critical to be able to measure the proton-flow vector relative to the magnetic-field direction. We are looking for cases where $v_\perp \approx 0$ in the reference frame of the magnetic structure in the presence of a large value of $v_{||}$ in that reference frame. The main source of error in $v_\perp$ is the fact that the magnetic-field direction at the spacecraft changes during the time interval when a flow measurement is made. An analysis of a CDE in Figure 3 of Borovsky (2020d) found that the rms change in the field direction during a 3-s proton measurement was 4.8^o; if this 4.8^o is taken as the uncertainty in the magnetic-field direction then the rms $v_\perp$ value of 5.2 km/s for that CDE is entirely consistent with perpendicular-versus-parallel orientation uncertainty for the observed $v_{||}$ of 75 km/s. Hence, the $v_\perp$ measurements in the CDE in Borovsky (2020d) were consistent with the noise level in the velocity measurements. To fix this difficulty, either 1) accurate proton measurements that are much faster than 3 s must be made or 2) the moving magnetic-field orientation during the proton measurement interval must be accounted for in the proton-count-rate data analysis. More accurate measurements of the proton flow vector will also yield more-accurate third-order moment calculations of solar-wind heating rates (e.g., Sorriso-Valvo et al., 2007; MacBride et al., 2008; Podesta et al., 2009; Smith et al., 2009). Third-order moments are products of inward- and outward-propagating Elsässer modes: if in the reference frame moving outward with the magnetic structure $v_\perp = 0$ then the inward-propagating Elsässer mode has an amplitude of zero and the third-order moment vanishes. (See also Wang et al. (2018) for arguments that observed inward Elsässer modes may be measurement noise).

General Plasma Parameters: Lower-noise measurements of general plasma parameters like number density, temperature, and specific entropy would enable the identification of more tangential discontinuities. Higher-time-resolution (and lower-noise) measurements of typical plasma parameters such as number density, temperature, particle pressure, and proton

TABLE 2 | The current state of the art in ion and electron instrumentation. All are ESA based except the faraday cups of BMSW.

Instrument	Heritage	Factor (cm^2 sr eV/eV)	Time resolution normal (burst)	References
Proton ESA	Specktr-R BMSW		0.031 s	Zastenker et al. (2013)
	MMS FPI	$1–2 \times 10^{-5}$	0.030 s (7.5 ms)	Pollock et al. (2016)
	PSP SPAN-I	6×10^{-4}	0.435 s	Livi et al. (2021)
Electron ESA	MMS FPI	$1–7 \times 10^{-5}$	0.030 s (7.5 ms)	Pollock et al. (2016)
	PSP SPAN-Ae	6×10^{-4}	0.437 s	Whittlesey et al. (2020)
Heavy-ion charge-state spectrometer	Solar orbiter SWA-HIS	1×10^{-5}	30 s/4 s	Owen et al. (2020)
Magnetometer	MMS		7.8 msec	Russell et al. (2016)

flow velocity would enable current sheets to be well resolved in quantities other than **B**. Current sheets are typically ~1,000 km thick, and so resolution considerably better than 1-s is desirable. If current sheets and the co-located plasma boundaries could both be well resolved so that their spatial profiles could be compared, then the door would be opened to the study of evolutionary processes such as particle diffusion, resistivity, and viscosity to learn how and why current-sheet and plasma-boundary thicknesses evolve with distance from the Sun. There are also evolutionary processes for current sheets related to plasma expansion and compression (e.g., Schindler and Birn, 2002; Schindler and Hesse, 2008, Schindler and Hesse, 2010): these result in fine-scale structuring of the current sheet profile. Higher-resolution plasma measurements may open the way to investigating the fine-scale fingerprints of such processes. The higher-resolution plasma measurements would also make possible new studies about the processes that create and evolve magnetic holes in the solar wind (Turner et al., 1977; Winterhalter et al., 2000; Neugebauer et al., 2001).

Total Particle Pressures: Accurate fast measures of ion and electron total particle pressures would enable new studies of the true compressibility in the solar wind and new studies about pressure-balance structures in the solar wind.

Strahl Intensities: Faster and lower-noise measurements of strahl intensities at one AU would enable the identification of more tangential discontinuities and of more current sheets that are coherent back to the Sun. The energetic-electron strahl moving out from the Sun (and the backscattered strahl moving back toward the Sun) both provide very unique information about the structure of the heliosphere. Whereas the proton plasma and the magnetic-field structure seen at one AU left the corona ~100 h ago, the strahl measured at one AU left the Sun only a few hours ago: in that time difference there could be changes in the magnetic connection of one AU into the corona that the strahl can uncover. Note that strahl measurements suffer from the same magnetic-field-direction changes during a measurement interval of the electron distribution function as do the proton-velocity-vector measurements.

5 INSTRUMENTATION: LARGE GEOMETRIC FACTORS

To make progress analyzing the heliospheric, structure measurements of ion and electron properties that are low noise with appropriate time resolutions are needed. For evaluating current sheets (as in **Table 1**) lower-noise measurements with time resolutions of a fraction of a minute will suffice. If time resolutions of less than 1-s with low noise can be obtained, then the fingerprints of current-sheet evolutionary processes can be obtained.

An overview of the state of the art of particle instruments appears in **Table 2**. For some desired measurement quantities (e.g., heavy-ion charge-state ratios) the state of the art will need to be exceeded.

To simultaneously satisfy the need for higher time resolution and high signal to noise, instruments must have higher effective collecting areas, typically called geometric factors. In instruments with curved plate electrostatic analyzers (ESAs), the geometric factor includes effects from both the physical size of the instrument and detectors, as well as electrostatic effects, known as ion optics. These include steering, focusing, and transmission through the instrument much in the same way as photons through a telescope, hence the use of the word "optics". Increasing the geometric factor is as simple as increasing the size of the instrument aperture and ion optical flight path through the instrument. However, there is a key trade off: the energy resolution of the instrument is reduced as the spacing between ESA plates is increased. Energy resolution fundamentally determines the accuracy of the energy spectrum measured by any ion instrument since if effectively determines the uncertainty in the measurement. For ion composition instruments, energy resolution propagates into time of flight (TOF) uncertainty. For charge-resolving composition (TOF-energy) instruments, it also propagates into the uncertainly in the residual energy measurement (E_{SSD}) on the solid-state detectors (SSDs), the intrinsic uncertainty in the SSD energy measurement typically makes the ESA energy resolution negligible. Larger TOF uncertainty affects the ability to identify individual charge states, which is typically done from peaks in TOF-E_{SSD}, as well as suitability for addressing more general problems in plasma physics. As such, general purpose instruments typically need high energy resolutions, ideally 5%–10% for ion instruments and 10%–15% for electron instruments, fundamentally limiting ability to increase geometric factor.

There are several approaches to remove this limitation. The first is to simply add ESA duplicate ESA channels either through multiple copies of full sensor heads or through sensors that incorporate multiple ESAs. The current standard in high time resolution and high signal to noise is the Fast Plasma

Investigation (FPI) instrument suite on MMS (Pollock et al., 2016). It employs 8 sensors heads per spacecraft for both ions and electrons, 16 total. There are 4 instruments for each species as each has dual sensor heads. For this primarily magnetospheric instrument, this arrangement allows sampling of many directions simultaneously, at a much higher cadence than would be possible by relying on spacecraft spin alone. While designed primarily for high time resolution, this design also increases the effective geometric factor for each species by a factor of 8. This represents one extreme, applicable only where resources (e.g., mass, power and budget) are abundant. The other extreme is also very straightforward: simply accept lower energy resolutions to increase geometric factor. For example, decreasing the energy resolution by two gives a two-fold increase in geometric factor due to the increase in the energy pass band. For science questions that can be addressed primarily through moments of the particle velocity distribution, i.e., density, velocity and temperature, this might not be a serious limitation. Additional improvements in time resolution can be achieved by limiting the energy range of the instrument. For solar wind heavy ions, limiting the speed range to 1,100 km/s and mass per charge (m/q) to a maximum of Fe^{6+} (9.33) requires E/q stepping only up to 15 keV/e. The current state of the art Heavy Ion Sensor (HIS) on Solar Orbiter (Owen et al., 2020) goes to much higher E/q, 78 keV/e. The proton instruments in **Table 2** go up to 30 keV/e. Limiting the energy range reduces the high voltages that must be applied as well as possibly the number of E/q steps in an energy scan. There are trade offs of a more limited energy range of course. For composition instruments limiting to 15 keV/e greatly limits the usefulness of the instrument for suprathermal or pick-up ion studies, as well as extreme CME analysis.

There are a few other factors can affect time resolution and signal to noise, but they are typically more minor. The analyzer constant, the ratio of the E/q passband peak to the voltage applied to the ESA plates, can affect time resolution. Designs with higher ratios require less voltage which often leads to shorter ramp up times and smaller voltage settling times. For spinning spacecraft, the top hat design, originally described by Carlson et al. (1982) and refined by Young et al. (1988), is an excellent choice at it has a high analyzer constant (~12–15). For 3-axis stabilized spacecraft, the choice is less clear. A top hat design requires additional deflector plates, causing the uniformity of response across the FOV to suffer. Other designs, such as MESSENGER/FIPS (Andrews et al., 2007), have more uniform response but low analyzer constants (e.g., 1.33 for FIPS) which may limit the maximum speed achievable to 5–10 s scans. In principle, the speed at which the ESA power supplies can be switched through voltages is an important consideration, but in practice very fast designs are available so that these are not limiting factors.

6 HELIOSPHERIC STRUCTURE ANALYZER

Heliospheric Structure Analyzer (HSA) is envisioned as a single spacecraft that takes low-noise measurements of ions and electrons in the solar wind at one AU. Low-noise particle measurements means instrumentation with large geometric factors. In this report the motivation is given for those measurements, which will help to answer outstanding questions about the magnetic structure of the heliosphere and the origins of that structure. Much of the measurement strategy is collected in **Table 1**.

The objective of HSA would be to collect low-noise solar-wind measurements, but the data set need not be continuous. Hence a single Earth-orbiting spacecraft that makes excursions into the solar wind (out of the Earth's foreshock) could suffice.

A pathway forward would be to form a team of scientists 1) to quantify the needed measurement parameters and 2) to explore possible instrument designs to attain those measurement objectives.

DATA AVAILABILITY STATEMENT

The original contributions presented in the study are included in the article/Supplementary Material, further inquiries can be directed to the corresponding author.

AUTHOR CONTRIBUTIONS

JB initiated this project. JB and JR researched and wrote the manuscript.

FUNDING

JB was supported at the Space Science Institute by the NASA HERMES Interdisciplinary Science Program *via* grant 80NSSC21K1406 and by the NSF GEM Program *via* grant AGS-2027569. JR was supported by NASA through the Wind, Advanced Composition Explorer, and Solar Orbiter missions.

REFERENCES

Adhikari, L., Khabarova, O., Zank, G. P., and Zhao, L.-L. (2019). The Role of Magnetic Reconnection-Associated Processes in Local Particle Acceleration in the Solar Wind. *ApJ* 873, 72. doi:10.3847/1538-4357/ab05c6

Andrews, G. B., Zurbuchen, T. H., Mauk, B. H., Malcom, H., Fisk, L. A., Gloeckler, G., et al. (2007). The Energetic Particle and Plasma Spectrometer Instrument on the MESSENGER Spacecraft. *Space Sci. Rev.* 131, 523–556. doi:10.1007/s11214-007-9272-5

Artemyev, A. V., Angelopoulos, V., and Vasko, I. Y. (2019). Kinetic Properties of Solar Wind Discontinuities at 1 AU Observed by ARTEMIS. *J. Geophys. Res. Space Phys.* 124, 3858–3870. doi:10.1029/2019ja026597

Artemyev, A. V. (2008). Evolution of a Harris Current Sheet in an Electric Field. *Mosc. Univ. Phys.* 63, 193–196. doi:10.3103/s0027134908030089

Birn, J. (1991). Stretched Three-dimensional Plasma Equilibria with Field-aligned Flow. *Phys. Fluids B Plasma Phys.* 3, 479–484. doi:10.1063/1.859891

Boldyrev, S., Forest, C., and Egedal, J. (2020). Electron Temperature of the Solar Wind. *Proc. Natl. Acad. Sci. U.S.A.* 117, 9232–9240. doi:10.1073/pnas.1917905117

Borovsky, J. E., and Burkholder, B. L. (2020). On the Fourier Contribution of Strong Current Sheets to the High-Frequency Magnetic Power SpectralDensity of the Solar Wind. *J. Geophys. Res. Space Phys.* 125, e2019JA027307. doi:10.1029/2019JA027307

Borovsky, J. E. (2020e). Compression of the Heliospheric Magnetic Structure by Interplanetary Shocks: Is the Structure at 1 AU a Manifestation of Solar-Wind Turbulence or Is it Fossil Structure from the Sun? *Front. Astron. Space Sci.* 7, 582546. doi:10.3389/fspas.2020.582564

Borovsky, J. E. (2010b). Contribution of Strong Discontinuities to the Power Spectrum of the Solar Wind. *Phys. Rev. Lett.* 105, 111102. doi:10.1103/physrevlett.105.111102

Borovsky, J. E., and Denton, M. H. (2016). The Trailing Edges of High-Speed Streams at 1 AU. *J. Geophys. Res. Space Phys.* 121, 6107–6140. doi:10.1002/2016ja022863

Borovsky, J. E. (2006). Eddy Viscosity and Flow Properties of the Solar Wind: Co-rotating Interaction Regions, Coronal-Mass-Ejection Sheaths, and Solar-Wind/magnetosphere Coupling. *Phys. Plasmas* 13, 056505. doi:10.1063/1.2200308

Borovsky, J. E. (2021b). Exploring the Properties of the Electron Strahl at 1 AU as an Indicator of the Quality of the Magnetic Connection between the Earth and the Sun. *Front. Astron. Space Sci.* 8, 646443. doi:10.3389/fspas.2021.646443

Borovsky, J. E., Halekas, J. S., and Whittlesey, P. L. (2021). The Electron Structure of the Solar Wind. *Front. Astron. Space Sci.* 8, 69005. doi:10.3389/fspas.2021.690005

Borovsky, J. E. (2012). Looking for Evidence of Mixing in the Solar Wind from 0.31 to 0.98 AU. *J. Geophys. Res.* 117, A06107. doi:10.1029/2012ja017525

Borovsky, J. E. (2021c). Magnetospheric Plasma Systems Science and Solar Wind Plasma Systems Science: The Plasma-Wave Interactions of Multiple Particle Populations. *Front. Astron. Space Sci.* 8, 780321. doi:10.3389/fspas.2021.780321

Borovsky, J. E. (2020d). On the Motion of the Heliospheric Magnetic Structure through the Solar Wind Plasma. *J. Geophys. Res.* 125, e2019JA027377. doi:10.1029/2019ja027377

Borovsky, J. E. (2010a). On the Variations of the Solar-Wind Magnetic Field about the Parker-spiral Direction. *J. Geophys. Res.* 115, A09101. doi:10.1029/2009ja015040

Borovsky, J. E. (2020c). Plasma and Magnetic-Field Structure of the Solar Wind at Inertial-Range Scale Sizes Discerned from Statistical Examinations of the Time-Series Measurements. *Front. Astron. Space Sci.* 7, 20. doi:10.3389/fspas.2020.00020

Borovsky, J. E., and Podesta, J. J. (2015). Exploring the Effect of Current Sheet Thickness on the High-frequency Fourier Spectrum Breakpoint of the Solar Wind. *J. Geophys. Res. Space Phys.* 120, 9256–9268. doi:10.1002/2015ja021622

Borovsky, J. E. (2021a). Solar-Wind Structures that Are Not Destroyed by the Action of Solar-Wind Turbulence. *Front. Astron. Space Sci.* 8, 721350. doi:10.3389/fspas.2021.721350

Borovsky, J. E., and Steinberg, J. T. (2014). No Evidence for the Localized Heating of Solar Wind Protons at Intense Velocity Shear Zones. *J. Geophys. Res. Space Phys.* 119, 1455–1462. doi:10.1002/2013ja019746

Borovsky, J. E. (2008). The Flux-Tube Texture of the Solar Wind: Strands of the Magnetic Carpet at 1 AU? *J. Geophys. Res.* 113, A08110. doi:10.1029/2007ja012684

Borovsky, J. E. (2020b). The Magnetic Structure of the Solar Wind: Ionic Composition and the Electron Strahl. *Geophys. Res. Lett.* 47, e2019GL084586. doi:10.1029/2019GL084586

Borovsky, J. E. (2016). The Plasma Structure of Coronal Hole Solar Wind: Origins and Evolution. *J. Geophys. Res. Space Phys.* 121, 5055–5087. doi:10.1002/2016ja022686

Borovsky, J. E. (2020a). What Magnetospheric and Ionospheric Researchers Should Know about the Solar Wind. *J. Atmos. Solar-Terrestrial Phys.* 204, 105271. doi:10.1016/j.jastp.2020.105271

Bruno, R., Carbone, V., Veltri, P., Pietropaolo, E., and Bavassano, B. (2001). Identifying Intermittency Events in the Solar Wind. *Planet. Space Sci.* 49, 1201–1210. doi:10.1016/s0032-0633(01)00061-7

Burlaga, L. F. (1971). Hydromagnetic Waves and Discontinuities in the Solar Wind. *Space Sci. Rev.* 12, 600–657. doi:10.1007/bf00173345

Burlaga, L. F., and Ness, N. F. (1969). Tangential Discontinuities in the Solar Wind. *Sol. Phys.* 9, 467–477. doi:10.1007/bf02391672

Burton, M. E., Neugebauer, M., Crooker, N. U., von Steiger, R., and Smith, E. J. (1999). Identification of Trailing Edge Solar Wind Stream Interfaces: A Comparison of Ulysses Plasma and Composition Measurements. *J. Geophys. Res.* 104, 9925–9932. doi:10.1029/1999ja900049

Byhring, H. S. (2011). The Helium Abundance in Polar Coronal Holes and the Fast Solar Wind. *ApJ* 738, 172. doi:10.1088/0004-637x/738/2/172

Carlson, C. W., Curtis, D. W., Paschmann, G., and Michel, W. (1982). An Instrument for Rapidly Measuring Plasma Distribution Functions with High Resolution. *Adv. Space Res.* 2 (7), 67–70. doi:10.1016/0273-1177/(82)90151-X10.1016/0273-1177(82)90151-x

Chandrasekhar, S. (1961). *Hydrodynamic and Hydromagnetic Stability*. New York: Oxford University Press. Sect. 113.

Di Matteo, S., Viall, N. M., Kepko, L., Wallace, S., Arge, C. N., and MacNeice, P. (2019). Helios Observations of Quasiperiodic Density Structures in the Slow Solar Wind at 0.3, 0.4, and 0.6 AU. *JGR Space Phys.* 124, 837–860. doi:10.1029/2018ja026182

Feldman, W. C., Asbridge, J. R., Bame, S. J., Gary, S. P., Montgomery, M. D., and Zink, S. M. (1976). Evidence for the Regulation of Solar Wind Heat Flux at 1 AU. *J. Geophys. Res.* 81, 5207–5211. doi:10.1029/ja081i028p05207

Feldman, W. C., Asbridge, J. R., Bame, S. J., Montgomery, M. D., and Gary, S. P. (1975). Solar Wind Electrons. *J. Geophys. Res.* 80, 4181–4196. doi:10.1029/ja080i031p04181

Fu, H., Madjarska, M. S., Li, B., Xia, L., and Huang, Z. (2018). Helium Abundance and Speed Difference between Helium Ions and Protons in the Solar Wind from Coronal Holes, Active Regions, and Quiet Sun. *Mon. Not. R. Astron. Soc.* 478, 1884–1892. doi:10.1093/mnras/sty1211

Geiss, J., Gloeckler, G., and von Steiger, R. (1995). Origin of the Solar Wind from Composition Data. *Space Sci. Rev.* 72, 49–60. doi:10.1007/bf00768753

Gosling, J. T., de Koning, C. A., Skoug, R. M., Steinberg, J. T., and McComas, D. J. (2004a). Dispersionless Modulations in Low-Energy Solar Electron Bursts and Discontinuous Changes in the Solar Wind Electron Strahl. *J. Geophys. Res.* 109, A05102. doi:10.1029/2003ja010338

Gosling, J. T., Skoug, R. M., McComas, D. J., and Mazur, J. E. (2004b). Correlated Dispersionless Structure in Suprathermal Electrons and Solar Energetic Ions in the Solar Wind. *ApJ* 614, 412–419. doi:10.1086/423368

Greco, A., Chuychai, P., Matthaeus, W. H., Servidio, S., and Dmitruk, P. (2008). Intermittent MHD Structures and Classical Discontinuities. *Geophys. Res. Lett.* 35, L19111. doi:10.1029/2008gl035454

Greco, A., Matthaeus, W. H., Servidio, S., Chuychai, P., and Dmitruk, P. (2009). Statistical Analysis of Discontinuities in Solar Wind ACE Data and Comparison with Intermittent MHD Turbulence. *Astrophysical J.* 691, L111–L114. doi:10.1088/0004-637x/691/2/l111

Horbury, T. S., Burgess, D., Fränz, M., and Owen, C. J. (2001). Three Spacecraft Observations of Solar Wind Discontinuities. *Geophys. Res. Lett.* 28, 677–680. doi:10.1029/2000gl000121

Kasper, J. C., Lazarus, A. J., Steinberg, J. T., Ogilvie, K. W., and Szabo, A. (2006). Physics-based Tests to Identify the Accuracy of Solar Wind Ion Measurements: A Case Study with the Wind Faraday Cups. *J. Geophys. Res.* 111, A03105. doi:10.1029/2005ja011442

Kepko, L., Viall, N. M., Antiochos, S. K., Lepri, S. T., Kasper, J. C., and Weberg, M. (2016). Implications of L1 Observations for Slow Solar Wind Formation by Solar Reconnection. *Geophys. Res. Lett.* 43, 4089–4097. doi:10.1002/2016gl068607

Khabarova, O., Malandraki, O., malova, H., Kislov, R., Greco, A., Bruno, R., et al. (2021). Current Sheets, Plasmoids and Flux Ropes in the Heliosphere. *Space Sci. Rev.* 217, 38. doi:10.1007/s11214-021-00814-x

Khabarova, O., Zank, G., Li, G., Le Roux, J. A., Webb, G. M., Dosch, A., et al. (2015). Small-scale Magnetic Islands in the Solar Wind and Their Role in Particle Acceleration. I. Dynamics of Magnetic Islands Near the Heliospheric Current Sheet. *Astrophys. J.* 808, 181. doi:10.1088/0004-637X/808/2/181

Khabarova, O., Zank, G., Li, G., MalandrakiLe Roux, O. E. J. A., and Webb, G. M. (2016). Small-scale Magnetic Islands in the Solar Wind and Their Role in Particle Acceleration. II. Particle Energization inside Magnetically Confined Cavities. *Astrophys. J.* 827, 122. doi:10.3847/0004-637X/827/2/122

Khabarova, O., Zharkova, V., Xia, Q., and Malandraki, O. E. (2020). Counterstreaming Strahls and Heat Flux Dropouts as Possible Signatures of Local Particle Acceleration in the Solar Wind. *Astrophysical J. Lett.* 894, L12. doi:10.3847/2041-8213/ab8cb8

Knetter, T., Neubauer, F. M., Horbury, T., and Balogh, A. (2003). Discontinuity Observations with Cluster. *Adv. Space Res.* 32 (4), 543–548. doi:10.1016/s0273-1177(03)00335-1

Knetter, T., Neubauer, F. M., Horbury, T., and Balogh, A. (2004). Four-point Discontinuity Observations Using Cluster Magnetic Field Data: A Statistical Survey. *J. Geophys. Res.* 109, A06102. doi:10.1029/2003ja010099

Komar, C. M., and Cassak, P. A. (2016). The Local Dayside Reconnection Rate for Oblique Interplanetary Magnetic Fields. *J. Geophys. Res. Space Phys.* 121, 5105–5120. doi:10.1002/2016ja022530

Lapenta, G., and Brackbill, J. U. (1996). Contact Discontinuities in Collisionless Plasmas: A Comparison of Hybrid and Kinetic Simulations. *Geophys. Res. Lett.* 23, 1713–1716. doi:10.1029/96gl01845

Lazarian, A., Eyink, G. L., Jafari, A., Kowal, G., Li, H., Xu, S., et al. (2020). 3D Turbulent Reconnection: Theory, Tests, and Astrophysical Implications. *Phys. Plasmas* 27, 012305. doi:10.1063/1.5110603

Lazarian, A., and Vishniac, E. T. (1999). Reconnection in a Weakly Stochastic Field. *ApJ* 517, 700–718. doi:10.1086/307233

Lepping, R. P., and Behannon, K. W. (1986). Magnetic Field Directional Discontinuities: Characteristics between 0.46 and 1.0 AU. *J. Geophys. Res.* 91, 8725. doi:10.1029/ja091ia08p08725

Li, G., and Qin, G. (2011). A Solar Wind Model with Current Sheets. *Asp. Conf. Ser.* 444, 117.

Livi, R., Larson, D. E., Kasper, J. C., Abiad, R., Case, A. W., Klein, K. G., et al. (2021). The Solar Probe ANalyzer -Ions on Parker Solar Probe. *Earth Space Sci.* doi:10.1002/essoar.10508651.1

MacBride, B. T., Smith, C. W., and Forman, M. A. (2008). The Turbulent Cascade at 1 AU: Energy Transfer and the Third-Order Scaling for MHD. *Astrophysical J.* 679, 1644–1660. doi:10.1086/529575

Maksimovic, M., Zouganelis, I., Chaufray, J. Y., Issautier, K., Scime, E. E., Littleton, J. E., et al. (2005). Radial Evolution of the Electron Distribution Functions in the Fast Solar Wind between 0.3 and 1.5 AU. *J. Geophys. Res.* 110, A09104. doi:10.1029/2005ja011119

Malandraki, O., Khabarova, O., Bruno, R., Zank, G. P., Li, G., Jackson, B., et al. (2019). Current Sheets, Magnetic Islands, and Associated Particle Acceleration in the Solar Wind as Observed by Ulysses Near the Ecliptic Plane. *ApJ* 881, 116. doi:10.3847/1538-4357/ab289a

McComas, D. J., Bame, S. J., Barker, P., Feldman, W. C., Phillips, J. L., Riley, P., et al. (1998). Solar Wind Electron Proton Alpha Monitor (SWEPAM) for the Advanced Composition Explorer. *Space Sci. Rev.* 86, 563–612. doi:10.1007/978-94-011-4762-0_20

McCracken, K. G., and Ness, N. F. (1966). The Collimation of Cosmic Rays by the Interplanetary Magnetic Field. *J. Geophys. Res.* 71, 3315–3318. doi:10.1029/jz071i013p03315

McIntosh, S. W., Kiefer, K. K., Leamon, R. J., Kasper, J. C., and Stevens, M. L. (2011). Solar Cycle Variations in the Elemental Abundance of Helium and Fractionation of Iron in the Fast Solar Wind: Indicators of an Evolving Energetic Release of Mass from the Lower Solar Atmosphere. *ApJ* 740, L23. doi:10.1088/2041-8205/740/1/l23

Michel, F. C. (1967). Model of Solar Wind Structure. *J. Geophys. Res.* 72, 1917–1932. doi:10.1029/jz072i007p01917

Moncuquet, M., Meyer-Vernet, N., Issautier, K., Pulupa, M., Bonnell, J. W., Bale, S. D., et al. (2020). First *In Situ* Measurements of Electron Density and Temperature from Quasi-Thermal Noise Spectroscopy with Parker Solar Probe/FIELDS. *Astrophysical J. Suppl. Ser.* 246, 44. doi:10.3847/1538-4365/ab5a84

Nemecek, Z., Durovcova, T., Safrankova, J., Nemec, F., Matteini, L., Stansvy, D., et al. (2020). What Is the Solar Wind Frame of Reference? *Astrophys. J.* 889, 163. doi:10.3847/1538-4357/ab65f7

Neugebauer, M., and Giacalone, J. (2010). Progress in the Study of Interplanetary Discontinuities. *AIP Conf. Proc.* 1216, 194. doi:10.1063/1.3395834

Neugebauer, M., Clay, D. R., Goldstein, B. E., Tsurutani, B. T., and Zwickl, R. D. (1984). A Reexamination of Rotational and Tangential Discontinuities in the Solar Wind. *J. Geophys. Res.* 89, 5395. doi:10.1029/ja089ia07p05395

Neugebauer, M. (2006). Comment on the Abundances of Rotational and Tangential Discontinuities in the Solar Wind. *J. Geophys. Res.* 111, A04103. doi:10.1029/2005ja011497

Neugebauer, M. (2012). Evidence for Polar X-Ray Jets as Sources of Microstream Peaks in the Solar Wind. *ApJ* 750, 50. doi:10.1088/0004-637x/750/1/50

Neugebauer, M., and Giacalone, J. (2015). Energetic Particles, Tangential Discontinuities, and Solar Flux Tubes. *J. Geophys. Res. Space Phys.* 120, 8281–8287. doi:10.1002/2015ja021632

Neugebauer, M., Goldstein, B. E., Winterhalter, D., Smith, E. J., MacDowall, R. J., and Gary, S. P. (2001). Ion Distributions in Large Magnetic Holes in the Fast Solar Wind. *J. Geophys. Res.* 106, 5635–5648. doi:10.1029/2000ja000331

Ogilvie, K. W., Chornay, D. J., Fritzenreiter, R. J., Hunsaker, F., Keller, J., Lobell, J., et al. (1995). SWE, a Comprehensive Plasma Instrument for the WIND Spacecraft. *Space Sci. Rev.* 71, 55–77. doi:10.1007/bf00751326

Owen, C. J., Bruno, R., Livi, S., Louarn, P., Al Janabi, K., Allrgrini, F., et al. (2020). The Solar Orbiter Solar Wind Analyzer (SWA) Suite. *Astron. Astrophys.* 642, A16.

Owens, M. J., Wicks, R. T., and Horbury, T. S. (2011). Magnetic Discontinuities in the Near-Earth Solar Wind: Evidence of In-Transit Turbulence or Remnants of Coronal Structure? *Sol. Phys.* 269, 411–420. doi:10.1007/s11207-010-9695-0

Parker, E. N. (1979). *Cosmical Magnetic Fields*. Oxford: Clarendon Press. Sect. 7.2.

Paschmann, G., Haaland, S., Sonnerup, B., and Knetter, T. (2013). Discontinuities and Alfvénic Fluctuations in the Solar Wind. *Ann. Geophys.* 31, 871–887. doi:10.5194/angeo-31-871-2013

Pecora, F., Greco, A., Hu, Q., Servidio, S., Chasapis, A. G., and Matthaeus, W. H. (2019). Single-spacecraft Identification of Flux Tubes and Current Sheets in the Solar Wind. *ApJ* 881, L11. doi:10.3847/2041-8213/ab32d9

Pilipp, W. G., Miggenrieder, H., Montgomery, M. D., Mühlhäuser, K.-H., Rosenbauer, H., and Schwenn, R. (1987). Characteristics of Electron Velocity Distribution Functions in the Solar Wind Derived from the Helios Plasma Experiment. *J. Geophys. Res.* 92, 1075. doi:10.1029/ja092ia02p01075

Podesta, J. J., and Borovsky, J. E. (2016). Relationship between the Durations of Jumps in Solar Wind Time Series and the Frequency of the Spectral Break. *J. Geophys. Res. Space Phys.* 121, 1817–1838. doi:10.1002/2015ja021987

Podesta, J. J., Borovsky, J. E., Steinberg, J. T., Skoug, R., Birn, J., Gary, S. P., et al. (2012). "High-resolution, High Accuracy Plasma, Electric, and Magntic Field Measurements for Discovery of Kinetic Plasma Structures and Processes in the Evolving Solar Wind," in *Solar and Space Physics: A Science for a Technological Society* (Washington, D. C: National Academies Press). 433. paper 222.

Podesta, J. J., Forman, M. A., Smith, C. W., Elton, D. C., Malécot, Y., and Gagne, Y. (2009). Accurate Estimation of Third-Order Moments from Turbulence Measurements. *Nonlin. Process. Geophys.* 16, 99–110. doi:10.5194/npg-16-99-2009

Pollock, C., Moore, T., Jacques, A., Burch, J., Gliese, U., Saito, Y., et al. (2016). Fast Plasma Investigation for Magnetospheric Multiscale. *Space Sci. Rev.* 199, 331–406. doi:10.1007/s11214-016-0245-4

Rakowski, C. E., and Laming, J. M. (2012). On the Origin of the Slow Speed Solar Wind: Helium Abundance Variations. *ApJ* 754, 65. doi:10.1088/0004-637x/754/1/65

Riazantseva, M. O., Khabarova, O. V., Zastenker, G. N., and Richardson, J. D. (2005a). Sharp Boundaries of Solar Wind Plasma Structures and an Analysis of Their Pressure Balance. *Cosm. Res.* 43 (3), 157–164. doi:10.1007/s10604-005-0030-8

Riazantseva, M. O., Zastenker, G. N., Richardson, J. D., and Eiges, P. E. (2005c). Sharp Boundaries of Small- and Middle-Scale Solar Wind Structures. *J. Geophys. Res.* 110, A12110. doi:10.1029/2005ja011307

Riazantseva, M. O., Zastenker, G. N., and Richardson, J. D. (2005b). The Characteristics of Sharp (Small-scale) Boundaries of Solar Wind Plasma and Magnetic Field Structures. *Adv. Space Res.* 35, 2147–2151. doi:10.1016/j.asr.2004.12.011

Russell, C. T., Anderson, B. J., Baumjohann, W., Bromund, K. R., Dearborn, D., Fischer, D., et al. (2016). The Magnetospheric Multiscale Magnetometers. *Space Sci. Rev.* 199, 189–256. doi:10.1007/978-94-024-0861-4_8

Safrankova, J., Memecek, Z., Cagas, P., Pavlu, J., Zastenker, G. N., Riazantseva, M. O., et al. (2013). Short-scale Variations of the Solar Wind Helium Abundance. *Astrophys. J.* 778, 25. doi:10.1088/0004-637X/778/1/25

Schindler, K., and Birn, J. (2002). Models of Two-Dimensional Embedded Thin Current Sheets from Vlasov Theory. *J. Geophys. Res.* 107, 1193. doi:10.1029/2001ja000304

Schindler, K., and Hesse, M. (2010). Conditions for the Formation of Nongyrotropic Current Sheets in Slowly Evolving Plasmas. *Phys. Plasmas* 17, 082103. doi:10.1063/1.3464198

Schindler, K., and Hesse, M. (2008). Formation of Thin Bifurcated Current Sheets by Quasisteady Compression. *Phys. Plasmas* 15, 042902. doi:10.1063/1.2907359

Sheeley, N. R., and Rouillard, A. P. (2010). Tracking Streamer Blobs into the Heliosphere. *ApJ* 715, 300–309. doi:10.1088/0004-637x/715/1/300

Simunac, K. D. C., Galvin, A. B., Farrugia, C. J., Kistler, L. M., Kucharek, H., Lavraud, B., et al. (2012). The Heliospheric Plasma Sheet Observed *In Situ* by Three Spacecraft over Four Solar Rotations. *Sol. Phys.* 281, 423. doi:10.1007/s11207-012-0156-9

Siscoe, G. L., Davis, L., Coleman, P. J., Smith, E. J., and Jones, D. E. (1968). Power Spectra and Discontinuities of the Interplanetary Magnetic Field: Mariner 4. *J. Geophys. Res.* 73, 61–82. doi:10.1029/ja073i001p00061

Smith, C. W., Stawarz, J. E., Vasquez, B. J., Forman, M. A., and MacBride, B. T. (2009). Turbulent Cascade at 1 AU in High Cross-Helicity Flows. *Phys. Rev. Lett.* 103, 201101. doi:10.1103/physrevlett.103.201101

Smith, E. J. (2001). The Heliospheric Current Sheet. *J. Geophys. Res.* 106, 15819–15831. doi:10.1029/2000ja000120

Söding, A., Neubauer, F. M., Tsurutani, B. T., Ness, N. F., and Lepping, R. P. (2001). Radial and Latitudinal Dependencies of Discontinuities in the Solar Wind between 0.3 and 19 AU and −80° and +10°. *Ann. Geophys.* 19, 667–680. doi:10.5194/angeo-19-667-2001

Sonnerup, B. U. O. (2022). Reflections by Bengt Ulf Osten Sonnerup. *Front. Astron. Space Sci.*, 943401. submitted to.

Sorriso-Valvo, L., Marino, R., Carbone, V., Noullez, A., Lepreti, F., Veltri, P., et al. (2007). Observation of Inertial Energy Cascade in Interplanetary Space Plasma. *Phys. Rev. Lett.* 99, 115001. doi:10.1103/physrevlett.99.115001

Stverak, S., Maksimovic, M., Travnicek, P. M., Marsch, E., Fazakerley, A. N., and Scime, E. E. (2009). Radial Evolution of Nonthermal Electron Populations in the Low-Latitude Solar Wind: Helios, Cluster, and Ulysses Observations. *J. Geophys. Res.* 114, A04104. doi:10.1029/2008JA013883

Tamano, T. (1991). A Plasmoid Model for the Solar Wind. *Sol. Phys.* 134, 187–201. doi:10.1007/bf00148747

Telloni, D., Perri, S., Carbone, V., and Bruno, R. (2016). Selective Decay and Dynamic Alignment in the MHD Turbulence: the Role of the Rugged Invariants. *AIP Conf. Proc.* 1720, 040015. doi:10.1063/1.4943826

Tenerani, A., Velli, M., Matteini, L., Reville, V., Shi, C., Bale, S. D., et al. (2020). Magnetic Field Kinks and Folds in the Solar Wind. *Astrophys. J. Suppl. Ser.* 246, 3. doi:10.3847/1538-4365/ab53e1

Trenchi, L., Bruno, R., Telloni, D., D'amicis, R., Marcucci, M. F., Zurbuchen, T. H., et al. (2013). Solar Energetic Particle Modulations Associated with Coherent Magnetic Structures. *ApJ* 770, 11. doi:10.1088/0004-637x/770/1/11

Tsurutani, B. T., and Ho, C. M. (1999). A Review of Discontinuities and Alfvén Waves in Interplanetary Space: Ulysses Results. *Rev. Geophys.* 37, 517–541. doi:10.1029/1999rg900010

Tu, C.-Y., and Marsch, E. (1993). A Model of Solar Wind Fluctuations with Two Components: Alfvén Waves and Convective Structures. *J. Geophys. Res.* 98, 1257–1276. doi:10.1029/92ja01947

Tu, C. Y., Wang, X., He, J., Marsch, E., and Wang, L. (2016). Two Cases of Convecting Structure in the Slow Solar Wind Turbulence. *AIP Conf. Proc.* 1720, 040017. doi:10.1063/1.4943828

Turner, J. M., Burlaga, L. F., Ness, N. F., and Lemaire, J. F. (1977). Magnetic Holes in the Solar Wind. *J. Geophys. Res.* 82, 1921–1924. doi:10.1029/ja082i013p01921

Turner, J. M., and Siscoe, G. L. (1971). Orientations of 'rotational' and 'tangential' Discontinuities in the Solar Wind. *J. Geophys. Res.* 76, 1816–1822. doi:10.1029/ja076i007p01816

Vasquez, B. J., Abramenko, V. I., Haggerty, D. K., and Smith, C. W. (2007). Numerous Small Magnetic Field Discontinuities of Bartels Rotation 2286 and the Potential Role of Alfvénic Turbulence. *J. Geophys. Res.* 112, A11102. doi:10.1029/2007ja012504

Vasquez, B. J., and Hollweg, J. V. (1999). Formation of Pressure-Balanced Structures and Fast Waves from Nonlinear Alfvén Waves. *J. Geophys. Res.* 104, 4681–4696. doi:10.1029/1998ja900090

Vasquez, B. J., Markovskii, S. A., and Smith, C. W. (2013). Solar Wind Magnetic Field Discontinuities and Turbulence Generated Current Layers. *AIP Conf. Proc.* 1539, 291. doi:10.1063/1.4811045

Viall, N. M., and Borovsky, J. E. (2020). Nine Outstanding Questions of Solar Wind Physics. *J. Geophys Res. Space Phys.* 125, e2018JA026005. doi:10.1029/2018JA026005

Viall, N. M., Spence, H. E., Vourlidas, A., and Howard, R. (2010). Examining Periodic Solar-Wind Density Structures Observed in the SECCHI Heliospheric Imagers. *Sol. Phys.* 267, 175–202. doi:10.1007/s11207-010-9633-1

Viall, N. M., and Vourlidas, A. (2015). Periodic Density Structures and the Origin of the Slow Solar Wind. *ApJ* 807, 176. doi:10.1088/0004-637x/807/2/176

Vocks, C., Salem, C., Lin, R. P., and Mann, G. (2005). Electron Halo and Strahl Formation in the Solar Wind by Resonant Interaction with Whistler Waves. *Astrophysical J.* 627, 540–549. doi:10.1086/430119

von Steiger, R., Fisk, L. A., Gloeckler, G., Schwadron, N. A., and Zurbuchen, T. H. (1999). Composition Variations in Fast Solar Wind Streams. *AIP Conf. Proc.* 471, 143. doi:10.1063/1.58791

von Steiger, R., Zurbuchen, T. H., Geiss, J., Gloeckler, G., Fisk, L. A., and Schwadron, N. A. (2001). The 3-D Heliosphere from the ULYSSES and ACE Solar Wind Ion Composition Experiments. *Space Sci. Rev.* 97, 123–127. doi:10.1007/978-94-017-3230-7_20

Wang, X., Tu, C. Y., He, J. S., Wang, L. H., Yao, S., and Zhang, L. (2018). Possible Noise Nature of Elsässer Variable Z − in Highly Alfvénic Solar Wind Fluctuations. *JGR Space Phys.* 123, 57–67. doi:10.1002/2017ja024743

Wang, Y.-M. (2016). Role of the Coronal Alfvén Speed in Modulating the Solar-Wind Helium Abundance. *Astrophysical J. Lett.* 833, L21. doi:10.3847/2041-8213/833/2/l21

Wang, Y.-M., Sheeley, N. R., Howard, R. A., Rich, N. B., and Lamy, P. L. (1999). Streamer Disconnection Events Observed with the LASCO Coronagraph. *Geophys. Res. Lett.* 26, 1349–1352. doi:10.1029/1999gl900177

Wang, Y. M. (2008). Relating the Solar Wind Helium Abundance to the Coronal Magnetic Field. *Astrophysical J.* 683, 499–509. doi:10.1086/589766

Whittlesey, P. L., Larson, D. E., Kasper, J. C., Halekas, J., Abatcha, M., Abiad, R., et al. (2020). The Solar Probe ANalyzers-Electrons on the Parker Solar Probe. *ApJS* 246, 74. doi:10.3847/1538-4365/ab7370

Wimmer-Schweingruber, R. F., von Steiger, R., and Paerli, R. (1997). Solar Wind Stream Interfaces in Corotating Interaction Regions: SWICS/Ulysses Results. *J. Geophys. Res.* 102, 17407–17417. doi:10.1029/97ja00951

Winterhalter, D., Smith, E. J., Neugebauer, M., Goldstein, B. E., and Tsurutani, B. T. (2000). The Latitudinal Distribution of Solar Wind Magnetic Holes. *Geophys. Res. Lett.* 27, 1615–1618. doi:10.1029/1999gl003717

Young, D. T., Bame, S. J., Thomsen, M. F., Martin, R. H., Burch, J. L., Marshall, J. A., et al. (1988). 2π-radian Field-of-view Toroidal Electrostatic Analyzer. *Rev. Sci. Instrum.* 59, 743–751. doi:10.1063/1.1139821

Zastenker, G. N., Safrankova, J., Nemecek, Z., Prech, L., Cermak, I., Vaverka, I., et al. (2013). Fast Measurements of Parameters of the Solar Wind Using the BMSW Instrument. *Cosm. Res.* 51, 78–89. doi:10.1134/s0010952513020081

Zelenyi, L. M., Malova, H. V., Artemyev, A. V., Popov, V. Y., and Petrukovich, A. A. (2011). Thin Current Sheets in Collisionless Plasma: Equilibrium Structure, Plasma Instabilities, and Particle Acceleration. *Plasma Phys. Rep.* 37, 118–160. doi:10.1134/s1063780x1102005x

Zelenyi, L. M., Malova, K. V., Popov, V. Y., Grigorenko, E. E., and Büchner, J. (2021). Albert Galeev: The Problem of Metastability and Explosive Reconnection. *Plasma Phys. Rep.* 47, 857–877. doi:10.1134/s1063780x21090075

Zhang, T. L., Russell, C. T., Zambelli, W., Vörös, Z., WangCao, C. J. B., Cao, J. B., et al. (2008). Behavior of Current Sheets at Directional Magnetic Discontinuities in the Solar Wind at 0.72 AU. *Geophys. Res. Lett.* 35, L24102. doi:10.1029/2008gl036120

Zhao, L., Zurbuchen, T. H., and Fisk, L. A. (2009). Global Distribution of the Solar Wind during Solar Cycle 23: ACE Observations. *Geophys. Res. Lett.* 36, L14104. doi:10.1029/2009gl039181

Zhdankin, V., Boldyrev, S., Mason, J., and Perez, J. C. (2012). Magnetic Discontinuities in Magnetohydrodynamic Turbulence and in the Solar Wind. *Phys. Rev. Lett.* 108, 175004. doi:10.1103/physrevlett.108.175004

Zurbuchen, T. H., Hefti, S., Fisk, L. A., Gloeckler, G., and von Steiger, R. (1999). The Transition between Fast and Slow Solar Wind from Composition Data. *Space Sci. Rev.* 87, 353–356. doi:10.1007/978-94-015-9167-6_62

Conflict of Interest: The authors declare that the research was conducted in the absence of any commercial or financial relationships that could be construed as a potential conflict of interest.

Publisher's Note: All claims expressed in this article are solely those of the authors and do not necessarily represent those of their affiliated organizations, or those of the publisher, the editors and the reviewers. Any product that may be evaluated in this article, or claim that may be made by its manufacturer, is not guaranteed or endorsed by the publisher.

APPENDIX: A FALSE ARGUMENT

As stated in **Section 3**, for particle-counting instruments the combination of lower noise and higher time resolution is difficult, with poorer counting statistics being a consequence of shorter measuring intervals. For the solar wind there is an argument that presents a further difficulty, concluding that higher-frequency fluctuations in the solar wind have smaller amplitudes, making the higher-time-resolution measurements need even more accuracy and lower noise. But that "extra difficulty" argument may be wrong. Looking at a Fourier power spectral density of the solar wind it is very noticeable that the power amplitude decrease with increasing frequency f. A natural interpretation of this is that higher-frequency fluctuations in the solar wind have smaller amplitudes (hence the extra measurement difficulty). In terms of the needed accuracy of high-frequency solar-wind measurements, that argument is made in Podesta et al. (2012). That interpretation of the power spectral density would be correct if the solar-wind time series was comprised of randomly-phased fluctuations: however, the solar-wind time series is highly intermittent and is not comprised of random-phase fluctuations. The counter example to the argument comes from an examination of the high-frequency breakpoint in the solar-wind magnetic power spectral density at a breakpoint frequency of $f_{break} \sim 0.5$ Hz: analysis shows that the power spectral density break at f_{break} is owed to the temporal thicknesses τ_{cs} of strong current sheets in the solar-wind time series, thicknesses $\tau_{cs} \sim 1/f_{break}$ (Borovsky and Podesta, 2015; Podesta and Borovsky, 2016). Instead of the solar-wind time series containing constant low-amplitude random-phased fluctuations with frequency f_{break}, a spacecraft occasionally crosses a large-amplitude current-sheet signal with a transition time of $1/f_{break}$. The measured signals of interest at high frequency need not be of small amplitude, they can be of large amplitude and the "extra difficulty" requiring extra accuracy when measuring signals at high time resolution may not be real.

In conclusion, to study jump properties across current sheets the "even higher accuracy and lower noise" is probably not necessary. However, for survey purposes the exploration of small signals with high time resolution is still desirable, if possible.

frontiers | Frontiers in Astronomy and Space Sciences

TYPE Methods
PUBLISHED 15 July 2022
DOI 10.3389/fspas.2022.919798

OPEN ACCESS

EDITED BY
Luca Sorriso-Valvo,
Institute for Space Physics (Uppsala), Sweden

REVIEWED BY
Anders Eriksson,
Institute for Space Physics (Uppsala), Sweden
Anton Artemyev,
University of California, Los Angeles, United States

*CORRESPONDENCE
Solène Lejosne,
solene@berkeley.edu

SPECIALTY SECTION
This article was submitted to Space Physics,
a section of the journal
Frontiers in Astronomy and Space Sciences

RECEIVED 13 April 2022
ACCEPTED 27 June 2022
PUBLISHED 15 July 2022

CITATION
Lejosne S, Auslander DM, Bonnell JW, Klumpar DM, Mozer FS, Pankow DH and Sample JG (2022), Grotifer: A new electric field instrument design to address the need for highly accurate three-component electric field measurements.
Front. Astron. Space Sci. 9:919798.
doi: 10.3389/fspas.2022.919798

Grotifer: A new electric field instrument design to address the need for highly accurate three-component electric field measurements

Solène Lejosne[1]*, David M. Auslander[2], John W. Bonnell[1], David M. Klumpar[3], Forrest S. Mozer[1], David H. Pankow[1] and John G. Sample[3]

[1]Space Sciences Laboratory, University of California, Berkeley, Berkeley, CA, United States, [2]Mechanical Engineering Department, University of California, Berkeley, Berkeley, CA, United States, [3]Space Science and Engineering Laboratory, Department of Physics, Montana State University, Bozeman, MT, United States

Accurate knowledge of the full, three-dimensional electric field vector is of fundamental importance in understanding electrodynamics of a vast variety of space plasmas. However, heliophysics research still lacks access to the reliable parallel electric field measurements required to close many significant science questions. This uncertainty represents a significant barrier to progress in the field. The only way to close this major observational gap is a profound change in electric field instrument design. A new electric field instrument called Grotifer is now being designed to address the need for highly accurate three-dimensional electric field measurements while enabling lower cost missions and constellation missions in deep space. Grotifer (Giant rotifer) is a reference to the rotifer, also known as the "wheel animalcule." Similarly, Grotifer consists of mounting detectors on two rotating plates, orthogonal to each other, on a non-rotating central body. The two rotating plates provide continuous high-accuracy three-dimensional measurements of both electric fields and magnetic fields. The Grotifer design leverages more than 50 years of expertise in delivering highly accurate spin plane electric field measurements, while overcoming inaccuracies generated by spin axis electric field measurements. Our current efforts focus on designing Grotifer as a SmallSat (27U CubeSat). That said, Grotifer could also become part of the payload on a much larger platform. In the future, one could imagine fleets of Grotifers studying electrodynamics at many points, facilitating differentiation between spatial and temporal dynamics. Plasma detectors could also be added to the rotating plates to cover the full phase space better than is done on spinning spacecraft, leading to more complete correlation studies of the fields and plasmas.

KEYWORDS

electric fields, double probes, parallel electric field, instrument design, CubeSat

1 Motivation

Complete and accurate understanding of the electrodynamics of space plasmas requires a complete and accurate measurement of the three-dimensional electric and magnetic fields, as well as the velocity distribution functions of the charged particles that interact with those fields. While one can often infer the presence and magnitude of poorly measured components of the electromagnetic fields, such inference is model-dependent and can obscure the true physics that are active in a given region or phenomenon. In this paper, we describe the current state of the art in three-dimensional electric field measurements and make the case that current designs and methods are inadequate to achieve the accuracies required to solve the remaining fundamental questions of space plasma electrodynamics. We then describe a new design for electric field measurements, Grotifer, which easily addresses the current issues, and represents a path forward towards resolving these questions.

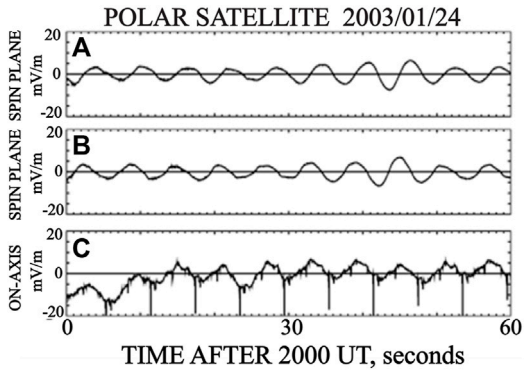

FIGURE 1
(A,B) Spin plane and **(C)** Spin axis E-field components measured by Polar. While the signal in the spin plane corresponds to a geophysical signal, the signal along the spin axis presents a large error, leading to a large uncertainty in the 3D E-field measurement.

1.1 Current electric field instrument design limits measurement accuracy

Electric field (E-field) measurements in the heliosphere are usually made on spinning spacecraft equipped with two disparate types of double probe antennas: 1) long wire booms in the spin plane, and 2) ~10 times shorter rigid booms along the spin axis. These designs, with current-biased antennas, were invented and first flown on a sounding rocket 55 years ago (Mozer and Bruston, 1967). Since then, this detector design has flown on many missions, either with or without a rigid pair of booms along the spin axis, such as: S3-3 (Mozer et al., 1977), ISEE-1 (Mozer et al., 1978), CRRES (Wygant et al., 1992), Polar (Harvey et al., 1995), FAST (Ergun R. et al., 2001), the four Cluster spacecraft (Gustafsson et al., 1997), the five THEMIS satellites (Bonnell et al., 2009), the two Van Allen Probes (Wygant et al., 2013), and the four MMS satellites (Ergun et al., 2016a; Lindqvist et al., 2016).

On such systems, the potential difference (signal + noise) is divided by the boom length to produce a resultant E-field. Because the spacecraft-associated errors are larger nearer the spacecraft, the spin plane components of the E-field are well measured while the spin axis component is either not measured or poorly measured. This asymmetry in measurement quality is also due to the fact that measuring electric fields using spinning antennas rather than rigid booms presents additional advantages such as the possibility to use thin wire booms, thereby minimizing the detrimental aspect of support structures, and the possibility to remove DC offsets in the electronics via spin fits. As a result, the accuracy of 2D E-field measurements in the spin plane is routinely better than the larger of ±1% or a fraction of a mV/m (Mozer et al., 1978; Gustafsson et al., 2001; Mozer, 2016). On the other hand, the short axial antennas see offsets 1 to 2 orders of magnitude larger than the relevant field strengths (several to tens of mV/m). A similar situation exists for magnetic field (B-field) measurements, where stray B-fields from the spacecraft (~10 nT or larger) create offsets and noise that are larger nearer the spacecraft.

An example of the failure to make useful E-field measurements along the spin axis is provided in Figure 1, where 60 s of E-field components measured by the Polar satellite are displayed. The top two panels (Figures 1A,B) give the spin plane measurements of a 5 mV/m DC E-field, producing a sinusoidal signal at the satellite spin rate. The bottom plot (Figure 1C) presents the spin axis data: It should be a DC signal having no power at the spin frequency, yet spin dependent variations of the spacecraft potential are felt by the short on-axis sensors as different elements of the spacecraft rotate in and out of sunlight. Due to the non-rotating short antennas and spacecraft generated electrical signals, there is no useful data in this component of the measurement.

An example of the current state of the art is provided in Figure 2 (Adapted from (Øieroset et al., 2016)). It displays the estimated DC uncertainty in the parallel E-field measured by MMS during a 9 s crossing of the magnetopause reconnection region. The estimated error in the parallel E-field measurement is a data product of MMS E-field data. Figure 2 shows that the estimated DC uncertainty in the parallel E-field (in green) is usually greater than its measured value. This significant uncertainty in the parallel E-field restricts the analysis of the associated electrodynamics to the largest-amplitude events.

Because of these limitations, no existing instrument is capable of measuring all three components of the DC and low

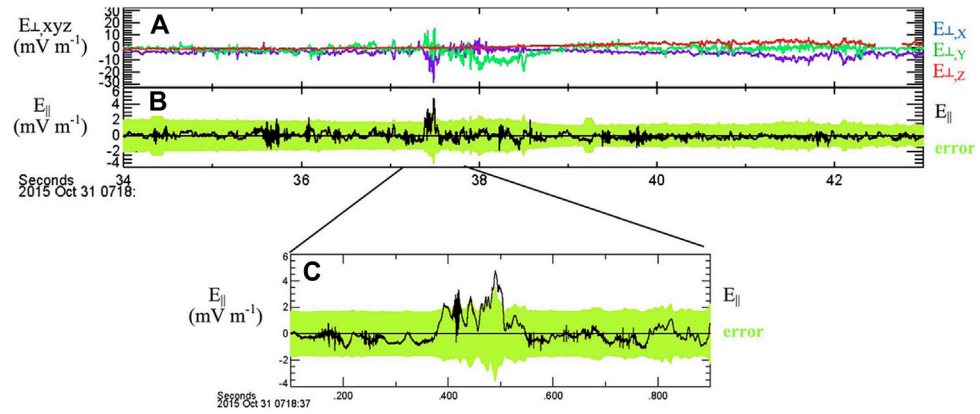

FIGURE 2
MMS **(A)** perpendicular E-field, **(B)** parallel E-field **(C)** zoom-in. The estimated DC uncertainty in the parallel E-field (in green) is usually greater than its measured value. Adapted from (Øieroset et al., 2016).

frequency E-field throughout the heliosphere with sufficient accuracy to determine the smallest and most consequential component: the E-field component parallel to the background B-field.

1.2 The closure of many significant science questions from various heliophysics research areas is hampered by the lack of accurate 3D E-Fields

Parallel E-fields exist in a multitude of plasma regimes in the heliosphere. These regions include such important loci of plasma acceleration and heating as reconnection sites (e.g., Egedal et al., 2012; Argall et al., 2015; Fox et al., 2018; Phan et al., 2018; Wilder et al., 2018), shocks (e.g., Goodrich and Scudder, 1984; Bale and Mozer, 2007; Mozer and Sundkvist, 2013; Schwartz et al., 2021), the auroral acceleration region (e.g., Mozer and Fahleson, 1970; Knight, 1973; Mozer et al., 1977; Gorney et al., 1985; Hultqvist and Lundin, 1987; Koskinen et al., 1996; Ergun R. E. et al., 2001; Andersson, 2002; Williams et al., 2006; Vedin and Ronnmark, 2007), the magnetosphere (e.g., Stark et al., 2011; Kropotkin, 2018; Arnold et al., 2019), the solar wind and corona (e.g., Hesse et al., 2005, Halekas et al., 2012, Mozer and Chen, 2013). Parallel E-fields have been observed at Earth and at other planets, including in the ionosphere of Mars (e.g., Dubinin et al., 2008; Akbari et al., 2019), and in the Jovian magnetosphere (e.g., Ergun et al., 2009; Underwood, 2017). They have been measured in standing waves (e.g., Damiano et al., 2019), in Alfvén waves and turbulence (e.g., Rankin et al., 1999; Ergun et al., 2005; Bian et al., 2010; Chaston, 2021), and in time domain structures (e.g, Mozer et al., 2015). Because parallel E-fields are essential components of the electrodynamics in all these regions, their measurement is required for understanding the acceleration and heating of the plasma that occupies these regions and that plays a significant role in the coupling of momentum and transport of mass and energy between and within the heliosphere, magnetosphere and ionosphere. This demonstrates the urgent need to accurately measure the three-dimensional (3D) E-field that is vital to a complete understanding of plasma dynamics. Instances of science questions that illustrate the need for a profound change in E-field instrument design are provided in the following.

1.2.1 Shock studies—Terrestrial bow shock, interplanetary shocks

1. Do quasi-DC fields or fluctuations dominate the electrodynamics of energy conversion in shock acceleration, reflection, and heating of electrons and ions?
2. Do the two sorts of processes produce significant quantitative or qualitative differences in energy partition?
3. Under what conditions does each mechanism dominate?

Recent studies utilizing MMS have begun to address these questions, but they have also suffered from significant uncertainties in the cross-calibration of 3D E-fields (e.g., Mozer and Sundkvist, 2013; Mozer and Sundkvist, 2014; Schwartz, 2014; Goodrich et al., 2018; Cohen et al., 2019; Hanson et al., 2019; Schwartz et al., 2021).

1.2.2 Reconnection studies—Terrestrial magnetopause

1. What is the partition of energy conversion between processes that are perpendicular and parallel to the B-field?
2. What is the partition of acceleration, scattering, and heating between quasi-DC fields and fluctuations?

Various MMS studies have shown how E-field uncertainties obscure the science, or restrict detailed analysis to the largest-amplitude events (Ergun et al., 2016b; Torbert et al., 2016; Øieroset et al., 2016; Gao et al., 2021). Cluster's 2D ecliptic normal attitude allowed the inference of Electron Diffusion Regions (EDR) at the magnetopause, but not direct measurement of parallel vs. perpendicular electrodynamics. Similarly, the THEMIS E-field instrument allowed investigation of Ion Diffusion Region (IDR) scale electrodynamics (perpendicular E-field), but not the 3D electrodynamics of the EDR (Mozer et al., 2005; Mozer et al., 2008).

1.2.3 Auroral acceleration region studies—Parallel potential drops and small-scale perpendicular structures in the upward and downward current regions

1. What is the partition of parallel acceleration into localized and distributed structures (Debye-scale double layers vs. ambipolar fields)?
2. What is the local development and dynamics of small-scale perpendicular structure in parallel potential drops?

The need for particular spacecraft orientation has limited the depth and breadth of studies on the occurrence and properties of the quasi-DC parallel potential drops associated with auroral electron and ion acceleration (Hull et al., 2003a; Hull et al., 2003b; Ergun et al., 2004; Andersson and Ergun, 2006; Chaston et al., 2007). Large parallel E-fields have been measured at higher altitudes on auroral field lines (Mozer et al., 1977) but their extension to lower altitudes is unknown. Theoretical and observational studies (e.g., Chaston and Seki, 2010; Chaston et al., 2011) show that small-scale structures in the perpendicular component of the E-field and the development of a parallel E-field component and significant parallel potential drops are intimately linked, further demonstrating the need for simultaneous highly accurate 3D E-field measurements in the auroral acceleration region.

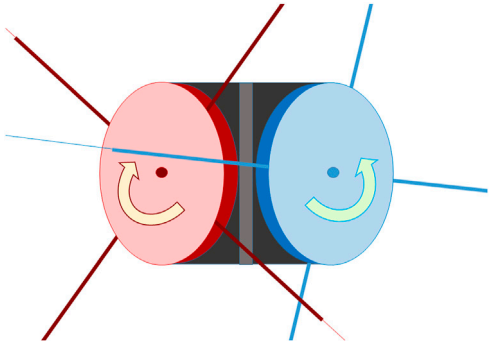

FIGURE 3
An illustration of the Twin Orthogonal Rotating Platforms (TORPs) on a non-rotating central body. The TORPs are oriented at 90° degrees with respect to each other, and they are both equipped with crossed double probes (only partially shown).

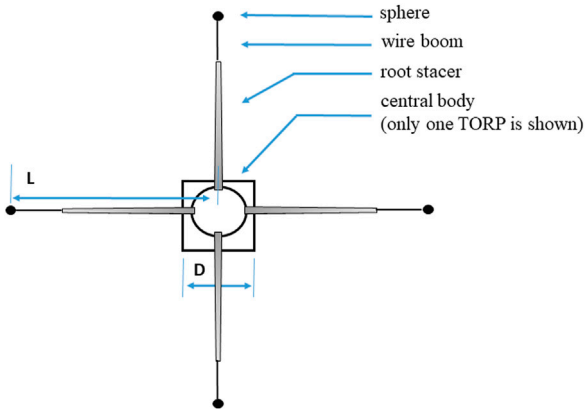

FIGURE 4
Definition of a single boom length, L, and spacecraft diameter, D. The components of each boom (root stacer, wire boom and sphere) are also defined.

2 Solution: Grotifer, the future of electric field instruments

2.1 Proposed design

We propose a new E-field instrument design that addresses the need for highly accurate 3D E-field measurements while enabling lower cost missions and constellation missions in deep space. That is why we aim to develop a new E-field instrument that fits in a 27U ($0.3 \times 0.3 \times 0.3$ m^3) CubeSat to provide accurate 3D E-field measurements in all environments of the heliosphere.

Grotifer (Giant rotifer) is a reference to the rotifer, also known as the "wheel animalcule," which has antenna-like cilia that appear to rotate in all directions. Grotifer's design consists of mounting detectors on two rotating plates, oriented at 90° with respect to each other, on a non-rotating central body. An illustration is provided in Figure 3. Each rotating plate has two component measurements of the E-field such that the Twin Orthogonal Rotating Platforms (TORPs) provide four instantaneous measurements of the E-field. That way, the three components are well-measured by the rotating detectors and redundant E-field measurements in the direction sampled by both TORPs can be used to estimate the time-varying measurement uncertainty. Grotifer's main requirements are described below, together with current design choices.

2.1.1 Minimum boom length

The accuracy of the double probe E-field measurement increases with the boom length because the signal increases and the spacecraft

FIGURE 5
A deployed stacer.

noise decreases with distance. In addition, the spacecraft noise at a fixed distance from the spacecraft increases with spacecraft size. Thus, a reasonable starting point for the characterization of E-field measurement accuracy is the dimensionless ratio between the single boom length, L, and the spacecraft diameter, D, i.e., L/D (see Figure 4 for an illustration of these definitions). Even though E-field measurement accuracy is ultimately determined by a variety of factors, highly accurate E-field measurements are facilitated by the instrument design when L/D is large, as is the case for spin plane wire booms. On the other hand, when the ratio is small, as is the case for axial rigid booms, spacecraft noise likely dominates in most situations of interest. For instance, L/D for the E-field component along the spin axis of Polar is 2.5, while it is 27 in the spin plane (Figure 1). The minimum length requirement for each Grotifer antenna is determined by scaling the L/D of Grotifer to that of other spacecraft that made successful spin plane E-field measurements. We find that a single boom length of $L = 6.75$ m from the center of the TORP to the sphere, compared to Grotifer's 0.3 m diameter, provides antennas that are long enough to favor high-quality E-field measurements.

2.1.2 Boom design and deployment

The booms on the rotating platforms consist of 5 m stacers with spheres connected to wires that extend through the stacers in what is known as a wire boom plus root stacer design. The stacers are cold-formed from spring-grade metal strip material to produce a constant helix angle and free coil diameter. They are then stowed in a canister with no helix. When released the coils progressively stack on an attached tip piece to produce a slight taper. This stacking provides significant inter-coil friction such that this formed tube compares favorably in stiffness and strength to the equivalent (solid) thin wall tube. An important characteristic of the device is the observation that the boom forms one coil at a time, such that a fully formed tubular element emerges from the housing. A picture of a deployed stacer is provided in Figure 5.

Once the stowed stacer is released, it expands to its 5 m length along with the sphere. After the stacer has fully deployed, and the TORP is spun up to its initial spin rate, the wire boom is then played out with a motor another 1.75 m for a total deployed single boom length of 6.75 m. The wire booms are kept short enough that they cannot entangle under any circumstance. The spheres become the E-field sensor, held radially outward by the centrifugal force of the rotating platform.

An antenna system made from a boom plus wire has two important advantages over a boom alone: First, the antenna length is greater than with a boom alone. Second, the extended wire allows separation of the boom, at the spacecraft potential, from the spherical sensor, which greatly decreases its sensitivity to spacecraft noise.

2.1.3 Proposed boom mounting

The mounting of the boom systems on the rotating platforms is illustrated in Figure 6. Each rotating platform has two levels on which the boom systems are mounted, and each level holds two antennas. The stacers are mounted inside the cylinders and their wire spools and spheres are mounted at their ends. The rotating plates are nested at launch and they swing out and latch to make the angle between the plates equal to 90°. In Figure 6, the upper 2/3 of the bus is mostly occupied by the stowed TORPs while the lower third is reserved for bus avionics.

2.1.4 Angular momentum balance

Once the stacers are deployed on the rotors, the rotors are spun up using the motors between each rotor and the spacecraft bus. The torque required to spin up the rotors and maintain their spin rate against friction produces a counter-torque on the spacecraft bus. If uncompensated, the counter-torque would spin up the spacecraft bus to unacceptably large spin rates and complicate operations significantly. In order to counteract that spin up, the Grotifer bus will carry two orthogonal air core torque coils. The spin period for the TORPs is 5 s (12 RPM). The central body attitude control will maintain pointing towards the Sun for the side of the satellite with the primary solar array and with sufficient stability that the boom wires do not oscillate through more than a few degrees. It will also stabilize the platform against torques generated in the control of the rotating booms. The design and control problems for Grotifer are already under study: Mao et al. (2015) developed an initial model of the Grotifer attitude determination and control system; and a NASA Instrument Technology Development award supports the current development and testing of prototype versions of the root-stacer/wire-boom system and the TORP drive and control systems from a start TRL of 3 to an anticipated end TRL of 5. All this past and current work serves to mature our knowledge of the Grotifer design as a direct prelude to a flight test model within the next 5 years.

2.2 Proposed applications

Some of the benefits of the Grotifer development are the following:

1. Grotifer will measure the parallel E-field to an accuracy comparable to that of the perpendicular E-field, enabling a significant increase in science return (see also Section 1.2)
2. Fleets of Grotifers can study electrodynamics at many points, facilitating differentiation between spatial and temporal dynamics.

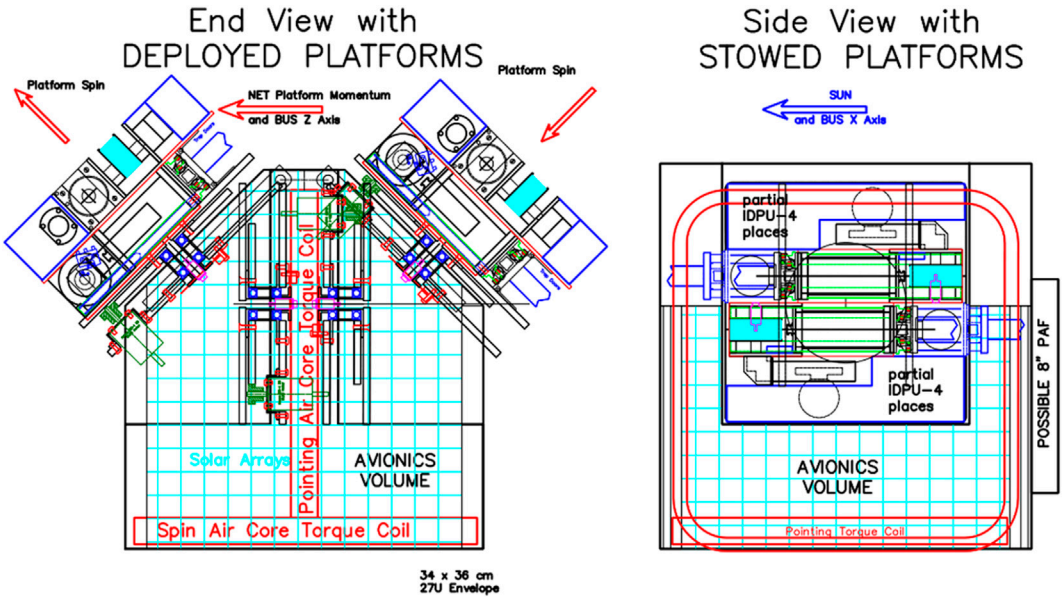

FIGURE 6
27U bus concept.

3. The current-biased, spherical, double probe E-field measurement is proven to work at reconnection sites, in the auroral acceleration region, at shocks, in the solar wind (see Section 1.2 and references therein) and at low L-values in the magnetosphere (e.g., Lejosne et al., 2022). Thus, Grotifer can become an important component of future space missions throughout the heliosphere.
4. TORPs easily allows accommodation of spinning and despun-preferring instrumentation on the same spacecraft (e.g., remote sensing limb/nadir/zenith looking imagers and charged particle detectors).
5. TORPs may also host plasma detectors so as to cover the full phase space more completely and continuously than on current spinning spacecraft. This would lead to more complete correlation studies of the fields and plasmas.

Data availability statement

The original contributions presented in the study are included in the article, further inquiries can be directed to the corresponding author.

Author contributions

We describe contributions to the paper using the CRediT (Contributor Roles Taxonomy) categories (Brand et al., 2015): Conceptualization: FM, DP, DA, and JB. Funding acquisition: all authors. Project administration: SL. Visualization: FM, DP, JB, and SL. Writing—original draft: SL, FM, JB, and DP. Writing—review and edition: all authors.

Funding

The work on Grotifer is supported by the NASA Heliophysics Technology and Instrument Development for Science program *via* award 80NSSC22K0640.

Conflict of interest

The authors declare that the research was conducted in the absence of any commercial or financial relationships that could be construed as a potential conflict of interest.

Publisher's note

All claims expressed in this article are solely those of the authors and do not necessarily represent those of their affiliated organizations, or those of the publisher, the editors, and the reviewers. Any product that may be evaluated in this article, or claim that may be made by its manufacturer, is not guaranteed or endorsed by the publisher.

References

Akbari, H., Andersson, L., Peterson, W. K., Espley, J., Benna, M., and Ergun, R. (2019). Ambipolar electric field in the martian ionosphere: MAVEN measurements. *JGR space Phys.* 124, 4518–4524. doi:10.1029/2018JA026325

Andersson, L. (2002). Characteristics of parallel electric fields in the downward current region of the aurora. *Phys. Plasmas* 9, 3600. doi:10.1063/1.1490134

Andersson, L., and Ergun, R. E. (2006). Acceleration of antiearthward electron fluxes in the auroral region. *J. Geophys. Res.* 111, A07203. doi:10.1029/2005JA011261

Argall, M. R., Torbertt, R. B., LeContel, O., Russell, C. T., Magnes, W., Strangeway, R. J., et al. (2015). *Parallel electric fields and wave phenomena associated with magnetic reconnection*. San Francisco: AGU. Fall meeting, SM51A-2548.

Arnold, H., Drake, J. F., Swisdak, M., and Dahlin, J. (2019). Large-scale parallel electric fields and return currents in a global simulation model. *Phys. Plasmas* 26, 102903. doi:10.1063/1.5120373

Bale, S. D., and Mozer, F. S. (2007). Measurement of large parallel and perpendicular electric fields on electron spatial scales in the terrestrial bow shock. *Phys. Rev. Lett.* 98, 205001. doi:10.1103/PhysRevLett.98.205001

Bian, N. H., Kontar, E. P., and Brown, J. C. (2010). Parallel electric field generation by Alfvén wave turbulence. *A&A* 519, A114. doi:10.1051/0004-6361/201014048

Bonnell, J. W., Mozer, F. S., Delory, G. T., Hull, A. J., Ergun, R. E., Cully, C. M., et al. (2009). "The electric field instrument (EFI) for THEMIS," in *The THEMIS mission*. Editors J. L. Burch and V. Angelopoulos (New York, NY: Springer). doi:10.1007/978-0-387-89820-9_14

Brand, A., Allen, L., Altman, M., Hlava, M., and Scott, J. (2015). Beyond authorship: Attribution, contribution, collaboration, and credit. *Learn. Pub.* 28, 151–155. doi:10.1087/20150211

Chaston, C. C. (2021). An auroral Alfvén wave cascade. *Front. Astron. Space Sci.* 8, 618429. doi:10.3389/fspas.2021.618429

Chaston, C. C., Hull, A. J., Bonnell, J. W., Carlson, C. W., Ergun, R. E., Strangeway, R. J., et al. (2007). Large parallel electric fields, currents, and density cavities in dispersive Alfvén waves above the aurora. *J. Geophys. Res.* 112, A05215. doi:10.1029/2006JA012007

Chaston, C. C., Seki, K., Sakanoi, T., Asamura, K., Hirahara, M., and Carlson, C. W. (2011). Cross-scale coupling in the auroral acceleration region. *Geophys. Res. Lett.* 38, L20101. doi:10.1029/2011GL049185

Chaston, C. C., and Seki, K. (2010). Small-scale auroral current sheet structuring. *J. Geophys. Res.* 115, A11221. doi:10.1029/2010JA015536

Cohen, I. J., Schwartz, S. J., Goodrich, K. A., Ahmadi, N., Ergun, R. E., Fuselier, S. A., et al. (2019). High-resolution measurements of the cross-shock potential, ion reflection, and electron heating at an interplanetary shock by MMS. *J. Geophys. Res. Space Phys.* 124, 3961–3978. doi:10.1029/2018JA026197

Damiano, P. A., Kim, E.-H., Johnson, J. R., and Porazik, P. (2019). Electron energization by parallel electric fields in poloidal standing waves. *J. Geophys. Res. Space Phys.* 124, 6691–6700. doi:10.1029/2019JA026849

Dubinin, E., Chanteur, G., Fraenz, M., and Woch, J. (2008). Field-aligned currents and parallel electric field potential drops at Mars scaling from the Earth's aurora. *Planet. Space Sci.* 56 (6), 868–872. doi:10.1016/j.pss.2007.01.019

Egedal, J., Daughton, W., and Le, A. (2012). Large-scale electron acceleration by parallel electric fields during magnetic reconnection. *Nat. Phys.* 8, 321–324. doi:10.1038/nphys2249

Ergun, R., Carlson, C., Mozer, F., Delory, G. T., Temerin, M., McFadden, J. P., et al. (2001). The FAST satellite fields instrument. *Space Sci. Rev.* 98, 67–91. doi:10.1023/A:1013131708323

Ergun, R. E., Goodrich, K., Wilder, R., Holmes, J., Stawarz, J. E., Eriksson, S., et al. (2016b). Magnetospheric multiscale satellites observations of parallel electric fields associated with magnetic reconnection. *Phys. Rev. Lett.* 116 (23), 235102. doi:10.1103/PhysRevLett.116.235102

Ergun, R. E., Andersson, L., Su, Y -J., Newman, D. L., Goldman, M. V., Lotko, W., et al. (2005). Localized parallel electric fields associated with inertial Alfven waves. *Phys. Plasmas* 12, 072901. doi:10.1063/1.1924495

Ergun, R. E., Andersson, L., Main, D., Su, Y.-J., Newman, D. L., Goldman, M. V., et al. (2004). Auroral particle acceleration by strong double layers: The upward current region. *J. Geophys. Res.* 109, A12220. doi:10.1029/2004JA010545

Ergun, R. E., Ray, L., Delamere, P. A., Bagenal, F., Dols, V., and Su, Y.-J. (2009). Generation of parallel electric fields in the Jupiter–Io torus wake region. *J. Geophys. Res.* 114, A05201. doi:10.1029/2008JA013968

Ergun, R. E., Su, Y.-J., Andersson, L., Carlson, C. W., McFadden, J. P., Mozer, F. S., et al. (2001). Direct observation of localized parallel electric fields in a space plasma. *Phys. Rev. Lett.* 87, 045003. doi:10.1103/PhysRevLett.87.045003

Ergun, R. E., Tucker, S., Westfall, J., Goodrich, K. A., Malaspina, D. M., Summers, D., et al. (2016a). The axial double probe and fields signal processing for the MMS mission. *Space Sci. Rev.* 199, 167–188. doi:10.1007/s11214-014-0115-x

Fox, W., Wilder, F. D., Eriksson, S., Jara-Almonte, J., Pucci, F., Yoo, J., et al. (2018). Energy conversion by parallel electric fields during guide field reconnection in scaled laboratory and space experiments. *Geophys. Res. Lett.* 45, 677–684. doi:10.1029/2018GL079883

Gao, C.-H., Tang, B.-B., Li, W. Y., Wang, C., Khotyaintsev, Y. V., Graham, D. B., et al. (2021). Effect of the electric field on the agyrotropic electron distributions. *Geophys. Res. Lett.* 48. e2020GL091437. doi:10.1029/2020GL091437

Goodrich, C. C., and Scudder, J. D. (1984). The adiabatic energy change of plasma electrons and the frame dependence of the cross-shock potential at collisionless magnetosonic shock waves. *J. Geophys. Res.* 89 (A8), 6654–6662. doi:10.1029/JA089iA08p06654

Goodrich, K. A., Ergun, R., Schwartz, S. J., Wilson, L. B., III., Newman, D., Wilder, F. D., et al. (2018). MMS observations of electrostatic waves in an oblique shock crossing. *J. Geophys. Res. Space Phys.* 123, 9430–9442. doi:10.1029/2018JA025830

Gorney, D. J., Chiu, Y. T., and Croley, D. R. (1985). *Trapping of ion conics by downward parallel electric fields*. Los Angeles: Aerospace Corporation Report ADA155306. https://apps.dtic.mil/sti/pdfs/ADA155306.pdf.

Gustafsson, G., André, M., Carozzi, T., Eriksson, A. I., Fälthammar, C.-G., Grard, R., et al. (2001). First results of electric field and density observations by Cluster EFW based on initial months of operation. *Ann. Geophys.* 19, 1219–1240. doi:10.5194/angeo-19-1219-2001

Gustafsson, G., BostrÖM, R., Holback, B., Holmgren, G., Lundgren, A., Stasiewicz, K., et al. (1997). The electric field and wave experiment for the Cluster mission. *Space Sci. Rev.* 79, 137–156. doi:10.1023/A:1004975108657

Halekas, J., Poppe, A., Delory, G., Farrell, W. M., and Horányi, M. (2012). Solar wind electron interaction with the dayside lunar surface and crustal magnetic fields: Evidence for precursor effects. *Earth Planet Sp.* 64, 3. doi:10.5047/eps.2011.03.008

Hanson, E. L. M., Agapitov, O. V., Mozer, F. S., Krasnoselskikh, V., Bale, S. D., Avanov, L., et al. (2019). Cross-shock potential in rippled versus planar quasi-perpendicular shocks observed by MMS. *Geophys. Res. Lett.* 46, 2381–2389. doi:10.1029/2018GL080240

Harvey, P., Mozer, F. S., Pankow, D., Wygant, J., Maynard, N. C., Singer, H., et al. (1995). The electric field instrument on the polar satellite. *Space Sci. Rev.* 71, 583–596. doi:10.1007/BF00751342

Hesse, M., Forbes, T. G., and Birn, J. (2005). On the relation between reconnected magnetic flux and parallel electric fields in the solar corona. *Astrophysical J.* 631, 1227. doi:10.1086/432677

Hull, A. J., Bonnell, J. W., Mozer, F. S., and Scudder, J. D. (2003b). A statistical study of large-amplitude parallel electric fields in the upward current region of the auroral acceleration region. *J. Geophys. Res.* 108 (A1), 1007. doi:10.1029/2001JA007540

Hull, A. J., Bonnell, J. W., Mozer, F. S., Scudder, J. D., and Chaston, C. C. (2003a). Large parallel electric fields in the upward current region of the aurora: Evidence for ambipolar effects. *J. Geophys. Res.* 108, 1265. doi:10.1029/2002JA009682

Hultqvist, B., and Lundin, R. (1987). Parallel electric fields accelerating electrons and ions in the same direction. *Atmos. Space Sci.* 144, 149–154.

Knight, S. (1973). Parallel electric fields. *Planet. Space Sci.* 21 (5), 741–750. doi:10.1016/0032-0633(73)90093-7

Koskinen, H. E. J., Toivanen, P. K., and Pulkkinen, T. I. (1996). "Parallel electric fields during the substorm growth phase," in Proc. Third International Conference on Substorms (ICS-3), Versailles, France. May 12–17, 1996, ESA SP-389 (October 1996).

Kropotkin, A. P. (2018). Parallel electric field and electron acceleration: An advanced model. *Geomagnetism Aeronomy* 58, 16–27. doi:10.1134/s0016793218010103

Lejosne, S., Bonnell, J. W., Wygant, J. R., and Mozer, F. S. (2022). Maximizing the accuracy of double probe electric field measurements near perigee: The case of the Van Allen Probes instruments. *J. Geophys. Res. Space Phys.* 127. e2021JA030099. doi:10.1029/2021JA030099

Lindqvist, P. A., Olsson, G., Torbert, R. B., King, B., Granoff, M., Rau, D., et al. (2016). The spin-plane double probe electric field instrument for MMS. *Space Sci. Rev.* 199, 137–165. doi:10.1007/s11214-014-0116-9

Mao, Y. T., Auslander, D., Pankow, D., Vega, K., Mozer, F. S., and Turin, P. (2015). "Modeling and control design for a new spacecraft concept for measuring particles and fields with unprecedented resolution and accuracy," in AIAA 2015-1588, Kissimmee, FL: Session: Modeling of Vehicle Dynamics II. doi:10.2514/6.2015-1588

Mozer, F. S., Agapitov, O. V., Artemyev, A., Drake, J. F., Krasnoselskikh, V., Lejosne, S., et al. (2015). Time domain structures: What and where they are, what they do, and how they are made. *Geophys. Res. Lett.* 42, 3627–3638. doi:10.1002/2015GL063946

Mozer, F. S., Angelopoulos, V., Bonnell, J., Glassmeier, K. H., and McFadden, J. P. (2008). THEMIS observations of modified Hall fields in asymmetric magnetic field reconnection. *Geophys. Res. Lett.* 35, L17S04. doi:10.1029/2007GL033033

Mozer, F. S., Bale, S. D., McFadden, J. P., and Torbert, R. B. (2005). New features of electron diffusion regions observed at subsolar magnetic field reconnection sites. *Geophys. Res. Lett.* 32, L24102. doi:10.1029/2005GL024092

Mozer, F. S., and Bruston, P. (1967). Electric field measurements in the auroral ionosphere. *J. Geophys. Res.* 72, 1109–1114. doi:10.1029/JZ072i003p01109

Mozer, F. S., Carlson, C. W., Hudson, M. K., Torbert, R. B., Parady, B., Yatteau, J., et al. (1977). Observations of paired electrostatic shocks in the polar magnetosphere. *Phys. Rev. Lett.* 38 (6), 292–295. doi:10.1103/physrevlett.38.292

Mozer, F. S., and Chen, C. H. K. (2013). Parallel electric field spectrum of solar wind turbulence. *Astrophysical J.* 768 (1), L10, 5 pp. doi:10.1088/2041-8205/768/1/l10

Mozer, F. S. (2016). DC and low-frequency double probe electric field measurements in space. *J. Geophys. Res. Space Phys.* 121, 10942–10953. doi:10.1002/2016JA022952

Mozer, F. S., and Fahleson, U. V. (1970). Parallel and perpendicular electric fields in an aurora. *Planet. Space Sci.* 18 (11), 1563–1571. doi:10.1016/0032-0633(70)90031-0

Mozer, F. S., and Sundkvist, D. (2013). Electron demagnetization and heating in quasi-perpendicular shocks. *J. Geophys. Res. Space Phys.* 118, 5415–5420. doi:10.1002/jgra.50534

Mozer, F. S., and Sundkvist, D. (2014). Reply to comment by S. Schwartz on "Electron demagnetization and heating in quasi-perpendicular shocks". *J. Geophys. Res. Space Phys.* 119, 1513. doi:10.1002/2013JA019694

Mozer, F. S., Torbert, R. B., Fahleson, U. V., Falthammar, C. G., Gonfalone, A., and Pedersen, A. (1978). Measurements of quasi-static and low-frequency electric fields with spherical double probes on the ISEE-1 spacecraft. *IEEE Trans. Geoscience Electron.* 16 (3), 258–261. doi:10.1109/TGE.1978.294558

Øieroset, M., Phan, T. D., Haggerty, C., Shay, M. A., Eastwood, J. P., Gershman, D. J., et al. (2016). MMS observations of large guide field symmetric reconnection between colliding reconnection jets at the center of a magnetic flux rope at the magnetopause. *Geophys. Res. Lett.* 43, 5536–5544. doi:10.1002/2016GL069166

Phan, T. D., Eastwood, J. P., Shay, M. A., Drake, J. F., Sonnerup, B. U. Ö., Fujimoto, M., et al. (2018). Publisher Correction: Electron magnetic reconnection without ion coupling in Earth's turbulent magnetosheath. *Nature* 569, E9. doi:10.1038/s41586-018-0091-5

Rankin, R., Samsona, J. C., and Tikhonchuk, V. T. (1999). Parallel electric fields in dispersive shear Alfven waves in the dipolar magnetosphere. *Geophys. Res. Lett.* 26 (24), 3601–3604. doi:10.1029/1999gl010715

Schwartz, S. J. (2014). Comment on "Electron demagnetization and heating in quasi-perpendicular shocks" by Mozer and Sundkvist. *J. Geophys. Res. Space Phys.* 119, 1507–1512. doi:10.1002/2013JA019624

Schwartz, S. J., Ergun, R. E., Harald, K., Wilson, L. B., Chen, L.-J., Goodrich, K. A., et al. (2021). Evaluating the de Hoffmann-Teller cross-shock potential at real collisionless shocks. *Earth Space Sci. Open Archive* 126. doi:10.1002/essoar.10506367.2

Stark, C. R., Cran-McGreehin, A. P., and Wright, A. N., 2011, Contributions to the magnetospheric parallel electric field, *J. Geophys. Res. Space Phys.* 116 A07216. doi:10.1029/2010JA016270

Torbert, R. B., Burch, J. L., Giles, B. L., Gershman, D., Pollock, C. J., Dorelli, J., et al. (2016). Estimates of terms in Ohm's law during an encounter with an electron diffusion region. *Geophys. Res. Lett.* 43, 5918–5925. doi:10.1002/2016GL069553

Underwood, E. (2017). Can large electric fields power Jupiter's X-ray auroras? *Eos* 98. doi:10.1029/2017EO084241

Vedin, J., and Ronnmark, K. (2007). Parallel electric fields: Variations in space and time on auroral field lines. *J. Plasma Phys.* 74, 53–64. doi:10.1017/S0022377807006538

Wilder, F. D., Ergun, R. E., Burch, J. L., Ahmadi, N., Eriksson, S., Phan, T. D., et al. (2018). The role of the parallel electric field in electron-scale dissipation at reconnecting currents in the magnetosheath. *J. Geophys. Res. Space Phys.* 123, 6533–6547. doi:10.1029/2018JA025529

Williams, J. D., MacDonald, E., McCarthy, M., Peticolas, L., and Parks, G. K. (2006). Parallel electric fields inferred during a pulsating aurora. *Ann. Geophys.* 24, 1829–1837. doi:10.5194/angeo-24-1829-2006

Wygant, J. R., Bonnell, J. W., Goetz, K., Ergun, R. E., Mozer, F. S., Bale, S. D., et al. (2013). The electric field and waves instruments on the radiation belt storm probes mission. *Space Sci. Rev.* 179, 183–220. doi:10.1007/s11214-013-0013-7

Wygant, J. R., Harvey, P. R., Pankow, D., Mozer, F. S., Maynard, N., Singer, H., et al. (1992). CRRES electric field/Langmuir probe instrument. *J. Spacecr. Rockets* 29 (4), 601–604. doi:10.2514/3.25507

Frontiers in
Astronomy and Space Sciences

Explores planetary science and extragalactic astronomy in all wavelengths

Advances the understanding of our universe - from planetary science to extragalactic astronomy, to high-energy and astroparticle physics.

Discover the latest Research Topics

See more →

Frontiers

Avenue du Tribunal-Fédéral 34
1005 Lausanne, Switzerland
frontiersin.org

Contact us

+41 (0)21 510 17 00
frontiersin.org/about/contact